Revisiting heterodyne mid-infrared interferometry for the imaging of protoplanetary environments

Guillaume Bourdarot

▶ **To cite this version:**

Guillaume Bourdarot. Revisiting heterodyne mid-infrared interferometry for the imaging of protoplanetary environments. Astrophysics [astro-ph]. Université Grenoble Alpes [2020-..], 2021. English. NNT : 2021GRALY052 . tel-03555838

HAL Id: tel-03555838

https://theses.hal.science/tel-03555838

Submitted on 3 Feb 2022

HAL is a multi-disciplinary open access archive for the deposit and dissemination of scientific research documents, whether they are published or not. The documents may come from teaching and research institutions in France or abroad, or from public or private research centers.

L'archive ouverte pluridisciplinaire **HAL**, est destinée au dépôt et à la diffusion de documents scientifiques de niveau recherche, publiés ou non, émanant des établissements d'enseignement et de recherche français ou étrangers, des laboratoires publics ou privés.

Université Grenoble Alpes

THÈSE

Pour obtenir le grade de

DOCTEUR DE L'UNIVERSITÉ GRENOBLE ALPES

Spécialité : Astrophysique et Milieux Dilués

Arrêté ministériel : 25 mai 2016

Présentée par

Guillaume BOURDAROT

Thèse dirigée par **Hugues GUILLET DE CHATELLUS**, Université Grenoble Alpes
et codirigée par **Jean-Philippe BERGER,** Université Grenoble Alpes
préparée au sein du **Laboratoire Interdisciplinaire de Physique**
dans **l'École Doctorale de Physique**

Interférométrie hétérodyne moyen-infrarouge pour l'imagerie des environnements protoplanétaires

Revisiting heterodyne mid-infrared interferometry for the imaging of protoplanetary environments

Thèse soutenue publiquement le **29 Septembre 2021**, devant le jury composé de :

Monsieur Jean-Louis MONIN
PROFESSEUR DES UNIVERSITÉS, Université Grenoble Alpes, Examinateur, Président du Jury

Monsieur Rafael MILLAN-GABET
INGENIEUR DE RECHERCHE, Giant Magellan Telescope corporation, Rapporteur

Monsieur Mehdi ALOUINI
PROFESSEUR DES UNIVERSITÉS, Université de Rennes, Rapporteur

Monsieur Carlo SIRTORI
PROFESSEUR DES UNIVERSITÉS, École Normale Supérieure, Examinateur

Monsieur Vincent PIÉTU
ASTRONOME-ADJOINT, Institut de Radio-Astronomie Millimétrique, Examinateur

Revisiting heterodyne mid-infrared interferometry for the imaging of protoplanetary environments

---

Guillaume Bourdarot

Supervisors :
Hugues Guillet de Chatellus
Jean-Philippe Berger

December 12, 2021
Version: v2.0

À ma famille,

In the meantime, every today, with only tentative understanding and in the face of uncertainty and change, how can we live gloriously and act decisively ? [...] How well we can commit our lives to ideas which we recognize in principle as only tentative represents a real test of mind and emotions.

— Charles H. Townes
THINK, IBM Magazine

"S'i' era sol di me quel che creasti
novellamente, amor che 'l ciel governi,
tu 'l sai, che col tuo lume mi levasti.

Quando la rota che tu sempiterni
desiderato, a sé mi fece atteso
con l'armonia che temperi e discerni,

Parvemi tanto allor del cielo acceso
de la fiamma del sol, che pioggia o fiume
lago non fece alcun tanto disteso.

La novità del suono e 'l grande lume
di lor cagion m'accesero un disio
mai non sentito di cotanto acume."

— Dante Alighieri
La Divina Commedia (Paradiso, Canto I, 73-84)

Abstract

This thesis work focuses on the study of young stars and their protoplanetary disks at the astronomical unit scale with infrared interferometry. It includes both observational and instrumental aspects. In the observational part, we focus on the accretion outburst occurring in the formation of young stars through a temporal monitoring of the star FU Orionis with 20 years of near-infrared interferometric data, in order to put constraints on the instability mechanisms at play in its accretion disk. Although infrared interferometry is a powerful technique to constrain the structure of the inner region of young objects, its capability to perform complete image reconstruction of protoplanetary disks is still limited. In the instrumental part of this work, we explore the extension of infrared interferometers to the recombination of a large number of telescopes and kilometric baselines in the mid-infrared, such as proposed in the framework of the Planet Formation Imager (PFI) initiative. In this perspective, infrared heterodyne interferometry represents a potential interesting technology, despite its sensitivity limits. In this work, we propose the revisit the architecture of an infrared heterodyne interferometric system at the light of the recent progresses in the field of mid-infrared technologies. On a theoretical level, we analyze the sensitivity performances of an interferometer integrating these recent progresses, and clarify the fundamental limitations in sensitivity due to the intrinsic quantum noise of this technique. Among the different technological challenges of heterodyne interferometry, we propose to address the problem of bandwidth limitation and of correlation of a large number of wideband radiofrequency (RF) signals by introducing the use of analog photonic correlation. We first describe the principles and the experimental demonstration of a simple, double-sideband analog correlator. We then present the extension of this concept to a wideband multi-delay correlator for RF signal processing based on a bidirectional fiber frequency shifting loop. In a last part, we present the preliminary implementation of a laboratory demonstrator at $10\,\mu\mathrm{m}$ dedicated to the validation of the complete detection and correlation chain devised in this thesis. Finally, based on the scalability of this technique, we describe the concept of a technological pathfinder combining the 8 telescopes of the Very Large Telescopes Interferometer (VLTI) at $10\,\mu\mathrm{m}$. We discuss its potential application to the imaging of bright young stars and its implications in the perspective of a Planet Formation Imager.

Résumé

Ce travail de thèse porte sur l'étude des étoiles jeunes et de leur disque protoplanétaire à l'échelle de l'unité astronomique par interférométrie infrarouge. Il inclut à la fois des aspects observationnels et instrumentaux. Dans la partie observationnelle, nous nous concentrons sur les sursauts d'accrétion intervenant dans la formation des étoiles jeunes, à travers l'analyse de 20 ans de données d'observations interferométriques de l'étoile FU Orionis, afin d'apporter des contraintes sur le mécanisme d'instabilité à l'oeuvre dans son disque d'accrétion. Bien que l'interferométrie soit une technique puissante pour contraindre les parties internes des objets jeunes, sa capacité de reconstruction d'images de disques protoplanétaires est encore limitée. Dans la partie instrumentale de ce travail, nous explorons la capacité d'étendre la technique d'interférométrie infrarouge à un grand nombre de télescopes et des lignes de bases kilométriques dans le moyen-infrarouge, comme proposé dans le cadre de l'initiative internationale "Planet Formation Imager" (PFI). Dans cette perspective, la technique d'interferométrie hétérodyne présente un potentiel intéressant, malgré ses limites de sensibilité intrinsèque. Dans ce travail, nous proposons de revoir l'architecture d'un système interferométrique hétérodyne à la lumière des récents progrès dans le domaine des technologies moyen-infarouge. D'un point de vue théorique, nous analysons les performances en sensibilité attendues d'un système intégrant ces progrès techniques récents, et proposons de clarifier les limites de sensibilité fondamentales de cette technique dues au bruit quantique inhérent à ce schéma de détection. Parmi les différents défis technologiques de l'interferométrie hétérodyne, nous proposons d'aborder le problème de la limitation en bande-passante et de corrélation d'un grand nombre de signaux radio-fréquences (RF) à large bande passante, en introduisant l'utilisation d'un schéma de corrélation analogique photonique. Nous commencons par décrire le fonctionnement et l'implémentation d'un corrélateur analogique (double-sideband) simple. Nous présentons ensuite l'extension de ce concept à un corrélateur multi-délai de signaux RFs à grande bande passante, reposant sur une architecture de boucle à décalage de fréquence bi-directionnelle. Dans une dernière partie, nous présentons l'implémentation d'un démonstrateur de laboratoire à $10\,\mu\mathrm{m}$ dédié à la validation de la chaîne complète de détection et de corrélation proposée dans cette thèse. Pour finir, nous décrivons le concept d'un instrument pouvant combiner les 8 télescopes de l'interferomètre du Very Large Telescope (VLTI) à $10\,\mu\mathrm{m}$. Nous discutons l'application potentielle de ce concept à l'imagerie d'étoiles jeunes brillantes, et les implications de ce concept dans la perspective d'un grand interferomètre destiné à l'imagerie de la formation planétaire tel que le Planet Formation Imager.

Remerciements

Il y a différentes façons de commencer une thèse, mais généralement une manière de la terminer : en écrivant les remerciements qui concluent ces trois années d'aventure. Les personnes présentes tout au long du chemin constituent le vrai coeur de ce travail.

Je remercie tout d'abord mes directeurs de thèse, Hugues Guillet de Chatellus et Jean-Philippe Berger. Pouvoir faire une thèse en astrophysique était un rêve en soi : il l'était encore plus avec des encadrants alliant à la fois les qualités scientifiques et humaines qui sont les vôtres. Je remercie Hugues pour avoir accepté de diriger cette thèse et de s'aventurer sur des sentiers inexplorés : le temps passé au laboratoire ensemble, tes connaissances et ta gentillesse infinis ont été des moments marquants et extrêmement formateurs dans cette thèse. Je remercie Jean-Philippe, pour son modèle de vision scientifique, qui a structuré cette thèse, et son attention constante, malgré un emploi du temps chargé. Les discussions et les réflexions permanentes ensemble, à l'IPAG, sur le trajet d'un observatoire ou dans les rues de Santiago sont et resteront des souvenirs précieux et inspirants, au-delà même de la thèse. À tous les deux, encore une fois : merci.
Je remercie également Etienne Le Coarer, sans qui cette thèse n'aurait pas non plus été possible. Un immense merci, pour avoir donné sa chance à un étudiant pas sûr de lui, pour m'avoir initié au travail de physicien, et pour ta passion qui déplacerait les montagnes. Surtout, merci pour les discussions constantes durant ces années, faisant s'élever toujours un peu plus.
Je remercie les membres du jury pour avoir consacré le temps et l'énergie à l'examen de ce travail, aux rapporteurs Rafael Millan-Gabet et Mehdi Alouini pour leur travail de relecture attentive du manuscrit, aux examinateurs, Carlo Sirtori et Vincent Piétu, pour leurs échanges lors la soutenance, et à Jean-Louis Monin, pour avoir accepté d'être président du jury et mené cette soutenance dans une ambiance particulièrement chaleureuse.

Je remercie les laboratoires de l'IPAG et le Liphy pour m'avoir accueilli dans leurs murs. Un remerciement spécial aux nombreuse personnes de l'IPAG avec qui j'ai eu la chance de travailler, de me former, de discuter et de rire, et tout particulièrement à la (nouvellement nommée) équipe instrumentale CHARM. Ces années à l'IPAG garderont une place toute particulière dans mon parcours. Je remercie en particulier Laurent Jocou ("Chef"), pour son modèle de professionnalisme et son énergie, Patrick Rabou ("Maître") pour m'avoir enseigné les fondamentaux du métier d'opticien, Guillermo pour sa générosité et pour m'avoir initié à l'enseignement, David pour ses conseils et ses idées toujours extrêmement fécondes, Mathieu et l'ensemble du CSUG pour les explorations au dessus de l'atmosphère, Karine pour les observations ensemble, Jean-Baptiste pour les brainstormings interferométriques, Jean-Jacques pour son aide en mécanique, Alexis, Titi & Alain, Yves, François, Eric... Un remerciement à Marie-Hélène pour nous éviter d'être trop sérieux et à Fabienne, Séverine, Aline et l'ensemble des services administratifs et techniques. Un très grand merci aux instrumentalistes, et en particulier, Silvère, Sandra, Mélanie et Hélène, ainsi qu'à tous les thésards pour ces trois années ensemble, en particulier mes co-bureaux Alois et Jonatan. Un

merci et beaucoup d'encouragements à Myriam & Martin, ainsi qu'à Tituan pour donner une nouvelle direction à ce travail. Un grand merci également à Azzurra (et Carlo) pour nos (trop) courts échanges, dans les circonstances que réglait l'actualité.
I would also like to thank Frank Eisenhauer, Linda Tacconi and Pr. Reinhard Genzel, for giving me the opportunity to continue this journey in infrared interferometry among their team at the Max Planck for Extraterrestrial physics.
Je remercie les enseignants tout au long de mon parcours, pour avoir su me transmettre le goût pour leur matière. Un remerciement tout particulier à mes professeurs de l'Institut d'Optique et aux encadrants de la filière "apprenti" pour avoir mis en place un mode de formation unique dans l'enseignement supérieur. En fin de thèse, un remerciement très respectueux aux Pr. Philippe Grangier et Pr. Alain Aspect pour leur contribution.
Je tiens à remercier les étudiants et les stagiaires avec qui j'ai eu la chance de travailler, ainsi que les personnes que j'ai eu la chance de rencontrer à l'occasion d'une conférence ou d'une nuit d'observation, et qui par leur regard apportent un sens tout particulier à ce métier. Je tiens à remercier les nombreux bénévoles qui ne comptent pas leur temps pour organiser ces évènements et qui font réellement vivre notre passion commune.

Merci évidemment à mes amis de longue date, pour un soutien qui dépasse le simple déroulement de cette thèse. Chronologiquement, merci à Adrien et Nicolas (grâce à qui en partie je me suis intéressé à l'astronomie !). Un merci à Noé, Florence et Thomas, sans qui je ne serai pas le même, malgré la distance. Un merci évident à Airbrain™ : Pierre-Alexis, Grégoire et Alexandre, pour de sacrés moments et beaucoup de soutien pendant cette thèse. Un merci aux amis Grenoblois, tout particulièrement Martin pour ses conversations rares mais lumineuses, Hadri pour un séjour de confinement (et ses couscous !), et aux anciens – Johary et Rémi ! Merci à quelques insomnies tenaces et leurs ombres. Merci à tous mes autres amis, du lycée, de master, et d'ailleurs, que je remercie collectivement.
Enfin, merci à ma famille, à qui je dois tout. À ceux qui ne sont plus là, mais dont la lumière est toujours : Grand-Père pour tout, Grand-Mère, Papi, Mamie, José, Josiane. À ma tante et ma cousine, Odile et Mathilde, pour leur sensibilité et leur force, et pour être là dans les moments difficiles. À mes tantes et mes oncles, Jojo, François, Pierre, Gilles & Geneviève, et mes cousines Caroline et Véronique. Merci également à Olivier et Grégoire pour leur présence nouvelle.
Pour finir, comment dire merci aux personnes qui me sont les plus proches et qui ont toujours été là. À mes grandes soeurs Gaëlle & Valérie : merci pour m'avoir toujours guidé, merci pour s'être construits et avoir grandi ensemble, et pour rester soudés. Enfin, merci à mes parents, Eric & Marie-Thérèse, sans qui rien de ce travail ne serait, pour avoir toujours accordé une très grande place et un grand souci à notre éducation, mais aussi, d'un livre au sommet d'une montagne, à toujours faire en sorte que nous soyons des personnes accomplies et vraies. En somme, pour nous avoir élevé avec l'amour de connaître, et avec amour simplement.

Munich, le 12 Décembre 2021

Contents

Abstract ix

Remerciements xiii

List of acronyms xxi

I Protoplanetary disks through infrared interferometry 3

1 Protoplanetary disks and the environment of young stars (Introduction Pt. I) 6
1.1 Formation of young low mass stars . . . 6
1.2 Protoplanetary disks . . . 7
1.2.1 Accretion & angular momentum transport . . . 7
Steady accretion disk . . . 7
Wind . . . 10
Layered disk model . . . 11
The problem of accretion in T Tauri stars . . . 11
1.2.2 Planet formation . . . 12
Planet formation scenarii . . . 13
Migration . . . 14
1.2.3 Imaging the astronomical unit-scale (AU) and sub-AU scale of protoplanetary disks . . . 16
1.3 The inner AUs of protoplanetary disks . . . 16
1.3.1 The large scale picture of protoplanetary disks studies . . . 16
1.3.2 The inner AU of protoplanetary disks with infrared interferometry . . . 17
1.4 The image of protoplanetary disks with sub-AU resolution : science case of the Planet Formation Imager . . . 18

2 Infrared Interferometry (Introduction Pt. II) 22
2.1 Instrument science requirements for a Planet Formation Imager (PFI) . . . 22
2.2 Interferometry and coherence . . . 22
2.2.1 Image formation as an interferometric process . . . 23
2.2.2 Zernike van-Cittert theorem . . . 24
2.2.3 Interferometric observables . . . 25
2.2.4 Temporal coherence & delay compensation . . . 25
2.3 Introduction to infrared interferometry . . . 26
2.3.1 Amplitude interferometry . . . 28
Atmosphere & fringe tracking . . . 29

Monomode interferometry and field of view . . . 30
The Very Large Telescope Interferometer (VLTI) infrastructure . . . 31
2.3.2 Heterodyne interferometry . . . 31
Heterodyne detection . . . 31
Heterodyne interferometry . . . 32
2.3.3 Implementation of infrared heterodyne interferometer . . . 33
The Infrared Spatial Interferometer (ISI) . . . 34
2.4 Heterodyne interferometry : correlation and interferometric signal . . . 35
Delay and sky rotation . . . 41
Atmospheric phase fluctuations . . . 41
2.5 Conclusion . . . 42

3 Temporal monitoring of FU Orionis with 20 years of near-infrared interferometry data 44
3.1 Introduction . . . 44
3.2 Observations . . . 46
3.2.1 Interferometric archival data . . . 46
3.2.2 Dedicated interferometric observing programs . . . 48
3.2.3 Data-reduction on archival data . . . 48
3.2.4 Spectral Energy Distribution . . . 49
3.3 Methodology of the geometrical modeling and of the temporal analysis . . . 49
3.3.1 Geometrical modeling of FU Orionis . . . 50
Extended envelope . . . 50
Resolved emission . . . 50
Central unresolved component . . . 51
3.3.2 Fitting strategy . . . 52
3.4 Results . . . 55
3.4.1 Size estimate of the resolved emission . . . 55
3.4.2 Chromatic dispersion of the extended envelope . . . 56
3.4.3 Compact unresolved component . . . 57
3.5 Analysis . . . 58
3.5.1 Thermal instability model . . . 58
3.5.2 MRI+GI in layered disk model . . . 59
3.5.3 Observables . . . 60
3.5.4 Size of the emission and temporal variation . . . 62
3.5.5 Origin of the compact emission . . . 64
3.5.6 Extended envelope . . . 64
Spectral variation and temperature of the extended envelope . . . 64
3.6 Conclusion and prospects . . . 66
3.6.1 Results . . . 66
3.6.2 Perspectives . . . 67
3.7 Appendix : FU Orionis' Spectral Energy Density (SED) . . . 69
3.8 Appendix : output of the bootstrap analysis in H and K band . . . 69

II Mid-infrared heterodyne interferometry for astronomical aperture synthesis **75**

4 A revisit of mid-infrared heterodyne interferometry **78**
4.1 Specifications of a PFI . . . 78
4.2 System architecture of a heterodyne PFI . . . 79
4.3 Heterodyne interferometry : signal to noise ratio . . . 81
4.3.1 Single channel SNR . . . 82
4.3.2 Two channel SNR . . . 84
4.3.3 Incoherent integration . . . 86
4.3.4 Point source sensitivity & imaging . . . 87
4.4 Sensitivity performance . . . 88
4.4.1 Imaging sensitivity & brightness temperature . . . 89
4.4.2 Comparison with direct interferometry . . . 91
4.4.3 Impact of the spectral resolution . . . 93
4.4.4 Impact of the number of telescopes . . . 94
4.4.5 Conclusion on heterodyne interferometry sensitivity . . . 95
4.5 Technological challenges . . . 96
4.5.1 Fundamental noise . . . 97
4.5.2 Detection . . . 97
4.5.3 Mid-infrared laser combs . . . 98
4.5.4 Correlation . . . 99
4.5.5 Laser synchronisation . . . 100
4.5.6 Fringe-tracking . . . 100
4.5.7 Fiber delay-lines . . . 101
4.5.8 Additional technologies . . . 101
4.6 *A workshop that never happened : HIFAAS 2020* . . . 102
4.7 Appendix . . . 103
4.7.1 Signal-to-noise ratio in SSB and DSB correlation . . . 103
4.7.2 Equivalent noise temperature of direct detection . . . 103

5 Noise analysis of heterodyne detection **106**
5.1 Quantum noise analysis . . . 106
5.1.1 Position of the problem . . . 106
Context . . . 106
Goal of this chapter . . . 108
5.1.2 Quantization of the electromagnetic field . . . 108
5.1.3 Quantum theory of detection and coherence [Glauber] . . . 112
5.1.4 Generalized measurement . . . 114
5.1.5 Quantum description and SNR of a heterodyne detection . . . 116
5.1.6 SNR in quantum formalism : two telescopes . . . 121
5.1.7 Conclusion . . . 124
5.1.8 Annex : Comment on optical amplification in astronomy . . . 126

III Photonic correlation **128**

6 Correlation I : Introduction of photonic correlation **130**
6.1 Motivation . . . 130
6.2 General picture . . . 131
6.3 Photonic correlation with phase modulation . . . 132
6.3.1 Phase modulation . . . 133
6.4 Experimental demonstration . . . 134
6.4.1 Generation of heterodyne test signals . . . 134
6.4.2 Phase correlation . . . 137
6.5 Amplitude modulation . . . 141
6.5.1 Amplitude modulation scheme . . . 141
6.5.2 Experimental demonstration of amplitude correlation . . . 144
6.6 Perspectives . . . 147
6.6.1 Delay compensation through a fiber delay lines . . . 147
6.6.2 Extension to a large number of telescopes . . . 149
Pairwise combination . . . 149
All-in-one with frequency encoding . . . 151
Direct-imager . . . 151
6.6.3 Extension to a large number of spectral channels . . . 152
Frequency multiplexing . . . 153
6.7 Annex : stability of the phase stabilization loop . . . 155
6.8 *Paper A&A : Toward a large bandwidth photonic correlator for infrared heterodyne interferometry (published)* . . . 156
6.9 *SPIE proceedings: MACH II: Mach-Zehnder analog correlator for heterodyne infrared interferometry (published)* . . . 157
6.10 *Paper JOSA : Architecture of photonics correlation for infrared heterodyne interferometry (under review)* . . . 157

7 Correlation II : Analog photonic correlator **160**
7.1 Motivation . . . 160
7.2 Principles . . . 162
7.2.1 Frequency Shifting Loop (FSL) . . . 162
7.2.2 Photonic correlator . . . 163
7.3 Characterisation . . . 167
7.3.1 Reminder of the properties of gain saturation and Amplified Spontaneous Emission (ASE) in FSL . . . 167
7.3.2 Experimental characterisation of the functioning regimes . . . 169
7.3.3 Small power regime . . . 169
7.3.4 Normal "flat" regime . . . 170
7.3.5 High-power regime : saturation effects . . . 171
7.3.6 Control of the loop . . . 171
7.3.7 Dynamic range & PRBS signal . . . 172
7.3.8 Dynamical correlation . . . 173
7.3.9 Correlation of wideband RF signals . . . 174
7.3.10 Antennas correlation and time of arrival . . . 176

7.4 Extension and perspectives . . . 179
7.4.1 Phase of the correlation function, interferometric observations at high-spectral resolution . . . 179
7.4.2 Application to infrared heterodyne interferometry . . . 181
Demonstration with 2 radio-antennas . . . 181
Sensitivity . . . 182
Scale-up to a large number of telescopes and multiple spectral channels : prospective ideas . . . 182
7.4.3 Other applications . . . 184
7.5 *Paper : Wideband multi-delay analog photonic correlator for RF signal processing (submitted)* . . . 185

IV Technological pathfinders **186**

8 Demonstrator for a 2T interferometer at 10µm **188**
8.0.1 Goal & specifications . . . 188
8.0.2 Description of the bench . . . 189
General description . . . 189
Components . . . 189
8.1 Sensitivity of the preliminary detection chain . . . 191
Amplifier noise in heterodyne detection [Kingston 1978] . . . 192
8.1.1 Noise analysis . . . 194
8.1.2 SNR estimation . . . 195
8.2 Preliminary developments . . . 195
8.3 Conclusion . . . 196
8.4 Appendix . . . 196
8.4.1 Proceedings SF2A: V8 concept and photonic correlation for mid-infrared interferometry (published) . . . 196
8.4.2 Components of the photonic correlator . . . 196

9 V8 concept : a 8 telescopes mid-infrared heterodyne instrument for the VLTI **200**
9.1 Introduction . . . 200
9.2 The V8 concept . . . 201
9.2.1 Instrument concept . . . 201
9.2.2 Subsystems and VLTI infrastructure . . . 201
9.2.3 Possible development phase . . . 202
9.3 Sensitivity budget . . . 203
Methodology . . . 203
9.3.1 Sensitivity of V8, comparison with current direct instrument . . . 205
9.4 Simulation of the observations . . . 206
9.4.1 Code . . . 206
9.4.2 Typical results . . . 208
9.4.3 Improvements of the simulator . . . 209
9.5 Perspectives : a pathfinder for the Planet Formation Imager . . . 210
9.5.1 Massive stars dense imaging : V8 with incoherent integration . . . 211

9.5.2 V8 with coherent integration : the mid-infrared image of the brightest Young Stellar Objects (YSOs) with 2AU resolution 211
V8 coherent integration : sensitivity limits on YSO 211
Brightness temperature 212
Imaging the mid-infrared environment of the brightest YSOs at 2 AU scale 213
Comment on brightness temperature : V8 as a precursor of PFI science case ? 214
9.5.3 Perspectives for PFI 215
9.6 Conclusion 216
9.7 *Proceedings : V8: an 8 beam mid-infrared heterodyne instrument concept for the VLTI (published)* 216
9.8 Appendix 217
9.8.1 Simulated point source observation with V8 217
9.8.2 *SPIE proceedings : "V8: an 8 beam mid-infrared heterodyne instrument concept for the VLTI "* 218
Comparison with direct interferometry in the N band 222

Annex: List of publications **224**

Bibliography **282**

Table of acronyms

Acronym	Name
ADC	Analog-to-Digital Converter
AGB	Asymptotic Giant Branch
AM	Amplitude Modulator
AO	Adaptive Optics
AOM	Acousto-Optic Modulator
ASE	Amplified Spontaneous Emission
AWG	Arbitrary Waveform Generator
–	OR Array-Waveguide Grating (depending on the context)
AT	Auxiliary Telescope
AU	Astronomical Unit
CW	Continuous Wave
DSB	Double-Side Band
EDFA	Erbium Doped Fiber Amplifier
EOM	Electro-Optic Modulator
ExAO	Extreme Adaptive Optics
FCL	Frequency Comb Laser
FSL	Frequency Shifting Loop
FT	Fourier Transform
FWHM	Full Width at Half Maximum
GI	Gravitational Instability
IF	Intermediate Frequency
ISI	Infrared Spatial Interferometer
LNA	Low-Noise Amplifier
LO	Local Oscillator
LSB	Lower-Side Band
MCT	Mercury Cadmium Telluride (detector)
MHD	Magneto-Hydrodynamic
MRI	Magneto-Rotational Instability
MZI	Mach-Zehnder Interferometer
MZM	Mach-Zehnder Modulator
NFF	Natural Fringe Frequency
OPD	Optical Path Difference
OTF	Optical Tunable Filter
PFI	Planet Formation Imager

PID	Proportional Integral Derivative
PLL	Phase-Locked Loop
PMS	Pre-Main Sequence
PSD	Power Spectral Density
PSF	Point Spread Function
PZT	Piezo Transducer
QCD	Quantum Cascade Detector
QCL	Quantum Cascade Laser
QWIP	Quantum Well Infrared Photodiode
RF	Radio-Frequency
RIN	Relative Intensity Noise
RON	Read-Out Noise
RSG	Red Supergiant Branch
Rx	Receiver
SED	Spectral Energy Density
SNR	Signal-to-Noise Ratio
TBPF	Tunable Bandpass Filter
TDoA	Time Delay Difference of Arrival
TI	Thermal Instability
Tx	Transmitter
USB	Upper-Side Band
UT	Unitary Telescope
VLBI	Very Long Baseline Interferometry
VLT(I)	Very Large Telescope (Interferometer)
VODL	Variable Optical Delay Line
YSO	Young Stellar Object

Infrared Bands	
J band	1.1 to 1.4μm
H band	1.5 to 1.8μm
K band	2.0 to 2.4μm
L band	3.0 to 4.0μm
M band	4.6 to 5.0μm
N band	8 to 14μm
Q band	17 to 25μm

Tab. 0.1: List of the acronyms used in the manuscript.

Introduction

Can we understand the processes leading to the diversity of stars and their planetary systems ? This question is at the heart of our understanding of the formation of planetary systems, and of the physical conditions that set their birth. This implies that we are capable of obtaining details of the spatial structure of these objects with an unprecedented angular resolution, and requires the implementation of dedicated *high-angular resolution* instruments.

In the past few years, following decades of research in instrumentation, the advent of large (sub)-millimetric arrays and extreme adaptive optics on large telescopes have profoundly changed our vision of these objects, producing in particular the image of their structures at large spatial scales. This revolution will continue with the advent of extremely large telescopes, enabling to reach ultimately a few astronomical units of resolution in the next decade. However, the systematic study of essential physical processes of star and planet formation, including the physics of disk accretion and mass ejection, the process of disk migration or the formation of planetary embryos, occurs at even smaller spatial resolutions, of the order of the astronomical unit and below, beyond the ultimate diffraction limit of these facilities.
Infrared interferometry, which consists in the recombination of separated telescopes in order to reach a higher angular resolution, is a powerful technique in this perspective. However, due to its complex implementation, its ability to reconstruct images is still limited. The long-term development of a future interferometer capable of producing the image of young stars will imply the recombination of a large number of telescopes, with kilometric baselines, and a high contrast imaging capability. This represents a considerable challenge for current astronomical instrumentation, and requires to reconsider deeply the architecture of a future infrared interferometers.

The founding motivation of this thesis is the exploration of the practical path that could enable to make the image of young stars environment with sub-astronomical unit resolution in the infrared. This begins with the understanding of these objects by the observation with current interferometers, which provides both state of the art astrophysical information and a good understanding of the limitations of current facilities. As initially proposed by the Planet Formation Imager (PFI) initiative, two possible complementary schemes can be envisioned in the perspective of an interferometer combining a large number of telescopes and kilometric baselines : direct interferometry and heterodyne interferometry. The first one consists in the extension of current infrared interferometers, based on the direct interference of astronomical

light. Although it is the most sensitive and most widespread interferometric scheme in the infrared, its extension to kilometric baselines and a large number of telescopes is difficult, in particular due to the complex infrastructure that this scheme necessitates. The second possible architecture is based on the use of a coherent - so-called heterodyne - detection, where the electric field of the light is detected at the level of each telescope, and transported in the form of a radio-frequency or a digitalized signal, before being processed. This scheme, usually used in radio-astronomy, was demonstrated as soon as the 70s at $10\,\mu\mathrm{m}$ at U.C. Berkeley by the team of C.H.Townes (M A Johnson, Betz, and C H Townes, 1974), inventor of the maser and Nobel Prize in physics, where it was the first technique enabling to combine two telescopes in an interferometric mode in the mid-infrared. However, this technique suffers from known limitations in sensitivity and bandwidth coverage, highly dependent on the available technology, which limits the use of this scheme. In this context, the recent rise of the mid-infrared technologies and the constant breakthroughs in this field considerably modify the previous limitations considered for heterodyne interferometry.

In this thesis, we will focus on the application of infrared heterodyne interferometry to the study of the environment of young stars and protoplanetary disks at the astronomical unit scale. Building on the profound and pioneering ideas led by C.H. Townes and his team, the goal of this work is to evaluate the feasibility and to propose a renewed approach of infrared heterodyne interferometry to the study of young stars through aperture synthesis, at the light of the recent progresses in mid-infrared technologies.

In Part I, we give a general introduction on Young Stellar Objets (YSOs) and protoplanetary disks (Chapter 1) and on the principles of infrared interferometry (Chapter 2). In Chapter 3, we focus on the problematic of accretion in YSOs, through the observational study of the inner astronomical units of FU Orionis outburst with existing near-infrared interferometric facilities.
In Part II, in Chapter 4 we revisit the architecture of a mid-infrared heterodyne interferometer and its subsystems at the light of the recent developments in mid-infrared technologies, and precise the typical sensitivity expected in this framework. In Chapter 5, we try to clarify the fundamental origin of the quantum noise of heterodyne interferometry.
In Part III, we focus on one challenge associated to these subsystems, the correlation of wideband RF signals. In Chapter 6, we describe the principle and the implementation of photonic schemes at telecom wavelengths in order to obtain an analog double-sideband simple correlator. In Chapter 7, we describe the extension of this concept to a wideband analog correlator at multiple delays, along with its experimental implementation.
In Part IV, we propose a path to validate the key technological building blocks of an infrared heterodyne interferometer. In Chapter 8, we describe the design of a preliminary laboratory demonstrator at $10\,\mu\mathrm{m}$ combining two heterodyne channels and including a simple photonic correlator. Finally in Chapter 9, we describe the concept of a pathfinder instruments combining the 8 telescopes of the VLTI in the N band, and discuss its potential in the perspective of PFI.

Part I

Protoplanetary disks through infrared interferometry

> *What is going on inside a thunderstorm ? We will describe this insofar as it is known. As we get into this marvellous phenomenon of real nature – instead of the idealized spheres of perfect conductors inside of other spheres that we can solve so neatly – we discover that we don't know very much. Yet it is really quite exciting. Anyone who has been in a thunderstorm has enjoyed it, or has been frightened, or at least has had some emotion. And in those places in nature where we get an emotion, we find that there is generally a corresponding complexity and mystery about it. It is not going to be possible to describe exactly how a thunderstorm works, because we do not yet know very much. But we will try to describe a little bit about what happens.*
>
> **— Richard Feynman**
> Lectures on Physics (Vol II), Lecture 9

1 Protoplanetary disks and the environment of young stars (Introduction Pt. I)

1.1 Formation of young low mass stars

Stars form inside dense cores resulting from the gravitational collapse of molecular clouds. Inside these cores, thermonuclear reactions are eventually triggered as the temperature and the pressure of the gas increase, leading to the birth of a star. In the whole process, the *angular momentum* of the initial cloud has to be conserved. This angular momentum is in fact much larger than the angular momentum of the final star. The collapse thus leads to the formation of a massive rotating disk of gas around the newly formed star, in order to conserve the total angular momentum of the system, in about $10^4 - 10^5\,\mathrm{yrs}$. This disk is known as the *protoplanetary disk*, in which planet formation take place in $10^6 - 10^7\,\mathrm{yrs}$.

The ensemble of a star and its surrounding disk is designated as a Young Stellar Object (YSO). Depending on the mass regimes of the pre-main sequence star, YSOs are divided in different categories :

- **T Tauri stars :** initially discovered by (Joy, 1945), these young stars have a mass similar to the Sun ($< 3\,\mathrm{M}_\odot$), with a spectral type between F and M. These stars show photometric variability and large surrounding nebulosity.

- **Herbig Ae/Be stars :** first classified by (George H. Herbig, 1960), these intermediate mass stars ($3\,\mathrm{M}_\odot < M < 8\,\mathrm{M}_\odot$) are more massive than T Tauri stars. They correspond to a spectral type A or B.

- **massive young stars :** these massive objects ($> 8\,\mathrm{M}_\odot$) evolve quickly to the main sequence. They have a spectral type O or B.

The classification of the different stages of evolution of a YSO was established by (Lada, 1987), and revised by (Andre and Montmerle, 1994). This classification is based on the Spectral Energy Distribution (SEDs) of these objects. This classification is divided in four classes (the timescale associated to each class is indicated in Fig 1.1) :

- **Class 0 :** the SED is dominated by the flux of the infalling envelope and peaks in the far-IR and mm part of the spectrum ($\sim 100\mu\mathrm{m}$). This corresponds to the initial phase of accretion of the star, which is buried in its envelope.

- **Class I :** The infalling envelope is partly accreted in the form a disk which radiates energy, visible as a mid-infrared counterpart in the SED.

- **Class II :** The envelope is optically thin and the SED is dominated by the contribution of the optically thick accretion disk, which peaks in the near-infrared. An ultraviolet (UV) excess due to the accretion of gas on the star can be seen, and the star contributes to the part of the spectrum in the visible. This class corresponds to the classical T Tauri phase.

- **Class III :** The accretion disk is optically thin or has simply vanished, with little or no infrared excess in the SED. This phase corresponds to the so-called weak line TTauri phase.

1.2 Protoplanetary disks

1.2.1 Accretion & angular momentum transport

The conservation of the angular momentum in actively accreting disk can be performed in two ways :

- by the redistribution of angular momentum i.e. the transport of material in the external part of the disk. This requires that some friction forces or *viscosity* exist in the disk.

- by the loss of material through ejection processes. The main mechanism imagined in this case is the existence of a magnetically driven disk wind.

Steady accretion disk

Viscous accretion
The viscosity of molecular origin yields a typical accretion time scale of the order of $10^{13}\,\mathrm{yrs}$, obviously incompatible with the typical evolution time scale ($10^6 - 10^7\,\mathrm{yrs}$) of protoplanetary disks (Armitage, 2020). Hence, the molecular viscosity can not explain accretion in disks. Instead, it is supposed that *turbulence* can provide an effective viscosity much larger than molecular viscosity. This is the origin of the standard α-disk model (Shakura and Sunyaev, 1973), where the viscosity ν is parametrized as a function of the basic parameters of the disk, c_s the speed of sound in the disk, h the typical scale height of the disk, and α, a dimensionless constant which encloses the effect of turbulence :

$$\nu = \alpha c_s h \tag{1.1}$$

Observationally, the typical lifetime of a disk (a few Myr) indicates a value α of the order of 10^{-2} (Lee Hartmann et al., 1998; Armitage, 2020). This parametric description is however

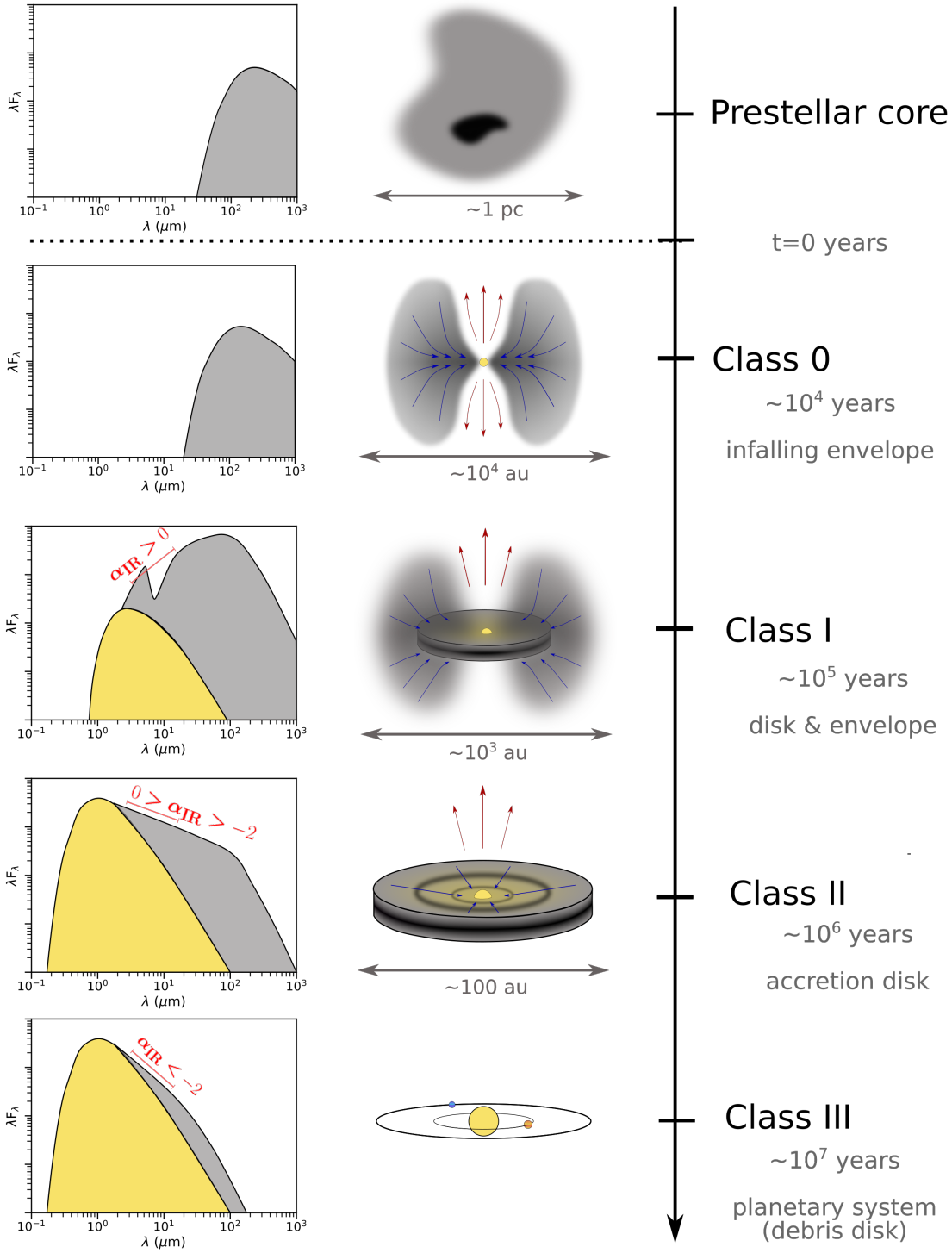

Fig. 1.1: Classes of Young Stellar Objects (Lada, 1987; Andre and Montmerle, 1994). Figure from A. de Valon (2021).

completely agnostic to the origin of turbulence. In this picture, describing and constraining observationally the exact physical mechanism behind the parameter α is one of the most important challenges in the study of accretion disks.

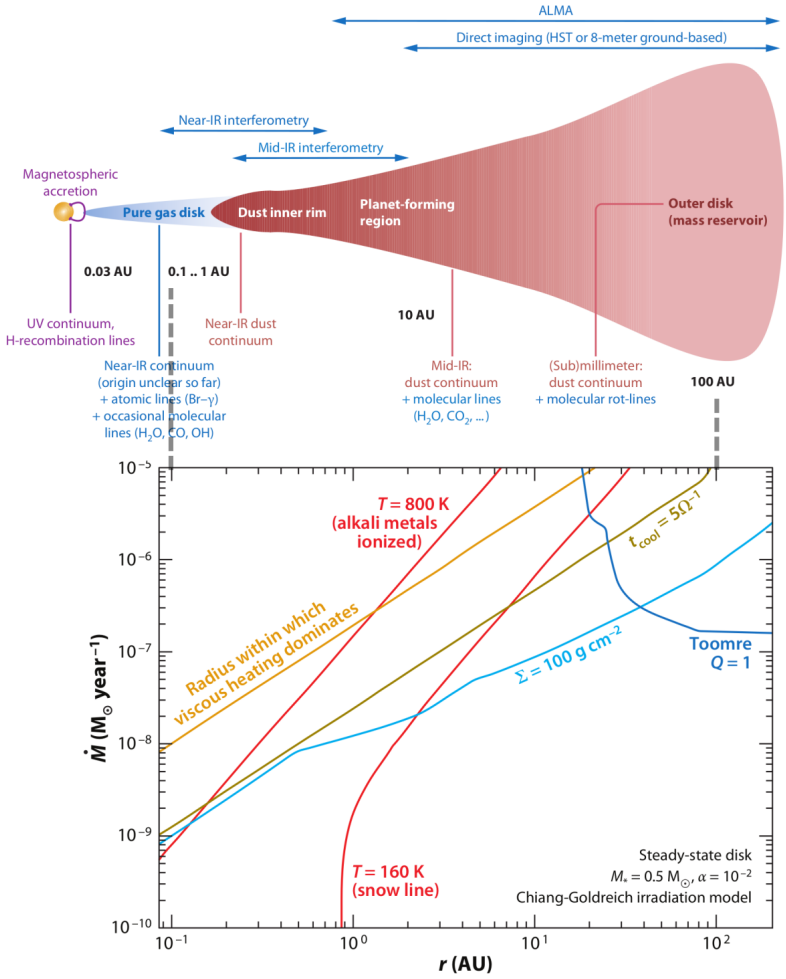

Fig. 1.2: *Up :* Structure of a protoplanetary disks and resolution range of each high-angular resolution techniques, from (C. Dullemond and J. Monnier, 2010). *Bottom :* Physical regimes relevant to angular momentum transport in disks (from (Armitage, 2011)). In the inner region of the disk and for high accretion rates, viscous accretion dominates the transport of angular momentum. The temperature of ionization of alkali metals provide the range where MRI can be activated. In the outer part, the disk is gravitationally unstable (Q<1). The overall conditions of the disk set the environment where planet formation occurs e.g. location of the snowline.

Different scenarii are identified to drive the turbulence and transport angular momentum in the disk, in particular Magneto-Rotational Instability (MRI) in the ionized parts of the disk, hydrodynamical instability, and self-gravitational instability in the outer part (Kratter and Giuseppe Lodato, 2016; Turner et al., 2014). The exact regions where these instabilities are efficient depend on the physical properties of the disk, and are summarized in part in Fig 1.2.

In the following, we will focus only on MRI and disk winds, as they are considered as the most efficient processes to provide the bulk of the angular momentum transport.

Magneto-Rotational Instability (MRI)
MRI is a magneto-hydrodynamic process that leads to turbulence in the ionized part of disk (Balbus and Hawley, 1991). The classical analogy in order to present MRI consists in considering two particle cells of fluid placed on the same vertical line of the magnetic field. In order to understand the effect of an instability, let us consider that these two particle are slightly separated from each other radially, as shown in Fig 1.3. The outer particle cell is decelerated and the inner cell is accelerated due to the conservation of angular momentum, so that these two cells move apart from each other azimuthally. In the case of a conducting (ionized) fluid, the magnetic field will act as a restoring force between these those cells moving apart azimuthally. The inner cell is decelerated by this restoring force, and thus moves to inner regions of the disk due to the loss of its angular momentum. Conversely, the outer cell is accelerated and moves to outer regions. The initial radial separation of the two cells leads to a larger radial separation, so this is indeed an unstable configuration. We note that this mechanism supposes that the magnetic restoring force is sufficiently weak not to stabilize completely the system. MRI is sustained only in the ionized parts of the disk. The primary sources are the thermal ionization, only effective in the innermost regions of the disk since it is the only part that reaches the activation temperature of MRI $T_{\rm MRI} \approx 800 - 1000\,{\rm K}$ (few tenths of AU, alkali metal ionization in Fig 1.2), and the ionization by X/far-UV radiations and cosmic rays, mostly effective in the surface layer of the disk. In the case of disk regions at sufficiently large radii not to reach $T_{\rm MRI}$, and sufficiently dense to be shielded from high-energy radiation, ionization will be too low to sustain MRI : this is the *dead-zone* (Gammie, 1996). MHD turbulence is damped in this region, and accretion only occurs at the surface layer of the disk, or is even totally suppressed (Turner et al., 2014). We will come back later on this point when introducing the layered-disk model

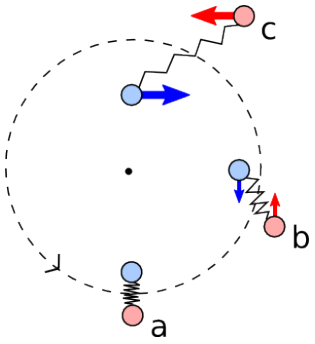

Fig. 1.3: Mechanism of magnetorotational instability (MRI). Extracted from Harvard Astronomy 201b lecture.

Wind

The second mechanism enabling accretion is the loss of angular momentum through a magnetically driven disk wind (Blandford and Payne, 1982; Ferreira, Dougados, and Cabrit, 2006). The mechanism powering disk winds is based on the coupling of the disk rotation with the magnetic field. In the case of vertical magnetic field lines crossing the disk midplane, the field lines are bended due to the rotation of the disk. This magnetic tension slows down the

disk rotation and generates radial accretion. The angular momentum lost during accretion is converted in magnetic pressure through a Lorentz force with a poloidal component (magneto-centrifugal force), which ejects matter from the surface of the disk to the outer regions, thus removing angular momentum out of the disk. There are now increasing observational evidences of disk winds, in particular through the study of gas kinematics through CO with ALMA in Class II objects (Louvet et al., 2018; Valon et al., 2020).

Layered disk model

The application of these ideas and the different regimes where MRI can be sustained have led to the introduction of a model of accretion in a layered structure (Gammie, 1996). In this model, three different zones can be distinguished in the disk :

- an inner zone (< 0.1 - 1 AU typically), where the temperature is sufficiently high ($T = 800 - 1000\,K$) to ionize the disk and for MRI to be active.

- an outer zone (> 3 - 10 AUs typically) where MRI is activated by non-thermal sources of ionization (X, UV), due to the lower surface density which is not sufficient to provide an efficient shielding of the disk. Gravitational instability also occur in this outer region if the disk is massive enough (Toomre Q<1 in Fig 1.2).

- an intermediate zone (1 - 10 AU typically), where the surface density is high enough to provide an efficient shielding from the radiation, and where the disk temperature is not high enough to thermally activate MRI. MRI is not effective in this region of the disk, even in surface in layers probably (Turner et al., 2014), where disk wind may appear as the main source of accretion. This intermediate zone is called the dead-zone, and plays an important role in the structure and the evolution of the disk.

More observational constraints are needed in order to confirm or infirm this current model of accretion in protoplanetary disk. The layered structure of a protoplanetary disk and in particular the presence of a dead-zone have potentially major ramifications in the scenario of planet formation, in particular on the formation of planetesimals in this region (1-10 AU) of the disk (Chiang and Youdin, 2010), and in providing a potential mechanism for massive accreting outbursts in young objects.

The problem of accretion in T Tauri stars

Thus far, we have considered a standard disk steadily accreting gas onto the star. Assuming a steady accretion rate, the accretion luminosity of T Tauri stars can be compared to their bolometric luminosity. This comparison shows that the bolometric luminosity of T Tauri stars is about one order of magnitude smaller than the luminosity expected from a star

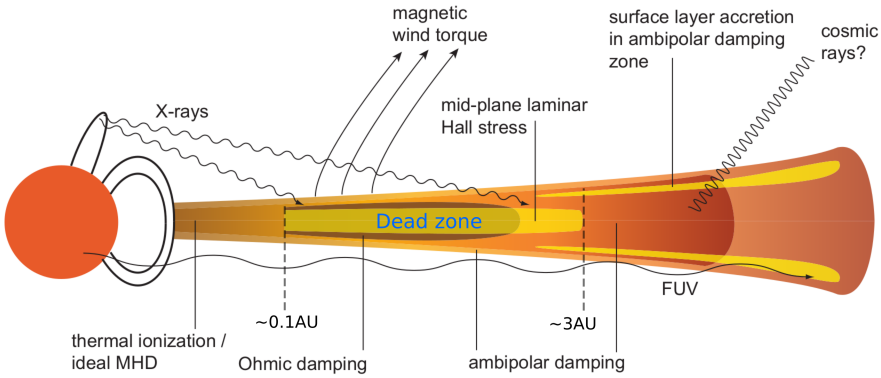

Fig. 1.4: Layered disk model and dead zone in protoplanetary disks (from (Armitage, 2011), and initially proposed in (Gammie, 1996)).

formed during the Class I phase, with an estimated accretion rate in the disk of typically $10^{-7}\,M_{\odot}.\mathrm{yrs}^{-1}$ (Nuria Calvet, Lee Hartmann, and Stephen E. Strom, 1999). This fundamental difficulty, known as the *luminosity problem* of Class I sources, and first identified by (Kenyon and L. W. Hartmann, 1990), necessitates that accretion should occur through massive episodic events rather than a steady process, in order for the star to form in the time-scales observed through disk evolution surveys (Nuria Calvet, Lee Hartmann, and Stephen E. Strom, 1999). As suggested by (Kenyon and L. W. Hartmann, 1990), these episodes could potentially be explained by FU Orionis events (abbrev. FUors), where the luminosity of the star increases by several magnitudes in only a few years, due to a massive accreting event in the disk with typical accretion rate $\sim 10^{-4}\,M_{\odot}.\mathrm{yrs}^{-1}$ during $\sim 100\,\mathrm{yrs}$, adding $\sim 0.01\,M_{\odot}$ onto the central star during the outburst(Lee Hartmann and Nuria Calvet, 1995a). However, the exact mechanism powering FU Orionis outburst, which is tightly linked to our knowledge of the physics of turbulence and to the supposed physical structure of the disks, is still poorly understood.

In Chap 3, we make use of more than twenty years of near-infrared interferometric observations to constrain the mechanisms at the origin of FU Orionis outbursts.

1.2.2 Planet formation

So far, we have described the structure of the protoplanetary disk during the phase of accretion in Class I/II. During its evolution, the dust contained in the disk will also progressively coagulate to form planetesimals, and ultimately, planets. In this section, we detail the mechanisms put forward to explain the transition from a disk made of gas and dust to the formation of planets.

Planet formation scenarii

Rocky core formation

The first step to go from dust particles to planetesimals is the *dust settling* : due to the relative motion of dust relative to gas, dust particles experienced a drag force and settle in the midplane (Weidenschilling, 1977). In this regime, small grains are strongly coupled to the gas so that the relative velocity between grains is relatively small, which favours their coagulation. This increase in mass favours their decoupling from the gas and settling towards the disk midplane. Inversely, turbulence occurs in the disk mid-plane and tends to mix the grains, whose signature at the surface is visible in the mid-infrared for example (tracing micrometric grains). At the same time, dust experiences radial drift, due to the friction with gas : this radial drift is maximum for cm to m-size bodies, with a typical fall time on the star much smaller than the time needed for grains to coagulate in m-size body. This problem is known as the *meter size problem*, whose exact solution still remains unclear (Weidenschilling, 1977). The existence of gravitational instability (Peter Goldreich and Ward, 1973), or pressure maxima due to turbulence (MRI), that would act as traps for dust, or vortices at the edge of the dead zone due to Rossby instabilities, are invoked as potential solutions to these problems (Lyra and Klahr, 2011). Beyond this m-size barrier, planetesimals accrete the dust in their neighbourhood through gravitational focusing and pebble accretion (Lambrechts and Johansen, 2012). The typical characteristic scale in which accretion on planetesimal occurs is given by the *Hill radius*, which defines the region where the gravity of the planetesimals dominates :

$$r_H = \left(\frac{M_p}{3M_*}\right)^{1/3} a \tag{1.2}$$

with M_p the mass of the planetesimal and a its semi-major axis. The accretion on planetesimals go through a phase of runaway, followed by a phase of *oligarchic growth* between the planetesimals, and ends with the phase of collision between the proto-planets. The final evolution of the planetary system is then shaped by the availability of gas and the migration torques induced by massive gas giants, which we will present later in this section.

The scenario described so far explained the formation of rocky cores, which can either constitute rocky planets or the core of gas giant planets. Two competing mechanisms are put forward to explain the formation of gas giant planets : *core-accretion* model and *gravitational instability* model, that we are going to present briefly. It is however possible that these two models co-exist in the same disk (Armitage, 2020), as they occur in relatively different regimes.

Core-accretion model

The core accretion starts from an initial rocky core, but unlike rocky planets, as core grows it becomes massive enough to hold an envelope of gas, this accretion of gas being favoured in the external part of the disk. The core continues to accrete gas and dust via planetesimal and pebble accretion, up to a *critical mass* beyond which the envelope can not remain in hydrostatic equilibrium. It follows that the core contracts and accretes even more gas from its environment. The proto-planet radiates a large fraction of energy during this phase, released from gravitational and core accretion energy, as shown in Fig 1.5, which makes planets more

easily detectable during this period. This process continues up until the proto-planet has depleted the gas in its neighbourhood and opened up a gap in the disk. The core accretion model is the most widely accepted theory of planet formation and is known in its broad outline, but its detailed scenario is still sensitive to key characteristics : the initial conditions of the disk (surface density in particular), the opacity assumed for the calculation of the critical mass, or the effect of planet migration, in particular in the formation of hot Jupiters. In that respect, observational constraints are crucial in order to provide a complete picture of the formation of proto-planets.

Gravitational instability model

The alternative formation scenario of gas giant planets is the gravitational instability (GI) model. In outer and sufficiently massive regions, a disk can become gravitationally unstable, resulting either in the transport of angular momentum or fragmentation. The idea at the basis of GI model is that giant planets could form directly and very rapidly from disk fragmentation, without requiring the initial formation of a core. The question of whether the required conditions to form planets through GI are met is still debated. This model could potentially provide a formation scenario of gas giant planets observed at very large separation 50 AU - 100 AU (e.g. HR8799 in Marois et al., 2008), although the formation of brown dwarfs and stellar companions from GI fragmentation is more likely than the formation of planets (Kratter and Giuseppe Lodato, 2016).

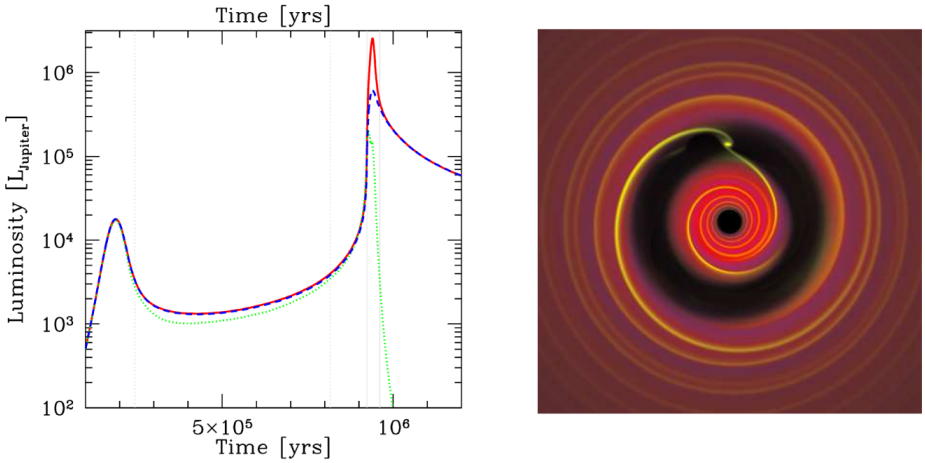

Fig. 1.5: *Left :* Accretion luminosity of a 1 M_J proto-planet at 5.2 AU. (Mordasini et al., 2012) (blue : core luminosity, green : envelope luminosity, red : total luminosity). The luminosity peak on the right corresponds to the runaway accretion following the collapse of the core. *Right :* Type II migration, with the opening of a gap and the apparition of disk Lindblad resonances (Armitage, 2020).

Migration

In their formation and evolution, proto-planets exchange angular momentum with their environment : dust, planetesimals, gas, or other planets. In turn, this leads to the modification of the orbit of these proto-planets, a process described as the *migration* process. Migration

is particularly important in planetary formation, as it is now clear that a large fraction of the planets currently observed (in particular hot-jupiters) could not have formed at the initial location predicted by planet formation scenarii (Lin, Bodenheimer, and Richardson, 1996). In the following, we will focus only on the interaction of the forming planet with the protoplanetary disk i.e. migration in gaseous disks.

The exchange of angular momentum between a planet and the disk is done through a gravitational torque. Following the presentation done in (Armitage, 2020), this idea can first be understood in the simplified *impulse approximation* (Lin and Papaloizou, 1979), by considering the perturbation due to gravitation of a portion of gas passing by a planet. In the case of the interaction with gas exterior to its orbit, the angular momentum of the gas increases while the angular momentum of the planet decreases, so that the planet moves inwards. Conversely, considering gas interior to the orbit, the gas loses angular momentum while the angular momentum of the planet increases. The computation of the total torque shows that the typical timescale for a forming planet at 5AU with earth mass to migrate on a star is ~ 1 Myr, and a few ~ 0.1 Myr in the case of a planet with Jupiter's mass, which shows that migration should have an important impact during the timescale in which a planet forms. The detailed treatment of the gas-disk interaction (P. Goldreich and Tremaine, 1979) shows that the total torque is in fact the result of the torques exerted at resonant locations, known as *Lindblad resonances*[1], co-orbital resonances, and thermal torques. Depending on the mass of the planet, these resonant interactions have been defined as Type I and Type II migration, the transition occurring for a planet mass of the order of Saturn approximately.

- **Type I :** in this regime, the local surface density of the disk is almost unperturbed by the planet, the most visible sign of interaction being the presence of a spiral wave which exerts a torque.

- **Type II :** in this regime, the mass of the planet is sufficiently large to open a gap in the disk and to deplete the gas in the resonances close to the planet. Once the gap is opened, the planet migrates at the same rate as the radial flows of the disk due to accretion.

The modelling of planet migration has seen considerable progresses in the recent years. Its comparison with observations remains however difficult and different models can reproduce the same observations, as different physical processes (migration, accretion, etc.) occurs at the same time and are sensitive to the initial conditions of the problem. This motivates the direct observation of planet forming systems *during* planet migration over a significant sample of planet-forming system.

[1] In the same manner as the impulse approximation, interaction with interior Lindblad resonances leads to an increase of the angular momentum of the planet, and a decrease in the case of exterior resonances

1.2.3 Imaging the astronomical unit-scale (AU) and sub-AU scale of protoplanetary disks

The astronomical unit (AU) and sub-AU scales are the natural scales at which the physics of planet formation occurs. In the following, we summarize the general driving questions related to planet formation occurring at these scales and which will motivate this work :

- **What is the structure of the protoplanetary disks in the inner AU and what is the mechanism driving accretion in this region of the disk ?** This mechanism is necessary to understand the the luminosity problem in young stars.

- **What are the physical conditions (temperature, surface density, dust composition) of the protoplanetary disk in the inner AU ?** Planet formation scenario are particularly sensitive to these initial conditions.

- **How do planets interact their disk and migrate, and how does migration impact their formation scenario ? What is the image of a typical planetary system in formation, as it is happening *now*, and *with AU and sub-AU resolution* ?** This picture is for the moment limited to few tens of AU resolution typically.

1.3 The inner AUs of protoplanetary disks

1.3.1 The large scale picture of protoplanetary disks studies

The past few years have seen a revolution in the observational study of protoplanetary disks. This revolution has been made possible by the advent of high-angular resolution instruments.

The current part of planetary system of which we can reconstruct a proper image are primarily the thermally heated dust in the equatorial plain of disks and the CO lines emission of the gas with ALMA, and micrometric dust in surface with high-contrast imaging. These observations reach typically a maximum resolution of 10 milli-arcsecond (mas), thus focusing on the region of the disk ranging from 10 AU to 1000 AU typically (Andrews et al., 2018). In the mm and sub-mm domain, ALMA observations, tracing the mm-size grains of the disk, revealed the presence of large disk structures (Andrews, 2020), such as gaps (ALMA Partnership et al., 2015), spirals (Perez et al., 2016), or cavities in almost every young objects. The observations of large samples of objects now enables to place constraints on the spatial segregation of grains and the time-scale of dust settling. The study of CO lines emission, which gives access to the kinematics of the gas in the disk, also revealed the existence of powerful disk winds in some Class II objects (Valon et al., 2020). In the infrared domain, observations with high-contrast imaging (VLT/SPHERE, GEMINI/GPI, Subaru/HiCiao), probes dust particles at the surface layers of the disk, revealing dust structures that are or not infrared counterpart of ALMA's structures (Andrews, 2020), and could be related to large-scale dynamical spiral structures

possibilty originating from the trail of a forming planet (Boccaletti et al., 2020). Extreme adapative optics and submm interferometry have also proven to be powerful techniques to observe young giant planet forming at large separation. In the case of ALMA, the study of gas kinematics enable to detect proto-planets by the deviation of the disk dynamics from keplerian velocity (Pinte et al., 2020). Moreover, high-contrast imaging in the infrared gives access to the direct emission of young planets at large separation (Chauvin, 2018), including proto-planets still embedded in their forming disk e.g. in TTauri star PDS 70 (Keppler et al., 2018). In this latter case, this detection can be complemented in the visible with integral-field spectrograph (VLT/MUSE) with the observation of the accretion luminosity of these proto-planets in the Hα line (Haffert et al., 2019).

Overall, submm interferometry and high-contrast imaging now enable to add constraints on the physical properties of the disk (dust distribution, dynamical structures, kinematics of gas) and to detect most massive young planets ($10\,M_J$ typically) at large separation. However, these observations are ultimately limited to imaging resolution of the order of approximately 10 AU on average. Essential physical process of planet formation occurs at much smaller scales, which elude current direct detection capabilities.

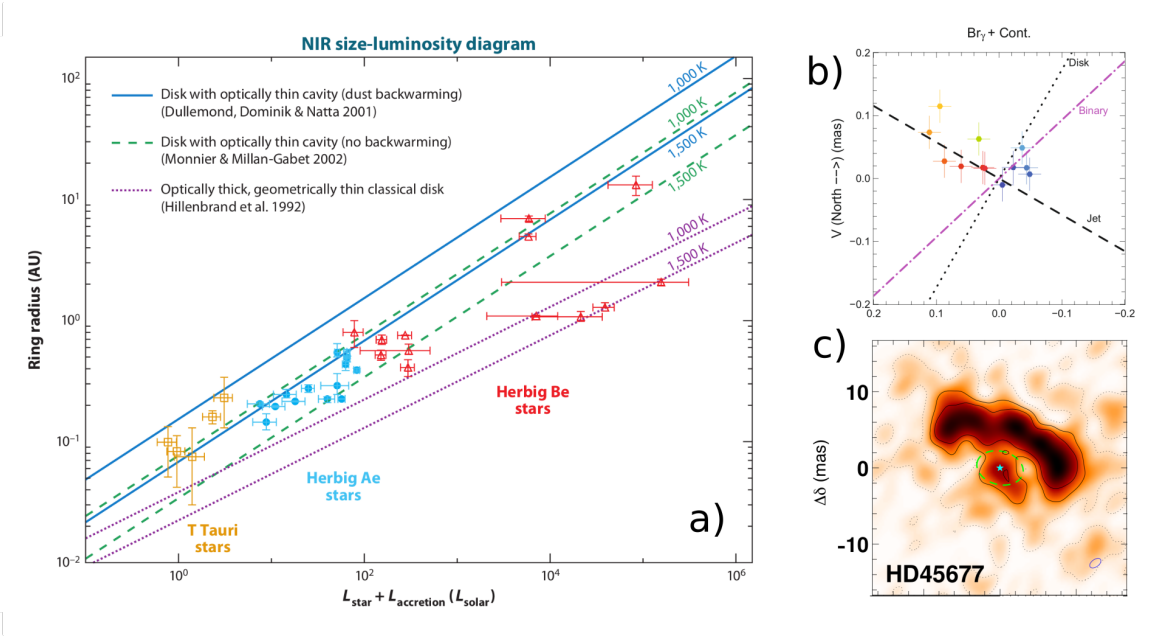

Fig. 1.6: **a)**: Size-luminosity relation in YSOs (C. Dullemond and J. Monnier, 2010) **b)**: Spectro-astrometry of bipolar wind in ZCma (Benisty et al., 2010) **c)**: Image reconstruction of a Herbig Ae/Be star (Kluska et al., 2020).

1.3.2 The inner AU of protoplanetary disks with infrared interferometry

Infrared and optical interferometry are the only technique able to spatially resolve the *inner AU* of protoplanetary disks. First, these observations have enabled to refine the geometry of the infrared emission arising from the inner astronomical unit (Rafael Millan-Gabet, Schloerb, and Traub, 2001). The comparison of the typical size of the disk emission measured by

interferometry in the near-infrared with the luminosity of the star + disk is consistent with a disk model with an optically thin innermost gaseous cavity and an inner rim composed of heated dust in direct sight of the star. In the case of T Tauri stars the observed infrared emission is significantly higher than the size-luminosity relations. Several explanations can be invoked including the additional contribution of accretion luminosity, a stronger dust backwarming, dust truncation by the magnetic field. (C. Dullemond and J. Monnier, 2010). Infrared interferometry also enabled to complement our picture of the accretion and ejection processes at stake in the inner AU of the disk. At a few stellar radii, spectro-interferometry observations with VLTI/GRAVITY have been able to locate the compact emission in Brγ arising from magnetospheric funnel flows(Bouvier et al., 2020; Gravity Collaboration et al., 2020). At larger radii, the study of Brγ (S. Kraus et al., 2008) enables to constrain the keplerian dynamics of the inner gaseous cavity in young stellar objects through Brγ or CO lines (Collaboration et al., 2020). At AU scale, the study of Brγ emission also revealed the presence of bipolar winds during massive ExOr accretion event (Benisty et al., 2010). Finally, in the mid-infrared, at larger spatial scales (few AUs typically), interferometric observations enabled to study the evolution of the radial distribution of disk mineralogy (Boekel et al., 2004), providing direct evidences that crystallization should occur in a large fraction of the disk and early in its evolution, during the phase of accretion.

In each cases, the power of infrared interferometry resides in its capability to spatially resolve astrophysical objects with milli-arcsecond resolution. Recently, the combination of a large number of observations enabled for the first time to reconstruct images of Herbig Ae/Be stars with sub-AU resolution (Lazareff et al., 2017; Kluska et al., 2020), adding constrain on the morphology of the inner-rim, and highlighting the presence of non-axisymmetric and temporally variable structures in the region of the inner rim. However, these images are ultimately limited by the dynamical range and the image complexity that can be reached by current infrared interferometers. As we will see in the next chapter, interferometry with a small number (<6) of telescopes is best suited for morphological and spectroscopic studies of photocenter position (spectro-astrometry), but is restricted to a sparse baseline coverage and thus low image reconstruction capability, in particular when compared to single telescope observations or radio-submm interferometry. This severely limits the capability of infrared interferometers to restore the emission of the inner AUs of disks in their full complexity.

1.4 The image of protoplanetary disks with sub-AU resolution : science case of the Planet Formation Imager

The image reconstruction of a disk with sub-AU resolution would provide a complementary and still missing access to the physical processes of planet formation that occur at these essential scales. In 2014, the Planet Formation Imager (PFI) initiative proposed to explore the fundamental questions in planet formation that could be addressed by a dedicated mid-infrared interferometric infrastructure producing an image with sub-AU resolution (John D. Monnier et al., 2018b). The choice for mid-infrared is guided by the imaging of the thermal

emission of the warm dust (μm-sized grains) of the disk, the detection of the accretion luminosity of proto-planets, and the higher angular resolution compared to mm-wavelength. This initial reflection of a PFI also included how this infrastructure would complement current and future observatories e.g. ALMA, ELT, JWST in terms of angular resolution and imaging capability. The fundamental questions that could be addressed by a PFI are summarized below (Stefan Kraus et al., 2014; Stefan Kraus et al., 2016). These points have to be seen has long-term driving axis :

- **protoplanetary disk physics :** trace warm μm-sized dust located in the disk surface layer, constrain disk temperature and density profile, resolve the spatial distribution of disk mineralogy, put constrain on the position of the snow-line

- **circum-stellar and circum-*planetary* structures :** resolve disk substructure (gaps, spirals,..) and kinematics tracing on-going planet formation, resolve accretion process down to the circum-planetary disk scale

- **proto-planets detection & migration :** detect thermal emission of accreting planets, reconstruct system architecture during its formation and constrain its migration process

As we have seen previously, these properties of disks are not yet within reach of current infrastructures. The initial proposition of the Planet Formation Imager is to examine the infrared interferometric facility which would be capable of addressing these questions by producing an image of protoplanetary disks with sub-AU resolution. This major facility would require the recombination of a large number of telescopes, with kilometric baseline, and calls for a renewed architecture of an infrared interferometer. In the next chapter, we present how these scientific questions convert into technical requirements of a future PFI, and we introduce the general principles at the basis of infrared interferometry.

> *... d'où, pour le dire en passant, il est peut-être permis d'espérer qu'en s'appuyant sur ce principe et en formant [...] des franges d'interférence au foyer de grands instruments destinés à observer les étoiles, il deviendra possible d'obtenir quelques données nouvelles sur les diamètres angulaires de ces astres.*
>
> **— Hippolyte Fizeau**
> Note aux Comptes rendus de l'Académie des sciences (1864)

2 Infrared Interferometry (Introduction Pt. II)

2.1 Instrument science requirements for a Planet Formation Imager (PFI)

Interferometry is the only technique capable of reaching milli-arcsecond resolution in the infrared. Existing infrastructures lack the angular resolution, surface brightness sensitivity and the ability to restore a complex astrophysical scenery (due the limited number of baselines). The long-term development of an infrared interferometer in the perspective of an imaging array of planet formation will be based on three main science requirements (John D. Monnier et al., 2018b) : high-contrast capability, image reconstruction fidelity, and kilometric baselines

- **Imaging arrray :** Image the dust distribution of the disk in the mid-infrared i.e. reconstruct an image with an ultimate brightness temperature sensitivity of 150K
- **Kilometric baseline :** Resolve the details of planet accretion at its typical scale, the Hill sphere i.e. with 0.3 AU for a Jupiter-mass planet at 5 AU, equivalent to 2 mas resolution at a typical distance d=140 pc (Taurus)
- **High-contrast :** Directly detect the thermal emission of accreting protoplanets with Jupiter mass

These points translates in the technical requirements given Tab. 2.1, extracted from (John D. Monnier et al., 2018b). These requirements will be at the basis of the research work on interferometric instrumentation carried out in this thesis. In this work, we will focus primarily on the instrumental development required for the case of dust imaging in the N band.

In the following, we introduce the basic principles of infrared interferometry, and introduce two interferometric architectures - amplitude interferometry and heterodyne interferometry - envision in the perspective of a PFI.

2.2 Interferometry and coherence

Parameter	Dust Imaging	Young Exoplanets
Wavelengths	5-13 μm	3-5 μm
Typical Source Distance	140 pc	50-500 pc
Spatial Resolution	2 mas $\equiv$ 0.3 AU	0.7 mas $\equiv$ 0.1 AU (for 140pc)
Point-Source Sensitivity (t= 10^4s)	$m_N \sim 12.5$ (5-σ)	$m_L \sim 18.5$ (5-σ)
Goal Surface Brightness (K) (t= 10^4s)	150 K	$--$
Spectral Resolving Power		
Continuum	R> 100	R> 100
Spectral Lines	R> 10^5	R> 10^5
Field-of-view	> 0.15"	> 0.15"
Minimum Fringe Tracking Limit	$m_H < 9$ (star only)	$m_H < 9$ (star only)
Fringe tracking star	$\phi < 0.15$ mas	$\phi < 0.15$ mas

Fig. 2.1: Top level requirements of a Planet Formation Imager, extracted from (John D. Monnier et al., 2018b).

2.2.1 Image formation as an interferometric process

In order to introduce the principles of interferometry and of interferometric imaging, it may be helpful to take a step back and first introduce the formation of an image through a single-dish optical system. The impulse response $I(\boldsymbol{\theta})$ of a telescope (with $\boldsymbol{\theta}$ the angular coordinate in the sky) is the Fourier Transform of the field $E(\mathbf{r}, t)$ in the pupil of the telescope (Born and Wolf, 1980; Lena et al., 2012), with $\mathbf{r}$ the position vector in the pupil :

$$I(\boldsymbol{\theta}) = \Big| \int_{\text{pup}} E(\mathbf{r}, t) \exp\Big(-2i\pi \frac{\mathbf{r}\boldsymbol{\theta}}{\lambda} \Big) \mathrm{d}\mathbf{r} \Big|^2 \tag{2.1}$$

In that respect, according to the basic properties of the Fourier Transform, the transfer function of an optical system[1] at a spatial frequency $\mathbf{f}$ is the auto-correlation of the electrical field with a physical separation $\mathbf{w} = \lambda\mathbf{f}$ in the pupil :

$$I(\mathbf{f}) \equiv \mathrm{FT}\left[I(\boldsymbol{\theta})\right] = \int_{\text{pup}} E(\mathbf{r}, t) E^*(\mathbf{r} + \lambda\mathbf{f}, t) \mathrm{d}\mathbf{f} \tag{2.2}$$

This impulse response function contains all the information of the spatial content of the image observed (filtered) through the optical system. In particular, it gives the maximum spatial frequency reached by the system, inversely proportional to the *angular resolution* of the optical system. In the case of a single-dish telescope with a circular aperture, the maximum spatial frequency of the optical system is naturally given by the diameter of the telescope. The practical resolution criteria used for single dish telescope, the Rayleigh criteria, provides the typical resolution limit of a telescope :

$$\Delta\theta = 1.22 \frac{\lambda}{D} \tag{2.3}$$

The relation Eq 2.2 can be viewed from another point of view, as pointed out by (Goodman, 1985). Considering the left term of Eq 2.2, the image through the optical system - more

[1] We will define the transfer function as the Fourier Transform of the impulse response of the optical system.

specifically, its content at a given spatial frequency $\mathbf{f}$ - is equal to the sum of the spatial coherence function of the field with a physical separation $\mathbf{w} = \lambda\mathbf{f}$. In the following, the spatial coherence is defined as :

$$C\Big((\mathbf{r},t);(\mathbf{r}+\lambda\mathbf{r},t)\Big) = \int E(\mathbf{r},t)E^*(\mathbf{r}+\lambda\mathbf{f},t)\,\mathrm{d}\mathbf{r} \tag{2.4}$$

In that sense, the image formed by a single-dish telescope can be viewed as the sum of large number of two hole Young interferometers, with separations probing all the possibilities provided by the pupil dimension. This is equivalent to an interferometric combinations, in which, however, a lot of redundant baselines are superimposed to each other. On the other hand, a Young interferometer, which indeed measures the coherence of two electrical fields, can be seen as an imager which measures only *one* spatial frequency. In between, the auto-correlation of a different set of apertures can be seen as an imaging system which paves a certain portion of the spatial frequency space. Interferometric arrays, including non-redundant aperture masking, infrared long baseline interferometers or radio-interferometers, can all be seen as this particular form of optical system. The essential features of these systems is their ability to measure the spatial coherence of an electric field.

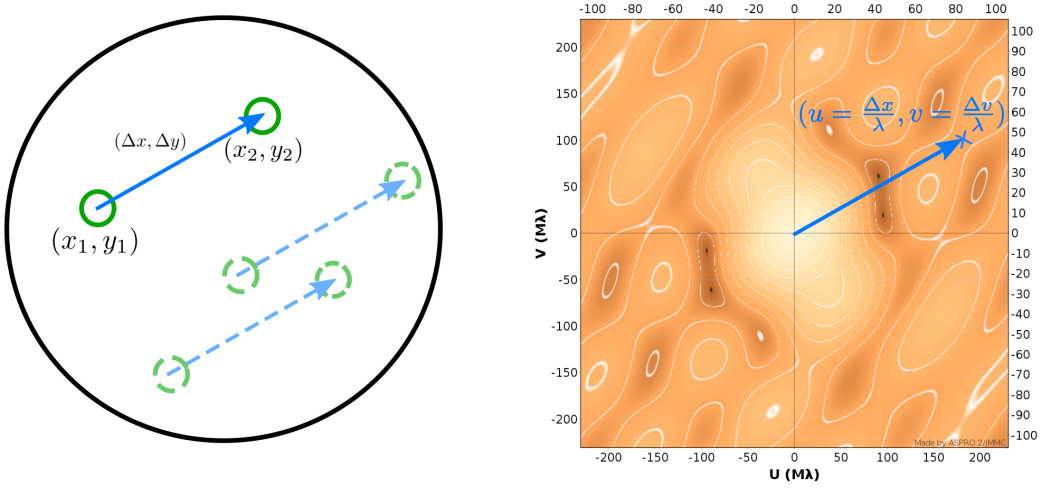

Fig. 2.2: *Left :* Pupil-plane of an optical system : the pupil can be seen as the decomposition of a multiple two element Young interferometer. *Right :* Frequency space of the image (so-called UV plane), in which one separation corresponds to the measurement of one spatial frequency. As an example, the visibility function of an arbitrary object was generated using `Aspro2` (developed by JMMC).

2.2.2 Zernike van-Cittert theorem

An imaging system is essentially an optical system that measures the spatial coherence of light, as we have seen in the previous paragraph. The amplitude of the coherence evaluated for a given separation of two apertures is related to the measurement of a certain spatial frequency by the system, and should thus be related to the measurement of a given component of the spatial spectrum of the observed object. More rigorously, this relation between the normalized coherence $\gamma(u,v)$ - also called the *complex visibility* - and the brightness distribution of the

object $I_o(\alpha, \beta)$ is exactly described by the Zernike van-Cittert theorem (Zernike, 1938; Lena et al., 2012) :

$$\gamma(u, v) = \frac{\int I_o(\alpha, \beta) e^{-2i\pi(\alpha u + \beta v)} \mathrm{d}\alpha \mathrm{d}\beta}{\int I_o(\alpha, \beta) \mathrm{d}\alpha \mathrm{d}\beta} \tag{2.5}$$

where we have introduced the angular coordinates $\boldsymbol{\theta} = (\alpha, \beta)$ and the spatial frequency coordinates $\mathbf{f} = (u, v) = \left(\frac{\Delta x}{\lambda}, \frac{\Delta y}{\lambda}\right)$. This corresponds to the measurement of the first order spatial coherence. In the same manner as in the previous paragraph, we can see that by cumulating a sufficient amount of coherence measurements over different spatial frequencies, the image of the initial object can be reconstructed. More rigorously, this image can be reconstructed by the inversion of Eq 2.5, which constitutes on its own the domain of image reconstruction in interferometry (J.-P. Berger et al., 2012). In the following, the spatial frequency space will be designated as the (u,v)-plane, in which the interferometric measurement are usually performed. An essential aspect of interferometers is that, even if they show less redundancy of the spatial content of an image, and as a consequence are less sensitive at a given spatial frequency than what would be an equivalent full aperture dish, their maximum spatial frequency - or conversely, their smallest *angular resolution* - is no more limited by the maximum telescope diameter, but by the *separation* of the apertures. We will come back on this point in Sec 2.3.1.

2.2.3 Interferometric observables

The essential observable extracted from the measurement of coherence is the *complex visibility* of an object, as we have seen in Sec 2.2.2. In practice, there is a diverse family of observables that are usually used, due both to the practical limitations when measuring this spatial coherence, and depending on the exact spatial and/or spectral property of interest in the astrophysical object. These observables are listed in Tab. 2.1.

2.2.4 Temporal coherence & delay compensation

Thus far, we have considered that the measurement of the coherence of the field gives access directly to the spatial coherence of the source. This supposes either that the sources are perfectly monochromatic, or that the *optical path difference* (OPD) between each interferometric channel is perfectly matched. In the more general case, the coherence of the field is the product of the spatial and the spectral coherence of light[2]. In the following, the temporal coherence is defined as :

$$C\Big((\mathrm{r}, t), (\mathrm{r}, t + \Delta\tau)\Big) = \langle E(t) E^*(t + \Delta\tau) \rangle \tag{2.6}$$

where the bracket refer to the temporal average. The exact expression of the measured spectral coherence is given by the Wiener-Khintchin theorem, and depends on the filtering

[2]We acknowledge that this is is not the most general expression of the coherence. However, this expression remains true in the case of a spatially and spectrally incoherent field, which will be the case considered in the rest of this thesis.

Complex visibility	$\gamma(u,v) = V(u,v) = \|V\|e^{\phi_v}$	General observable, contains the information on the coherence (amplitude and phase).
Coherent flux	$F(u,v) = \|F\|e^{\phi_v} = \int I_o(\alpha,\beta)e^{-2i\pi(\alpha u+\beta v)}\mathrm{d}\alpha\mathrm{d}\beta$	Non-normalized complex visibility, can be used when the photometric calibration can not be easily done or is too noisy
Squared visibility	$V^2 = \|V(u,v)\|^2$	Modulus squared of the complex visibility ; used when the interferometric phase can not be exploited due atmospheric phase fluctuations. The morphology of the object (disk, binary, etc.) can be constrained using the Zernike van-Cittert theorem.
Bispectrum	$\mathrm{B}(\overline{uv}_1,\overline{uv}_2,\overline{uv}_3) = \gamma(u_1,v_1)\cdot\gamma(u_2,v_2)\cdot\gamma^*(u_3,v_3)$	Product of the complex visibility over a triangle
Closure phase	$\phi_{CP} = \phi_v(u_1,v_1) + \phi_v(u_2,v_2) + \phi_v(u_3=-(u_1+u_2),v_3=-(v_1+v_2))$	Sum of the interferometric phase over a closed triangle of 3 telescopes, equivalent to the phase of the bispectrum. In theory, this observable is immune to the atmospheric phase fluctuations. This observable is much more noisy, as this is a moment of order of the field (R. Lachaume, 2003).

Tab. 2.1: Interferometric observables obtained from the measurement of the spatial coherence of light.

of the interferometric channel. A convenient order of magnitude is the typical width of this coherence function is given by the coherence length :

$$l_c = R\lambda = \frac{\lambda^2}{\Delta\lambda} = \frac{c}{\Delta\nu} \tag{2.7}$$

with $\Delta\lambda$ the spectral width of the detection channel (i.e. a bandwidth $\Delta f = \frac{c}{\lambda^2}\Delta\lambda$), and $R = \frac{\lambda}{\Delta\lambda}$) the spectral resolution.

The major consequence is that the relative delays of an interferometer have to be precisely matched, within the coherence length, in order to preserve the contrast of the fringes. This requires the introduction of a fundamental element of an astronomical interferometer, the *delay lines*, in order to compensate for this relative delay. This delay has also to be compensated in real time, given that it is continuously varying due to the rotation of the sky. We will come back later on this point when presenting the practical implementation of an interferometer.

2.3 Introduction to infrared interferometry

The function of an interferometer is to extract the coherence of an incident astronomical field. As mentioned in the last section, this consists in measuring:

$$g^{(1)} \propto \langle E(\mathbf{r},t)E^*(\mathbf{r}+\lambda\mathbf{f},t)\rangle$$

This quantity is proportional to the first order of coherence of the light (Goodman, 1985), related to the distribution of intensity of the object (the image) through the Zernike van-Cittert theorem. More generally, higher degrees of coherence of light can be measured, such as the second order of coherence $g^{(2)} \propto \langle I_1(t) I_2(t) \rangle$ (Hanbury Brown, 1956), and linked to the distribution of intensity of the object (Goodman, 1985). Unlike the first order of coherence, second-order of coherence is not sensitive to the interferometric phase. In practice, higher degree of coherence than order 2 are not considered, because leading to too small signal-to-noise ratio.

The measurement of coherence of light can thus be achieved through different techniques, whose main domain of application are shown on Fig. 2.2. The main interferometric schemes already demonstrated on-sky in optical interferometry (visible and infrared) at the time of writing are summarized in Tab. 2.2.

Interferometric technique	**Degree of coherence**	**Wavelength**	**Principle**	**Reference**
Amplitude	$g^{(1)}$	0.45μm to $\sim 13\mu$m	Direct combination of light to form interference fringes.	[1,2,3]
Heterodyne	$g^{(1)}$	$\sim 11\mu$m to radio-domain	Coherent detection scheme: astronomical signal is mixed with a local oscillator, converted to the RF domain, and correlated.	[4,5,6]
Upconversion	$g^{(1)}$	1.55μm and 3.39μm	Upconversion of the photon frequency through its mixing with a laser pump in a non-linear medium (crystal).	[7,8]
Intensity	$g^{(2)}$	Visible / near-IR (0.780μm)	Detection of the intensity of the light, and cross-correlation the detected signals	[9,10]

Tab. 2.2: Summary of astronomical interferometric techniques demonstrated in the visible and the infrared. References: (1):Fizeau (1864) ; (2): Michelson and Pease, 1921 ; (3): Labeyrie, 1975 ; (4): M A Johnson, Betz, and C H Townes, 1974 ; (5): J. Gay et al., 1973; (6): Thompson, Moran, and Swenson, 2017 ; (7):Darré et al., 2016 ; (8): Szemendera et al., 2017 ; (9): Hanbury Brown, 1956 ; (10): Guerin et al., 2018

In the perspective of a Planet Formation Imager, we are mainly interested in techniques sensitive to the interferometric phase, as they enable to reconstruct an image. In this way, we will primarily focus on the techniques sensitive to the first order of coherence. Amplitude interferometry and heterodyne interferometry represent two potential techniques to this end, and potentially offer complementary domains in terms of wavelength and operability for an infrared PFI. In the following, we will focus on these two techniques and introduce briefly the functioning principle of each of them [3].

[3] At the time of writing, up-conversion techniques are currently evolving fast, however they are primarily demonstrated with decent up-conversion efficiency in the L ($3.5\,\mu$m) and M ($4.2\,\mu$m) band. This technique could potentially represents an interesting techniques in these mid-infrared domains, depending on the evolution of the conversion efficiency with on-going or future technological developments (Lehmann et al., 2019).

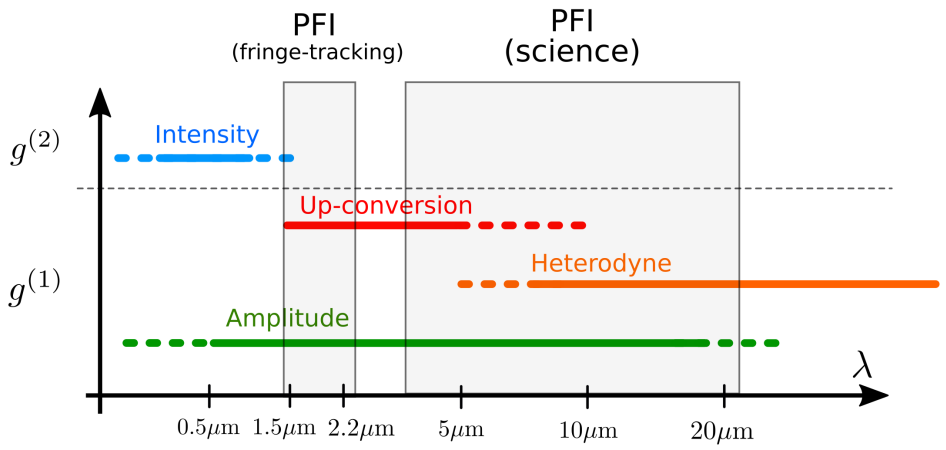

Fig. 2.3: Domain of application of the astronomical interferometric techniques demonstrated at the time of writing. For each technique, the solid line represents the domain where the technique has been demonstrated (cf Tab 2.2), the dashed line represents the domain could be potentially extended, but where the demonstration is not yet done or is on-going. The order of coherence measured by each technique is indicated on the y-axis.

2.3.1 Amplitude interferometry

This scheme consists in the physical transport of light to a recombination unit, where the beams are superimposed and the resulting interference fringes are detected (Michelson and Pease, 1921; Labeyrie, 1975), as shown in Fig 2.5. The spatial coherence of the astronomical object is then extracted from the contrast of the fringes. Considering E_1 and E_2 the field of the astronomical light collected at the level of each telescopes (with $I_1 = |E_1|^2$ and $I_2 = |E_2|^2$ the related intensity), the signal measured at the level of the combiner is :

$$\left|E_1 + E_2\right|^2 = |E_1|^2 + |E_2|^2 + 2|E_1||E_1|\cos\left(\frac{2\pi}{\lambda}\mathbf{B}\cdot\boldsymbol{\sigma}\right) \tag{2.8}$$

$$= (I_1 + I_2)\Big(1 + V_{\rm ins}\cdot \mathrm{Re}\left(|V(u,v)|e^{i\phi(u,v)}\right)\Big) \tag{2.9}$$

with $V_{\rm ins} = \frac{2\sqrt{I_1 I_2}}{I_1+I_2}$ the instrumental contrast, $\mathbf{B}$ the vector baseline and $\boldsymbol{\sigma}$ the angular vector position of the point source object in the sky. The coherence of light is then extracted from the amplitude and the phase of the fringes. In order to compensate for the relative delay between each telescope due to the elevation of the astronomical object, an additional delay is introduced at the level of *optical delay lines*.

In the case of an interferometer, the angular resolution $\Delta\theta$ resolution depends of the baseline B between each pair of telescopes :

$$\Delta\theta = \frac{\lambda}{B} \tag{2.10}$$

In this way, interferometers are prime instruments to probe the spatial content of astronomical images at the highest angular resolution possible. The sensitivity depends on the diameter of each individual apertures (collecting area) and on the redundancy of the array, and the image fidelity depends on the capability to recombine a sufficiently large number of separations

to pave the frequency spaces. For a number of telescope N_t, the number of baselines in the array is :

$$\binom{N_t}{2} = \frac{N_t(N_t-1)}{2} \tag{2.11}$$

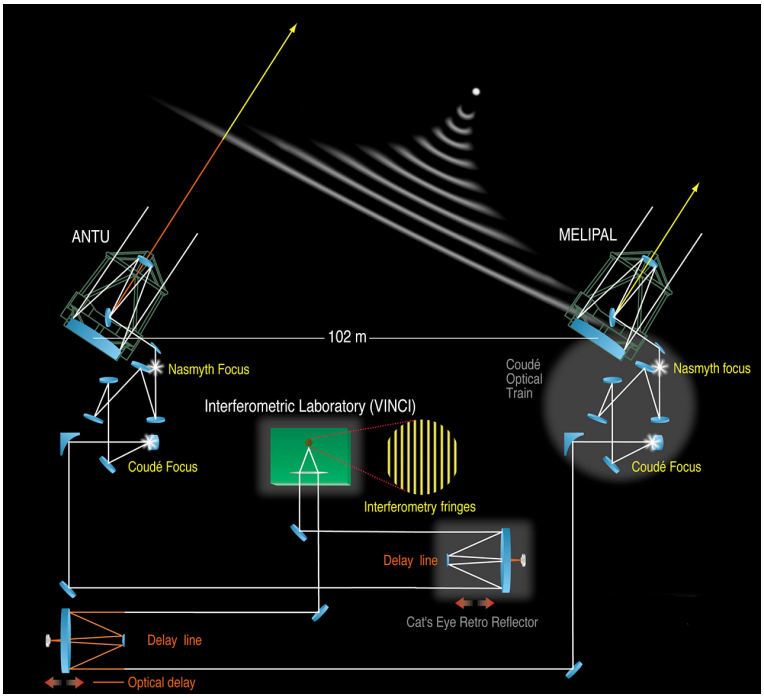

Fig. 2.4: Principles of infrared interferometer (amplitude interferometry), credits ESO.

Atmosphere & fringe tracking

Atmosphere above the telescopes introduces relative phase difference between each arm of the interferometer, which constantly perturbs the phase of the interferometric signal. This phase perturbation is also called the *atmospheric piston*. The typical timescale during the atmospheric piston remains constant, thus allowing a coherent integration of the signal, is called the *coherence time*. In the infrared, the typical value of the coherence time is typically $t_0 = 15\,\mathrm{ms}$ in good conditions (at $\lambda = 1.6\,\mu\mathrm{m}$). This implies that, without a mechanism which compensates for this perturbation, the measurement of an interferometric signal has to be performed in a integration time smaller than t_0. This severely restricts the sensitivity of the measurement as the noise budget is generally limited by the read-out-noise of the detector. In addition, the phase measured in each coherence time can not be averaged together, and only the closure phase can be exploited, but is an intrinsically noisier observable.

There is thus a very strong motivation to compensate for this atmospheric phase perturbation. This is usually done by a second combiner, which measures the perturbation introduced the atmosphere and feed a control loop which stabilizes the fringes. This system is called a *fringe-tracker*.

In the rest of this work, we will assume that all the incident astronomical fields are projected on a gaussian profile before the combination. In the case of amplitude interferometry, this filtering is usually done by monomode waveguides (optical fibers), whose dimension matches the Point Spread Function (PSF) of one telescope (Shaklan and Roddier, 1988). In this case, the typical extent of the field of view observed by an interferometer is thus given by the diffraction lobe of one telescope[4] (Mège, 2002; Perrin and J. Woillez, 2019). The typical extent of the interferometric field of view is thus :

$$\Delta\theta_{\text{fov}} \approx \frac{\lambda}{D} \tag{2.12}$$

In practice, as the measured signal has a limited coherence length, the relative OPD at the edge of the interferometric field of view has to remain smaller than the coherence length, otherwise decreasing the contrast of signal at the edge of the field of view. This effect is called the *beam smearing*. The typical angular extension in the sky corresponding to an OPD equal to one fringe is $\frac{\lambda}{B}$, the number of fringes in one coherence length is R (spectral resolution), and the total angular field of view is $\frac{\lambda}{D}$. As a consequence, the minimum spectral resolution required to avoid beam smearing is :

$$R \times \frac{\lambda}{B} = \frac{\lambda}{D} \Rightarrow R \sim \frac{B}{D} \tag{2.13}$$

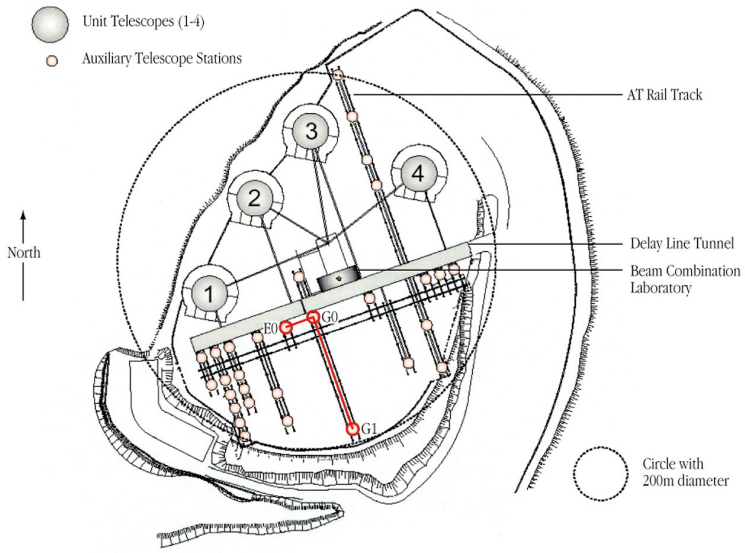

Fig. 2.5: Overview of the Very Large Telescope Interferometer (VLTI) at Cerro Paranal.

[4] As shown in (Perrin and J. Woillez, 2019), this situation is in fact more complex, and requires also to take into account the aberrations introduced by the atmospheric turbulence.

The Very Large Telescope Interferometer (VLTI) infrastructure

The Very Large Telescope Interferometer (VLTI) is an interferometric facility, located at the top of the Cerra Paranal, in the Atacama desert in Chile (Fig 2.5). It is composed of 4 Unitary Telescopes (UT) of 8.2m diameter, and 4 Auxiliary Telescopes (AT) with 1.8m diameter. Contrarily to the UTs, the ATs can be punctually moved on different stations, in order to target specific spatial frequency of the (u,v)-plane. After having been collected by the telescopes, the light is guided through tunnels, where the delay compensation is performed at the level of *optical delay lines* (6 available delay lines at VLTI). These delay lines, composed of curved mirror transported on moveable carriage, require a few tens of nanometer precision and are continuously moving to compensate for sky rotation. At the output of the delay lines, 3 different interferometric instruments are located in the VLTI laboratory, and can be chosen to recombine four ATs our four UTs. At the time of writing, 3 instruments are available at VLTI : PIONIER instrument in H band (Le Bouquin et al., 2011), GRAVITY in K band (Gravity Collaboration et al., 2017) and MATISSE which covers L-M-N band (Lopez et al., 2014).

The measurement over a large number of telescopes translates in an increasing combination complexity, as the number baselines to be measured is proportional to the square of the number of telescopes[5]. At the time of writing, the maximum number of telescopes combined in the infrared is 4 at VLTI, and 6 at the CHARA observatory (Center for High Angular Resolution) on the Mount Wilson.

2.3.2 Heterodyne interferometry

Heterodyne detection

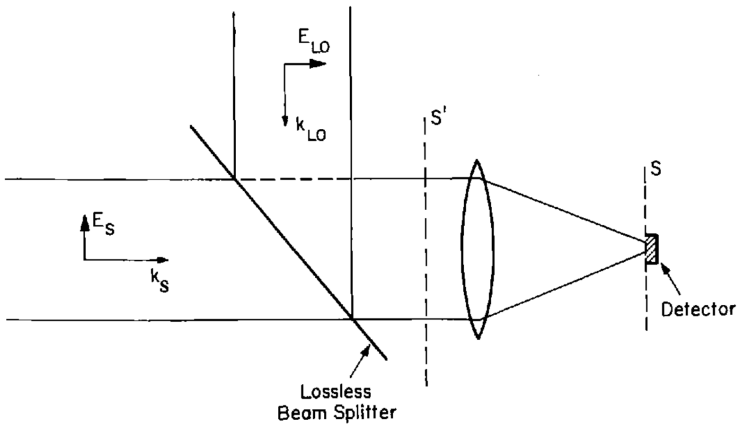

Fig. 2.6: Schematic of a infrared heterodyne detection (from (Kingston, 1978)).

[5]This is not true in the case of *direct imager*, which proposes to form directly an image of the object through the interferometer. This supposes the simultaneous cophasing of the whole array, which has not yet been demonstrated for the moment.

The heterodyne scheme relies on a different paradigma compared to amplitude interferometry. At the level of each telescope, the electric field of the incident astronomical signal is directly measured by the use of a *coherent* or so-called *heterodyne detection*. Heterodyne detection consists in the mixing on a diode of a very pure monochromatic signal with pulsation ω_{LO} - the *local oscillator* - and the astronomical field, as shown on Fig 2.6. Assuming a monochromatic astronomical signal $E_s(t) = E_s e^{i(\omega_s t+\phi)}$ for the sake of simplicity, the resulting detected intensity is :

$$s(t) = \left|E_{\rm OL}(t) + E_s(t)\right|^2 \tag{2.14}$$

$$= |E_{\rm OL}|^2+|E_s|^2+2|E_{\rm OL}||E_s|\cos\Big((\omega_s-\omega_{LO})t+\phi\Big) \quad = i_{\rm OL}+i_s+2\sqrt{i_{\rm OL}i_s}\cos\Big((\omega_s-\omega_{LO})t+\phi\Big) \tag{2.15}$$

with $i_{\rm LO}$ the detected photocurrent of the LO, and $i_{\rm s}$ the photocurrent of the signal. The beating signal at the output of the mixer is an RF signal which is a down-converted version of the incident astronomical field : its frequency is equal to the frequency difference of the field and the local oscillator, its phase is equal to the phase difference of the astronomical signal and of the local oscillator, and its amplitude is proportional to the amplitude of the astronomical field. This detection scheme is thus sensitive to the electric field of the astronomical signal : this is a *coherent detection* scheme. As the incident field is down-converted in the radio-frequency (RF) domain, the total bandwidth on which is detected is given by the RF bandwidth of the photodiode, hence requiring wideband detectors[6].

Heterodyne interferometry

The heterodyne signals at the level of each telescope are sensitive to the electric field $E(r,t)$ of the astronomical object. As a consequence, the degree of spatial coherence can be extracted by integrating in time the multiplication product of the RF heterodyne signal :

$$\langle s_1(t)s_2(t)\rangle \propto \langle E(\mathbf{r},t)E(\mathbf{r}+\lambda\mathbf{f},t\rangle \tag{2.16}$$

This operation is done at the level of a correlator, whose role is to extract the degree of coherence of the object. The relation Eq 2.16 is in fact a bit simplistic[7] : the exact derivation of the correlation signal will be detailed given in more details in Sec 2.4.

As the incident signal is converted in the RF domain, the delay compensation can be performed in the RF domain, or even a posteriori by registering the RF signals and processing them afterwards, as it is done in Very Long Baseline interferometry (VLBI). In the correlation process, the *relative* phase of the local oscillator has to remain stable in time, as the phase of the heterodyne signal measures the phase difference of the astronomical signal with the

[6] As an example, the total bandwidth of a 1 GHz photodiode observing a radiation at $10\,\mu$m (30 THz) is equivalent to a spectral channel with a spectral resolution $R = 30\,\mathrm{THz}/1\,\mathrm{GHz} = 30\,000$

[7] The beating signal described in Eq 2.16 essentially measures one quadrature of the field, rather than the complete electric field.

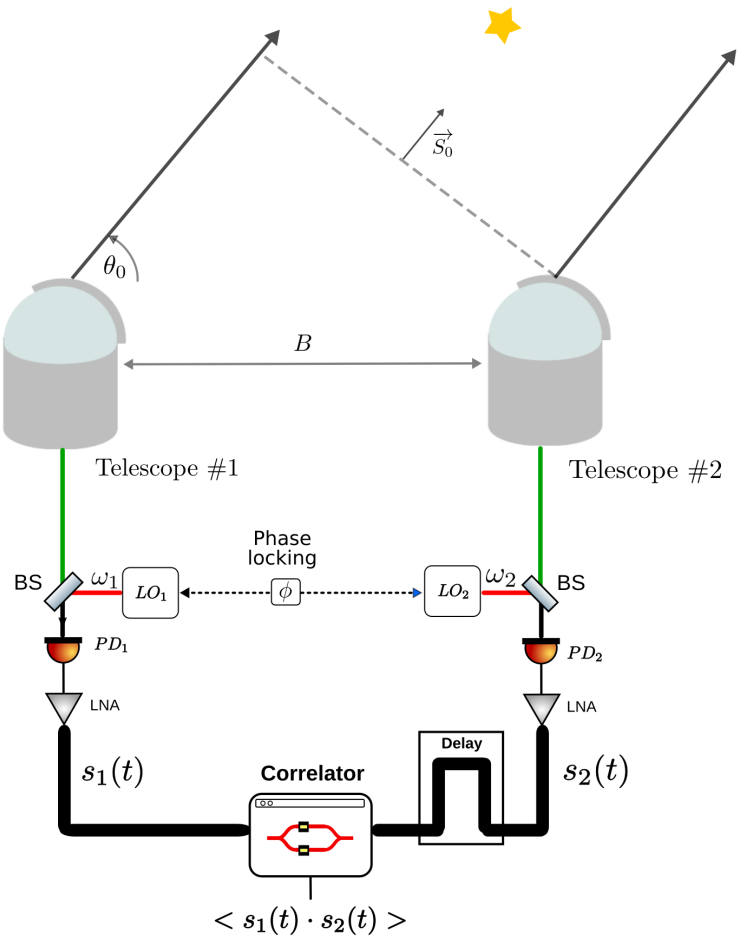

Fig. 2.7: General layout of a two element infrared heterodyne interferometer.

phase of the local oscillator. This requires a relative *phase-locking* of the local-oscillator, which is achieved by dedicated stabilization loop (see Sec 2.3.3).

The general layout describing a heterodyne interferometer is shown in Fig. 2.7 . In the next section, we show how this scheme was implemented in practice in the mid-infrared, in particular on the Infrared Spatial Interferometer.

2.3.3 Implementation of infrared heterodyne interferometer

The first demonstrations of infrared heterodyne interferometry go back to early 70s (J. Gay et al., 1973; M A Johnson, Betz, and C H Townes, 1974), and were initiated simultaneously in two separate groups, in France with Jean Gay at Calern observatory (Soirdété, now C2PU, J. Gay and Journet, 1975), and in the USA in Pr. C.H.Townes' group at UC Berkeley on the Infrared Spatial Interferometer (ISI) (M A Johnson, Betz, and C H Townes, 1974; C. H. Townes, 1984)[8]. Different technological hurdles limited the development of this scheme in

[8]We also note that in the same period, single dish mid-infrared heterodyne spectroscopy provides important results in the field of spectroscopic study of planetary atmosphere (De Graauw and Van De Stadt, 1973; Kaeufl,

J.Gay's group, which progressively abandoned this technological path, despite early on-sky demonstrations at $10.6\,\mu\mathrm{m}$ on the Sun (Gay and Rabbia, 2014).

The Infrared Spatial Interferometer (ISI)

The ISI provides one of the first astronomical interferometers operating in the infrared. The ISI was an interferometric array combining up to 3 telescopes at a wavelength $\lambda = 11\,\mu\mathrm{m}$, which observed routinely during more than ten years from the early 90s at Mount Wilson. Despite clear sensitivity limitations (50 - 100 Jy in one hour incoherent integration time), the ISI was scientifically productive throughout all its existence, primarily focusing on the study of massive evolved stars. It was also the first interferometer observing in the N band (C. H. Townes and Sutton, 1981), and also the first instrument to measure closure phase in this wavelength range (David D. S. Hale et al., 2003). In the following, we give a brief description of the ISI system, which was an essential inspiration of the work presented in this thesis.

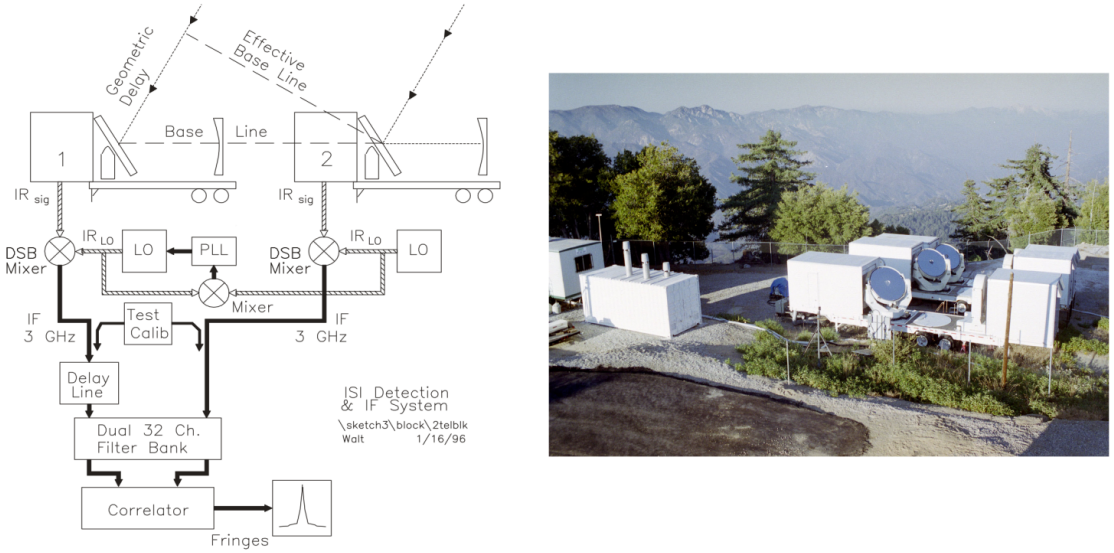

Fig. 2.8: *Left :* Simplified block diagram of the Infrared Spatial Interferometer (ISI, figure from **Danchi2002**). *Right :* ISI on the Mt Wilson : the periscopes from which the local-oscillators are launched are visible on the left.

The essential features of the architecture of the ISI could be listed as follows and are summarized in the block diagram of 2.8. We also refer the reader to a detailed description of the system in (D. D. S. Hale et al., 2000).

- *telescopes :* the array was composed of 3 siderostats with 1.65m diameter which could be moved (mounted on trucks), so that the array was easily re-configurable.

1984), in particular providing the first evidence of natural laser gain emission in the CO2 atmosphere of Mars (Mumma et al., 1981). We will not focus on these applications in spectroscopy in the rest of this thesis.

- *local oscillator :* a CO2 laser was located at each telescope to serve as a local oscillator. CO2 lasers were chosen for their very high stability and very high power. In order to act as a coherent array, the relative phase of the local oscillators were locked together. To do so, part of the local oscillator were sent through periscope and interfered on a detector : the beating term was then locked on a stable frequency reference at 1 MHz (quartz oscillator) and fed a phase locked loop (PLL) acting on the cavity of the lasers. This scheme supposed a phase stabilization of the link on which were propagated the CO2 laser : this stabilization was ensured by a dedicated metrology with He-Ne lasers. Importantly, the exact frequencies of the CO2 lasers differ by exactly 1 MHz, a feature which will be used later in the fringe encoding.

- *detectors :* the detectors were MCT detectors (HgCdTe photodiode) whose bandwidth and IF circuitry were sensitive on 0.2 - 2.8 GHz. Both sidebands of the system were detected (double sideband correlation, see below)

- *correlators :* the initial implementation was an analog correlator based on a wideband RF components and a hybrid mixer ("magic T"). This early correlator enables to extract the correlation product, integrated over the whole detection bandwidth of the photodiodes (see Chap 6 for a more detailed discussion on ISI's analog correlator). In a later version, this correlator was later equipped with a filterbank module (John David Monnier, 1999), in order to perform high-resolution spectroscopy. More recently, FPGA-based correlator (3 GHz bandwidth, 63 channels) were under development.

2.4 Heterodyne interferometry : correlation and interferometric signal

We describe the correlation of the signals of a heterodyne interferometer. This description is largely based on the introduction given in Thompson, Moran, and Swenson, 2017 and in John David Monnier, 1999.

The signal detected at the level of each telescope is the result of the down-conversion of the astronomical signal through a heterodyne detection. In the most general way, the heterodyne signal detected at the level of each telescope, originating from an angular direction θ with central mid-infrared frequency (or angular frequency ω_s), can be written :

$$\begin{cases} s_1(t) &= g_1 \cdot E_{\mathrm{LO},1} \left(E_s(\theta, \omega_s) e^{i\Phi_1(\theta,\omega_s,t)} + \mathrm{c.c.} \right) \\ s_2(t) &= g_2 \cdot E_{\mathrm{LO},2} \left(E_s(\theta, \omega_s) e^{i\Phi_2(\theta,\omega_s,t)} + \mathrm{c.c.} \right) \end{cases} \tag{2.17}$$

with g_k the total complex gain of the detection chain at telescope k (including the quantum efficiency of the detector), $E_{\mathrm{LO,k}}$ the amplitude of the LO field (real scalar), $E_s(\theta, \omega_s)$ the astronomical field (real scalar), $\Phi_k(\theta, \omega_s, t)$ the phase of the down-converted signal at the entrance of the correlator, and c.c. the abbreviation of complex conjugate.

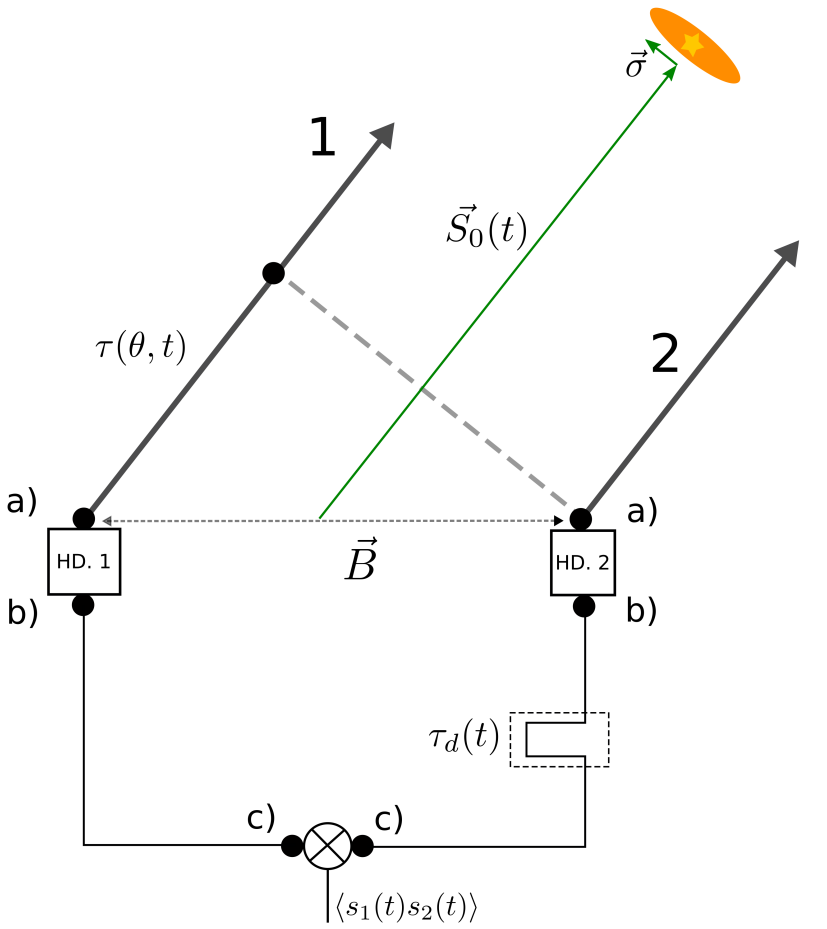

Fig. 2.9: Simplified schematic of the propagation of signals in a heterodyne interferometer, inspired from Thompson, Moran, and Swenson, 2017. The different points a), b) and c) are used in the calculation of the phase in the text. HD: Heterodyne Detection, see the text for the definition of $\tau(\theta,t)$ and $\tau_d(t)$.

The phase difference $\Phi_k(t)$ takes into account the frequency and the phase of the signal after the down-conversion in the heterodyne detection, as well as the different delays introduced along its path, due both to the elevation of the object in the sky and additional delays in the instrumental chain. We describe this phase along the path of the interferometer, which is a fundamental step in order then to describe the correlation of the signals.

Phase of the interferometric signals

The path of the interferometric signals, introduced in Fig. 2.7, is reproduced in a simple fashion in Fig. 2.9 for the sake of clarity. The phase at the different steps of the interferometer are the following:

(a) *Propagation:* the phase of the incident astronomical signal at telescope 1 is the phase of the astronomical signal $\omega_S t$, shared with telescope 2, delayed in time $t \rightarrow t - \tau(\theta,t)$, with $\tau(\theta,t)$ the geometrical delay associated to the position of the object in sky. The

phases of the electromagnetic field right before the heterodyne detection at the level of each telescope is thus:

$$\begin{cases} \Phi_{1,a}(\theta,\omega_s,t) & = \omega_s(t-\tau(\theta,t)) \\ \Phi_{2,a}(\theta,\omega_s,t) & = \omega_s t \end{cases}$$

(b) *Heterodyne detection:* the signal is then detected at the level of each telescope by an heterodyne detection, which down-converts the incident infrared signal in the RF domain. Writing the instantaneous phase of each LO as $\omega_{\mathrm{LO,k}}t + \phi_{\mathrm{k}}$, and based on the previous description of a heterodyne detection in Sec 2.3.2, the phase in each interferometric channel becomes :

$$\begin{cases} \Phi_{1,b}(\theta,\omega_s,t) & = \omega_s\Big(t-\tau(\theta,t)\Big) - \Big(\omega_{\mathrm{LO},1}t+\phi_1\Big) \\ & = (\omega_s-\omega_{\mathrm{LO},1})t - \omega_s\tau(\theta,t) - \phi_1 \\ \Phi_{2,b}(\theta,\omega_s,t) & = \omega_s t - \Big(\omega_{\mathrm{LO},2}t+\phi_2\Big) \\ & = (\omega_s-\omega_{\mathrm{LO},2})t - \phi_2 \end{cases}$$

(c) *Instrumental delay:* in order to compensate[9] for the delay due to the elevation of the object in sky, a relative delay $\tau_d(t)$ is introduced in channel 2, which results in a change of $t \to t-\tau_d$ in channel 2:

$$\begin{cases} \Phi_{1,c}(\theta,\omega_s,t) & = (\omega_s-\omega_{\mathrm{LO},1})t - \omega_s\tau(\theta,t) - \phi_1 \\ \Phi_{2,c}(\theta,\omega_s,t) & = (\omega_s-\omega_{\mathrm{LO},2})\Big(t-\tau_d(t)\Big) - \phi_2 \end{cases} \tag{2.18}$$

The geometrical delay $\tau(\theta,t)$ is related to the position of the object in sky. It can be described by introducing $\vec{S}_0$, which locates the center of the interferometric field of view, and the vector $\vec{\sigma}$ which corresponds to the angular position relative to the center of this field of view, see Fig. 2.9. The phase associated to this phase delay is:

$$\begin{aligned} \omega_s\tau(\theta,t) &= \omega_s\frac{\vec{B}}{c}\Big(\vec{S}_0(t)+\vec{\sigma}\Big) \\ &= \underbrace{\omega_s\frac{\vec{B}}{c}\vec{S}_0(t)}_{\omega_s\tau_B(t)} + \underbrace{\omega_s\frac{\vec{B}}{c}\vec{\sigma}}_{\phi(\theta,\omega_s)} \end{aligned} \tag{2.19}$$

with $\tau_B(t)$ the main delay associated to elevation of the object in the sky (i.e. the delay associated to the center of the field of view $\vec{S}_0$), and $\phi(\theta,\omega_s)$ the astrophysical phase of the object, which will enter into account when describing the spatial coherence of light (see later, Eq. 2.27).

[9] In other words, in order to match the coherence length of detected signal, as detailed in Eq.2.28 in "Correlation Signal".

Finally, the frequency at which the incident signal is downconverted is usually called the intermediate frequency (IF) (Thompson, Moran, and Swenson, 2017), written $\omega_{\rm if}$, which verifies the relation :

$$\omega_s = \omega_{\rm LO} \pm \omega_{\rm if} \tag{2.20}$$

The $\pm$ refers to the two possible incident optical frequency which can be folded on the same intermediate frequency $\omega_{\rm if}$ in the RF domain. The higher and lower frequency refer to the Upper-Sideband (USB) and the Lower Sideband (LSB) respectively.

Correlation product

The correlator performs the multiplication product of the heterodyne signals. For one incident frequency ω_s of the intermediate frequency bandwidth and one angular direction θ in the interferometric field of view, this product is written :

$$\langle s_1(t) s_2(t) \rangle_{\omega_s,\theta} \propto \left(g_1 g_2^* |E_s(\omega_s,\theta)|^2 e^{i[\Phi_1(\theta,\omega_s,t) - \Phi_2(\theta,\omega_s,t)]} + \text{c.c.} \right) \tag{2.21}$$

where here the sum terms $\Phi_1(t) + \Phi_2(t)$ vanished in the integration by the detector.

Based on the previous Eq 2.18, we can compute the phase difference of the phase of each interferometric channels :

$$\begin{aligned}
\Phi_1(\theta,\omega_s,t) - \Phi_2(\theta,\omega_s,t) &= (\omega_s - \omega_{\rm LO,1})t - (\omega_s - \omega_{\rm LO,2})(t - \tau_d(t)) - \omega_s \tau(\theta,t) - (\phi_1 - \phi_2) \\
&= \Big[(\omega_s - \omega_{\rm LO,1})t - (\omega_s - \omega_{\rm LO,2})t \Big] + (\omega_s - \omega_{\rm LO,2})\tau_d(t) - \omega_s \tau(\theta,t) - (\phi_1 - \phi_2) \\
&= (\omega_{\rm LO,2} - \omega_{\rm LO,1})t + (\omega_s - \omega_{\rm LO,2})\tau_d(t) - \omega_s \tau(\theta,t) - (\phi_1 - \phi_2) \\
&= (\omega_{\rm LO,2} - \omega_{\rm LO,1})t - \omega_s(\tau(\theta,t) - \tau_d(t)) - \omega_{\rm LO,2}\tau_d(t) - (\phi_1 - \phi_2)
\end{aligned} \tag{2.22}$$

By using the expression of $\tau(\theta,t)$ in Eq.2.19 and the definition of the intermediate frequency Eq. 2.20, the terms related to the delays can be re-written:

$$\begin{aligned}
-\omega_s(\tau(\theta,t) - \tau_d(t)) - \omega_{\rm LO,2}\tau_d(t) &= -(\omega_{\rm LO,2} \pm \omega_{\rm if})(\tau_B(t) - \tau_d(t)) - \phi(\theta,\omega_s) - \omega_{\rm LO,2}\tau_d(t) \\
&= \mp\omega_{\rm if}(\tau_B(t) - \tau_d(t)) - \phi(\theta,\omega_s) - \omega_{\rm LO,2}\tau_B(t)
\end{aligned} \tag{2.23}$$

By summarizing the different terms, the final phase difference is :

$$\begin{aligned}
\Phi_1 - \Phi_2 &= \underbrace{(\omega_{\rm LO,2} - \omega_{\rm LO,1})t}_{\substack{\text{Frequency difference} \\ \text{of LOs : } \Delta\omega_{21}}} \mp \omega_{\rm if} \underbrace{(\tau_B(t) - \tau_d(t))}_{\substack{\text{Delay difference} \\ \Delta\tau(t)}} - \underbrace{\phi(\theta,\omega_s)}_{\substack{\text{Astrophysical} \\ \text{Phase}}} - \underbrace{\omega_{\rm LO,2}\tau_B(t)}_{\substack{\text{Natural} \\ \text{Fringe Frequency}}} + \underbrace{(\phi_2 - \phi_1)}_{\substack{\text{Phase difference of LOs} \\ \Delta\phi_{21}}} \\
&= \Delta\omega_{21}t \mp \omega_{\rm if}\Delta\tau(t) - \phi(\theta,\omega_s) - \omega_{\rm LO,2}\tau_B(t) + \Delta\phi_{21}
\end{aligned} \tag{2.24}$$

At the level of the correlator, the correlation product Eq. 2.21 is then integrated over all the angular directions θ as well as all the frequencies ω_s :

$$\langle s_1(t)s_2(t)\rangle \propto \int_{\omega_{\rm IF}}\int_{\theta}\langle s_1(t)s_2(t)\rangle_{\theta,\omega_s}\ \mathrm{d}\theta\mathrm{d}\omega_{\rm IF} \tag{2.25}$$

$$\propto \int_{\omega_{\rm IF}}\int_{\theta}\left(g_1 g_2^*|E_s(\theta,\omega_s)|^2 e^{i[\Phi_1(\theta,\omega_s,t)-\Phi_2(\theta,\omega_s,t)]}\right.\ \mathrm{d}\theta\mathrm{d}\omega_{\rm IF} \tag{2.26}$$

We can identify the complex coherent flux $F_c(B/\lambda,\omega_s)$ from the integration over all the angular directions (Zernike van-Cittert theorem) :

$$|F_c(B/\lambda,\omega_s)|e^{i\phi_{\rm V}(B/\lambda,\omega_s)} = \int_{\theta}|E_s(\theta,\omega_s)|^2 e^{-i\phi(\theta,\omega_s)}\ \mathrm{d}\theta \tag{2.27}$$

Using this expression of the coherent flux, and isolating the terms related to $\omega_{\rm IF}$ in order to perform the integration :

$$\langle s_1(t)s_2(t)\rangle \propto \int_{\omega_{\rm IF}}\left(g_1 g_2^*|F_c(B/\lambda,\omega_s)|e^{i\phi_{\rm V}(B/\lambda,\omega_s)}e^{\mp i\omega_{\rm if}\Delta\tau(t)}e^{i[\Delta\omega_{21}t+\Delta\phi_{21}-\omega_{{\rm LO},2}\tau_B(t)]}+\text{c.c.}\right)\mathrm{d}\omega_{\rm IF} \tag{2.28}$$

The signal is then integrated over the full RF bandwidth. The complex gains g_1 and g_2 of the instrumental chain can in fact depend on $\omega_{\rm if}$, which can also be included in the total response of the chain. The total complex gain averaged over the bandwidth is (Thompson, Moran, and Swenson, 2017; John David Monnier, 1999) :

$$|G(\Delta\tau(t))|e^{i\phi_G}e^{\pm i\omega_c\Delta\tau(t)} = \int_{\omega_{\rm IF}} g_1(\omega_{\rm IF})g_2^*(\omega_{\rm IF})e^{-(\mp i\omega_{\rm IF}\Delta\tau(t))}\ \mathrm{d}\omega_{\rm IF}$$

where we have written ω_c the central angular frequency of the detection bandwidth. We note that this terms is maximal when the delay difference is perfectly matched in the interferometer $\Delta\tau = 0$ (maximization of the contrast associated to the temporal coherence of the signal).

Finally, the expression of the correlation product integrated over the total bandwidth is :

$$\langle s_1(t)s_2(t)\rangle \propto |G(\Delta\tau(t))|\cdot|F_c(B/\lambda,\omega_s)|e^{i\phi_{\rm V}(B,\omega_s)}e^{i\phi_{\rm G}}e^{\pm i\omega_c\Delta\tau(t)} \tag{2.29}$$

$$\times\, e^{i[\Delta\omega_{21}t+\Delta\phi_{21}-\omega_{{\rm LO},2}\tau_B(t)]} + \text{c.c.} \tag{2.30}$$

In the following, this expression will give the basis to describe the output of the correlator.

Fringe frequency & lobe rotation

The frequency of the fringes at the output of the correlator is related to the time-varying terms in Eq. 2.24, which includes different contributions:

- the frequency difference of the local oscillators $\Delta\omega_{21}t$
- the term $\omega_{{\rm LO},2}\tau_B(t)$, which varies in time as the source crosses the sky, and is denominated the *natural fringe frequency*.

- the phase difference of the LOs $\Delta\phi_{21}(t)$: in practice, this phase difference is indeed time-varying (intrisic phase fluctuations of the laser, relative path difference fluctuations between each LO, etc.), compared to the ideal case introduced previously (constant phase: $\phi_2 - \phi_1$). In addition, the term related to the additional time delay introduced in the RF domain $\omega_c \Delta\tau(t)$ is also contributing to the total phase term: the goal however is to nullify this term in order to maximize the temporal coherence of the signal.

In this ensemble of terms, we can see that a small frequency difference between the mid-infrared LOs can compensate for the natural fringe frequency, an operation usually called *lobe rotation*. This operation is commonly implemented at the level of the correlator, as it was done on ISI, so that the fringes can be encoded at a given frequency. In the following, we will write f_{12} this frequency at which the fringes are encoded :

$$\Delta\omega_{21}t + \Delta\phi_{21}(t) - \omega_{\mathrm{LO},2}\tau_B(t) \pm \omega_c\Delta\tau(t) = 2\pi f_{12}t \tag{2.31}$$

As mentioned above, it can be seen from Eq 2.31 that the relative phase difference of the LOs has to be stable in time. This relative phase stabilization of the LOs is exactly the operation that we designate as the phase stabilization of the LOs. We note that $\Delta\Phi(t)$ has not necessarily to be set to zero, and can be locked on a frequency reference[10].

Single-sideband (SSB) correlation

The response of the correlator written in Eq 2.25 is :

$$\begin{aligned}\langle s_1(t)s_2(t)\rangle_{\mathrm{SSB}} = |F_c(B/\lambda,\omega_s)|\cdot|G(\Delta\tau(t))|\times \\ \cos\Big(2\pi f_{12}t + \omega_c\Delta\tau(t) + \phi_{\mathrm{V}}(B/\lambda,\omega_s) + \phi_G\Big)\end{aligned} \tag{2.32}$$

The expression Eq(2.32) represents the response of a correlator for a single sideband (upper or lower) separately, which provides the basis to describe the correlator response. In practice, these sidebands are not necessarily measured separately, which will require to introduce a distinction between single-sideband and double-sideband operation.

Double-sideband (DSB) correlation

In the case where the two signals are multiplied and integrated without additional operations, the upper- and the lower-sideband are added. In this case, the response of the correlator is :

$$\begin{aligned}\langle s_1(t)s_2(t)\rangle_{\mathrm{DSB}} &= |F_c(B/\lambda,\omega_s)|e^{i\phi_{\mathrm{V}}(B/\lambda,\omega_s)}e^{2i\pi f_{12}t}|G(\Delta\tau(t))| \\ &\quad\times\Big(e^{+i\phi_{\mathrm{G}}}e^{+i\omega_c\Delta\tau(t)} + e^{-i\phi_{\mathrm{G}}}e^{-i\omega_c\Delta\tau(t)}\Big) + \text{c.c.} \\ &= |F_c(B/\lambda,\omega_s)|\cdot|G(\Delta\tau(t))|\cos\Big(\omega_c\Delta\tau(t) + \phi_G\Big) \\ &\quad\cos\Big(2\pi f_{12}t + \phi_{\mathrm{V}}(B/\lambda,\omega_s)\Big)\end{aligned} \tag{2.33}$$

[10] This was the case on the ISI, where the $\Delta\phi(t)$ was compared with a 1 MHz reference (crystal oscillator) (D. D. S. Hale et al., 2000).

In the following, in particular in Chap 6 and Chap 7, most of the operations considered here will correspond to DSB operation.

Delay and sky rotation

Delay compensation
As written in Eq 2.19, the elevation of the object in sky introduces a relative delay between each telescopes, which is written :

$$\tau(t) = \frac{\vec{B}}{c} \cdot \vec{S_0} = \frac{B}{c} \cos(\theta_0(t)) \tag{2.34}$$

with $\theta_0(t)$ the elevation angle of the star above the horizon. This delay has to be compensated in order to observe fringes within the coherence length $c/\Delta\nu$. The minimum coherence length in the case of heterodyne detection is of the order of a cm (assuming $\Delta\nu = 30\,\mathrm{GHz}$), down to a few mm in the extreme case (assuming $\Delta\nu = 30\,\mathrm{GHz}$) : this is the advantage of narrow detection. In addition, this delay can be introduced after the detection stage, for example in the correlator.

Natural fringe frequency
As introduced in Eq. 2.31, and irrespective of the delay compensation $\tau_d(t)$ introduced at the level correlator, an additional term, the natural fringe frequency (see paragraph "Fringe frequency & lobe rotation"), also varies in time as the source crosses the sky [11]. The typical order of magnitude of the maximum rate of these fringes (when the object is at zenith), is given by John David Monnier, 1999 :

$$\nu_{FF} \leq \left(\frac{d}{100\,\mathrm{m}}\right)\left(\frac{\lambda}{10\,\mu\mathrm{m}}\right) \cdot 727\,\mathrm{kHz} \tag{2.35}$$

This relation gives the typical rate at which the fringes have to be corrected, as mentioned in Eq 2.31.

Atmospheric phase fluctuations

In the same way as for amplitude interferometry, atmosphere introduces relative phase fluctuations, which limits the coherent integration time and the sensitivity of the interferometer (see Sec 2.3.1). As for amplitude interferometry, the only way to correct it is to use a fringe-tracker. In Chap 4 ("Technological challenges"), we discuss the possible technological option in this perspective.

[11] Fundamentally, this term is due to the frequency difference between the optical signal, where the geometrical delay due to the elevation of the object in the sky occurs ($\omega_s \tau(t)$), and the frequency at which this delay is compensated for ($\omega_{\mathrm{if}} \tau_d(t)$). See calculations for the exact derivation.

2.5 Conclusion

Infrared interferometry is the only technique enabling the imaging of planetary environment with mas resolution in the mid-infrared. Its implementation requires the combination of a large number of telescopes, at high-contrast, with kilometric baselines. This problem represents a major open challenge of current astronomical instrumentation, which requires a profound reassessment of the architecture of infrared interferometer in this perspective, as proposed in the Planet Formation Imager initiative.

In this work, we propose to explore the application of heterodyne infrared interferometers to the recombination of a large number of telescopes and kilometric baselines in the mid-infrared (N band). Based on the initial proposition of (Swenson, 1986) and (Ireland and John D. Monnier, 2014), we propose to assess the feasibility of a renewed architecture of a heterodyne interferometer, based on the recent evolution of mid-infrared technologies in the field of detection, laser physics, and photonics. The reassessment of heterodyne interferometry in this perspective will be the object of Chap 4.

> *C'est entendre le ciel sans y monter jamais.*
>
> — **Marceline Desbordes-Valmore**
> Les Séparés

3

Temporal monitoring of FU Orionis with 20 years of near-infrared interferometry data

3.1 Introduction

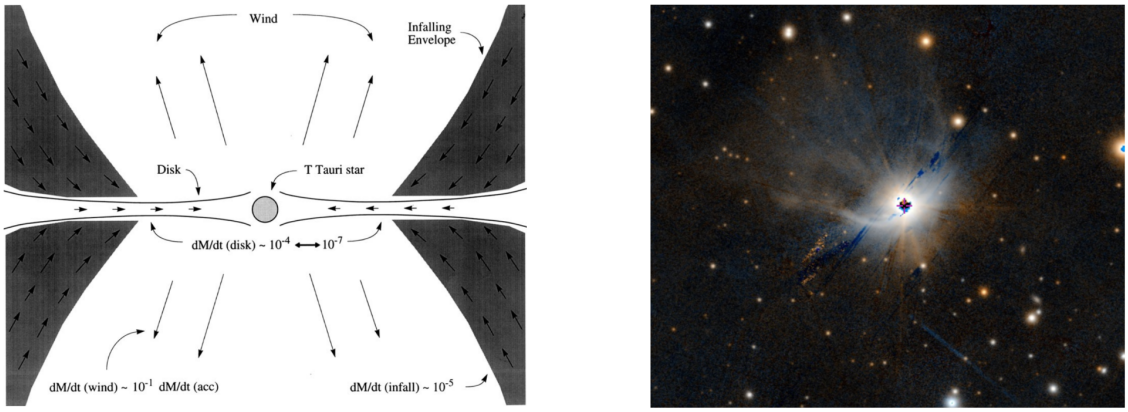

Fig. 3.1: *Left* : Classical picture of FU Orionis outburst, exctracted from (Lee Hartmann and Kenyon, 1996). *Right* : Optical image of FU Orionis at large spatial scales (PanSTARRS/DR1). The remnant of the infalling envelope in which FU Orionis is embedded is visible.

FU Orionis is a variable star, located at 450 parsec near the λ Orionis star forming region. It is the prototype of a small class of pre-main sequence (PMS) objects referred to as FU Ori objects (FUors). The main characteristic of FUors is to display an outburst of several magnitude at visible wavelengths over short timescales (1 year to 20 years typically), followed by a decay in luminosity over several decades, and more than 100 years in the case of FU Orionis (Lee Hartmann and Kenyon, 1996), as shown on Fig.3.2 . In our current understanding of the phenomenon, FU Orionis is composed of an accretion disk, outshining the star by several order of magnitudes, and is surrounded by the remnant of large infalling envelope, feeding the accretion disk, and extending up to hundreds of AU. The favoured explanation for the FUors outbursts is that the disk experiences a considerable rise in the accretion rate, from $10^{-10} - 10^{-7} \mathrm{M}_{\odot}.\mathrm{yr}^{-1}$, typical for a T Tauri star, to $10^{-4} \mathrm{M}_{\odot}.\mathrm{yr}^{-1}$ caused by a major instability within the disk, before returning to quiescence. As it is now clear that steady accretion rates deduced from T Tauri luminosity are not sufficient to build up a low-mass star over timescales of few million of years (Kenyon and L. W. Hartmann, 1990), it has been proposed that a large fraction of T Tauri stars must go through episodic accretion events, possibly several times during their early existence (N. Calvet, L. Hartmann, and S. E. Strom, 2000). FU Orionis may

thus represent a crucial stage of the process of star and disk formation, although the exact mechanism at the origin of this phenomenon still remains elusive.

In particular, the origin of the instability is still poorly understood. Bell and Lin, 1994 have proposed thermal instabilities (TI) very close to the central star ($\approx 0.1\,\mathrm{AU}$) to be the main cause of the disk overheat. Armitage, Livio, and Pringle, 2001, Zhu et al., 2009, Bae et al., 2014 make the case for a gravitational instability on the external parts of the disk that cause pile-up of material in the inner disk ($\approx 1-2\,\mathrm{AU}$), triggering massive Magneto-Rotational Instability and thus an accretion outburst (MRI-GI). In all theories, the return to quiescence corresponds to a state where the inner disk drains out and the physical conditions cannot longer sustain MRI, gravitational or thermal instabilities. We refer to Audard et al., 2014 for a complete review of the different scenarios for FU Orionis outbursts. This scenario was first supported by the presence of an infrared excess which can be modeled by a simple steady accretion disk in FU Orionis. In addition, spectroscopic features are well explained by a keplerian disk in rotation, in particular double-peaked line profiles, rotationally broadened CO bands, and increasing line broadening at shorter wavelength, probing inner regions of the disk with larger rotation velocity (Lee Hartmann and Kenyon, 1996).

The only technique able to spatially resolve the inner AU (<2 mas) of FU Orionis, where the outburst takes place, is near-infrared interferometry. As a relatively bright object in the near-infrared, FU Orionis has been a prime target of interferometry, and was the first YSO to be spatially resolved (F. Malbet et al., 1998), which gave a direct evidence of the presence of an accretion disk. The initial study by F. Malbet et al., 1998 was then confirmed and refined in F. Malbet et al., 2005, which provided a first estimation of the temperature profile of the disk, and explored the potential detection of an embedded hot spot. This estimation was recently complemented by Labdon et al., 2020, based in particular on J-band interferometric data on CHARA/MIRC-X, which confirmed the $T \propto r^{-3/4}$ temperature profile expected in the case of a standard accretion disk. In addition, the presence of an extended flux as a general features of FUors in interferometric data, corresponding to the remnant of the infalling envelope, was first revealed by R. Millan-Gabet et al., 2006 on a sample of three FUors. The properties of the dusty envelope of FU Orionis itself was examined in the mid-infrared by Quanz et al., 2006, and more recently by Liu et al., 2019 through ALMA and GRAVITY data, both of which inferred the presence of a cold envelope. However, at this time, none of these interferometric studies specifically focused on identifying the origin of the disk instability.

In this study, we propose to take advantage of more than 20 years of interferometric observations to perform a temporal monitoring of the outbursting region of FU Orionis. The goal of this work is to measure the typical size of the outbursting region of the disk and to put constrain on its variation of size in time. We compare these observations with the numerical simulations of a disk obtained with pure TI and MRI-GI models in order to distinguish between these different scenarios, and to add constrain on the value of the physical parameters of instability.

Section 3.2 describes the data set used in our study. The global geometrical modeling of FU Orionis, as well as the methodology used to analyze our data sample is presented in

Section 3.3. The results of this analysis are presented in Section 3.4. Finally, in Section 3.5, we compare these results with MHD simulation of FU Orionis outburst, and we discuss the implications of these observations on the origin of the instability mechanism at play in FU Orionis.

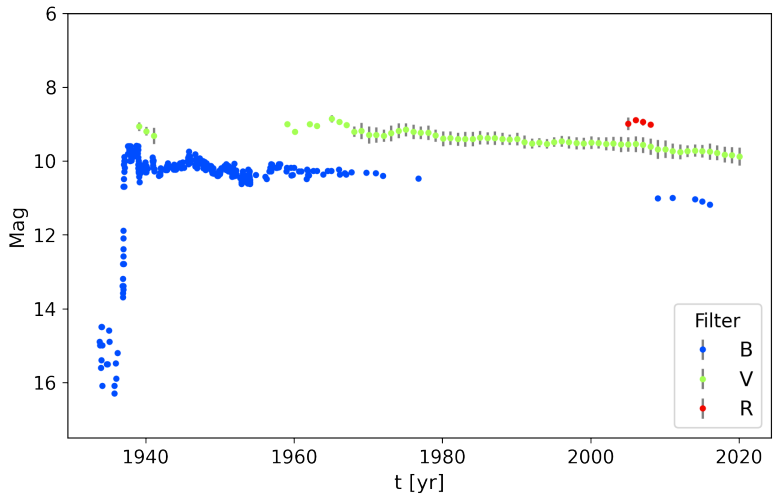

Fig. 3.2: Lightcurve of FU Orionis, extracted from G. H. Herbig, 1977 and AAVSO database (https://www.aavso.org).

3.2 Observations

We based our analysis on three classes of data : archival data, dedicated observing programs on VLTI/PIONIER and GRAVITY, and additional archival data, for which data reduction has been redone. Given the heterogeneity of the dataset, a specific emphasis was put on the examination of the data quality, in order to identify potential sources of bias for each observation. The different information relative to the data as well as the acronym by which they will be designated in the following are provided in Tab.3.1.

3.2.1 Interferometric archival data

The majority of the archival data originates from the legacy study of F. Malbet et al., 2005. This dataset is essentially based on IOTA and PTI observations. These observations were carried between 1998 and 2003, which enables to add valuable constraints on the longer time scale in this study. These observations consist in 2 apertures observations, at low spectral resolution in H and K band. IOTA and PTI observations cover complementary spatial scales (respectively small baselines $\sim 30\,\mathrm{m}$ and large baselines $\sim 120\,\mathrm{m}$). These observations were initially gathered as a unique temporal point in the original study of F. Malbet et al., 2005, in order to obtain the most complete coverage of the (u,v)-plane. In the present study, we have chosen to separate temporally the PTI observations for each year, and when IOTA data were available, to gather them with PTI data of the closest year in order to benefit

Date	Instrument	Acronym	Telescopes	Stations	Filter	$R = \lambda/\Delta\lambda$	Data	Flag
2019/10/03	MIRC-X	MIRCX19	5	S1-S2-E1-W1-W2	H	50	(Labdon et al., 2020)	
2019/02/20	PIONIER	PION19	4	A0-G1-J2-J3	H	30	**ESO ID : 2102.C-5036** (PI : Bourdarot) *data reduced*	
2018/11/27	MIRC-X	MIRCX18	6	S1-S2-E1-E2-W1-W2	H	50	(Labdon et al., 2020)	
2017/12/25	PIONIER	PION17	4	D0-G2-J3-K0	H	5	ESO archive (PI : Garcia-Lopez) *data reduced*	dome-seeing effect ?
2010/12/03	PIONIER	PION10	4	E0-G0-H0-I1	H	5	Commissioning data *data reduced*	
1999/11/23 to 1999/12/01	PTI	IOTA+PTI	2	NS	H	5	(F. Malbet et al., 2005)	
1998/12/13 to 1998/12/26	IOTA	IOTA+PTI	2	S15-N15, S15-N35	H	5	(F. Malbet et al., 2005)	
2021-01-09	GRAVITY-SCI	GRAVI21	3	U1-U3-U4	K	4000	**ESO ID : 106.212G.004** (PI : Perraut) *data reduced*	Problem on U2
2017-02-02	GRAVITY-FT	GRAVI17	4	A0-G1-J2-K0	K	20	ESO archive (PI : Garcia-Lopez) *data reduced*	large phase shift during acquisition
2016-11-25	GRAVITY-SCI	GRAVI16	4	K0-G2-D0-J3	K	500	Commissioning data *data reduced*	
2011-10-27	CLIMB	CLIMB11	3	S2-E2-W2	K	5	(Labdon et al., 2020)	
2010-11-30	CLIMB	CLIMB10	3	S1-E1-W1	K	5	(Labdon et al., 2020)	large dispersion, discrepancy with CLIMB2011 at high spat. scales
2003/11/19 to 2003/11/27	PTI	PTI03	2	NS, SW	K	5	(F. Malbet et al., 2005)	
2002/10/28	VINCI	VINCI02	2	UT1-UT3	K	5	(F. Malbet et al., 2005) (PI : F.Malbet) *data reduced*	
2000/11/18 to 2000/11/27	PTI	PTI00	2	NS, NW	K	5	(F. Malbet et al., 2005)	
1999/11/23 to 1999/12/01	PTI	PTI99	2	NS	K	5	(F. Malbet et al., 2005)	
1998/11/14 to 1998/11/27	PTI	IOTA+PTI	2	NS	K	5	(F. Malbet et al., 2005)	
1998/12/13 to 1998/12/26	IOTA	IOTA+PTI	2	S15-N15, S15-N35	K	5	(F. Malbet et al., 2005)	

Tab. 3.1: Logs of FU Orionis interferometric observations in H and K Band. The data for which the data-reduction was done in this study are indicated with '*data reduced*'.

simultaneously from constrain on small and high spatial scales. Given the specific format of these observations, the reduced data included in this analysis were provided by Regis Lachaume (private communication).

In addition to IOTA and PTI observations, we have included CHARA/CLIMB observations (PI : R.Millan-Gabet) which were conducted on 2 nights on 2010-11-30 and 2011-10-27. Due to the larger number of telescopes and the larger baselines, these observations offer a more complete sampling of the (u,v)-plane in a single observation. In the case of CLIMB10 data, a large dispersion can be seen in the visibility data, as well as a significant discrepancy at high spatial scales (low visibilities) for the same baselines with respecti to CLIMB11 data. We will keep CLIMB10 and CLIMB11 in our sample in the following, as they enable to constrain the disk around year 2010 in the K band, however a higher level of confidence will be given

on CLIMB11 in the analysis given its lower dispersion in visibility data. These observations were provided by A.Labdon and S.Kraus (private communication), and were reduced using J.D.Monnier's pipeline at University of Michigan.

Finally, we also include two CHARA/MIRCX observations, conducted on 2018-11-27 and 2019-10-03, and initially published in Labdon et al., 2020. The data were reduced and provided by A.Labdon and S.Kraus (private communication) using the MIRC-X standard reduction pipeline [1].

3.2.2 Dedicated interferometric observing programs

In order to add two contemporary reference observations in H and K band respectively, we performed two dedicated observations of FU Orionis on PIONIER and GRAVITY instruments on VLTI.

The PIONIER observation was obtained through a specific DDT proposal awarded in winter 2019 (PI:Bourdarot), which was conducted on night 2019-02-20 (ESO run 2102.C-5036). PIONIER observation with large configuration on the 1.8m Auxiliary Telescopes (ATs) was specifically chosen in order to reach the highest angular resolution and to obtain the most complete (u,v)-coverage on VLTI. Data were reduced using the standard `pndrs` pipeline (Le Bouquin et al., 2011) and exhibit a low statistical dispersion. GRAVITY observations were obtained on GTO time (ESO run 106.212G.004, PI:Perraut) on the 8.2m Unitary Telescopes (UTs) and reduced through the standard ESO pipeline. This dataset benefits from the exquisite low errorbars reached by the UTs, however the difference between AT and UT data is significantly higher than the errorbars of each dataset. This discrepancy is most likely originating from the different interferometric field of views (Perrin and J. Woillez, 2019), given the difference in terms of telescope diameter in each observations. This effect is made even more apparent given that FUors objects are embedded in large envelopes, which cover the whole field of view and contribute to a non-negligible fraction of the interferometric flux. This difference will be taken into account in the geometrical modeling of the interferometric visibility in Sec.3.3.

3.2.3 Data-reduction on archival data

We also include in our analysis different datasets for which it was possible to perform a new data reduction.

In the H band, two PIONIER observations were included. PION10 originates from commissioning observations, retrieved from the OIdB platform of the Jean-Marie Mariotti Center (JMMC) [2]. PIONIER 2017 data were retrieved from the publicly available ESO archive [3] (PI: Garcia-Lopez, ESO run ID 0100.C-0278(J)). We reduced both datasets using the standard

[1] https://gitlab.chara.gsu.edu/lebouquj/mircx_pipeline
[2] http://oidb.jmmc.fr
[3] http://archive.eso.org

pndrs pipeline (Le Bouquin et al., 2011). PION10 shows a relatively large dispersion, but visibility values consistent with other small baselines observations such as IOTA. On the contrary, relatively low data dispersion and small errorbars are seen on PION17 data, but with significantly higher visibility values than comparable PIONIER observations on ATs. Such high values in PION17 observation would correspond to an almost non-resolved object. A careful inspection of the calibrators did not show anomalies in the calibration procedure. However, intermediate products of the data reduction highlights strong phase variations during that night, which are likely to bias the visibility of the fringes. Surprisingly, these phase variations occur during particularly good seeing conditions <0.6". We postulate that these variations could originate from a dome-seeing effect, similar to the low-wind effect known on the UTs for high-contrast imaging (Milli et al., 2018), which would explain such degradation specifically in very good atmospheric conditions. To the best of our knowledge, this effect was not reported in previous interferometric observations. In the following, we analyse PION17 dataset but we caution that data may be biased (see Tab.3.1).

In the K band, three additional archival datasets were included. We reduced VINCI observation originally included in F. Malbet et al., 2005 using the standard vndrs pipeline (Kervella, D. Segransan, and Coude du Foresto, 2004). VINCI data were obtained on the UTs so that similar remarks concerning the difference of interferometric field of view apply here. We also reduce two GRAVITY datasets on the ATs. For both observations we used the fringe-tracker (FT) channel rather than scientific (SCI) channel of GRAVITY. In the case of GRAVI17, we used the fringe-tracker data only, due to insufficient SNR in the science channel in high-resolution mode ($R \approx 4000$). Concerning GRAVI2016, a careful inspection of the intermediate product of data reduction highlights large discrete phase fluctuations of the fringe tracker away from the zero Optical Path Differrence (OPD) reference. This perturbation potentially creates or amplify the chromatic dependency seen in the visibilities : this point is discussed in more details in Sec.3.4.

3.2.4 Spectral Energy Distribution

In order to complement our analysis, we also provide a recent SED of FU Orionis using Gaia DR2, DR3 and TESS photometric data. A particular attention has been drawn to gather data originating from a limited range of time (2015-2019) in order to avoid potential temporal variation. These data are summarized in Appendix in Tab.3.6 .

3.3 Methodology of the geometrical modeling and of the temporal analysis

In this section, we describe the geometrical modeling of FU Orionis and the fitting strategy used in our temporal analysis. The final goal of this analysis is an estimation of the full-width-at-half-maximum (fwhm) size of the emission as a function of time. In addition, given the heterogeneity of the dataset, particular attention is paid to provide a reliable estimation of

the statistical and systematics errors of the fwhm, in particular through a dedicated bootstrap analysis.

3.3.1 Geometrical modeling of FU Orionis

In order to introduce the geometrical modeling of FU Orionis, we present one observation which exhibits the archetypal features of our sample, as shown on Fig.3.3. In the following, the different components of the model are described from the largest spatial scale (i.e. smallest spatial frequency) to the smallest spatial scales (highest spatial frequency). Three main components can be identified in the visibility : a fully resolved component, designated as the *extended envelope* ; a *resolved emission* ; and a central *unresolved component*. This model is in fact very similar to the picture deduced from NIR interferometric observations over a large sample of Herbig Ae/Be stars (Lazareff et al., 2017; Gravity Collaboration et al., 2019).

Extended envelope

FU Orionis is embedded in a large extended emission, also visible on high-contrast images at very large spatial scales (Takami et al., 2018). This emission corresponds to the large infalling envelope which feeds the disk in the classical picture of FUors (Lee Hartmann and Kenyon, 1996). In the case of interferometric observations, this extended flux fills the whole interferometric field of view, whose extension corresponds typically to the diffraction limit of one telescope (Perrin and J. Woillez, 2019), of the order of $250\,\mathrm{mas} \equiv 100\,\mathrm{AU}$ for an ATs in H band. Finally, in the visibility space, the extended component corresponds to a low spatial frequency object, fully resolved in our observations, which will be modeled as a dirac function with a certain amplitude f_e, centered on zero spatial frequency. In Fig 3.3, this component appears indeed as an apparent offset between the maximum of the resolved visibility and the $V^2 = 1$ visibility at null spatial frequency. Given the apparent spectral dependency visible in GRAVITY data, also reported in (Liu et al., 2019) with the same dataset, f_e will be modeled by a second order polynomial, with coefficients (f_0, f_1, f_2) (see Tab 3.2). The detailed of the visibility functions used in the models are given in Tab 3.2.

Resolved emission

The second component visible on the interferometric observations is a regularly decreasing visibility profile, whose extent is inversely proportional to the typical size of the emission zone. This component is marginally resolved on spatial frequencies $45\mathrm{M}\lambda \equiv 100\,\mathrm{m}$ in K band, and therefore will be modeled as a gaussian elongated disk $V_d(\alpha, \beta)$, with a the full-width-at-half-maximum (fwhm) of the gaussian, θ the position angle of the disk and i the inclination angle of the disk (cf Tab 3.2) . The coordinates (α, β) are expressed in the reference frame of

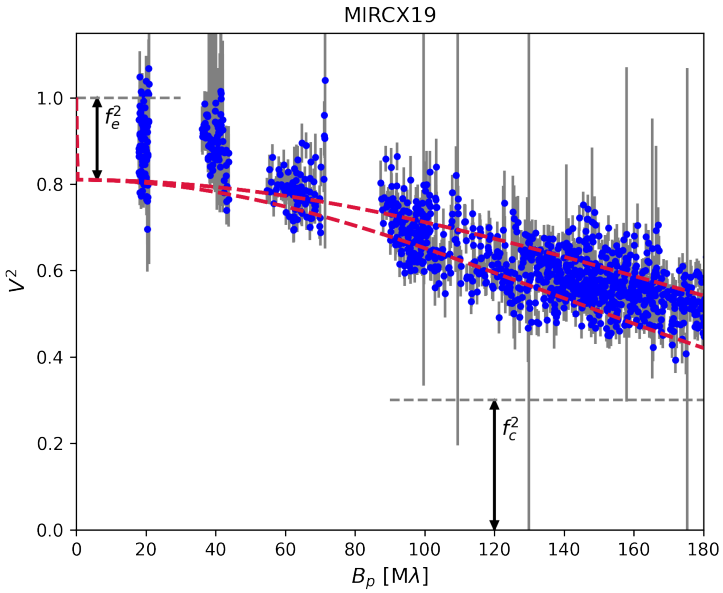

Fig. 3.3: Visibility squared as a function of the projected baseline, observed with MIRCX instrument in year 2019 (see logs Tab 3.1). Red dashed line shows the minor and major axis of the gaussian inner disk ; black solid lines and black arrows show the contribution of the compact flux f_c and of the over-resolved flux f_e.

the (u,v)-plane, following the description introduced in F. Malbet et al., 2005; J. P. Berger and Damien Segransan, 2007 :

$$\begin{cases} \alpha &= u\cos\theta - v\sin\theta \\ \beta &= \Big(u\cos\theta + v\sin\theta\Big)\cos i \end{cases} \tag{3.1}$$

In the geometrical model, this component will be designated as the *resolved emission*. In the common picture of FU Orionis, this resolved component is associated to the inner disk of the inner disk surrounding FU Orionis that constitutes the brightest component of the object, where the instability at the origin of the outburst takes place. In this respect, the primary goal of the present study is to constrain the size of this emitting region as a function of time. A further physical interpretation of this component will be given in 3.5.

Central unresolved component

The last component of the object is associated to the smallest spatial scales i.e. highest spatial frequencies. The MIRC-X and CLIMB visibility data shows an asymptote in the visibility that betrays the presence of a component that can be considered as unresolved at the angular resolution of this facilities ($150\,\mathrm{M}\lambda$). This unresolved component corresponds to a very compact emission in the inner part of the disk, below the resolution of the interferometer $< 0.1\,\mathrm{AU}$, which could originate from the natural peak of luminosity of a disk following a $T^{-3/4}$ profile, or even from a boundary layer (see 3.4.3). In the following, we model this floor as a pure unresolved component i.e. a constant in visibility f_{uc} (see Tab 3.2). This unresolved

Component	Visibility Model	Fitted Parameters
Extended envelope	$f_e(\lambda) = (f_0 + f_1(\lambda - \lambda_0) + f_2(\lambda - \lambda_0)^2) \cdot \delta(0,0)$	(f_0, f_1, f_2)
Resolved emission	$\exp\left(-\frac{\pi a \sqrt{\alpha^2+\beta^2}}{4 \log 2}\right)$	a, θ, i
Central unresolved component	f_c	f_c

Tab. 3.2: Components of the geometrical model used to fit FU Orionis visibility.

component is visible for the largest baselines ($\mathrm{m} = 150\,\mathrm{M}\lambda\,320$) of MIRC-X observations in H band, as seen on Fig 3.3, and CLIMB observations in K band.
Finally, the total visibility is written as the sum of the three individual components :

$$V(u,v,\lambda) = \Big(1 - f_{uc} - f_e(\lambda)\Big) \cdot V_d(u,v) + f_e(\lambda) \cdot \delta(0,0) + f_{uc} \tag{3.2}$$

These three components are centered on the same reference position. In the following, the interferometric data consist in visibility squared, so that we will fit the modulus squared of Eq(3.2) to these observations.

3.3.2 Fitting strategy

The major constraint of this study arises from the large heterogeneity of the dataset, and in some cases from the sparsity of the uv-coverage of the oldest data (IOTA, PTI). These constraints call for a specific fitting procedure. We first present the global methodology used in this study to fit the interferometric data. We then detail this procedure for each particular datasets in H and K band.

General procedure

Our goal is to provide a robust estimation of a for each observation. For some observations, this estimation is degenerate, due for example to an insufficient coverage of the small spatial frequencies, which constrain the contribution of the extended envelope, or due to a limited coverage of the highest spatial frequencies, which constrain the contribution of the central unresolved component. Our general strategy consists in fitting the geometrical model to the most complete dataset, which provides an estimation of the whole set of parameters for these observations **(Step 1)**, and to fix part of these parameters in order to fit the sparse datasets **(Step 2)** e.g. IOTA and PTI. In the latter case, the parameters that are assumed to be constant in time are typically : the position and inclination angles (θ and i), the spectral variation of the envelope (f_1 and f_2 coefficients, f_0 is fitted individually when small baselines are available), and the flux of the central unresolved component (f_c), which leaves only a and f_0 (when small baselines available) to be estimated. The validity of this approximation is discussed in Sec.3.4, and the exact parameters that are fixed depend on each particular dataset and will be detailed in the next paragraph. Finally, the errorbars of each parameters are obtained through a bootstrap analysis **(Step 3)** (Efron, 1982; Kervella, D. Segransan, and

Coude du Foresto, 2004; Regis Lachaume et al., 2019) : for each observation, we draw with repetition a number of visibility points equal to the number of visibility points in the initial observation, and we fit the model to these points, in the same order (Step 1 and Step 2) than mentioned above. The fitted parameters are then registered, and the whole procedure is repeated from the start over a large number of trials (typically 1000). For each observation, the final parameters are estimated with the median value of the fitted parameters, and the upper and lower 1σ-errobars with respectively the 16% and 84% percentile of the distribution. At the end of the process, this method enables us to reconstruct the probability distribution of our fitted parameters and to evaluate their errorbars without any assumptions on their properties. In addition, it is possible to identify from the output probability distribution potential bi-modal or multi-modal results, which could trace potential biases or local minima in our parameter estimation.

The list of the fitted parameters, which shows also which parameters are fitted independently or fixed by an other observation, are summarized in Tab 3.3. The exact fitting procedure in each band is now detailed in the following section.

Fit of the H band data set

The whole set of parameters of the model are fitted in MIRCX19, PION19, MIRCX18 and PION17 independently (Step 1), considering the (u,v)-coverage and the spectral resolution available with this dataset. Given their limited baselines, PIONIER observations barely estimate the contribution of the unresolved component shown in Fig 3.3, so that f_c parameter in PION19 and PION17 are fixed by MIRCX18. A bi-modal distribution can be seen at the output of MIRCX19 bootstrap, which may originate from an issue with the calibrator, so that we prefered to select MIRCX18 as a reference for the value of f_c ; nevertheless, the values of f_c obtained with MIRCX19 and MIRCX18 are consistent between each other. PION17 was both tested with independent and fixed parameters, but in both case this fit does not enable to obtain a reliable size estimation, for reasons explained in Sec 3.2. PION10, PTI00 and IOTA+PTI exhibit a sparse (u,v)-coverage, so that their parameters are fixed on a reference observation (Step 2). The fit on these three points was tested by choosing successively the parameters estimated in MIRCX19, MIRCX18 and PION19 as a reference. We finally chose the observation that minimizes the χ_2 of the fit of PION10, PTI00 and IOTA+PTI, which appears to be PION19. Due to the lack of small baselines, the contribution of the extended envelope in PION10 and PTI00 was fixed on PION19, and only the size a was fitted for these two observations. IOTA observations conducted in 1998 and PTI observations conducted in 1999 (Tab 3.1) were combined in the same point IOTA+PTI, as they enable to constrain both small and intermediate baselines respectively, at the price of a relatively low decrease in time resolution, which enables to provide an independent estimation of a and f_c. The results of the bootstrap (Step 3) are computed after $N = 1000$ iterations, and are shown in Tab 3.3. The output of the bootstrap analysis of our reference observation PION19 is also provided in a corner plot in appendix (Fig 3.15).

Fit of the K band data set

In the K band, GRAVITY and CLIMB data provide independent fits of the whole set of parameters. The estimate of the position and inclination angles in K band appears to be more

H Band			Fitted parameters						
			a	θ	i	f_{uc}	f_0	f_1	f_2
		Obs	[mas]	[°]	[°]	[%]	[%]	[%]/μm	[%]/μm^2
	(1)	MIRCX19	$0.46^{+0.01}_{-0.01}$	82^{+2}_{-3}	77^{+1}_{-1}	$15.9^{+0.2}_{-0.2}$	$8.5^{+0.1}_{-0.1}$	$-0.0^{+0.1}_{-0.1}$	$0.0^{+0.0}_{-0.0}$
	(2)	**PION19**	$\mathbf{0.62^{+0.03}_{-0.03}}$	$\mathbf{89^{+11}_{-9}}$	$\mathbf{56^{+8}_{-6}}$	**16.7**	$\mathbf{2.7^{+1.0}_{-1.0}}$	$\mathbf{1.7^{+2.0}_{-2.0}}$	$\mathbf{0.0^{+0.0}_{-0.0}}$
	(3)	MIRCX18	$0.49^{+0.01}_{-0.01}$	98^{+3}_{-3}	71^{+2}_{-2}	$16.7^{+0.4}_{-0.5}$	$10.2^{+0.2}_{-0.2}$	$0.0^{+0.1}_{-0.1}$	$0.0^{+0.0}_{-0.0}$
	(4)	PION17	$0.90^{+0.45}_{-0.21}$	98^{+23}_{-21}	157^{+50}_{-50}	16.7	$3.1^{+1.6}_{-1.6}$	$-32.5^{+12.0}_{-12.0}$	$0.0^{+0.0}_{-0.0}$
	(5)	PION10	$0.63^{+0.23}_{-0.18}$	89	56	16.7	2.7	1.7	0.0
	(6)	PTI00	$0.82^{+0.10}_{-0.06}$	89	56	16.7	2.7	1.7	0.0
	(7)	IOTA+PTI	$0.68^{+0.06}_{-0.06}$	89	56	16.7	2.7	1.7	0.0
K Band			Fitted parameters						
			a	θ	i	f_{uc}	f_0	f_1	f_2
		Obs	[mas]	[°]	[°]	[%]	[%]	[%]/μm	[%]/μm^2
	(1)	GRAVI21	$0.61^{+0.01}_{-0.01}$	45^{+1}_{-1}	35^{+1}_{-1}	30.0	$0.2^{+0.1}_{-0.1}$	$3.6^{+0.1}_{-0.1}$	$0.0^{+0.0}_{-0.0}$
	(2)	**GRAVI17**	$\mathbf{0.67^{+0.05}_{-0.04}}$	$\mathbf{62^{+9}_{-16}}$	$\mathbf{33^{+4}_{-3}}$	**30.0**	$\mathbf{5.0^{+1.0}_{-1.0}}$	$\mathbf{0.0^{+1.0}_{-1.0}}$	$\mathbf{0.0^{+0.0}_{-0.0}}$
	(3)	GRAVI16	$0.62^{+0.01}_{-0.01}$	61^{+2}_{-2}	35^{+1}_{-1}	30.0	$2.4^{+0.1}_{-0.1}$	$4.2^{+0.1}_{-0.1}$	$0.0^{+0.0}_{-0.0}$
	(4)	CLIMB11	$0.62^{+0.06}_{-0.05}$	49^{+3}_{-5}	55^{+5}_{-3}	$30.0^{+1.1}_{-0.5}$	$5.2^{+1.6}_{-1.6}$	$4.0^{+0.1}_{-0.1}$	$0.0^{+0.0}_{-0.0}$
	(5)	CLIMB10	$0.64^{+0.06}_{-0.04}$	13^{+6}_{-4}	44^{+10}_{-15}	$29.8^{+1.5}_{-0.4}$	$2.3^{+3.0}_{-3.0}$	$1.9^{+0.1}_{-0.1}$	$0.0^{+0.0}_{-0.0}$
	(6)	PTI03	$0.93^{+0.15}_{-0.14}$	62	33	30.0	5.0	0.0	0.0
	(7)	VINCI02	$0.65^{+0.08}_{-0.09}$	45	35	30.0	0.2	3.6	0.0
	(8)	PTI00	$0.80^{+0.06}_{-0.08}$	62	33	30.0	5.0	0.0	0.0
	(9)	PTI99	$0.84^{+0.05}_{-0.08}$	62	33	30.0	5.0	0.0	0.0
	(10)	IOTA+PTI	$1.10^{+0.10}_{-0.13}$	62	33	30.0	5.0	0.0	0.0

Tab. 3.3: Fitted parameters of the geometrical modeling of FU Orionis. The reference datasets in each band, on which are fixed the sparse dataset (see text), are indicated in bold.

sensible to their initial guess θ_0 and i_0 than in H band, so that the initial guess were chosen close to the output estimate in H band $\theta_0 = 50°$ and $i_0 = 35°$. In contrast to H band MIRC-X data, the contribution of the compact unresolved component is much less constrained in CLIMB data, due to a smaller number of visibility points at high spatial frequency (lower spectral resolution and lower number of baselines and spectral channels) and higher errorbars. As a consequence, f_c parameter of GRAVI21, GRAVI17 and GRAVI16 were fixed to a value close to the estimate provided in H band ($f_c = 0.25$). For CLIMB data, f_c is let as a free parameter, but appears to almost not deviate from the initial guess, whatever the value of this guess, which is finally chosen equal to $f_c = 0.25$. The parameters of PTI observations were fixed on GRAVI17, given the sparsity of these datasets, with only a let as a free parameter. GRAVI17 was preferred over GRAVI16 given the fringe-tracking issue in this observation (Sec 3.2), and over GRAVI21 given that the field of view of the ATs are closer to the field of view of PTI and IOTA observations. For the same reason, GRAVI21 was chosen as a reference for VINCI data, which were obtained on the UTs. In a similar fashion than data in H band, the IOTA and PTI observations conducted in 1998 were combined in a single point, which enables to provide an estimation of both a and f_e. Finally, the results of the bootstrap in Tab 3.3 are also computed over $N = 1000$ iterations, and the corner plot of GRAVI17 is shown in Fig 3.16).

3.4 Results

In this section, we present the results of the temporal fitting, and we evaluate the validity of these results. The complete output of the fit can be found in Appendix 3.8, on Fig. 3.12, Fig. 3.13 and Fig. 3.14.

	H band	K band
Mean fwhm [AU]	$0.33^{+0.04}_{-0.08}$	$0.34^{+0.03}_{-0.03}$
Slope [AU/100yr]	$-0.56^{+0.14}_{-0.36}$	$-0.30^{+0.19}_{-0.19}$

Tab. 3.4: Estimation of the size and the temporal slope of the resolved emission

3.4.1 Size estimate of the resolved emission

The size a of the resolved emission as a function of time is shown in Fig 3.4. On average, the mean size a over all the observations is $0.33^{+0.04}_{-0.08}$ AU in the H band and $0.34^{+0.03}_{-0.03}$ AU in the K band, which are consistent with previous estimates based on comparable models ((Labdon et al., 2020)). The errorbars and the validity of each individual data point can be inspected through the output of the bootstrap. These output distributions follow overall a gaussian distribution in both H and K band, MIRCX19 and PION17 excepted, due to the above-mentioned observational biases. In the following, we will discard PION17, given that this size estimate is clearly inconsistent with the rest of the sample and that an observational bias is identified for this point. From Fig 3.4, the size estimate of the oldest datapoints in the the early 2000s differ significantly from the most recent points, in particular in K band. On the other hand, the errorbars of IOTA and PTI points tends to be underestimated by the bootstrap analysis, given that two parameters are fitted at the most. Hence, this temporal trend has to be considered with great caution. From this set of fwhm sizes, we estimate the temporal slope in H and K band. In order to provide a reliable estimate of the slope, we perform a bootstrap estimate of the temporal slope in each band, by drawing with repetition a subset of size estimate and by applying a linear fit on this subset. Given that the errorbars of the different points are not symmetric, we take into account the maximum errorbar of each point in the linear fit. This conservative approximation is consistent with the statistical distribution evaluated with bootstrap for almost all points. The temporal slopes resulting from the bootstrap are respectively $-0.57^{+0.14}_{-0.33}$ AU/100yr and $-0.30^{+0.19}_{-0.19}$ AU/100yr in H and K band. These two values differ but remain in the 1σ range of each other. In H and K band respectively, the mean temporal slope is mostly constrained by the points with the smaller uncertainty i.e. MIRC-X and GRAVITY resp. Although the uncertainties of the first points in the 2000s are large, they contribute to draw the uncertainty contours of the temporal estimate, and are important to cover a large time span and to set upper and lower bounds on the size variation of the resolved emission. Finally, the overall consistency of this temporal slope with the mean estimate of a can be evaluated by comparing the points lying in the 1σ and 3σ estimate of the temporal slope in Fig.3.4. In K band, IOTA+PTI point lies outside the 3σ region, which confirms the caution to be taken with this point.

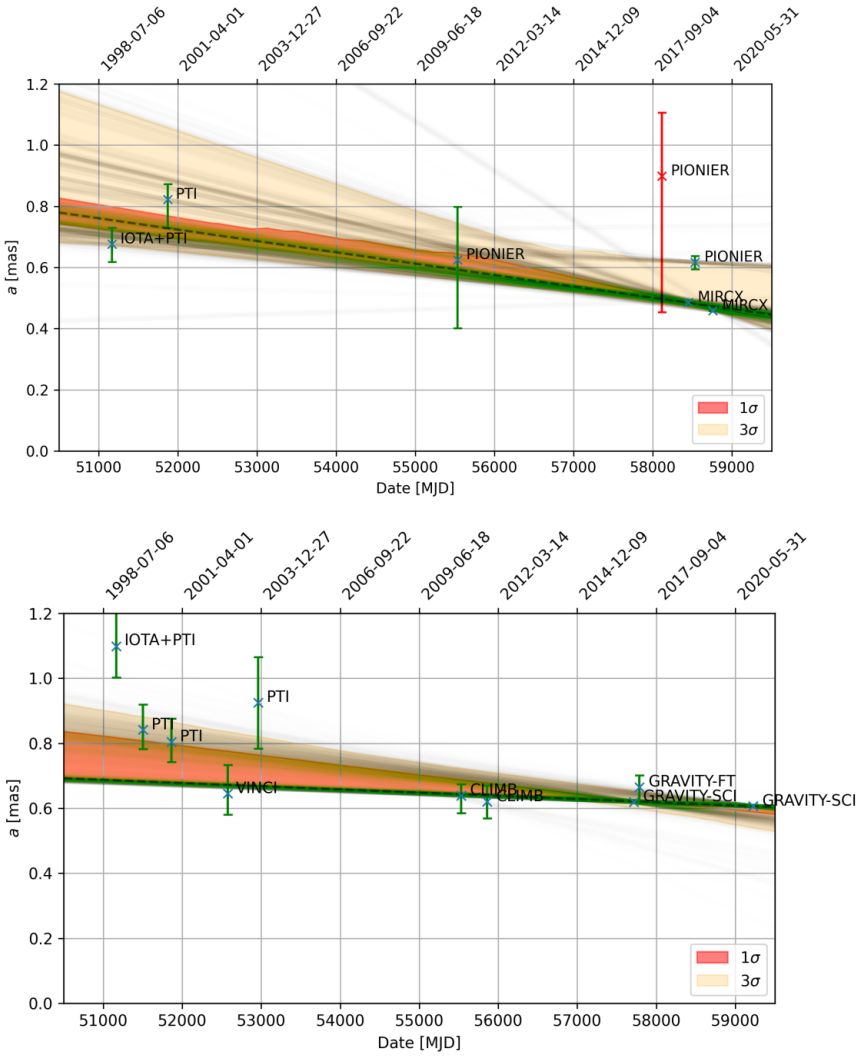

Fig. 3.4: Size of the resolved emission as a function of time, plotted in H band *(up)* and K band *(bottom)*. The temporal slope is estimated through bootstrap (dashed line : median of the bootstrap trials), the individual trials being over-plotted in the graph (green lines). Yellow and red regions highlight respectively the 1σ and 3σ contours of the fit. The red point in H band (PIONIER, 2017) is discarded from the estimation of the slope with bootstrap, due to an observational bias identified for this point.

3.4.2 Chromatic dispersion of the extended envelope

The fit in the K band highlights a spectral dependency of the extended envelope in the GRAVI16 high-resolution data, as reported by Liu et al., 2019, who analyzed the same Gravity dataset. As pointed out in Sec 3.2, the raw interferometric data for this observation exhibit strong discrete shifts in OPD away from the zero OPD reference. These strong discrete shifts can translate into a chromatic decrease of the visibility, which could reproduce the chromatic effect observed in the visibility data (private communication with Jean-Baptiste Le Bouquin and Karine Perraut). No chromatic dependency of the extended envelope could be detected

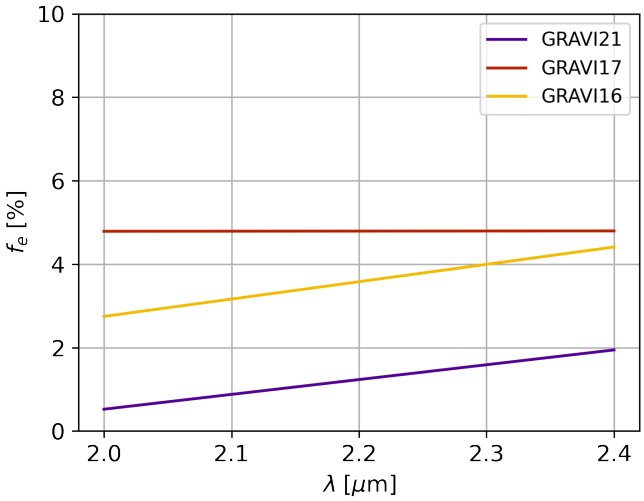

Fig. 3.5: Proportion of the flux of the extended envelope over the total flux measured in the interferometric field of view, in K band. A chromatic dependency is visible in GRAVI21 and GRAVI16 data. The offset between these two curves is due to the smaller interferometric field of view in GRAVI21.

in GRAVI17 : however, only low-resolution was available for this dataset (fringe tracker channel), which can barely constrain such chromatic effect. GRAVI21 enables to shed a light on this ambiguity. Although the total contribution of the extended flux is smaller in GRAVI21, due to the smaller interferometric field of view of the UTs, we detect a comparable chromatic variation to that of GRAVI16 (see Tab 3.3). The fit of the extended flux as a function of wavelength is also shown in Fig 3.5. GRAVI21 tends to confirm that the flux of the extended envelope increases for longer wavelengths. Conversely, although we detect an extended flux contribution in H band, we do not detect any significant chromatic effect of this envelope in H band (see Tab3.3), neither in MIRC-X nor in PIONIER data. However, this lack of detection can also be attributed in part to the low spectral resolution at our disposal in these two bands ($R < 50$). The implication of the spectral dependency of the extended flux on the properties of the envelope will be discussed in Sec 3.5.6.

3.4.3 Compact unresolved component

The unresolved flux of the disk is better estimated in the CHARA/MIRC-X observations. The mean unresolved flux for these observations are $f_{uc} = 27.8^{+0.3}_{-0.3}\,\%$ and $f_{uc} = 29.1^{+0.7}_{-0.8}\,\%$ in the H band. This compact unresolved component thus represents a significant proportion of the total flux $\sim 30\,\%$. All this flux should be encircled within a radius smaller than $\sim 0.1\,\mathrm{AU}$ (i.e within the inner disk), according to the maximum spatial frequency measured in MIRC-X observation.

3.5 Analysis

In this section, we compare our interferometric observations with two models of outburst, in order to put constraints on the accretion mechanism at play in FU Orionis. Two main scenarios have been put forward in the case of FUors : an outburst driven by Thermal Instability (TI) (Bell and Lin, 1994), and an outburst driven by Magneto-Rotational Instability and triggered by Gravitational Instability (MRI+GI) in a magnetically layered disk model (Armitage, Livio, and Pringle, 2001). In the following, we compare the predictions of numerical simulations of the near-infrared emission spatial evolution for both mechanisms to our observations. These numerical simulations were provided by Geoffroy Lesur, with whom we collaborate on this project, and that will be described in the following section.

3.5.1 Thermal instability model

The first historical model is an outburst driven by TI (Bell and Lin, 1994) : in this model, the outburst is triggered as the disk temperature increases up to the point where hydrogen is ionized, creating an abrupt change of opacity, which traps the thermal energy generated by the viscous disk and results in a thermal run-away of the disk. Since thermal instability requires a temperature $\sim 5000\,\mathrm{K}$ to be triggered, the instability starts at few stellar radii in the disk, and propagates outwards as the whole disk becomes unstable. Given that the accretion rate increases with the temperature in a standard accretion disk (Lynden-Bell and Pringle, 1974), this large increase in temperature is equivalent to a large increase of the accretion rate. Ultimately, the instability front stops its propagation, and moves backwards onto the star. Once all the matter in the disk has been accreted onto the star (decrease of the accretion rate, and equivalently of the temperature), the disk returns to its lower state, until a new cycle begins. We note that TI instability is a general mechanism which can be applied to different type of astrophysical models, for example eruptions in dwarf novae. This instability model was implemented by Geoffroy Lesur in a 1D numerical model of standard disk, based on the model and the opacities prescription described in (Bell and Lin, 1994) and assuming a star with a mass $\mathrm{M} = 0.5\,\mathrm{M}_{\odot}$. This 1D model assumes that the disk is axisymmetric. To sample both inner and outer regions, a logarithmic radial grid is used, from $0.1\,\mathrm{AU}$ to 30 AU. The output of the simulation is radial profile of several parameters of the disk as a function of time (effective temperature, Toomre, parameter, surface density, etc.). In the following, we will use the effective temperature of the disk to simulate a visibility profile and a SED that we can then compare to our observations. The exact method used to compare this simulation with the observation is similar to MIR+GI simulation and will be described in more extent in Sec 3.5.3.

On a general basis, the comparison of TI models with the observations highlights two main difficulties. First, the size of the emission of the disk is typically $< 0.1\,\mathrm{AU}$ in the TI model, compared to $\sim 0.3\,\mathrm{AU}$ measured in the interferometric observations. This smaller emission zone is inherent to thermal instability, which is triggered only in the innermost region of the disk, close to the star, where temperature is sufficiently high for hydrogen to be ionized. As seen on Fig 3.7, TI cannot sustain effective temperatures much higher than 4000 K up

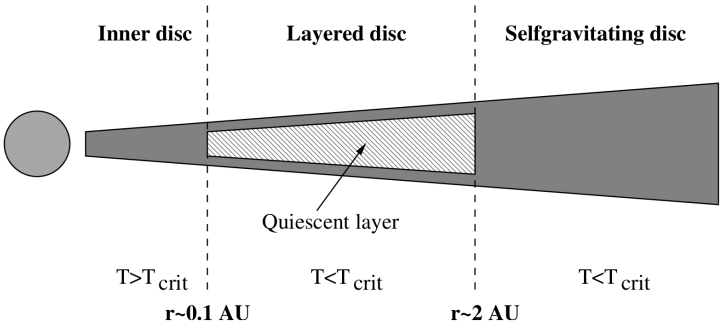

Fig. 3.6: Schematic of the disk structure in a layered disk model. Figure extracted from Armitage, Livio, and Pringle, 2001.

to a maximum extent of $\sim 0.1\,\mathrm{AU}$. Second, as shown also in Fig 3.7, the instability fronts propagates inside-out, which should translate in a slow rise of magnitude over few tens to one hundred years, followed by a decay of luminosity over a similar timescale. This obviously contradicts the purely asymmetric profile in FU Orionis visible lightcurve, where a fast rise of magnitude (few years in the case of FU Orionis) is followed by a slow photometric decay (few hundred years). Different mechanisms have been proposed to trigger the instability in the outer edge of the disk, so that the instability can propagate outside-in and reproduce the lightcurve of the outburst. The most notable scenario is an instability triggered by an external perturbation, which could be compatible with the presence of a stellar companion FU Ori S at large separation (Bonnell and Bastien, 1992; Cuello et al., 2020), or by an internal perturbation, in particular a planet of a few Jupiter mass (G. Lodato and Clarke, 2004). A review on these different models can be found in Audard et al., 2014. The implementation of such triggering perturbations in the code is out of the scope of this study. Finally, on a more fundamental level, an other difficulty of the TI model is related to physical justification of the value of α. The TI model implies a change of the value α between the hot state and the quiescent state, driven by the change in opacities. The values needed in this case have to be as low as 10^{-3} in the hot state and 10^{-4} in the cold state, in order to be compatible with the typical timescale of the eruption seen in FUors (Bell and Lin, 1994), but the exact physical justification of these particularly low values of α remains problematic (Hirose, 2015).

In view of these different elements, and following the advise of Geoffroy Lesur, we investigated a second instability model based on MRI+GI, in order to explain the outburst mechanism at play in FU Orionis.

3.5.2 MRI+GI in layered disk model

The second model considered in this work is a magnetically layered disk driven by MRI-GI (Armitage, Livio, and Pringle, 2001). In the lower state, the disk is structured with a thin surface layer, in which accretion occurs, and a dead zone from 0.1AU to 2AU (Gammie, 1996), as shown in Fig 3.6. As a magnetically inactive region, the dead zone can not sustain MRI and is quiescent. Conversely, the outer region of the disk is considered as gravitationally unstable for radii larger than $\sim 3\,\mathrm{AU}$. Material from the outer of the disk thus flows inwards and accumulates on the outer edge of the dead zone. As material piles up, the temperature

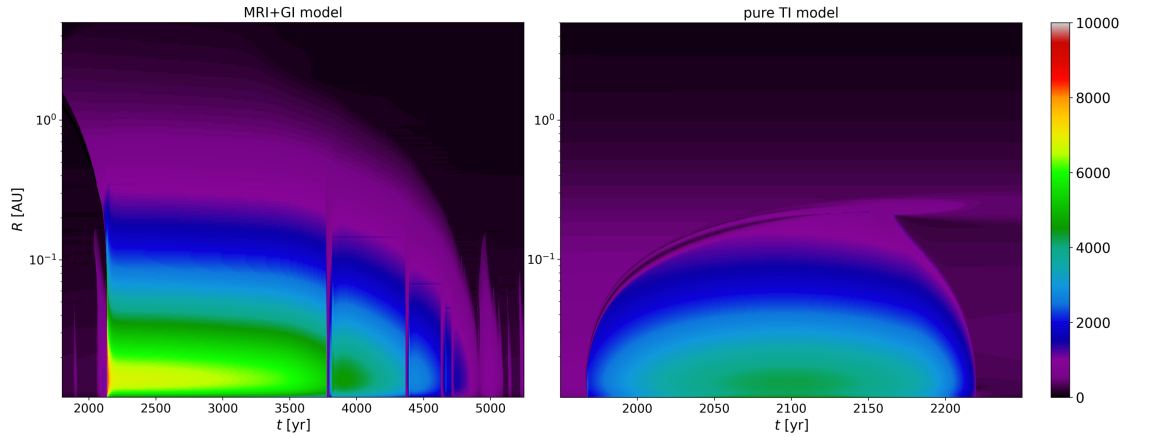

Fig. 3.7: Radial profile of the effective temperature of the disk as function of time (y-axis : radius, x-axis : time). *Left :* MRI+GI model, including TI instability at the innermost scale *Right :* pure TI model, based on the opacities provided in (Bell and Lin, 1994).

increases, up to a point where it reached the activation temperature of MRI ($T_{\rm MRI}$), which triggers the instability. This instability front propagates inwards and place the entire disk in a hot turbulent state. After the outburst, once all matter has been accreted onto the star, the inner disk returns to its initial quiescent state, until a new cycle is triggered. In addition to MRI, TI could locally be activated in the hottest and innermost region of the disk < 0.1 AU, although it is not essential in triggering and sustaining the outburst (Armitage, Livio, and Pringle, 2001). The MRI+GI was also implemented in a 1D numerical simulation by Geoffroy Lesur similar to the model described in Sec 3.5.1 (axisymmetric, logarithmic scale) , based on the model given in (Martin and Lubow, 2011). The two parameters which are the least constrained in the models are $T_{\rm MRI}$ and $\Sigma_{\rm crit}$ (Martin and Lubow, 2011). In the following, we provide a preliminary exploration of these parameters by comparing different simulations obtained with $T_{\rm crit} = 800\,{\rm K}$ and $600\,{\rm K}$, and $\Sigma_{\rm crit} = 10\,{\rm g.cm^{-2}}$ and $40\,{\rm g.cm^{-2}}$. The parameters of these different simulations are given in Tab 3.5, and the comparison of these simulations with our observations will be detailed in Sec 3.5.3.

3.5.3 Observables

SED, visibility and lightcurve from $T_{\rm eff}$

In order to compare the outputs of the simulations to our observations, we produced the SED, the interferometric visibility and the photometric lightcurve associated to each simulation. The SED and the interferometric visibility are obtained following the method described in (F. Malbet et al., 2005), by integrating the flux of successive infinitesimal rings of the disk, whose effective temperature profile is given by the output of the numerical simulation. By doing so, the total flux as a function of time is :

$$F_\lambda(i,t) = \frac{2\pi}{d^2}\cos i \int_{r_{\rm min}}^{r_{\rm max}} r B_\lambda[T_{\rm eff}(r,t)]{\rm d}r \tag{3.3}$$

and the interferometric visibility :

$$V_\lambda(B_p,t) = \frac{1}{F_\lambda(0)}\frac{2\pi}{d^2}\int_{r_{\rm min}}^{r_{\rm max}} rB_\lambda[T_{\rm eff}(r)]J_0\Big(\frac{2\pi}{\lambda}B_p\frac{r}{d}\Big)\mathrm{d}r \tag{3.4}$$

, with B_λ the Planck function, J_0 the zeroth-order Bessel function, d the distance to FU Orionis, $r_{\rm max}$ and $r_{\rm max}$ the inner and outer radius of the simulation, and $B_p = \sqrt{B_u^2 + B_v^2\cos^2 i}$ the projected baseline, where B_u and B_v are the coordinates (in [m]) of the baselines in the (u,v)-plane. Finally, the SED is corrected from interstellar extinction by a reddening the spectrum with $A_v = 1.4$, as described in (Pueyo et al., 2012). In addition to the visibility, the photometric lightcurves are constructed from the simulation by computing $F_\lambda(i,t)$.

Correction of $T_{\rm eff}$ profile

The computation of the total SED and of the interferometric visibility is sensible to the temperature of the innermost regions of the disk, given that the temperature varies as a power-law of radius $T \propto r^{-q}$. The rigorous treatment of this inner region in FU Orionis requires a dedicated model of boundary layer (Popham et al., 1996), whose implementation in our numerical model of the outburst is out of the scope of this work. As a consequence, in the current simulation, the temperature profile in the innermost region of the disk (<0.03 AU) is likely to be underestimated. On the other hand, in order to correct the temperature down to a few stellar radii in the simulation, it could be reasonably approximated that the effect of a boundary layer is a corrective factor of the power-law temperature profile $T \propto r^{-q}$ in the first 0.1 AU of FU Orionis, as also visible in (Popham et al., 1996). In order to correct the temperature profile, we fitted the parameters q of the power law to the temperature profile of the inner region where the outburst occurs, so that the temperature profile in the innermost regions appears as the continuation of the profile given by the simulation. Given that this parameter appears to change slightly during the outburst in the simulation, q is fitted at each timestep of the simulation. We then extrapolate this profile down to an inner radius $r_{\rm in}$, the value of $r_{\rm in}$ being set by fitting the observed SED of FU Orionis to the SED obtained with the corrected effective temperature profile. The values of $r_{\rm in}$ and $T(r_{\rm in})$ obtained from this procedure for each observation are given in Tab 3.5.

At this stage, we obtain the corrected SED, interferometric visibilities and photometric lightcurves, which can now be compared to the data. An example of the output of the model is given in Fig. 3.8 for one simulation in the MRI+GI scenario.

Fit of the simulated visibility profile

Finally, in order to provide a size estimate of the disk emission comparable to that of our interferometric observations, we fitted a geometrical model composed of a gaussian disk and a compact unresolved component to the visibility profile obtained from the simulations, at the central two central wavelengths of H and K band ($\lambda = 1.65\,\mu$m and $= 2.2\,\mu$m respectively). The estimation of a is sensible to the contribution of the compact component in this model. In order to provide consistent estimates between the simulation and the observations, we fixed the contribution of the compact flux during the fit of the simulated visibilities. We chose the value $f_c = 0.3$ at $\lambda = 1.65\,\mu$m and $\lambda = 2.2\,\mu$m , which are close to the value obtained in the observations in H and K band (see Sec 3.4. Finally, the only free parameter in the fit is

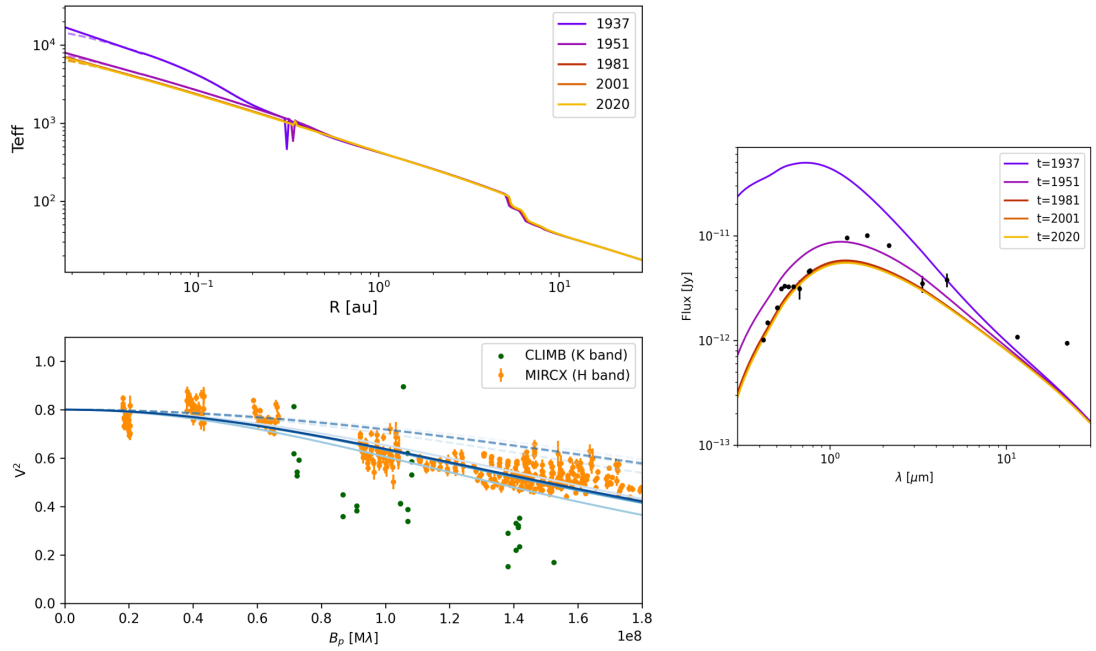

Fig. 3.8: Typical observables deduced from the simulation, here given for Simulation 5. *Upper left :* Effective temperature profiles (solid line) obtained at the output of the numerical simulation of the outburst, corrected in the inner part of the disk (dashed line). *Lower left :* Visibility profiles deduced from the corrected effective temperature profile. The dashed line corresponds to the minor axis of the disk (less resolved), solid line to the major axis (more resolved). *Middle right :* SED deduced from the corrected effective temperature profile. Effective temperature profiles, Visibilities, and SEDs are plotted at the different time stamp, that are indicated in the legend to show the evolution of these observables in time.

the size a of the resolved emission, which is fitted at each time-step of the simulation. This enables us to reconstruct the variation of the size of the disk emission as a function of time, which can be compared to our observations.

3.5.4 Size of the emission and temporal variation

The results of the fit of the simulated visibility profile described in the previous section is shown in Fig 3.9.

Simulation	$T_{\rm MRI}$ [K]	$\Sigma_{\rm crit}$ [g.cm^{-2}]	R_* [$R_\odot$]	MRI+GI	TI	$r_{\rm in}$ [$R_\odot$]	$T(r_{\rm in})$ [K]
1	800	40	2.24	yes	no	7.6	5689
2	600	10	2.24	yes	no	5.1	6819
3	800	10	2.24	yes	yes	2.8	8631
4	800	10	5.17	yes	no	3.0	6915
5	800	10	5.17	yes	yes	5.3	4317
6	-	-	2.24	no	yes	5.0	3411

Tab. 3.5: Parameters of the different numerical simulations of FU Orionis outburst. These simulations were performed by Geoffroy Lesur.

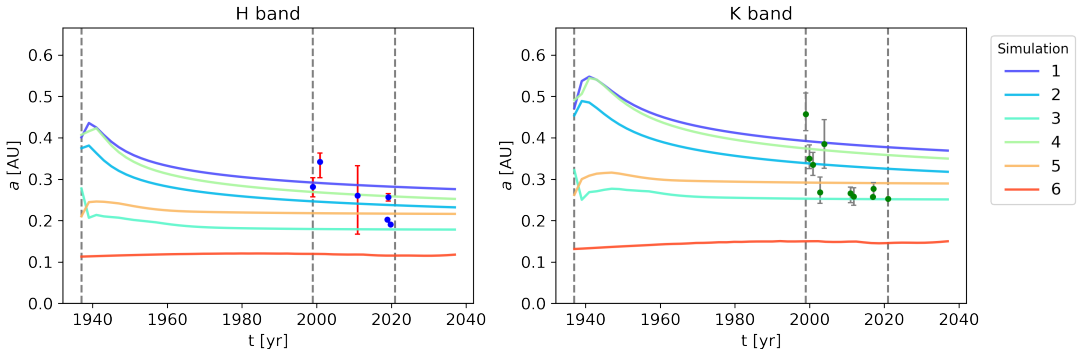

Fig. 3.9: Simulated size of the emission zone compared to interferometric observations. The simulations are labeled with the number provided in Tab.3.5.

The different estimates of the size of the emission in the interferometric observations range between 0.19 AU and 0.38 mas in H band, and between 0.25 AU and 0.46 AU in K band. These values are compatible with the different simulations in MRI+GI, but shows a significant discrepancy of about a factor 2 with pure TI model (Fig 3.9). In both TI and MRI+GI, the disk exhibits a theoretical profile $T \propto r^{-3/4}$ during the outburst. This profile is observed in interferometric observations presented (F. Malbet et al., 2005) and (Labdon et al., 2020). However, the sole knowledge of $r^{-3/4}$ dependency does not differentiate these two models. The main difference between TI and MRI-GI arise from the maximum temperature that can be sustained by each type of instability, which reach respectively $< 4500\,\mathrm{K}$ and $\sim 8500\,\mathrm{K}$ at the innermost truncation radius in the simulations, and translates in a difference of the typical extent of the emission zone in the disk, as observed here. **The size estimate of the inner AU region of FU Orionis outburst indicate that TI, whose typical extent is confined to $< 0.1\,\mathrm{AU}$ in the disk, can not sustain a temperature sufficiently high to match the typical size observed in out interferometric sample. Conversely, the predictions of the size estimate of the outburst of MRI-GI instability in a layered disk model are consistent with our observations, which strongly favour this model.**

In addition to this static view, the slope presented in Sec 3.4 is compatible with a constant size or a slow decrease. This slow decrease is better reproduced by the simulations labeled 1-2-4 in Tab 3.5. Simulations 3-5, where both MRI-GI and TI in the inner of the disk are included, are however better matched to the mean size observed in the sample. This plateau is in tension with the slow decrease observed in visible photometry, and very likely in K band photometry[4]. In that respect, this comparison should favour Simulation 2, which has the smallest size estimate among the simulations exhibiting a significant size variation (1-2-4). In order to compare these simulations more objectively, we computed the χ_2 between the simulation and our estimated size samples. In H band and K band respectively, the simulation 5 and simulation 4 (resp.) have the lower χ_2, but are mainly constrained by the recent points with low errorbars, and can not enable to reach a clear conclusion on the best estimate of MRI-GI parameters. The exact comparison between the different simulations and the data is still on-going at the time of writing. On the observational side, the exact differentiation between the models is made difficult by the large dispersion of the dataset, and in particular

[4]We note that at the time of writing very sparse photometric data are available for FU Orionis in H and K band in the literature.

the most ancient data-points. On the simulation side, a better understanding is needed on the origin of the plateau when MRI-GI and TI instability are included in the same model, which contradicts the photometric data. In addition, in the case where TI is included in MRI-GI, very abrupt eruptions can be seen in the simulation as the outburst start to decrease, these eruptions being likely purely numerical artefacts.

3.5.5 Origin of the compact emission

As mentioned in Sec 3.4, the compact unresolved component observed in the interferometric data contributes to $\sim 30\,\%$ of the total flux in the H band, and is enclosed in a region smaller than 0.1 AU in the disk, this upper limit being set by the maximum angular resolution at our disposal. The physics of this region and of the boundary layer is not captured in the simulation discussed previously. As already mentioned in (Fabien Malbet, 1992), a standard $T \propto r^{-3/4}$ profile naturally produces a steep increase of flux when going in the innermost region of the disk, so that an unresolved compact emission should naturally arise in the visibilities. However, given that this region is not spatially resolved, relative loose constraints on the geometry of this region can be drawn. In particular, these inner regions do not enable to distinguish a $T \propto r^{-3/4}$ from more elaborated models of boundary layers developed in (Popham et al., 1996). Labdon et al., 2020 fitted a standard disk profile with $T \propto r^{-3/4}$ and deduced from it the existence of a boundary layer, although the typical extent of this boundary layer as defined in (Popham et al., 1996) ranges from up to $\sim 10\,R_*$, one order of magnitude smaller than the maximum resolution in MIRC-X observations. In particular, other processes than a boundary layer could produce a large increase of flux at 0.1 AU, such as TI or accretion mechanisms close to the star, below the resolution of interferometric observations. More conservatively, we will restrict our conclusion by saying that a large fraction of flux is emitted within 0.1 AU, which could originate from both accretion processes such as TI close to the star and/or a boundary layer.

3.5.6 Extended envelope

Infalling envelope in FUors

The contribution of an extended flux was first revealed as a general feature of FUors by R. Millan-Gabet et al., 2006 in near-IR interferometric data. This extended flux is the signature of a extended envelope covering the interferometric field of view, which can be clearly attributed to the remnant infalling envelope visible in high-contrast observations AO observations at larger spatial scales. Our interferometric datasets confirm the presence of this envelope in FU Orionis.

Spectral variation and temperature of the extended envelope

In addition, the presence of chromatic variation of the envelope, already put forward in (Liu et al., 2019), appears to be confirmed in new GRAVITY data in 2021. In the H band,

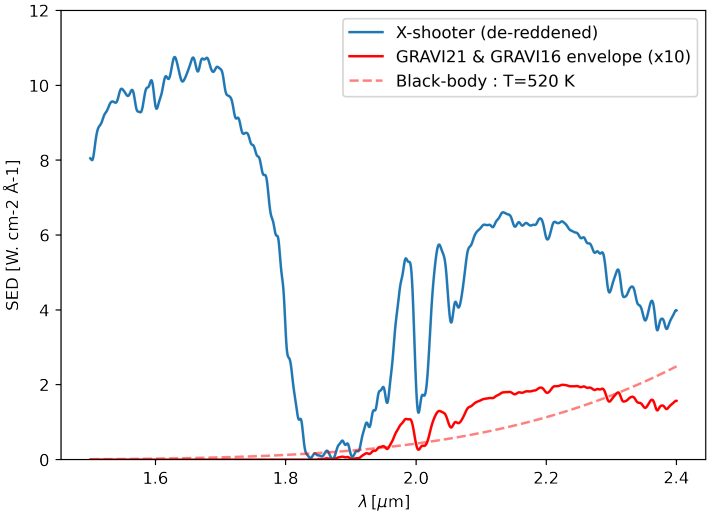

Fig. 3.10: SED of the extended envelope deduced from GRAVITY observations in K band, and MIRC-X and PIONIER non-detection in H band. The total SED of FU Orionis was obtained with archival X-shooter data.

no chromatic variation is detected, which could be attributed to the low spectral resolution available in our observations, as mentioned in Sec.3.4. Concomitantly, this lower spectral variation in H band would also be expected in the case of an extended envelope with a relatively low temperature of the order of few hundreds of Kelvin. In the following, we take into account the spectral variation in both H and K band to try to set a preliminary constrain on the temperature of the extended envelope.

We obtained the spectrum of FU Orionis in H and K band from publicly available observations of X-Shooter (ESO ID: 094.C-0233(A)). We de-reddened this spectrum using the same interstellar extinction as described earlier, and multiplied the total spectrum by the proportion of extended flux in the interferometric field of view $f_e(\lambda)$ which is measured in our observation. The resulting spectrum provides an estimation of the SED of the extended envelope, in the same way as (Liu et al., 2019), but including also the constraint by the H band data. Finally, we fit a black-body spectrum to the envelope.

We finally estimate the temperature of the envelope by fitting a blackbody to the average of the extended flux contribution observed with GRAVI21 and GRAVI16. We obtain a temperature $T_{\rm env} = 520\,{\rm K}$, an estimation consistent with the value expected in the dust model discussed in (Liu et al., 2019). The uncertainty in our estimation of the temperature is certainly dominated by the uncertainty on the estimation of the slope in $f_e(\lambda)$ rather than data uncertainty in X-shooter spectrum. The uncertainty on the slope is itself probably larger than the uncertainty provided by the chi-squared. In order to provide an order of magnitude of the errorbars on the temperature, we fitted independently the extended envelope SED deduced from GRAVI16 and GRAVI21. We obtain respectively $T_{\rm env,16} = 578\,{\rm K}$ and $T_{\rm env,16} = 282\,{\rm K}$ (Fig. 3.10). The estimation of the spectral variation of $f_e(\lambda)$ shows a significant discrepancy between GRAVI16 and GRAVI21, which could be attributed in part to uncertainty in the slope estimation, but also to the fact that these two observations probe significantly different field of view, GRAVI21 being focused on much more closer region of the envelope than GRAVI16 ($\sim 20{\rm AU}$

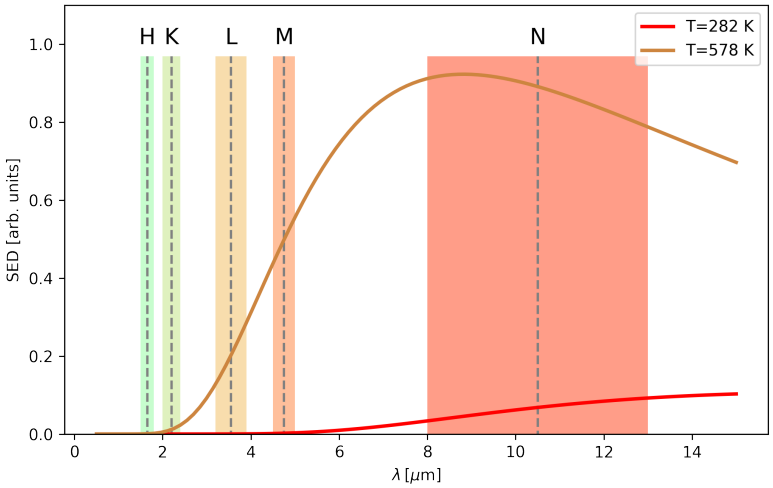

Fig. 3.11: Extrapolation of the flux of the extended envelope deduced from interferometric observations, and available spectral bands in the mid-infrared.

and $\sim 100\mathrm{AU}$ respectively). Consequently, a smaller fraction of the extended envelope is measured in GRAVI21, while the constrain of a zero flux in H band remains identical between GRAVI21 and GRAVI16, which leads to a smaller estimated temperature in GRAVI21. In principle, a higher temperature should be measured in GRAVI21, which is closer to the hot inner part of the disk. Such a temperature measurement would require the observation of the extended contribution in H band and K band with the field of view of the UTs, in order to measure the SED of the extended flux also in H band, rather than approximating this flux to zero. In the next paragraph, we propose some prospects to put more constrains on the physical properties of this extended envelope.

3.6 Conclusion and prospects

3.6.1 Results

In this chapter, we have presented the temporal monitoring of FU Orionis through more than 20 years of interferometric data in H and K band. First, this analysis has enabled us to complement the classical picture of FU Orionis, from $0.2\,\mathrm{AU}$ (maximum angular resolution) up to $20\,\mathrm{AU}$ (interferometric field of view of the ATs). Our modelisation leads us to distinguish three components in FU Orionis : an extended envelope, which corresponds to the remnant of the infalling envelope feeding the accretion disk ; a resolved emission in the accretion disk, where the outburst occur ; and a compact unresolved component below $\sim 0.1\,\mathrm{AU}$ which enclosed up to $30\,\%$ of the total flux of the accretion disk. Second, we evaluated the typical size of the resolved emission in the disk and put boundaries on its temporal variation. We measured a typical fwhm size of the resolved emission of $\sim 0.3\,\mathrm{AU}$, and a temporal slope between $-0.55\,\mathrm{AU}/100\mathrm{yr}$ and $-0.3\,\mathrm{AU}/100\mathrm{yr}$, whose errorbars are compatible with a constant or slowly decreasing size of the emission in time. We then compared these

measurements with the expectation of size variation obtained with two models of disk instability, based respectively on pure TI instability and a MRI-GI occurring in a magnetically layered disk. Our observations strongly favour MRI-GI model over pure TI instability, which predicts emission sizes significantly smaller than our observation, by approximately a factor 2. We also explored different MRI-GI parameters in order to put preliminary constrains on the fundamental parameters of MRI. Our observations are compatible with $T_{\rm MRI}$ ranging from 600 K to 800 K and $\Sigma_{\rm crit}$ ranging from 10 $\rm g.cm^{-2}$ to 40 $\rm g.cm^{-2}$, although the differentiation of these models remains difficult due to the heterogeneity of our interferometric sample. Finaly, our new observation on GRAVITY confirm the presence of an extended envelope, and tends to confirm the spectral variation of its flux in the K band, which would fit a temperature $T \sim 500\,K$ for the envelope included below ~ 20 AU.

3.6.2 Perspectives

Three main axis could be explored following this study. First, the temporal analysis could crucially benefit from the continuity of stable interferometric instruments in the next 15 years such as GRAVITY, PIONIER or MIRC-X, by performing observations of FU Orionis every year or 2 years with an homogeneous instrumental set-up. As shown in Sec 3.5.4, the comparison between the size predicted by the numerical model and the data is made difficult by the heterogeneity of the dataset. However, as seen for the most recent period in K band, regularly spaced measurements with comparable instruments on the same instrumental configuration enable to significantly refine these estimates, with a data dispersion potentially compatible with the distinction of different instability models (Fig 3.9), which are sensitive to the fundamental parameters driving accretion, in particular $T_{\rm MRI}$ and $\Sigma_{\rm crit}$. Such observations would represent a crucial step in order to put constraints on the fundamental parameters of the MRI, on which only a few observational constrains exist. Importantly, this monitoring would have to include both small and large baselines, in order to simultaneously constrain the extended envelope of the disk, the resolved emission and the unresolved component, otherwise introducing potential biases in the estimation of the size of the emission.
Second, the confirmation of a spectral variation of the extended flux observed in GRAVI21 would greatly benefit from new GRAVITY observations with the field of view of the ATs. In addition, the advent of MATISSE instrument could enable to add constraints on the temperature of the envelope through the use of medium spectral resolution in mid-infrared L,M and N band, in which the flux of a cold envelope is expected to rise (Fig 3.11). These mid-infrared interferometric observations could be compared to high-contrast imaging data, which probes comparable spatial scales in J/H band. These observations, or even an ambitious imaging program coupling the two techniques, would be of particular interest to study the extended envelope of FUors and to clarify the link between these structures and the outburst.
Finally, as demonstrated in Gravity et al., 2020 or (Benisty et al., 2010), and in a complementary manner to the temporal monitoring, the observations of the dynamics of the inner AU with high-spectral resolution near-infrared interferometry could enable to constrain the rotation velocity of the disk, and potentially additional parameters of the instability models (temperature, density). Such observations could also probe the deviation from keplerian velocity in the disk, indicating the presence of disk winds, whose existence are likely in FU

Orionis (Lee Hartmann and Nuria Calvet, 1995b).

As a unique laboratory of accretion physics in protoplanetary disks, FU Orionis will remain a particularly interesting object to study in the following years.

3.7 Appendix : FU Orionis' Spectral Energy Density (SED)

Tab. 3.6: Table of photometric data used in our SED of FU Orionis.

λ [μm]	Flux [Jy]	Catalog	Ref.
0.53	0.55	Gaia DR1	(Gaia Collaboration et al., 2016)
0.42	0.14	Gaia DR1	(Gaia Collaboration et al., 2016)
0.77	1.2	Gaia DR2	(Gaia Collaboration et al., 2018)
0.62	0.68	Gaia DR2	(Gaia Collaboration et al., 2018)
0.50	0.35	Gaia DR2	(Gaia Collaboration et al., 2018)
0.76	1.16	Gaia DR3	(Gaia Collaboration, 2020)
0.58	0.64	Gaia DR3	(Gaia Collaboration, 2020)
0.50	0.35	Gaia DR3	(Gaia Collaboration, 2020)
22.11	6.95	TESS	(Stassun et al., 2019)
11.57	4.16	TESS	(Stassun et al., 2019)
4.60	5.82	TESS	(Stassun et al., 2019)
3.35	3.91	TESS	(Stassun et al., 2019)
2.17	5.83	TESS	(Stassun et al., 2019)
1.63	5.46	TESS	(Stassun et al., 2019)
1.25	3.97	TESS	(Stassun et al., 2019)
0.55	0.61	TESS	(Stassun et al., 2019)
0.44	0.22	TESS	(Stassun et al., 2019)
0.67	0.70	Gaia DR1	(Zari et al., 2017)

3.8 Appendix : output of the bootstrap analysis in H and K band

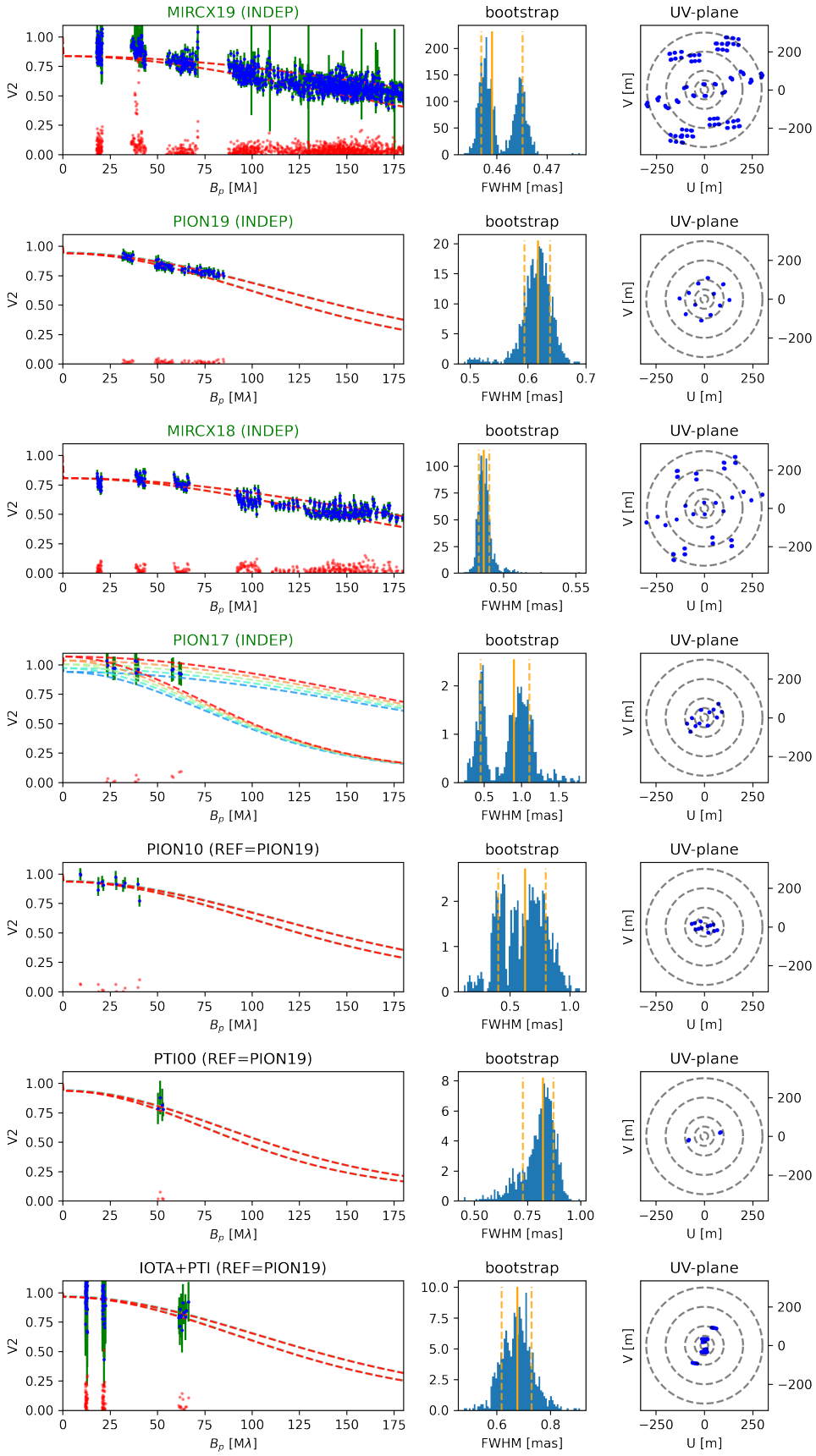

Fig. 3.12: H band : output of the fitting procedure of the interferometric observations. **Left :** The visibility model is represented in dashed line, the minor axis of the gaussian disk is associated to the upper visibility curve and the major axis to the lower visibility curve. Residuals are shown in red scattered points. **Middle :** Bootstrap values of the fwhm estimate. **Right :** (u,v)-coverage associated to each observation.

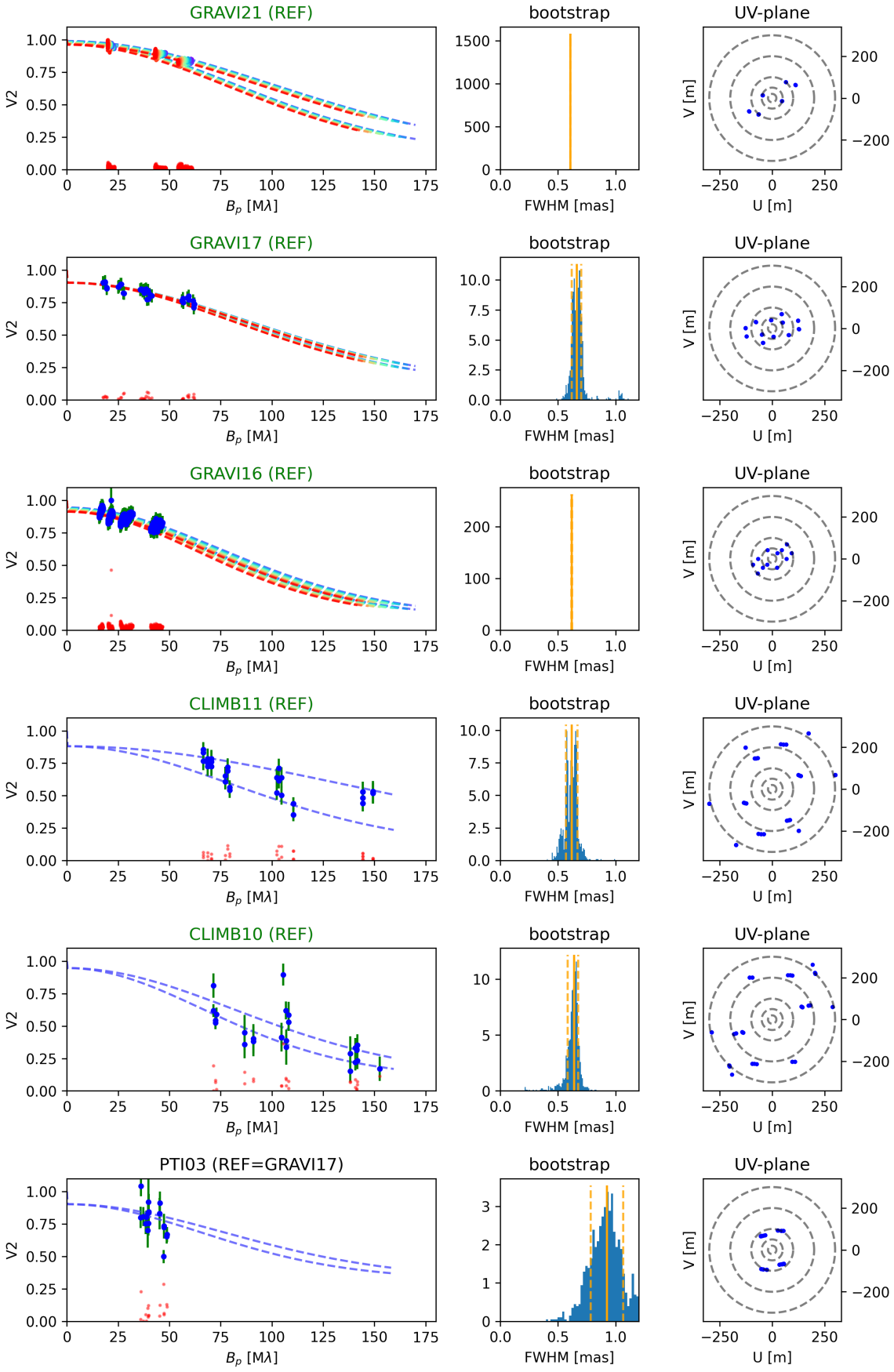

Fig. 3.13: K band : output of the fitting procedure. See Fig.3.14 for the second part.

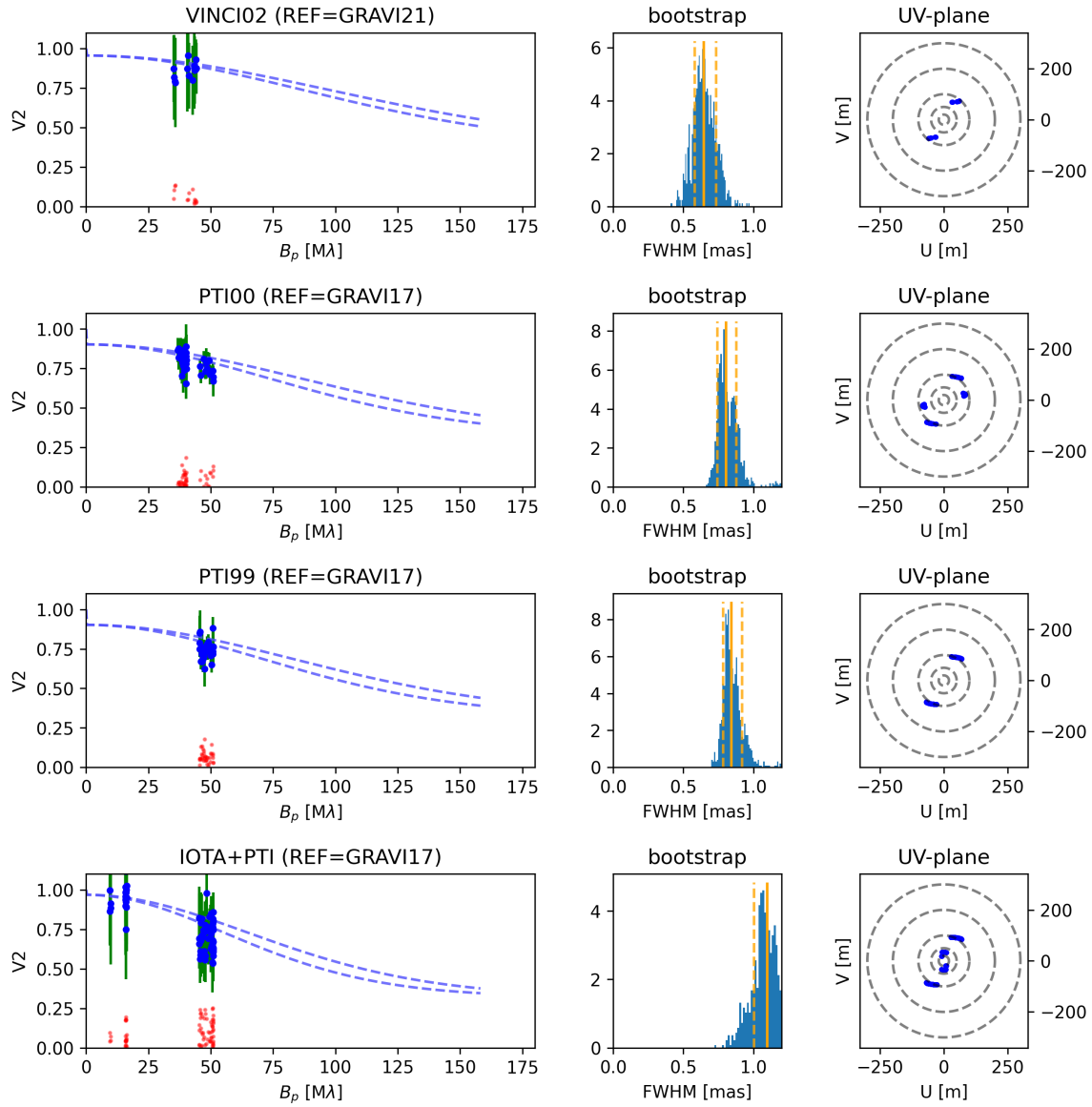

Fig. 3.14: K band (continuation).

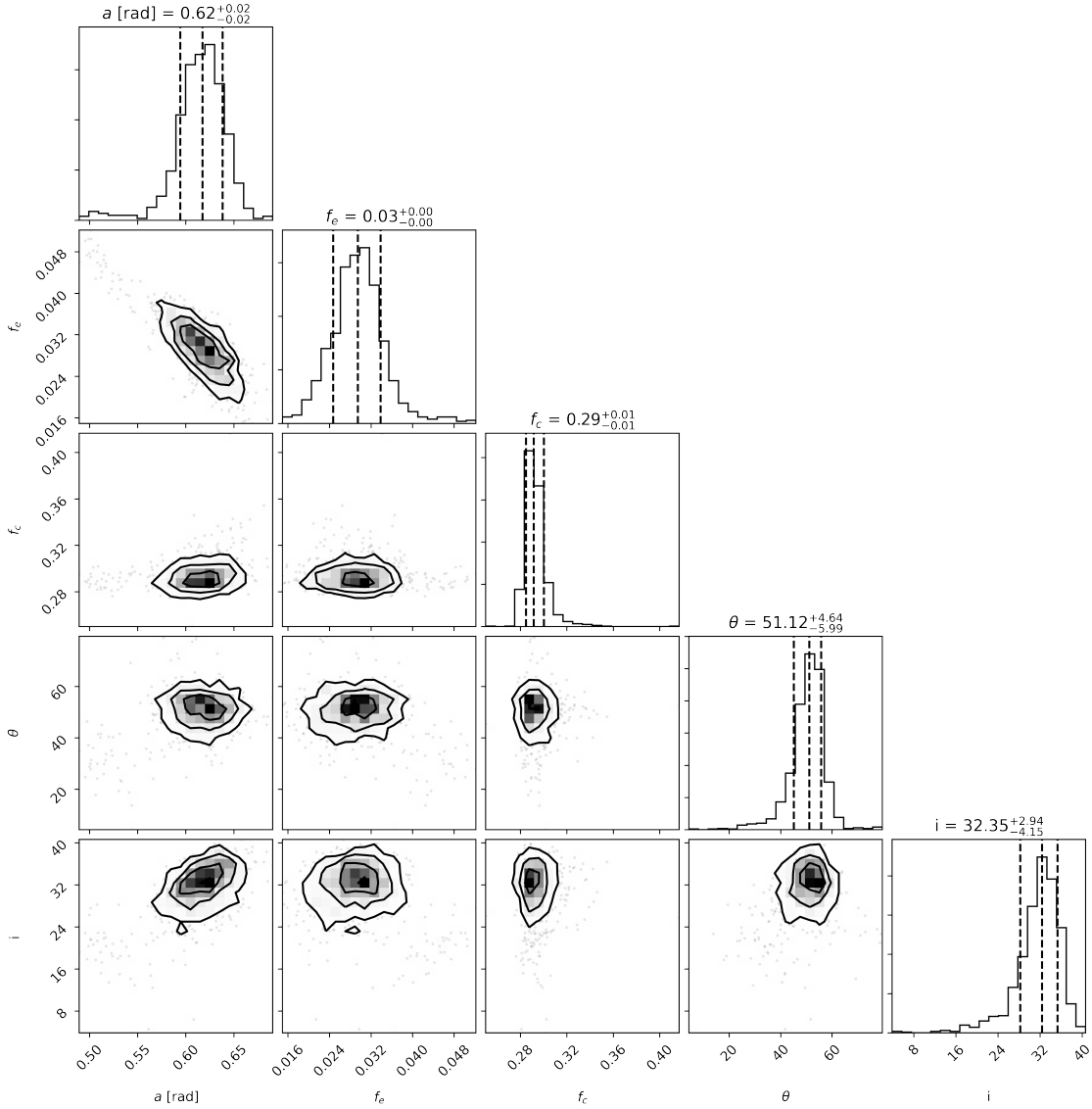

Fig. 3.15: PION19 bootstrap output, computed over $N = 1000$ iterations.

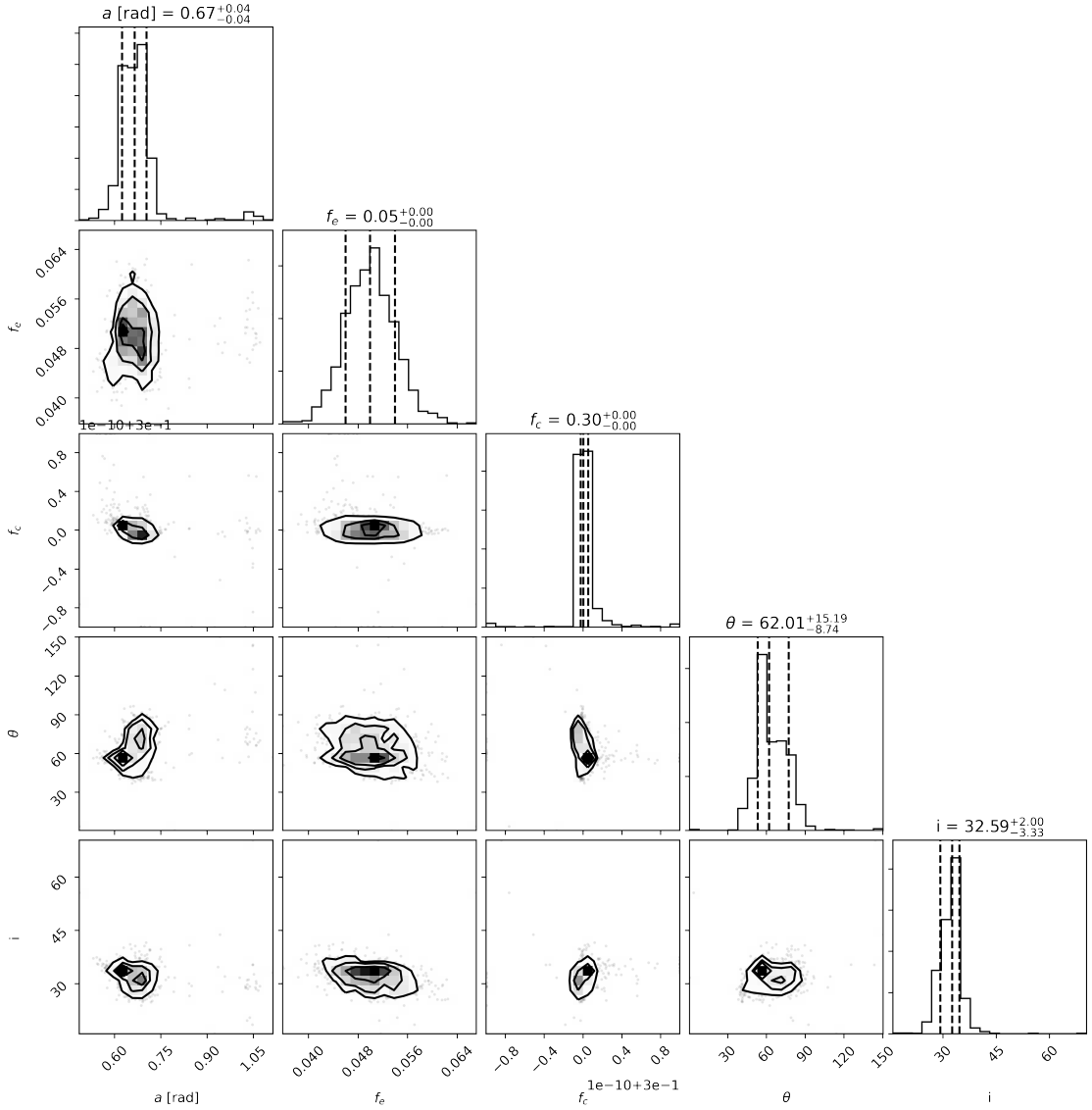

Fig. 3.16: GRAVI17 bootstrap output, computed over $N = 1000$ iterations.

Part II

Mid-infrared heterodyne interferometry for astronomical aperture synthesis

> ***Andrea**: Aber ich sehe doch, daß die Sonne abends woanders hält als morgens. Da kann sie doch nicht stillstehn! Nie und nimmer.*
> ***Galilei**: Du siehst! Was siehst du? Du siehst gar nichts. Du glotzt nur. Glotzen ist nicht sehen.*

— Bertolt Brecht
Das Leben des Galilei

4 A revisit of mid-infrared heterodyne interferometry

In this chapter, we propose to revisit the architecture of mid-infrared interferometry in light of the recent and rapid developements in mid-infrared technologies. We confirm the signal-to-noise ratio (SNR) relations commonly used in the literature, based on basic relations of heterodyne detection and radio-astronomy, and apply it to a preliminary sensitivity estimation of an array with the technical specifications of the Planet Formation Imager. Finally, we give an overview of the potential technological developments enabling the implementation of this architecture.

4.1 Specifications of a PFI

The imaging of the key stages of planet formation translates into general science requirements that were described in Chap 2. These, in turn, translates into general technical specifications of the interferometric architecture required for a Planet Formation Imager.

Parameter	Value
Number of telescopes	12 to 21
Maximum baseline	1.2km
Science wavelengths	N band (possible ext. to Q band)
Sensitivity (point source, $5\,\sigma$)	$m_N \sim 12.5$ (0.36 mJy) in $t = 10^4\,s$
Surface brightness	$150\,K$ in $t = 10^4\,s$
Spectral resolution	$R = 100$ (300 GHz) to $R = 1 \times 10^5$ (300 MHz)
Number of spectral channel	50 to 10 000
Fringe tracking wavelengths	H and K band
Fringe tracking limits	$m_H < 13$ (point source)
Field of view	0.7" in N band

Tab. 4.1: Technical requirements of a baseline PFI architecture in the mid-infrared (N and Q band)

These requirements are driven by three main aspects :

- **large number of telescopes** : the reconstruction of an interferometric image with sufficient complexity requires the recombination of a large number of telescopes. The baseline number assumed in the following will be comprised between 12 and 20

telescopes. This number still has to be consolidated, with a trade-off between sensitivity, image reconstruction complexity, and total cost.

- **kilometric baseline** : the minimum baseline is 1.2 km in order to reach 2 mas resolution in the N band. Further increase of the maximum baseline remains interesting for unresolved sources, but is in tension with the goal surface brightness temperature of 150 K in the case of imaging (for further details on the notion of temperature brightness, refer to Sec 4.4.1).

- **bandwidth coverage & sensitivity** : the minimum spectral resolution is fixed to R=100, and corresponds approximately to the lower bound constrained by bandwidth smearing. The maximum spectral resolution is set to $R = 10^5$, which corresponds to a bin of resolution of 3 km/s.

These technical requirements are summarized in Tab 4.1, and are based on the initial study of (John D. Monnier et al., 2018b). We emphasize that these requirements does not constitute the final design parameters of an array, but have to be considered as the framework of the system and technological developments better suited for a PFI. The final choice of the optimal characteristics of a definite PFI array is still an open problem, that will have to take into account multiple parameters (e.g. cost, technical feasibility, uv-coverage...).

Concerning the array configuration, both "Y-array" and "ring-array" were initially considered in (John D. Monnier et al., 2018b), based on the optimization of the fringe tracking limit. This question of the optimal geometry of an array was further investigated in Julien Woillez et al., 2017, which favoured circular geometry, based on the analysis of the noise propagation and the robustness of the array to a flux dropout on one of the telescope in the array.

4.2 System architecture of a heterodyne PFI

The technical requirements described in Tab 4.1 go well beyond the capability of previous existing heterodyne facilities such as ISI, limited to typically 50-100 Jy in t=1h *incoherent* integration. The perspective of a PFI thus requires the introduction of a profoundly renewed architecture, which would also integrate the massive evolution of mid-infrared technologies. In the following, we introduce the general heterodyne system which will constitute the framework of our study.

The architecture considered is shown in Fig 4.6, and is based on the architecture initially presented in (Swenson, 1986) and in (Ireland and John D. Monnier, 2014). The two main features of this configuration, in order to overcome the previous limitations of sensitivity of heterodyne interferometers, are the implementation of a massive spectral multiplexing of the spectral channel by the use of the laser comb, and the phase-referencing of the heterodyne array on an external fringe-tracker in the H / K band based on direct interferometry, implemented in a fibred design in order to release the design complexity of this system. The spectral multiplexing is achieved by using a laser frequency comb whose teeth are spectrally

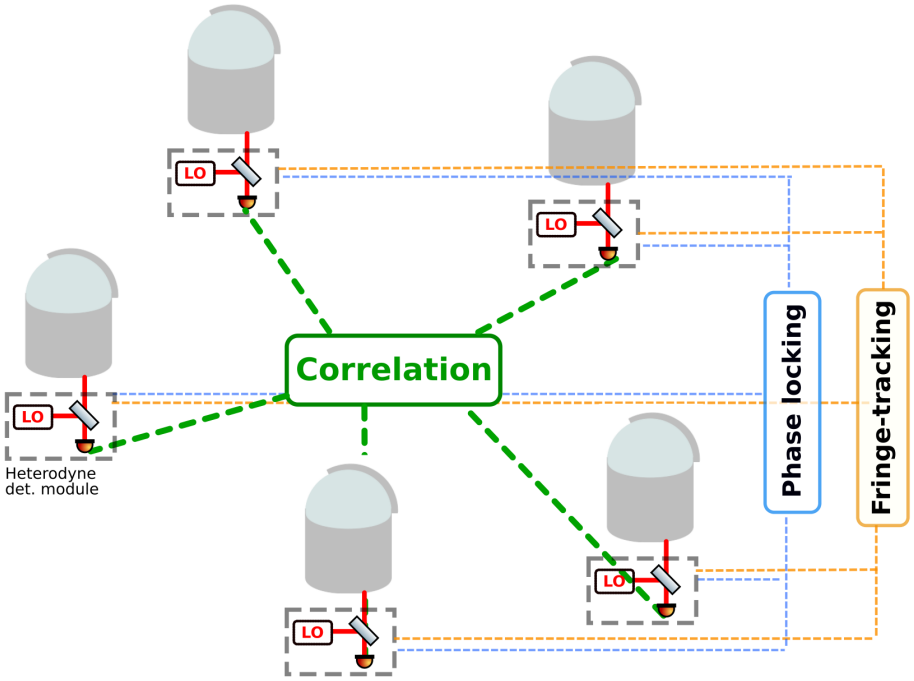

Fig. 4.1: System architecture of the mid-infrared heterodyne interferometer considered in this work for a PFI.

dispersed, and mixed with the corresponding spectral channel of the astronomical signal on a photodiode. Then, the output signal of each photodiode is either transmitted in an analog transmission link and processed in an analog correlator, or digitalized by an Analog-to-Digital Converter (ADC) and transmitted to a digital correlator (e.g. as ALMA or NOEMA arrays), or stored for later processing (in a similar way to Very Long Baseline Interferometry). For low spectral resolution mode, the correlator would compute the correlation product integrated over the bandwidth of the photodiodes. The correlation signal associated to each spectral channel could then be averaged in order to maximize the sensitivity. In the case of high-resolution spectral resolution observations, the correlator computes the correlation in spectral bins inside the detection bandwidth of the photodiode, as it is done in ALMA or NOEMA correlators. The goal of this architecture is to increase the spectral coverage of heterodyne detection and/or its sensitivity, by increasing the number of spectral channels. This increase of sensitivity and instantaneous bandwidth can also be achieved in part by an increase of the detection bandwidth of the photodiode, given that the detected RF signal of a heterodyne detection is proportional to the field of the incident astronomical signal. The second main aspect in order to increase the sensitivity in this heterodyne architecture is the referencing of the science channel on an external near-infrared fringe-tracker. In this process, the atmospheric piston (relative phase fluctuations between each telescope due to the atmosphere, see Chap 2) is measured by the near-infrared fringe tracker and the correction is applied directly on the science signal, in the correlator for example. A similar system is demonstrated at VLTI in direct interferometry, where the GRAVITY instrument (K band) acts as a fringe-tracker for the MATISSE instrument (L, M and N band). Although the use of a direct interferometer to cophase a heterodyne interferometer may appear counter-intuitive, the

major guess behind this architecture is that the fringe tracker can be implemented with near-infrared fibered technology which relaxes massively the requirement on the infrastructure, such as (Julien Woillez et al., 2017), which will be discussed in Sec. 4.5.

The essential subsystems shown in Fig 4.6 and their general function are :

- *Local oscillator & signal synchronization :* a frequency comb is placed at each telescope, and each tooth of the comb acts as a local oscillator (see 'Focal instrumentation'). The frequency comb can operate in Continuous Wave (CW) regime, the essential function being that the relative phase between each tooth is stable over time in order to guarantee the phasing of the array. The relative phase of each comb has to be stabilized between each telescope by a dedicated phase locking system, possibly using a transport of the locking signal in the near-infrared rather than in the mid-infrared (see Sec 4.5). This relative phase has to be stable over the maximum coherent integration time set either by the atmosphere (no fringe-tracker) or by the fringe tracker (coherent integration).

- *Focal Instrumentation :* the light in H-K band and in N band are separated and directed to the fringe-tracker and the science channel respectively. For the science channel, the focal instrument is composed of a spectrograph and an array of mid-infrared photodiodes, with as many photodiodes as the number of comb teeth. The total number of channels and comb teeth depends on the bandwidth of the photodiodes.

- *Signal transport & storage :* the signal transport of the wideband RF heterodyne signals can be performed both in analog or digital systems, whose relative technological advantages are discussed in Sec 4.5. From a purely system point of view, an additional feature of digital systems is the capability to register the signal for later processing.

- *Correlation :* Its essential function is to compute the correlation product of each pair of signals, and in the case of high spectral resolution observations, to perform spectroscopy inside a detection bandwidth. The correlation can both be performed in the analog or digital domain, depending on the technological solution envision.

- *Fringe-tracking :* the fringe-tracker measures the atmospheric piston between each pair of telescopes and provides the error signal to be applied on the science channel to correct this relative phase fluctuation.

4.3 Heterodyne interferometry : signal to noise ratio

We now recall the computation of the SNR of heterodyne detection with one telescope. Given that a heterodyne detection is sensitive to the electric field, it is necessary to measure the modulus square of the photo-current i.e. the RF power, in order to have access to the intensity of the incident field, in a so-called "radiometer mode" :

$$P_k(\nu) \propto \langle E_k(t) E_k^*(t) \rangle \tag{4.1}$$

The calculation of the SNR of this quantity is given in Kingston, 1978 specifically for an infared detection, and is in fact analogous to the so-called *radiometer equation* in the radio-domain. The result at one telescope will give us a basis to introduce the SNR on the interferometric signal, which in an analogous way results from the multiplication product of two signals :

$$C_{12}(\tau) \propto \langle E_1(t) E_2^*(t-\tau) \rangle \tag{4.2}$$

In the literature, it is generally assumed that the SNR computed for one telescope directly applies to the SNR on the correlation of telescopes. In the following, we will try to give a little more detail on this point, based on the treatment of a heterodyne detection (Kingston, 1978) and of a radio-interferometer (Thompson, Moran, and Swenson, 2017).

4.3.1 Single channel SNR

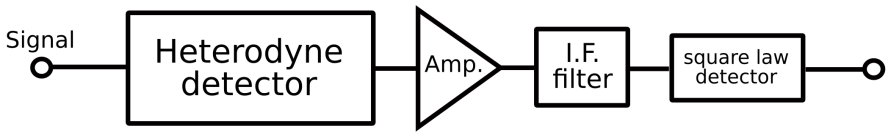

Fig. 4.2: Block diagram of a single channel heterodyne detection chain in radiometer mode, adapted from Kingston, 1978.

The general set-up to measure a heterodyne signal with a single detector in radiometer mode (as opposed to two detectors in interferometry) is depicted in 4.2. After the detector, the photocurrent is amplified and filtered, and then passes through a square law detector. The voltage output of the square-law detector is proportional to the square of the input photocurrent $v = k\overline{i^2}$, with k a given constant of the diode, so that it is indeed proportional to $v \propto |E_s(t)|^2$. In this way, the heterodyne detection chain with a single detector acts as a *radiometer*. The current at the output of the photodiode is sensitive directly to the electric field E_s of the incident light. Because the field considered in this study will be incoherent, E_s oscillates in the phase space in a Gaussian manner, in a similar way to a random walk in a two dimensional plane, with two quadratures of the field being independent. The statistical distribution of the output photocurrent is thus described by a gaussian distribution[1] with a variance $k\overline{i_N^2}$ equal to the noise power :

$$p(i) = \frac{1}{\sqrt{2\pi \overline{i_N^2}}} \exp\Big(-\frac{i^2}{2\overline{i_N^2}}\Big) \tag{4.3}$$

The result averages to zero when measuring only the voltage of the photocurrent (centered gaussian distribution), but to non-zero value when measuring the signal power $v \propto |E_s(t)|^2$. Following Eq 2.14, the power of the heterodyne beating signal is :

$$\overline{i_s^2} = \frac{(2\sqrt{i_{LO} i_s})^2}{2} = 2 i_{LO} i_s \tag{4.4}$$

[1] This statistical distribution will be verified experimentally in Chap 6

The power of the noise is dominated by the shot noise of the laser[2] :

$$\overline{i_N^2} = 2ei_{LO}\Delta\nu \tag{4.5}$$

The signal-to-noise ratio can then be obtained by computing the noise on the measurement of v, which can be obtained by computing the moments of the probability distribution of v, deduced from Eq 4.3 by setting $p(v)\mathrm{d}v = p(i)2i\mathrm{d}i$ [3], which enables to compute the rms noise on the measurement of $\overline{v}$:

$$v_{rms} = \frac{k\overline{i_N^2}}{\sqrt{2\Delta\nu t}} = k\frac{2ei_{LO}\Delta\nu}{\sqrt{2\Delta\nu t}} \tag{4.6}$$

which can be simply seen physically as the noise power at the output of the detector averaged over $2\Delta\nu t$ samples (Nyquist criteria). The signal is $v_s = k\overline{i_s^2}$. Finally, expressing the photocurrent i_s as a function of the power density P_ν [W.Hz^{-1}] and η of the quantum efficiency of the detector :

$$i_s = \frac{\eta}{h\nu}P_\nu\Delta\nu \tag{4.7}$$

The SNR of a single detector heterodyne radiometer is :

$$\mathrm{SNR} = \frac{v_s}{v_{rms}} = \frac{\eta P_\nu}{h\nu}\sqrt{2\Delta\nu t} \tag{4.8}$$

This results is also known in radio-astronomy as the *radiometer* equation[4].

In practice, the detection and amplification chain adds supplementary noise. Following Kingston, 1978, the total noise power is :

$$\overline{i_N^2} = 2ei_{LO}\Delta\nu + \frac{4kT_N\Delta\nu}{R} \tag{4.9}$$

with T_N the noise temperature of the detection chain. T_N is equal to the temperature of a load that would produce the same noise power than the detector and the amplification chain. In particular in Chap 8, this will enable us to take into account the noise power of the amplification chain in the total noise budget[5]. In the following, we will take into account

[2] The power fluctuation associated to an incoherent field can be neglected here, given that we will only consider a weak thermal field in the following, and thus very low occupancy number of the photons. The power fluctuations being at the basis of the Hanbury-Brown Twiss effect, this highlights the intrinsically different physical nature of these two types of interferometry, heterodyne detection remaining a form of amplitude interferometry.

[3] The calculation of the moments is provided in Kingston, 1978 Chap 11.2 (pp 126-130). See also Boyd, 1983, which converges to a similar result.

[4] The radiometer equation in radio-astronomy is usually without the factor 2 in the square root $\frac{T_A}{T_S+T_A}\sqrt{\Delta\nu t}$. T_A and T_S are the antenna and system temperatures, which corresponds to the load temperatures that produce the signal and noise power respectively (kT_A and kT_S resp.), see Thompson, Moran, and Swenson, 2017. The presence of the factor 2 in this case is justified in Kingston, 1978, Chap 11.2, p129, which comes itself from the choice of convention of the low-pass filter (real integrator filter, rather than ideal filter, see also Bracewell, 1965).

[5] We refer the reader to (Kingston, 1978), Chap 4, for more details on this notion.

these non-ideal effects by expressing the final SNR in comparison to the SNR limited by the shot noise, by introducing a noise penalty factor n_p :

$$\mathrm{SNR} = \frac{\eta P_\nu}{n_p h\nu}\sqrt{2\Delta\nu t} \tag{4.10}$$

This noise factor penalty n_p can also be seen as the ratio of the total noise power over the noise power with shot noise only.

Importantly, we note that the calculation of the SNR for a infrared heterodyne interferometer is exactly analogous to the derivation of the moments in the demonstration of the radiometer equation in radio-astronomy ((Thompson, Moran, and Swenson, 2017), Appendix 1.1 46-48). This should not be surprising, given that the detector output in radio-astronomy can also be assumed to be Gaussian (incoherent field). In the radio-domain, the noise budget is however mostly dominated by the noise temperature of the detection system (right term in Eq.4.5). This also explains why it is convenient to express the signal and the noise power in terms of noise temperature in radio-astronomy. Conversely, in the infrared domain, the optimum signal to noise ratio is reached when the photon noise of the LO dominates the noise. Importantly, given that the typical magnitude of the shot noise can be relatively high (see Chap 8), this allows the noise temperature of the amplification and processing stages after the detector to be relatively high in infrared heterodyne interferometry, contrary to radio-astronomy, where specific cryogenic temperature have to be reached to maintain an acceptable noise level on the detector and amplification stages. The question whether the shot noise really is a fundamental limit in heterodyne detection is particularly important, and related to the very fundamental nature of light and of the detection process. This question will be treated in more details in Chap 5.

Usually, the Eq 4.8 is directly applied to 2 telescopes to justify the SNR on the interferometric signal. This is consistent with the fact that Eq 4.8 describes the SNR on the product of two signals, as for the interferometric signals. Based on the treatment provided in radio-astronomy, we will try to detail further the physical ground of the expression of the SNR of the interferometric signal.

4.3.2 Two channel SNR

The signal measured at the output of an heterodyne interferometer is the correlation of the RF signals $s_1(t)$ and $s_2(t)$ coming from the two telescopes :

$$C_{12}(\tau) = \langle s_1(t) s_2(t+\tau) \rangle \tag{4.11}$$

Signal to noise ratio

We want to evaluate the SNR of this quantity. Following Thompson, Moran, and Swenson, 2017, the expression of the noise can be obtained by expressing the power spectrum of $C_{12}(\tau)$, which in turn can be derived from the Fourier transform of the auto-correlation of $C_{12}(\tau)$,

according to the Wiener-Khintchin theorem. The auto-correlation $A(\tau)$ of the interferometric signal is :

$$A(\tau) = \langle s_1(t)s_2(t)s_1(t-\tau)s_2(t-\tau)\rangle \tag{4.12}$$

The different waveforms $s(t)$ are Gaussian signals, so that this expression can be split into a combination of simple 2-terms correlation function using the Wick-Isserlis theorem :

$$\begin{aligned} A(\tau) &= \langle s_1(t)s_2(t)s_1(t-\tau)s_2(t-\tau)\rangle \\ &= \langle s_1(t)s_2(t)\rangle \times \langle s_1(t-\tau)s_2(t-\tau)\rangle \\ &+ \langle s_1(t)s_1(t-\tau)\rangle \times \langle s_2(t)s_2(t-\tau)\rangle \\ &+ \langle s_1(t)s_2(t-\tau)\rangle \times \langle s_2(t)s_1(t-\tau)\rangle \\ &= C_{12}^2(0) + C_{11}(\tau)\cdot C_{22}(\tau) + C_{12}(\tau)\cdot C_{12}(-\tau) \end{aligned} \tag{4.13}$$

The power spectrum of $A(\tau)$ can then be obtained by a Fourier-transform of Eq 4.13. This exact calculation, which would be relatively cumbersome to reproduce in details here, can be found in (Thompson, Moran, and Swenson, 2017) Section 6.2.1 (pp 224-226), in the case of a radio-signal, considering that only one sideband is measured. The result in that case is :

$$\mathrm{SNR} = \sqrt{\frac{T_{A1}T_{A2}}{T_{S1}T_{S2}}}\sqrt{2\Delta\nu t}$$

with T_{Ak} and T_{Sk} the antenna and system temperatures of each channel. By expressing the signal and the noise amplitudes of a heterodyne signal corresponding to the antenna and noise temperature in Eq 4.3.2 (see the radiometer equation to obtain the transposition of these amplitudes), this SNR can be directly written :

$$\mathrm{SNR} = \frac{P_\nu}{h\nu}\sqrt{\frac{\eta_1\eta_2}{n_{p1}n_{p2}}}\sqrt{2\Delta\nu t} \tag{4.14}$$

with η_1, η_2 the quantum efficiency at telescopes 1 and 2, and n_{p1}, n_{p2} the noise factors of each channel.

Noise

The noise power in $[\mathrm{W.Hz}^{-1}]$ for *one polarisation* of the field can be finally defined as the equivalent power that produces $\mathrm{SNR} = 1$:

$$N_\nu = \frac{h\nu}{\sqrt{2\Delta\nu t}} \tag{4.15}$$

The interferometric visibility is characterised by its amplitude and its phase i.e. it is a complex quantity, whose noise on both quadratures has an amplitude σ and is uncorrelated. Following (Thompson, Moran, and Swenson, 2017), the measurement of the visibility can be represented in the complex plane as the addition of noise ϵ to a coherent flux S, which can be considered to lie on the real axis (arbitrary phase reference). The modulus squared of the total signal $Z = S + \epsilon$, is :

$$\left\langle |Z|^2 \right\rangle = S^2 + 2N_\nu^2 \tag{4.16}$$

The noise on each quadrature is N_ν, which adds together, decreasing the total SNR in Eq 4.14 by a factor $\sqrt{2}$. Thus, in the case of a single-sideband signal measured with a complex correlator (measurement of the two quadratures), the SNR on the amplitude of the complex visibility is :

$$\mathrm{SNR}_{\mathrm{SSB,complex}} = \frac{P_\nu}{h\nu}\sqrt{\Delta\nu t} \tag{4.17}$$

In the same way, a DSB signal measured with a simple correlator, where the fringes are encoded on a sinusoidal modulation, such as in ISI or in the photonic correlator that we will introduced in Chap 6, can be shown to have a relative sensitivity of $\sqrt{2}$ compared to $\mathrm{SNR}_{\mathrm{SSB,complex}}$:

$$\mathrm{SNR}_{\mathrm{DSB,simple}} = \frac{P_\nu}{h\nu}\sqrt{2\Delta\nu t} \tag{4.18}$$

In order to summarize these different results, our reference expression of the SNR in the following will be :

$$\boxed{\mathrm{SNR} = \frac{P_\nu}{h\nu}\sqrt{\Delta\nu t}} \tag{4.19}$$

where $\Delta\nu$ is equal to detector bandwidth B in the case of single-sideband correlation $\Delta\nu = B$, and $\Delta\nu = 2B$ in the case of DSB signal. Eq.4.19 has an expression similar to the SNR provided in John David Monnier, 1999 and C. H. Townes, 1984; D. D. S. Hale et al., 2000.

The different results concerning SSB with complex correlator, DSB with simple correlator, etc. are summarized in Tab 4.5 in Appendix, although we refer to Thompson, Moran, and Swenson, 2017 for a precise discussion on these specific points.

4.3.3 Incoherent integration

The signal-to-noise ratio described so far is valid for a coherent integration of a complex visibility i.e. a measurement of visibility during which the phase remains stable over time and can be measured. This provides the elementary expression of the SNR.

This situation corresponds however to a relatively limited number of measurement in infrared interferometry. Unlike radio-arrays, in which the interferometric phase can remain relatively stable in time due to the relatively slow atmospheric piston, infrared interferometers are often limited to integration of the order of $t_0 = 100\,\mathrm{ms}$ at $10\,\mu\mathrm{m}$. As a consequence, the measurement of a visibility is typically limited to the measurement of the modulus squared of the visibility, averaged over N samples of the coherence times ($t = N\tau_c$) - an operation called *incoherent* integration, given that the phase is thrown away in the process. In this way, this type of measurement is similar to incoherent integration in VLBI observations, which shares analogous problematic on phase stabilization due to the atmosphere. The results derived in this case directly applies to incoherent integration in infrared heterodyne interferometry.

The exact derivation of the SNR in incoherent integration can be found in (Thompson, Moran, and Swenson, 2017) Chap 9.3.5 pp 415-418, of which we will only recall the very basic

results that will be used in the following. According to Eq 4.16, the unbiased coherent flux amplitude S_e is :

$$|S_e| = \sqrt{Z^2 - 2N_\nu^2} \tag{4.20}$$

Similarly, the second order moment on the modulus square of the visibility, from which the expression of the noise on $|S_e|^2$ can be deduced, is (Thompson, Moran, and Swenson, 2017):

$$\left\langle |S_e|^4 \right\rangle = |S|^4 + 4N_\nu^2 \frac{|S|^2 + N_\nu^2}{\sqrt{N}} \tag{4.21}$$

The signal-to-noise ration on the incoherent integration of visibility square modulus is finally :

$$\mathrm{SNR}_{\mathrm{inc}} = \frac{\langle |S_e|^2 \rangle}{\sqrt{\langle |S_e|^4 \rangle - \langle |S_e|^2 \rangle}} = \frac{|S|^2}{2N_\nu^2} \frac{1}{\left(1 + \frac{|S|^2}{N_\nu^2}\right)} \sqrt{N\tau_c} \tag{4.22}$$

Finally, it can be expressed as a function of the incident signal power using our reference expression on the SNR in Eq 4.19, assuming that the signal to noise is small $\frac{S}{N_\nu} \ll 1$:

$$\mathrm{SNR}_{\mathrm{inc}} = \left(\frac{P_\nu}{h\nu}\right)^2 \Delta\nu \sqrt{t\tau_c} \tag{4.23}$$

This expression is equivalent to the SNR on incoherent integration provided in (C. H. Townes, 1984; D. D. S. Hale et al., 2000), based on different arguments. As pointed out in (C. H. Townes, 1984), this SNR can be simply interpreted as the square of the coherent SNR (modulus squared, incoherent integration) multiplied by $\sqrt{N}$, the number of independent coherent chunks in the total integration time. This expression and its connection with equivalent relations in radio-astronomy and VLBI is made clear in the present derivation.

We note that incoherent integration is a particularly inefficient process : the SNR of the visibility squared scales as the power $1/4$ with the total integration time. As an order of magnitude, assuming a coherence time $t_0 = 100\,\mathrm{ms}$, a $1\,\mathrm{h} = 3600 \times 10\, t_0$ incoherent integration represents an increase of ~ 13 of the SNR, compared to ~ 190 in coherent integration. These considerations emphasize the fundamental necessity of coherent integration, and thus fringe-tracking, in order to obtain good point source sensitivity.

4.3.4 Point source sensitivity & imaging

The SNR of an unresolved point with an interferometer with N_t telescopes is equal to the SNR over a single baseline, averaged over the total number of independent samples, which corresponds here to the total number of baselines $N_B = \frac{N_t(N_t-1)}{2}$. Here, we will express the point source sensitivity n_{ps} in [W.m^{-2}.Hz^{-1}], so that $N_\nu = n_{\mathrm{ps}} \times A$, with A the collecting area of each individual telescopes. Using Eq 4.19, the point source sensitivity of the interferometer is[6] :

$$n_{\mathrm{ps}} = \frac{h\nu}{\eta A \sqrt{\Delta\nu t}} \frac{1}{\sqrt{N_t(N_t-1)/2}} \tag{4.24}$$

[6] In the case of a combination of telescopes with different areas or transmissions efficiencies, quantum efficiencies, etc., the factor in Eq 4.24 is replaced by the geometrical mean of the two channels : $\eta A \to \sqrt{\eta_1 \eta_2 A_1 A_2}$

Notably, we remark that the global sensitivity in heterodyne interferometry scales as $\propto N_t$, compared to $\propto \sqrt{N_t}$ using classical interferometry[7]. This is due to the fundamental fact that signals in heterodyne interferometry can be amplified and split without further loss in SNR, unlike direct interferometry. This adds a relative gain to heterodyne interferometry compared to classical interferometry, of $\sqrt{\frac{N_t-1}{2}}$ (see (Ireland et al., 2016) for a detailed discussion), which is typically ~ 2.5 for $N_t = 12$.

To conclude, as an order of magnitude, the typical point source sensitivity of a heterodyne array with simple DSB correlator, defined as the equivalent object flux [W.m^{-2}.Hz^{-1}] to obtain a SNR $= 1$, is :

$$n_{\rm ps} = \frac{1}{\eta}\left(\frac{1\,\mathrm{m}}{D}\right)^2\left(\frac{1\,\mathrm{GHz}}{B}\right)^{1/2}\left(\frac{100\,\mathrm{ms}}{t_c}\right)^{1/2}\left(\frac{t_c}{t_i}\right)^{1/4}\cdot\frac{1}{\sqrt{N_t(N_t-1)/2}}\times 170\,\mathrm{Jy} \tag{4.25}$$

with D the telescope diameter, B the bandwidth of the detector, t_c the coherent integration time, and t_i the incoherent integration time.

In the following, we will further discuss the relative advantages related to the optimization of each parameter of a heterodyne system in order to increase the point source sensitivity.

4.4 Sensitivity performance

In this section, we discuss the sensitivity performances of the heterodyne scheme devised for a Planet Formation Imager in the N band. Based on the theoretical noise analysis in Sec 4.3, we discuss the scaling of the sensitivity performances relative to each parameter of the array, assuming technological hypothesis on the future development of these subsystems. We then compare these sensitivity performances to the requirements of a PFI. The feasibility of our technological hypothesis at the light of the current state of the mid-infrared technologies is addressed in Sec 4.5. Finally, we discuss some general considerations generally assumed in the literature when comparing the sensitivity of heterodyne and direct interferometry. Overall, the goal of this section can be seen as a first estimation of the sensitivity increase that can be expected for heterodyne interferometry, weighted by the technological challenge necessary for each technological subsystems.

Performance scale-up The scale-up of the sensitivity of a heterodyne interferometer can be estimated with Eq 4.25. The relative impact of each parameters in the final sensitivity of the heterodyne architecture can be seen in Tab 4.2, where we chose typical values for the different items envisioned in the heterodyne architecture of a PFI.

We remark that the total sensitivity increase with the detection bandwidth is of the order of $\sqrt{\frac{2.5\,\mathrm{THz}}{2.5\,\mathrm{GHz}}} \approx 30$. Here, we separated the contribution of the bandwidth increase in two contributions : first, the increase of the individual bandwidth, second the increase of the

[7] With the exception of densified pupil, whose implementation in mid-infrared on a large number of telescopes has not yet been envisioned.

number of comb teeth. In the first case, the sensitivity increase can be obtained without requiring the use of a frequency comb, and is thus interesting for immediate application. This also highlights the massive impact on the sensitivity budget of the telescope diameter $\propto D^2$ and of coherent integration with the use of a fringe-tracker. This can motivate the adaptation of pathfinder demonstrators to existing infrastructure, as explored in 9, even without the implementation of a massive multiplexing in a first time. Finally, the recombination of a large number of telescopes also appears as an important factor of sensitivity increase, comparable with the spectral multiplexing.

Item	Parameter	Gain	Comment
Detector bandwidth	$\Delta\nu$	$\sqrt{10} = \times 3$	QCD, QWIP and wide-bandwidth correlators
Telescope diameter	D	$\times 1$ to $\left(\frac{4.5}{1.6}\right)^2 = \times 7.9$	moving from 1.6m ISI to 4.5m diameter telescopes
Number of telescopes	N_t	$\times 1$ to $\sqrt{\frac{N_t(N_t-1)}{2}} = \times 8.1/\times 15$	moving from ISI 2T to PFI 12T / 21T telescopes
Spectral channels	N_{sp}	$\times 1$ to $\sqrt{100} = \times 10$	1 to 100 spectral channels QCL combs, photonic comb, mode-locked laser
Coherent integration	t_c	$(60 \times 10)^{1/4} = \times 4.9$ and $(3600 \times 10)^{1/4} = \times 14$	moving from incoherent to coherent int. 1min and 1h with $t_0 = 100\,\mathrm{ms}$

Tab. 4.2: Scaling of the performances on the point-source sensitivity of a heterodyne interferometer. The point source sensitivity of the ISI was typically 50-100 Jy in t=1h *incoherent* integration.

4.4.1 Imaging sensitivity & brightness temperature

Technological hypothesis The typical technological parameters assumed to compute the sensitivity of a PFI array are summarized in Tab 4.3. We assumed an array of 12 telescopes with 4.5m diameter. We assume a detector with 25 GHz and 0.4 quantum efficiency, whose values were chosen compared to the value reachable with QCD technology. We integrate the non-ideal factors of degradation of the SNR (noise penalty, telescope transmission) based on the numbers reported on the ISI (D. D. S. Hale et al., 2000). The number of telescopes and their diameter are chosen for indicative purpose. Overall, the goal of this choice is to provide the right order of magnitude of sensitivity of a PFI architecture[8], in order to ensure that this sensitivity is compatible with the sensitivity criteria defined in PFI.

Brightness temperature The final goal is a point source sensitivity of $m_N \sim 12.5$ in $10^4\,\mathrm{s}$. In the context of imaging, in a similar way to radio-imaging, this sensitivity limit should be related to the minimum brightness that can be detected in an image, a "point" being defined by the minimum element of resolution of the image. Assuming that the uv-coverage

[8] In addition, this value of point source sensitivity can be scaled by the reader to a different set of parameters using Eq 4.24.

Item	Parameter	Value
Wavelength	λ	$10.5\,\mu$m
Angular resolution	θ	2 mas
Number of telescopes	N_t	12
Diameter	D	4.5m
Quantum efficiency	η	0.4
Telescope transmission	T_t	0.6
Noise penalty	n_p	1.5
Bandwidth	$\Delta\nu$	25 GHz
Spectral channels	N_{sp}	100

Tab. 4.3: Technological parameters chosen for the sensitivity calculation of the array.

is sufficient to obtain a reconstructed beam with Gaussian shape, with typical FWHMs θ_1,θ_2 in each direction, the solid angle Ω of an element of resolution of the image is :

$$\Omega = \frac{\pi\theta_1\theta_2}{4\ln(2)} \tag{4.26}$$

Assuming that the flux limit is detected in one resolution element $n_{ps} = \frac{\Omega}{\lambda^2} \times 2h\nu/\left(e^{\frac{h\nu}{k_B T}} - 1\right)$, this point source sensitivity can be conveniently converted into a brightness temperature i.e. the equivalent temperature of an optically thick medium emitting this flux limit in an element of resolution (Ravi et al., 2011; Lobanov, 2015; Thompson, Moran, and Swenson, 2017) :

$$T_b = \frac{h\nu}{k_B \ln\left(1 + \frac{2h\nu\Omega}{c^2 n_{ps}}\right)} \tag{4.27}$$

The above mentioned point source sensitivity requirement is thus equivalent to a brightness temperature of $\sim 150\,\mathrm{K}$ for an angular resolution of $2\,\mathrm{mas} \equiv 0.3\,\mathrm{AU}$ in the Taurus ($d = 140\,\mathrm{pc}$). This goal on brightness temperature is even more demanding for higher angular resolution.

The point source sensitivity as well as the temperature brightness of an array based of a heterodyne architecture of a PFI are indicated in Fig 4.3, based on the technological parameters of Tab 4.3.

Comments This analysis converges with the initial estimation provided in (Ireland and John D. Monnier, 2014). The result of the present sensitivity estimation is compatible with the sensitivity requirements of Chap 2 provided that two essential technological developments are implemented : first, a long-time coherent integration, which supposes stable relative phase of local oscillators on time scale of $10^4\,\mathrm{s}$ and the compensation of atmospheric phase fluctuations with an external fringe tracker ; second, massive multiplexing (100 channels), based on a dispersed heterodyne detection scheme. These two specific developments will be detailed in 4.5.

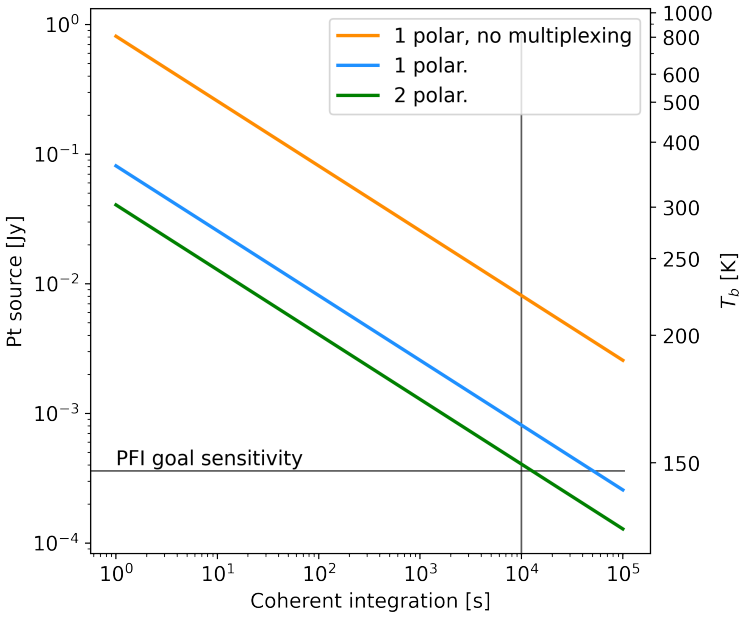

Fig. 4.3: Point source sensitivity and brightness temperature for an angular resolution $\theta = 2\,\mathrm{mas}$, based on the parameters in Tab 4.3.

4.4.2 Comparison with direct interferometry

How does heterodyne noise compare with direct detection noise ? It is often stated that heterodyne detection suffers from an incommensurable sensitivity penalty compared to direct detection. This is definitely the case when moving to a short wavelength regime ($< 5\,\mu\mathrm{m}$), as the equivalent noise temperature of heterodyne detection is inversely proportional to the wavelength[9] This is also obviously true at $\lambda = 10\,\mu\mathrm{m}$ when comparing a single channel heterodyne system to a direct detection one in low spectral resolution mode, the archetypical example being the comparison between ISI and MIDI instruments. However, in the more general case, a detailed look provides a more nuanced picture. In the following, we focus on the relative sensitivity of direct interferometry and heterodyne interferometry, in particular taking into account the effect of spectral resolution and of the number of telescopes. We highlight the importance of taking into account the read-out noise when comparing these systems, a point which is generally neglected in the literature.

The sensitivity penalty of heterodyne detection compared to direct detection can be evaluated by computing the ratio of the noise density associated to each technique, in a similar way to (Lawson, 2000). Following our description of the noise in heterodyne detection, the noise density in heterodyne detection is :

$$N_{\nu,\mathrm{het}} = \frac{1}{\eta}\frac{h\nu}{\sqrt{2\Delta\nu t}} \tag{4.28}$$

[9] Or in space, where the absence of background noise boosts massively the sensitivity of any direct system.

using the same notation introduced before, and η the total transmission and noise penalty of a practical detection chain (including telescope transmission, mode matching, etc.).

In the same way, the SNR of direct detection (considering an all-in-one combiner) is expressed as (Petrov et al., 2020) :

$$\frac{S}{N_{\nu,\mathrm{dir}}} = \frac{n^I V}{\sqrt{N_t(n_b + n^I) + n_{\mathrm{pix}} \cdot \mathrm{RON}^2}} \tag{4.29}$$

with $n^I = \frac{P_\nu \Delta\nu t}{h\nu}$ the number of photons in the interferometric channel, n_b the number of background photon, N_t the number of telescopes, n_{pix} the number of pixels on which the signal is encoded in all-in-one combination, RON the Read-Out-Noise of the detector. In the following, we will neglect the contribution of the signal photon noise, given that background photon noise and RON are always prevailing. In this way, we can express the noise density of direct detection :

$$N_{\nu,\mathrm{dir}} = \frac{1}{\eta}\frac{h\nu}{\Delta\nu t}\sqrt{N_t \cdot n_b + n_{\mathrm{pix}} \cdot \mathrm{RON}^2} \tag{4.30}$$

The ratio of the noise density of heterodyne detection over direct detection is shown in Fig . The parameters used for this comparison are the typical parameters reported on ISI and the design parameters of MATISSE N-band ; these parameters are summarized in the Appendix in Tab 4.4. This same ratio was in fact computed in Lawson, 2000, but without including RON, which has a significant impact on this comparison, as we will see in the following.

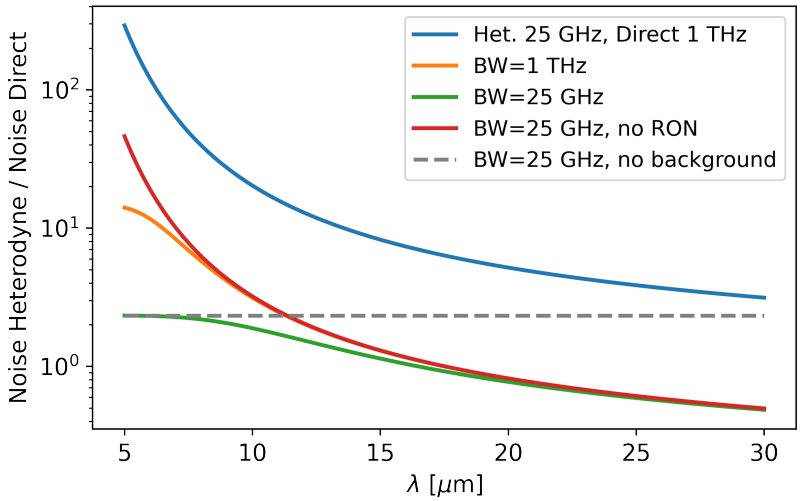

Fig. 4.4: Ratio of the noise density in heterodyne and direct interferometry. The exact parameters used in this comparison are provided in Tab 4.4.

The Fig 4.4 highlights the different regimes of this comparison. The comparison of two usual systems generally considered - a direct interferometer at low spectral resolution ($R \sim 30$) in direct detection, with a single heterodyne channel with 25 GHz - shows the large advantage of direct detection, of more than one order of magnitude, due both to the larger bandwidth and

the lower noise of direct detection (limited by background photon noise, small contribution of RON compared to background). When considering equal bandwidth (orange line) with low resolution[10] (1 THz), direct detection remains more sensitive but by a factor 3 to 4 at $10\,\mu\mathrm{m}$. In this regime at $10\,\mu\mathrm{m}$ the noise budget of direct detection is mainly dominated by background photon noise, a feature that can also be seen when comparing the noise ratio computed with a different detection bandwidth and suppressing read-out-noise (25 GHz, red curve). In this case, the two curves (orange and red) are superimposed at $\sim 10\,\mu\mathrm{m}$, which is consistent with the fact that the noise ratio does not depend on the detection bandwidth when considering that direct detection is limited by background photon noise only (Lawson, 2000). However, this noise budget is getting saturated by read-out-noise, an effect seen at lower spectral resolution (25 GHz, green curve). In this regime, the gain of direct detection is approximately a factor 2 compared to heterodyne detection due to RON, whose relative contribution increased at smaller wavelength (orange curve that diverges from red curve).

To sum up, three points can be retained :

- the comparison of typical performances of archetypal instruments in direct and heterodyne interferometry - MIDI and ISI typically- is not exactly informative in the perspective of a PFI, given that two extreme cases are compared in terms of detection bandwidth (and telescope diameter in the case of MIDI).

- at comparable bandwidth, the sensitivity gain of direct interferometry over heterodyne is typically a factor of 3 and 4, when dominated by photon noise of the background, assuming the transmission obtained on each technique in practice.

- this gain of direct detection is affected by the contribution of the read-out-noise, which becomes important when increasing the spectral resolution, up to a regime where heterodyne detection is more favourable in terms of sensitivity.

The impact of the spectral resolution on the relative comparison between direct and heterodyne interferometry is provided in the next paragraph.

4.4.3 Impact of the spectral resolution

This simple comparison highlights the importance of read-out-noise in the budget of direct interferometry, which prevails at higher spectral resolution. In order to compare the relative gain when considering higher spectral resolution, we can compare the noise ratio as a function of the detection bandwidth, in a similar way to (John David Monnier, 1999), but including the parameter of MATISSE (Tab 4.4). The gain as a function of bandwidth is shown in Fig 4.5. The relative advantage of direct detection is strongly affected by RON at higher spectral resolution, the exact limit between heterodyne and direct detection being largely dependent on the number of pixels used to encode the fringe signal, on the value on the read-out-

[10] This supposes already that we consider a dispersed heterodyne system covering 1 THz

Item	Parameter	Value	
	Wavelength	λ	$10.5\,\mu$m
	Integration time (one frame)	$t_{\rm int}$	100ms
	Number of telescopes	N_t	2
Heterodyne			
	Quantum efficiency	η	0.4
	Noise penalty	Np	1.5
	Bandwidth	$\Delta\nu$	25 GHz
	Telescope transmission	T_t	0.6
	Number of polarization detected		2
Direct			
	Bandwidth	$\Delta\nu$	1 THz and 25 GHz (R=30 and 1200)
	Total transmission	t_d	0.04
	Read-out-noise	RON	210
	Number of pixels	$n_{\rm pix}$	468
	Transmission of the background	T_{bb}	0.28
	Background emissivity	ϵ	0.8
	Background temperature	T_{bb}	270 K

Tab. 4.4: Parameters of the array considered for the comparison of direct and heterodyne detection sensitivity. The values of direct detection are based on the design of the MATISSE instrument in N band.

noise of the detector and of the maximum integration time of one frame of the detector (saturated by background). In order to highlight the impact of RON, we plot the relative noise factor with both a number of pixel $n_p = 6$ and $n_p = 468$ (MATISSE). In the latter case, the comparison shows that a single channel of a heterodyne and a direct system have comparable sensitivity for typical bandwidth between $\sim 10\,$GHz and $\sim 20\,$GHz (typically $10\,$GHz in this graph[11]). This exact number is also highly dependent on the maximum integration time allowed on MATISSE in N band (maximum time limited by the saturation of the detector due to background), chosen typically equal to 100 ms here. We emphasize that this comparison gives an order of magnitude and the tendency of each regime, with parameters chosen as close as possible to practical implementations, the definite optimum range of each regime in the case of a PFI design being highly dependent of the final design parameters.

4.4.4 Impact of the number of telescopes

It is also often stated that heterodyne detection has an advantage compared to direct detection when the number of telescopes increases. In the case of an all-in-one combiner as considered here, where all the baselines are formed simultaneously on a detector via a non-redundant spatial encoding, this statement is not exactly true at high-spectral resolution. Since the number of photons is not divided (unlike pairwise combination) and that the noise is dominated by RON, no further penalty is added from the background noise with a

[11] This value is comparable but slightly larger than the value derived in (John David Monnier, 1999), likely due to a larger number of pixels considered here.

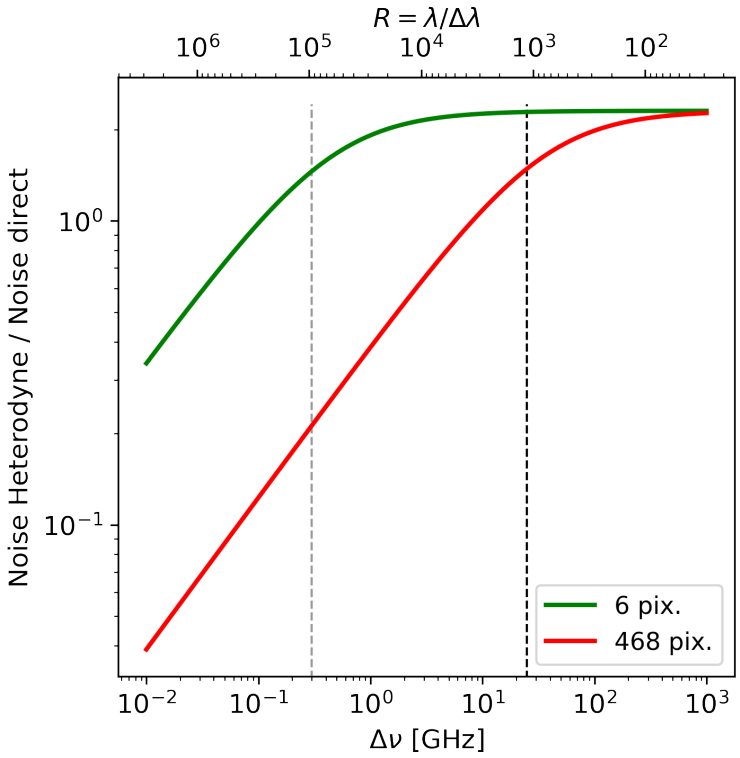

Fig. 4.5: Ratio of the noise density in heterodyne and direct interferometry for a single spectral channel as a function of detection bandwidth, with the same parameters as in Fig 4.4.

larger number of telescopes, as long as the background noise remains significantly smaller than read-out-noise[12]. In the case of low spectral resolution, dominated by background or signal photon noise, the background noise increases as $\sqrt{N_t}$, the number of baselines as $\sqrt{\frac{N_t(N_t-1)}{2}}$, so that the total SNR increases typically as $\sqrt{(N_t-1)/2}$, compared to $\sqrt{\frac{N_t(N_t-1)}{2}}$ in heterodyne interferometry. In this case, direct interferometry is indeed affected by an additional penalty of the order of $\sqrt{N_t}$ compared to heterodyne detection. For a large number of telescopes, the theoretical advantage of direct detection over heterodyne at low spectral resolution shown in Fig 4.4 is potentially significantly affected for a large number of telescope (>12, $\sqrt{12} \approx 3.5$). In the case of pair-wise combiner, given that each beam is divided in $(N_t - 1)$ channels, this penalty is always present.

4.4.5 Conclusion on heterodyne interferometry sensitivity

At $10\,\mu$m, the comparison of the noise budget of heterodyne and direct interferometry gives a more nuanced picture of the relative advantage of both techniques. The theoretical advantage of direct interferometry is tempered by the larger noise of a practical infrastructure, the background noise and the read-out-noise of the detector. At low spectral resolution, direct interferometry (when limited by background photon noise) does have sensitivity advantage, although this advantage is attenuated when combining a larger number of telescopes. At high

[12] We do not consider any additional technical penalty factors due to the practical implementation of an instrument combining a large number of telescopes in direct interferometry.

spectral resolution, this penalty when combining a larger number of telescopes disappears in all-in-one combination when the noise is dominated by read-out-noise, but in this case direct interferometry sensitivity is comparable or even smaller than heterodyne detection, unless considering a direct interferometer with a larger transmission, smaller RON and significantly smaller number of pixels on which the fringes are encoded. In particular, the impact of the read-out-noise in direct detection for only 4 telescopes raises the question of the optimum combiner for 12 telescopes and more, for which the design complexity and the number of pixels required in an all-in-one combiner dramatically increase.

These considerations qualify the generally admitted overwhelming superiority of direct interferometry in the N band for ground-based interferometers. Overall, the practical gain advantage of direct over heterodyne interferometry when considering direct interferometer combining a small number (<4) with low spectral resolution is clearly an upper limit in the theoretical comparison of the two techniques. This pure sensitivity advantage tends to be attenuated when combining a larger number of telescope (N>12) at modest high spectral resolution (R>3000), and favours heterodyne detection at high spectral resolution ($R > 10^4$). Fundamentally, in the N-band, the key advantage of direct interferometry lies not really in its much larger sensitivity, considering a practical infrastructure with generally low total transmission, but in its capability to naturally detect signals over THz bandwidth, and/or to multiplex easily a large number of spectral channels, a point which remains a major technical challenge of heterodyne detection. In that sense, the comparison of heterodyne and direct interferometry at $10\,\mu\mathrm{m}$ should revolve around the technical challenge associated to each technique, rather than the intrinsic sensitivity of each technique. These challenges are respectively the capability to synchronize and multiplex a large number of spectral channels in the case of heterodyne detection, and the capability to recombine a large number of telescopes and to transport and delay signals over kilometric baseline in the case of direct interferometry. In this sense, heterodyne detection is a path worth considering.

4.5 Technological challenges

The realisation of heterodyne array in the mid-infrared for the study of planet formation relies on major technological developments, related to the different subsystems that we have previously described. Considerable advances in the field of mid-infrared technologies have been achieved since the start of the development of ISI heterodyne interferometer in the mid 80s, almost forty years ago. This evolution follows the current rise of mid-infrared technologies in the last decade, pushed essentially by other communities, in fundamental physics, solid-state physics, laser physics and with strong applicative drivers such as gas sensing, communication or lidar. This development of mid-infrared technologies could be crucial in the frame of astronomical applications, and in particular in the perspective of the renewed picture of a heterodyne interferometer.

The goal of the following subsections is to give a panorama of the challenges of an infrared heterodyne interferometer and how new technologies could enable to overcome these chal-

lenges. This section will provide the context of the specific points that we have developed in the rest of this thesis.

4.5.1 Fundamental noise

A first fundamental challenge of heterodyne detection concerns its sensitivity limitation. This limitation arises from the fundamental quantum nature of the field, and is typically of the order of one photon per mode of detection. The exact understanding of the quantum origin of this noise remains relatively elusive in the field of infrared heterodyne interferometry, and different propositions were made to try to overcome this fundamental limitation (Michael and Besser, 2018; Le Coarer, Chalabaev, and G. Duvert, 2014). In Chap 5, we propose to investigate this question and to show that this quantum noise arises indeed from the fundamentally quantum nature of the field, which sets a lower bound to the value of the noise with this current detection scheme. Potentially more work could be envisioned to better understand the nature of this noise in the field of quantum optics, with interesting similarities with the field of Continuous Variable Quantum Communications (CVQC) for example. The existence of a protocol (analogous to squeezing techniques for example) allowing to increase in a significant manner the sensibility of heterodyne detection while keeping its practical advantages would represent a groundbreaking advance in infrared interferomertry.

4.5.2 Detection

The intrinsically narrow bandwidth available in heterodyne detection is both a major limitation both in sensitivity and in spectral coverage, as seen previously. The typical bandwidth of ISI system was 2.5 GHz based on MCT detectors, equivalent to a single channel at a spectral resolution of $R = 12\,000$. Ultimately, the bandwidth in MCT detectors is set by the recombination time of electrons and holes. Since 2000s, a different technologies based on intersubband transitions with Quantum Well Infrared Detectors (QWIP) and Quantum Cascade Detectors (QCD) has now demonstrated a potential increase of this bandwidth limit by more than one order of magnitude. The very heart of these technologies is based on the confinement and wave-function engineering of electrons in semi-conductors (Bigioli, 2021), enabling to reduce the capacitance and so to increase the speed of such detectors. Concerning QWIPs, recent developments show the demonstration of few GHz bandwidth at room temperature with QWIP (Palaferri et al., 2018), and up to 70 GHz (equivalent to $R = 430$) and responsivity $1.5\,\mathrm{A/W}$ with a detector cooled at $T = 77\,\mathrm{K}$ (Hakl et al., n.d.). Demonstrations with QCD also show very promising perspectives, with preliminary results in a heterodyne mode with $1.4\,\mathrm{GHz}$ bandwidth (Bigioli et al., 2020). Ultimately, these different technologies have the potential to reach bandwidth up to $100\,\mathrm{GHz}$ and even beyond, limited by the return to the equilibrium of the system, of the order of ps timescale.

The field of QWIP/QCD is a vibrant and fast evolving field of research, with potentially rapid improvements to be expected in the near term. The group of C.Sirtori at LPENS is one of the world-leading group in this field, who demonstrated the first detection at $9\,\mu\mathrm{m}$ with GHz bandwidth and room-temperature with QWIP (Palaferri et al., 2018). The exchanges with

this group are currently taking the form of a collaboration, in the exciting perspective of developing detectors with >20 GHz bandwidth and a quantum efficiency $\eta = 0.4$, which could be tested on a true on-sky demonstration.

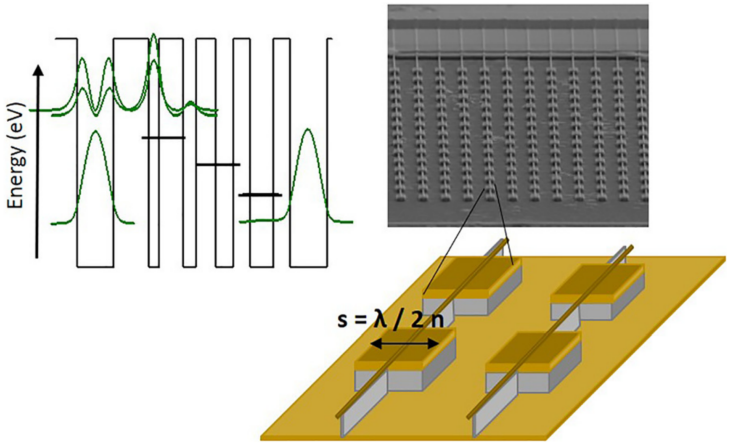

Fig. 4.6: QCD technology, from Bigioli, 2021. Upper-left: band diagram of the detector; Upper-right: SEM (Scanning Electron Microscope) image of an array of detector; Lower right: sketch of the array

4.5.3 Mid-infrared laser combs

The development of mid-infrared frequency comb lasers is currently a major and very active field of research in the laser physics community. Mode-locked lasers in the $10\,\mu\mathrm{m}$ range are now commercially available (Menlo System), with typical repetition rate of 100 MHz. However, larger repetition rates, equal to the detection bandwidth of our wideband detectors i.e. of the order of 10 GHz to 100 GHz, are preferable in the case of a dispersed heterodyne interferometer. Two possible alternatives are being developed in this direction, based on electro-combs (Parriaux, Hammani, and Millot, 2020) and QCL frequency combs (Consolino et al., 2019). The first one consists in generating a comb with telecom photonic modulator, which enables to obtain repetition rates of 10 GHz to 100 GHz and a hundred lines typically, which would then be converted in the mid-infrared through non-linear process. These schemes were demonstrated at $2\,\mu\mathrm{m}$ (Parriaux, Hammani, and Millot, 2019), but still need to be demonstrated in the $10\,\mu\mathrm{m}$ range, which depends mainly on the non-linear process available in this wavelength domain. The second technological developments (QCL combs based on Fabry-Pérot cavities) potentially offer very close properties to our requirements for a heterodyne interferometer : a frequency repetition rate of 10 GHz to 100 GHz, about 100 teeth, and an optical power of the order of mW per teeth ((Hugi et al., 2012), and now commercially available[13]). This type of technology represents also a currently active field of research and potentially very interesting avenue for infrared heterodyne interferometry.

[13] https://www.alpeslasers.ch/?a=28,126,191

4.5.4 Correlation

The correlation of tens of telescopes, with instantaneous bandwidths of 50 to 100 GHz such as the one expected with new generation detectors, and tens to hundreds of spectral bands is a major challenge of a heterodyne array. This correlation can be implemented in two different architectures : analog correlation and digital correlation. In analog correlation, the processing is directly performed on the analog RF signal, which generally enables to use broadband analog components with cheaper implementation, such as in ISI. In digital correlation, the RF signal is first digitalized, and then processed in a high-computing unit.

Digital architecture would be a prime option for infrared heterodyne interferometry, given its perfect stability, less SNR losses than analog correlation, and the capability to perform spectroscopy. In addition, the digitalization of the signal offers the capability to store the signal and to correlate it a posteriori. The two main challenges related to digital correlation are : first, the analog-to-digital conversion (ADC) at high rate ($> 20\,\mathrm{GSa/s}$ to $> 100\,\mathrm{GSa/s}$) and in particular the requirement on the timing of the clock in the ADC ; second, the total computing power necessary to correlate few bit Pflop data, larger than current supercomputer (Ireland and John D. Monnier, 2014). Currently, the NOEMA/PolyFIX correlator is currently the one accepting the widest instantaneous bandwidth per antenna, with 32 GHz wide digitized signals coming from 12 antennas (8 GHz per receptor for the two polarizations and two sidebands). ALMA can process 8 GHz wide signals coming from up to 64 antennae. These performances have to be compared to the perspective of correlating N=20 telescopes with 100 spectral channels and tens of GHz bandwidth each. The estimated requirements at the level of the digital correlator in the initial PFI studies pointed toward a computing power more than two orders of magnitude larger than the current correlator on ALMA (Ireland and John D. Monnier, 2014), which represents still a major challenge for the existing technology.

Conversely, the ISI correlator was relying on an analog correlation scheme that enables to process 2.5 GHz in a simple double-sideband correlator, later equipped with filterbank modules to perform spectroscopy. The main advantage of analog correlation is its capability to process relatively wide bandwidth in a simple instrumental set-up. In the case of ISI, the correlator was based on the use of wide-bandwidth RF and microwave components with GHz bandwidth. However, this capability is also limited when considering tens of GHz to 100 GHz bandwidth. Recently, analog lag-correlator developed in the frame of Cosmological Microwave Background (CMB) interferometry reached up to 20 GHz bandwidth (Holler et al., 2011). Although these developments could constitute immediate attractive solutions for infrared heterodyne instrument, they rely on specific RF design (custom-made Gilbert cell multiplier, Wilkinson splitter tree, etc.) at the limit of the current technology, and are unlikely to go far above 40 GHz any time soon. RF parasitic frequency, although not a fundamental limit, could also turn out to be a disadvantage of wideband RF systems.

Both approaches, digital and RF analog correlation, are worthwhile exploring for infrared interferometry when considering an array of a few telescopes, but their extrapolation to a large number of telescope and larger spectral coverage may call for a different approach. In the following (Chap 6 and Chap 7), we propose to revisit the analog correlation scheme by

introducing the idea of photonic correlation in infrared heterodyne interferometry, based on the use of photonic components developed by the telecom industry, and capable of transporting and processing bandwidths up to 100 GHz.

4.5.5 Laser synchronisation

The measurement of interferometric signals requires a stabilization of the relative phase of the local oscillator during one coherent integration time (Eq 2.31). This stabilization can be performed by measuring directly the beating between the local oscillators at each telescopes and a master oscillator, and then by applying an error signal on each local oscillators (Phase Lock Loop, abrev. PLL). This technique was effective on ISI, but requires a free-space propagation of the local oscillators, launched with periscope on each station, which goes against our vision of an infrastructure with fiber propagation.

Importantly, the possibility to phase stabilize a QCL through 43km optical-fibre link at telecom wavelength on a primary reference (in this case a frequency comb) was recently demonstrated (Argence et al., 2015). The general idea consists in propagating the reference in a compensated fibre link (phase stabilized link), and then in mixing the reference with the QCL through sum-frequency generation. The up-converted QCL is mixed with another tooth of the comb, whose beating note generate the error signal which enables to phase lock the QCL. A similar concept could be transposed in heterodyne interferometry, where the relative phase of each local oscillator has to be stabilized : a reference stable monochromatic laser could be distributed to each station, through a compensated fibre link (stable phase) at telecom wavelength, and mixed locally with the local oscillator at $10\,\mu\mathrm{m}$ using similar type of non-linear cristal as (Argence et al., 2015). The up-converted signal would then be propagated backwards in the same fibre link and mixed with the up-converted signal coming from a different station. The beat note would produce an error signal which could be applied to one of the QCL, so that the relative phase between the mid-infrared LOs and the reference at $1.55\,\mu\mathrm{m}$ is stable over a coherent integration time, every station being stabilized on a common reference, the relative phase between each station is stabilized.

4.5.6 Fringe-tracking

One of the very important assumption of the heterodyne architecture presented previously is the use of a fibred, near-infrared fringe-tracker, in order to compensate for the atmospheric piston. The fringe-tracker will be an essential building block of any future interferometric facility. As shown in Tab 4.2, excepting the telescope diameter, fringe-tracking is the most important element with the detector bandwidth in order to increase the sensitivity limit of an interferometer. We did not developed specific architecture or technologies in this thesis, which would have represented a work on its own, although this development remains a very high-priority. The design of a completely fibred interferometer in the near-infrared for a large number of telescopes was recently investigated in Julien Woillez et al., 2017, which could be the precursor of the fringe tracker required in the perspective of a PFI. In addition, new

architectures of fringe-tracker, called hierarchical fringe-tracker, were also investigated in Petrov et al., 2016.

In addition, the ability to reference a N band instrument (MATISSE) on GRAVITY K band fringe tracker was recently demonstrated in the GRA4MAT project at VLTI (Petrov et al., 2020). At the time of writing, the GRAVITY instrument (Gravity Collaboration et al., 2017) includes the most advanced fringe-tracker in near-infrared interferometry, reaching Kmag=10.5 on 8.2m telescopes with $\sim 150\,\mathrm{nm_{rms}}$. Such developments of a sensitive fringe-tracker combining a large number of telescopes, benefiting from GRAVITY experience and exploring the technologies needed in the AGILIS concept, would be a crucial step towards an infrared imaging array, and would benefit both to direct and heterodyne interferometry.

4.5.7 Fiber delay-lines

In direct interferometry, the delay compensation of the signals is performed in free-space delay lines, whose design would represent a major technological challenge in the perspective of a direct interferometer with kilometric vacuum delay in the mid-infrared. In heterodyne detection, this delay can be performed in the correlator itself, which represents a major practical advantage over direct interferometry.

Concerning the near-infrared fringe tracker, there would be a major interest in performing this delay in fiber components to relax the need on the infrastructure. We note that there is an interest to design such fiber delay lines both in the perspective of a fiber fringe tracker and of a photonic correlator. The major difference between these two types of developments concerns the compensation of spectral dispersion, over a very large spectral domain in the first case (the whole H band or K band), and a relatively narrow bandwidth similar to telecom applications for the photonic correlator.

4.5.8 Additional technologies

The development of an infrared heterodyne interferometer will involve additional technologies which are not mentioned here. The first technology in this perspective is the manufacturing of large and cost-effective telescopes, as investigated in (Bayo et al., 2020). The dominant cost of existing telescopes is driven by the cost of the primary mirror. A potential path of research, detailed in (Bayo et al., 2020), could consist to use Carbon Fiber Reinforced Polymer (CFRP) to replicate a large number of mirrors using a single reference mold. The second technology that we do not detailed here is the development of dedicated focal instrumentation (dichroic and spectrograph), scalable to a large number of telescopes. The exact design parameters of the spectrograph depends on the detector bandwidth that will finally fixed in the architecture (2 GHz bandwidth being equivalent to $R = 12\,000$; 20 GHz equivalent to $R = 1\,500$).

4.6 *A workshop that never happened : HIFAAS 2020*

The review of the different key technologies and the actors on these thematics led to the organization of the international workshop HIFAAS 2020, whose goal was to gather the different developments and potentially to define a roadmap in the perspective of an infrared heterodyne interferometer with kilometric baseline and a large number of telescopes. This workshop was planned in Grenoble on March 9th to 11th, hosting 49 participants and the very specialists of this field. Unfortunately, this workshop could not happen due to the outburst of the first wave of the Covid-19 pandemic in France at this exact date. Nonetheless, the interest to gather the specialists of the different key thematics that we have identified remain very high, in particular in the perspective of an on-sky pathfinder combining the 8 telescopes of VLTI (see Chap 9). This workshop will be re-scheduled one day or another.

4.7 Appendix

4.7.1 Signal-to-noise ratio in SSB and DSB correlation

System type	relative SNR	SNR
SSB complex	1	$\frac{P_\nu}{h\nu}\sqrt{\Delta\nu t}$
SSB simple and fringe fitting	$\frac{1}{\sqrt{2}}$	$\frac{P_\nu}{h\nu}\sqrt{\frac{\Delta\nu t}{2}}$
DSB simple and fringe fitting	$\sqrt{2}$	$\frac{P_\nu}{h\nu}\sqrt{2\Delta\nu t}$

Tab. 4.5: Signal-to-noise ratio in SSB and DSB correlation.

4.7.2 Equivalent noise temperature of direct detection

The equivalent noise temperature of heterodyne detection due to fundamental quantum noise is typically $T \sim 1500\,\mathrm{K}$. In the case of a practical system, this large noise is in addition affected by non-ideal factors (transmission, detector noise, etc.), typically a factor 6 in ISI. This gives a noise temperature of $T = 6 \times 1500\,\mathrm{K} \sim 9000\,\mathrm{K}$ (Kingston, 1978; Boyd, 1983), a value which appears very much larger than the background noise temperature in direct detection $T = 270\,\mathrm{K}$, while the two techniques appear to have comparable SNR at higher spectral resolution.

Is this result physically consistent? This would imply that RON introduces an equivalent noise temperature of the order of heterodyne detection quantum noise with non-ideal parameters, which appears not to be intuitive.

We can verify this point by expressing the RON as an equivalent background noise temperature in the noise density of direct detection[14], in Eq 4.29. Assuming that only RON is contributing to the noise (noise budget dominated by RON), this equivalent background noise temperature T_b should verify :

$$\frac{2}{e^{\frac{h\nu}{k_b T_b}} - 1} \times \Delta\nu t = \frac{n_{\mathrm{pix}}\mathrm{RON}^2}{t_d}$$

where t_d is included in the equivalent noise, in the same way that in the computation of the equivalent noise temperature in heterodyne detection. Following this condition, the noise temperature is :

$$T_b = \frac{h\nu}{k_b \ln\left(\frac{2\Delta\nu t}{n_{\mathrm{pix}}\cdot\mathrm{RON}^2} + 1\right)} \tag{4.31}$$

The value of T_b as a function of detection bandwidth is shown on Fig 4.7. This temperature reaches 9500 K at $\sim 5\,\mathrm{GHz}$ i.e. the value at which direct and heterodyne have equal noise in Fig 4.4. Thus, the contribution of RON is indeed comparable to the photon noise of a background source with a temperature 9000 K. This highlights the fact that the RON affects very significantly the noise budget a direct interferometer, with a value comparable or larger than the fundamental noise of heterodyne detection at for spectral resolution $R \sim 5000$.

[14] In a way, this method is quite comparable to the comparison of noise in direct and heterodyne detection done in (Boyd, 1983).

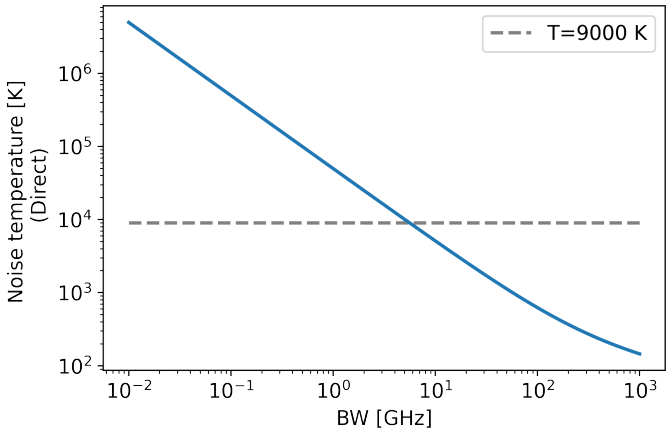

Fig. 4.7: Equivalent background noise temperature of direct detection, computed with the same parameters as Fig 4.4.

> *Ring the bells that still can ring*
> *Forget your perfect offering*
> *There is crack, a crack in everything*
> *That's how the light gets in*

f

— **Leonard Cohen**
Anthem

5 Noise analysis of heterodyne detection

5.1 Quantum noise analysis

We have described so far the classical signal and the classical noise emanating from an infrared heterodyne detection. This analysis exhibits the surprising property that, as long as the LO power is sufficiently high, the final SNR does not depend on the LO power, even if the main the contribution of the noise comes from the shot noise of the LO. The SNR appears intrinsically limited by the detection scheme itself (coherent detection). Recently, different propositions arose to question that this noise was a fundamental limitation of coherent detection scheme (Michael and Besser, 2018; Le Coarer, Chalabaev, and G. Duvert, 2014), and to implement strategies to overcome this noise. The goal of this chapter is to propose a complete justification of the fundamental nature of the noise in heterodyne interferometry, both at the focus of a single telescope and for the correlation signal of two telescopes. Even if the ideas presented here are very well-known from different fields outside astronomy (in particular, from the quantum optics community), the goal of this chapter is to precise some of these ideas in the context of infrared heterodyne interferometry.

5.1.1 Position of the problem

Context

The fundamental noise limitations in heterodyne detection is a recurring question of infrared interferometry, for which a complete justification in literature is still difficult to find.

The origin of the noise in heterodyne detection has been largely studied in the frame of lidar (Teich, 1968) or telecom applications (Kikuchi, 2016) based on laser signals. In the classical approach, this treatment is usually extended to the description of an incoherent field by decomposing this incoherent field on a set of pure monochromatic fields (Boyd, 1983), whose phases vary randomly between each wavelengths (spectrally incoherent). In this way, this approach is fundamentally identical to the description for a laser field, generalized by the incoherent integration over the RF bandwidth. As described in the previous section, this approach provides a classical model of the noise, which is identical both in radio and heterodyne interferometry (Thompson, Moran, and Swenson, 2017).

The weak incoherent signals involved in infrared interferometry contains typically only a few photons per integration time [1], so that these weak signals are usually thought in terms of simple photons impinging the detector. This picture does not apply in heterodyne detection, which measures the *field amplitude* of the incident signal at the level of each telescopes. This could lead to difficult physical interpretations : where and when do we detect the "photons" in the interferometer ? For a small number of photons, is the number of signal photoelectrons somehow "amplified" by the photons from the LO ? And ultimately, could we avoid part of the shot noise electrons from the LO, which sets the sensitivity limit of heterodyne detection ? In this somehow difficult interpretative framework, different schemes, supported by preliminary experimental demonstrations, were proposed ((Michael and Besser, 2018), (Le Coarer, Chalabaev, and G. Duvert, 2014) cited in **Monnnier2014** PFI initial paper), putting forward the idea that the fundamental noise in heterodyne detection could be overcome.

In a more general manner, three main treatments of the fundamental noise could be identified in the community of infrared interferometry :

1. **Zero-point fluctuations / Heisenberg inequalities :** This analysis relies mainly of the work developed by C.H.Townes and his team (C. H. Townes, 1984; D. D. S. Hale et al., 2000), and consists in interpreting the detection noise in terms in uncertainty relation $\Delta n \Delta\phi \geq 1/2$, or equivalently in terms of zero-point fluctuations. Here the "uncertainty relation" refers to the number of photons in the state of the incident field, which is only a qualitative relation in quantum mechanics [2]. A quantitative justification on this basis thus remains problematic. On the other hand, the interpretation based on zero-point fluctuations implies to add an additional *ad hoc* field corresponding to void fluctuations in the classical field description (M. A. Johnson and C. H. Townes, 2000), or to introduce by hand 1 photon of noise per mode of detection (Lawson, 2000). These two last cases are physically identical, and take as a premise that quantum fluctuations contribute to one photon per detection mode. This photon is then added by hand in the noise budget [3] The conclusion of this chapter will converge to this class of analysis, by showing explicitly how this noise is related in a fundamental manner to the quantum property of the electromagnetic field.

2. **Optical amplification :** A second interpretation, partly related to the first class, consists in interpreting the whole detection chain as a linear amplifier. This approach is justified by the fact that there is indeed a linear relation between the input and output field in a coherent detection $\hat{E}_{\text{out}} = G\hat{E}_{\text{in}}$. As indicated by quantum mechanics (Heffner, 1962; Caves, 1982), noiseless amplification is impossible [4], and is shown to introduce a

[1] One can notice that that a source at $\lambda = 10\mu\text{m}$ with 1 Jy/polar ($N_{\text{mag}} = 3.14$), observed over 1 GHz bandwidth during 1ms brings 1 photon over the entire surface of 1 AT (1.8m diameter, with an unrealistic ideal transmission of 100%).

[2] This is due to the fact that there is no tangible operator associated to the phase of a field in quantum mechanics.

[3] We also remark that in the context of radio-astronomy, a close approach, based on statistical physics arguments, enable to go a step further in the justification of this "zero-point fluctuations". This argument is based on the Callen-Welton formula, and is based on the quantization of energy level of an harmonic oscillator. We will comment on this point later in this chapter.

[4] We comment on this aspect later in this chapter and in the appendix.

fundamental noise of the order of half an energy level $\hbar\omega/2$. Notably, the exact stage at which the addition of this noise is added is not identified in Caves, 1982 (see (Tucker and Marc J. Feldman, 1985) for a comment on this point), and should occur at some point in "internal modes" of the amplification process. This approach constitutes the most prevalent argument in the treatment of the fundamental noise in radio-interferometry (Tucker and Marc J. Feldman, 1985; Thompson, Moran, and Swenson, 2017). However, the exact formalization of this argument is not a straightforward problem even in radio-astronomy (Tucker and Marc J. Feldman, 1985; Kerr' and M J Feldman, 1997; Kerr, 1999). Furthermore, such arguments do not take into account the correlation process , which is put forward by some authors to avoid the noise at the level of each detectors (Michael and Besser, 2018). These reasons motivate at least a refinement of this approach to be applied to infrared heterodyne interferometry.

3. **Noise reduction :** The last class of arguments e.g. (Michael and Besser, 2018) is based on the idea that the fundamental noise of heterodyne detection can be reduced below the quantum limit. Such approaches would represent ground-breaking results, as they would surpass limitations that were thought irreductible. Through this chapter, we will see how a quantum description of light seems to invalidate these approaches in their current form. A potentially detrimental point in this class of analysis is to reduce the quantum description of light to a corpuscular picture (i.e. "photons"), where the description of quantized field seems to provide a more faithful insight. We will conclude this chapter with the potential perspectives and limitations to reduce this noise, which appears for the moment related to the field coined as "quantum assisted interferometry", whose exact application to infrared heterodyne interferometry go beyond the scope of the present work.

Goal of this chapter

The goal of this chapter is to determine the fundamental noise of infrared heterodyne detection by taking into account the quantum properties of light, based on a quantum theory of detection (Glauber, 1963b) and of the measurement process (Gardiner, Zoller, and Zoller, 2004). This chapter is largely based on the work of Tsang, 2011, and can be seen as an effort to situate the ideas related to the quantum theory of measurement in the context of radio and infrared heterodyne interferometry. Based on Tsang, 2011, a specific effort is put on the clarification of the fundamental nature of the noise in infrared heterodyne interferometry, on the explicit derivation of the SNR in infrared heterodyne interferometry from first principles, and its formulation in terms of practical SNR relations usually used in infrared interferometry.

5.1.2 Quantization of the electromagnetic field

The goal of this section is to recall very elementary notions of quantum optics which will be used all along this chapter. These notions can be found in most of the introductory

books on Quantum Optics, and are mainly based here on the lecture of Chris Westbrook and Antoine Broaweys at Institut d'Optique. The reader familiar with these concepts and the quantum theory of optical coherent (Sec 5.1.5) can directly go to the description of heterodyne detection in the quantum formalism (Sec 5.1.5).

Classical electromagnetic field

We will first describe a *classical* field, which will familiarise us with the notion of mode. To describe such a field, we suppose that it is contained in a box of dimension L, which set the boundary conditions of the field[5]. In this case, the electromagnetic field can be decomposed on set of plane wave with wave-vector $k = \frac{2\pi}{L}m$, with m a integer :

$$E = \omega\vec{\epsilon}_x m \left(ce^{i(kz-\omega t)} + c^* e^{-i(kz-\omega t)}\right) \tag{5.1}$$

These are the solutions of the Maxwell equation in absence of charge. The number m has nothing to do with a quantum treatment here, but just arise from the decomposition of a classical solution in plane wave. However, this number is related to the very important notion of *mode* : the field is completely described by a set of a wave-vector and a polarisation, which defines a **mode** of the field.

We can write the energy (hamiltonian) associated to each mode of the field :

$$H = \frac{1}{2}\int \mathrm{dV}\left(\epsilon_0 E^2 + \frac{B^2}{\mu_0}\right) \equiv \frac{1}{2}\left(\frac{p^2}{\tilde{m}} + \tilde{m}\omega^2 q^2\right) \tag{5.2}$$

where the canonical variables p and q enable to write the hamiltonian of the field as the hamiltonian of an harmonic oscillator. It is important to note that, since the modes are orthognals between each others, the total hamiltonian of the field is simply the sum of the hamiltonian of each mode. This remark will be particularly useful to describe the hamiltonian of a black body for example. The formal relations defining these variables are :

$$2\omega\sqrt{V\epsilon_0}c = \omega\sqrt{\tilde{m}}q + i\frac{p}{\sqrt{\tilde{m}}}$$
$$2\omega\sqrt{V\epsilon_0}c^* = \omega\sqrt{\tilde{m}}q - i\frac{p}{\sqrt{\tilde{m}}}$$

Physically, these two numbers c and c^* are related to the quadrature of the electromagnetic field.

Quantization of the electromagnetic field

We now consider a quantized field : starting from a classical field as described in previous section, the quantization consist in considering that the general coordinate describing the field are no more complex numbers, but operators, coined as $\hat{P}$ and $\hat{Q}$:

$$\hat{P} = \frac{\hat{p}}{\sqrt{\hbar\omega\tilde{m}}} \quad , \quad \hat{Q} = \frac{\omega\tilde{m}}{\sqrt{\hbar\omega\tilde{m}}}\hat{q} \tag{5.3}$$

[5]The description over a box of dimension L does not limit at all the generality of this description : L can be chosen as large as needed against any other physical quantity of the problem.

The fundamental quantum nature of the field lies in the non-commutativity of these operators i.e. that they have a non-zero commutator :

$$\left[\hat{Q}, \hat{P}\right] = i \tag{5.4}$$

Notably, these operators $\hat{P}$ and $\hat{Q}$ can be interpreted as the quadrature of the field :

$$\hat{E} = \vec{\epsilon}_x \sqrt{\frac{\hbar\omega}{\epsilon_0 V}} \left(\hat{Q}\cos(kz - \omega t) + \hat{P}\sin(kz - \omega t)\right) \tag{5.5}$$

The non-commutativity concerns thus the *quadrature* of the field. A direct consequence of the non-commutativity of hermitian operators is the existence of a so-called uncertainty relation between these variables[6], which limits the precision on the simultaneous measurement of these variables. In this case, the uncertainty relation concerns the *measurement of the quadrature* of the field, which thus fundamentally contrasts with a classical description.

Quantum harmonic oscillator

The hamiltonian described in Eq 5.2 is the hamiltonian of an harmonic oscillator. Quantifying the energy of the field amounts to quantifying the energy of an harmonic oscillator. This very well-known result of quantum mechanics leads to introduce the creation and annihilation operators :

$$\begin{cases} \hat{a} = \frac{1}{\sqrt{2}}\left(\hat{Q} + i\hat{P}\right) \\ \hat{a^\dagger} = \frac{1}{\sqrt{2}}\left(\hat{Q} - i\hat{P}\right) \end{cases} \tag{5.6}$$

In this the form, the field is written :

$$\hat{E}(\vec{r}, t) = \hat{E}^{(+)}(\vec{r}, t) + \hat{E}^{(-)}(\vec{r}, t) = \sum_k \sqrt{\frac{\hbar\omega}{2\epsilon_0 V}} \vec{\epsilon}_{xk} \left(\hat{a}_k e^{-i\omega t} + \hat{a}_k^\dagger e^{-i\omega t}\right) \tag{5.7}$$

where the $\hat{E}^{(-)}$ and $\hat{E}^{(+)}$ have been introduced :

$$\begin{cases} \hat{E}^{(+)}(\vec{r}, t) & = \sum_k \sqrt{\frac{\hbar\omega}{2\epsilon_0 V}} \vec{\epsilon}_{xk} \hat{a}_k e^{-i\omega t} \\ \hat{E}^{(-)}(\vec{r}, t) & = \sum_k \sqrt{\frac{\hbar\omega}{2\epsilon_0 V}} \vec{\epsilon}_{xk} \hat{a}_k^\dagger e^{+i\omega t} \end{cases} \tag{5.8}$$

The form of Eq 5.7 and Eq 5.8 is analogous to the description of classical field verifying Maxwell equations, decomposed in positive and negative frequency. This form will be used in particular for the description of coherent state, used to describe a perfect local oscillator.

Finally, the energy of the field can be written :

$$\hat{H} = \hbar\omega\left(\hat{N} + \frac{1}{2}\right) \tag{5.9}$$

[6] In the following, we will write the uncertainty relations using the Robertson-Schrödinger relation applied to two hermitian operators $\hat{X}$ and $\hat{Y}$: $\Delta\hat{X}\Delta\hat{Y} \geq \frac{1}{2}\left|\left\langle\left[\hat{X}, \hat{Y}\right]\right\rangle\right|$.

with $\hat{N} = \hat{a}^\dagger \hat{a}$ the number operator. The $+1/2$ is the fundamental term of this chapter : it arises directly from the non-commutativity of $\hat{a}$ and $\hat{a}^\dagger$, and implies that even the vacuum state $|0\rangle$ with no photons has a non-zero energy level $\frac{\hbar\omega}{2}$. This energy is commonly coined as the "zero-point energy" of the field.

In the next paragraph, we give a physical interpretation of this term for a black-body, which will be the type of radiation which will be of primary interest in an astronomical context.

Apllication to a black-body : the Callen-Welton formula

The $+1/2$ is the direct manifestation of the fluctuations of the vacuum state, which appears in the mean energy of a black-body, as shown in the Callen-Welton formula. This formula is particularly used in radio-interferometry to justify the fundamental noise of a heterodyne detection.

Callen & Welton (Callen and Welton, 1951) deduce the mean energy of a black-body by computing the energy density $\rho(E)$ in the neighbourhood $[E\,;\, E + \delta\, E]$, multiplied by the probability to populate this state (Boltzmann law) $f(E) = e^{-\beta E}$ (with $\beta = \frac{\hbar}{kT}$) and E_n the energy of the mode, as defined in Eq 5.9. The mean energy of a mode is thus :

$$\overline{E}_m = \sum_n E_n e^{-\beta E_n} = \sum_n \hbar\omega(n + 1/2)e^{-\beta E_n} \tag{5.10}$$

According to the well known property of the partition function $Z = \sum_n e^{-\beta(n+\frac{1}{2})\hbar\omega}$, the mean energy of the field is :

$$\overline{E}_m = -\frac{\partial \ln Z}{\partial \beta} = \hbar\omega \left(\frac{1}{e^{\beta\hbar\omega} - 1} + \frac{1}{2} \right) \tag{5.11}$$

For a black body, we retrieve the fact that the mean energy of a vacuum state (no photons[7]) is $\frac{\hbar\omega}{2}$, not zero. This gives a more precise insight of the notion of quantum fluctuations associated to a black-body.

This formula is in fact widely used in radio-astronomy (Thompson, Moran, and Swenson, 2017) in order to justify the quantum limit of detection. *In fine*, this formula enables to describe the mean energy of mode of a field of a black-body, but do not take into account any physics of the detection nor the correlation process.

The goal of the next section is precisely to see how to introduce the notions of detection and coherence in a quantum description of the field. In the following, we will thus see how we choose to separate the contribution of the signal power $\frac{\hbar\omega}{e^{\beta\hbar\omega}-1}$ from the zero-point energy $\frac{\hbar\omega}{2}$.

[7] Photons designate here the quantum of energy necessary to go from each energy level of the harmonic oscillator. Regarding the third class of interpretation detailed in introduction, we see that the terms photons has to be considered with caution : in particular, this notion does not render the notions of uncertainty between quadratures, related to the notion of noise in phase measurement. The term photons renders the notion of an exchange of a discrete amount of energy, which is indeed a quantum property, as well as the implicit notion of mode.

5.1.3 Quantum theory of detection and coherence [Glauber]

Glauber

We recall here the quantum theory of detection and coherence as proposed by Glauber (Glauber, 1963b; Glauber, 1963a). This paragraph is largely inspired by these two historical papers, where these ideas were introduced.

A complete description of the interaction of a field and a detector calls on the second golden rule of Fermi : the whole description would lengthen this chapter, but can be found in detail in (Cohen-Tannoudji, Diu, and Laloë, 1973). Instead, we will introduce this interaction as proposed in (Glauber, 1963b) : the detection of a photon can be seen simply as the annihilation of a photon of the field. As a consequence, the probability to detect a photon i.e the probability of a photodetector to go from state $|i\rangle$ to $|f\rangle$ is :

$$w_{i\to f}^{(1)} = \left| \langle f|\hat{E}^{(+)}(r,t)|i\rangle \right|^2 \tag{5.12}$$

This is made natural by the fact that $\hat{E}^{(+)}$ is proportional to $\hat{a}^\dagger$, as shown in Eq 5.8. The probability that a detection signal is triggered when any of the final state is reached. The total probability of detection is thus the sum over the final states :

$$w_i^{(1)} = \sum_f \left| \langle f|\hat{E}^{(+)}(r,t)|i\rangle \right|^2 = \langle i|\hat{E}^{(-)}(r,t)\hat{E}^{(+)}(r,t)|i\rangle \tag{5.13}$$

The probability of Eq 5.13 is proportional to the field "intensity", which is consistent with the physical interpretation of this term. In the same vein, if this probability is evaluated in two different point of space (r_1,r_2), the above formula corresponds to the first degree of spatial coherence of the field, proportional to $g^{(1)}$. In a similar manner, higher degree of coherence can be defined :

$$w_i^{(n)} = \langle i|\hat{E}^{(-)}(r_n,t)...\hat{E}^{(-)}(r_1,t)\hat{E}^{(+)}(r_1,t)...\hat{E}^{(+)}(r_n,t)|i\rangle \tag{5.14}$$

In the following we will mainly focus on $g^{(1)}$, which is the main quantity of interest in heterodyne detection. $g^{(2)}$ described the correlation associated to the detection of two photons, which is the specific interest of intensity interferometry experiment, such as the seminal Hanbury-Brown & Twiss experiment. The same degree of coherence can be define in the temporal domain, changing (r_1,r_2) coordinates with (t_1,t_2).

State representation with density matrix

The previous paragraph implicitly considered that the incident field was in a pure quantum state $|i\rangle$. This situation is far from being general, and for example a black body can not be considered as a pure quantum state. The goal of this paragraph is to introduce the notion of *mixed* states, to introduce the most general description of detection process proposed by Glauber.

Let us consider a quantum system which could prepared in successive different state $|\psi_i\rangle$ with a certain probability p_i. In this way, the system is in state $|\psi_1\rangle$ with probability p_1, $|\psi_2\rangle$ with probability p_2, etc. Here, p_i is considered in *classical* way. In the general case, the

probability to measure an observable $\hat{A}$ in state $|\psi_1\rangle$ is $\langle\psi_i|\hat{A}|\psi_i\rangle$. The mean value of the output measurement is thus the sum of this mean value, weighted by the probability to have the system in state $|\psi_i\rangle$:

$$\left\langle \hat{A} \right\rangle = \sum_i p_i \langle\psi_i|\hat{A}|\psi_i\rangle = \sum_i p_i \text{tr}\left[A |\psi_i\rangle \langle\psi_i|\right] = \text{tr}\left[\hat{A} \sum_i p_i |\psi_i\rangle \langle\psi_i|\right] \tag{5.15}$$

By introducing ρ, the *density matrix* representing the quantum system, the result of the measurement of the observable $\hat{A}$ is, in the more general manner :

$$\rho = \sum_i p_i |\psi_i\rangle \langle\psi_i| \quad , \quad \left\langle \hat{A} \right\rangle = \text{tr}\left[\rho \hat{A}\right] \tag{5.16}$$

This enables to refine the first description of a detection process in the last paragraph : the field has a probability p_i to be in state $|i\rangle$ (once again, still in a *classical* sense), so that the final detection probability is the sum of the probability to generate a photo-events, weighted by the probability of the field to be in state $|i\rangle$:

$$w^{(1)} = \sum_i p_i w_i^{(1)}$$

In this more general case, the first order correlation function of the field between to point (r_1, t_1) et (r_2, t_2) can be written :

$$\boxed{G^{(1)} = \text{tr}\left[\rho E^{(-)}(r_2, t_2) E^{(+)}(r_1, t_1)\right]} \tag{5.17}$$

In the same manner, the second order correlation can be written :

$$G^{(2)} = \text{tr}\left[\rho E^{(-)}(r_3, t_3) \rho E^{(-)}(r_4, t_4) E^{(+)}(r_1, t_1) E^{(+)}(r_2, t_2)\right] \tag{5.18}$$

Example of a density operator : the thermal field An example of density matrix of particular importance in our case is the density matrix of thermal state. The statistical distribution of such a state is naturally described by a Maxwell-Boltzmann law :

$$\rho_{th} = \frac{e^{-\beta\hbar\omega\hat{a}^\dagger\hat{a}}}{Z} \tag{5.19}$$

with Z the partition function of the system $Z = \text{tr}\left[e^{-\beta\hbar\omega\hat{a}^\dagger\hat{a}}\right] = \left(1 - e^{-\beta\hbar\omega}\right)^{-1}$.
As n is an eigenvalue of the operator $\hat{a}^\dagger\hat{a}$, the former expression gives an intuitive description of the matrix density of a thermal state :

$$\rho_{th} = \sum_n p_n |n\rangle \langle n| = \sum_n \frac{e^{-\beta\hbar\omega n}}{Z} |n\rangle \langle n|$$

The diagonal value of this matrix are the Maxwell-Boltzmann coefficients (population), and the off-diagonal terms $|m\rangle \langle n|$ (coherences) appears as zero terms ($n \neq m$), which is consistent with the fact that there is no correlation between these states.

5.1.4 Generalized measurement

Generalized measurements

The measurement of an observable consists in evaluating the mean of an observable through a density matrix as described in Eq 5.15, which has enabled to generalize description of the detection process in Eq 5.17.

In the same manner, we can ask ourselves if there is a mean to generalize the description of any *measurement process*. This is enabled by the notion a *generalized measurement* (Landi, n.d.) and Kraus operators in quantum theory of measurement.

From quantum theory of measurement, it can be shown that any measurement can be described through a Kraus operator whose only condition is to verify :

$$\sum_k M_k M_k^\dagger = 1 \tag{5.20}$$

The probability of obtaining a certain output k is :

$$\boxed{p_k = \mathrm{tr}\left[M_k \rho M_k^\dagger\right]} \tag{5.21}$$

At this stage, we note that the expression of the detected flux and of first degree of coherence of light is an exact illustration of this property[8].

The final state of the system affected by the measurement can finally be written :

$$\boxed{\rho \to \frac{M_k \rho M_k^\dagger}{p_k}} \tag{5.22}$$

Based on this description of the detection and of the measurement processes, we will see how to describe the measurement through a coherent detection. To do so, we need to describe the sate of the local oscillator, which is the subject of the next paragraph.

Coherent states

Going back into the initial publication of Glauber (Glauber, 1963a), the coherent states have been introduced by Glauber in order to find a simple solution to the Maxwell equations applied to a quantum field. As we have seen in Eq 5.8, the solutions of the quantized Maxwell equations can be decomposed on a basis of solutions proportional to $\hat{a}$ (or $\hat{a}^\dagger$, which is the same problem). Naturally, Glauber poses the question to find eigensolutions of $\hat{a}$: indeed, in this case, the eigenvalues of these states would give the eingesolutions of the Maxwell equations. In a certain manner, this is the analogous approach to the decomposition on a basis of plane wave for classical Maxwell equation, in other words, the ideal monochromatic solutions, representing an ideal laser for example.

[8] Using the cyclic permutation property of the trace : $\mathrm{tr}\left[M_k \rho M_k^\dagger\right] = \mathrm{tr}\left[\rho M_k^\dagger M_k\right]$.

The coherent states are thus defined as the eigenstates of $\hat{a}$ [9]

$$\hat{a}\,|\alpha\rangle = \alpha\,|\alpha\rangle \tag{5.24}$$

Several important properties of coherent states will be used directly or implicitly in the following :

1. A coherent state can be written over a basis of number states :

$$|\alpha\rangle = e^{-\frac{|\alpha|^2}{2}} \sum_k \frac{\alpha^n}{\sqrt{n!}} |n\rangle \tag{5.25}$$

2. Using the description over a basis of number state, the mean occupation number i.e. the number of photons detected follows a Poisson distribution, consistent with the mean and the standard deviation of photons detected in the semi-classical picture :

$$|\langle n|\alpha\rangle|^2 = \frac{|\alpha|^{2n}}{n!} e^{-|\alpha|^2}$$

3. Finally, a coherent state can also be conveniently represented by the mean of a unitary operator, the displacement operator $D(\alpha)$. This operator will be implicitly used in the calculation using generalized measurements. The name of this operator comes from the fact that α is represented as a "displaced-vacuum":

$$|\alpha\rangle = D(\alpha)\,|0\rangle$$

The displacement operator can be shown to be written as :

$$D(\alpha) = e^{\alpha\hat{a}^\dagger - \alpha^*\hat{a}} \tag{5.26}$$

Non-orthogonality, complete basis of coherent sates

We note finally the two last properties of coherent states that will enlighten our description of heterodyne detection as a generalized measurement. These properties are related to the representation of $|\alpha\rangle$ as a "basis" of states.

It can be shown (Gardiner, Zoller, and Zoller, 2004) that $|\alpha\rangle$ fulfil the closure relation :

$$\int \frac{\mathrm{d}^2\alpha}{\pi} |\alpha\rangle\langle\alpha| = 1 \tag{5.27}$$

[9] This is the way of defining a coherent state in the Heisenberg picture (time-independent operators, time-dependent states). The similarity with classical monochromatic signals is even more striking in the Schrödinger picture (time-dependent operators, time-independent states) :

$$a(t) = e^{-i\omega t} a(0) \tag{5.23}$$

In the following, we will stay in the Heisenberg picture for more convenience.

This property will be of primary importance when defining the general measurement associated to an heterodyne detection. However, contrary to number state for example, coherent states do not form an orthogonal basis :

$$\langle\beta|\alpha\rangle = e^{\beta^* - \frac{|\beta|^2}{2} - \frac{|\alpha|^2}{2}} \tag{5.28}$$

$$|\langle\beta|\alpha\rangle|^2 = e^{-|\alpha-\beta|^2} \tag{5.29}$$

The $\{|\alpha\rangle\}$ is in fact "over-complete" : there is more coherent states that need to pave the whole space of states. The representation over a "basis" of coherent states will be central when introducing the P and Q representations in particular[10]

5.1.5 Quantum description and SNR of a heterodyne detection

The goal of this section is to derive the SNR of a heterodyne detection with one telescope, based on the very fundamental quantum principles that we have introduced in the first section. We will first start with a simple model of balanced detection, allowing us to derive the fundamental noise with one telescope. We will then extrapolate this description with the notion of generalized measurement, of which will make use for the description of the interferometric SNR with 2 telescopes.

Balanced detection

We start by the description of balanced detection.

First, the two incident inputs, the local oscillator and the astronomical signal, are superposed on the two output ports of beam-splitter (BS). Based on the creation/annihilation introduced in first section, the transformation through the BS is :

$$\begin{pmatrix} \hat{c} \\ \hat{d} \end{pmatrix} = \frac{1}{\sqrt{2}} \begin{pmatrix} 1 & 1 \\ -1 & 1 \end{pmatrix} \begin{pmatrix} \hat{a} \\ \hat{b} \end{pmatrix} \tag{5.30}$$

Then, using the expression of each output, and the expression Eq 5.17, the photocurrent detected at each output is :

$$\begin{cases} \hat{i}_1 = \hat{c}^\dagger\hat{c} = \frac{1}{2}\left(\hat{a}^\dagger\hat{a} + \hat{b}^\dagger\hat{b} + \hat{b}^\dagger\hat{a} + \hat{a}^\dagger\hat{b}\right) \\ \hat{i}_2 = \hat{d}^\dagger\hat{d} = \frac{1}{2}\left(\hat{a}^\dagger\hat{a} + \hat{b}^\dagger\hat{b} - \hat{b}^\dagger\hat{a} - \hat{a}^\dagger\hat{b}\right) \end{cases} \tag{5.31}$$

The difference signal of these two photocurrent enables to remove the dc component :

$$\hat{i} = \hat{c}^\dagger\hat{c} - \hat{d}^\dagger\hat{d} = \left(\hat{b}^\dagger\hat{a} + \hat{a}^\dagger\hat{b}\right) \tag{5.32}$$

[10] As a well-known property of coherent states, it can be seen from Eq.5.28 that the "scalar product" of two coherent states tends exponentially towards 0 i.e. two coherent states tend to be orthogonal as these states are more "distant" in the complex plane.

Measurement description

What we want now is to evaluate the average of this operator. This is usually done by bracketing the operator by the input state[11] $|\psi\rangle = |\psi_1, \psi_2\rangle$. Here, the local oscillator can be assumed to be represented by a coherent state $|\psi_2\rangle = |\alpha\rangle$. Noting $\alpha = |\alpha|e^{i\phi}$:

$$\langle \alpha, \psi_2 | \hat{i} | \alpha, \psi_2 \rangle = |\alpha| \langle \psi_2 | \hat{a} e^{-i\phi} + \hat{a}^\dagger e^{i\phi} | \psi_2 \rangle = 2|\alpha| \langle \psi_2 | \hat{Q} \cos\phi + \hat{P} \sin\phi | \psi_2 \rangle$$

In the following, in order to deal only with well normalized operator, we will assume that the observable of our balanced detection is :

$$\hat{x} = \hat{Q} \cos\phi + \hat{P} \sin\phi \tag{5.33}$$

The detected photocurrent thus gives access to the quadratures of the field in the signal port, which is consistent with the classical interpretation.

Thus far, we have thought as if the signal port was in a pure state. Here we have to keep in mind that our input (astronomical) signal is a mixed state (thermal state). In the same manner as we have described the detection probability through density matrix in the Glauber formalism in Sec 5.1.3, our mean average should thus be the sum of the average of the operator, weighted by the probability to have the system in state $|n\rangle$, which is the probability p_n :

$$\langle \hat{x} \rangle = \sum_n p_n \langle n | \hat{x} | n \rangle = \sum_n p_n \mathrm{tr} \left[\hat{x} | n \rangle \langle n | \right] = \mathrm{tr} \left[\rho \hat{x} \right] \tag{5.34}$$

More generally the different moments, from which we will deduce the variance (noise power) in particular, can be simply expressed :

$$\left\langle \hat{x}^k \right\rangle = \mathrm{Tr} \left[\rho \hat{x}^k \right] \tag{5.35}$$

Measurement over one quadrature

To start with, we will simplify the problem by assuming that the phase of the local oscillator is $\phi = 0$, which turns out to measure only one quadrature of the incident state. By doing so, the measurement is :

$$\mathrm{Tr} \left[\rho \hat{x}^k \right] = \int \mathrm{d}x \, \langle x | \rho \hat{x}^k | x \rangle \tag{5.36}$$

$$= \int \mathrm{d}x \, \langle x | \rho | x \rangle \, x^k \tag{5.37}$$

$$= \int \mathrm{d}x \, \rho(x) x^k \tag{5.38}$$

[11] Here, our input state is the tensor product of the state at the two inputs $|\psi_1\rangle \otimes |\psi_2\rangle$, that we will shorten with the notation $|\psi_1, \psi_2\rangle$

The integral in Eq 5.36 is very well-known in quantum mechnanics : it corresponds the measurement of the mean position $\langle \hat{x} \rangle$ of an harmonic oscillator. By applying directly the results in this case Cohen-Tannoudji, Diu, and Laloë, 1973, we obtain :

$$\begin{cases} \langle \hat{x} \rangle & = 0 \\ \langle \hat{x}^2 \rangle & = \frac{\coth(\frac{\hbar\omega}{2kT})}{2} = \overline{n} + \frac{1}{2} \end{cases} \tag{5.39}$$

This provides a first very important result. The variance (i.e. noise power) of the measurement of a quadrature is $\overline{n} + \frac{1}{2}$, with $\overline{n} \ll 1$ in infrared astronomy. **At the level one balanced detection, the fundamental quantum noise on the measurement of thermal state with a heterodyne balanced detection over one quadrature is $\frac{1}{2}$ i.e. half a photon per mode of detection.**

Measurement over two quadratures and Husimi distribution

We will now suppose that we measure the two quadratures of the incident field. This is what is done in practice in a correlator measuring both the real part and the imaginary part of the field, as we have seen in the classical treatment in Chap 4. Instead of projecting the signal field over a single quadrature, the signal state is projected in the complex plane, over a coherent state. Recalling from Eq 5.27 that the coherent state forms a complete basis, this ensures that $M = \frac{1}{\sqrt{\pi}} |\alpha\rangle \langle\alpha|$ is a Kraus operator. We can verify that this relation is consistent with our initial assumption :

$$\rho \rightarrow \frac{M_\alpha \rho_{th} M_\alpha^\dagger}{p_\alpha} = \frac{|\alpha\rangle \langle\alpha|\rho|\alpha\rangle \langle\alpha|}{\langle\alpha|\rho|\alpha\rangle} = |\alpha\rangle \langle\alpha| \tag{5.40}$$

The output is indeed a coherent state. In this case, the probability distribution of our output measurement is :

$$p_\alpha = \mathrm{tr}\left[\rho_{th} M^\dagger M\right] = \frac{1}{\pi} \langle\alpha|\rho_{th}|\alpha\rangle \tag{5.41}$$

p_α is also known has the *Husimi* quasi-probability distribution and will be noted $Q(\alpha, \alpha^*)$ in the following. For a thermal state, writing Eq 5.41 over number state enables to obtain directly the expression :

$$\boxed{Q(\alpha, \alpha^*) = \frac{1}{\pi} \langle\alpha|\rho_{th}|\alpha\rangle = \frac{1}{\pi(1+\overline{n})} \exp\left(-\frac{|\alpha|^2}{1+\overline{n}}\right)} \tag{5.42}$$

The mean, the variance, and more generally the different moments can be deduced in the same way from this distribution. This distribution being gaussian, the immediate result is :

$$\begin{cases} \overline{m}_\alpha & = 0 \\ \sigma_\alpha^2 & = \overline{n} + 1 \end{cases} \tag{5.43}$$

This results looks very much like the result for the measurement over one quadrature, excepting that $+\frac{1}{2}$ has been replaced by $+1$. We can summarize this result by saying that **the fundamental quantum noise of thermal state with a heterodyne balanced detection over two quadratures is +1 i.e. one photon of noise per mode of detection**. This is

consistent with the interpretation that we have added the fundamental noise of the two quadratures.
As Husimi function can be conveniently interpreted as a probability distribution, it can be represented in the 2D phase plane, as shown in Fig 5.1. It corresponds to the probability density to measure the thermal state (harmonic oscillator) around a small region $\alpha + \mathrm{d}\alpha$. The fundamental quantum noise appears as a finite lower bound imposed on the width of

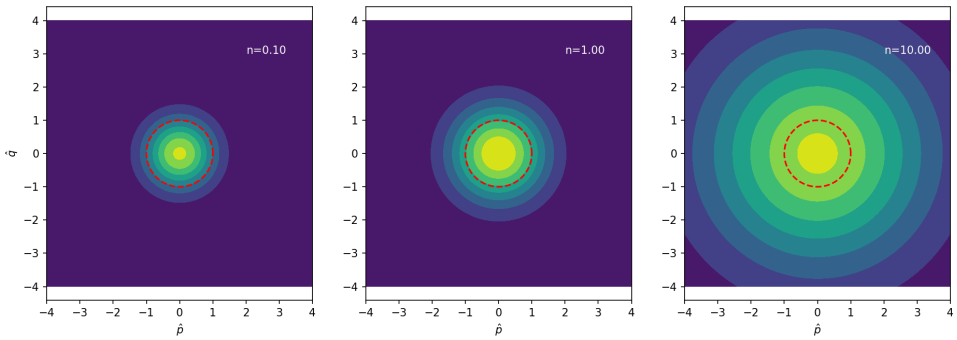

Fig. 5.1: Probability distribution to measure a thermal field with a coherent deteciton in phase space.

the probability distribution of the thermal field in phase space. In particular, for regimes where $\hbar\omega \gg kT$ (e.g. infrared domain), the width saturates to a limit $+1$, so that the incident thermal field measured by a coherent detection can not be located in an arbitrary small region of phase space. The fundamental quantum noise corresponds to the smallest width in which the field can be measured, and is of the order of 1 photon. Conversely, in the case where the energy of a photon is smaller than thermal energy (e.g. radio domain) (radio $\hbar\omega \ll kT$, this fundamental quantum limit is no more perceptible, and converge with the classical limit. Interestingly, a detailed description of a thermal density operator in terms of coherent states can be found in (Glauber, 1963a), sect. VIII.

We also note that in their pioneering derivation of the quantum limits of a coherent amplifier, which can well be adapted to the description of a coherent detection, Serber & Townes (Serber and C. H. Townes, 1960) derive the limitation of measurement of phase and amplitude (gathered in $\Delta n \Delta\phi > 1/2$) through a description of the limits in the measurement of the quadratures of an harmonic oscillator. This already captures the essence of the development presented here, even if not expressed through the same formalism, Glauber's paper being published 4 years after Serber & Townes' paper.

Intermediate conclusion

The intermediate conclusion of this section is :

- a measurement of a thermal state with a heterodyne detection can be interpreted as the measurement of the quadratures of a quantum harmonic oscillator.

- as a consequence, the fundamental limit on the measurements of the field is 1 per mode of deteciton when measuring the two quadratures of the field.

- this quantum limit can be interpreted as a fundamental limit to locate the state of the field in an arbitrary small region of the phase space (quantum harmonic oscillator), translating into an error on the measurement of its quadratures i.e of its phase and amplitude.

- in terms of radio notation, the fundamental noise temperature due to the measurement of two quadratures at the level of one telescope is $T_N = \frac{\hbar\omega}{k}$.

Generalization

The analysis would naturally take advantage of a description of the state of the signal in terms of coherent states. That is precisely the point of the Sudarshan-Glauber representation (Glauber, 1963a; Sudarshan, 1963), or P-representation. In P-representation, every state can be represented in a decomposition over coherent states :

$$\rho = \int \mathrm{d}^2\alpha \, P(\alpha) \, |\alpha\rangle \, \langle\alpha| \tag{5.44}$$

In the case of thermal state, it can be shown (Glauber, 1963a; Mandel and Wolf, 1995) that $P(\alpha)$ has a very natural expression over the mode of the field :

$$P(\alpha) = \frac{1}{\pi}\left(e^{\beta\omega} - 1\right) \exp\left(-|\alpha|^2 \left(e^{\beta\omega} - 1\right)\right) \tag{5.45}$$

Going back on Eq 5.41, and deriving the probability distribution in terms of coherent state, we have :

$$\begin{aligned} p_\alpha &= \mathrm{tr}\left[\rho M^\dagger M\right] && (5.46)\\ &= \frac{1}{\pi}\int \mathrm{d}^2\beta \, |\langle\beta|\alpha\rangle|^2 P(\beta) && (5.47)\\ &= \frac{1}{\pi}\int \mathrm{d}^2\beta \exp\left(-|\alpha-\beta|^2\right) P(\beta) && (5.48) \end{aligned}$$

In this way, the P-representation, i.e. the representation of the density matrix in terms of coherent states, enables us both to express in a natural way the state in terms of the mode of the field, and to provide a simple derivation of the Husimi function. This approach will be particularly useful when dealing with the description of the noise with two telescopes observation.

Additional comments

We conclude the previous paragraph by introducing the P-representation. In fact, the description with Eq
refeq:HO_quadrature is equivalent to a decomposition through so-called Wigner functions $\langle x|\rho|x\rangle = \int \mathrm{d}pW(x,p)$:

$$\mathrm{Tr}\left[\rho\hat{x}^k\right] = \int \mathrm{d}x\mathrm{d}p \, W(x,p)x^k \tag{5.49}$$

whose variance is shown to be $\langle|\alpha|^2\rangle = \overline{n} + \frac{1}{2}$ (Gardiner, Zoller, and Zoller, 2004). Finally, the description with Eq 5.41 is equivalent to a decomposition over Husimi functions, whose

variance is shown to be $\langle|\alpha|^2\rangle = \overline{n} + 1$. All these 3 representations can be used to describe these measurements.

In the following, we will suppose that we measure two quadratures, so we will use a description based on Husimi functions, which also provides a convenient interpretative framework in terms of probability distribution. With the measure of only one quadrature, similar type of calculations could be made using a Wigner decomposition, which would finally lead to replace $+1$ in the noise term with $+\frac{1}{2}$. In fact, both rigorous approaches can be found in (Helstrom and Helstrom, 1976) VIII.3.a and VIII.3.b .

5.1.6 SNR in quantum formalism : two telescopes

Thus far, we have started with the description of a measurement over a single balanced coherent detection to derive the calculation of its moment. The calculation of the moments was made more systematic by the introduction of Husimi distribution, which has the property to be interpreted as a probability distribution in phase space. Finally, the derivation of Husimi function can be related to the representation of the density matrix in terms of coherent states (P-representation), whose advantage is to provide a natural expression of the mode of the field in terms of Gaussian distribution. This final representation can be easily generalized to multimode field, which is precisely the situation in which we will have to deal in this part. In our case, we will limit ourself to to a bi-modal field, in order to describe the field at the two telescopes of the interferometer, through the use of a very similar formalism compared to the classical description, based on a representation of the interferometric measurement as a coherence matrix. In this section, we will start by the description of the state detected by two telescopes (bi-modal field), following the initial formalization by (Tsang, 2011), and then perform backwards the method followed for one telescope.

Formalization of the problem [Tsang]

The formalization of the problem for a field measured with two telescopes consists to cast the density operator into a diagonal form over a coherent state representation, here over a basis of two coherent states. This description can be naturally done in P-representation, which is precisely a representation in terms of coherent states, the expression of which is provided in (Mandel and Wolf, 1995) 13.1.5. Equivalently, this representation is designated as a "bi-partite thermal light" in (Tsang, 2011). In this way, the density matrix is written :

$$\rho = \int P(\alpha_1, \alpha_2) \, |\alpha_1, \alpha_2\rangle \, \langle\alpha_1, \alpha_2| \tag{5.50}$$

with $P(\alpha_1, \alpha_2)$:

$$P(\alpha_1, \alpha_2) = \frac{1}{\pi^2 \det\Gamma} \exp\left[- \begin{pmatrix} \alpha_1^* & \alpha_2^* \end{pmatrix} \Gamma^{-1} \begin{pmatrix} \alpha_1 \\ \alpha_2 \end{pmatrix} \right] \tag{5.51}$$

and Γ :

$$\Gamma = \begin{pmatrix} \left\langle \hat{a_1}^\dagger \hat{a_1} \right\rangle & \left\langle \hat{a_2}^\dagger \hat{a_1} \right\rangle \\ \left\langle \hat{a_1}^\dagger \hat{a_2} \right\rangle & \left\langle \hat{a_2}^\dagger \hat{a_2} \right\rangle \end{pmatrix} = \begin{pmatrix} \epsilon & \gamma\epsilon \\ \gamma^*\epsilon & \epsilon \end{pmatrix} \tag{5.52}$$

Here again, we note that this description is very close to the classical description of an interferometer such as (Bouquin, 2005), all the information of the interferometric measurement being encoded in the coherence matrix.
Finally, the probability distribution can be evaluated in (β_1,β_2) in the same way as we have done for one telescope [12] :

$$p_{\beta_1,\beta_2} = \frac{1}{\pi^2}\int \mathrm{d}\alpha_1\mathrm{d}\alpha_2 \, \exp\left(-|\beta_1-\alpha_1|^2 - |\beta_2-\alpha_2|^2\right) P(\alpha_1,\alpha_2) \tag{5.53}$$

$$= \frac{1}{\pi^2}\int \mathrm{d}\alpha\mathrm{d}\beta \, \Pi(\beta_1-\alpha_1,\beta_2-\alpha_2) P(\alpha_1,\alpha_2) \tag{5.54}$$

$\Pi(\beta_1-\alpha_1,\beta_2-\alpha_2)$ is finally also a gaussian distribution with covariance matrix :

$$\tilde{\Gamma} = \begin{pmatrix} 1 & 0 \\ 0 & 1 \end{pmatrix} \tag{5.55}$$

As seen by Tsang, the detection probability is thus the convolution of two gaussian distribution. According to the properties of gaussian multivariate distributions, the results is also a gaussian distribution, whose covariance matrix is the sum of the initial covariance matrices :

$$\Gamma' = \Gamma + \tilde{\Gamma} = \begin{pmatrix} \epsilon+1 & \gamma\epsilon \\ \gamma\epsilon & \epsilon+1 \end{pmatrix} \tag{5.56}$$

This result contains the essence of the description of the noise and signal properties through the interferometer. We note the similarity of this description compared to the treatment with one telescope, and above all the presence of a fundamental noise term $+1$ in the diagonal elements of the covariance, associated to the fundamental quantum limit in the noise power. As suggested by Tsang, this complement also the interpretation of the probability distribution p_{β_1,β_2}, which can seen as a conditional probability of measuring a gaussian state in (α,β) with respect to (α,β), and cannot restricted to an arbitrarily small area of the phase space.

Moments estimation

The final step to derive the signal to noise ratio is to compute the moment of the probability distribution associated to the interferometric measurement. The moments of a gaussian multivariate distribution are shown to be :

$$\left\langle \hat{X}_i\hat{X}_j\hat{X}_k\ldots \right\rangle = \frac{(2N)!}{N!\,2^N}\left\{\sigma_{ij}\sigma_{kl}\sigma_{mn}\ldots\right\} \tag{5.57}$$

Once again, this is interesting to see the similarity with the classical derivation of the SNR. The upper relation is the direct transcription in a quantum framework of the Isserlis-Wick theorem used in the *classical* derivation of the SNR, as it can be found in the derivation of the SNR in (Thompson, Moran, and Swenson, 2017) to which we referred in Chap 4.

[12] Using a different phrasing, this would consist in considering that we perform a generalized measurement using now the Kraus operator $M = \frac{1}{\pi}|\beta_1,\beta_2\rangle\langle\beta_1,\beta_2|$, and then retrieve the probability $p_{\beta_1,\beta_2} = \mathrm{Tr}\left[\rho M^\dagger M\right] = \frac{1}{\pi^2}\int \mathrm{d}\alpha\mathrm{d}\beta \, \exp\left(-|\mu-\alpha|^2 - |\nu-\beta|^2\right) P(\alpha,\beta)$

We can deduce in particular the two moments in which we are interested in our derivation of the interferometric SNR :

$$\begin{cases} \overline{m} = \left\langle \hat{b}^\dagger \hat{a} \right\rangle & = \gamma\epsilon \\ V = \left\langle \left| \hat{b}^\dagger \hat{a} \right|^2 \right\rangle & = \left\langle \hat{b}^\dagger \hat{a} \hat{a}^\dagger \hat{b} \right\rangle \\ & = \left\langle \hat{b}^\dagger \hat{a} \right\rangle \left\langle \hat{a}^\dagger \hat{b} \right\rangle + \left\langle \hat{b}^\dagger \hat{b} \right\rangle \left\langle \hat{a}^\dagger \hat{a} \right\rangle + \underbrace{\left\langle \hat{b}^\dagger \hat{a}^\dagger \right\rangle \left\langle \hat{a} \hat{b} \right\rangle}_{=0} \\ & = (1+\epsilon)^2 + |\gamma|^2 \epsilon^2 \end{cases} \tag{5.58}$$

Interferometric SNR

From Eq 5.58, we can deduce the signal and standard-deviation on the interferometric measurement :

$$\begin{cases} S \equiv \gamma\epsilon \\ \sigma = \sqrt{V - |\overline{m}|^2} = 1 + \epsilon \end{cases} \tag{5.59}$$

The SNR for one mode of detection of an heterodyne interferometer observing a thermal state is :

$$\boxed{\frac{S}{N} = \frac{|\gamma|\epsilon}{1+\epsilon}} \tag{5.60}$$

- with $\epsilon = \eta_{\text{tot}} \cdot S(\nu) \cdot \Delta\nu \cdot t_m$
- $S(\nu)$ the optical power of the astronomical signal W.Hz^{-1}
- $\Delta\nu$ the bandwidth of detection. This value differs between SSB and DSB detection.
- t_m the duration of one temporal mode of detection. This value is set by the bandwidth $\frac{1}{2\Delta\nu_{IF}}$ (Shannon criterion), and do not change between DSB and SSB.
- η_{tot} the total efficiency of the detection chain

Comparison with classical expression of the SNR

In the following, we clarify the link between the expression deduced from a quantum treatment and the common expression of the heterodyne SNR that can be found in the literature. Our result will slightly differ from (Tsang, 2011) from this point.
The results given Eq 5.60 is deduced for one temporal mode of detection. The duration associated to this "temporal mode" is the response time of the detector : following the Shannon criterion, two events separated by a smaller amount of time $t_m = \sqrt{2\Delta\nu_{IF}}$ can not be distinguished. As a consequence, for a total integration time t, the number of independent modes measured is $N_m = \frac{t}{t_m} = 2\Delta\nu_{\text{IF}} t$ (Thompson, Moran, and Swenson, 2017; C. H. Townes, 1984). These N_m independent modes are averages in time, which leads to :

$$\left(\frac{S}{N}\right)_{\text{coh}} = \left(\frac{S}{N}\right)\sqrt{N_m} = \left(\frac{S}{N}\right)\sqrt{2\Delta\nu_{\text{IF}} t} \tag{5.61}$$

For a DSB signal, $\Delta\nu = 2\Delta\nu_{\text{IF}}$ and the SNR over a coherent integration time t is :

$$\left(\frac{S}{N}\right)_{\text{coh,DSB}} = |\gamma| S(\nu)\sqrt{2\Delta\nu_{\text{IF}} t} \tag{5.62}$$

We converge here with the previous expression derived in Chap 4 through a classical approach.

The noise limitation in the interferometric observables thus arise from the same the very fundamental quantum limitations derived in this chapter. From a physical point of view, this should not be surprising, given that the astronomical signal considered here corresponds to a classical state of light : both calculations should thus deliver the same results[13] Moreover, the formalism and the method used to derive the expression and the statistical properties of the signal shares strong similarities between classical and quantum approaches.

5.1.7 Conclusion

The following conclusions can be drawn from the analysis through the quantum formalism of the SNR of a two-telescopes heterodyne interferometer :

1. the noise analysis derived for single telescope can be generalized to an interferometric signals obtained with two separate telescopes. The contribution of the noise due to quantum fluctuations is shown to be of 1 photon per mode of detection.

2. the SNR extrapolated from this quantum analysis converges with the expression derived from a purely classical approach, in particular the expression provided by Townes and in the radio-interferometry framework, with notable analogies in the derivation of the statistical properties of these signals.

3. as in the radio-domain, the fundamental noise term of can be expressed in terms of noise temperature, in this case equals to $T_N = \frac{\hbar\omega}{k}$.

Overall, this analysis confirms the initial intuition of Townes, where it was taken as a premise that the fundamental noise contribution was equal to one photon per mode. This postulate is confirmed through this analysis, starting from the very fundamental properties of the quantized electromagnetic field and of the detection process. This treatment exhibits the fundamental similarity of this problem with the estimation of the quadrature of a quantum harmonic oscillator (the quantized electromagnetic field) in the phase space. This noise contribution is inherent to both the sate of the field (thermal state) and to the *measurement* process. This phenomenon is commonly coined as the "zero-fluctuation" contribution of a quantum harmonic oscillator : noticeably, this is one of the few measurements in physics in which quantum zero-fluctuations have such a direct and practical manifestation. Importantly,

[13] It is interesting to note that, even if the focus of the approach developed in this manuscript was to derive the SNR for a thermal state, it could be generalized to other states of astronomical light which would not have classical equivalent (squeezed states, etc.), which would also bring different expression of the SNR.

the generalization of this quantum analysis also highlights that such noise do no not vanish in the correlation process, as stated by (Michael and Besser, 2018).

Local and non-local interferometric schemes

To conclude, we mention a more general results shown by Tsang : in fact, it can be shown that *any* local measurement (i.e. where the field is estimated at the level of each telescope) is less sensitive than a non-local scheme (e.g direct interferometry, where photons are detected only at the level of the recombination unit). In the case of *local* measurement, Tsang shows that heterodyne detection saturates the detection limit : even if heterodyne detection remains less sensitive than direct interferometry, this is the optimal detection scheme of *local* measurements in the case of a thermal field. Several propositions are currently emerging in the class of *non-local* schemes, based on the use of quantum repeaters (Gottesman, Jennewein, and Croke, 2012) or quantum memories (Khabiboulline et al., 2019). These technologies have their own constrains in terms of practical implementation (a detailed analysis can be found in (Khabiboulline et al., 2019) for example) or sensitivity (bandwidth limitation for example), and at the time of writing are not yet available for a practical implementation in astronomy. Depending on the near and mid-term evolution of these quantum technologies, such schemes could provide interesting additional alternatives to direct interferometry.

5.1.8 Annex : Comment on optical amplification in astronomy

As mentioned in the introduction of this section, a coherent detection can be conveniently considered as an amplification process, given that a coherent detection measured directly the *amplitude* of the input field. This treatment has an advantage of providing simple arguments that a fundamental noise should be present in a coherent detection, although it is difficult to clearly describe the detection process nor the correlation process with this treatment. We will rapidly recall this argument, and mention that it should also apply to other type of measurements, for example the detection of astronomical signals through optical amplifiers.

From an heuristic argument, (Heffner, 1962) shows through a simple argument that an amplification process should necessarily introduce an additional noise. Let us consider an input with n_1 photons and a phase ϕ_1, are amplified by a factor G to obtain a number of photons $n_2 = Gn_1$. If no specific source of noise was introduced during the amplification process, n_2 and ϕ_2 should saturate the inequality relation :

$$\Delta n_2 \Delta \phi_2 \geq \frac{1}{2}$$

Given that $n_2 = Gn_1$, this would mean that the uncertainty relation on n_1 and ϕ_1 is :

$$\Delta n_1 \Delta \phi_1 \geq \frac{1}{G} \cdot \frac{1}{2}$$

For $G > 1$, this clearly violates this fundamental inequality $> 1/2$. Some noise has necessarily to be introduced in the measurement process. A rigorous treatment is derived by the historical paper of Caves (Caves, 1982), based on the idea that the input and output observables should both be unitary operators. Considering $\hat{x}$ and $\hat{y}$ the input and output observables, the amplification reduced to :

$$\hat{x} = \hat{x}_1 + i\hat{x}_2 \quad \underset{\text{AMP}}{\rightarrow} \quad \hat{y} = \hat{y}_1 + i\hat{y}_2 = (\sqrt{G_1}\hat{x}_1 + \sqrt{G_2}\hat{x}_2) + \hat{\mathcal{I}}_1 + \hat{\mathcal{I}}_2 \tag{5.63}$$

with $\hat{x}_i$ and $\hat{y}_i$ the input and output quadratures, and $\hat{\hat{\mathcal{I}}}_i$ the noise that has necessarily to be introduced by the amplification process. The output observables has to be unitarian, which means :

$$\begin{cases} [\hat{x}_1, \hat{x}_2] & = \frac{1}{2}i \\ [\hat{y}_1, \hat{y}_2] & = \frac{1}{2}i \end{cases} \tag{5.64}$$

The uncertainty relation verified by every observables is fundamentally linked to the value of their commutator, through the Robertson-Schrödinger relation. Using Eq 5.63 and Eq 5.64 :

$$\left[\hat{\mathcal{I}}_1, \hat{\mathcal{I}}_2\right] = \frac{1}{2}i\,(1 - G) \tag{5.65}$$

This sets the lower bound on the error $\Delta\hat{\mathcal{I}}_1$ and $\Delta\hat{\mathcal{I}}_2$ introduced in the amplification process :

$$\Delta\hat{\mathcal{I}}_1 \Delta\hat{\mathcal{I}}_2 \geq \frac{1}{2}\left|\left\langle\left[\hat{\mathcal{I}}_1, \hat{\mathcal{I}}_2\right]\right\rangle\right| = \frac{1}{4}|1 - G| \tag{5.66}$$

This added amplification noise can also be reduced to an equivalent "input noise" $\hat{a}_i = \hat{\mathcal{I}}_i/\sqrt{G}$:

$$\Delta\hat{a}_1\Delta\hat{a}_2 \geq \frac{1}{4}|1 - G^{-1}| \to 1/4 \tag{5.67}$$

The equivalent input noise added by a coherent amplification on each quadrature is thus $\Delta\hat{a}_i = +\frac{1}{2}$, which is consistent with the quantum analysis detailed in the upper sections.

Fundamentally, the noise introduced in the amplification process also originate from the same zero-point fluctuations present in Eq 5.64. Both derivations thus highlights the generality of the origin of noise. Interestingly, the description of such a coherent amplifying process can be applied to other types of measurement, in particular the amplification of an incident optical signal by an optical amplifier (e.g. a telecom amplifier, such an EDFA). Following the same analysis, a necessary fundamental noise of the order of 1 photon per mode should be introduced by the amplifier. In the case of thermal signal with a low occupation number $\overline{n} \ll 1$, the use of such device thus become prohibitive, with an increasing noise penalty as the central wavelength of observation shortens e.g. in the near-infrared, were most of the telecom optical amplifiers are available.

Part III

Photonic correlation

- Seulement, le tout venant a été piraté par les mômes... Qu'est-ce qu'on fait, on se risque sur le bizarre ? [...]
- Ah faut reconnaître ... c'est du brutal.
- Vous avez raison, il est curieux hein.
- J'ai connu une polonaise qu'en prenait au petit-déjeuner.

— Les Tontons Flingueurs
(G.Lautner, dialogues M.Audiard)

6 Correlation I : Introduction of photonic correlation

6.1 Motivation

The general picture of an infrared heterodyne interferometer combining a large number of telescopes, given in Chapter 4, has highlighted the need to develop a dedicated correlation scheme going beyond the capabilities of current analog or digital correlators. This motivated a specific work in this direction, which is the object of the two following chapters.

The starting point of this work was an initial questioning on the architecture that would be best suited to the following drivers :

1. **Correlation of wide-bandwidth signals**, compatible with typical bandwidth achieved by QCD or QWIP, of the order of 50 GHz, and up to 100 GHz.

2. **Transport over kilometric distances**, the easiest way to perform such a transport would be to use telecom technologies, as it is also done in radio-submm facilities such as NOEMA or ALMA.

3. **Delay compensation**, integrated inside the correlator in the form of RF or fibered delay line, and which would substitute the free-space optical delay line in direct interferometry (see also Chapter 4).

Conversely, photonic technologies enables to process and to transport wide-bandwidth RF signals, taking advantage of the decades of developments in the field of telecom industry. Such applications have seen a significant developments in the past decade, grouped under the name of *microwave photonics* (Capmany et al., 2013; Marpaung, Yao, and Capmany, 2019).

These different elements, guided by the approach followed on ISI with analog correlation, have led us to introduce the concept of **photonic correlation** in the context of infrared heterodyne interferometry. The goal of this chapter is to present the basic concepts and the experimental demonstration of simple analog two-element demonstrators, and how they could be extended to a larger number of telescopes and spectral channels.

6.2 General picture

The idea at the basis of a photonic correlation is to encode the RF signal at the output of each heterodyne detection, which is directly proportional to the optical field, onto a monochromatic optical carrier which can be propagated over fibers, and processed with photonic components to recover the correlation product of two wide-bandwidth RF signals (Fig 6.1). In this scheme, the optical carrier is a monochromatic laser, modulated by an electro-optic modulator, which is then propagated with low loss and over kilometric distances via optical fibers. In this sense, this technique is truly compatible to the standard operation operation of telecom fibers and telecom components, which are capable of handling routinely up to 40 GHz, and more than 200 GHz with dedicated laboratory experiments (Burla et al., 2019). It should be noted that the exact wavelength of this correlation stage would not be constrained by the incident astronomical signal, which depends on the central wavelength of the mid-infrared local oscillator and of the detector, but can be chosen at the wavelength which is the most convenient to process, in this case telecom wavelength.

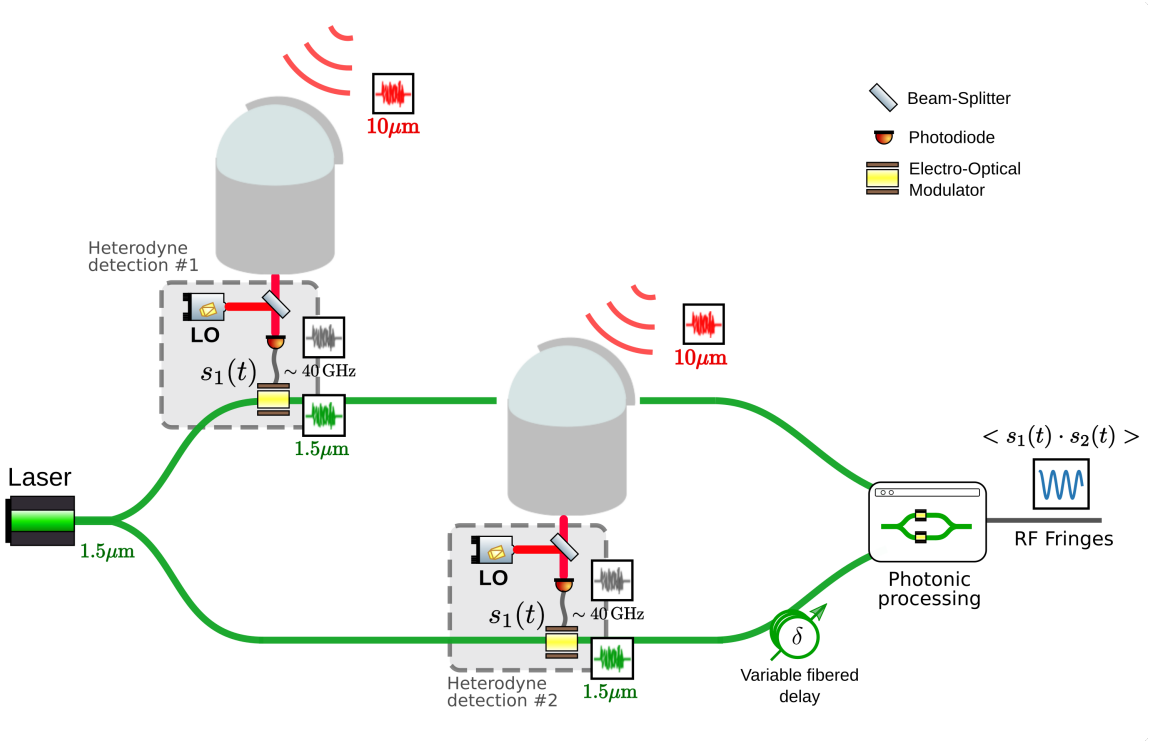

Fig. 6.1: General picture of a photonic correlator scheme.

The basic operation required at the level of this analog correlator unit consists in computing the correlation product of one detection bandwidth at one given delay, which means **to perform the multiplication product of two wide-bandwidth RF signals and to integrate the results in time**. At this stage, this operation differs from the so-called digital correlators of sub-millimetric arrays such as ALMA and NOEMA, which recover the complete correlation function of the input signals[1].

[1] This type of operation will be investigated in the next chapter.

6.3 Photonic correlation with phase modulation

The goal of this section is to detail the principle of a photonic processing which would effectively implement this function. In a general way, photonic processing can be based either on phase and or on amplitude modulation. Both schemes will be presented in the following. Phase modulation is introduced first.

Intuition

The intuition at the basis of the first implementation of photonic correlation -through phase modulation- can be captured by the encounter of the analog RF concept of correlation used on ISI, and the working principle of a Mach-Zehnder interferometer, whose is in fact a common building block of a variety of photonic systems.

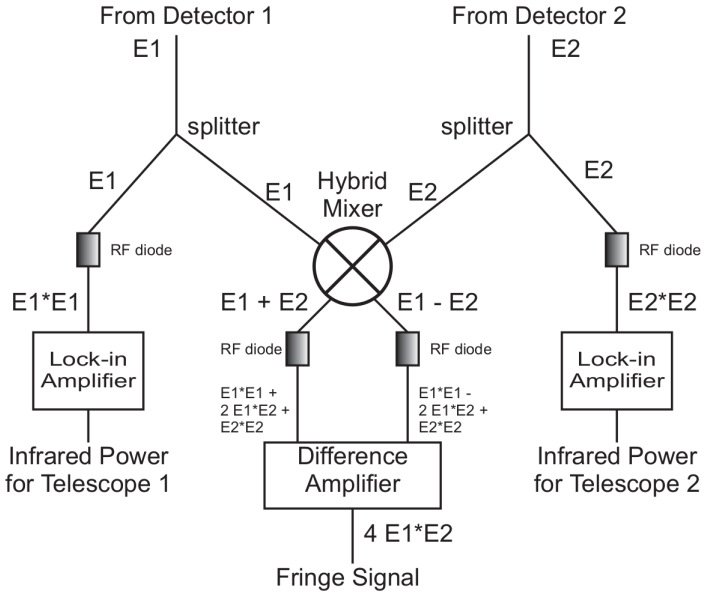

Fig. 6.2: Principle of the ISI analog correlator (from (Danchi, 2003)).

The correlation system of ISI was based on an analog processing, whose goal was first to extract the multiplication product of two wide-bandwidth RF signals, through the use of radio-frequency components. The correlation is obtained through the following successive operations :

1. Making the sum $V_1 + V_2$ and the difference $V_1 - V_2$ of the incident voltages of each pair of telescope. This was done in an hybrid mixer ("magic T"), which has to bear a wide input bandwidth ≈ 2 GHz.

2. Obtaining the modulus square of these signals using a non-linear component : $|V_1 \pm V_2| = |V_1|^2 + |V_2|^2 \pm 2V_1V_2$. In this case, the non-linear component is an RF diode with a wide input bandwidth.

3. Subtracting these signals to filter out the square terms : $|V_1 + V_2|^2 - |V_1 - V_2|^2 = 4V_1V_2$. This operation is done in a difference amplifier, which can be a low frequency component, the multiplication term being already formed (diode stage), and is generally encoded at a low frequency.

The key idea thus consists in performing the sum of the input voltages, and then to square the total. This should remind the analogy of a Mach-Zehnder : for a sufficiently small range around a minimum or a maximum of intensity, **the ouptut intensity of the Mach-Zehnder evolves as the square of the phase difference between each arms**. This idea is the starting point of an analog optical correlation with phase modulation.

6.3.1 Phase modulation

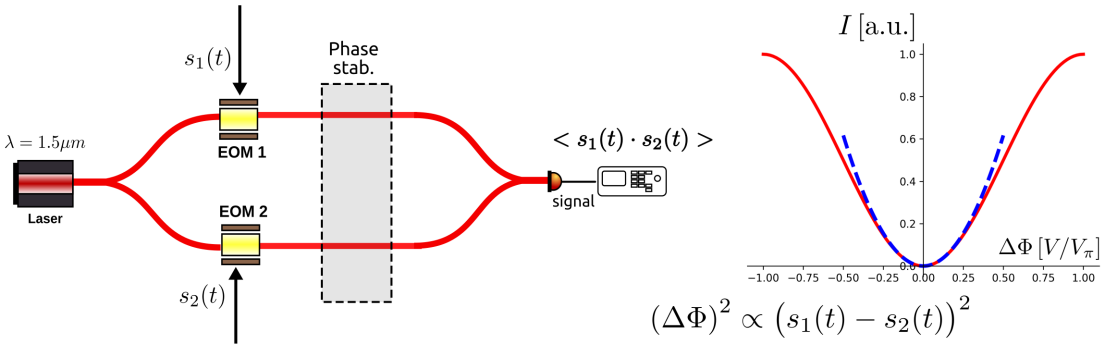

Fig. 6.3: Principle of a photonic correlation based on phase modulation

According to the previous paragraph, let us consider a Mach-Zehner interferometer, in which each arm is modulated by a phase modulator whose characteristic voltage is $V_{\pi,k}$. Assuming an incident laser E_0 at frequency ω_0, and a transmission t_k for each channel, the field at the output of the interferometer is :

$$E(t) = E_0 e^{i\omega_0 t}(t_1 e^{i\beta_1 s_1(t)} + t_2 e^{i\beta_2 s_2(t)} e^{i\phi_0}) \tag{6.1}$$

with $\beta_k = \frac{\pi}{V_{\pi,k}}$. Using a balanced detection, which enables to reject common mode noise and DC component, the intensity detected is :

$$I(t) = 4I_0 \mathrm{V}_t \cos(\beta_1 s_1(t) - \beta_2 s_2(t) - \phi_0) \tag{6.2}$$

with $\mathrm{V}_t = 2t_1t_2/(t_1^2 + t_2^2)$. Assuming that the relative phase between each arm is set at $\phi_0 = 0$ or $\phi_0 = \pi$, and that the incident RF signal is sufficiently small compared to V_π, Eq (6.2) becomes :

$$I(t) = 4I_0 \mathrm{V}_t \Big(\frac{1}{2}(\beta_1^2 s_1^2(t) + \beta_2^2 s_2^2(t)) \pm \beta_1\beta_2 s_1(t)s_2(t)\Big) \tag{6.3}$$

where the $+$ sign corresponds to $\phi_0 = 0$, and $-$ sign to $\phi_0 = \pi$. The multiplication product $s_1(t)s_2(t)$ appears at this functioning point : it corresponds to the correlation product of the two incident signals that we seek to compute. Two broad noise signals $s_k^2(t)$ are also present in the spectrum, but can be considered as negligible as their power is distributed over the

entire detection bandwidth, whereas the correlation product can encoded in a narrow RF fringe peak around a frequency f_k, as detailed in Chap 4, Eq 2.31. The width Δf of this fringe peak is given by the total integration time $\Delta f \approx 1/t$, set ideally by the maximum time during which the relative phase between the two telescopes channel is stable i.e. the coherence time.

In practice, the modulators can be located directly at each telescope at the RF output of the heterodyne detection unit, the modulated optical signal being then propagated through fibre to the recombination unit. This assumes that each arm can be phase-stabilized over the distance to the recombination unit : such a condition is not trivial to fulfil. We address this point in the practical implementation of the correlator in Sec 6.4.2, for which we have conceived a dedicated phase stabilization loop, which enables to lock the Mach-Zehnder to a null, and to compensate for rapid and arbitrarily large phase perturbations. Such phase-stabilization scheme is particularly suited to propagation of signals over several kilometres of optical fibre. The experimental demonstration of the phase modulation scheme, as well as the phase-stabilization loop, is presented in the next section.

6.4 Experimental demonstration

The idea of a photonic correlation originates from experimental considerations, when initiating the first exploratory experiments (see Sec.6.4.1) whose goal was simply to generate two heterodyne signals, first at telecom wavelength for practical reasons, to get familiar with a preliminary heterodyne chain. The goal of this first experiment was to include the different functional elements of an heterodyne interferometric instrument. The question that arose from this first preliminary experiment was how to correlate easily widebandwidth signals. Hence, this first experiment preceded the idea of a photonic correlation. We start this section by this initial experiment, which enables us to generate wideband correlated heterodyne signals, and then present the demonstration of the phase correlation scheme.

6.4.1 Generation of heterodyne test signals

Goal

The general goal of this experiment was to simulate and get familiar with a complete heterodyne interferometric set-up, from a broad spectrum source to the correlation stage. More specifically, the purpose of this two-telescope simulator is to produce a correlated signal on two seperated detectors, whose signal can reproduce the beating between a broadband source of radiation and two LOs with a stable relative phase. By registering directly the voltage at the output, these signals can be correlated *a posteriori*, and can even be regenerated in a future analogic experiment. This will be of particular use in Sec.6.4.2 and Sec.6.5.2 .

For the ease of use, this set-up was chosen at telecom wavelength, as the focus here is on the architecture aspects, rather than the sensitivity limits and the detection aspects, which will be

investigated at $10\,\mu$m (see Chap 8, and are theoretically unfavourable in the near-infrared compared to the mid-infrared, as shown in 4.

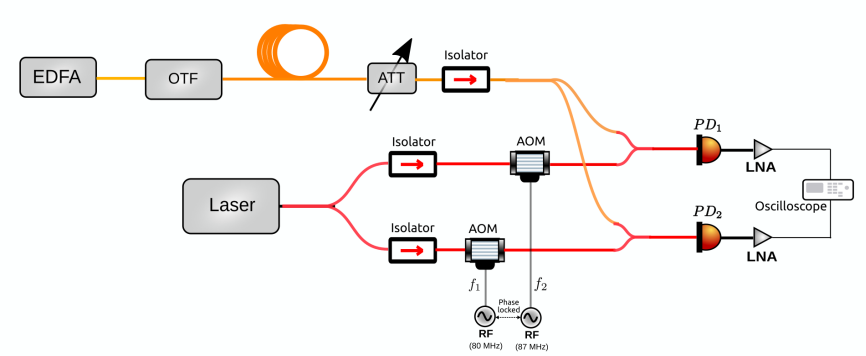

Fig. 6.4: Two-telescope interferometric set-up at telecom wavelength.

Set-up

The interferometric set-up is described in Fig 6.4 and is based exclusively on telecom fibered components. The different functional stages of the two-telescopes are :

- **Local oscillator :** The local oscillators are obtained by separating in two arms a stable laser at $1.55\,\mu$m. Given the sub-kHz linewidth of the laser and the maximum propagation length difference in each arm (<1m), the two equivalent LOs distributed on each arm are naturally in phase. In addition, as in ISI, a small frequency difference is applied by means of one AOM placed in each arm. These AOMs are driven around a frequency shift of $+80\,$MHz with a $\pm 5\,$MHz range of tunability. This introduces a relative frequency difference between each arm $\Delta f = f_2 - f_1$ which is also the modulation frequency of the fringes and enables to encode them at a tunable frequency. It was experimentally chosen to be $\Delta f = 7\,$MHz with $f_1 = 80\,$MHz and $f_2 = 87\,$MHz, in order to avoid environmental parasitic RF frequencies which are present in the RF spectrum.

- **Broadband source :** The broadband input source is an erbium-doped fiber amplifier (EDFA) without optical input. Without any input, the EDFA emits a broadband light spectrum of amplified spontaneous emission (ASE) radiation. The ASE then passes through an optical tunable filter (OTF) adjusted to the few GHz bandwidth of the detector to limit the shot noise of the EDFA. This source is finally divided in two arms, and distributed to two detectors. Once again, this source of radiation is not used to evaluate the sensitivity limit of a heterodyne detection in the near-infrared, as we would do with a black-body radiation in the mid-infrared, but rather to reproduce representative coherence properties of a heterodyne signal.

- **Detection:** The local oscillator and the input broadband source signals are then combined and detected on two separate commercial high-speed InGaAs detectors, with a detection bandwidth of 5 GHz (Thorlabs DET08), each one followed by a Low-Noise-Amplifier (LNA). This simple, fiber-coupled mono-pixel photodiode exhibit a relatively

large NEP, but this contribution is not a limiting factor compared to other factors of the set-up (mainly quantization and Johnson noise).

- **Signal recording and a posteriori generation:** Finally, the output signals of each detectors can be either sent to an analog correlator unit, or sampled in an ADC (here embedded in the fast oscilloscope) and stored for future processing. The two options were used : the first for analogic correlation with RF components (as in ISI), the second one for numerical correlation and signal regeneration through arbitrary-waveform generators (AWGs) for photonic correlation demonstration.

In the following section, we detail the correlation of these signals through analog RF components, and through numerical processing, which were the two first solutions enabling the correlation. The same signals will then be correlated *a posteriori* (in fact, months later) in the photonic correlation experiments in Sec.6.4.2 and Sec.6.5.2 by means of the regeneration through AWGs.

Results

Analog RF correlation

As a first step, we used a passive RF mixer in order to form directly the multiplication product of the two signals, which enables to observe in real-time the correlation peak at 7 MHz. In order to assess that this correlation peak was not a parasitic frequency of the setup, multiple RF cables were successively used to introduce a delay $\sim 1/\Delta\nu$ to scan the coherence length.

The RF mixer suffers from a limited bandwidth (0.5 - 400 MHz) and a sensibility to parasitic RF signals. In practice, such a component enables to obtain the first fringes and to set-up the demonstrators, but leads to prohibitive performances for further demonstrations. Smaller insertion losses and larger bandwidth could be obtained through the use of more sophisticated analog RF components. However, as seen in Chap 4, these components are ultimately limited to a few tens GHz bandwidth at best (<40 GHz) and are still sensitive to parasitic RF signals.

Numerical correlation

In a second step, the output of each detector was simultaneously recorded on a fast oscilloscope at a sampling rate of 2 Gb/s, with an analog bandwidth $\Delta\nu = 400$ MHz, which set the upper bandwidth limit in our detection scheme. In this case, the correlation could be computed numerically by processing the acquisition traces in the oscilloscope or on a computer. This processing enables to retrieve the correlation peak and to evaluate it at multiple delays, which could be compared to the analog measurements, in order to check the consistency of the results. As a remark, the two signals at the output of the rapid photodiodes appear basically as noise -or more precisely as a temporal speckle- signals for broadband optical source, which is consistent with the inherent nature of the detection used here.

6.4.2 Phase correlation

We present here the proof-of-principles of the phase modulation introduced in Sec.6.3.1. This demonstration was done in two steps : first, the development of a robust phase stabilization scheme in order to lock the Mach-Zehnder at a minimum (resp. maximum) output ; second, the regeneration of the correlated heterodyne signals, previously registered in Sec.6.4.1, to obtain the correlation signals.

Set-up

The principle of the set-up is shown in Fig 6.7, and its actual implementation is shown in Fig. 6.6. This implementation was done at telecom wavelength $\lambda = 1.55\,\mu$m with commercially available components. In this case, a CW laser with sub-kHz linewidth is divided in two arms with a 50:50 fibered splitter, each arm being modulated by an EOM, in this case IXBlue phase modulators with 10 GHz bandwidth, on which are applied the RF signals that will be correlated. A feedback loop is used to stabilize the phase of the Mach-Zehnder (see next paragraph), and the two arms are recombined with another 50:50 fibered coupler. Finally, at the null output of this fibered Mach-Zehnder, the flux is splitted in two parts with a 90:10 fibered splitter, where 90% of the flux is sent to the signal photodiode and 10% of the flux to a detector used in the stabilization loop detector. The output of the photodiode can either be registered on an ADC, a lock-in amplifier, or a Fourier-transform oscilloscope, the latter solution being adopted most of the time.

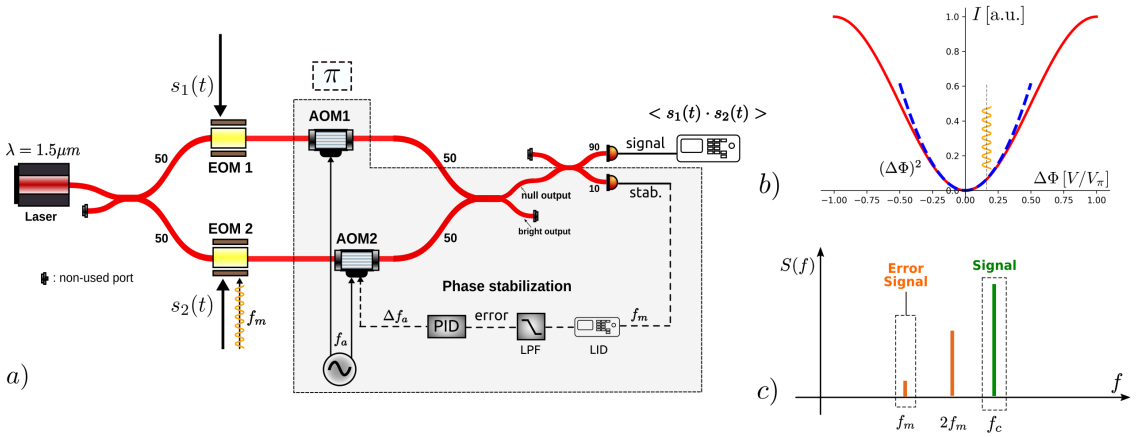

Fig. 6.5: a) Set-up of the photonic correlator based on phase modulation. Abbreviations as follows: LO: local oscillator; BS: beam splitter; PD: photo-diode; LNA: low-noise amplifier; LID: lock-in detection; LPF: low-pass filter; PID: proportional integral derivator; AOM: acousto-optic modulator; EOM: electro-optic modulator. b) Quadratic regime of the Mach-Zehnder output : at the exact null, the second harmonic (first harmonic respectively) of any sinusoidal phase modulation (orange signal) will be maximized (resp. minimized). The first harmonic can then be used as an error signal of the PID (c) that drives the frequency difference between each arm of the interferometer.

Phase stabilization loop

The goal of the phase stabilization loop is to maintain the photonic correlator at the null

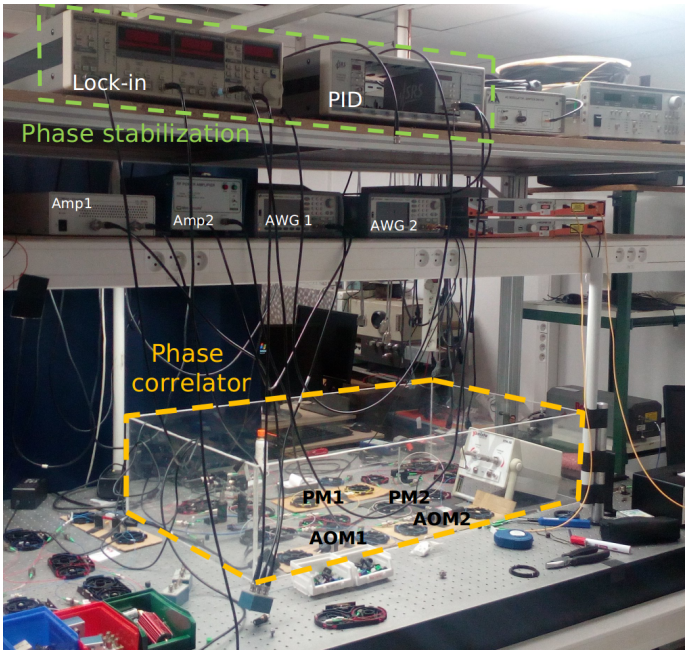

Fig. 6.6: Implementation of the phase modulation scheme in the lab.

intensity of the Mach-Zehnder. In the intensity null, the output intensity varies quadratically with the input voltage. The basic idea of the stabilization thus consists in generating a small amplitude phase modulation signal at a defined frequency f_m in one arm, and using the real part of the first harmonic signal as an error signal to be minimized (Fig 6.5).

Usually, the command signal is applied on a phase modulator (e.g., PZT, fiber stretcher, or EOM) to compensate for OPD variations. The problem of this solution based on *phase* modulation is the limited speed and/or the limited range of phase amplitude on which the correction can be applied. In this case, we set up a phase stabilization based on *frequency* modulation, composed of two AOMs, where one AOM is modulated in frequency by a proportional-integral-derivative (PID) controller. The basic idea of the frequency modulation scheme is that, integrated over a small of time $\mathrm{d}t$, a frequency modulation Δf_m acts as a small phase modulation :

$$\mathrm{d}\Phi_m = \Delta f_m \mathrm{d}t \tag{6.4}$$

Noticeably, this modulation is not restricted neither in amplitude nor in speed, in contrast to an OPD modulator system. The amplitude of modulation depends of Δf_m and of the time during which the modulation is applied, and the speed is set by the PID and the driving electronics. The results Fig 6.7 represents the closure of the phase stabilization loop. In Sec 6.7, we present a characterisation of the stability of the loop, by estimating the phase residuals and phase variations of the loop, in order to check its performances.

Results and characterisation

At this stage, the photonic correlator is stabilized at the null point through the phase stabilization loop, and operates following the principle described in Sec.6.3.1.

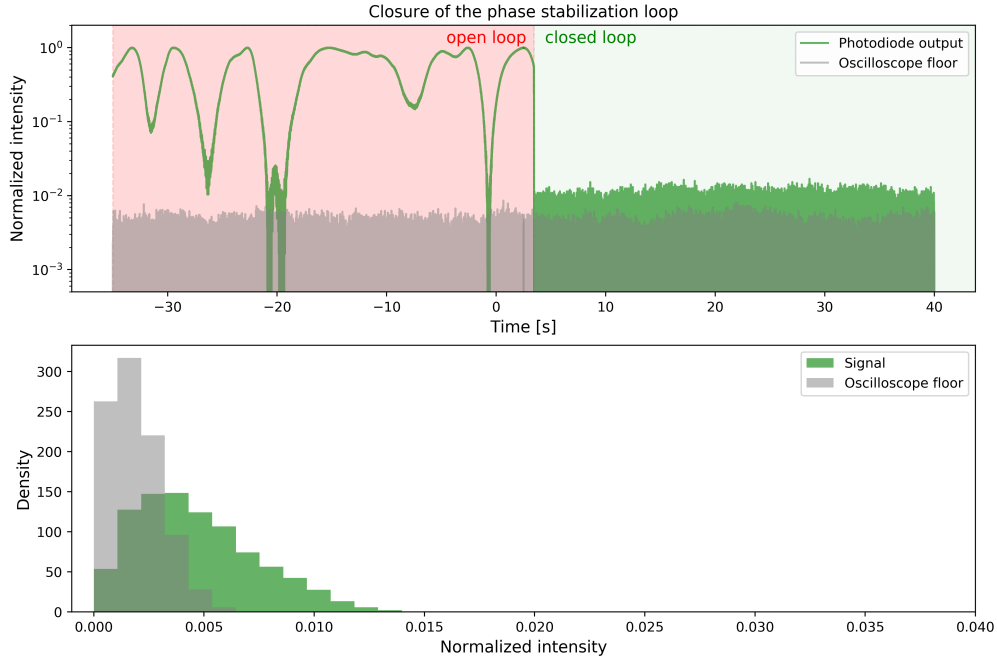

Fig. 6.7: Closing of the phase stabilization loop Top: Open-loop is highlighted in red, closed-loop in green. The photodiode output signal (green line) is just above the oscilloscope dark current (gray), which limits the effective contrast of the null. Bottom: Histogram of the photodiode output is shown. Asymmetric shape of the photodiode output is typical of a null output.

Signal generation

In order to demonstrate the working principles of the correlator, and after having tested the set-up with simple signals (sinus, square, etc.), the heterodyne signals obtained previously were generated with AWGs, and applied directly to the EOMs, in order to obtain the *a posteriori* correlation of heterodyne signals. Given the limited memory of the AWG, a set of 2^{16} points were generated at a sampling rate of 50 MHz. Taking into account the dilatation factor between registration and regeneration, the peak frequency (initially at 7 MHz) was thus placed at a frequency 175kHz after regeneration. The resulting fringe signal is visible in the power spectral density (PSD) of the photocurrent, as shown in Fig 6.8.

Results and SNR preservation

In order to estimate the degradation introduced by the photonic correlator on the signal, we estimate the ratio r between the output and the input SNR of the correlation signal :

$$r = \frac{(S/N)_{out}}{(S/N)_{in}} \tag{6.5}$$

The fringe signal can then be compared to the numerical correlation of the same signal. We estimated the input S/N on the numerical correlation of the two registered waveforms. Fringe power and noise are estimated on two defined frequency windows, as shown if Fig.6.8, by computing the integrated power in the peak and the standard deviation of the noise

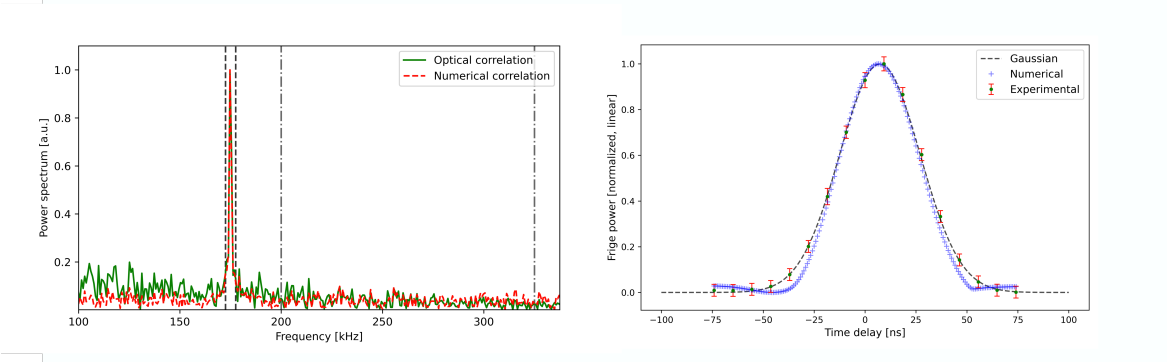

Fig. 6.8: Left: Fringe peak at the ouptut of the correlator (linear scale in y-axis). The red dashed line indicates the numerical correlation of the input signal. The green solid line shows the correlation of the signal through the optical correlator. Right: The coherence envelope of the fringe signal (green dot), and the envelope computed numerically (blue cross) are shown.

floor, respectively. Output S/N is then estimated with the same method on the PSD of the photodiode output, on the same exact frequency windows. This analysis provides a ratio of the input S/N on the output S/N : $r = 87\% \pm 5\%$ that is, a S/N degradation of 13%. This result is limited by a non-negligible oscilloscope dark current, as seen in the histogram of Fig 6.7, and a strong contribution of a low-frequency $1/f$, as visible in Fig 6.8, which artificially degrades the S/N of the fringe peak. However, these two factors are not fundamentally due to the optical correlator, and could be optimized further relatively easily.

Coherence envelope

Finally, we assessed the temporal properties of our correlation signal to observe its coherence envelope. To do so, a numerical delay is introduced at the level of one AWG, for each value of which we measured the fringe peak power. The coherence envelope is shown on Fig 6.8, and superposed to the coherence envelope computed numerically. The experimental envelope fits a Gaussian profile, which differs from the numerical computation only at the feet of the envelope. This could be imputed both to the experimental measurement uncertainties and to the estimation of the impulse response of the AWG. The full width at half maximum (FWHM) of the fitted profile is $\tau \approx 20\,\text{ns}$, which corresponds to an equivalent bandwidth $\Delta f = 1/\tau \sim 50\,\text{MHz}$. This is consistent with the maximum bandwidth of our regenerated signal through the AWGs, with a sampling frequency $f_S = 50\,\text{MS/s}$. Moreover, this measurement removes the possibility that the fringe peak is a parasitic signal coming within the photonic correlator itself.

Conclusion

In this section, we have demonstrated the functioning principles of the photonic correlation scheme through phase modulation, and proposed and demonstrated a dedicated phase-stabilization scheme, which could potentially be extended to propagation distances targeted in a practical infrastructure.

Photonic correlation through phase modulation appears as an interesting path towards the transport and correlation of wide-bandwidth signals for an infrared heterodyne interferometer.

In addition, the operation at a null output of the interferometer is an interesting feature of this scheme, in order to reduce the noise contribution (amplitude noise and shot noise) of the photonic correlator (Marpaung et al., 2012). However, as mentioned previously, the need for a locking on a precise phase point appears as a strong practical constrain. In the next section, we will see how this constraint is relaxed through the implementation of the photonic correlation through amplitude modulation.

6.5 Amplitude modulation

6.5.1 Amplitude modulation scheme

As seen in Sec.6.3.1, the relative phase stabilization is a strong constraint of the phase modulation scheme. This should enjoin to encode the information on the *amplitude* of the electromagnetic field, rather than on its *phase*.

In fact, the analogy with ISI correlator also gives a clue in this direction : the method used to compute the multiplication product in the ISI analog correlator could be exactly transposed in the photonic domain on the amplitude of the electric field, at the condition to be able to modulate linearly the amplitude of the optical carrier with respect to the output voltage of the heterodyne detection unit. This is the function that an amplitude modulator at a linear functioning point can achieved.

Amplitude modulation without frequency shift

Amplitude modulator consists in integrated Mach-Zehnder, whose relative phase difference between each arm can be driven by a RF voltage. In a general way, the output of such amplitude modulator can be written (using the same notation than Sec.6.3.1) :

$$E_k(t) = t_k E_0 e^{i\omega_0 t} e^{i\phi_k} (1 - e^{i\beta_k s_k(t)}) \approx -i t_k E_0 \beta_k s_k(t) e^{i\omega_0 t + i\phi_k(t)} \tag{6.6}$$

Amplitude modulator can be implemented in compact integrated optics components, with a stable functioning point over time, so that they can be easily set to a minimum or a maximum of transmission. In the presence of residual phase perturbations or phase drifts, these components can also be stabilized and locked to an arbitrary phase position, and commercial systems are now also available to achieve this function.

Assuming that the Mach-Zehnder is placed and stabilized at a minimum of transmission, the electric field at the output of the amplitude modulator can finally be written :

$$E_k(t) \approx -i t_k E_0 \beta_k s_k(t) e^{i\omega_0 t + i\phi_k(t)} \tag{6.7}$$

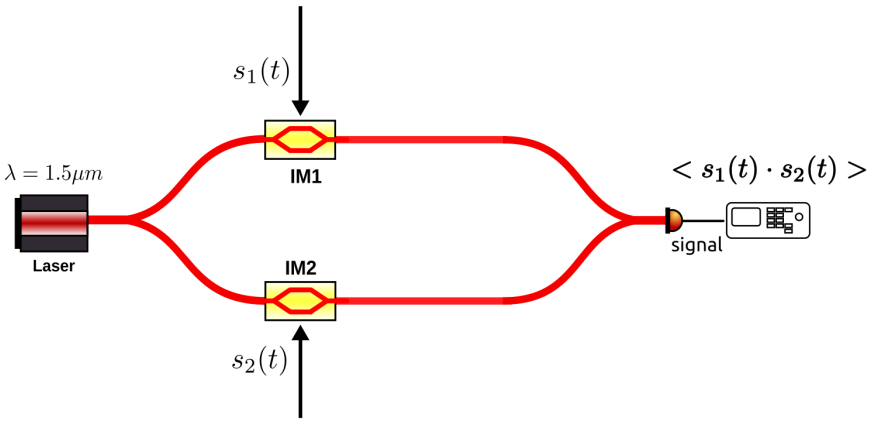

Fig. 6.9: Principle of a photonic correlation based on amplitude modulation, with no additional frequency modulation

We now come back to our original photonic correlator set-up, in which each arm of a Mach-Zehner is modulated, replacing the phase modulators of Sec.6.3.1 by amplitude modulators in the linear regime. In this case, the intensity detected is, using a single-photodiode :

$$I(t) = I_0\Big(t_1^2\beta_1^2 s_1^2(t) + t_2^2\beta_2^2 s_2^2(t) + 2t_1t_2\beta_1\beta_2 s_1(t)s_2(t)\cos\left(\Delta\phi(t)\right)\Big) \tag{6.8}$$

This signal is almost identical to Eq (6.2) : here again, we can see that it enables to retrieve the multiplication product of the input wide-bandwidth signals. However, we can also notice that the amplitude of this fringe signal is modulated by a term $\cos\left(\Delta\phi(t)\right)$. This means that such a scheme also necessitates the Mach-Zehnder to be phase stabilized at a given functioning point. This requires the same kind of stabilization loop than in phase modulation, in order to maintain the contrast of the correlation product to a maximum value. Contrarily to the phase modulation scheme, the square components $s_k^2(t)$ can be removed here by the use of a balanced detection. However, regarding the requirements on phase-stabilization, this amplitude modulation scheme and the phase modulation scheme are very similar. We will now see how this requirement on phase-stabilization can in fact be circumvented in amplitude modulation.

Amplitude modulation with frequency shift

Principles

We now assume that a frequency shift is applied between each arm of the Mach-Zehnder, upstream or downstream the amplitude modulator. In practice, this frequency shift can be applied through an Acousto Optical Modulator (AOM) in one arm, or two AOMs driven with slightly different frequencies, the latter solution being generally preferred in order to obtain a

lower frequency encoding the fringes (equal to the frequency difference of the two AOMs). In this case, the electric field is :

$$E_k(t) = -it_k E_0 \beta_k s_k(t) e^{i(\omega_0 + \Delta\omega_k)t + i\phi_k(t)}$$

Using a single photodiode, the detected signal becomes :

$$I(t) = I_0\Big(t_1^2\beta_1^2 s_1^2(t) + t_2^2\beta_2^2 s_2^2(t) + 2t_1t_2\beta_1\beta_2 s_1(t)s_2(t)\cos\left(\Delta\omega_k t + \Delta\phi(t)\right)\Big) \tag{6.9}$$

Using a balanced detector, this signal is :

$$I(t) = 4I_0 \mathrm{V}_t \beta_1\beta_2 s_1(t)s_2(t)\cos\left(\Delta\omega_k t + \Delta\phi(t)\right) \tag{6.10}$$

Here, the fringes are encoded directly at the frequency difference of the AOMs, that can be changed easily through the driving frequency of AOMs. At this point, we note three fundamental advantages of this type of recombination over phase modulation. First, the correlation product does not depend of a particular functioning point, but only needs to be relatively phase-stabilized over a coherent integration time. Second, it enables to have an other degree of freedom on the frequency encoding of the fringes, which does not necessitate to be controlled exclusively at the level of the infrared LOs. Third, it definitely eliminates the broadband terms $s_k^2(t)$.

These reasons, along with its ease of use in a practical set-up, tend to favor the use of amplitude modulation over phase modulation. We will see how this translates effectively in a practical implementation in Sec.6.4.

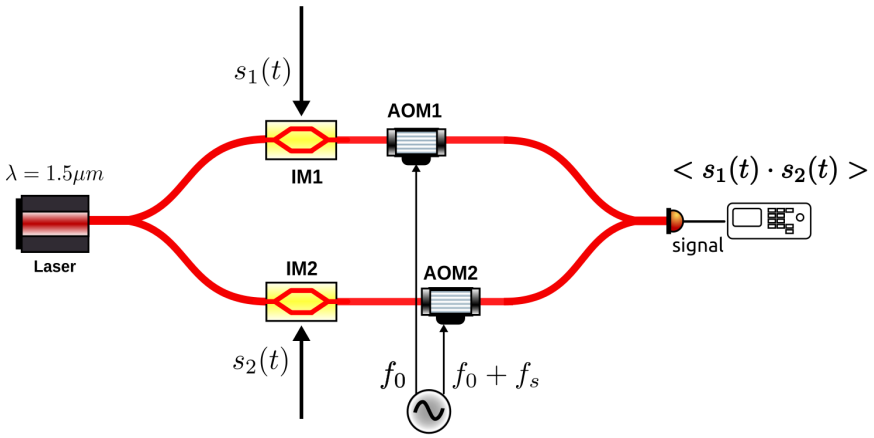

Fig. 6.10: Principle of a photonic correlation based on amplitude modulation, with two AOMs which encode the fringe frequency.

Observables

The description of an amplitude modulation scheme with frequency shift in Eq 6.10 finally enables to retrieve the common interferometric observables that we seek to measure.

In this case, the response of the correlator is given by the response of a DSB correlator (see Chap 4), that we can inject in the expression Eq 6.10. Finally, it enables to obtain the phase which encodes the fringes :

$$\phi_{\pm}(t) = \Delta\omega_k t \pm 2\pi f_k t \pm \phi_{\mathrm{V}}(B/\lambda, \omega_s) + \Delta\phi(t) \tag{6.11}$$

For $f_k = 0$, the correlation product is encoded on a single peak at angular frequency $\Delta\omega_k$; for $f_k \neq 0$, the correlation product is encoded on two peaks centered on both sides of ω_k. Following Eq 6.11, the coherent flux and the interferometric phase can be extracted from these two peaks at frequencies $\Delta\omega_k t \pm 2\pi f_k t$:

$$\begin{cases} \tilde{I} & = 2I_0 \mathrm{V}_t \beta_1 \beta_2 |F_c(B/\lambda, \omega_s)| \cdot |G(\Delta\tau(t))| \cos\left(\omega_c \Delta\tau(t) + \phi_G\right) \\ \tilde{\phi}_V & = \frac{1}{2}(\phi_+ - \phi_-) \end{cases} \tag{6.12}$$

The usual observables of astronomical interferometry can finally be constructed from the amplitude and phase of the coherent flux extracted from photonic correlation.

6.5.2 Experimental demonstration of amplitude correlation

Set-up

Here, we implemented the amplitude modulation scheme with frequency shift, following the scheme depicted on Fig 6.10, which enabled to test both amplitude modulation with frequency shift and without frequency shift (no AOM). The implementation of the bench is shown on Fig. 6.11. The set-up was implemented with similar standard fibred components than the demonstration for phase modulation, at telecom wavelength 1.55μm. Each arm is modulated in amplitude using commercial fibered Mach-Zehnder Interferometer (MZI) modulators with 10 GHz bandwidth (IXBlue MXAN-LN-10 series), then shifted in frequency through AOMs. The AOMs are fed at 81 MHz and 82.7 MHz respectively, which were chosen to avoid potential parasitic RF signals at 80 MHz of the driving electronics and small residual amplitude modulation signals of the AOMs at 80 MHz. Finally, the signal is recombined through a 50:50 combiner on a balanced photodiode, and processed on a rapid oscilloscope.

Results and characterisation

Fringe signal

We then generated *a posteriori* the two correlated heterodyne signals obtained in our first heterodyne experiment (Sec 6.4.1) through AWGs and applied these signals to the MZIs. A set of 2^{16} samples were generated at a rate of $100\,$MSa/s, which encodes the fringes at a frequency difference of $350\,$kHz after generation. When no driving voltage is applied on the AOMs, the signal is encoded in a single frequency peak at $350\,$kHz. In the absence of phase stabilization loop, the amplitude of this fringe peak is not maximal and varies in time (slow drift on the timescale of a few seconds typically). In the case where a driving voltage is applied on the AOMs, the fringe signal is encoded in two fringe peaks at 1.7 ± 0.35MHz, according to Eq 6.10, and whose contrast remains maximal for integration time smaller than the typical time-scale of the phase drifts.

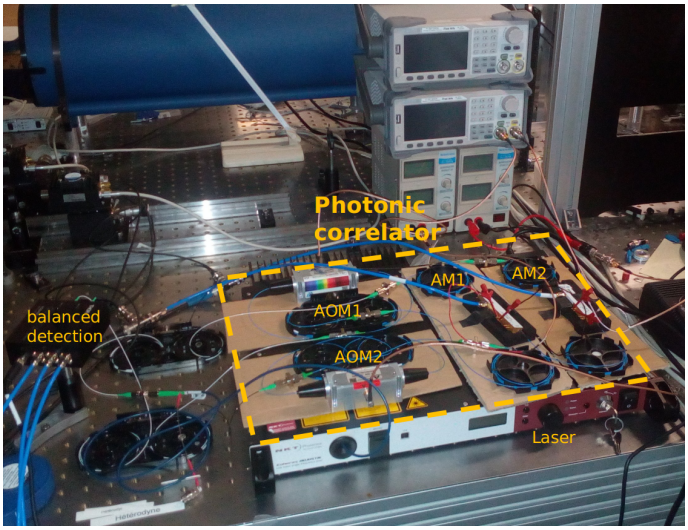

Fig. 6.11: Implementation of the amplitude modulation scheme in the lab.

The output of the balanced detection is then registered on the oscilloscope and processed on a computer in order to extract the coherent flux. The amplitude modulus and phase signal of the fringes are shown in Fig 6.12. In this demonstration, the amplitude of the fringes constitutes the main observable. We will leave aside the phase signal, which could be exploited, but do not contain particular information in this demonstration.[2]

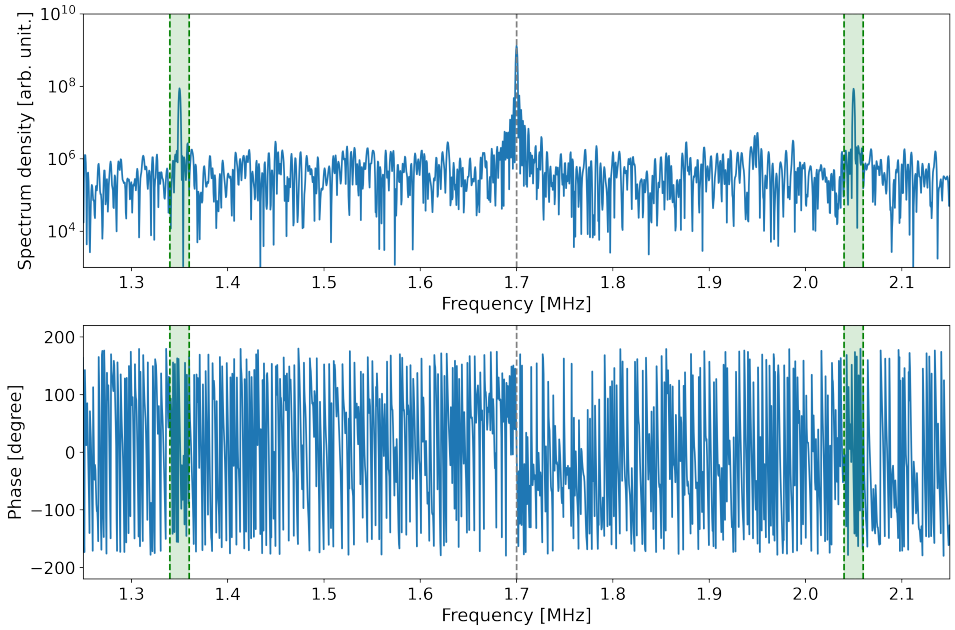

Fig. 6.12: Top : Spectrum modulus of the output signal of the photonic correlator with amplitude modulation. Bottom : phase signal. The position of the peak encoding the fringe information are highlighted in green. These peaks are centered around the central AOM frequency difference at 1.7MHz.

[2]We will return on the information contained in the phase when discussing potential extension to 3 telescopes and more.

Coherence envelope

Using the same methodology than the one used in the demonstration of the phase modulation scheme, we can explore the coherence envelope $G(\Delta\tau)$ of the incident signals by introducing a numerical ns-delay at the level of the AWGs. Similarly to phase modulation, the coherence envelope retrieved in Fig 6.13 from this measurement exhibits a Gaussian shape with a typical FWHM of 12ns, consistent with the sampling rate and the minimum rise-time of the AWGs.

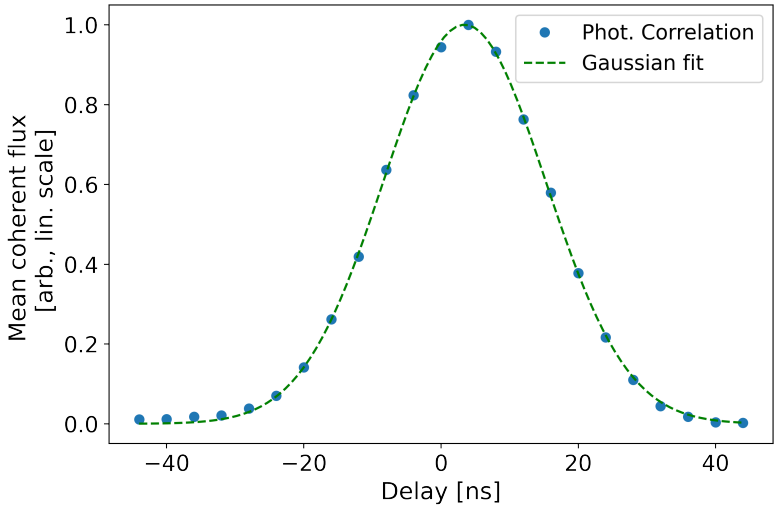

Fig. 6.13: Coherence envelope of the correlated heterodyne signals, obtained by measuring the coherent flux for different numerical delays in the correlator.

SNR preservation

Using the same methodology as for phase modulation, we evaluated the preservation of the SNR between the input and the output of the correlator by comparing the numerical SNR and the experimental SNR obtained through the photonic correlator. We obtain a ratio $r = \frac{(S/N)_{out}}{(S/N)_{in}} \geq 92\%$. This number is comparable or better than in phase modulation, and enables to ensure that the amplitude modulation exhibit a SNR preservation compatible with sensitive applications.

Further improvements

Phase-stabilization for long integration times

Considering the good performances demonstrated by the amplitude modulation scheme with frequency shifts, the experimental set-up tested in this case could be applied to the correlation of rapid detectors in a mid-infrared set-up. In fact, given its relative advantage over the phase modulation scheme, we will choose the amplitude modulation scheme for the demonstrator of a 2-telescopes combiner at 10.6μm presented in Chap 8.

However, this set-up would remain affected by phase fluctuations and phase drifts for long integration time (typically >100 ms). A further improvements would consist in implementing a phase stabilization loop for such time-scales, in order to prevent a decrease of the interferometric contrast. Such phase stabilization could be inspired by the loop developed for phase modulation in Sec 6.4.2, but could also be based on a simpler design with a slower correction

(<10 kHz). The range of correction would have to be sufficiently large, requiring a fibred delay line or a PZT with a sufficient stroke.

3 telescopes
Finally, as it will be discussed in more details in the next section, the amplitude scheme could be rapidly extended to the recombination of a larger number of telescopes. With 3 telescopes, a potential solution consists in combining the 3 channels on the same photodiode, and to encode the fringe peak through a non-redundant frequency encoding (i.e. multiplexing the baseline information in the frequency domain). The requirements to extend this scheme to 3 telescopes are minimal, as it requires only 1 additional MZI, 1 additional AOM with its driver, and the necessary recombination couplers. This possibility offers a simple and effective solution to demonstrate the correlation with more than 2 telescopes. In the case of a demonstration with 3 modulators, the phase information could be exploited, and could enable to obtain one closure phase (3 telescopes), from the phase signal originating from the different pairs of telescope.

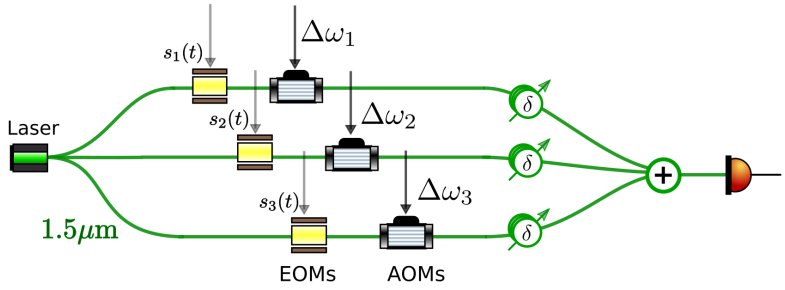

Fig. 6.14: Principles of a photonic correlation with amplitude modulation and frequency shift, extended to 3 telescopes. The encoding of the fringes is ensured by choosing a non-redundant frequency shift differences.

6.6 Perspectives

6.6.1 Delay compensation through a fiber delay lines

The different path between each telescopes will necessarily introduce a delay, which will vary as the source crosses the sky, due to the combination of the object declination and earth rotation. This delay will have potentially two effects : a decrease of the fringe contrast and a modulation of the phase of the fringes, which can be compensated respectively by a relative delay between and a relative frequency shift between each channel.

Delay compensation
As shown in the expression of the single and double-sideband correlator (Eq (2.32) and Eq (2.33) respectively), the amplitude of the fringes are modulated by the amplitude of the coherence envelope ($|G(\delta\tau)|$ and $|G(\Delta\tau(t))|\cos\left(\omega_c\Delta\tau(t)+\phi_G\right)$ respectively), whose typical width is inversely proportional to the detection bandpass $\sim c/\Delta\nu$. This imposes to match the optical delay between each arm within a coherence length $\ll c/\Delta\nu$. In the case of a

practical astronomical interferometer, the relative delay $\Delta\tau(t)$ between each channel varies continuously as the source crosses the sky. The delay compensation has to be adjusted by switching fixed time delays regularly (quasi-static compensation). For a typical bandwidth ranging from 1 GHz to 100 GHz, the coherence length ranges from 30cm to 3mm, which set the typical precision within which the delay has to be matched. For B_{eq} ranging from $100\,\text{m}$ to $1\,\text{km}$, the typical rate at which the fringes move ranges from $5\,\text{mm}$ to $50\,\text{mm}$, which gives an order of magnitude of the speed at which this delay has to be compensated.

Rate of change of the delay and natural fringe frequency
Irrespective of the delay compensation introduced at the level of the correlator, a phase modulation of the fringes would remain due to the natural fringe frequency (see Chap 4). This additional frequency shift changes the frequency at which the fringes are modulated within the correlator: this can be compensated by introducing an additional frequency shift downstream in the photonic processing chain, as detailed below. Such an operation amounts to saying that the lobe rotation is handled in the photonic chain directly.

Practical implementation with fiber delay-lines

The compensation of the delay between the different telescopes is a significant challenge in direct interferometry. In heterodyne interferometry, this problem takes advantage of the fact that this delay can be compensated after the detection stage, numerically in the case of digital correlation, in the RF domain with cables of different lengths in the case of analog RF correlation, or in the photonic processing chain with a fibred optical delay in the case of photonic correlation (Zhao et al., 1995). For analog correlation, the latter solution will be our preferred option to handle large delays, given the low propagation loss of optical fibers compared to RF cables and the fact that fibres are immune to RF parasitic signals.

Multistage fibred delay line
This delay line could consist in a first stage, introducing large delays through incremental fiber lengths, switched at a relatively low rate (of the order of few seconds). This first stage could benefit from standard fibered components developed in the framework of telecom industry or phased array applications, in order to introduce incremental delays, with a typical maximum delay of $\Delta\tau_{\text{res}} \times 2^N$, with N the number of switches implemented in the fiber component. In this scheme, the delay resolution $\Delta\tau_{\text{res}}$ would be set by the minimum tolerance of contrast decrease $|G(\Delta\tau_{\text{res}})|$.

Given the constraint imposed by the minimum resolution element $\Delta\tau_{\text{res}}$, which limits the total range of this first stage and possibly imposes frequent switches which could perturb the correlation, this stage could be complemented by a second continuous stage with a smaller stroke. The maximum stroke of this second stage would set the minimum resolution element of the first stage, thus enabling a potentially large increase of the delay range covered by the first stage. This second stage would introduce a continuous delay variation, covering a smaller range but with a precision of the order of the coherence length.

Fringe rotation
Finally, as above-mentioned, a last consequence of earth rotation is the non-zero phase velocity

of the fringes. In the case where a second continuous stage is tracking the fringes, this stage also naturally compensates for the NFF. In the case of a compensation by an incremental static delay, the NFF would have to be compensated by a frequency shift, either at the level of the LOs or downstream in the photonic correlator itself. In particular, in the case of the amplitude correlation with frequency shift, this effect can be simply compensated by computing the frequency correction in advance and applying it to the AOMs.

6.6.2 Extension to a large number of telescopes

The combination schemes described so far enable the correlation of signals coming from two detectors i.e. only two telescopes, each one with one spectral channel. In the perspective of an imaging heterodyne interferometer, the concept of photonic correlation has to be compatible with the correlation of a large number of telescopes ($N_t \approx 30$ i.e. 435 baselines), themselves including a large number of detectors ($N_s > 100$) each one being associated to one spectral channel. The goal of the following section is to present the potential concepts enabling the scale-up of photonic correlation to a large number of telescopes and a large number of spectral channels.

We present three types of solutions which could enable to combine a large number of telescopes. The combination of a multiple number of baselines is in fact a question that was investigated in the case of classical infrared interferometry, as described in LeBouquin et al., 2004. The different methods in this case can be categorised according to the type of flux encoding (spatial, temporal or static-phase shifting, also known as matricial) and the beam routing (pair-wise, all-in one, hybrid). All these architectures could be applied to a photonic correlator, provided that they can handle a sufficiently large number of baselines.

In practice, the photonic correlation scheme presented so-far will necessarily require a metrology signal in order to probe and stabilized the fringes. Such a metrology system would require either a dedicated metrology sub-system or to use a beam combination architecture compatible with high cadence single-pixel telecommunication detectors, of the order of few kHz at least.

In the following, we will use the same wording than direct interferometry to describe three combination concepts applied to photonic correlation, as summarized on Fig.6.15.

Pairwise combination

The first immediate transpose of photonic correlation to a larger number of telescopes consists in the pairwise correlation of each telescopes signals individually. This could be done both in phase and amplitude modulation (respectively), and basically consists in forming each pair of telescope signals, as described in Eq (6.3) (resp. Eq (6.10)) in a combiner. At the output of the combiner, $N_t(N_t-1)/2 \times n_c$ outputs are simultaneously detected, with n_c the number of

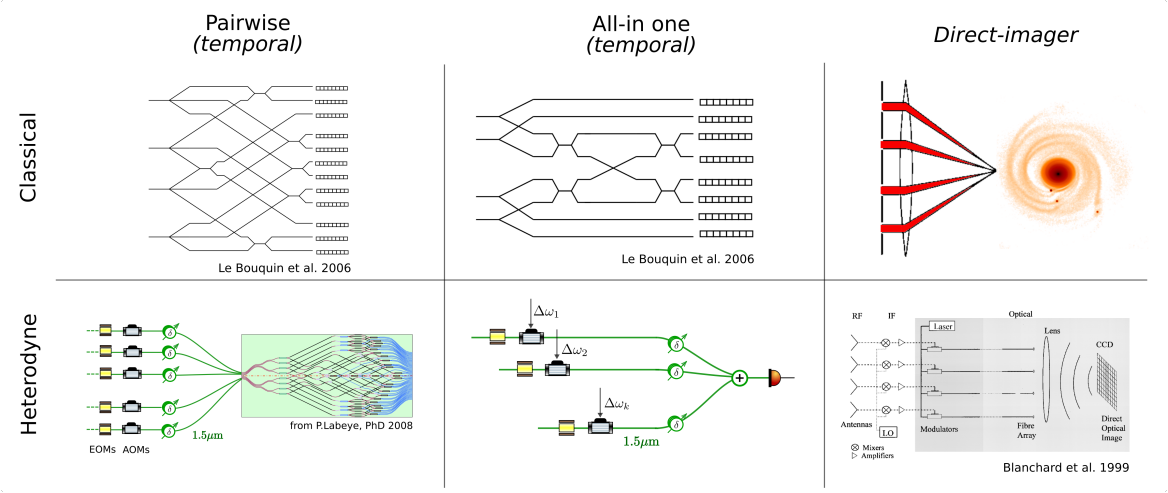

Fig. 6.15: Analogy between classical and heterodyne multi-telescopes combinations.

outputs registered simultaneously at one baseline. In particular, $n_c = 2$ for operations using balanced detection, corresponding to two opposite phase outputs.

In both phase and amplitude modulations, the overall photonics (fibres) link still has to be phase-stabilized, as described in each respective section. The phase correlation scheme (and the amplitude modulation scheme without frequency-shift) requires a locking of the relative phase between the arms at a precise functioning point and a relative phase stabilization, while amplitude correlation with frequency modulation requires only a relative phase stabilization, but no specific functioning point.

The use of photonics technologies borrowed from the telecommunication industry allows integrated-optics-based beam-combination solutions to be used for the final beam interference function of the correlator. In practice, such a pairwise correlation of photonic signals is already done in classical interferometry for more than two decades, and the IO combiners developed for this purpose Benisty et al., 2009; Labeye, 2008 could be directly used in photonic correlation. For example, four beam combiners have been developed for astronomical direct interferometry (Benisty et al., 2009) and 8 beam combiners have been designed (Labeye, 2008). In particular, the AC combination scheme, which offers two opposite phases outputs per baseline, would be favored as they are perfectly adapted to operate with a balanced detector. The fact that, here, the correlation works with a narrow spectral line laser simplifies the chromaticity and throughput constraints previously encountered in astronomical broadband applications.

Notably, contrary to classical interferometry, the splitting of the telescope signals, which induces a decrease of the optical carrier flux coming from each telescope, does not induce a fundamental loss of sensitivity, as long as the noise figure of the photonic processing does not dominate the budget of the detection chain. Nonetheless, a pairwise combination scheme for more than 12 telescopes might prove a technological challenge since the integrated optics would need to ensure at least 66 beam interferences. Massive progresses in the field of highly confined photonics (e.g. silicon based, see (**Miller2020**)) might provide a way out but this remains to be explored and led us to examine us with a particular attention the all-in-one scheme. Finally, the major limitation of the direct imager scheme scalability of this system

with the number of spectral channel n_s, for which no clear solution is identified, expected the replication of this system n_s times.

All-in-one with frequency encoding

The alternative to this pair-wise concept consists in summing together all the telescope signals at once, and then separating each baseline with a non-redundant frequency encoding. This is the so-called all-in-one combiner. More formally, this combination could be written :

$$\left|\sum_k \beta_k s_k(t) e^{i\Delta\omega_k t}\right|^2 = \sum_k (\beta_k s_k(t))^2 + 2\mathrm{Re}\left(\sum_{k\neq l} \beta_k \beta_l s_k(t) s_l(t) e^{i[(\Delta\omega_k - \Delta\omega_l)t + \phi_k(t) - \phi_l(t)]}\right) \quad (6.13)$$

where the frequency differences $(\Delta\omega_k - \Delta\omega_l)$ are chosen so that they are non-redundant for every $k \neq l$.

The fundamental advantages here comes from the fact that the information is encoded in the frequency domain, which can bear a massive multiplexing capability with simple hardware requirements and less complex combination routing, since it could rely on a cascade of directional couplers. Considering an array with $N_t = 30$ telescopes, the ratio between the smallest to the largest spacing in the frequency domain for a non-redundant encoding is typically of the order of 1000 (Ribak et al., 1988) ; fixing a teeth separation of 10 kHz typically, constrained by the smallest desired coherent integration time (usually limited by the atmospheric coherence time), the typical extent of the non-redundant frequency encoding extend to $1000 \times 10\,\mathrm{kHz}$, compatible with standard telecom photodiodes and electronics. Such a combination would represent a major simplification of the design of the combiner compared to pairwise correlation, as it would only require to sum together N_t channels, rather than physically performing $N_t(N_t - 1)/2$ combinations. This combination can be performed in a cascade of coupler or in a multichannel combiner/divider.

Direct-imager

The two previous correlation techniques inherit from current radio and optical infrastructure architectures, which are built with the goal to measure the spatio-spectral coherence of the incoming electro-magnetic field at as many spatial frequencies as possible. This, in turn, makes it possible to reconstruct an image. A significantly different option could consist in forming directly the image of the astronomical object. This could be done by arranging the outputs of the fibers coming from each telescope in a scaled-down version of the entrance pupil of the telescope array and imaging the direct combination. In this way, the image is convolved by the response of the array and forms in the focal plane of the lens, where it can be recorded on a camera. This principle was already proposed in the context of millimeter wave

imaging by Blanchard et al. (Blanchard et al., 1999) and shares intrinsic similarities with optical beamforming technologies. In principle, it also shares analog ideas with the Fizeau and densified pupil (hypertelescope) modes in classical interferometry (Labeyrie, 1996).
Direct-imager mode requires stringent operating conditions on the fiber link in order to observe a proper image of the object. First and foremost, every baseline has to be coherenced and cophased simultaneously, otherwise introducing a blur of the final image. This condition imposes a simultaneous phase stabilization of the entire fibered link, based either on a potential external phase stabilization mechanism, or on Redundant Phase Calibration (RSC) as proposed in Blanchard et al., 1999. The extrapolation of this second solution remains problematic in the case of an astronomical array with low redundancy. Phase stabilization still remains an open question to be solved in the case of the direct imager.
Notably, the principle proposed by Blanchard et al., 1999 was further developed in the context of millimeter wave imaging, and enables to combine simultaneously 224 apertures with a 75 GHz bandwith and a NETD compatible with sensitive imaging in this wavelength regime (Christopher Schuetz et al., 2013). An additional nuance of this method lies in the fact that one of the sideband of the modulated optical carrier has to be suppressed in order to avoid the superposition of two centro-symmetric replica of the image (Blanchard et al., 1999), which can be performed by the use of dual parallel Mach-Zehnder modulators or by very narrowband optical filters (C.A. Schuetz et al., 2005).

Overall, it is more likely that the direct combination is fully advantageous for a significantly large number of telescopes ($N_t > 30$), for which pairwise correlation would appear cumbersome. For $N_t \leq 30$, pair-wise and all-in-one schemes appear as the preferred options, as they enable to control and to register independently each baseline, and to post-process the whole visibility information in the (u,v)-plane. Given its much less demanding requirements on the beam combination unit, all-in-one appears as a particularly interesting perspective for both a small and a large number of telescopes.

6.6.3 Extension to a large number of spectral channels

In the last section, we described the different approaches that could enable the correlation of a large number of telescopes. In this section, we propose two main strategies to extend the concept of photonic correlation to a large number of spectral channels.

Wavelength multiplexing

The first approach consists in multiplexing the information associated to the mid-infrared spectral channel in the wavelength domain of the photonics correlator. In practice, at the level of each telescopes, the modulators associated to one mid-infrared detector (i.e. one teeth of the frequency comb) could be associated to one telecommunication wavelength in the photonic chain. Then, all the telecommunication wavelengths could be transported in the same transport fiber, and injected in the same pair-wise or all-in-one combiner. At the

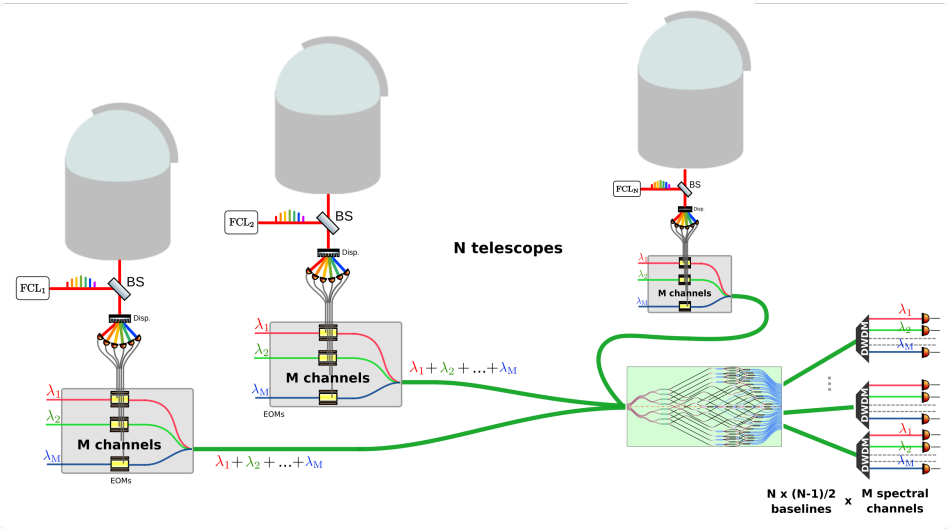

Fig. 6.16: Processing of multiple spectral channels in the photonics correlator through wavelength multiplexing.

output of the combiner, the spectral information would then be recovered by dispersing the light, producing $n_s \times N_t(N_t-1)/2$ outputs (resp. n_s for an all-in-one combiner), with n_s the number of spectral channels processed simultaneously. To this end, the dense wavelength multiplexing/demultiplexing could benefit from the dedicated DWDM technologies of telecom industry. The principal constrain here would be to limit the chromatic dispersion during the propagation through the fiber, a task which could be facilitated by the relatively modest distance considered here (up to 1km or a few kms typically) compared to typical distances in telecom (several 100kms).

Frequency multiplexing

A second potential path could consist in encoding the spectral information non-redundantly in the frequency domain. In particular, this strategy could build in the continuity of ideas developed in the framework of dual comb spectroscopy.
Let us first consider a pair-wise combination (Sec 6.6.2), and a telescope array where a mid-infrared frequency comb is placed at each telescope station. As in dual comb spectroscopy, given that the output RF signals are encoded at the frequency difference between each LO frequency, plus a possible adjustment at the level of the AOM, the correlation signal between two telescopes produced at the output of the combiner will consist in the difference of two combs with slightly distinct frequency spacing $f_{s,1}$ and $f_{s,2}$. This frequency difference results in a RF comb with frequency spacing $f_{s,2}-f_{s,1}$. In that respect, N_t (number of telescopes) distinct values have to be chosen for the repetition rate f_s of each comb in order to encode the signals of each baselines. In this way, the output of the combiner will be made of $N_t(N_t-1)/2$ physical outputs, from which n_s spectral channels could be extracted from such a RF comb. Here, we have implicitly considered that the carrier envelope offset frequency (f_{ceo}) of each mid-infrared combs were set to a same, fixed common value. The main advantage of the frequency multiplexing approach would be to put aside the need of physical demultiplexing with

DWDM at the output of the beam combiner, the signal being multiplexed in the RF frequency domain. This approach would take full benefit of the massive multiplexing capability that can be performed in the RF domain, and would relax the requirements on the hardware.

On a prospective basis, it could be envisioned that a specific non-redundant computation of both the repetition rate and of the carrier envelope offset frequency (f_{ceo}) of the frequency combs of each telescope could enable to multiplex both the different spectral channels and the different baselines, possibly avoiding part or all of the need of a pair-wise combiner, at the benefit of an all-in-one combiner.

6.7 Annex : stability of the phase stabilization loop

Methodology
Intuitively, we have seen that the ratio between the amplitude of the first and the second harmonic should depend on the functioning point of the Mach-Zehnder.

In a more formal way, the intensity on the output photodiode can be written :

$$I(t) = I_m \left[1 + V_{ins} \cos\left(m \sin(\omega_m t + \phi_m) + \Delta\phi\right)\right] \tag{6.14}$$

with

- $I_m = \frac{I_{\max}+I_{\min}}{2}$ the mean intensity, and $I_{\max}$ and $I_{\min}$ the minimum and mawimum intensity respectively.
- $V_{\text{ins}} = \frac{I_{\max}-I_{\min}}{I_{\max}+I_{\min}}$ the global instrumental contrast.
- $m = \frac{\pi A V}{V_\pi} = \frac{\pi V}{V_{\pi,\text{eff}}}$ the modulation depth of the EOM, with V the input modulation voltage, V_π the characteristic voltage of the EOM, and A the potential attenuation of the RF chain before reaching the modulator.
- ϕ_m the phase term associated to RF probe modulation signal.
- $\Delta\phi$ the phase term at which the interferometer is placed.

The cosinus term could be treated through the use of Bessel function : assuming a that the modulation amplitude is small, we will simply Taylor-expand Eq 6.14 : We neglect the terms of order 3, an approximation that has been verified in practice.

Mean-value and standard deviation
In this approximation, the mean ratio between A_I, the amplitude associated to the first harmonic term (ω_m), and A_{II} the amplitude of the second harmonic ($2\omega_m$), is written :

$$\frac{A_I}{A_{II}} = \frac{4}{m(V)} \tan(\Delta\phi) \approx \frac{4}{m(V)} \Delta\phi \tag{6.15}$$

The dependency with m and V appears clearly in this ratio, and enables to retrieve the functioning point $\Delta\phi$. In the following, in order to evaluate $\Delta\phi$, we will fit $\frac{A_I}{A_{II}}$ with our experimental data for different known voltage V.

In the same way, a measure of the RMS standard deviation of the amplitude of the first harmonic enables to retrieve the standard deviation $\sigma_{\Delta\phi}$ of the functioning point :

$$\frac{\sigma(P_I)}{A_{II}} = \frac{4}{m(V)}\sigma(\Delta\phi) \tag{6.16}$$

Calibration of $V_{\pi,eff}$
Before fitting the Eq.6.15 and Eq.6.16 with experimental data, we need to calibrate the value of $V_{\pi,\text{eff}}$ in this model. To do so, we fit Eq.6.14 for different acquisitions in open-loop and different known driving voltage V, as shown in Fig.6.17. From this fit, we obtain a

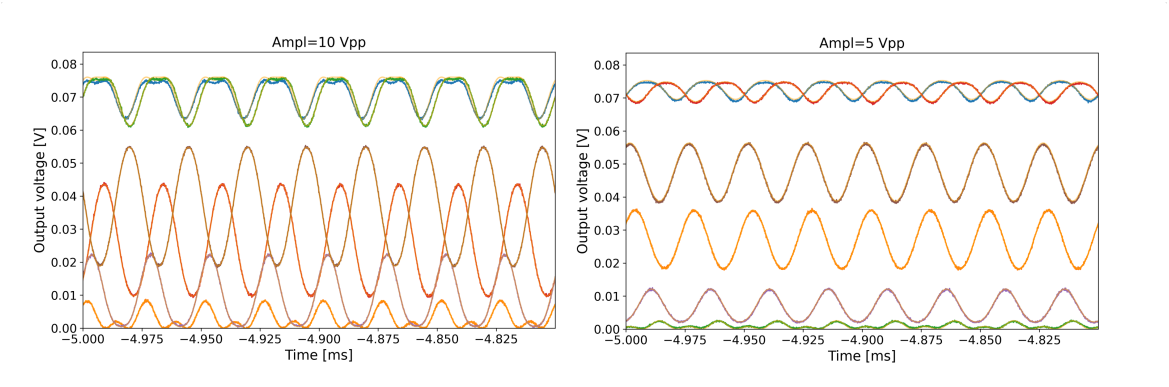

Fig. 6.17: Calibraiton of $V_{\pi,\text{eff}}$ for different functioning point in open-loop. Left : acquisitions with $10\,Vpp$ driving amplitude ; Right : $5\,Vpp$ amplitude.

value $V_{pi,\text{eff}} = 31.7 \pm 1.1\,V$. At first glance, this results seems inconsistent with the typical $V_\pi \approx 7\,V$ given by the manufacturer : however, our fitted value also takes into account the RF attenuation of the chain. Considering a $V_\pi \approx 7\,V$, the attenuation would be effectively $A \approx 0.25 \approx 6\,dB$, compatible with the typical RF attenuation of the set-up.

Fit and results
We then measure the experimentally the mean value and the standard deviation of the peak amplitude of the harmonic I and II, for different driving voltages ranging from 0.1 to $10\,V$, and fit this value to Eq.6.15 and Eq.6.16, as shown on Fig.6.18.

The values that we finally obtained for characterizing the stability of the loop are :
- Mean : $\overline{\phi} = \lambda/240$
- Standard-deviation : $\sigma_\phi = \lambda/440$.

6.8 *Paper A&A : Toward a large bandwidth photonic correlator for infrared heterodyne interferometry (published)*

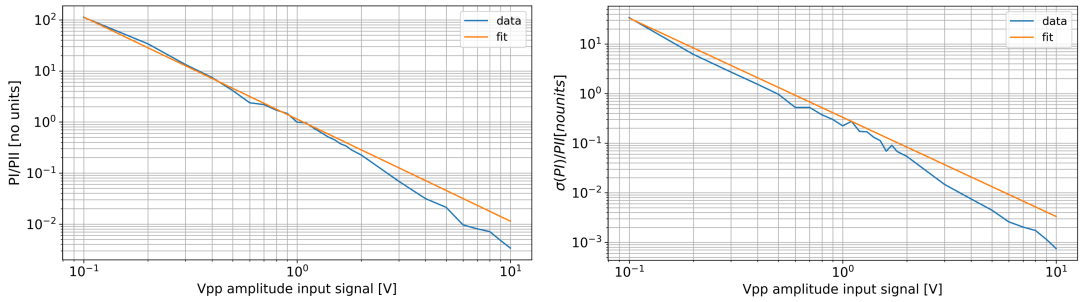

Fig. 6.18: Left : Fit of $\frac{A_I}{A_{II}}$ data with the model of Eq.6.15. Right : fit of the standard deviation experimental data with Eq.6.16. A noticeable deviation between the model starts to be visible for large Vpp, where the driving voltage is not negligible against V_π of the modulators.

6.9 *SPIE proceedings: MACH II: Mach-Zehnder analog correlator for heterodyne infrared interferometry (published)*

6.10 *Paper JOSA : Architecture of photonics correlation for infrared heterodyne interferometry (under review)*

Les choses ont leur secret, les choses ont leurs légendes,
Mais les choses murmurent si nous savons entendre

— **Barbara**
Drouot

7 Correlation II : Analog photonic correlator

7.1 Motivation

Motivation

In the last section, we introduced the use of photonic schemes in order to perform the transport and the analog correlation of wide-bandwidth RF signals. More precisely, this correlation -equivalent to the analog RF correlation performed on the ISI- was essentially restricted to the computation of the correlation function $C_{12}(\tau)$ at one delay τ :

$$C_{12}(\tau) = \langle s_1(t) s_2(t+\tau) \rangle \tag{7.1}$$

The computation of the complete correlation function requires to measure this product for a complete set of time-delays. If the interferometric phase is preserved, the Fourier Transform of this function gives access to the complete visibility function over the bandwidth (or spectro-visibility) (John David Monnier, 1999)

$$\int_\tau \Big[\int_{\mathrm{BW}} |V(\omega_s)| e^{i\phi_V(\omega_s)} e^{i\omega'_{\mathrm{i.f.}}\tau} \mathrm{d}\omega'_{\mathrm{i.f.}} \Big] e^{-i\omega\tau} \mathrm{d}\tau = V(\omega) e^{i\phi_V(\omega)} \tag{7.2}$$

The measurement of the complete temporal correlation could be performed by introducing successive delays between the different channels and repeating this measurement successively, point by point[1]. However, such a method suffers from a lack of reconfigurability, a high degree of complexity and the need for successive measurements.

Context

More generally, the methods at our disposal to compute a cross-correlation product can be grouped in two categories, as summarized in Fig.7.1, divided between time-domain approaches and frequency-domain approaches. The time-domain approach consists in measuring either successively or simultaneously the multiplication product of the two signals at different time delay, which gives access to the complete correlation function. The frequency-domain approach consists in computing the Fourier transform of each signal $s_k(f)$, and then performing the product $s_1(f)s_2^*(f)$, which is equal to the Fourier transform of the cross-correlation.

In this context, a wide range of solutions have been developed, based on analog RF and digital techniques : we refer the reader to the Chap 4, which discusses the status and the limitations of these techniques applied to heterodyne interferometry, which are restricted to

[1] This measurement was done when characterising the coherence envelope of the simple 2 element correlator in Chap 6 for example.

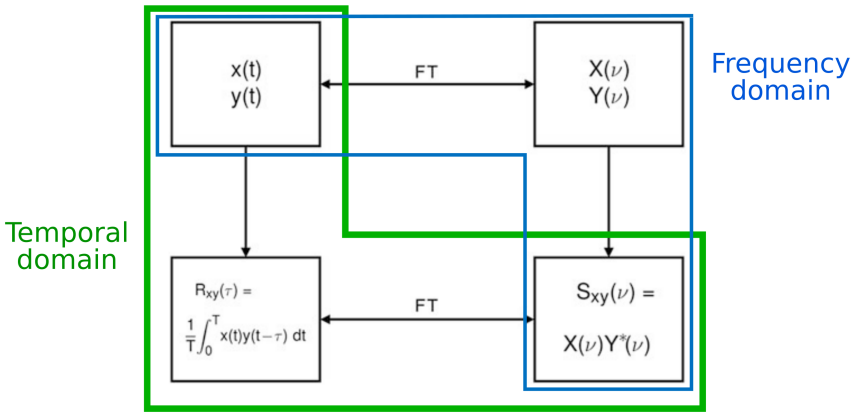

Fig. 7.1: Schematic diagram of the two possible correlation approaches. The temporal approach (green) consists in retrieving the value of the correlation function at each time step τ by multiplying and integrating the two signals delayed by a relative amount τ ; in the case where the correlation function is mapped for a large number of delays τ, the spectro-visibility can be obtained by computing the Fourier transform of the correlation function $C_{12}(\tau)$. The frequency approach consists in computing directly the Fourier transform of each signals, and in multiplying one spectrum with the complex conjugate of the other. At the end, temporal and frequency approach enables to obtain the same observable.

bandwidth of the order to 10 GHz typically. In the case of radio-astronomy, digital correlators are developed for decades and constitutes the prime solutions for most of the contemporary interferometers (ALMA, NOEMA, VLA, etc.). These correlators are implemented through XF and FX architectures, which corresponds respectively to the aforementioned temporal- and frequency-approaches [2]. Concerning analog RF solutions[3] the most advanced solutions are based on the parallelized multiplication of channels, which enables to perform the correlation in real-time : these solutions mainly belong to the temporal approach.

In the following, we present the joint reflection and demonstration with Hugues Guillet de Chatellus and Jean-Philippe Berger of an analog correlator computing the real-time correlation of wide-bandwidth signals in a simple photonic set-up. In Section 7.2.2, we recall some basic properties of Frequency Shifting Loop (FSL), and then introduce the principles of the analog photonic correlator. In Section 7.3, we present a characterisation of the different properties of the correlator, in particular of its different functioning regimes and dynamical range. In Section 7.3.9, we present the experimental demonstration of the analog photonic correlator on different type of signals and on the correlation of simple monopole antenna. Finally, we conclude in Section 7.4 by presenting the applications of the correlator and potential perspectives and ideas to scale-up this concept to a large number of telescopes.

[2] X is designating the multiplication, and F the Fourier transform. XF correlator are also known as *lag correlator*.
[3] See for example the analog lag correlator developed in the frame of CMB interferometry mentioned in Chap 4, (Holler et al., 2011).

7.2 Principles

The general principles of the analog photonic correlator consists in computing simultaneously the multiplication product at several delays of two RF signals, each relative delay being encoded at a specific frequency in the output trace of the correlator. The fundamental block of the correlator, which enables to create multiple replica of the input signals, is the so-called *frequency shifting loop* (FSL). In the following, we first describe the functioning principle of a generic FSL, which will then enable us to introduce the principle of the analog photonic correlator.

7.2.1 Frequency Shifting Loop (FSL)

The general FSL, represented in Fig 7.2, consists in an optical loop in which a frequency shifting element is placed, generally an AOM, and a gain medium, such as a telecom amplifier, which compensates for the optical losses during a loop. At each loop, the electric field acquires a delay τ and is shifted by a frequency f_s. This translates by a frequency shift of the optical carrier $e^{i2\pi(nf_s)t}$, and the addition of a phase delay seen at the optical frequency $f_0 + nf_s$ i.e. the multiplication by a phase term $e^{-i2\pi(f_0+nf_s)\tau_c}$, assuming that the field is first shifted in frequency, and then delayed by τ_c[4]. A fraction is transmitted at the output, so that the resulting field is the sum of the fields that have been shifted by an amount nf_s, and that have accumulated the different phase shifts (Schnebelin, 2018) :

$$
\begin{aligned}
E_{\text{out}}(t) = \; & \epsilon(0)E_{\text{in}}(t)e^{i2\pi f_0 t} \\
& + \epsilon(1)E_{\text{in}}(t-\tau_c)e^{i2\pi(f_0+f_s)(t-\tau_c)} \\
& + \epsilon(2)E_{\text{in}}(t-2\tau_c)e^{i2\pi(f_0+2f_s)(t-\tau_c)} \times e^{-i2\pi(f_0+f_s)\tau_c} \\
& + \dots \\
& + \epsilon(n)E_{\text{in}}(t-n\tau_c)e^{i2\pi(f_0+nf_s)(t-\tau_c)} \times e^{-i2\pi\left(nf_0+(1+2+..+(n-1))f_s\right)\tau_c} \\
& = e^{i2\pi f_0 t} \times \Big(\epsilon(0)E_{\text{in}}(t) \\
& + \epsilon(1)E_{\text{in}}(t-\tau_c)e^{i2\pi f_s t}e^{-i2\pi f_s\tau_c}e^{-i2\pi f_0\tau_c} \\
& + \epsilon(2)E_{\text{in}}(t-2\tau_c)e^{i2\pi(2f_s)t}e^{-i2\pi f_s(1+2)\tau_c}e^{-i2\pi f_0(2\tau_c)} \\
& + \dots \\
& + \epsilon(n)E_{\text{in}}(t-n\tau_c)e^{i2\pi(nf_s)t}e^{-i2\pi f_s(1+2+..+n)\tau_c}e^{-i2\pi f_0(n\tau_c)}\Big)
\end{aligned}
$$

with $\epsilon(n)$ the cumulated gain and losses after n loops.

[4] In the more general case where the AOFS is not at zero-time, the only difference is the introduction of a global phase shift $e^{-i2\pi f_0\tau_i}$ due to the delay τ_i between the entrance in the loop (implicitly chosen as the phase reference) and the AOFS. In fact, this phase term is arbitrary, as the time and phase references are always chosen arbitrarily.

The cumulated sum of delay creates a quadratic phase term $(1+2+3+...+n)\tau_c = \frac{n(n+1)}{2}\tau_c$, so that the output field is finally written :

$$E_{\text{out}}(t) = e^{i2\pi f_0 t} \sum_{n=0}^{N} \epsilon(n) E_{\text{in}}(t - n\tau_c) e^{i2\pi n f_s t} e^{-i\pi f_s \tau_c n(n+1)} e^{-i2\pi f_0 (n\tau_c)} \tag{7.3}$$

In fact, the starting time τ_0 of an acquisition is always arbitrary $t \to t - \tau_0$, so that Eq (7.3) is always defined with an arbitrary linear phase term $e^{-i2\pi n f_s \tau_0}$. In the following, we will consider that the starting time τ_0 is always chosen in such a way that all the linear terms $e^{-i\pi f_s \tau_c n} e^{-i2\pi f_0 (n\tau_c)}$ are canceled. Actually, this is what is done in practice when we process the experimental data numerically. In this way, the output electric field can finally be written, still in the general case :

$$E_{\text{out}}(t) = e^{i2\pi f_0 t} \sum_{n=0}^{N} \epsilon(n) E_{\text{in}}(t - n\tau_c) e^{i2\pi n f_s t} e^{-i\pi f_s \tau_c n^2} \tag{7.4}$$

Eq (7.4) summarizes the properties of the FSL : the output field consists in a frequency comb of spacing f_s, starting from frequency f_0, and exhibits a quadratic phase which can be tuned[5] through the choice of f_s and τ_c. This frequency comb is represented in Fig 7.2 . FSLs have already been extensively studied, and have proven many applications in spectroscopy (Duran, Schnebelin, and Guillet de Chatellus, 2018), ranging distance (Clement et al., 2019), or in microwave photonics (Schnebelin, Azana, and Guillet de Chatellus, 2019; Guillet de Chatellus, Cortes, and Azana, 2016), which includes the present work.

7.2.2 Photonic correlator

General principle

The architecture of the photonic correlator, whose principle is shown in Fig 7.3, is based on a pair of FSLs, which produce two combs with repetition rates f_1 and f_2 and time delays τ_1 and τ_2 respectively. The general principle of the correlator consists in encoding the input RF signals on an optical carrier through the use of an amplitude modulator, and generate replicas $s_k(t - n\tau)$ of the input signals at multiple time delays. For each input RF signals, the replicas are shifted by slightly different time delays τ_1 (associated to signal $s_1(t)$) and τ_2 (associated to signal $s_2(t)$). The key idea consists in associating at each round trip a *frequency shift* f_1 (resp. f_2), so that a signal experiencing n delays is shifted by a frequency

[5] Such quadratic phase term is in fact equivalent to the effect of dispersion, which can be easily tuned here. The physical property of this quadratic phase term is interesting by itself e.g. for the generation of chirped signal (Guillet de Chatellus et al., 2018). See in particular (Schnebelin, 2018) for a detailed discussion about the properties related to the quadratic phase.

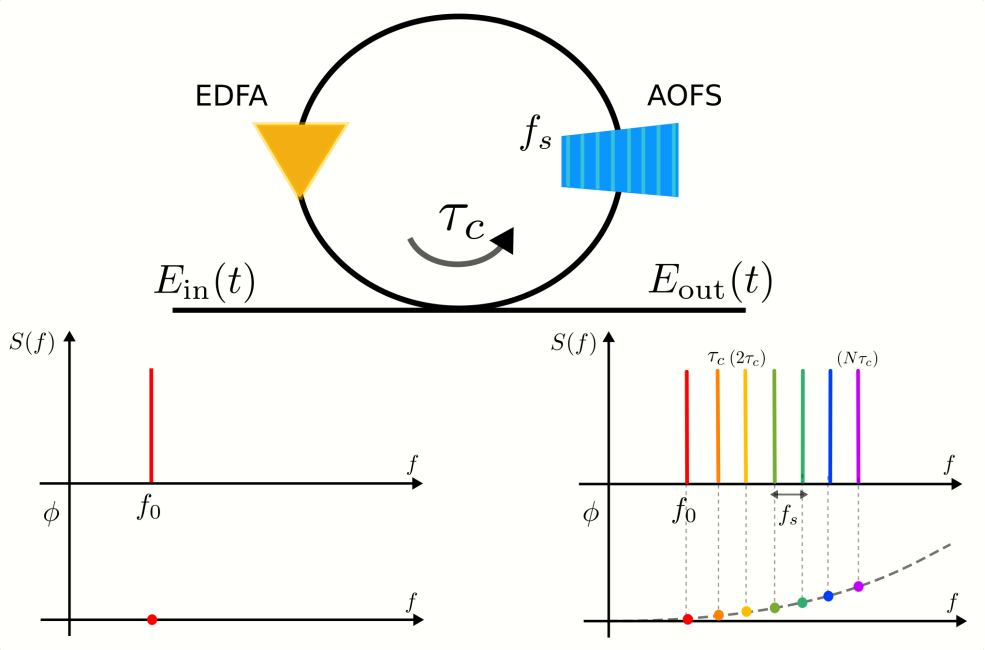

Fig. 7.2: Principle of a Frequency Shifting Loop (FSL) : an input field $E_{\text{in}}(t)$ enters the loop, where it is shifted in frequency f_s by the AOFS and delayed by a time τ_c. An optical amplifier (EDFA : Erbium Doped Fiber Amplifier) is inserted in the loop in order to compensate for the propagation losses and the output coupling losses to extract part of the flux. The output field E_{out} is carried by a comb with frequency separation f_s and which exhibits a quadratic phase (see text), where each tooth is associated to a replica of the incident field delayed by a time $n\Delta\tau$.

nf_1. (resp. nf_2). By recombining all channels on a photodiode, the multiplication product $s_1(t)s_2(t+n\Delta\tau)$ associated to the delay difference $\Delta\tau = \tau_2 - \tau_1$ is encoded at a different frequency difference $n\Delta f$, with $\Delta f = f_2 - f_1$. In this manner, by computing the Fourier transform of the photocurrent, one can extract the amplitude and the phase of each of these peaks, which are proportional to the value of the cross-correlation over a complete set of N time-delays, $N \approx 200$ typically.

Implementation

The two FSLs which constitute the comb could be implemented in two independent loops. However, in this case, such a configuration would introduce relative phase drift between each loops, perturbing the coherence of the output signal. Here, the two loops are implemented in a bidirectional configuration (Duran, Djevarhidjian, and Guillet de Chatellus, 2019; Billault et al., 2021) the two signals travel in opposite direction in the same portion of fiber, except a short non-reciprocal section where they experience different time delays and frequency shifts. In this manner, the two combs experience almost similar phase perturbations, which guarantees the relative phase stability between the two loops. The FSLs are seeded with a CW laser modulated with amplitude modulator on which are applied the two RF signals to be correlated, so that the amplitude of the input field is of the form $E_{\text{in}} = E_0 s(t)$. According to

the description of the FSL, and assuming the ideal case of a constant gain $\epsilon(n)$ at each loop, the combs extracted from the couplers at the output of each FSL (numbered k) are :

$$E_k(t) = E_0 e^{i2\pi f_0 t} \sum_{n=0}^{N} s_k(t - n\tau_k) e^{i2\pi n f_k t} e^{-i\pi f_k \tau_k n^2} \tag{7.5}$$

The outputs of the two FSLs are then combined on a balanced detector :

$$I(t) \propto \langle E_1(t) E_2^*(t) \rangle = \sum_{n,m} s_1(t - n\tau_1) s_2(t - m\tau_2) e^{i2\pi(nf_1 - mf_2)t} e^{-i\pi(f_1\tau_1 n^2 - f_2\tau_2 m^2)} \tag{7.6}$$

This leads to the second fundamental idea of the photonic correlator, which shares similarity with the principle of dual-comb techniques (Picque and Hänsch, 2019; Coddington, Newbury, and Swann, 2016) : assuming that the frequency difference $\Delta f = f_1 - f_2$ are tuned so that the maximum frequency difference remains smaller than the comb separation $N\Delta f \ll f_1/2, f_2/2$, only the closer tooth n of comb 1 can interfere with the tooth of comb 2. In this way, only terms with $n = m$ remain n the previous beating term :

$$I(t) = I_0 \sum_{n=0}^{N} \langle s_1(t - n\tau_1) s_2(t - n\tau_2) \rangle e^{-i2\pi n\Delta f t} e^{-i\pi n^2(f_1\tau_1 - f_2\tau_2)} \tag{7.7}$$

$$= I_0 \sum_{n=0}^{N} \langle s_1(t) s_2(t - n\Delta\tau) \rangle e^{-i2\pi n\Delta f t} e^{-i\pi n^2(f_1\tau_1 - f_2\tau_2)} \tag{7.8}$$

The output consists itself in a RF comb with a separation Δf. Each tooth n of this comb at frequency $n\Delta f$ is associated to the value at a time delay $n\Delta\tau$ of the cross-correlation function of the input signals $s_1(t)$ and $s_2(t)$. This RF comb can be retrieved by a FT of the photocurrent, which finally gives access to the value of the cross-correlation function :

$$\tilde{I}(n\Delta f) \propto C_{1,2}(n\Delta\tau) e^{-i\pi n^2(f_1\tau_1 - f_2\tau_2)} \tag{7.9}$$

The system parameters can be tuned so that $f_1\tau_1 - f_2\tau_2$ is an even integer. In this case, the phase term vanishes and teeth amplitude is directly proportional to the complex value of the cross-correlation function. Otherwise, the square-modulus of the FT gives access to the modulus of the cross-correlation function. This proves that the cross-correlation of the input signals can be mapped at the output of the photonic correlator, over a number of points N.

The main features of the analog optical correlator are the following :

- **N $\approx$ 250 correlation values :** in practice, the maximum number of teeth is limited by the maximum bandwidth of the tunable bandpass filter (TBPF) inserted in the loop $Nf_1 \approx Nf_2$. This window has to be adjusted to the position and the extent of the comb in order limit the ASE coming from the EDFA. In addition, the non-homogeneous transmission of the TBPF over the spectral bandpass often introduces modulation of the teeth amplitude, and a too large window bring more ASE in the comb, which reduces its dynamic range. The maximum number of teeth is a compromise with respect to these

elements : in most of the experiment carried in the following, the typical number of teeth will be equal to $N \approx 250$.

- **tens of GHz correlation :** the minimum delay $\Delta\tau$ with which the cross-correlation function can be sampled is given by the minimum path *difference* between the two arms, which can be set in theory to an arbitrarily small value, enabling the correlation of signals with tens of GHz bandwidth. Furthermore, this delay difference can be easily reconfigured over a wide range of values, by introducing a variable optical delay line (VODL) between each arms, as demonstrated in the following in Sec 7.3.9.

- **Real-time operation**: the processing time of the photonic correlator is equal to the total life time of the photons in the loop $N\tau_1 \approx N\tau_2$, which here is typically equal to $20\,\mu$s ($N = 200$ and $\tau_1 \approx 100$ns). Thus, the photonic correlator operates in real-time, and enables the correlation of non-stationnary signals, with a maximum rate of the order the inverse processing time of the correlator (e.g. $1/20\mu\text{s} = 50\text{kHz}$), as demonstrated further in Sec 7.3.8.

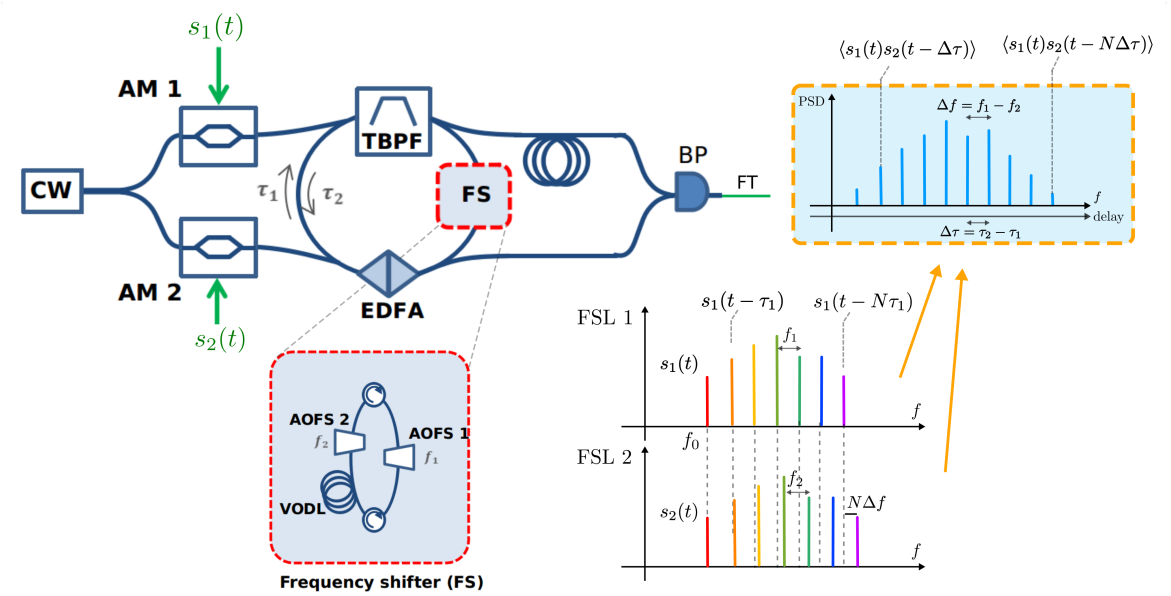

Fig. 7.3: Principle of the analog photonic correlator : the correlator consists in two FSLs, implemented in a bidirectional configuration. The input of the loop is composed of a CW laser seed, splitted in two arms, which are modulated by broadband amplitude modulator. The frequency shifts f_1 and f_2 and delays τ_1 and τ_2 are introduced in the non-reciprocal part of the loop, where the two respective loops are directed along two different paths by means of circulators. A Variable Optical Delay Line (VODL) is inserted in one arm, and enables to easily reconfigure the relative delay between each loops. Finally, the two arms are recombined on a balanced photodiode, which is low-pass filtered. The beating of the two combs with slightly different frequency separation creates a down-converted RF comb, in a similar way to dual-comb spectroscopy, where each tooth is here associated to the product of the input RF signals at different relative delays $\langle s_1(t)s_2(t-\tau)\rangle$. In this way, this output RF combs gives directly access to the value of the cross-correlation function, evaluated for a large number N of relative delays. An additional portion of fiber is introduced in one arm in order to position the zero delay $\Delta\tau = 0$ at the center of the frequency window.

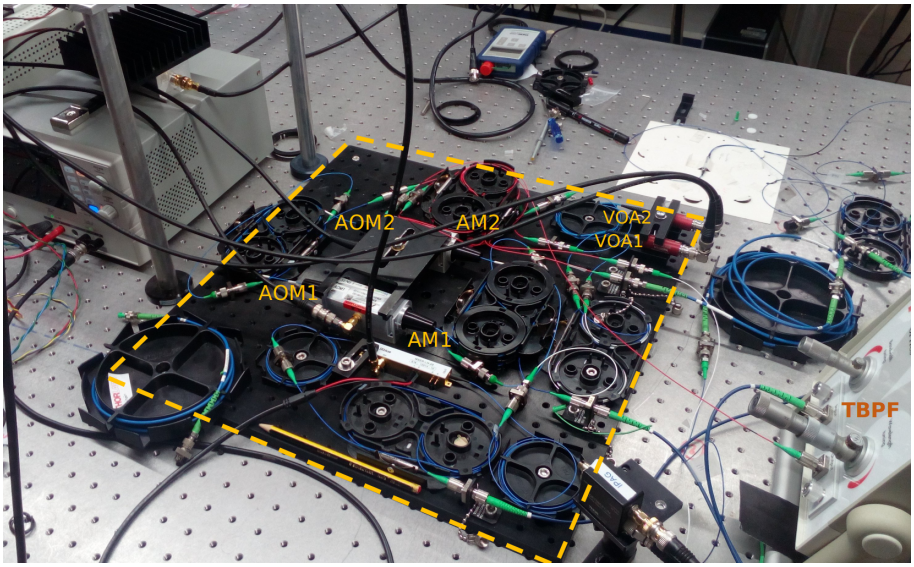

Fig. 7.4: Actual implementation of the analog photonic correlator in the laboratory.

The photonic correlator, whose principle is depicted in Fig 7.3, was then implemented in the lab through commercially available photonic components, as shown in Fig. 7.4 . In the following section, we start by focusing on the characterisation of the performances of the comb and its functioning regimes (Sec 7.3), and on the application of our set-up to the correlation of different type of broadband signals (Sec 7.3.9).

7.3 Characterisation

In this section, we focus on the characterisation of the analog photonic correlator and the factors limiting its performances, in particular in terms of sensitivity, saturation, dynamic range, and temporal response. In particular, we will describe the different functioning regimes of the correlator : small RF power regime, normal functioning regime, and high-power regime dominated by saturation. Before presenting the experimental characterisation of the comb, we briefly remind the reader some fundamental properties inherent to the gain and Amplified Spontaneous Emission (ASE) in FSL.

7.3.1 Reminder of the properties of gain saturation and Amplified Spontaneous Emission (ASE) in FSL

In this section, we briefly remind some fundamental properties inherent to the gain and Amplified Spontaneous Emission (ASE) in FSL, which will be important to understand the different regimes of the correlator (low, nominal and high power regime). In particular, we refer the reader to (Kanagaraj et al., 2019), who provides a detailed description of the gain, the ASE and the saturation effects in FSL, on which the present paragraph is largely based

and which is reproduced in part here. In this paragraph, we will keep most of the notations of (Kanagaraj et al., 2019) in order to remain consistent with this paper.

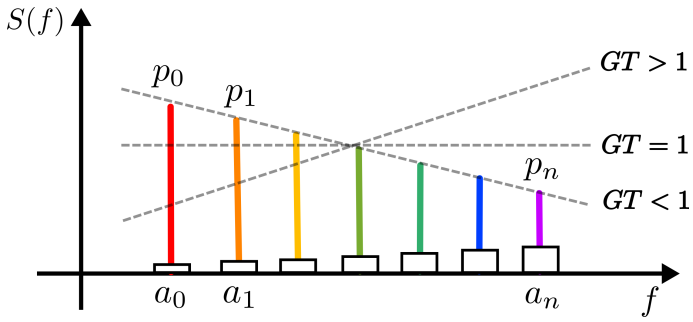

Fig. 7.5: Regimes of the FSL depending of the gain of the amplifier relative to the passive losses. The power of the teeth and of the ASE are both represented. Adapted from (Kanagaraj et al., 2019).

We start by describing the power of the comb. At each round-trip, the optical power of tooth is amplified by a gain G set by the EDFA, and attenuated by a factor T due to the passive losses. In that respect, the power p_n of the comb tooth numbered n is simply described by the relation :

$$p_k = (GT)^n \cdot p_0 \tag{7.10}$$

The general form of the amplifier gain G is written :

$$G = \exp\left(\frac{g_{ss}}{1 + \frac{P_{\text{tot}}}{P_{\text{sat}}}}\right) \tag{7.11}$$

with P_{tot} the total optical power in the loop, P_{sat} the saturation power of the loop, and g_{ss} the dimensionless small signal gain of the amplifier. A fundamental aspect in the following is that this gain evolves with the total optical power in the loop. More precisely, this gain *decreases* with the optical power P_{tot}, or in other words gets *saturated* by the optical power: the more light there is in the loop, the smaller G is. This property will lead to different operating regimes. In order to understand this, the amplification factor has simply to be compared to the total losses : in the case where the gain is larger than the optical losses ($GT > 1$), the teeth power increase with the number of round-trips ; when the gain exactly equals the losses ($GT = 1$), the teeth power is constant ; when the gain is smaller than the losses ($GT < 1$) the teeth power decrease with the number of round-trips. These regimes are summarized in Fig 7.5.

In addition, the amplifier is producing ASE, whose optical power a_0 adds a fixed contribution to the former power circulating in the loop at each round-trip :

$$a_n = (GT)^n \cdot a_{n-1} + a_0 \tag{7.12}$$

As we will see in the following, a consequence of this relation is that unlike the teeth power, the contribution of the ASE is strictly increasing with the number of round-trips, even in the case where $GT < 1$. This property is also schematically represented on Fig 7.5.

7.3.2 Experimental characterisation of the functioning regimes

In a general way, the PSD peak varies quadratically with the optical input power, which is itself proportional to the RF power. In order to study the different regimes of the comb versus the RF power, we measured the auto-correlation for a series of acquisition with regular increasing values of RF power. We repeat this series for a sinus waveform and a noise waveform : the sinus consists in a sinus voltage with frequency f=178 MHz, and the noise was 120 MHz-bandwidth noise waveform generated by the AWGs. In each case, we measure the comb at several increasing amplitude value of the voltage, all other parameters (driving current of the EDFA, passive attenuation, etc.) being kept constant.

In the following, we detail the different limitations associated to each regime, starting from small RF power ($\sim 5\,\mathrm{dBm}$) and going to higher RF power ($\sim 15\,\mathrm{dBm}$).

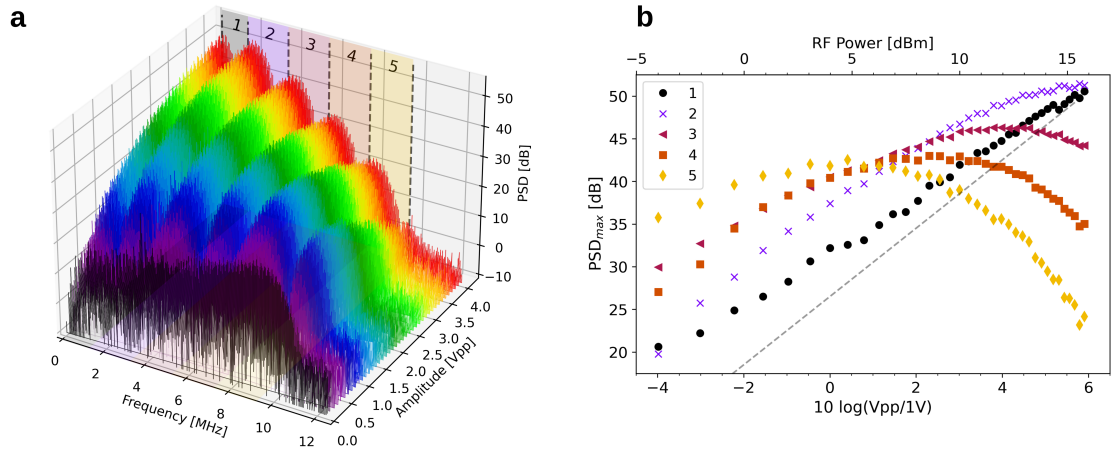

Fig. 7.6: a) Auto-correlation of a sine function for increasing amplitude value. The plot is divided in 5 frequency bins, corresponding to each local peak of the auto-correlation function (bin 1 : 0.2 to 1.5 MHz ; bin 2 : 1.5 to 3.5 MHz ; bin 3 : 3.5 to 5.5 MHz ; bin 4 : 5.5 to 7.5 MHz ; bin 5 : 7.5 to 9.5 MHz). b) The maximum PSD amplitude of each frequency bin is extracted for each voltage, and plotted versus corresponding input RF power. The dashed line corresponds to the theoretical quadratic growth of the auto-correlation PSD.

7.3.3 Small power regime

We first focus on the small RF-power regime (black and purple in Fig 7.6; red in Fig 7.7). The lower limit of input power for a signal to be exploitable is of the order of 5 dBm for a sinus waveform (Fig 7.6 b)), and 10 dBm in the case of a noise waveform (Fig 7.7 b)). This lower bound originates mostly from the ASE in the correlator. The ASE is amplified and added at each round-trip : as mentioned previously, the consequence is that the contribution of ASE always increases with frequency offset (contrary to the comb associated to the signal). As a result, ASE contribution appears as a broad noise contribution in the comb, which ultimately limits the sensitivity and the dynamic range of the correlator. Given that the contribution of ASE adds to the input seed power, it was also shown that in the case of a FSL (Kanagaraj

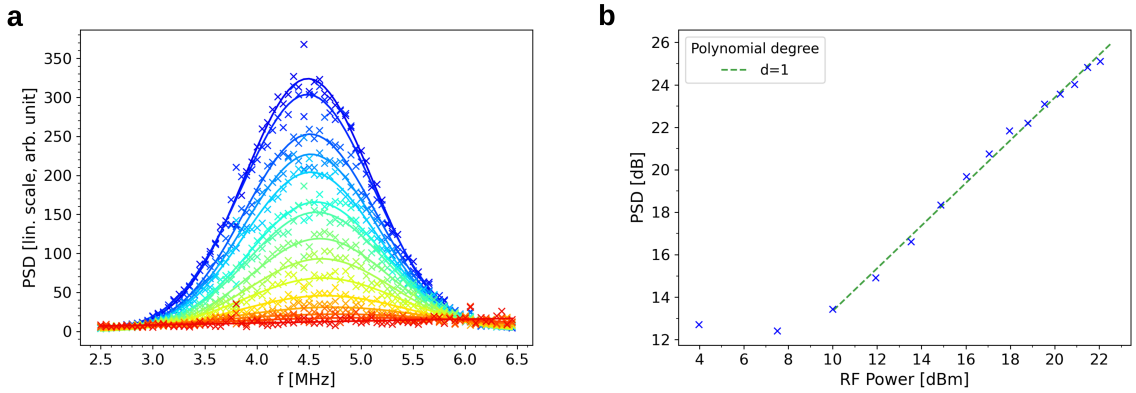

Fig. 7.7: a) Auto-correlation of a noise waveform signal with 120 MHz bandwidth. b) Maximum amplitude of the correlation envelope versus input input RF power. A dashed line corresponding to a linear growth is over-plotted in comparison.

et al., 2019) that ASE contributes to saturate the gain of the amplifier, which will appear as a limitation for high power.

The ASE increases with the bandwidth of the amplifier, set by the TBPF. The consequence of this latter point is a trade-off between N the total number of teeth (i.e. the number of points in the mapping of the correlation function) and the sensitivity that can be achieved. In practice, N is of the order of few hundreds ($N \approx 200 - 250$ in our set-up). On the other hand, ASE increases with the gain and the noise factor (NF) of the amplifier. In order to reduce ASE and thus to increase the sensitivity and/or the number of teeth (depending of the desired trade-off), it is of major importance to aim at low gain, in particular by lowering the passive losses in the correlator, and to use amplifiers with the lowest NF. In addition to ASE, when the RF power is set to zero, a residual comb is still visible in Fig 7.6, which results from the finite extinction ratio of the MZI, of the order of 25 - 30 dB typically, due to a small residual imbalance at the level of the AM. This small imbalance causes a leaking of the seed laser through the AM. Therefore, even in the absence of an input RF signal, a small part of the input seed is transmitted and produces a comb. The teeth of this comb appear to increase as the frequency offset increase (higher number of round-trips). This is due to the fact that the optical power is low in this regime, so the optical gain is high, leading to an increase of the teeth amplitude at each step.

7.3.4 Normal "flat" regime

The specific shape of the comb observed at the previous paragraph, where the teeth increase with the frequency offset, is visible when no RF signal is applied and for small amplitude signals (red and purple regions in Fig 7.6). Nevertheless, by increasing further the RF power, a larger total optical power circulates in the loop, which decreases the gain of the amplifier (gain saturation). As a result, the increase of the teeth power is less and less steep for larger RF power (i.e. total optical power in the loop). Ultimately, for a given functioning point, the gain compensates exactly for the losses at each round-trip, so that the net gain per round-trip

$\epsilon(n)$ equals 1. In this case, the comb appears perfectly "flat", which is the regime we seek to obtain. This shape enables to map the correlation and is the nominal regime of the comb.

7.3.5 High-power regime : saturation effects

The last regime of the correlator is a regime dominated by saturation at high RF power. As the RF-power increases, so does the total optical power in the loop, leading to saturation and reduction of the gain. As the gain per roundtrip is smaller than the losses, the teeth decrease exponentially with the offset frequency. This exponential decay due saturation is particularly visible on Fig 7.6 (yellow and red regions) as a linear slope in log scale, with a steepness which increases with the RF power. The effect of saturation is more predominant for the highest offset frequency of the spectrum. Ideally, the teeth peak amplitude should exhibit a quadratic growth with respect to RF power. This increase is relatively close to a quadratic growth for the very first teeth (frequency bin 1), in which the amplification is mainly due to the single pass (or few passes) amplification, so that the effect of saturation is difficultly visible (low number of round-trips). On the other hand, for higher frequency, the comb deviates strongly from the theoretical increase, and even exhibits a decrease of amplitude for higher RF power (frequency bins 3-4-5, Fig 7.6 b). The higher the frequency is, the smaller is the value of the RF power (i.e. the optical power) required to observe this inflexion point. This is due to the higher number of round-trips, which makes the effect of saturation more predominant and thus visible at lower optical power.
The effect of saturation is also visible on the noise waveform in Fig 7.7. In this case, the variation of the amplitude of the comb is linear with input RF power, as seen in Fig 7.7 b) (slope close to one in log-log scale). This is well consistent with the sinus waveform, which was close to a linear increase in the same frequency window 3.5 - 5.5 MHz (frequency bins 2 - 3 in Fig 7.6). In addition to the amplitude, the saturation effect also translates in a small narrowing and a slight shift of the mean position of the auto-correlation peak, as shown in Fig 7.7 . The measurement for the lowest voltage values (<2 Vpp) is subject to caution due to low output power value. Overall, the effect of saturation on peak width and mean position remains however relatively limited.

7.3.6 Control of the loop

The different regimes discussed in the last three sections potentially affect the quality of the comb, but they can be controlled. In particular, saturation is directly dependant of the total optical power of the loop. The comb can be kept in a regime where the gain of the amplifier is equal to the passive losses by adjusting in real time the light injected in the system through variable optical attenuator (VOA) at the input of the loop. Such system is the next step of the current version of the correlator. Concerning the ASE, as above-mentioned, the TBPF has to be adjusted with the narrowest window possible and the EDFA has to be chosen with the lowest NF possible in order to limit the contribution ASE.

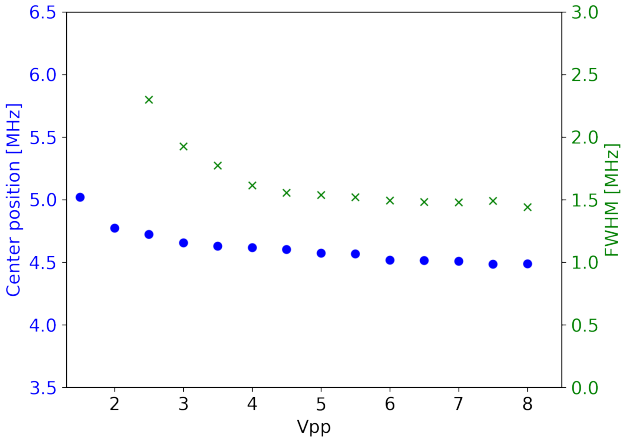

Fig. 7.8: a) Auto-correlation of a noise waveform signal with 120 MHz bandwidth. b) Maximum amplitude of the correlation envelope versus input input RF power. A dashed line corresponding to a linear growth is over-plotted in comparison.

7.3.7 Dynamic range & PRBS signal

The typical dynamic range of the comb is usually of the order of 20-30 dB. In the following, we apply the analog correlation to PRBS signal, which enables both to demonstrate the correlation for this type of signals and to probe the maximum dynamic range of loop.

Pseudo-Random Binary Sequence (PRBS) are periodic signals generated with a deterministic algorithm, which exhibits statistical properties very similar to random signals, and offer the capability to probe high dynamic range. More specifically, the auto-correlation function of PRBS signal has the property to be equal to -1 for every value, and to be proportional to K at delays multiple of $K\delta\tau$, with $\delta\tau$ the increment of delay of the sequence and $K = 2^k - 1$ the total length of the sequence. These signals are designated as PNk. A consequence of these properties is that the amplitude is increased by a factor 2 at each step k to $k+1$, which translates in an increase of $20\log(2) \approx 13.9$ in the PSD at each step.

Experimentally, we used an AWG to generate PN3 and PN4 (sampling rate 30 MSa/s, $200\,\mu$s acquisition time) and then measured the auto-correlation. We use the configuration of the analog correlator with large delays (resolution $\Delta\tau \sim 5\,$ns and total span $200 \times 5\,\text{ns} = 1\,\mu$s) previously introduced in this chapter. The theoretical auto-correlation function exhibits a characteristic triangular shape, crossing zero on both sides of the peak. In order to compare this theoretical expectation to the experimental data, we measured independently the PRBS signals generated by the AWGs (which enables to include the rise time of the AWGs) and compute the numerical auto-correlation. The square modulus of this numerical auto-correlation is then compared to the experimental acquisition, as shown on Fig 7.9. Both traces are in excellent agreement. In addition, the maximum difference between the main peak and the adjacent dips reaches typically 25 to 30 dB for 200ms. This constitutes the typical maximum dynamic range achieved by the correlator. In the case of PN4, one can

notice that the floor of the auto-correlation is slightly below the theoretical level : this effect is likely due to a small residual on the bias of the AM.

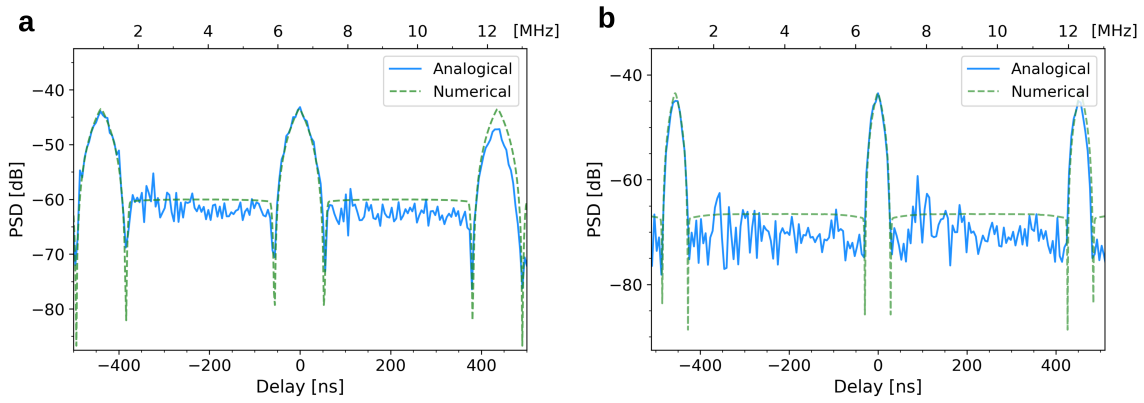

Fig. 7.9: Auto-correlation of PN3 (left) and PN4 signal (right).

7.3.8 Dynamical correlation

In practice, the analog photonic correlator enables to compute correlation function in so called "real time". In this section, we try to evaluate quantitatively the typical speed at which it is possible to perform a measurement.

To this end, we apply a known waveform, here a sinus waveform, of which we modulate the central frequency (frequency modulation) with different rates. We use a sinus waveform with central frequency $f = 100\,\mathrm{MHz}$, modulated with a depth equal to $f_\Delta = 10\,\mathrm{MHz}$, and an increasing modulation rate $f_r = 100\,\mathrm{Hz},\ 400\,\mathrm{Hz},\ 4\,\mathrm{kHz}$. The expected result is a correlation trace modulated in time at the rate f_r, around the zero delay (offset frequency $\sim 6\,\mathrm{MHz}$). The maximum rate for which an acquisition has a sufficient SNR is typically $f_r = 4\,\mathrm{kHz}$, which gives an estimate of the maximum refreshing rate of the correlator. Ultimately, the processing time is limited by the round-trip time, which is typically $N \times \tau_1$ ($\approx N\tau_2$), in this case $\sim 12.5\,\mu\mathrm{s}$. This round-trip time corresponds to a rate $1/12.5\mu\mathrm{s} = 80\,\mathrm{kHz}$. This rate is globally consistent with our measurement, given the fact that a number of round-trip larger than one is necessary to obtain a measurement with a sufficient SNR. The maximum refreshing rate should depend on the SNR of the input signal, so that a trade-off would have to be reached between the input RF power and the maximum refreshing rate required. In our case, we can suppose that we were placed in optimal conditions of SNR, so that our measurement set a maximum limit on the refreshing rate. Overall, this demonstrates the capability of the correlator to perform measurement at time-scales of the order of ms and below.

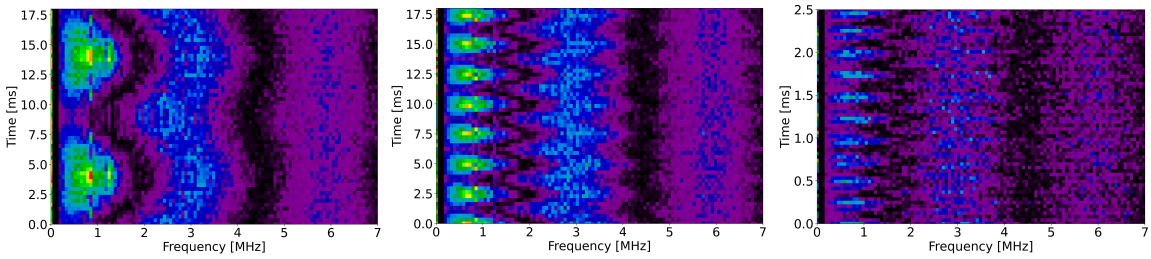

Fig. 7.10: Auto-correlation of sinusoidal signals modulated in frequency. The parameters of the input signals are (see text for the notation used) $f = 100\,\text{MHz}$, $f_\Delta = 10\,\text{MHz}$ and *(Left)* $f_r = 100\,\text{Hz}$; *(Center)* $f_r = 400\,\text{Hz}$; *(Right)* $f_r = 4\,\text{kHz}$ (note the different scale on time axis).

7.3.9 Correlation of wideband RF signals

In this section, we apply our set-up to the correlation of broadband signals. We first focus on the correlation of broad noise signals, then applied to the determination of time delay estimation, and finally to the correlation of monopole antennas in Sec 7.3.10.

Wideband correlation

We first apply the correlation scheme to broadband random noise signals. These RF signals were generated by an AWG and then applied to both AMs. In this configuration, the photonic correlator is computing the auto-correlation of the input RF waveform.

As described in Sec 7.2.2, the analog correlation is typically obtained over $N \approx 200$ values. Depending of the application, one can choose either to optimize the time resolution $\Delta\tau$ or to maximize of the time span $N\Delta\tau$ (respectively). This can be easily configured by adjusting the relative delay between each loop through the VODL. We choose to test these two types of configuration respectively with the delays $\tau = 115\,\text{ps}$ and $\tau = 4\,\text{ns}$.

Correlation of signals with 100s MHz bandwidth

The first series of acquisition ($\tau = 115\,\text{ps}$) is suitable with correlation bandwidth of approximately 8 GHz, and covers a delay range of approximately $200 \times 115\,\text{ps} = 23\,\text{ns}$, approximately equal to a propagation delay in free-space $\approx 7\,\text{m}$. An additional fiber delay $\approx 3\,\text{m}$ is introduced outside the loop in channel 1, in order to compensate the relative delay between the two arms i.e. to center the correlation trace in the output frequency window. In order to have a constant phase in the output comb, the value of the frequency rate of each FSLs is chosen to be $f_1 = 80.0000\,\text{MHz}$ and $f_2 = 80.0657\,\text{MHz}$ ($\Delta f = 65.7\,\text{kHz}$) so that they meet the condition $f_1\tau_1 = f_2\tau_2$. Finally, the correspondence between frequency and delay can be directly obtained with a scaling with the linear factor $\Delta\tau/\Delta f$.

In order to observe the effect of the signal bandwidth on the correlation signal, successive acquisitions were made with bandwidth ranging from 40 MHz to 120 MHz. The results are shown in Fig 7.11 : the output comb is encoded over $N \approx 200$ teeth, separated by a frequency Δf, and whose amplitude is proportional to square modulus of the correlation

function at delay $\Delta\tau$: $\tilde{I}(n\Delta\tau) \propto |C_{12}(\Delta\tau)|^2$. These experimental results were compared to the theoretical autocorrelations of the same signals. The theoretical auto-correlations were obtained by recording the input RF signals and computing numerically the autocorrelation, which enables to take into account the effect of the rise time of the AWGs on the RF waveforms. Experimental and theoretical auto-correlations shows an excellent agreement. In addition to the teeth, a broad noise pedestal is visible in the output trace, and mainly originates from the contribution of the ASE circulating in the loop. In practice, the experimental output trace exhibits a dynamic range of approximately $\approx 25\,\mathrm{dB}$. The factors which set the limit of the dynamical range will be investigated in details in Sec 7.3.7. Given that the repetition rate of the output RF comb Δf is precisely known, the acquisition (PSD) can be filtered, which is not applied in Sec 7.11 to show the noise background, but will be implemented in the rest of this chapter.

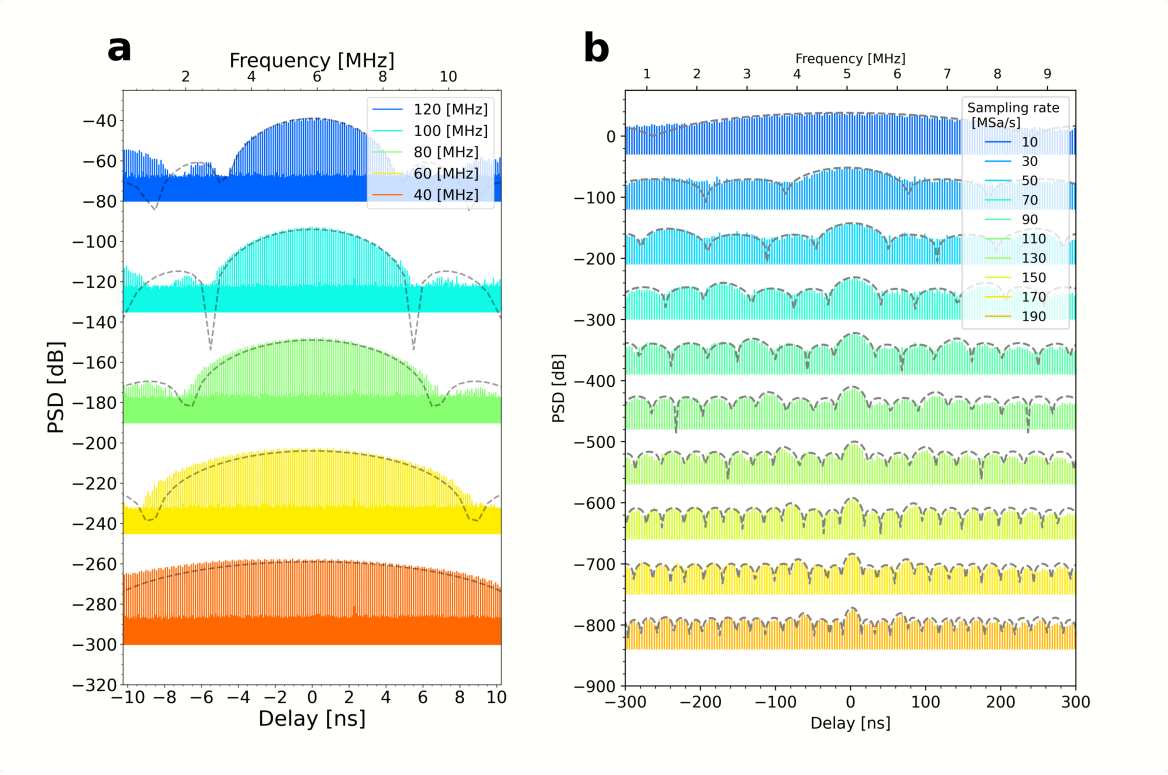

Fig. 7.11: a) Auto-correlation of broad noise signals with temporal resolution $\Delta\tau = 115\,\mathrm{ps}$. The PSD is proportional to the square modulus of the auto-correlation. b) Auto-correlation of noise signals (heterodyne signals generated in Sec 6.4.1) with temporal resolution $\Delta\tau = 4\,\mathrm{ns}$. Both : the theoretical autocorrelation traces are superimposed in dashed lines.

.

Autocorrelation of signals with 100s ns delay

In addition to the small delay configuration, the correlator was configured with a relative delay $\Delta\tau = 4\,\mathrm{ns}$ by introducing 1m fiber next to AOFS 2. In this configuration, we use one heterodyne signal generated in Sec 6.4.1, and applied it to both AMs. The particular feature of this signal is to exhibit multiple side-lobes, approximately $15\,\mathrm{dB}$ below the value of the

central lobe maximum. These side-lobes are mainly due to the non-uniform response of the detection and to the environmental parasitic signals mentioned in Sec 6.4.1 [6].

In this configuration, the correlation trace covers a time-span of approximately $200 \times 4\,\mathrm{ps} = 0.8\,\mu\mathrm{s}$, corresponding to a propagation delay 240m. An additional $\approx 100\,\mathrm{m}$ fiber was also introduced here at the output of channel 1 in order to center the output correlation trace. The results are shown in Fig 7.11. The larger value of $\Delta\tau$ enables to retrieve the complexity of the correlation function, which is compared to the numerical auto-correlation trace. In addition, successive sampling rate from 10 MSa/s to 190 MSa/s were applied in order to observe the effect of signal bandwidth on the auto-correlation.

Filtered signals & and narrow spectral features

Thus far, we have focused on the *auto*-correlation of noise signals : here, we focus on the *cross*-correlation of noise signals. In addition, in order to observe strongly non-symmetrical correlation function, we use two different noise signals : the first one is a noise with 120 MHz bandwidth, the second one is the same signal filtered with a stop-band filter (65 MHz - 85 MHz filter).

The result is shown in Fig 7.12. Similarly to the previous acquisition, a comparison with the numerical signal cross-correlation is done and shows a very good agreement, over a significant dynamical range (up to 30 dB). The analog auto-correlation signals were also obtained separately and are shown in comparison. We highlight that the second noise signal is similar to a source exhibiting an absorption line in a continuum. The experimental cross-correlation signal obtained here is not exactly equivalent to the correlation signal that would be obtained by a heterodyne interferometer observing such an object with a narrow spectral lines, given that the first channel is only a broad noise signal. However, interestingly, the capability to distinguish a narrow spectral lines in the correlation trace are comparable between these two situations [7]

7.3.10 Antennas correlation and time of arrival

We then applied this photonic scheme to the correlation of signals coming from two monopole antennas. The correlation of signals coming from two astronomical radio-antennas neces-

[6] These parasitic signals are mainly composed of sinusoidal, single-frequency signals (also visible in the PSD of each individual heterodyne signals), which explains the periodicity of the side-lobes. The contribution of these parasitic term was a difficult problem to solve, and was carefully checked in the experiment presented in Sec 6.4.1, first experimentally by introducing a relative delay between each channels and varying the relative contrast, and then numerically by computing the coherence envelope from the two recorded signal. Experimentally, a gaussian central side-lobe was effectively retrieved, and from the numerical trace, the contributions of these parasitic terms in the *coherent flux* was estimated to be at least $15\,\mathrm{dB}$ smaller than the contribution of the central lobe, part of this contribution being also simply due to the response of the detector itself. These results on the signal cross-correlation are consistent with the present result on auto-correlation presented in this chapter.

[7] In the case of astronomical signal, the typical linewidth (20 MHz, equivalent to $R = 1.5 \times 10^6$) tested here would correspond mainly to non-LTE (Local Thermal Equilibrium) processes e.g. natural laser gain in emission in planetary atmosphere (Mumma et al., 1981). The typical width of lines at LTE are generally of the order 2 GHz (equivalent to 20km/s or $R = 15 \times 10^3$), which would require to optimize the set-up to larger input bandwidth (typically 20 GHz).

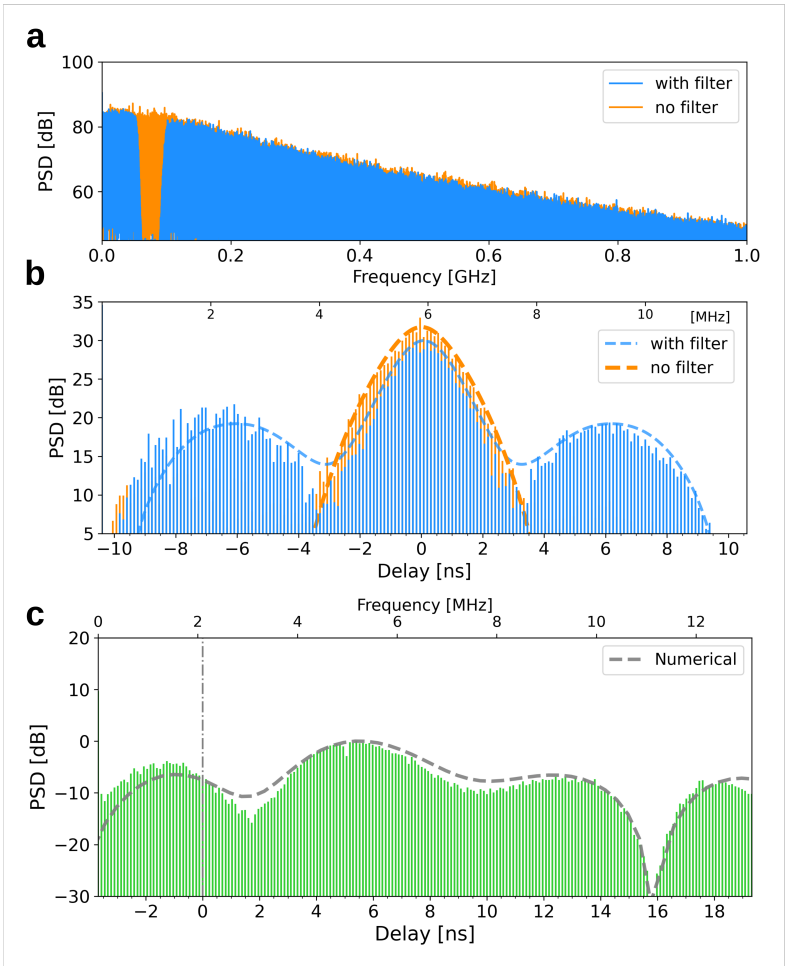

Fig. 7.12: a) Spectrum of noise signals with 120 MHz bandwidth (orange), and the same signal on which a notch filter is applied (65 MHz - 85 MHz). b) Square modulus of the auto-correlation function. One can notice the significant side-lobes on the filtered signal (acquisition time : 200ms). c) Square modulus of the cross-correlation of the two signals (acquisition time : 200ms). All : the theoretical autocorrelation traces are superimposed in dashed lines.

sitates dedicated parabolas and guiding systems which were under development but not available yet at the time of writing. Although, the measurement presented in the following differs from the type of observables in the case of astronomical antennas (resp., time delay difference of arrival (TDoA) vs. variation of visibility with respect to baseline in the case of radio-astronomy), this experiment was relevant in the perspective of a demonstration on astronomical radio-antennas, in particular regarding the very similar experimental set-up in these two experiments. A demonstration with two astronomical antennas would represent a logical follow-up of these experiments. Furthermore, the potential of the correlation of monopole antennas for applications outside astronomy (radar, localisation of RF transmitters) justified by itself such a demonstration.

First, we characterize the precision of the photonic correlator on time delay measurements by applying two replicas of a well-known noise signals generated with AWGs. We then present the results on the localization of real antennas.

Time delay measurements

Before describing the antenna set-up, we characterize the typical measurement precision of the photonic correlator by applying two replicas of known noise signals with 120 MHz bandwidth generated by the AWGs and applied on the AMs. In addition, the AWGs enable to apply a digital delay between each RF channels at the ns-scale, which allows to compare the delay scale of the photonic correlator to an exact reference. A linear time delay was applied between each channel, which shows that the delay retrieved from the photonic correlator agrees very well with the input numerical delay, as shown on Fig 7.13.

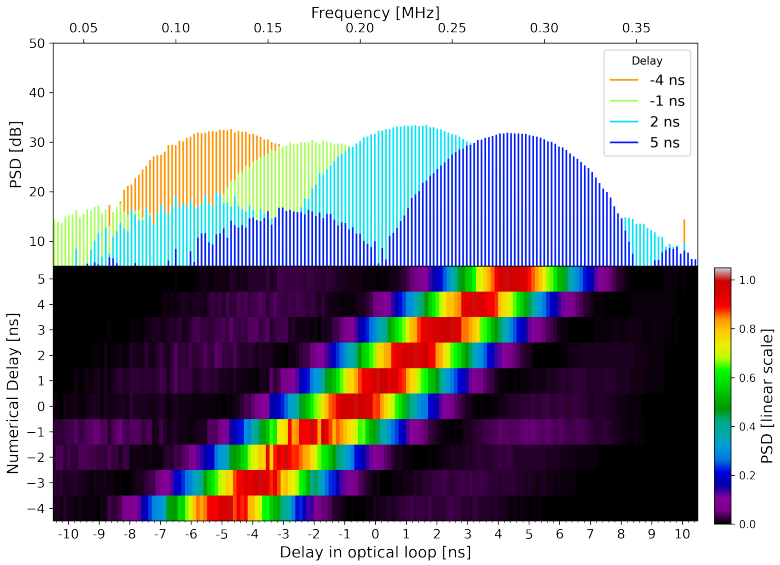

Fig. 7.13: Autocorrelation of 120 MHz noise signals : a relative digital delay is applied between each channel, which can be compared to the delay measured by the photonic correlator.

We then characterize the exact precision of the time delay estimation. The measurement of the time delay is done by estimating the centroid of the main lobe of the correlation function. More generally in TDoA, the typical measurement precision is set by the width of this correlation function, which is itself inversely proportional to the bandwidth of the signal and can be very narrow by using high bandwidth signals. In the following demonstration, given that the time resolution of the correlator (115 ps) is larger than the typical temporal resolution of the incident signal ($1/120\,\mathrm{MHz} \approx 9\,\mathrm{ns}$, the main lobe of the cross-correlation is sampled by approximately $\sim 100\,\mathrm{pts}$. This enables to enhance the precision on time delay below the typical width of the correlation function, by estimating the centroid position through a fit of the main lobe. In that respect, the precision on the estimation of the time delay also depends on the SNR of the correlation function, and thus on the integration time. This precision was measured by acquiring a long acquisition (1s), which was then divided

in individual sequences of a certain fixed duration, on which an estimate of the time delay is done by a fit of the envelope. The standard deviation of these individual estimates then provides the measurement precision for this typical integration duration. Experimentally, it was verified that the precision exhibits a precision inversely proportional to the square-root of the integration time, with a typical 100 ps for 1 ms integration time, and 10 ps for 100 ms integration. These values are significantly smaller than the width of the main lobe of the correlation function (<8 ns). In addition, this precision can be converted in terms of distance measurement, typically equal to 3mm with a 120 MHz signal (for 100ms integration time), which is about $\lambda/1000$ of the central RF carrier.

Correlation of antennas

The set-up, shown in Fig 7.14, consists in three identical monopole antennas : one transmitter (Tx) and two receivers (Rx), the latter being placed about 1 meter from Tx. A broad RF noise signal is applied to the transmitter, and generated by the multiplication of a relatively low frequency noise signal (<100 MHz) through RF multipliers, then filtered with low- and high-pass filters. These noise signals are detected by the Rxs, amplified, and applied on the AMs. The photonic correlator finally processed the cross-correlation function, whose centroid enables to retrieve the time delay difference of arrival of the signal at each antenna. In particular, the position of antenna Rx2 can be moved by approximately $\pm 10\mathrm{cm}$. As expected, the mean position of the centroid of the correlation function shifts, as shown clearly in Fig 7.14, and matches the geometrical delay between the antennas.

7.4 Extension and perspectives

7.4.1 Phase of the correlation function, interferometric observations at high-spectral resolution

In the previous experimental sections, we essentially focused on the the modulus of the correlation comb. As shown in the theoretical description Sec 7.2.2, the phase under each teeth also encodes the phase information of the correlation function.

In the case $f_1\tau_= f_2\tau_1$, the phase of the comb also contains the information on the phase of the correlation function, which contains information on the astrophysical object in the case of heterodyne interferometry (phase of the visibility). Since the amplitude modulation scheme used so far for the analog photonic correlator is identical to the Chap 6, but extended to a larger number of delays $\langle s_1(t)s_2(t+\Delta\tau)\rangle$, the expression of the correlation function is that of a double-sideband correlator and can be written :

$$\langle s_1(t)s_2(t+\Delta\tau)\rangle = |G(\Delta\tau)|\cos(\omega_c\Delta\tau(t)+\phi_G)\times\cos(2\pi f_k t+\phi_V)$$

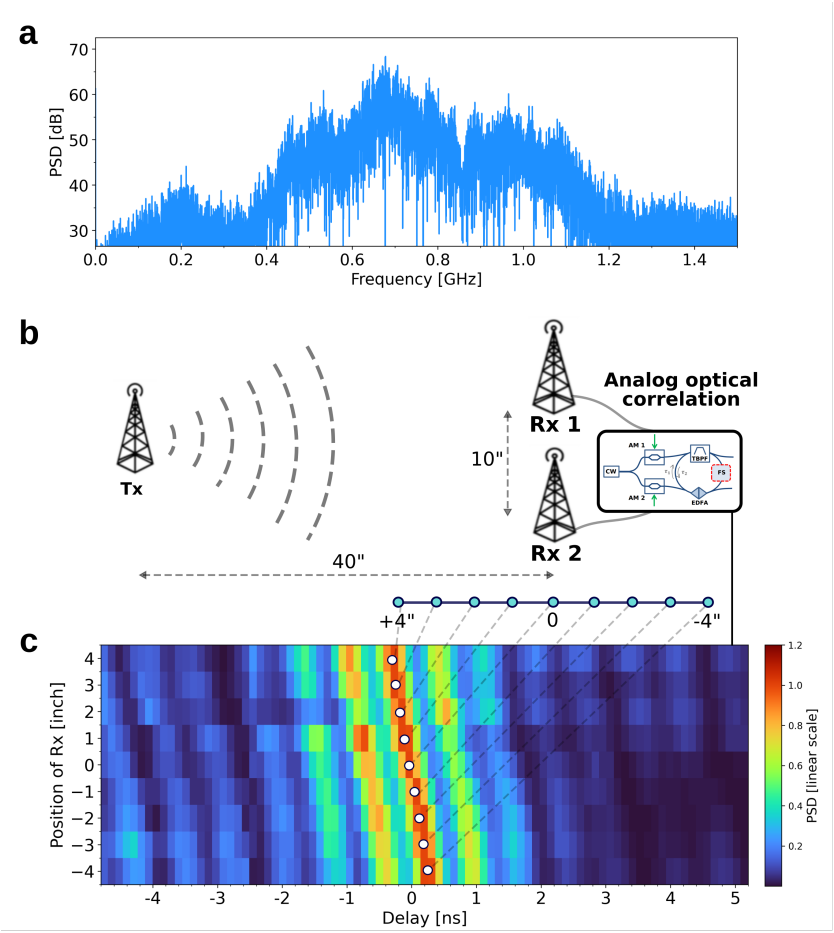

Fig. 7.14: a) Spectrum of the signal emitted by the Tx antenna. b) Experimental set-up used to correlate two monopole antennas. c) Plot of the cross-correlation traces with respect to their position (100ms acquisition time).

The correlator is measuring the real part of Eq (7.9). Combining these two equations :

$$\begin{aligned}\langle s_1(t)s_2(t+\Delta\tau)\rangle &= |G(\Delta\tau)|\cos\Big(\omega_c\Delta\tau(t)+\phi_G\Big)\\ &\quad\times\cos\Big(2\pi f_k t+\phi_V\Big)\\ &\quad\times\cos\Big(2\pi(n\Delta f)t+\phi(n^2)\Big)\\ &= |G(\Delta\tau)|\cos\Big(\omega_c\Delta\tau(t)+\phi_G\Big)\\ &\quad\frac{1}{2}\Big[\cos\Big(2\pi(n\Delta f-f_k)t+\underbrace{(\phi(n^2)-\phi_V)}_{\phi_1}\Big)+\cos\Big(2\pi(n\Delta f+f_k)t+\underbrace{(\phi(n^2)+\phi_V)}_{\phi_2}\Big)\Big]\end{aligned} \tag{7.13}$$

where the notation are identical to Sec 7.2.2 and Chap 6. By subtracting the phase ϕ_1 and ϕ_2 under each peak :

$$\phi_V = \frac{1}{2}(\phi_2-\phi_1) \tag{7.14}$$

In an analogous way to the basic amplitude modulation scheme in Chap 6, it is possible to avoid the calibration of the quadratic phase of the comb in order to retrieve the astrophysical phase associated to each correlation peak.

The simultaneous measurement of the amplitude and the phase at each delay of the correlation function would enable to reconstruct the complete spectro-visibility, as indicated in the introduction of this chapter, in Eq 7.2. This could enable to obtain both a spectrum of the source within the bandwidth of the detector (modulus $|V(\omega)|$), and the interferometric phase, which is related to the position of the emission photocenter at a given spectral channels. As the number of reconstructed points is equal to the number of teeth i.e. $N \approx 200$ spectral channels, this sets the spectral resolution of the correlator within the detection bandwidth of the mid-infrared detector (e.g. for a 40 GHz detector, $\Delta f = 40\,\mathrm{GHz}/200 = 200\,\mathrm{MHz}$, which is equivalent to $R = f/\Delta f = 150\,000$).

This feature has important observational consequences, for example in the study of astrophysical emission or absorption lines. In particular, the measurement of the differential phase between the line and the continuum enables to measure the relative location of the emission or absorption lines with respect to the object photo-center (continuum). With a sufficient number of baselines, this enables to retrieve the information on the spatial location of these lines (e.g. location of chemical species in the astrophysical objects), and also to constrain their dynamics (doppler shift), both informations are of high astrophysical interest.

7.4.2 Application to infrared heterodyne interferometry

Demonstration with 2 radio-antennas

In Sec 7.3.10, we demonstrated the correlation of wide noise RF signals with 2 separated antennas. The natural extension of this preliminary experiment would be to apply two signals originating from radio-astronomical parabolas on the analog photonic correlator, in order to retrieve the correlation function of a bright astronomical objects. This measurement gives access to the coherent flux associated to this object, and potentially to the visibility if an appropriate calibration is used. This calibration would greatly benefit to be done through the same photonic processing chain as the coherent flux. Such calibration can take advantage of the of the fact by applying the same signal to each AMs the correlator computes naturally the auto-correlation function.

The coupling of the analog correlator would be the next natural step in the perspective of a demonstration in an interferometric mode. The interest in measuring a correlation function with radio-parabolas would be the demonstration of the functioning principle of the correlator in the radio regime, with simpler on-sky constraints than in the infrared domain (delay lines, coherencing, target tracking, etc.), and better understanding of its calibration and sensitivity limits. This demonstration would provide a valuable experience of practical, on-sky constraints of an interferometric system, in the perspective of preliminary on-sky demonstrations with an infrared heterodyne interferometer. Such a radio-interferometer

was in fact developed independently at IPAG by Bernard Lazareff and Jean-Philippe Berger. Unfortunately, this system could not yet have been coupled to the correlator at the time of writing. The system consists in two commercial parabolas observing at a frequency of 9 GHz, and includes the heterodyne detection and amplification chain, enabling to produce an output RF power with $\sim 10\,\mathrm{dBm}$, compatible with the analog correlator.

Sensitivity

In parallel to a demonstration on a two elements radio-interferometer, the fundamental step towards the application of the correlator to infrared heterodyne interferometry consists in detailing the sensitivity analysis of the correlator, in particular taking into account the improvements on ASE mentioned in Sec 7.3.3. The sensitivity limit for a noise signals was estimated to be typically 5 dBm in Sec 7.3, and was later optimized to reach about -15 dBm. This limit can likely be reduced with a better noise factor of the amplifier, a reduction of passive losses in the loop, and a reflexion on the trade-off between the number of teeth and the maximum sensitivity. The fundamental parameter to be estimated in this perspective is the SNR preservation through the correlator, or equivalently an estimation of the noise temperature of the correlator. At this point, as already pointed out in Chap 4, the specification of the noise temperature of the correlator can benefit from the natural large noise temperature of the heterodyne detection. The fact that the correlator is preceded by different stages of amplification reduces significantly the weighting of the correlator noise temperature in the final budget (Friis formula) :

$$T_{\mathrm{ampl}} = T_1 + \frac{T_2}{G_1} + \frac{T_3}{G_1 G_2} + \ldots$$

with T_1, T_2, T_3 the noise temperature and G_1, G_2 the gain of the successive amplification stages. In this chain, the strongest noise requirements is put on the first amplifier (pre-amplifier) just after the detection (often a trans-impendance), which has to have a low noise compared to the noise temperature of heterodyne detection. The exact budget of the chain is at the heart of the sensitivity analysis of the detection chain. We will detail part of this budget in Chap 8 when introducing the 2 telescopes demonstrators at $10\,\mu\mathrm{m}$.

Scale-up to a large number of telescopes and multiple spectral channels : prospective ideas

The last step towards the application of the correlator to an infrared heterodyne array is the scale-up of the concept of analog correlation to a large number of telescopes and a large number of spectral channels. In this paragraph, we propose some prospects in this direction, based on the frequency multiplexing scheme proposed in the case of the simple two elements photonic correlator in Chap 6.

The basic idea is identical to the all-in-one combination proposed in amplitude modulation in Chap 6. We assume that each channel identified by the index k (with N_t telescopes times N_s spectral channels) is encoded on an independent AM and modulated at a frequency f_k by an AOM. Prior to the correlator, we suppose that all the channels are summed together (so called "all-in-one"). The resulting signal is then splitted in two arms wich are injected in the bi-directional loop. In this case, the resulting signal will have a form very similar to Eq.7.13 :

$$\langle s_1(t)s_2(t+\Delta\tau)\rangle = |G(\Delta\tau)| \sum_{k,l}^{N_t,N_s} \Big[\cos\Big(2\pi(n\Delta f - (f_k - f_l))t + (\phi(n^2) - \phi_V)\Big) + \cos\Big(2\pi(n\Delta f + (f_k - f_l))t + (\phi(n^2) + \phi_V)\Big)\Big] \tag{7.15}$$

The factor $\frac{1}{2}$ disappeared here because the operation is essentially an auto-correlation. We also supposed that $|G(\Delta\tau)| = |G(-\Delta\tau)|$ and that the $\cos\Big(\omega_c\Delta\tau(t) + \phi_G\Big)$ is removed by a control of the delay and is equal to 1, so that the two replicas of the correlation product are summed on the same tooth at frequency $n\Delta f + (f_k - f_l)$. In the case where the AOMs encode the fringes in a non-redundant pattern, the cross-correlation will appear as sets of non-redundant side-bands on both sides of the teeth $n\Delta f$. The auto-correlation will sum together on the teeth at $n\Delta f$ and will not be exploitable.

The total number of peaks will be limited by the number of non-redundant peaks that can be enclosed in a frequency span of $\Delta f/2$ (separation of two teeth of the comb). The minimum spacing between two peaks is ultimately set by the total integration time i.e. generally the coherence time of atmosphere or the maximum integration allowed by the fringe tracker, and can be assumed to be typically of the order of 1 Hz. In addition, the ratio N_{nr} between the shortest and the largest spacing in a non-redundant pattern is rapidly diverging : it reaches about 500 for 20 channels to encode in a non-redundant pattern, and about 1500 for 30 channels (Ribak et al., 1988). This translates in a total spacing of $1.5\,\mathrm{kHz}$, which is one order of magnitude below the teeth separation used in Sec 7.3.9 for example. The teeth spacing can also be set to a larger value by adjusting the frequency of the AOM, which could enable to increase significantly the number of elements that can be encoded in the comb. On the other hand, the total number of elements to correlate non-redundantly is typically $N_s \times N_t = 20 \times 100 = 2000$, which will largely exceed the maximum number of correlation peaks that could be encoded in the comb. In addition, the multiplication of the number of peaks in the comb will consume part of the gain of the amplifier, and may likely affect the gain, the saturation, and finally the SNR of the final comb, an effect which is not trivial to quantify. Overall, this scheme could potentially enables a massive multiplexing of information (high number of telescopes and spectral channels), even if this multiplexing may be limited to a number of a few tens of elements, a number that would also need a careful examination regarding the impact on the amplifier and the sensitivity of the analog correlator. Presumably, an hybrid solution, in which the correlator is replicated several times to cover several spectral sub-windows and to process only a part of the total number modulators, may be used.

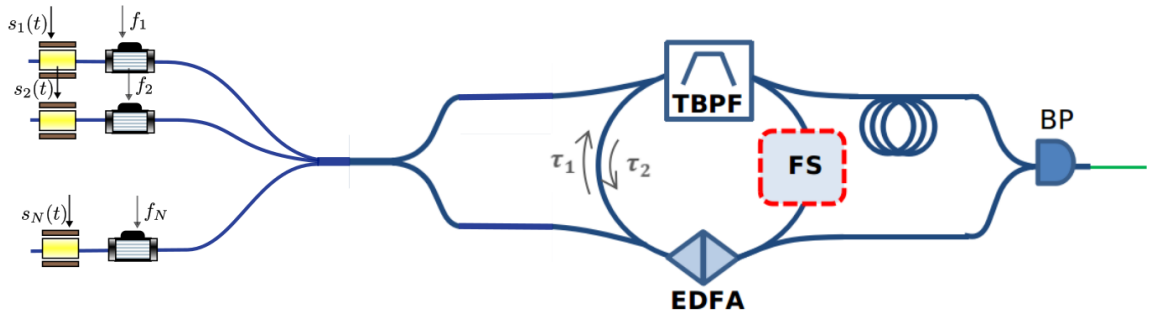

Fig. 7.15: Schematic diagram of the scale-up of the analog correlator to a large number of channels. In an analogous way to the simple amplitude photonic correlator, the basic idea consists in encoding each pair of correlation signal in a non-redundant frequency pattern at the output of the correlator.

7.4.3 Other applications

The wideband correlation of RF signals has a broad range of applications outside of astronomy, in particular in the estimation of time delays. The first type of this kind of applications is related to the passive positioning of RF transmitters based on the measurement of time difference of arrival between known antennas (Rx). By knowing the precise location of the receivers and measuring the time difference of arrival, it is possible to deduce the location of an unknown RF emitter. These passive systems are at the basis of a large number of applications, such as the location of victims in natural disasters (avalanches,...), location of RF jammer which perturbs communication, or military applications (location of an unknown RF transmitter). In the case of noise signal, the precision with which the time delay difference can be measured is related to the inverse of the emitters RF bandwidth, and can even be increased by an estimation of the correlation envelope (see Sec 7.3.10, with $\lambda/1000$ at $\sim 1\,\mathrm{GHz}$), potentially enabling the localization with mm precision for radio-wavelengths. Interestingly, the location of multiple emitters with multiple antennas with the analog optical correlator may share common processing strategies with interferometric image reconstruction : such study go beyond the present preliminary work but could offer interesting development perspectives. The second type of application related to time delay measurement is the measurement of time of flight of signals, between a given emitter (Tx) and a known or unknown target - these systems are thus active systems. By correlating the probe RF signals to the retro-reflected signals (an operation equivalent to matched filtering), the time delay that maximized the correlation signals gives an estimate of target distance. This correlation operation can be applied either to RF waveforms, or directly to the modulated optical signals at $1.55\,\mu\mathrm{m}$ (Billault et al., 2021), the first category being related to radar and sonar applications, the second one to lidar applications.

7.5 *Paper : Wideband multi-delay analog photonic correlator for RF signal processing (submitted)*

Part IV

Technological pathfinders

> *Seeing is in some respect an art, which must be learnt. To make a person see with such a power is nearly the same as if I were asked to make him play one of the Handel's fugues upon the organ.*

— W.Herschel
Letter to Sir W.Watson (7th January 1782)

8 Demonstrator for a 2T interferometer at 10µm

We have presented so far the system, the sensitivity and the correlation aspects associated to a mid-infrared heterodyne interferometer combining a large number of telescopes. This has enabled us to revisit the architecture of a potential heterodyne instrument at $10\,\mu\mathrm{m}$, based on the current state of mid-infrared technologies. In order to validate this architecture and the technologies associated with it, we describe in this chapter the preliminary design and implementation of a heterodyne bench which combines two interferometric channels at $10\,\mu\mathrm{m}$.

8.0.1 Goal & specifications

The general goal is to provide a technological demonstrator in the laboratory, which combines two heterodyne channels at $10\,\mu\mathrm{m}$, and enables to test the building blocks devised in the perspective of a PFI. The different essential elements that we aim to demonstrate in this demonstrator are :

- testing and validation of the **detector technology** (QCD and off-the-shelf VIGO[1] detectors)
- validation of the **correlator architecture** : amplitude photonic correlator, and numerical correlation for relatively small bandwidth (<1 GHz).
- validation of the **sensitivity analysis** : measurement and budget of the complete detection and correlation chain at $10\,\mu\mathrm{m}$, first on QCL source, then on a black-body source.
- validation of the **local oscillator** and **phase-locking scheme**
- validation of the **alignment protocol** of the bench, and **mode-matching** of the LO with the signal.
- validation of **operational strategies** in the perspective of on-sky observations : chopping strategy, piston mitigation.

[1] In the following, we refer as 'VIGO detectors' the detectors manufactured by the VIGO company. These detectors are the rare off-the-shelf high-bandwidth (up to 1GHz in our case) detectors commercially available in the mid-infrared (e.g. $10\,\mu\mathrm{m}$). See : https://vigo.com.pl/en/home/

At the end, an essential part of this demonstration is the validation of the sensitivity of the interferometric signal on a black-body. Following this validation in the laboratory, this experiment could provide the elements of a potential on-sky demonstrator that could be adapted to existing telescopes.

8.0.2 Description of the bench

General description

The general idea is to distribute two local oscillators on two detectors, where they are mixed with the signal channel. For practical reason, the initial version of H2T10 is based on a single laser splitted in two parts, which allows to obtain a local oscillator channel on each channel with only one laser[2]. In a second version, a complete version including two lasers and a phase-lock loop (PLL), in order to stabilize the relative phase of each QCL, is planned. The different phase of integration of the bench are :

- **Step 1** : a single QCL is splitted in two parts, which act as two local-oscillators with stable relative phase at the level of each detector. Off-the-shelf detector (VIGO) with 1 GHz bandwidth are used. At the time of writing, this version is currently aligned, and its characterisation is on-going, see Sec 8.2.

- **Step 2** : two QCLs act as two distinct local oscillator whose relative phase is stabilized by a PLL. Off-the-shelf VIGO detectors are still used.

- **Step 3** : two QCLs and two QCDs. This requires the specific development of QCDs, which could allow for major sensitivity increase of the bench compared to VIGO detectors.

The final optical set-up including two QCLs (Step 2 and Step 3) is represented in Fig 8.1. At each step, the source signal mixed on each detector can be either a laser source (QCL in our case), or a black-body, depending on the minimum sensitivity of the bench. In the following, these combinations will be designated respectively as QCL+QCL beating (QCL source) or QCL+black-body beating (black-body source).

Components

The different elements chosen for the bench are given in Tab 8.1. In the following, we detail briefly the functional aspects of these elements :

[2]The relative phase stability between the local oscillator is ensured by the fact that the coherence of the laser is relatively large. The exact linewidth of the QCL is not yet characterized, but the typical value reported in comparable set-up is of the order of a few MHz, which corresponds to a coherence length of $c/\Delta\nu = c/1\,\mathrm{MHz} \approx 300\,\mathrm{m}$, larger than the typical relative path difference between each LO.

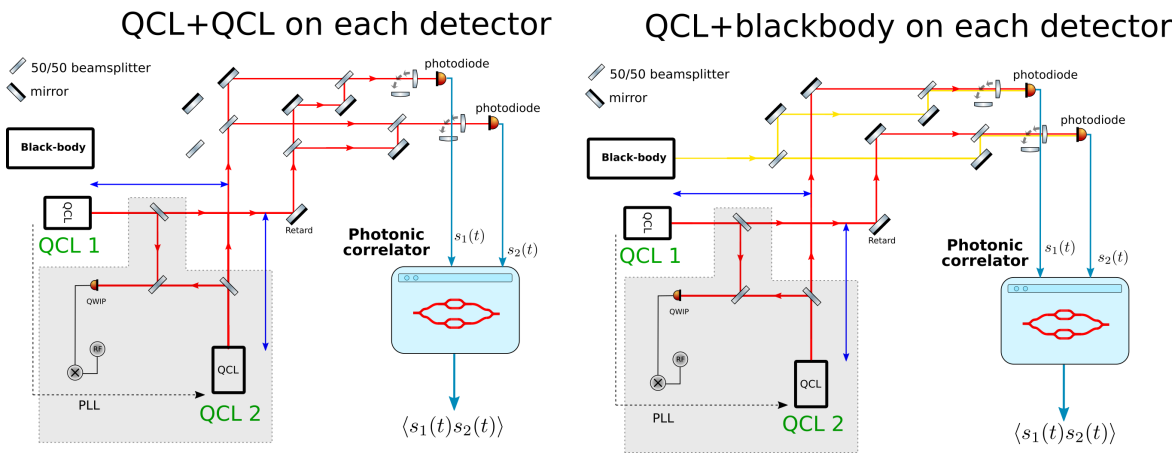

Fig. 8.1: Optical layout of H2T10 alignment *Left:* QCL+QCL beating *Right:* QCL+black body beating. *Gray area :* In the first implementation, only one QCL we be used as the same local oscillator for each detection channel. The final goal will be to phase-locked two QCLs together in order to obtain two separated local-oscillators. Schematic adapted from G. Bruel.

- *local oscillator :* we chose QCLs for their practical aspects, in particular their tunable power and their tunable wavelength over a small range ($5\,\mathrm{cm}^{-1}$).[3]

- *detectors :* the two requirements at the level of the detector for a heterodyne detection system are a high-bandwidth and a high quantum efficiency. We chose VIGO detectors, which reach relatively high-bandwidth (1 GHz) and exploitable quantum efficiency (0.08), and require only Pelletier cooling. Alternatively, MCT detectors with liquid nitrogen cooling can be used.

- *correlation :* we chose the 2T amplitude modulation scheme for the photonic correlator, whose performances were demonstrated in Chap 6, for its very simple implementation which does not require specific phase stabilization for relatively short integration time (<1s). Longer coherent integration will require the implementation of a slow phase stabilization loop in order to stabilize the relative phase of each arm of the Mack-Zehnder, still much less demanding than in the phase modulation scheme. Alternatively, the correlation of the signals can be performed numerically for relatively small bandwidth <1 GHz and small integration time (<10s), using a rapid numerical oscilloscope.

- *signal source :* the initial demonstration is based on a QCL+QCL heterodyne beating on each detector in order to set-up the detection, amplification and correlation chain. This QCL+QCL beating is obtained by splitting and combining the LO, as shown in Fig 8.1. Once this step is validated, a stabilized black-body source reaching temperature up to 900 K is installed on the bench.

[3] We remark that the tunability range of a QCL can be very significantly by coupling the QCL with an external Fabry-Pérot cavity. This was already demonstrated in the case of astronomical heterodyne, in the infrared spectrometer THIS at $10\,\mathrm{m}$ (Stupar et al., 2008), enabling the coverage the full N-band in a scanning mode.

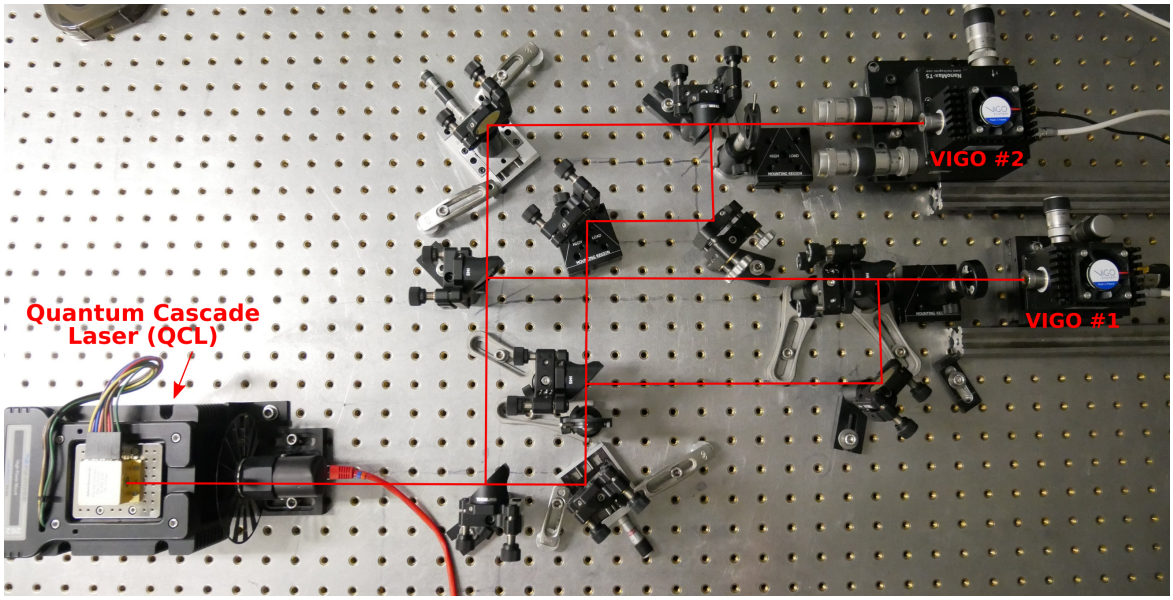

Fig. 8.2: Current implementation of the optical set-up of H2T10 at $10\,\mu\mathrm{m}$, with one QCL and two detection channels. See description in Sec 8.2.

Stage	Item	Ref.	Characteristics
$10\,\mu\mathrm{m}$	QCL	AdTech HHL-15-40	$\lambda = 10.59\,\mu\mathrm{m}$ $P_{\max} \approx 40\,\mathrm{mW}$ tunability $\approx 5\,\mathrm{cm}^{-1}$
	Detectors	Vigo PVI-4TE	BW = 1 GHz QE=0.08
	Black-body	RCN900	T=900K
Photonic correlator	Laser	NKT Koheras E15	power 40 mW linewidth $< 100\,\mathrm{Hz}$ RIN=135 dB
	Intensity modulator	MXAN-LN 10	BW = 10 GHz
	AOM	AA-Opto MT80	$f_s = 80 \pm 5\,\mathrm{MHz}$
	Balanced detector	PDB-450C	$R_{PD} = 1\,\mathrm{A/W}$ 20 dB common mode rejection
	Oscilloscope	Tektronix MSO64B-6-BW-1000	1 GHz analog bandwidth

Tab. 8.1: Characteristics of the main optical components of the bench.

8.1 Sensitivity of the preliminary detection chain

We evaluate the theoretical sensitivity of the demonstrator on a black-body, based on the description in Sec 8.0.2. We recall the sensitivity budget of the heterodyne detection stage,

based on (Kingston, 1978), including the amplification stages. This will also enable us to take into account the impact of the correlation stage, which will be included in the chain as an amplification stage. Finally, we give the typical number expected for the measurement with a black-body source.

A critical component in the sensitivity budget is the detector, regarding its properties in bandwidth, quantum efficiency and noise. In the following, we emphasize the first version of H2T10 based on VIGO detectors (Step 1 and Step 2) will be substantially limited in sensitivity compared to a final version including state-of-the-art QCD detectors[4] (Step 3). In addition, we emphasize that the present noise analysis has not yet been confronted to experimental results : it has thus to be seen as a preliminary noise budget calculation, but has to be considered with caution.

Amplifier noise in heterodyne detection [Kingston 1978]

We base this analysis on the treatment of a heterodyne detection given in (Kingston, 1978). Using the same notation as (Kingston, 1978), the signal to noise of a heterodyne detection is :

$$\frac{S}{N} = \frac{\overline{i_{if}^2}}{i_{\mathrm{SN}}^2 + 4kT_A B/R} \quad ; \quad \begin{cases} \overline{i_{if}^2} = & 2i_{\mathrm{LO}} i_s \\ i_{\mathrm{SN}}^2 = & 2ei_{LO}B \end{cases} \tag{8.1}$$

with i_{LO} the photocurrent of the LO, i_s the photocurrent of the signal, B the detection bandwidth, R the load resistance of the system, e the electric charge, k the Boltzmann constant. Based on (Kingston, 1978), T_A the noise temperature of the amplification chain is defined as :

$$T_A = T_R + (F-1)T_{290\mathrm{K}} \tag{8.2}$$

with T_R the load temperature of the detector and F the noise factor associated to the amplification chain, in which we will also include the contribution of the photonic correlator. In fact, different noises can be added by the detector in addition to Johnson noise, which we will include in T_R in the following.

We will also express the shot noise as a noise temperature $T_{\mathrm{SN}} = \frac{ei_{\mathrm{LO}}R}{2k}$, so that the signal to noise ratio can be written :

$$\frac{S}{N} = \frac{\eta P_\nu}{(1 + T_A/T_{\mathrm{SN}})} \tag{8.3}$$

In this way, the goal is to give an estimate T_A, which implies to also to give an estimate of F. We will first describe the noise associated to the detection stage, and then the amplification stage including the photonic correlator.

[4] As an order of magnitude, compared to a detector with 25 GHz and QE=0.4, the point source sensitivity of our current instrument is smaller by a factor $\frac{0.4}{0.085} \times \left(\frac{25\,\mathrm{GHz}}{1\,\mathrm{GHz}}\right)^{1/2} \approx 23.5$. For a given SNR and integration time, this corresponds to a telescope diameter 4.85 smaller, or a coherent integration time 550 times larger.

Amplification chain

The noise associated to the amplification stage will be set by the Friis formula, which can also be written in terms of noise temperature :

$$\begin{cases} F = F_1 + \frac{F_2 - 1}{G_1} + \frac{F_3 - 1}{G_1 G_2} + ... \\ T = T_1 + \frac{T_2}{G_1} + \frac{T_3}{G_1 G_2} + ... \end{cases} \tag{8.4}$$

The amplifier contributing the most to the noise of the amplification chain is thus the first amplifier (the pre-amplifier). The most constraining requirements on the noise is thus on the detector and the first amplifier (T_1 and G_1). As mentioned in Chap 7, even in the case of very noisy amplifiers downstream in the amplification chain, their contribution can be relatively small or even negligible if the cumulated gain is sufficiently large before this amplifier. This is particularly true in the case of the photonic correlator, which is generally equivalent to an amplifier with low gain and large noise factor, as we show in the next paragraph.

Photonic correlator

The photonic correlator can be modeled as an amplification stage : in order to give an estimation of the gain and noise contribution of the photonic correlator, we will follow the general description of Marpaung et al., 2012 of microwave photonics link. We will write the equivalent gain of the photonic correlator (Marpaung et al., 2012) :

$$G_{PC} = \left(\frac{\pi \mathrm{R}_{PD} R_L P_0 \sin \phi_b}{4 L_{MZ} V_\pi} \right)^2 \tag{8.5}$$

with R_{PD} the responsivity of the photodiode of the correlator, R_L the load resistance,P_0 the optical power of the laser, ϕ_b of the MZM (in the case of an amplitude modulation scheme, we will set $\sin \phi_b = 1$), L_{MZ} the insertion loss of the modulator, and V_π the characteristic voltage of the modulator.

The noise power p_N introduced by the photonic correlator is (Marpaung et al., 2012):

$$p_N = (1 + G_{PC}) p_{th} + \frac{1}{4} p_{\text{shot}} + \frac{1}{4} p_{\text{rin}} \tag{8.6}$$

with p_{th} the thermal noise power, p_{shot} the shot noise power, and p_{rin} the Relative Intensity Noise (RIN) of the laser. In our case, the RIN contribution will be diminished by 25 dB typically by the use of a balanced detectors at the output of the correlator.

The final noise figure of the photonic correlator will be taken equal to :

$$NF = 10 \log_{10} \left(\frac{p_N}{G_{PC} k T B} \right) \tag{8.7}$$

Stage	Item	Symbol	Unit	Value
Detection				
	Shot noise temperature	T_{SN}	K	355
	Amplifier gain	G_1	dB	44
	Detector & pre-amplifier noise	T_R	K	337*
Amplifier				
	Gain	G_2	dB	40
	Noise Factor	NF_2	dB	10
	Noise temperature	T_2	K	2610
	Added noise	$+T_2/G_1$	K	< 1
Photonic correlator				
	Gain	G_3	dB	-29
	Noise Factor	NF_3	dB	44
	Noise temperature	T_3	K	7.1×10^6
	Added noise	$+T_3/G_1G_2$	K	< 1
Total noise	Noise temperature	T_A	K	337
	Noise penalty (detection + amplification))	$1 + T_A/T_{\mathrm{SN}}$	no unit.	1.95

Tab. 8.2: Noise budget of the detection and amplification/correlation chain. *This number originates from the specifications of our detectors, but at not yet characterized in the lab. This noise contribution has the strongest impact on the total noise budget.

8.1.1 Noise analysis

Based on the analysis provided in the previous section, we designed and estimated a preliminary noise budget of the chain. The noise budget is given in Tab 8.2, based on the specifications of the component implemented in the bench.

The main results of this analysis is that the components with the largest noise contributions in the chain are the elements close to the detector : in this case, the detector itself and its pre-amplifier. These two components are thus critical to achieve the sensitivity requirements of the heterodyne detection chain. Conversely, the contribution of the photonic correlator, which naturally exhibits a low gain and a large noise factor (cf previous section), is small provided that the total gain between the detector photonic correlator is approximately equal or larger than the noise factor of the correlator (Friis law), which is the case here. This remark is also true for any amplifier after the first pre-amplifier (e.g. the amplifier with relatively large noise factor NF=10 dB). The parameters used to compute the gain and the noise factor of the photonic correlator are also provided in Tab 8.4, the gain and the noise factor of the photonic correlator being consistent with the values derived in the literature (Ridgway, Dohrman, and Conway, 2014).

Finally, the estimated noise penalty of the whole detection and correlation chain is $n_p = 1 + \frac{T_A}{T_{\mathrm{SN}}} = 1.9$, which is dominated by the noise of the detection stage. This noise penalty will then be taken into account in the SNR estimation of the chain. We remark that this value

of noise penalty is relatively consistent with the unaccounted noise penalty reported on ISI (factor $\times 1.5$), which may also originate in part from the detection stage.

We emphasize that this preliminary noise budget of the detection chain is based solely on the specifications of the component : this analysis has now to be characterized and validated in the lab. The final sensitivity will be highly dependent on the actual performances of the detection stage.

8.1.2 SNR estimation

We can finally provide the estimate of the SNR expected in H2T10, taking into the quantum efficiency of the detector, the different optical losses in the bench, and by including the contribution of the noise of the detection, amplification and correlation chain in the form of a noise factor n_p. These parameters are summarized in Tab 8.3.

Using the expression of the SNR of a heterodyne interferometer provided in Chap 4, Eq 4.14, the estimated SNR of H2T10 observing a black-body at 900 K is equal to SNR=15 in t=0.1s integration time. This integration is time is small compared to the typical time of fluctuation of the relative phase between each channel and in the photonic correlator in laboratory conditions. This analysis indicates that the sensitivity of the preliminary implementation of H2T10, based on commercial VIGO detectors, is theoretically compatible with a characterization of the bench on a black-body at 900K. However, this analysis has yet to be confirmed by a characterization of the testbench in the laboratory.

Stage	Item	Unit	Value
Optical transmission			
	BS1	–	0.5
	BS2	–	0.5
	Chopper	–	0.5
	extra losses alignment, mode-matching,...	–	0.7
Blackbody	Temperature	K	900
	flux/polar	W/Hz	9.3×10^{-21}
Detection & correlation	Quantum efficiency	–	0.08
	Bandwidth	GHz	1
	Noise penalty	–	1.9
Sensitivity	integration time	s	0.1
	SNR	–	15

Tab. 8.3: Signal-to-noise estimation of H2T10 on black-body at 900K.

8.2 Preliminary developments

The current implementation of Step 1 of the bench is shown in Fig 8.1. This initial phase has for the moment focused on the alignment of the bench and the characterisation of the

components. Heterodyne QCL+QCL signal are now measured on each channel, and the properties of the detectors (responsivity, saturation, etc.) are currently being characterised. This implementation was developed in part during the internship of Guillaume Bruel (M1 master student, Phelma), under the supervision of Jean-Philippe Berger and myself, who carried out the optimization of the alignment of the bench. The following steps are the implementation of the photonic correlator, in order to measure a correlation signal with QCL+QCL, before moving to QCL+black-body beating.

8.3 Conclusion

The implementation of H2T10 is on-going, with fringes expected on a laser source through a complete heterodyne detection and correlation chain in the short term. The detection of a blackbody radiation and the addition of a second QCL local-oscillators are the following steps of this development. At the end of this phase, this demonstrator could serve as a platform to integrate QCD detectors, in order to test their sensitivty performances in a heterodyne interferometer combination.

This initial laboratory demonstration could enable to demonstrate the essential building blocks of a simple heterodyne system, without spectral multiplexing, but easily scalable to a larger number of telescopes. This system could be potentially adaptable to current infrastructures, where it could recombine the light from multiple existing telescopes. In the next chapter, we investigate the extension of the building blocks developed in H2T10 to the recombination of the 8 telescopes of VLTI, so-called "V8 concept".

8.4 Appendix

8.4.1 Proceedings SF2A: V8 concept and photonic correlation for mid-infrared interferometry (published)

8.4.2 Components of the photonic correlator

Item	Symbol	Unit	Value
Wavelength	λ	μm	1.55
Laser intensity (input modulators)	P_0	mW	20
Laser RIN	RIN	dBc/Hz	-150
Common mode rejection (balanced detection)		dB	25
Modulator half-voltage	V_π	V	5.5
Insertion loss	L_{MZ}	dB	3.5
AOM optical loss		dB	3
Other optical losses		–	0.5
Detector responsivity	R_{PD}	A/W	1
Bias (amplitude modulation scheme)	ϕ_b	–	1

Tab. 8.4: Parameters of the photonic correlator implemented in H2T10.

Elle voit l'étendue du sable couleur d'or et de soufre, immense, pareil à la mer, aux grandes vagues immobiles. Sur cette étendue de sable, il n'y a personne, pas un arbre, pas une herbe, rien que les ombres des dunes qui s'allongent, qui se touchent, qui font des lacs au crépuscule. [...]
La lumière rutile et ruisselle de toutes parts, la lumière qui naît de tous les côtés à la fois, la lumière de la terre, du ciel et du soleil.
Dans le ciel il n'y a pas de fin.

— J.M.G Le Clézio
Désert

9 V8 concept : a 8 telescopes mid-infrared heterodyne instrument for the VLTI

9.1 Introduction

The advantage of heterodyne interferometry in the perspective of a PFI is the scalability of this scheme to the recombination of a large number of telescopes. This advantage is made tangible in H2T10, where scaling the concept to N telescopes would basically require the replication of the detection and the adaptation of the correlation scheme (if not digital).

In this chapter, we propose to explore the concept of a pathfinder heterodyne instrument combining the 8 VLTI telescopes in the N band (Jean-Philippe Berger, Bourdarot, and Guillet de Chatellus, 2020), so-called "V8" concept. We propose to take benefit of the incomparable mapping capability reached the simultaneous combination of 4 UTs and 4 ATs, in order to perform dense imaging on bright sources, with the possibility to couple it with high-spectral resolution. After a brief overview of the concept, we provide a preliminary sensitivity analysis of the concept, depending on the different step of technological development that could be reached, and simulate the typical interferometric observations integrating this noise analysis. Finally, in the perspective of PFI, we explore the implication of the V8 concept with fringe-tracking to the image reconstruction of the complex mid-infrared environment of bright young stars, with AU scale resolution (in the Taurus) and low surface brightness (150 K - 200 K).

Fig. 9.1: Overview of the VLT on Cerro Paranal, with the 4 UTs (8.2m diameter) and 4 ATs (1.8m diameter), and the VLTI infrastructure.

9.2 The V8 concept

9.2.1 Instrument concept

The schematic principle of V8 is shown in Fig 9.8. The combiner is placed at the VLTI laboratory, where the 8 beams would have to be brought back. In the instrument, the astronomical signals are mixed with a mid-infrared local oscillator, which consists in a single laser distributed on each channel, onto 8 high-bandwidth unipolar detectors. The wideband RF signals are then correlated in a wideband correlator, either based on photonic correlation or digital based, in which is performed the delay compensation and the extraction of the object visibility. A brief detail on these different subsystems, based on the renewed architecture and technology presented previously, is given below (paragraph "Subsystems and VLTI infrastructure").

The basic concept of V8 can be thought as the direct extension of H2T10 to a larger number of channels, based on the scalability of the heterodyne detection scheme, and adaptable on existing infrastructure. By circumventing the need of an optical delay line, this concept could relax the requirements on a hard infrastructure, and potentially enable full-sky coverage operation. By benefiting from a larger number of baselines (16 AT-UT combination, 6 UT-UT and 6 AT-AT) and of a boost of sensitivity due to UT collecting area in particular on AT-UT combination, the combiner could potentially benefit both from a better mapping capability (uv-coverage) and a potential global sensitivity in the image reconstruction : these two aspects will translate in a increase of surface brightness temperature sensitivity, discussed for example in Sec 9.4.

9.2.2 Subsystems and VLTI infrastructure

The different subsystems are based on the different technology identified throughout this work :

- *local oscillator :* the local oscillator could be based on a single QCL splitted in 8 channels, which requires in the bench that the relative phase of the different channels are stable in time. Given the losses due to splitting in 8 channels, multiple QCLs locked with a PLL could be used, in the same way to 8, in order to increase the available LO power on the different channel.

- *detector :* unipolar (likely QCD) are envisioned, with typical requirements of 25 GHz bandwidth and 0.4 quantum efficiency, in order to increase the sensitivity and/or to cover a larger frequency coverage in the case of high spectral resolution observation.

- *correlator :* the signal processing could be based either on analog or digital correlators. Analog correlator are preferred in the case of wideband continuum observation (cf Chap 6). In the case of observations at high-spectral resolution, digital correlation is

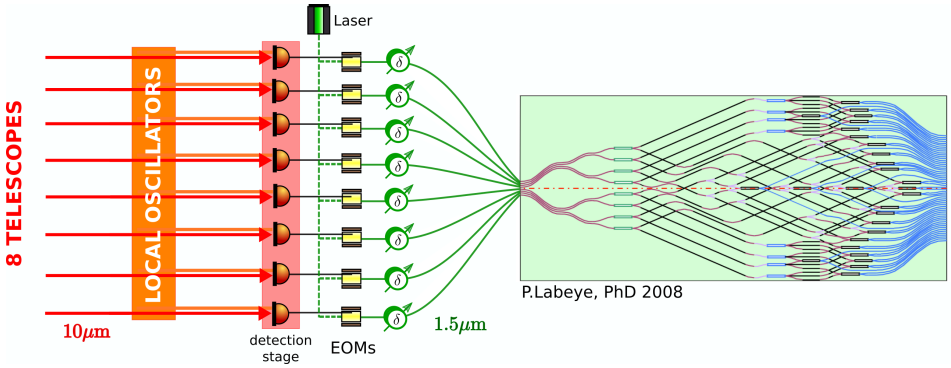

Fig. 9.2: General schematic of V8 concept.

potentially an interesting option, though more demanding in terms of computation power and sampling capability.

On the VLTI side, the V8 concept supposes a good knowledge of the propagation of the polarization in the VLTI beam train, as the signal is projected on the polarization of the LO (linear polarization) in the heterodyne mixing. The second point on the VLTI infrastructure is the addition of mirrors in order to guide the light of all the eight telescopes, and an adaptation of VLTI software in order to handle the operation of the eight telescopes simultaneously.

9.2.3 Possible development phase

The concept presented so far represents the baseline implementation of V8. In this form, it suffers from strong sensitivity limitations due to the absence of a fringe-tracker (incoherent integration) and to the location at the VLTI lab (40% transmission of the VLTI beam train), and still require the propagation of the beams in the VLTI infrastructure. Different development phase could be envisioned in order to overcome these limitations, and to exploit the full potential of the instrument. The impact of this upgrade on the sensitivity will be detailed in Sec 9.3 and Sec 9.5. This development can be decomposed in three possible phases, to which we will refer in the following :

- **V8 incoherent :** baseline implementation of V8 at VLTI lab, including only the heterodyne detection unit. The atmospheric phase fluctuations are not compensated, and the instrument performs incoherent integration.

- **V8 coherent :** the heterodyne combiner is coupled to a near-infrared fringe-tracker, which compensates for the atmospheric phase fluctuations and enables coherent integration. This upgrade potentially enables a massive increase of the sensitivity of the combiner, which will be evaluated in Sec 9.4. This requires the stabilization of the array with a 8 beam fringe-tracker, preferably implemented with fibred technology in order to relax the requirements on the VLTI infrastructure. As already discussed in Chap 4, this technological challenge has still to be solved at the time being.

- **V8+ :** In this final version, which shares strong similarities with the long-term implementation targeted in PFI (spectral multiplexing excepted), the heterodyne detection modules are placed at the level of each telescopes directly, which enables both a sensitivity increase ($\times 2.5$ transmission losses of VLTI beam train) and a lower requirement on VLTI infrastructure (no propagation in the tunnels). This supposes a phase synchronization mechanism of the mid-infrared local oscillators, preferably through telecom fibre, as evoked in Sec 4. This version of V8 would also include the fringe-tracker developed in the previous phase.

Intermediate steps could be envisioned on smaller infrastructure in order to validate on-sky operations and the global instrument concept. This demonstration would require >1m diameter telescope, such as C2PU observatory for example.

In the next section, we detail the sensitivity analysis associated to the V8 concept in order to evaluate its feasibility.

9.3 Sensitivity budget

In this section, we evaluate the sensitivity limits of a heterodyne instrument combining the 8 telescopes of VLTI, taking into account the current state of technology and the non-ideal factors of concrete operations, for which we based our analysis on the typical performances reported on ISI in (D. D. S. Hale et al., 2000; David D. S. Hale et al., 2003).

Methodology

This analysis is based on the sensitivity derivation presented in Chap 4 (in particular Eq 4.25). We defined the sensitivity limits as the lower flux to obtain a given SNR (e.g. SNR=10) in a given integration time on source (e.g. in t=1 min) in one polarization. We split the sensitivity analysis in two main scenarii, without and with coherent integration (fringe-tracking), each category being itself divided in two detection bandwidths (2.5 GHz and 25 GHz), corresponding respectively to ISI and what can be expected from QCD technology. We assume a quantum efficiency QE=0.4 corresponding to the ISI technology and to the current accessible technology. We took into account the non-ideal factors of practical operations using the results reported on ISI, most notably : a transmission T=0.6 taking into account optics transmission and the projection of the PSF on the mode of the local oscillator ; a transmission of the VLTI beam train of 0.4 at $10\,\mu\mathrm{m}$ (each cell of Tab 9.1 is divided in two parts : in the left part, we assume that light went through VLTI beam-train ; in the right part, that it is placed directly at the focus of each telescope) and a noise penalty (factor above the quantum noise, apart from the contribution of QE and T) of 1.5.

We also provide the comparison of the sensitivity obtained in heterodyne detection to the sensitivity performances in coherent flux of a single channel of MATISSE instrument reported

t=1 min, SNR=10		V8			MATISSE		
no FT	BW	AT-AT	AT-UT	UT-UT		AT	UT
	2.5 GHz	996 / 398	218 / 87	48 / 19	Low (950 GHz)	2.5	0.2
	25 GHz	315 / 126	69 / 28	15 / 6	High (137 GHz)	12	0.2
with FT	2.5 GHz	212 / 85	47 / 19	10 / 4	Low (950 GHz)	1.5	/
	25 GHz	67 / 27	15 / 5.9	3.2 / 1.3	High (137 GHz)	12	/

t=20 min, SNR=10		V8		
no FT	BW	AT-AT	AT-UT	UT-UT
	2.5 GHz	448 / 179	98 / 39	22 / 8.6
	25 GHz	142 / 57	31 / 12	6.8 / 2.7
with FT				
	2.5 GHz	47 / 19	10 / 4	2.3 / 0.9
	25 GHz	15 / 6.0	3.3 / 1.3	0.72 / 0.29

Tab. 9.1: SNR sensitivity limits (in Jy/polar), assuming $t_0 = 150\,\mathrm{ms}$ (at $\lambda = 10.5\,\mu\mathrm{m}$), QE=0.4, and a noise penalty of 1.5 (reported on ISI) ; each cell is divided in two, corresponding to $\mathrm{T} = 0.6 \times 0.4 = 0.24$ (total transmission, including VLTI beam train, left part) and $\mathrm{T} = 0.6$ (transmission to the telescope focus and projection on the mode of the laser, based on ISI typical results, right part) **Top :** sensitivity limits defined as the lowest flux to obtain a SNR=10 in t=1 min integration **Bottom :** idem with SNR=5 and t=20 min integration. For MATISSE, sensitivity limits are taken from (Petrov et al., 2020), and divided by two in order to compare both number in Jy/polarization. For heterodyne detection, the point source sensitivity is computed only for 2 telescope combinations. See the next section for a calculation including all the 8 telescopes of the array.

in (Petrov et al., 2020), in order to obtain a comparison with typical performances of current instrument. The number given in Tab 9.1 are divided by a factor two compared to (Petrov et al., 2020) in order to compare the flux measured in one polarisation. Due to the intrinsic larger bandwidth of direct detection, these performances are obtained with significantly larger detection bandwidth (Low resolution R=32 equivalent to 950 GHz, High resolution R=218 equivalent to $\sim 135\,\mathrm{GHz}$). In the case of MATISSE, the reported sensitivity in incoherent and coherent integration are comparable, due the capability to shift-and-add fringes (without fringe-tracker) when the SNR is sufficiently high in one *coherence time*, so that the use of fringe-tracker translates in a lower bias on the measurement of coherent flux (Petrov et al., 2020). Finally, we emphasize that this sensitivity is given for only one spectral channel : in the case of MATISSE instrument, multiple channels can be measured simultaneously (typically ~ 150 in low resolution, and ~ 850 in High resolution), enabling a larger spectral coverage and/or an increased sensitivity, which is an intrinsic advantage of direct interferometry. In the next paragraph, we discuss further how the sensitivity of heterodyne detection compares to direct detection.

9.3.1 Sensitivity of V8, comparison with current direct instrument

The sensitivity analysis Tab 9.1 summarizes the impact of the different possible technological developments on the sensitivity of a heterodyne detection, and how this compares to a direct instrument. Three main factors have a massive impact on the sensitivity of the heterodyne combiner : the detection bandwidth ($\sqrt{\Delta f}$), the coherent integration ($\propto t^2$, compared to $\propto t^4$ in incoherent integration), and the telescope diameter ($\propto D^2$). This can be illustrated by considering the sensitivity of a 2.5 GHz detection system with no fringe-tracker, which would be an equivalent of ISI detection system on VLTI. The sensitivity estimated on ATs in this case matches the typical sensitivity reported on ISI (50-100 Jy in 1 hour incoherent integration and 1.6m diameter telescope), with a penalty due to additional losses in VLTI beam train. This sensitivity increases theoretically by a factor $\times 3$ with the bandwidth increase, and by a factor $\times 10$ with fringe tracking when comparing sensitivity limits in incoherent and coherent integration in t=20min. This underlines the crucial impact of coherent integration on the sensitivity of the observations, the gain of fringe-tracker in t=20min being equivalent to half the gain of moving from ATs to UTs ($\times 20$). In addition, this sensitivity estimate highlights the potential gain with telescope diameter, especially interesting for AT-UT combination which represents the largest fraction of baselines (16 baselines over 28), for which UTs increase the sensitivity by a factor $\times 4.5$ compared to AT-AT combination.

This analysis provides the typical observing sensitivity limit that can be expected on V8. Here we will focus on the sensitivity limit of AT-UT combination, which provides the most useful estimate for imagery[1], as AT-UT combinations represent the largest fraction of baseline in the array, combined to a good sensitivity due UT collecting area. In the case of a 25 GHz detection bandwidth, the estimated sensitivity is of the order 30 Jy in 20min with SNR=10 in incoherent integration (V8 incoherent). In the case of the coupling with a fringe-tracjer, the sensitivity is of the order of a few Jys (V8 coherent) and typically 1 Jy in the case of a distribution of the the local oscillator (V8+). These two last numbers are comparable to a single spectral channel on MATISSE-High mode, although only one channel would be available in first instance in V8 without dispersed frequency comb.

These numbers illustrate the initial comparison presented in Chap 4, Sec 4.4.2 between heterodyne and direct detection, with which it converges. At first glance, heterodyne detection is obviously much less sensitive when compared directly to the low resolution mode of a direct interferometer, mainly due to the very large difference of integration bandwidth (e.g. 950 GHz compared to 25 GHz or 2.5 Ghz). However this situation changes significantly with higher resolution, even compared to the moderate R=220 in MATISSE (equivalent to 150 GHz). From pure sensitivity considerations, this change arise from the cumulated effects of a significantly lower total transmission of direct interferometry (typically 4% on MATISSE), and from the large fraction of background noise and detector noise in this wavelength regime. In addition, high to very high resolution (VHR) modes are difficult to implement and to exploit, due to the very large contribution of the background and the detector noise, and are

[1] We will come back more rigorously on this point in Sec 9.5 when looking at the equivalent brightness temperature of the array.

typically available only in L and M band with GRAVITY fringe-tracking in MATISSE. Finally, in the case of image reconstruction, the largest number of available baseline in heterodyne interferometry adds further sensitivity advantage[2] :

Despite the known sensibility disadvantage of heterodyne detection, these sensitivity numbers are compatible with the image reconstruction of astronomical targets on relatively bright targets, down to a few Jy coherent flux when coupled with an external fringe-tracker. In Sec 9.5, we explore the possible science case associated to V8, and the implication of this pathfinder concept for PFI. Heterodyne detection thus appears as a potential interesting technique to take full advantage of the 8 telescopes of VLTI in the mid-infrared. In the next section, we refine the expected performances that could be expected from a V8 combiner, by simulating the observations of V8 on VLTI integrating the noise budget of a heterodyne detection system.

9.4 Simulation of the observations

The goal of our simulator is to reproduce the interferometric observations of a realistic heterodyne interferometer installed at VLTI on input images or input user-defined models of astronomical objects. In particular, the final goal is to explore the uv-coverage allowed by the simultaneous 8 telescopes combination, in the perspective of applying image reconstruction tools to this simulated observations taking into account detection noise of the array, in an analogous way to (John D. Monnier et al., 2018a).

9.4.1 Code

We simulated the output interferometric observations of V8, based on the code `UTILS` developed by Antoine Mérand (ESO, VLTI Project Scientist) in Python[3]. We adapted the code in order to integrate the sensitivity calculation presented in Chap 4, both in a heterodyne and in a direct mode. The input of the simulation is either a parametric model of the astronomical object or a proper image, that is converted into a visibility map. The parameter of the instruments (quantum efficiency, bandwidth, noise penalty, etc.), as well as the integration mode (coherent, incoherent) and the VLTI configuration can be chosen by the user. The simulator then generates an observation, that can also be obtained in `OIFITS` format (Gilles Duvert, Young, and Hummel, 2017), so that it can be processed by classical data analysis tool and image reconstruction tools developed for interferometry. This structure is summarized in Fig 9.3, that we detail briefly in the following.

Object model and image
The input model can be chosen among a different collections of common geometrical models, in a similar way to `Aspro2` (point source, disk, elongated gaussian, etc.). In the case of an

[2]This advantage is even larger when one consider the sensitivity of an equivalent direct interferometer
[3]Publicly available on https://github.com/amerand/UTILS

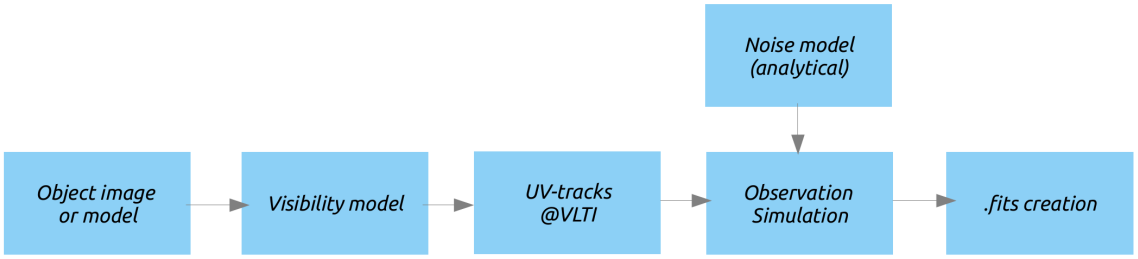

Fig. 9.3: Structure of the code (upper) and an example of a 8 telescopes uv-track (left) and the associated dirty map and the sampling of the input image (middle).

image, the visibility is computed with a simple 2D Fourier-Transform, which the visibility map is then sampled by the uv-tracks of the VLTI configuration.

UV-tracks

This part originates directly from `UTILS`, that we have slightly adapted to allow the UT-AT combination, and to remove the pointing limitations of the delay-lines. The telescope shadowing is also computed by `UTILS`. In addition, once the uv-coverage is computed, `UTILS` is able to draw the equivalent dirty-beam of the observations, in a similar way to radio-interferometry. At this stage, the theoretical values of complex visibilities measured with each baselines can be computed from the uv-tracks and the visibility model, and can be converted in coherent fluxes.

Noise model

The heterodyne noise is calculated with the detection noise due to the local oscillator only. In addition, the non-ideal noise are taken into account through a noise penalty, defined as the value of the noise above the theoretical shot noise of the laser (e.g. factor $\times 1.5$ reported in ISI). The transmission of the optical system (including the VLTI train) can be taken into account in the quantum efficiency, or in the nose penalty factor (e.g. $1/0.6 \times 1/0.4 \times 1.5 = \times 6.25$ in the case of a telescope transmission of 0.6 (number on ISI), a VLTI transmission of 0.4, and an additional 1.5 penalty). The exact parameters are indicated in the output of each simulations. For the direct mode, we implemented the noise and typical parameters used in `Aspro2` simulator[4], for which we benefited from the support of JMMC expertise center. We add the noise to the complex visibilities, and derive the interferometric observables from this noisy visibilities (visibility modulus and phase, closure phase, etc.).

Fits creation

The final observations can be saved in `OIFITS` format, which was implemented in the simulator based on the code of MIRCX-18 pipeline provided by Jean-Baptiste Le Bouquin[5]

[4] Available at http://www.jmmc.fr/aspro
[5] Available at : https://gitlab.chara.gsu.edu/lebouquj/mircx_pipeline

9.4.2 Typical results

In Appendix 9.8, we show the results of the simulation for three archetypal observations : a non-resolved point source, which can be compared to the sensitivity analysis in Sec 9.3 ; a partially resolved gaussian disk, similar to the morphology of a YSO ; and a massive star (α Sco). In the following, all the observations will assume that detector with 25 GHz bandwidth are used in the instrument, and placed at the VLTI laboratory (i.e. total noise penalty $1/0.6 \times 1/0.4 \times 1.5 = \times 6.5$). We assume that the signals are correlated with a simple double-sideband correlator, as investigated in Chap 6 for example.

Point source
The Fig 9.9 and Fig 9.10 show the simulated observations of a non-resolved point-source with 70 Jy/polar and 5 Jy/polar (respectively), observed in 5 sequences of 1 min integration time without fringe-tracker and 3 sequences of 20 min integration time with fringe-tracker. These numbers can be compared to Tab 9.1, in particular to the sensitivity limit of AT-UT in incoherent integration with 25 GHz bandwidth and 1min integration time, and the sensitivity limit of AT-UT in coherent integration for 25 GHz in 20 min. We also note the complementary of AT-AT, AT-UT and UT-UT combination in terms of sensitivity and uv-coverage. In particular AT-UT baselines represent the majority of the visibility measurements (16 points), while allowing decent sensitivity limits due to the sensitivity boost of UT. Overall, these simulations are consistent with the theoretical sensitivity estimates.

The simulator enables to explore the uv-coverage associated to the combination of the 8 telescopes of the VLTI. In the following simulations, we choose the combination of the UTs with the station B4-B5-J1-M0 in order to obtain one visibility point at small baseline (B4-B5) and AT-UT combination with both moderate large baselines. This choice results from a qualitative analysis of the uv-coverage, however more work should be done to optimize the choice of the AT stations. Ultimately, this optimization could be thought as an optimization of the brightness temperature of the array, also possibly depending of type of object observed and the brightness temperature targeted.

Massive stars (α Sco)
We simulated the typical observation of a massive star (in this case α Sco, 2800 Jy), by using directly the output of 3D hydrodynamical simulation of RSG/AGB stars performed with the code `CO5BOLD-OPTIM3D` of A.Chiavassa (Chiavassa et al., 2009; Chiavassa et al., 2011) available on MOIO AMHRA platform [6].

With a star diameter of 40mas, the simulation covers the first 4 interferometric lobes of α Sco in 5min acquisition without fringe tracker, for which the combiner benefits from the sensitivity boost of AT-UT baseline. This result is consistent with the previous sensitivity estimate : a contrast 10^{-3} in $|V|^2$ is compatible with the sensitivity limit of AT-UT combination $\sqrt{10^{-3}} \times 2800\,\mathrm{Jy} = 75\,\mathrm{Jy}$ (cf Tab 9.1). AT-AT on baselines larger than >50m are not exploitable and could be optimized to better cover the small spatial frequency.

[6] Service available at https://amhra.jmmc.fr/.

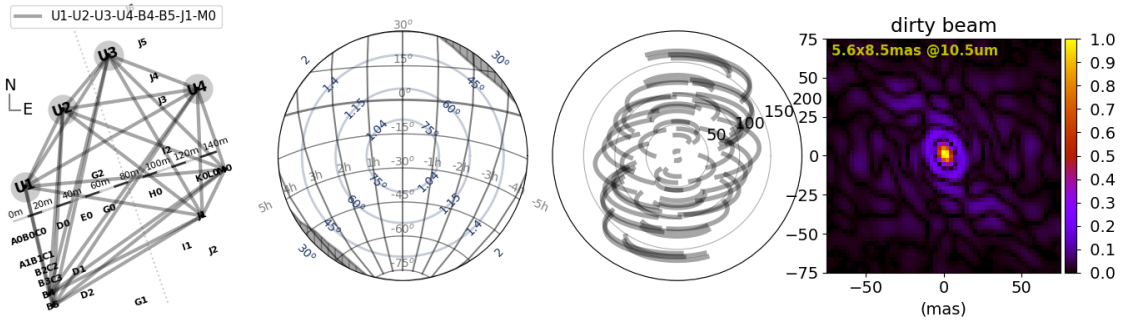

Fig. 9.4: **Left:** VLTI baseline map **Left (middle):** Sky-coverage of the 8 telescopes combination, the sky coverage is limited by the shadow of the UT only **Right (middle):** uv-plane associated to the 8 telescopes combination **Right:** Dirty beam associated to the 8 telescopes combination, the dimension of the beam at 10.5 μm are indicated in upper left corner.

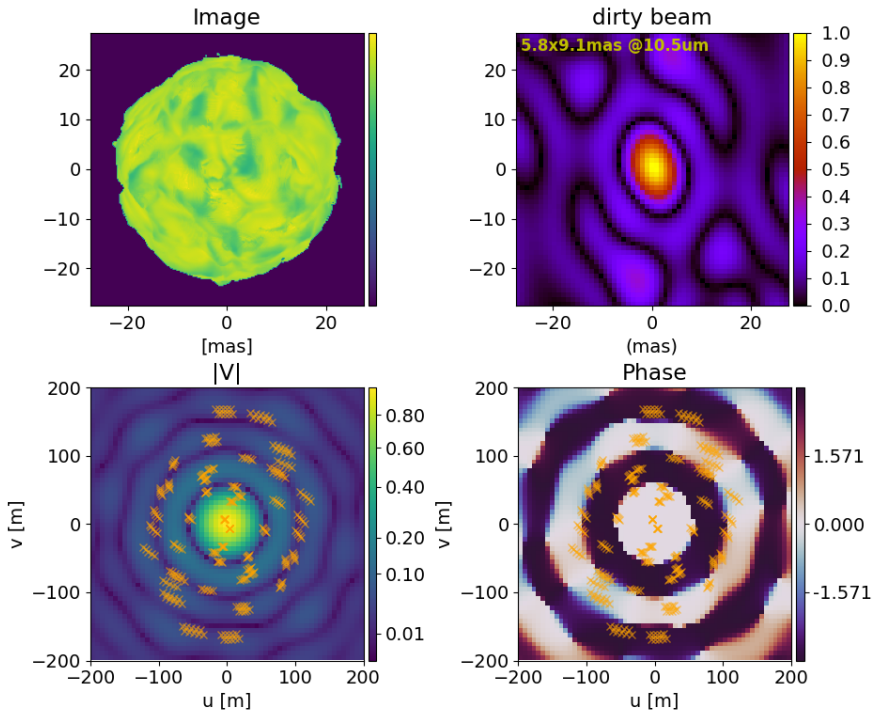

Fig. 9.5: The output image of `CO5BOLD-OPTIM3D` model (Chiavassa et al., 2009; Chiavassa et al., 2011) the visibility function (amplitude and phase) associated to this image. The image and the dirty beam are at the same spatial scale.

9.4.3 Improvements of the simulator

The preliminary results of the current simulator have to be taken with caution :

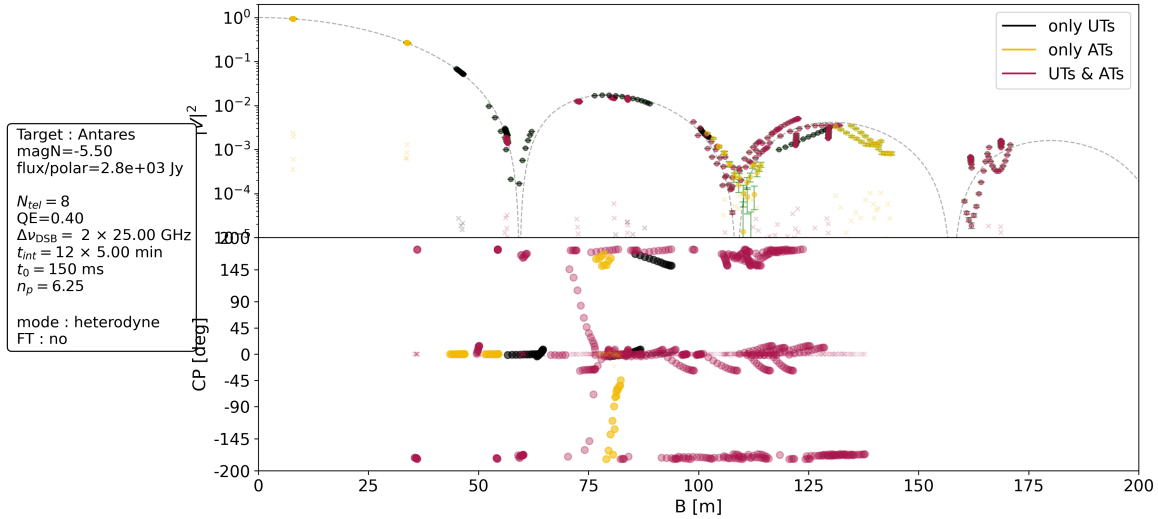

Fig. 9.6: Simulated observation of α Sco, 12 sequences of 5min incoherent integration.

- in the same way than the sensitivity estimates provided in Tab 9.1, with which the current simulations share the same input parameters, the definite sensitivity limits will be set by the experimental noise validated in laboratory.

- in the case of the simulation with fringe-tracking, the coherent integration in the simulator is for the moment implemented in a naive way, and does not take into account any instrumental effect of a practical fringe-tracker. More generally, the simulator would benefit from integrating both a heterodyne and a direct mode. The next potential step could be to start with a simple fringe-tracker model, as provided in (Julien Woillez et al., 2017).

- the remaining item in our analysis is to perform a proper image reconstruction, based either on the image reconstruction tools developed for infrared interferometry (John D. Monnier et al., 2014), or potentially benefiting from uv-coverage of an 8T combination to explore image reconstruction approach inspired from radio-interferometry (CLEAN, etc.).

9.5 Perspectives : a pathfinder for the Planet Formation Imager

In this section, we explore the possible science case associated to V8, and the implication of this pathfinder concept to PFI. We start by exploring the science cases that could be targeted with V8, that we will divide in the different development phase of the instrument (V8 incoherent, V8 coherent, V8+).

9.5.1 Massive stars dense imaging : V8 with incoherent integration

A unique feature of V8 is its capability to combine dense imaging with high-spectral resolution at $10\,\mu\mathrm{m}$. This property could be of high interest in the study of Red Supergiant Giants (RSG) and Asymptotic Giant Branch (AGB) stars. Despite the lower sensitivity of heterodyne interferometry compared direct interferometry at moderate resolution R<1000, the sensitivity of heterodyne detection becomes advantageous at high-spectral resolution. The sensitivity in Tab 9.1 are compatible with the mapping of tens of evolved stars even whithout fringe tracker. With the full-sky coverage capability of V8, these performances are compatible with the dense imaging of a significant sample of RSG/AGB stars in the Southern Hemisphere. This imaging capability can be coupled to the monitoring of the spatio-kinematic of the envelope through spectral lines, based on the capability of heterodyne detection to reach high-spectral resolution. In an analogous way, (Ohnaka, Weigelt, and Hofmann, 2017) reports strong velocity gradients ranging from -20 to +20 km/s (R=15 000, ∼2 GHz) spatially resolved at the surface of Antares, observed through CO bandheads in K band with AMBER instrument. These gas clumps extend up to 1.7 stellar radii which can not be explained by convection alone, the exact mechanism giving rise to this extension being likely related to the mass loss in RSG and still remains to be identified. In this perspective, systematic dense imaging and spectro-kinematic monitoring of a significant sample of RSG/AGB stars with V8 could enable to constrain the still poorly understood mass loss and dust production processes in RSGs.

9.5.2 V8 with coherent integration : the mid-infrared image of the brightest Young Stellar Objects (YSOs) with 2AU resolution

V8 coherent integration : sensitivity limits on YSO

In theory, the addition of a fringe-tracker should dramatically increase the sensitivity limits of the instrument, down to a few Jy in the case of "V8 coherent". This sensitivity limit is still higher than a large fraction of YSOs, but may be compatible with a restricted but relevant sample of YSOs with typical total flux of the order of $\sim$ 10 Jy/polar total flux, down to $\sim$ 2 Jy/polar coherent flux (Varga et al., 2018). In order to evaluate this point, we simulated the observation of a bright YSO (AB Aurigae), taking as an input the visibility profile deduced from previous MIDI observations and provided in (Varga et al., 2018). We show the typical observation obtained on 3 sequences of 20min with coherent integration on Fig 9.7, compared to the equivalent MIDI observation published in (Varga et al., 2018). These simulations highlight the fact that these observations should be restricted to maximum baseline of 100m typically, in order to obtain a sufficient sensitivity. In terms of imaging, this is the same as decreasing the spatial resolution in order to increase the sensitivity, thus focusing on more large spatial scales ($\sim$ 20mas, equivalent to $\sim 2.5\,\mathrm{AU}$ at 153pc). Following this initial finding, we generalize this sensitivity analysis in the context of image reconstruction by introducing the notion of brightness temperature.

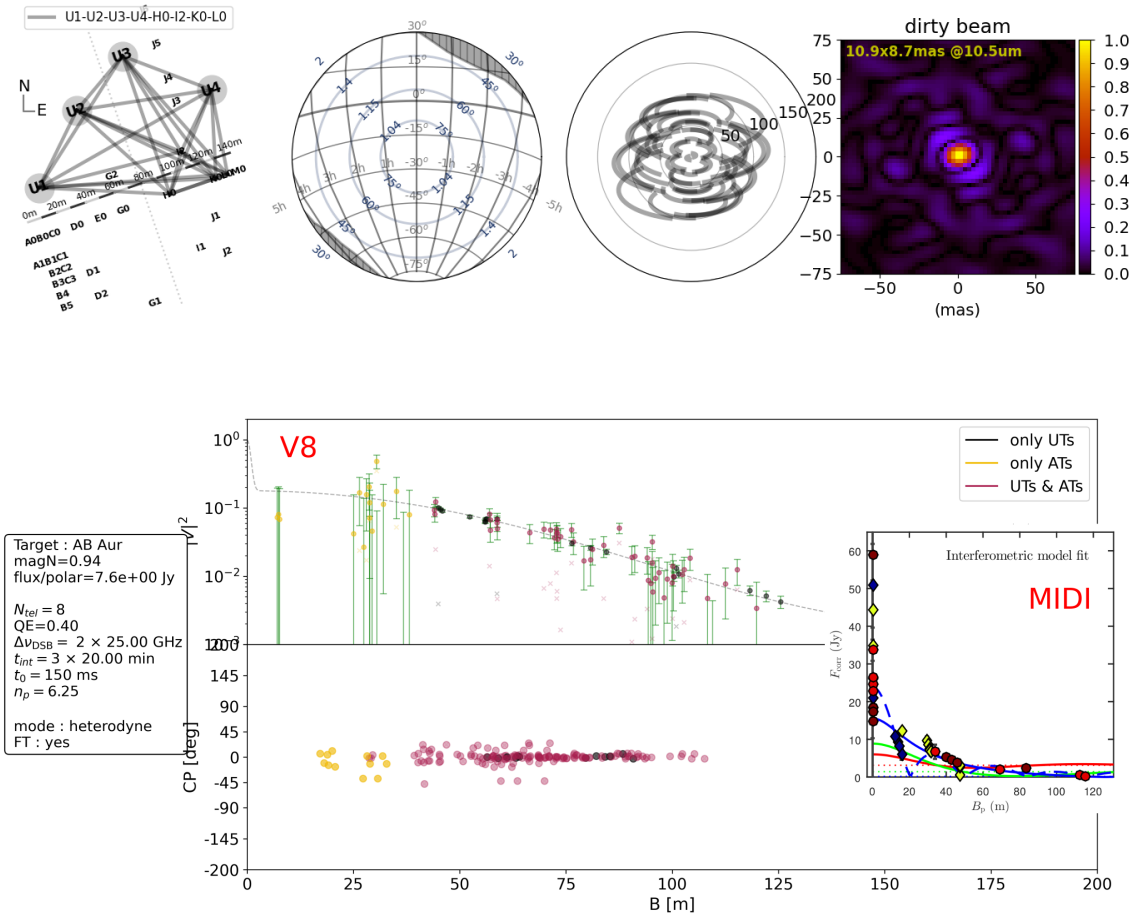

Fig. 9.7: *Up :* Compact VLTI telescope configuration chosen to simulate the YSO observations.*From left to right :* VLTI telescope base ; Sky coverage ; UV-coverage ; Dirty Beam. *(Bottom :)* Simulated observation of a bright YSO (AB Aurigae), whose morphology is taken from MIDI observation (Varga et al., 2018). The MIDI observation (coherent flux) is inserted on the right.

Brightness temperature

We can generalize this sensitivity analysis by computing the brightness temperature associated to V8, in order to compare it with the typical brightness temperature expected from YSO at 10mas resolution at $10\,\mu$m. We choose a more compact configuration than in the case of massive stars, with the goal to have most of the AT-UT on baselines <130m and AT-AT on baselines <30m, shown in Fig 9.7, with an interferometric lobe of dimension $10.9\,\mathrm{mas} \times 8.7\,\mathrm{mas}$, equivalent to a $1.7\,\mathrm{AU} \times 1.3\,\mathrm{AU}$ at d=153pc. The results of sensitivity computation for this size of interferometric lobe is shown on Fig 9.8, for the three development steps suggested previously (V8 incoherent, V8 coherent, and V8+)[7] :

[7]The theoretical sensitivity should be computed considering 16 AT-UT and 6 UT-UT combinations (AT-AT have an almost negligible contribution) : however Eq 4.25 and Eq 4.27 are only valid for pairs of telescopes with same

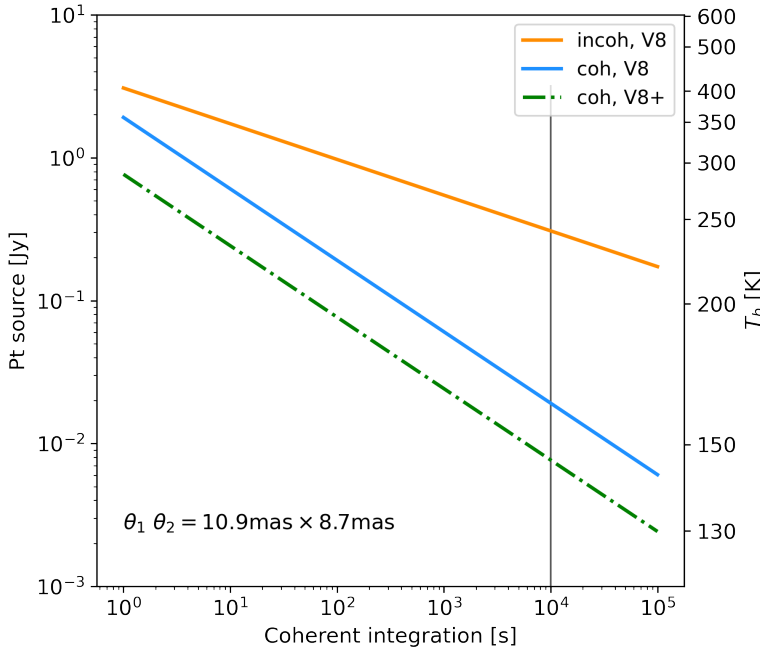

Fig. 9.8: Point source sensitivity and brightness temperature of a V8, assuming the telescope configuration shown in Fig 9.7. We note that the point source sensitivity is smaller than the point source sensitivity criteria given in Tab 9.1, which was assuming the combination of only 2 telescopes, whereas the present estimation take into account the 8 telescopes of the array for the image reconstruction.

Imaging the mid-infrared environment of the brightest YSOs at 2 AU scale

The typical limit on brightness temperature is of the order 160 K in 10^4 s coherent integration. In order to reach a decent SNR, a factor 5 on point source sensitivity (i.e. corresponding to SNR=5) can be accounted, giving $T \sim 200\,\mathrm{K}$ in $10^4\,\mathrm{s}$. In the following, we will keep the number $150 - 200\,\mathrm{K}$ as the limit in sensitivity. We comment this rather surprising results compared to PFI targeted brightness temperature (150K) in the next paragraph. This sensitivity criteria is obtained with an imaging resolution of $10.9\,\mathrm{mas} \times 8.7\,\mathrm{mas}$, equivalent to a $1.7\,\mathrm{AU} \times 1.3\,\mathrm{AU}$ at d=150pc. This brightness temperature is potentially compatible with the dense imaging of the gas and dust thermal emission of the brightest YSO with 2 AU angular resolution (in the Taurus), as shown by previous MIDI observations on similar spatial scales (Varga et al., 2018). In this perspective, the imaging capability of V8 would enable to add constrains on the radial and vertical structure of the inner disk, and potentially on the spatial inhomogeneities of the inner disk at spatial scales contiguous with near-infrared

point source sensitivity. In order to take into account this this effect into account, we computed the final point source sensitivity as :

$$n_{\mathrm{ps,tot}} = \left(1/n^2_{\mathrm{ps,AT-UT}} + 1/n^2_{\mathrm{ps,UT-UT}}\right)^{-1/2} \tag{9.1}$$

AT-AT are not taken into account in the computation of the point source sensitivity, as they are negligible compared to AT-UT and UT-UT combinations.

high-contrast imaging in J and H band. The case of AB Aurigae is the archetypal object of such relatively bright YSOs (15 Jy), with coherent fluxes of the order of a few Jy up to 100m baseline, as probed by MIDI observation (Varga et al., 2018). (Bitner et al., 2008) derived a disk temperature of 650K at 18 A, higher than the value predicted by theoretical disk models ($\sim 250\,\mathrm{K}$, (C. P. Dullemond, Dominik, and Natta, 2001)), and compatible with the brightness temperature limit of V8. This temperature was probed by mid-infrared TEXES observations of pure rotational H2 lines at 8, 12 and 17 microns (S(1), S(2) and S(4) resp.), at LTE at the local gas temperature (Bitner et al., 2008), whose relative high value may trace possible additional heating by X/UV radiation in this region of the disk. In J and H band, high-contrast imaging with extreme adaptive optics (Boccaletti et al., 2020) recently revealed impressive spiraling structures at 10 to 100 AU scale in the disk of AB Aurigae, and the presence of a strong point source structure at 200 mas of the central star. The reconstruction of an image in the mid-infrared would be sensitive to thermal emission of the disk, potentially revealing complementary structures at similar spatial scales compared to J/H band, and adding constrain on the temperature of the disk. In this complex picture of the earliest stage of planet formation, the complete reconstruction of an image at AU scale of the disk would enable to shed light on the disk structure in this crucial region of young objects, and their possible connexion to the mechanism of planetary formation.

As additional perspectives, heterodyne detection would be suited to the measurement of the disk structure in spectral lines in disks, focusing on disk kinematic and composition. However, this would likely require higher sensitivity and a greater range of tunability of the LO in order to center on the wavelength of a specific line[8]. Finally, in the case of the observation of low spectral features, characteristics of disk mineralogy (Boekel et al., 2004), V8 would necessitate the addition of multiple local oscillators (or frequency combs) in order to cover a sufficiently large wavelength range.

Comment on brightness temperature : V8 as a precursor of PFI science case ?

The theoretical brightness temperature reached in the case of V8 with coherent integration is of the order 160 K in $10^4\,\mathrm{s}$, a particularly surprising value compared to PFI specification of 150 K in $10^4\,\mathrm{s}$ obtained with massive multiplexing and a larger number of telescope. These numbers are however consistent with these previous sensitivity estimates and highlight two important facts : the brightness temperature is extremely dependent of the angular resolution (a resolution increase by a factor θ requires a point source sensitivity $\propto \theta^2$ smaller) and of the telescope diameter ($\propto D^2$). In terms of order of magnitude, V8 sensitivity benefit both from an 8.2m diameter telescope (factor $\left(\frac{8.2}{4.5}\right)^2 = 3.3$) and a resolution 10 times smaller than PFI (factor $10^2 = 100$) : cumulated together (factor ~ 300), these two factors are consistent with the larger sensitivity of an optimized PFI system with 1.2km baseline and 12 telescopes. Conversely, one can notice that the point source sensitivity in V8 is larger by a factor ~ 70 compared to PFI (and of course not compatible with the detection of planet), given that the

[8]The total span of a single 25 GHz is compatible with a velocity range of $\pm 200\,\mathrm{km/s}$ at $10\,\mu\mathrm{m}$.

V8 is obviously much less sensitive that PFI, the comparable brightness temperature being due to the difference in angular resolution. The number for point source sensitivity are also consistent with the sensitivity estimation shown previously in Chap 4 for PFI[9].

In conclusion, even if the final sensitivity of V8 will depend of the practical SNR achieved by the detection chain in the lab, these theoretical results highlight the fact that a relatively simple implementation of V8, even in the VLTI lab, based on a single detector with 25 GHz and near-infrared fringe tracking at 8 telescopes, could potentially reach brightness temperature comparable to the specification of PFI, due to the smaller angular resolution of V8 (factor 10 compared to PFI), and would appear potentially as a relevant demonstration of PFI long-term goal.

9.5.3 Perspectives for PFI

Beyond the intrinsic science case of V8, the development of an all-fibred combiner on existing telescopes would represent a potential path to develop PFI mid-infrared technologies. The experience and the technologies developed in this framework could then serve as a first test for a more ambitious PFI array, for which it could serve as precursor instrument.

On a more prospective basis, these sensitivity limits could be further increased by the multiplexing of the spectral channels ($\sqrt{N_s}$) and the distribution of the local oscillator directly at the level of the telescopes (avoiding the transmission of VLTI delay lines $\times 2.5$). These two steps could potentially enable the image reconstruction of a larger sample of YSO, whose typically coherent flux is around ~ 200 mJy/polar for a 130m baseline (Varga et al., 2018) and/or to exploit the full resolving capability of VLTI (200m baseline). These two technological steps would require specific developments on fibred phase-synchronization scheme of the local oscillators and in the implementation of multiple local oscillators or frequency comb in a dispersed detection scheme, two demonstrations required in the perspective of a PFI array and which could be tested on existing infrastructure.

With the modest point source sensitivity of an early demonstrator with single detector, the brightness temperature attained by V8 with fringe-tracking and 20 mas spatial resolution could also serve as a precursor of the science case targeted with PFI at 2 mas resolution. Even if not enough sensitive to detect young planets and resolve their accreting environment, this early demonstration could benefit from the unprecedented uv-coverage of VLTI to reconstruct for the first time an interferometric image of the complex environment of relatively bright protoplanetary disks, with effective temperature 150-200 K at 2 AU scale.

[9] In terms of order magnitude : PFI has a sensitivity increase of 10 due to spectral multiplexing ($\sqrt{(100)}$), a factor 2 due to local detection (VLTI transmission ~ 0.4), a factor 10 due 12 telescopes combination (compared to 4 telescopes combination), and a factor 3 penalty due to smaller telescope compared to UT $\left(\frac{8.2}{4.5}\right)^2$, so $10 \times 2 \times 10/3 \approx 70$ advantage in point source sensitivity. These order of magnitudes considerations are for illustrative purpose only, but show that the present results on the point source of V8 are physically consistent with previous estimation provided for PFI.

9.6 Conclusion

In this section, we explored the idea of using heterodyne detection to combine the 8 telescopes of VLTI in a coherent array at $10\,\mu\mathrm{m}$, so-called V8 concept. Based on the current state of the technology, we evaluate that the sensitivity of the simultaneous combination of the 8 telescopes of VLTI would be compatible with the image reconstruction of RSG/AGB without fringe-tracker, and with the imaging of bright YSOs with effective brightness temperature of 150-200 K at 2 AU scale in the Taurus with fringe-tracker.

The current state of mid-infrared technologies would be compatible with a short term development of V8. These developments could simultaneously push the development on the fringe-tracking aspects, which would dramatically increase the sensitivity of V8, pushing both heterodyne and direct interferometry developments. The simultaneous combination of the 8 telescopes in an imaging array with V8 could serve as a pathfinder for a more ambitious instrument, and could represent a precursor of the Planet Formation Imager.

9.7 *Proceedings : V8: an 8 beam mid-infrared heterodyne instrument concept for the VLTI (published)*

9.8 Appendix

9.8.1 Simulated point source observation with V8

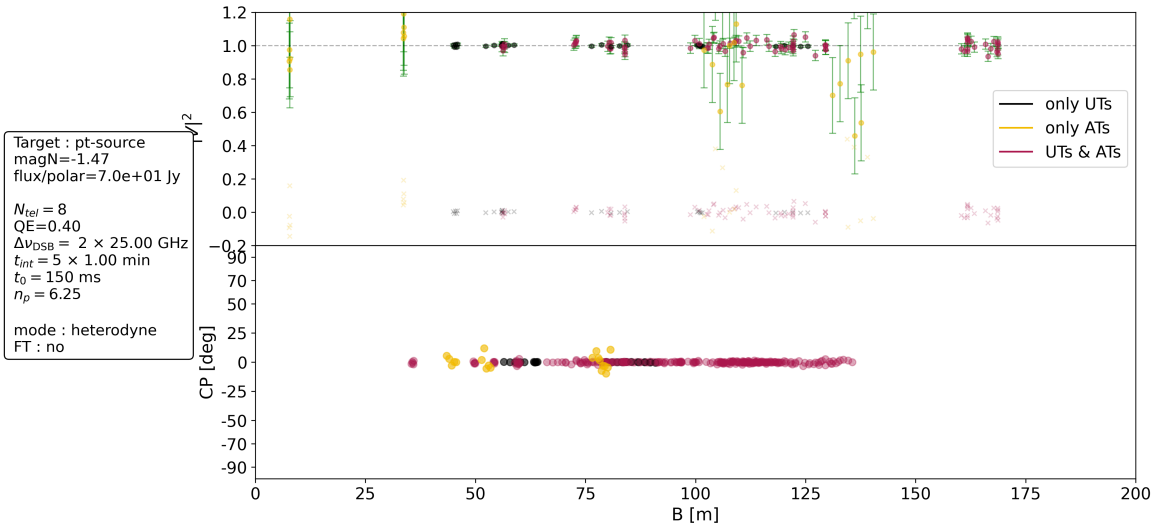

Fig. 9.9: Simulated observation of a non-resolved point source with a total flux of 70 Jy/polar. The parameters of the observation are indicated in the legend.

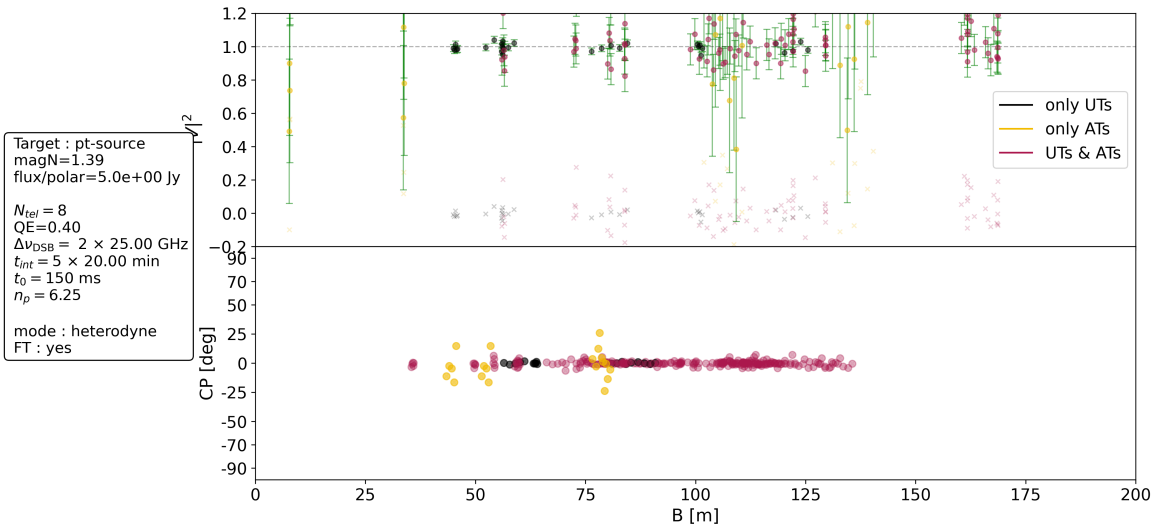

Fig. 9.10: Similar simulation to 9.9, with a total flux of 5 Jy/polar.

9.8.2 *SPIE proceedings : "V8: an 8 beam mid-infrared heterodyne instrument concept for the VLTI "*

> *Interroge la beauté de la terre, la beauté de la mer, la beauté de cette vaste et immense atmosphère, la beauté du ciel... interroge tout cela. Tout ne répond-il pas : Regarde, admire notre beauté ? Leur beauté même est une réponse.*

— St Augustin
Serm. 241, 2 - 3, c. 411 A.D

Conclusion

Results

FU Orionis outburst

In Chapter 3, our temporal monitoring of FU Orionis outbursting disk with near-infrared interferometry enabled to estimate the typical size of the emission zone and to put constraints on its evolution in time, compatible with a slightly decreasing size in time. The comparison of the typical size and dynamic of the outburst with simple 1D numerical models favours a combination of Magneto-Rototional Instability and Gravitational Instability (MRI-GI) occurring in a layered disk model, as proposed in (Armitage, Livio, and Pringle, 2001), rather than a canonical Thermal Instability (TI) model. Our current sample is limited by the systematics error due to heterogeneity of the instruments, in particular with regards to the oldest data in our dataset. A key opportunity in this direction is the programmed second generation instrument of VLTI in the next ten years, which could enable the regular observation (every years or 2 years) on a stable configuration. On the numerical side, more work is needed to explore the parameters space of these models, and also evaluate its potential sensitivity to the disk structure (external trigger in particular). The refinement of the size estimation would be potentially sensitive to different fundamental parameters of MRI (activation temperature), of the disk (surface density) or of the disk structure (external trigger), thus representing a unique laboratory to put constraints on the very fundamental properties of accretion in disks. A systematic study of the environment of the FUors, in order the role of the envelope in triggering the instability mechanisms, would greatly benefit from the systematics observation of the envelope on a larger sample of EXor/FUor with techniques probing intermediate spatial scales (mid-interferometry) and large spatial scales (ExAO). Finally, this study could also be complemented by the study of the dynamics of the inner disk, in particular through CO lines with spectro-interferometry, which could enable to put constraints on its keplerian dynamics, or its non-keplerian dynamics tracing a disk wind for example. Finally,

Infrared heterodyne interferometry

In **Chapter** 4 we investigated a renewed architecture of an infrared heterodyne system, initially based on (Swenson, 1986) and (Ireland and John D. Monnier, 2014), adapted to a large number of telescopes, with the long-term goal of an all-fibred infrastructure. Major innovations emerging in the field of mid-infrared technologies enable to profoundly modify the previous architecture of heterodyne interferometer. We identify in particular three essential mid-infrared technologies in this perspective : wide bandwidth detectors based on quantum engineered structures, in particular QCD detectors ; fibred synchronization of mid-infrared QCL through telecom fiber network ; frequency comb lasers, including frequency comb and QCL combs. We projected the sensitivity that could be expected from this long-term architecture and confirmed that it could be suitable to the technical requirements of a PFI with a massive spectral multiplexing. In **Chapter** 5, we try to clarify the fundamental origin of the noise in heterodyne detection based on Tsang, 2011, and converged with the analysis of Townes, confirming the very quantum nature of this noise. This study focuses on the observable of main interest in interferometry (complex visibility), but it does not exclude potential alternative protocols or noise reduction techniques on different set of observables, which go however well beyond the present work.
In **Part** III, we propose potential solutions to address the challenge associated to the transport and the correlation of signals with tens of GHz bandwidth, originating from hundreds of spectral channels, and tens of telescopes. In **Chapter** 6, we proposed and demonstrated the use in the laboratory of analog photonic correlation, in amplitude and phase modulation, in order to reproduce the function of an analog simple double-sideband correlator with off-the-shelf telecom components. In **Chapter** 7, we presented the extension of this technique to the wideband correlation of RF signals over multiple delays, enabling to map in real time (below ms) the correlation function of GHz signals over typically 200 values. More work is needed in order to assess the noise property of this last set-up and its compatibility with its use in infrared heterodyne interferometry. However, it offers already potential applications related to the correlation of wideband RF signals (emitters localization, lidar, etc.).
In **Part** IV, we presented technological pathfinders based on our renewed architecture of a heterodyne instrument. In **Chapter** 8, we presented the preliminary implementation of a laboratory demonstrator at $10\,\mu\mathrm{m}$, dedicated to the validation of a complete detection and correlation chain. This demonstrator includes a Quantum Cascade Laser (QCL), wideband (1 GHz) commercial detectors and a photonic correlator in amplitude modulation. The alignment of this demonstrator is completed and its characterisation is on-going. In the mid-term, this demonstrator could serve as a platform to test new technologies, and in particular wideband QCD and QCL phase-locking. In **Chapter** 9, based on the inherent scalability of infrared heterodyne interferometry, we presented the concept of a heterodyne instrument combining the 8 telescopes - so-called V8 concept- in order to exploit the full imaging capability of Very Large Telescope Interferometer (VLTI), and evaluated the sensitivity of this concept. In the case of the combination with a fringe tracker, we explored the possibility to apply V8 to the imaging of bright young stars with 150 K brightness temperature and 2 AU spatial resolution in the Taurus, which could represent a pathfinder instrument in the perspective of a Planet Formation Imager.

Perspectives

Technological development

More and more advanced technologies have now been demonstrated in the recent years, and bear the promise of a possible adaptation of these technologies in infrared heterodyne interferometry. The immediate development of a heterodyne interferometer would benefit from three major innovations. The first one is the advent of high-bandwidth detector, in particular QCD detectors. The development of detector with typically 25 GHz and a quantum efficiency of 40% enables the increase of the sensitivity of heterodyne detection, or the coverage of larger portion of the spectrum in the perspective of spectroscopy. The second major innovation is the development of a synchronization link at telecom wavelength in order to lock mid-infrared local oscillators. Demonstrations for spectroscopic applications with propagation in the telecom network have already been carried out for CO2 laser and QCL. Their possible adaptation to the stabilization of the relative phase of two mid-infrared local oscillators through fibred link would represent a major step in the direction of an all-fibred infrastructure, and could initiate the development of complete heterodyne detection modules, adaptable to existing telescopes, that could be deployed in an array. The last innovation is the use of frequency comb lasers in the mid-infrared, an active field of research in which new solutions are currently being developed, in particular based on mode-lock laser frequency comb and QCL combs.

Comparison with direct interferometry in the N band

Concerning the fundamental sensitivity penalty of heterodyne interferometry compared to direct interferometry, we have put forward several arguments (Chapter 4) to show that heterodyne detection remains an interesting detection mode in the N band, in particular when comparing the sensitivity of these two techniques at high and even at medium spectral resolution. Rather than an intrinsically larger sensitivity, the key advantage of direct interferometry lies in its natural capability to detect and multiplex signals over THz bandwidth. In the N band, we argue that the comparison of these two techniques in the case of a PFI should thus revolve around the *technical* feasibility of each technique, namely the transport of signals over kilometer vacuum delay lines and the combination of a large number of telescopes in direct detection, and the massive multiplexing of spectral channels in heterodyne interferometry.

Importance of the fringe-tracking

One fundamental aspects of a future array, that we did not solved in this study, is the development of a fringe-tracker combining a large number of telescopes. The fringe-tracker will be an essential element both in heterodyne and direct mid-infrared interferometers. The different sensitivity estimates presented in this work have shown that coherent integration,

requiring fringe-tracking, is one of the largest, if not the largest factor that increases the sensitivity of an array, with telescope diameter. In our long-term goal of an all-fibred infrastructure, this requires the development of a specific fringe-tracker fibred technologies. The cophasing of a V8 instrument could represent a near-term objective for this development, with an important feedback in the context of a PFI for both heterodyne and direct detection mode. As mentioned in Chapter 4, the 'OHANA and AGILIS concepts are two precursors in this direction.

Implications for PFI

On a more general level, the practical implementation of a heterodyne interferometer highlights two potential interesting aspects of this detection mode in the perspective of PFI. The first one is the ability in heterodyne mode to develop incremental demonstrations of PFI key building blocks, with validations in the laboratory, and intermediate on-sky demonstrations with scientific outputs. The second point is that the technological developments required in heterodyne interferometry for PFI could benefit from strong external drivers (spectroscopy, telecommunication), that push these technologies. A future PFI will rely in any case on heavy technological developments, which could benefit from the achievements originating from a broader community.

Finally, the present work, as a first practical attempt to a PFI, and especially the V8 concept, highlights some fundamental notions in the design of an infrared imaging array, and in particular the importance of the notion of brightness temperature. Fundamentally, it underlines the necessary trade-off between *angular resolution* and *sensitivity*. This consideration should motivate the logic of considering the array as an imager, and to proportion the angular resolution aimed in the interferometric image with the sensitivity that can be reached by the detection system. A prime infrastructure in that respect is the VLTI, which was envisioned as an interferometric imaging array with a large collecting area from the beginning (Léna, 1988). Exploiting the full interferometric imaging capability of this infrastructure would represent a first forming experience in the perspective of a Planet Formation Imager.

Annex: List of publications

List of publications

In the following, we list the publications directly related to the manuscript and cited in the main text. A complete list of publications, including collaborations, can be found here.

[1] "Toward a large bandwidth photonic correlator for infrared heterodyne interferometry"
Bourdarot G., Guillet de Chatellus H., Berger J-P, 2020, *A&A*, Vol. 639, A53

[2] "MACH II : MACH-Zehnder Analog Correlator for Heterodyne Infrared Interferometry"
Bourdarot G., J-P Berger, Guillet de Chatellus H., 2020, *SPIE Proceedings*

[3] "V8 : an 8 beam mid-infrared heterodyne instrument for the VLTI"
Berger J-P, **Bourdarot G.**, Guillet de Chatellus H., 2020, *SPIE Proceedings*

[4] "Architecture of photonics correlation for infrared heterodyne interferometry: demonstration of amplitude-modulation based correlation "
Bourdarot G., J-P Berger, Guillet de Chatellus H., 2021, *JOSAB*, Vol. 38, issue 10

[5] "V8 concept and photonic correlation for mid-infrared interferometry"
Bourdarot G., J-P Berger, Guillet de Chatellus H., 2021, *SF2A Proceedings*

[6] "Multi-delay photonic correlator for wideband RF signal processing"
Bourdarot G., J-P Berger, Guillet de Chatellus H., submitted to *Optica*

A&A 639, A53 (2020)
https://doi.org/10.1051/0004-6361/201937368
© G. Bourdarot et al. 2020

Astronomy & Astrophysics

Toward a large bandwidth photonic correlator for infrared heterodyne interferometry

A first laboratory proof of concept

G. Bourdarot[1,2], H. Guillet de Chatellus[2], and J-P. Berger[1]

[1] Univ. Grenoble Alpes, CNRS, IPAG, 38000 Grenoble, France
e-mail: guillaume.bourdarot@univ-grenoble-alpes.fr
[2] Univ. Grenoble Alpes, CNRS, LIPHY, 38000 Grenoble, France

Received 19 December 2019 / Accepted 17 May 2020

ABSTRACT

Context. Infrared heterodyne interferometry has been proposed as a practical alternative for recombining a large number of telescopes over kilometric baselines in the mid-infrared. However, the current limited correlation capacities impose strong restrictions on the sensitivity of this appealing technique.
Aims. In this paper, we propose to address the problem of transport and correlation of wide-bandwidth signals over kilometric distances by introducing photonic processing in infrared heterodyne interferometry.
Methods. We describe the architecture of a photonic double-sideband correlator for two telescopes, along with the experimental demonstration of this concept on a proof-of-principle test bed.
Results. We demonstrate the a posteriori correlation of two infrared signals previously generated on a two-telescope simulator in a double-sideband photonic correlator. A degradation of the signal-to-noise ratio of 13%, equivalent to a noise factor NF = 1.15, is obtained through the correlator, and the temporal coherence properties of our input signals are retrieved from these measurements.
Conclusions. Our results demonstrate that photonic processing can be used to correlate heterodyne signals with a potentially large increase of detection bandwidth. These developments open the way to photonic processing of wide bandwidth signals for mid-infrared heterodyne interferometry, in particular for a large number of telescopes and for direct imager recombiners.

Key words. instrumentation: interferometers – techniques: high angular resolution – techniques: interferometric

1. Introduction

Optical interferometry and Very Long Baseline Interferometry (VLBI) are the two techniques that currently achieve the highest angular resolution in astronomy. The scale-up of infrared interferometry to an imaging facility with milli-arcsecond resolution and below represents a long-term objective of major interest for astrophysics (Monnier et al. 2018). Such an instrument would require a large number of telescopes ($N \geq 12$), in order to obtain a (u, v)-coverage that is compatible with imaging, and a kilometric baseline, in order to reach milli-arcsecond resolution in the near- and mid-infrared. At the present time, current facilities have the capacity to recombine up to four telescopes in the near- and mid-infrared at the Very Large Telescope Interferometer (VLTI) (Lopez et al. 2014) and up to six telescopes in the near-infrared at the CHARA array (Che et al. 2012); these two facilities have a maximum baseline of 130 m and 330 m, respectively. However, the extension of this current direct detection scheme represents a major technical challenge, in particular because of the infrastructure requested to operate the vacuum delay lines and the recombination of a large number of telescopes, which cannot necessarily be extrapolated from current existing infrastructures.

In this context, heterodyne detection, in which incident light is coherently detected on each telescope, has been proposed as a potential alternative in the mid-infrared (Townes 1984; Swenson 1986; Ireland & Monnier 2014). Although heterodyne detection is commonly used in the radio to submillimeter domain, its extrapolation to higher frequencies (1 THz to several 10s THz) is limited by a radically different instrumentation compared to radio and submillimetric interferometry, and more fundamentally, by its lack of sensitivity at higher frequency. There are two reasons for this lack of performance. First, at equal bandwidth, there is a relative penalty in signal-to-noise ratio (S/N) between direct and heterodyne detection due to the fundamental quantum noise in heterodyne detection, which is a degradation that has been estimated to be on the order of ~40 by Hale et al. (2000). Second there is a very narrow instantaneous detection bandwidth in heterodyne detection (a few GHz typically) compared to the frequency (30 THz at 10 μm) of the incident radiation. On the other hand, heterodyne detection offers the advantage of recombining a large number of telescopes without a loss in S/N in contrast to direct detection.

The work presented in this paper should be placed in the context of a global effort to examine how present-day technology allows us to revisit the true performance of a mid-infrared heterodyne astronomical interferometer composed of tens of telescopes and how it can be fairly compared with a direct interferometry approach. In this work, we do not attempt a full comparison, that we reserve to a forthcoming paper. We do explore one novel approach to one of the building blocks of such an interferometer: the correlator.

Open Access article, published by EDP Sciences, under the terms of the Creative Commons Attribution License (https://creativecommons.org/licenses/by/4.0), which permits unrestricted use, distribution, and reproduction in any medium, provided the original work is properly cited.

Following the idea laid out by Swenson et al. (1986) and Ireland & Monnier (2014) we propose that part of the sensitivity issue of the heterodyne concept related to the bandwidth limitation can be overcome by using synchronized laser frequency combs as local oscillators (LOs) and detectors with much higher bandwidths. In this framework, the incoming celestial light interferes with a frequency comb and is dispersed to sample tens to hundreds of adjacent spectral windows. In addition, progress in mid-infrared technology has recently led to spectacular improvement of more than an order of magnitude of the detection bandwidth, in particular with the emergence of graphene detectors (Wang et al. 2019), which have a frequency response of up to 40 GHz, and quantum well infrared photodetectors (QWIP) (Palaferri et al. 2018) demonstrated at 20 GHz. These developments bear the promise of even higher bandwidths of up to 100 GHz, more than an order of magnitude larger than what has been used on sky. As a consequence, as pointed out by Ireland & Monnier (2014), this detection scheme raises the formidable challenge of correlating thousands of pairs of signals.

The three-beam Infrared Spatial Interferometer (ISI) was based on the use of an analog radio frequency (RF) correlator with an input bandwidth ranging from 0.2 GHz to 2.8 GHz, using passive RF components. In the same way, Cosmological Microwave Background (CMB) interferometry has a long history of developing analog RF wideband correlators (Dickinson 2012); an analog lag-correlator design recently reached up to 20 GHz bandwidth (Holler et al. 2011). Although these developments in CMB interferometry could constitute immediate attractive solutions, several difficulties inherent to wideband RF technology limit its use in the short and medium term, for infrared interferometry. The 20 GHz correlator presented in Holler et al. (2011) requires a specific RF design based on a custom-made Gilbert cell multiplier and Wilkinson splitter tree at the limit of the current technology and this design is unlikely to go far above 40 GHz any time soon. Parasitic frequency, although not a fundamental limit, could also turn out to be a disadvantage of wideband RF systems. On the numerical side the currently most advanced digital correlation systems are those developed for the Northern Extedend Array (NOEMA; Gentaz 2019) or for the Atacama Large Millimiter Array (ALMA; Escoffier et al. 2007). For NOEMA, the PolyFIX correlator currently accepts the widest instantaneous bandwidth per antenna. The PolyFIX correlator can process 32 GHz wide digitized signals coming from 12 antennas (8 GHz per receptor for the two polarizations and two sidebands). ALMA correlator can process 8 GHz wide signals coming from up to 64 antennae. Both approaches are worth exploring for infrared interferometry when considering an array of a few telescopes that have detector instantaneous bandwidths of a few 10 GHz and only a few spectral channels. However, their extrapolation to instantaneous bandwidths of 50 GHz–100 GHz such as the bandwidths expected with new generation detectors, tens of telescopes and tens to hundreds of spectral bands call for a different approach. As evaluated in Ireland & Monnier (2014), this requires custom made developments with computing power at least two orders of magnitude greater than the existing correlators.

In order to tackle this conundrum, we propose a photonic solution to the problem of the correlation of broadband RF signals. We exploit the old idea of transmitting RF signals over optical waveguides to encode the intermediate frequency (IF) beating between the incoming signal and the local oscillator onto a coherent optical carrier, which could then be processed by the means of photonic operations. Remarkably, the past decade has seen an impressive development of microwave photonics, which aims precisely at generating, routing, and processing broadband RF signals, using standard photonic techniques (Capmany & Novak 2007; Nova Lavado 2013). The ability to couple such analog processing with optical transport over fiber, compatible with standard telecom components, provides the building blocks of an analog correlator.

In this paper we introduce the idea of a correlator for infrared heterodyne interferometry that makes use of photonic phase modulators to encode the RF beating signal onto a coherent carrier. Our scheme is based on commercially available electro-optic phase modulators and fiber-optics components. These can handle up to 50 GHz (off the shelf) and bear the promises of hundreds of GHz capability (Burla et al. 2019). In Sect. 2, we present the principles of a simple correlation architecture with two telescopes, which reproduces the equivalent function of the initial ISI analog correlator. The experimental results of a proof of principle of this concept are presented in Sect. 3, where two heterodyne beating signals have been generated experimentally, and correlated a posteriori on a photonic correlator several months later. The perspective and limits of this technique are discussed in Sect. 4. Conclusions are drawn in Sect. 5. A theoretical sensitivity study, taking into account the instrumental parameters of a practical infrastructure, the gain in detection bandwidth introduced by a photonic correlator, the extrapolation in a multiplexed architecture, and its comparison with a direct detection scheme for a large number of telescope will be the object of a follow-up paper.

2. Principles of a photonic correlator

2.1. Principles of infrared heterodyne interferometry

As in radio astronomy, a single baseline heterodyne interferometer is composed of two distant telescopes on which the incident light is coherently detected by its mixing with a stable frequency reference, referred to as the local oscillator (LO), on a detector squaring the field. In the optical domain, the LO is a laser, and the detector a fast photodiode. Assuming a local oscillator $E_{\rm LO}$ and an incident field E_S the heterodyne signal at each telescope is written as

$$\begin{aligned} i_k &\propto |E_S(t) + E_{\rm LO}(t)|^2 \\ &\propto ||E_S|e^{-i((\omega_{\rm LO}\pm\omega_{\rm IF})t+\phi_S(t))} + |E_{\rm LO}|e^{-i(\omega_{\rm LO}t+\phi_{\rm LO}(t))}|^2 \\ &\propto |E_S|^2 + |E_{\rm LO}|^2 + 2|E_S||E_{\rm LO}|\,{\rm Re}\left(e^{-i(\pm\omega_{\rm IF}t+(\phi_S(t)-\phi_{\rm LO}(t))}\right), \end{aligned} \quad (1)$$

where $\omega_{\rm LO}$ is the laser angular frequency, $\omega_{\rm IF}$ the IF detected in the RF range, and ϕ_S and $\phi_{\rm LO}$ the phases of the signal and LO, respectively. The signal angular frequency is denoted as $\omega_S = \omega_{\rm LO} \pm \omega_{\rm IF}$ to highlight the lower and upper sidebands of the signal; these are downconverted at the same IF $\omega_{\rm IF}$. The measured optical intensity thus contains a beating term proportional to the electric field, enabling the detection of the phase. After filtering through the detection chain, with transfer function $H(\omega)$, the beating term $s_k(t)$ is written (Boyd 1983) as

$$s_k(t) = 2H(\omega_{\rm IF}) \cdot |E_S||E_{\rm LO}| \cos\left(\pm\omega_{\rm IF}t + (\phi_S(t) - \phi_{\rm LO}(t))\right). \quad (2)$$

As these signals coming from each telescope are proportional to the input electric field, their multiplication is proportional to the coherent flux $Fe^{i\phi_o}$ of the source, where $\phi_o = 2\pi\frac{\vec{B_p}\cdot\vec{\sigma}}{\lambda}$ the phase of the astrophysical object, $\vec{B_p}$ the projected baseline, $\vec{\sigma}$ the angular coordinate of the object from the phase center, and

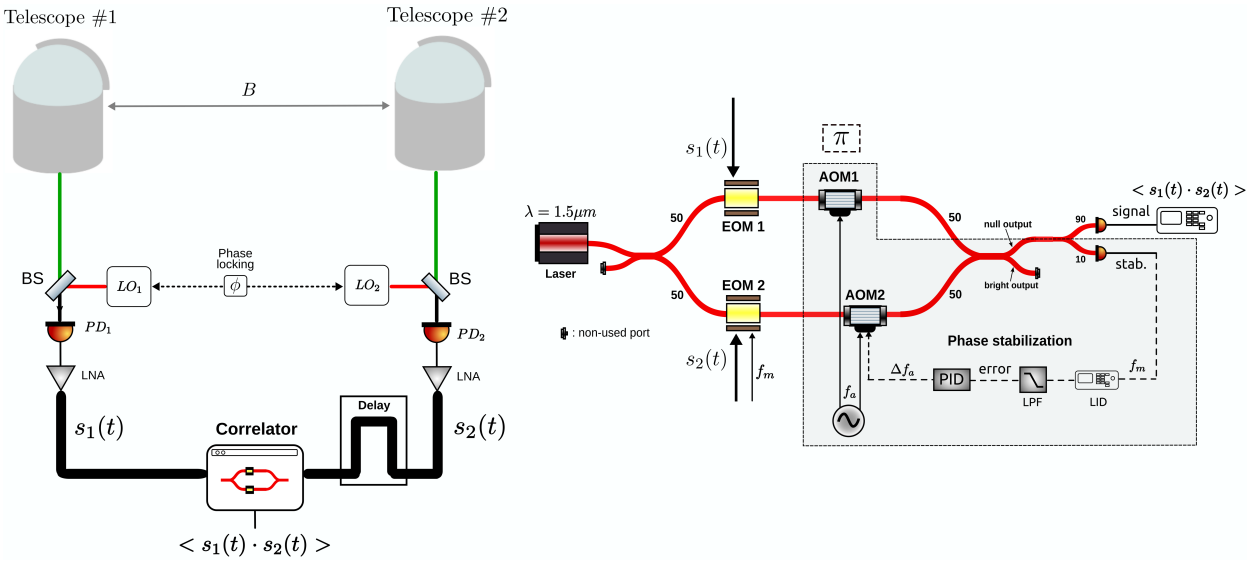

Fig. 1. *Left*: general layout of a 2 telescopes heterodyne interferometer. *Right*: general layout of an optical correlator. A Mach-Zehnder interferfermometer, stabilized at the zero null, is modulated by EOMs placed in each arm. In this configuration, the output of the photodiode contains a term proportional to the product of the RF signals at the input of each modulator. Abbreviations as follows: LO: local oscillator; BS: beam splitter; PD: photo-diode; LNA: low-noise amplifier; LID: lock-in detection; LPF: low-pass filter; PID: proportional integral derivator; AOM: acousto-optic modulator; EOM: electro-optic modulator.

λ the central wavelength. More specifically, in the case in which the two sidebands $\pm\omega_{\rm IF}$ are not separated, the product of the two voltages from each telescope is (Thompson et al. 2017; Monnier 1999)

$$r(t) = \langle s_1(t) \cdot s_2(t) \rangle = C|F||G(\tau)| \cos(\phi_o + \Delta\omega_{\rm LO} t) \cos(\phi_G + \omega_c \tau), \quad (3)$$

assuming the detection bandwidth could be modeled with a rectangular filter function of width $\Delta\omega$, centered around ω_c, where τ is the relative delay between the two optical signals, $\Delta\omega_{\rm LO}$ the frequency difference between the LOs, C a constant, and $|G(\tau)|e^{i\phi_G} = \frac{1}{2\pi} H_0^2 \Delta\omega \left[\frac{\sin(\Delta\omega\tau/2)}{\Delta\omega\tau/2}\right]$ the frequency response of the detection chain that has an amplitude H_0. This expression corresponds to the signal of a double-sideband correlator (DSB), in which the fringes are modulated at the frequency $\Delta\omega_{\rm LO}$. Importantly, we assume in Eq. (3) that the relative phase between the LOs $\Delta\phi_{\rm LO} = \phi_{L01}(t) - \phi_{L02}(t)$ is null and stable over the time of detection, that is, that the LOs are phase-locked to each other. In practice, this phase-locking can be obtained either by distributing the same LO or by measuring a beating signal between each distant LOs, in both cases on a phase-stabilized link. In addition, in the following, the object phase ϕ_o is assumed to be constant, that is, the atmospheric piston fluctuations are assumed to be negligible during an integration time.

2.2. Principles of a double-sideband photonic correlator

In its simple form, the function required at the level of the correlator thus consists in multiplying two input signals with a very wide bandwidth. In this section, we show that this multiplication product can be achieved with a simple photonic design.

We consider a Mach-Zehnder interferometer, as represented in Fig. 1, in each arm of which is inserted a phase modulator with a characteristic voltage V_π. In a phase modulator, the V_π is defined as the equivalent tension for which a phase shift of π is introduced. Each phase modulator transposes the wide bandwidth RF signal coming from a telescope onto a monochromatic optical carrier. Assuming that the voltage amplitude is small compared to V_π, and writing $\beta = \frac{\pi}{V_\pi}$, the optical field after each phase modulators is

$$E_k(t) = E_0 e^{i(\omega_0 t + \phi_k + \beta s_k(t))} \approx E_0 e^{i(\omega_0 t + \phi_k)}(1 + i\beta s_k(t)). \quad (4)$$

If a total relative phase shift of $\Delta\phi = \phi_2 - \phi_1 = \pi$ is applied between the arms, the interferometer is placed in a quadratic regime and the output intensity of the Mach-Zehnder can be simply written as

$$\begin{aligned} i(t) &= |E_1(t) + E_2(t)|^2 \\ &= |E_0|^2\beta^2\Big(s_2(t) - s_1(t)\Big)^2 \\ &= |E_0|^2\beta^2\Big(s_1^2(t) + s_2^2(t) - 2s_1(t)s_2(t)\Big). \end{aligned} \quad (5)$$

We note that if, for example, a phase shift of $\pi/2$ was used, there would not be a beat signal $s_1 \cdot s_2$ between the two signals in the output. The two first quadratic terms appear as noise signals spread out over the wide frequency range of phase modulators. In turn, the last term is the product of the incident signal coming from the telescope, which is proportional to the coherent flux, as described in Eq. (3). In the case in which $\Delta\omega_{\rm LO} \neq 0$, the DSB product signal is modulated at the frequency $\Delta\omega_{\rm LO}$, and thus gives access to a measurement of the coherent flux of the interferometer. This fringe peak can be integrated over a very restricted frequency range around $\Delta\omega_{\rm LO}$, in which the relative contribution of the quadratic terms $s_k^2(t)$ can be neglected. In the above developments, it is fundamental to note that the total bandwidth is now limited by the bandwidth of the phase modulators. In practice, current standard off-the-shelf, fibered, electro-optic modulators (EOMs) at telecom wavelength reach a bandwidth of 50 GHz, and EOMs with flat-frequency response beyond 500 GHz have been demonstrated (Burla et al. 2019). Such bandwidths would represent a crucial improvement of the input bandwidth at the level of the correlator.

2.3. Signal distribution and phase stabilization

In this correlation scheme, the telescope signals are converted at the level of each telescope on an optical carrier by means of an EOM. The signal could then propagate through telecom fibers over kilometric distance, avoiding the problem of bandwidth limitations. This scheme is only possible under the condition in which the optical link is phase-stabilized over large distance to guarantee a stable functioning point at the Mach-Zehnder's null; this stresses the importance of a robust phase stabilization scheme.

Given the similarities of the photonic correlation with the principle of operation of a nulling interferometer, the phase stabilization scheme developed in this frame (Gabor et al. 2008) could be adapted in the present case. However, stabilization through phase modulation, by the use of EOMs or a fiber stretcher, could only be applied on a limited optical path difference (OPD) range, which may be a limit for kilometric optical links. Alternatively, in Sect. 3.2.2, we detail the principle of a fast phase stabilization scheme of the null based on frequency modulation of the optical carrier, which can correct an arbitrary OPD amplitude variation.

3. Proof of concept and practical implementation

In this section, we present the proof of principle of a DSB photonic correlator dedicated to infrared heterodyne interferometry. In Sect. 3.1, we detail the test bed used on a broadband laboratory source to generate an equivalent heterodyne signal of a two element interferometer. Section 3.2 describes the practical implementation of the photonic correlator and its phase stabilization scheme based on frequency modulation. In Sect. 3.3, we finally present the a posteriori correlation through this photonic correlator of the two signals previously generated on the two-telescope test bed, together with a measurement of the temporal coherence of the broadband source initially used, and we provide an estimation of the S/N degradation through the correlator.

3.1. Two telescope heterodyne signal generation

The general purpose of the two-telescope simulator is to produce a correlated signal on two seperated detectors, whose signal could reproduce the beating between a broadband source of radiation and two LOs with a stable relative phase. The experiment was carried out at telecom wavelengths for practical reasons, but could be generalized to other optical wavelengths, in particular the N band, which is the target of the present study. We emphasize that the purpose of this test bed was not to evaluate the sensitivity limit of a complete detection chain from the detectors to the output of the photonic correlator, which would necessitate dedicated mid-infrared detectors and LOs, but to produce representative correlation signals in terms of coherence properties at the entrance of the photonic correlator. We acknowledge that typical astrophysical sources in the near- (H band) or mid-infrared (N band) are significantly fainter than in this proof of concept. The characterization of a complete mid-infrared detection chain, on objects at the detection limit and low S/N, would be the next step of this study.

This test bed is described on Fig. 2. The representative elements of a two-telescope interferometer in the test bed are the following:

Local oscillator. A laser at 1.55 μm is separated in two arms. Given the sub-kHz linewidth of the laser, the two equivalent LOs distributed on each arm are naturally in phase at the timescale of the measurement. In addition, as in ISI, a small frequency difference is applied between each arm by means of two acousto-optic modulators (AOMs). As this fequency difference is also the modulation frequency of the fringes, it has been experimentally set to $\Delta f = f_2 - f_1 = 7$ MHz, which is a spectrum region in which parasitic RF frequencies were absent. Since these modulators are designed so as to operate at 80 ± 10 MHz, their frequency are set to $f_1 = 80$ MHz and $f_2 = 87$ MHz.

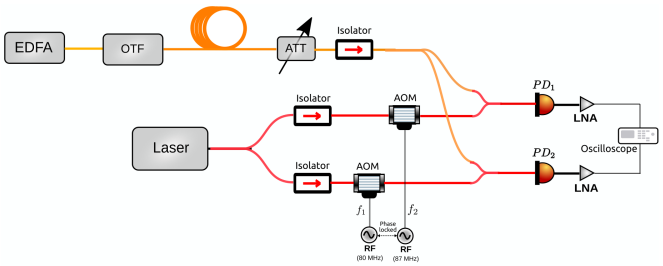

Fig. 2. Scheme of the simulator of a 2 telescopes interferometer at telecom wavelength. A shift of $\Delta f = 7$ MHz is introduced between each LO by the use of AOMs driven at $f_1 = 80$ MHz and $f_2 = 87$ MHz. The signal registered at the output of each PD has then been regenerated and correlated a posteriori on the optical correlator.

Broadband source. We used an erbium-doped fiber amplifier (EDFA), without an input signal, as a broadband input source. An EDFA is a pumped gain medium, usually used in telecom to amplify an incident radiation. Without any input, it emits a broadband light spectrum through amplified spontaneous emission (ASE) of radiation. The ASE then passes through an optical tunable filter (OTF) adjusted to the few GHz bandwidth of the detector to limit the shot noise associated with the incident source. This source is finally divided in two arms, and distributed to two detectors. Once again, we emphasize that this source of radiation was not used to evaluate the sensitivity limit of a heterodyne detection in the near-infrared, but to reproduce representative coherence properties of a heterodyne signal.

Detection. The local oscillator and the input broadband source signal are combined and detected on two separate fast detectors. As a first step, a correlation peak at 7 MHz was directly observed with an RF mixer, which multiplies the output of the two detectors. Multiple RF cables were successively used to introduce a delay $\sim 1/\Delta\nu$ to scan the coherence length and to assess that the signal was not a parasitic frequency of the setup. In a second step, the output of each detectors were simultaneously recorded on a fast oscilloscope at a sampling rate of 2 Gb s^{-1}, with an analog bandwidth $\Delta\nu = 400$ MHz, which is the upper bandwidth limit in our detection scheme.

A posteriori generation. Once registered, these two RF traces were electronically generated a posteriori by arbitrary-waveform generators (AWGs) to perform the a posteriori correlation on the photonic correlator. Given the limited memory of the AWG, a set of 2^{16} points were generated at a sampling rate of 50 MHz. Taking into account the dilatation factor between registration and regeneration, the peak frequency was thus placed at a frequency 175kHz after regeneration.

3.2. Experimental implementation of the photonic correlator and phase stabilization

In this subsection, we detail the experimental implementation of the photonic correlator described in Sect. 2. As this photonic

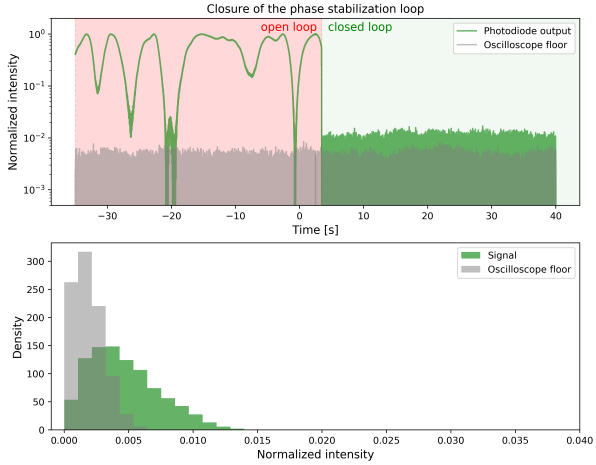

Fig. 3. Phase stabilization scheme. *Top*: open-loop is highlighted in red, closed-loop in green. The photodiode output signal (green line) is just above the oscilloscope dark current (gray), which limits the effective contrast of the null. *Bottom*: histogram of the photodiode output is shown. Asymmetric shape of the photodiode output is typical of a null output.

processing is independent of the carrier wavelength, its implementation could greatly benefit from the development of fibered components from telecom standards, which were also used in this proof of principle.

3.2.1. Photonic processing

The actual implementation is represented in Fig. 1. A sub-kHz linewidth laser at 1.55 μm is equally divided into two arms with a 50:50 fibered splitter. Each arm is then modulated by an EOM, on which is applied the RF signal generated a posteriori from one of the two-telescope simulator traces, as described in Sect. 3.1. A feedback loop is used to stabilize the phase of the Mach-Zehnder, and the two arms are recombined with another 50:50 fibered coupler. Finally, at the null output of this fibered Mach-Zehnder, the flux is split in two parts with a 90:10 fibered splitter, where 90% of the flux is sent to the signal photodiode and 10% of the flux to a detector used in the stabilization loop detector. After the signal photodiode, the fringes are modulated at the frequency $f = 175$ kHz, which can either be registered on an ADC, a lock-in amplifier, or a Fourier-transform oscilloscope. We adopted the latter solution.

3.2.2. Phase stabilization loop

The general goal of the phase stabilization loop is to maintain the photonic correlator at the null intensity of the Mach-Zehnder. In the intensity null, the output intensity varies quadratically with the input voltage. The basic idea of the stabilization consists in generating a small amplitude phase modulation signal at a defined frequency f_m in one arm, and using the real part of the first harmonic signal as an error signal to be minimized. Usually, the command signal is applied on a phase modulator (e.g., PZT, fiber stretcher, or EOM) to compensate for OPD variation. In this case, we set up a frequency modulation system, composed of two AOMs, where one is modulated in frequency by a proportional-derivative (PD) controller. Integrated over a small of time dt, this frequency modulation Δf_m acts as a phase modulation $\mathrm{d}\Phi_m = \Delta f_m \mathrm{d}t$, which is restricted neither in amplitude nor in speed in contrast to an OPD modulator system. Figure 3 represents the closure of the phase stabilization loop. We estimated its stability to a mean phase deviation of $\overline{\phi} = \lambda/240$, and RMS deviation of $\sigma_\phi = \lambda/440$.

It has though to be noted that in such a frequency modulation scheme, large OPD drifts, on the order of a fraction of the coherence length $l_c = c/\Delta\nu$, have to be corrected by a dedicated OPD offset. However, given a maximum spectral bandwidth of $\Delta\nu \approx 100$ GHz, the coherence length is on the order of millimeter scale, thus requiring only occasional offset correction after minute or hour timescales.

3.3. Noise factor and temporal coherence

Once stabilized on the null, the signals a posteriori generated by the AWGs are applied to the phase modulators. According to Eq. (5), a fringe peak is observed at the modulation frequency $\frac{f_G}{f_S}\Delta f_{\mathrm{OL}} = 175$ kHz, where f_S is the recording sampling frequency and f_G is the generation sampling frequency. This fringe signal is easily visible in the power spectral density of the photocurrent (PSD), as shown in Fig. 4. In order to estimate the degradation introduced by the photonic correlator on the signal, we measured the noise factor, defined as the ratio of input and output S/N, as follows:

$$\mathrm{NF} = \frac{(S/N)_{\mathrm{in}}}{(S/N)_{\mathrm{out}}}. \tag{6}$$

We estimated input S/N from the two recorded waveforms, by computing numerically the interference term in Eq. (5). Fringe power and noise are estimated on two defined frequency windows, as shown if Fig. 4, by computing the integrated power in the peak and the standard deviation of the noise floor, respectively. Output S/N is then estimated with the same method on the PSD of the photodiode output, on the same exact frequency windows. This analysis provides a ratio of the output S/N on the input S/N: $1/\mathrm{NF} = 87\% \pm 5\%$ that is, a S/N degradation of 13%, also corresponding to NF = 1.15. This result is limited by a non-negligible oscilloscope dark current, as seen in the histogram of Fig. 3, and a strong contribution of a low-frequency $1/f$, as visible in Fig. 4, which artificially degrade the S/N of the fringe peak, but are not fundamentally due to the optical correlator.

In addition, we assessed the temporal properties of our correlation signal to observe its coherence envelope and give an additional verification that the fringe peak observed could not be produced by a parasitic signal. To do so, a numerical delay is introduced at the level of one AWG, for each value for which we measured the fringe peak power. The coherence envelope is shown on Fig. 4, and superposed to the coherence envelope computed numerically. The experimental profile fits a Gaussian with a full width at half maximum (FWHM) $\tau \approx 20$ ns, which corresponds to an equivalent bandwidth $\Delta f = 1/\tau \sim 50$ MHz. This is consistent with the maximum bandwidth of our regenerated signal with a sampling frequency $f_S = 50\,\mathrm{MS\,s^{-1}}$. Moreover, this measurement removes the possibility that the fringe peak is a parasitic signal.

4. Discussion

4.1. Further developments

In this section, we discuss the further developments to be led in the path towards a practical correlator, dedicated to an imaging facility with kilometric baselines. In a second section, we discuss at a more general level the remaining open challenges of infrared heterodyne interferometry.

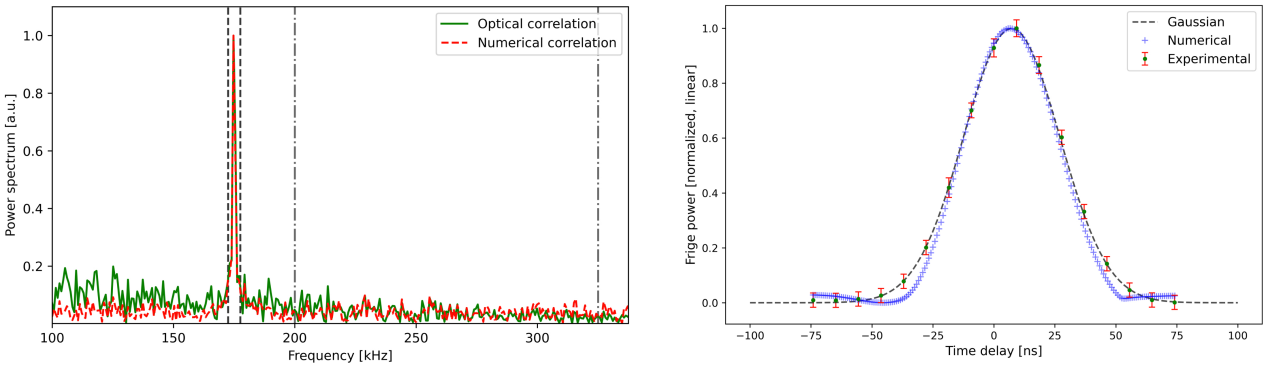

Fig. 4. *Left*: fringe peak at the ouptut of the correlator (y-axis, in linear scale). The red dashed line indicates the numerical correlation of the input signal. The green solid line shows the correlation of the signal through the optical correlator. *Right*: coherence envelope of the fringe signal (green dot), and envelope computed numerically (blue cross). The experimental envelope fits a Gaussian profile, which differs from the numerical computation only at the feet of the envelope. This could be imputed both to the experimental measurement uncertainties and to the estimation of the impulse response of the AWG.

4.1.1. Photometric calibration and delay compensation

In the continuity of our demonstration of signal correlation, the next steps of the development consist in measuring the spatial coherence of a laboratory object in the mid-infrared. For this purpose, a detailed procedure of photometric calibration will have to be carried out in order to normalize the coherent flux measured on the source and to deduce an estimate of the visibility. Furthermore, in this work we did not address the problem of delay compensation and earth rotation. Earth rotation translates into a phase velocity that can be computed and compensated at the level of a local oscillator by a dedicated frequency shift, which is also called lobe rotation. In addition, we did not address a group delay, which has to be compensated for in order to track the maximum of the correlation envelope within a coherence length l_c. This delay can be covered using a combination of switchable fibered delay, compensating for the large delays, and a continuously adjustable fibered delay line, covering small delays and relaxing the minimum resolution of the switchable module. We note that the design complexity of such a movable delay line, at telecom wavelength and on a very narrow spectral band, would be considerably lower than the design complexity of a direct mid-infrared vacuum delay line. As in telecom networks, dispersion could be managed with the use of dispersion compensating fibers, over a bandwidth of 100 GHz in this case, but with propagation distances significantly smaller than that encountered in telecom, up to a few kilometers in this case. The speed of the movable delay line could be relaxed by a careful control of the frequency shift of lobe rotation.

4.1.2. Measurements with $N \geq 3$

This measurement with two telescopes could then lead to a generalization of the method to more than two telescopes, and in particular to the measurement of closure phases with three telescopes, in a way that is analogous to the method performed on the ISI correlator (Hale et al. 2003). We note that from the perspective of achieving image reconstruction with a large number of telescopes ($N \geq 12$), the encoding of the signal on an optical carrier also offers the possibility to recombine all the fibers into an homothetic pupil plane, as in a Fizeau configuration, which would enable us to use the array in a direct imager mode. The transposition of the technique presented in this paper, where fringes are modulated at a given frequency (7 MHz), may be adapted by lowering the modulation frequency to a rate compatible with a 2D-matrix acquisition rate (typically smaller than kHz), although this method does not seem optimal. Instead, direct phase stabilization scheme, as experimentally demonstrated in Blanchard et al. (1999) may possibly allow for direct imager acquisitions without applying a frequency modulation. Signal-to-noise preservation has, however, not yet been considered for this scheme, nor has it been demonstrated in Blanchard et al. (1999).

4.2. Open challenges of infrared heterodyne interferometry

Although we addressed the problem of correlation and signal transportation by the introduction of a photonic correlator and photonic processing, several challenges remain open on the path to a practical mid-infrared heterodyne interferometer.

The first problem we did not address in the heterodyne system is the synchronization of distant LOs separated by kilometric distances. We recall that this requirement concerns at least the relative phase between the different local oscillator, which has to be constant during a coherent integration time. For this purpose, the beating of each LO with an LO that serves as a master and reference can be used to apply a correction to each LO through a dedicated phase-lock-loop (PLL), a strategy that was implemented in ISI with up to three telescopes (Hale et al. 2000, 2003). In practice, such a stabilization scheme would imply that we propagate each mid-infrared local oscillator on kilometric distances in our case, which imposes strong constraints in a practical infrastructure. The possibility to stabilize in phase each mid-infrared LOs with the distribution of a reference phase signal through a fiber link, in a way analogous to Chanteau et al. (2013) for example, would substantially simplify the infrastructure of a mid-infrared heterodyne interferometer.

The second problem that we did not address concerns the limit in sensitivity imposed by atmospheric phase fluctuations, which severely restricts the maximum coherent integration time. Previous studies (Ireland & Monnier 2014; Ireland et al. 2016) already raised this limitation, and proposed an out-of-band cophasing based on a companion instrument in the H band. Although this auxiliary instrument would be a direct interferometer, which is apparently in contradiction with the heterodyne detection scheme proposed, its implementation in the H band would surely be much easier than in the mid-infrared with the use of fiber components. In the case in which this atmospheric cophasing were absent, the *heterodyne* interferfometer would still be functional, but limited to bright objects.

Concerning the improvement of sensitivity, the introduction of this paper was based on the observation that current detectors now enable us to reach several tens of gigahertz of bandwidth in the mid-infrared. These compelling demonstrations will need further development to consolidate these results, in particular regarding the exact characterization and optimization of their quantum efficiency.

Finally, as proposed in Swenson (1986), revived in Ireland & Monnier (2014), and from a more prospective view, a promising but difficult method to further increase the sensitivity of an heterodyne interferometer would consist in multiplexing a large number of LOs, with the associated number of detectors, to potentially obtain a spectral coverage comparable to direct detection. This method supposes the generation of mid-infrared frequency combs that have sufficient power per teeth, which constitutes a present active field of research. We note that such a multiplexed architecture could be advantageously coupled to a photonic correlation.

5. Conclusions

Within the context of infrared heterodyne interferometry, we have introduced the use of photonic correlation in order to overcome the bandwidth limitation of the correlators developed so far. We proposed the architecture of a DSB correlator for two telescopes based on the use of a fibered Mach-Zehnder at telecom wavelength, precisely stabilized at the null of intensity, and demonstrated the a posteriori correlation of two signals previously generated on a dedicated two-telescope test bed in the near-infrared. For this purpose, we realized a dedicated phase stabilization loop based on frequency modulation. The final photonic processing chain exhibits a degradation of the S/N of 13%, corresponding to a noise factor NF = 1.15. The coherence properties of the initial input signals were also retrieved by introducing an incremental temporal delay. The next step of this development will consist in measuring the spatial coherence of an object in the mid-infrared with two telescopes, and to generalize this architecture to more than two telescopes and to the detection of closure phases. More generally, this proof of principle opens the way to the photonic processing and transportation of wide bandwidth signals for infrared heterodyne interferometry, which could constitute a valuable advance in the perspective of kilometric baseline interferometry with a large number of telescopes.

Acknowledgements. We thank the anonymous referee for his/her constructive remarks that improved our initial manuscript. This work was supported by the Action Spécifique Haute Résolution Angulaire (ASHRA) of CNRS/INSU, co-funded by CNES. We acknowledge the funding of Agence Nationale de la Recherche (“ANR FROST”, ANR-14-CE32-0022). The authors thank Jean-Baptiste Le Bouquin for his very relevant advice during the optimization of the set-up. The authors also thank Etienne Le Coarer for the always stimulating discussions with him and for having initiated our interest in this topic.

References

Blanchard, P. M., Greenaway, A. H., Harvey, A. R., & Webster, K. 1999, J. Lightwave Technol., 17, 418
Boyd, R. W. 1983, Radiometry and the detection of optical radiation, in Pure and Applied Optics (New York: Wiley)
Burla, M., Hoessbacher, C., Heni, W., et al. 2019, APL Photonics, 4, 056106
Capmany, J., & Novak, D. 2007, Nat. Photon, 1, 319
Chanteau, B., Lopez, O., Zhang, W., et al. 2013, New J. Phys., 15, 073003
Che, X., Monnier, J. D., Kraus, S., et al. 2012, Imaging from the First 6-beam Infrared Combiner, 8445 84450Z
Dickinson, C. 2012, Proc. meeting Resolving The Sky - Radio Interferometry: Past, Present and Future. April 17–20, 2012. Manchester, UK, 34, published online at http://pos.sissa.it/cgi-bin/reader/conf.cgi?confid=163
Escoffier, R. P., Comoretto, G., Webber, J. C., et al. 2007, A&A, 462, 801
Gabor, P., Chazelas, B., Brachet, F., et al. 2008, A&A, 483, 365
Gentaz, O. 2019, PolyFiX: Lessons learned from the NOEMA Wideband Correlator System, 16
Hale, D. D. S., Bester, M., Danchi, W. C., et al. 2000, ApJ, 537, 998
Hale, D. D. S., Fitelson, W., Monnier, J. D., Weiner, J., & Townes, C. H. 2003, Techniques for Measuring Phase Closure at 11 Microns, 4838, 387
Holler, C. M., Jones, M. E., Taylor, A.C., Harris, A. I., & Maas, S. A. 2011, ArXiv e-prints [arXiv:1112.1982]
Ireland, M. J., & Monnier, J. D. 2014, A Dispersed Heterodyne Design for the Planet Formation Imager, 9146, 914612
Ireland, M. J., Monnier, J. D., Kraus, S., et al. 2016, Status of the Planet Formation Imager (PFI) Concept, 9907 99071L
Lopez, B., Lagarde, S., Jaffe, W., et al. 2014, Messenger, 157, 5
Monnier, J. D. 1999, Infrared Interferometry and Spectroscopy of Circumstellar Envelopes, PhD thesis
Monnier, J. D., Kraus, S., Ireland, M. J., et al. 2018, Exp. Astron., 46, 517
Nova Lavado, E. 2013, PhD thesis, Universitat Politécnica de Catalunya, Spain
Palaferri, D., Todorov, Y., Bigioli, A., et al. 2018, Nature, 556, 85
Swenson, G. W. 1986, J. Opt. Soc. Am. A, JOSAA, 3, 1311
Swenson, Jr., G. W., Gardner, C. S., & Bates, R. H. T. 1986, Optical Synthesis Telescopes, 643, 129
Thompson, A. R., Moran, J. M., & Swenson, Jr., G. W. 2017, in Interferometry and Synthesis in Radio Astronomy, eds. A. Richard Thompson, J. M. Moran, & G. W. Swenson Jr., 3rd ed. (Springer), 2017
Townes, C. H. 1984, JApA, 5, 111
Wang, N., Cakmakyapan, S., Lin, Y.-J., Javadi, H., & Jarrahi, M. 2019, Nat. Astron., 3, 977

MACH II: MACH-Zehnder Analog Correlator for Heterodyne Infrared Interferometry

Guillaume Bourdarot[a,b], Jean-Philippe Berger[a], Hugues Guillet de Chatellus[b], and Jean-Baptiste Le Bouquin[a]

[a]Univ. Grenoble Alpes, CNRS, IPAG, F-38000 Grenoble, France
[b]Univ. Grenoble Alpes, CNRS, LIPhy, F-38000 Grenoble, France

ABSTRACT

The path toward a large imaging interferometer in the infrared, as proposed within the framework of the Planet Formation Imager initiative, represents an incredibly exciting and complex challenge of future infrared interferometry. In this context, heterodyne detection has been proposed as a potential alternative in order to recombine a large number of telescopes, with kilometric baselines, in a practical infrastructure, despite a poorer sensitivity compared to classical interferometry. Among the different building blocks necessary to an infrared heterodyne interferometer, the detection and correlation of wide-bandwidth signals remains a big obstacle, in particular to gain further in sensitivity. Here, we propose to address the problem of transport and correlation of wide-bandwidth signals over kilometric distances by presenting the concept of a photonic correlation dedicated to infrared heterodyne interferometry. We present the concept, the implementation and the experimental results for the correlation of two signals with a phase modulation implementation, its possible extrapolation to a larger number of telescopes and spectral channels, and an alternative correlation scheme based on amplitude modulation.

Keywords: Photonic, Infrared Interferometry, Heterodyne Detection, Planet Formation Imager

1. INTRODUCTION

The extension of infrared interferometry to an imaging facility with milli-arcsecond resolution and below, as proposed within the Planet Formation Imager initiative, represents a major objective of future interferometry [1]. Such an instrument would require a large number of telescopes (N $\geq$ 12), in order to obtain a (u,v)-coverage that is compatible with imaging, with kilometric baselines. The exact path towards such a facility remains an open challenge, with major aspects still to be solved, such as the infrastructure requested to operate the vacuum delay lines, or the recombination of a large number of telescopes [2].

In this context, heterodyne detection, in which incident light is coherently detected at the level of each telescope, has been proposed as a potential alternative in the mid-infrared [3]. Heterodyne interferometry was first proposed and demonstrated on the Infrared Spatial Interferometer (ISI) by C.H. Townes and his group at UC Berkeley [4, 5], and was the first method able to recombine 2 telescopes in the mid-infrared in the early 90s, then followed by 3 telescopes with closure phases in the early 2000s [6]. These observations have led to a notable science program for his time [7–9], but were ultimately limited by the poor sensitivity of heterodyne detection. This well-known limitation originate from two main reasons : 1) heterodyne detection suffers from a fundamental quantum noise, whose density is equivalent to one photon of noise per detection mode [5] 2) the very narrow detection bandwidth of heterodyne detection (of the order of the GHz typically), which means that the total signal is detected in a single spectral channel with a spectral resolution $R \sim 30\,000$. This bandwidth is limited by the instantaneous bandwidth of the mid-infrared detector, and by the correlation processing available downstream.

Further author information :
Guillaume Bourdarot : guillaume.bourdarot@univ-grenoble-alpes.fr

Two complementary ways can be envisioned to go beyond this sensitivity limitations. First, the massive multiplexing of the spectral channels using synchronized frequency comb, as proposed by [10] and revived in [3] within the PFI projet. Second, the increase of the instantaneous bandwidth of each detector. Spectacular progress have recently led to an improvement of more than an order of magnitude of the detection bandwidth in the mid-infrared, in particular with quantum well infrared photodetectors (QWIP) which have been demonstrated up to 70 GHz [11, 12] or graphene detector [13]. These developments bear the promise of even higher bandwidths, up to 100 GHz, and already more than one order of magnitude larger than what has been used on ISI. However, an architecture involving more than ten telescopes, tens to hundreds of spectral channel, and a total of instantaneous bandwidth of the order of the order of 1 THz, raises the formidable challenge of the correlation these signals, and in any case challenges the current capabilities of state of the art ADCs and available computing power. As estimated by [3], the requirement on the correlator tends towards specific major developments, with a total computing power at least two orders of magnitude larger than existing ALMA correlator.

In this context, we propose to address the problem of the transport and correlation of signals introducing the concept of a photonic processing dedicated to infrared heterodyne interferometry. We present the general concept in which these developments take place, and detail its experimental implementation, along with the results obtained with a demonstrator designed for two telescopes. We then explore the possible extrapolation of this correlation architecture to a large number of telescopes and a large number of spectral channel. Finally, we introduce succinctly a second concept of photonic correlation architecture based on amplitude modulation, which could overcome some limitations of the phase modulation scheme and could be explored as a second photonic correlation scheme.

2. GENERAL PRINCIPLE

The idea at the basis of a photonic correlation is to encode the RF signal coming from each mid-infrared detectors, which is directly proportional to the optical field according to heterodyne detection, onto a monochromatic optical carrier which can be propagated over fibers, and processed with photonic components to recover the correlation product of two wide-bandwidth RF signals Fig 1 . In this scheme, the optical carrier is a monochromatic laser, modulated by an electro-optical modulator, and in this sense, is truly compatible to the standard operation operation of telecom fibers and telecom components. It should be noted that the exact wavelength of this correlation stage would not be constrained by the incident astronomical signal, which depends on the central wavelength of the mid-infrared local oscillator and of the detector, but can be chosen at the wavelength which is the most convenient to process, in this case telecom wavelength.

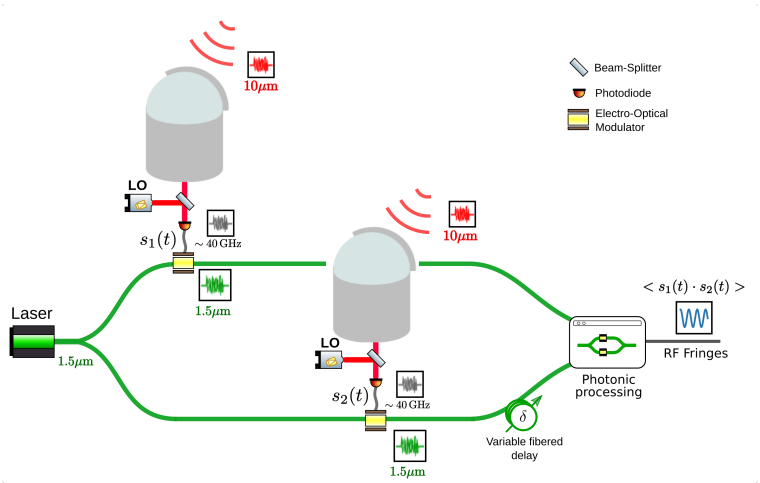

Figure 1. General principle of a photonic correlator for a 2 elements heterodyne interferometer.

The basic operation required at the level of this analogical correlator unit consists in computing the correlation product of one detection bandwidth at one given delay, which means to perform the product of two wide-bandwidth RF signals and to integrate the results in time. In particular, it would differ from the so-called digital correlators of sub-millimetric arrays such as ALMA and NOEMA, which recover the complete correlation function of the input signals. In this sense, such an analog unit perform an operation equivalent to the one pointed out by [3], which is specifically targeted for infrared heterodyne interferometry, given the different requirements in terms of spectral resolution between infrared and sub-millimetric interferometry. This results in a dramatic simplification of the correlation unit for infrared heterodyne interferometry, in particular with regards to the requirement at the level of the ADC (digitalization of 100 GHz signals) and computing power (100 GHz, and ultimately several 100 GHz to THz).

In the next section, we detail the principle and the practical implementation of a two element correlation unit based on a phase modulation scheme. We present the implementation of this idea on a demonstration testbed at telecom wavelength, along with preliminary results obtained on this demonstrator, also presented in [14].

3. PRACTICAL IMPLEMENTATION AND RESULTS

3.1 Coherent detection in heterodyne interferometry

As in radio astronomy, a single baseline heterodyne interferometer is composed of two distant telescopes on which the incident light is *coherently* detected by its mixing with a stable frequency reference, referred to as the *local oscillator* (LO), on a detector squaring the field. In the optical domain, the LO is a laser, and the detector a fast photodiode. The measured optical intensity thus contains a beating term proportional to the electric field, enabling the detection of the phase. Assuming a local oscillator E_{LO} and an incident field E_S, after filtering through the detection chain with transfer function $H(\omega)$, the beating term $s_k(t)$ is written as [15]

$$s_k(t) = 2H(\omega_{IF}) \cdot |E_S||E_{LO}| \cos\left(\pm\omega_{IF}t + (\phi_S(t) - \phi_{LO}(t))\right). \tag{1}$$

where ω_{LO} is the laser angular frequency, ω_{IF} the IF detected in the RF range, and ϕ_S and ϕ_{LO} the phases of the signal and LO, respectively. The signal angular frequency is denoted as $\omega_S = \omega_{LO} \pm \omega_{IF}$ to highlight the lower and upper sidebands of the signal; these are downconverted at the same IF ω_{IF}.

As these signals coming from each telescope are proportional to the input electric field, their multiplication is proportional to the coherent flux $Fe^{i\phi_o}$ of the source, where $\phi_o = 2\pi\overrightarrow{B_p} \cdot \overrightarrow{\sigma}/\lambda$ the phase of the astrophysical object, $\overrightarrow{B_p}$ the projected baseline, $\overrightarrow{\sigma}$ the angular coordinate of the object from the phase center, and λ the central wavelength. More specifically, in the case in which the two sidebands $\pm\omega_{IF}$ are not separated, this expression corresponds to the signal of a double-sideband correlator (DSB), in which the fringes are modulated at the frequency $\Delta\omega_{LO}$. The product of the two voltages from each telescope is [16, 17]

$$\langle s_1(t) \cdot s_2(t) \rangle = C|F||G(\tau)| \cos(\phi_o + \Delta\omega_{LO}t) \cos(\phi_G + \omega_c\tau),$$

where τ is the relative delay between the two optical signals, $\Delta\omega_{LO}$ the frequency difference between the LOs, C a constant, and assuming the detection bandwidth could be modeled with a rectangular filter function of width $\Delta\omega$, centered around ω_c, such that the frequency response of the detection chain is written $|G(\tau)|e^{i\phi_G} = \frac{1}{2\pi}H_0^2\Delta\omega\left[\frac{\sin(\Delta\omega\tau/2)}{\Delta\omega\tau/2}\right]$, with H_0 an amplitude constant. Importantly, we assume in Eq. (2) that the relative phase between the LOs $\Delta\phi_{LO} = \phi_{L01}(t) - \phi_{L02}(t)$ is null and stable over the time of detection, that is, that the LOs are phase-locked to each other. In practice, this phase-locking can be obtained either by distributing the same LO or by measuring a beating signal between each distant LOs, in both cases on a phase-stabilized link. In addition, in the following, the object phase ϕ_o is assumed to be constant, that is, the atmospheric piston fluctuations are assumed to be negligible during an integration time.

3.2 Principles of a double-sideband correlator based on phase modulation

As explained in the section [2], the function required at the level of the correlator consists in multiplying two input signals with a very wide bandwidth. Here, we show how this multiplication can be achieved with a simple phase modulation design.

We first consider a Mach-Zehnder interferometer, as represented in Fig.1, in each arm of which is inserted a phase modulator with a characteristic voltage V_π. In a phase modulator, the V_π is defined as the equivalent tension for which a phase shift of π is introduced. Each phase modulator transposes the wide bandwidth RF signal coming from a telescope onto a monochromatic optical carrier. Assuming that the voltage amplitude is small compared to V_π, the optical field after each phase modulators is

$$E_k(t) = E_0 e^{i\left(\omega_0 t + \phi_k + \frac{\pi}{V_\pi} s_k(t)\right)} \approx E_0 e^{i(\omega_0 t + \phi_k)} \left(1 + i\pi\, s_k(t)/V_\pi\right). \tag{2}$$

If a total relative phase shift of $\Delta\phi = \phi_2 - \phi_1 = \pi$ is applied between the arms, the interferometer is placed in a quadratic regime and the output intensity $i(t) = |E_1(t) + E_2(t)|^2$ of the Mach-Zehnder can be simply written as

$$i(t) = |E_0|^2 \left(\frac{\pi}{V_\pi}\right)^2 \Big(s_2(t) - s_1(t)\Big)^2 = |E_0|^2 \left(\frac{\pi}{V_\pi}\right)^2 \left(s_1^2(t) + s_2^2(t) - 2s_1(t)s_2(t)\right). \tag{3}$$

We note that if, for example, a phase shift of $\pi/2$ was used, there would not be a beat signal $s_1 \cdot s_2$ between the two signals in the output. The two first quadratic terms appear as noise signals spread out over the wide frequency range of the phase modulators. In turn, the product of the incident signal coming from the telescope, which is proportional to the coherent flux, as described in Eq.(2). In the case in which $\Delta\omega_{LO} \neq 0$, the DSB product signal is modulated at the frequency $\Delta\omega_{LO}$, and thus gives access to a measurement of the coherent flux of the interferometer. This fringe peak can be integrated over a very restricted frequency range around $\Delta\omega_{LO}$, in which the relative contribution of the quadratic terms $s_k^2(t)$ can be neglected. In the above developments, it is fundamental to note that the total bandwidth is now limited by the bandwidth of the phase modulators, which can typically reach 40 GHz with off-the-shelf component, and have been demonstrated up to 500 GHz in dedicated experiment [18].

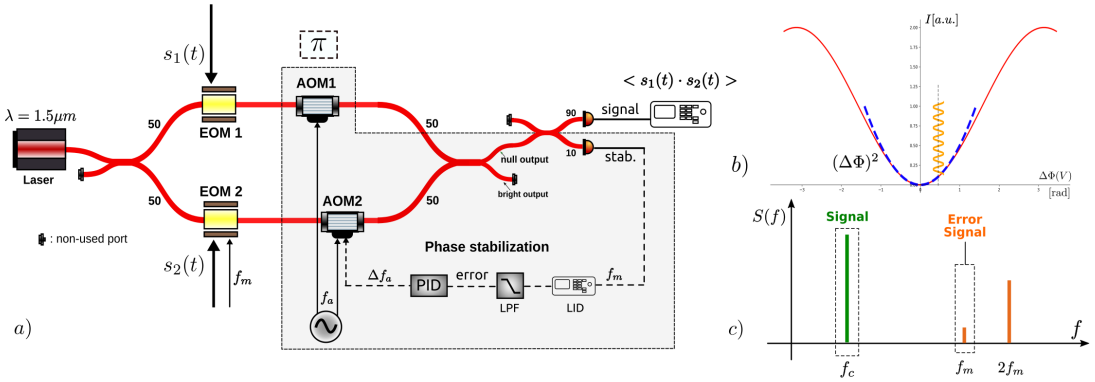

Figure 2. Proof-of-concept demonstrator implemented with phase modulation. a) Details of the optical set-up, including the phase stabilization loop, which locks precisely the output of the Mach-Zehnder to the null. b) Quadratic variation of the intensity with respect to the phase difference between the two arms of the Mach-Zehnder. The orange sinusoid is a small amplitude reference modulation at frequency f_m, which enables to probe the position of the interferometer in the quadratic profile, and thus to lock the fringes c) In the frequency spectrum (RF domain), a deviation from the null intensity is monitored with the amplitude of the 1st harmonic f_m, which constitutes the error signal of the phase stabilization loop. The amplitude of the fringes (signal) are encoded at the frequency f_c, which is independent from f_m.

3.3 Practical implementation & phase stabilization

3.3.1 Practical implementation

The correlation architecture was implemented on an experimental testbed, as described in Fig. A stable linewidth laser at 1.55 μm is equally divided into two arms with a 50:50 fibered splitter. Each arm is then modulated by an EOM, on which is applied one the RF signals to be correlated. A feedback loop is used to stabilize the phase of the Mach-Zehnder, and the two arms are recombined with another 50:50 fibered coupler. Finally, at the null output of this fibered Mach-Zehnder, the flux is split in two parts with a 90:10 fibered splitter, where 90% of the flux is sent to the signal photodiode and 10% of the flux to a detector used in the stabilization loop detector. This splitting was done for more convenience, but could also be done downstream the science photodiode without flux splitting. After the signal photodiode, the fringes are modulated at the frequency $f = 175\,\mathrm{kHz}$, which can either be registered on an ADC, a lock-in amplifier, or a Fourier-transform oscilloscope. We adopted the latter solution.

3.3.2 Phase stabilization

This scheme is only possible under the condition in which the optical link is phase-stabilized over large distance to guarantee a stable functioning point at the Mach-Zehnder's null; this stresses the importance of a robust phase stabilization scheme. Given the similarities of the photonic correlation with the principle of operation of a nulling interferometer, the phase stabilization schemes developed in this frame [19] could be adapted in the present case. However, stabilization through phase modulation (e.g., PZT, fiber stretcher, or EOM) could only be applied on a restricted range of optical path difference (OPD) perturbations, which may constitute a limitation of the setup given the phase perturbation accumulated on kilometric optical links. Alternatively, in order to avoid such limitations, both in amplitude and in speed, we propose a phase stabilization scheme based on frequency modulation instead, which can correct rapid and arbitrary amplitude OPD perturbations.

In the intensity null, the output intensity varies quadratically with the input voltage. The basic idea of the stabilization consists in generating a small amplitude phase modulation signal at a defined frequency f_m in one arm, and using the real part of the first harmonic signal as an error signal to be minimized. Usually, the command signal is applied on a phase modulator to compensate for OPD variation. In this case, we set up a frequency modulation system, composed of two AOMs, where one is modulated in frequency by a proportional-derivative (PD) controller. Integrated over a small of time dt, this frequency modulation Δf_m acts as a phase modulation $\mathrm{d}\Phi_\mathrm{m} = \Delta \mathrm{f_m dt}$, which is restricted neither in amplitude nor in speed in contrast to an OPD modulator system. This principle was implemented on our testbed, and used routinely to stabilize the experiment. Fig.3 represents the closure of the phase stabilization loop.

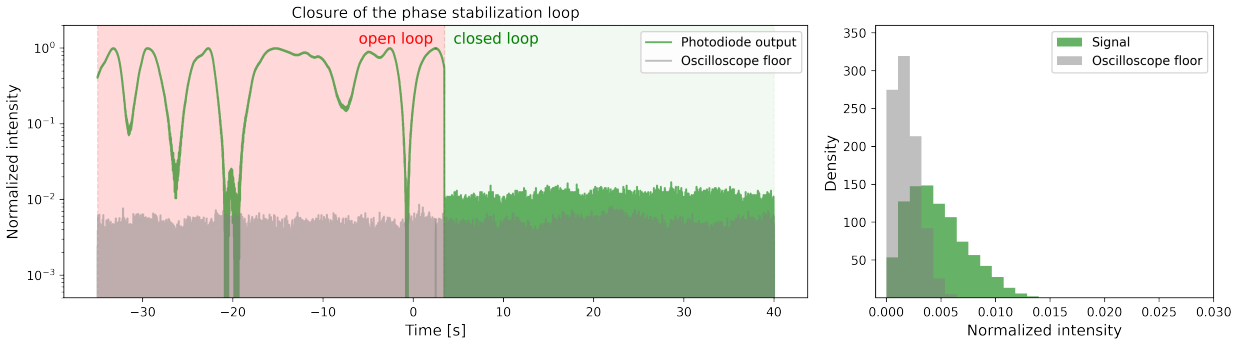

Figure 3. Laboratory results of the phase-stabilization loop. Left : Open-loop is highlighted in red, closed-loop in green. The photodiode output signal (green line) is just above the oscilloscope dark current (gray), which limits the effective contrast of the null. Right : Histogram of the photodiode output is shown. Asymmetric shape of the photodiode output is typical of a null output.

3.4 Results and SNR preservation

Once stabilized on the null, two correlated RF signals, originating from photodiode outputs of a heterodyne simulator at 1.5μ m (described [14]), are generated by two Arbitratry Waveform Generators (AWGs) and applied to the phase modulators. The goal of such a simulator was not to evaluate the sensitivity limit of a complete heterodyne detection chain at 1.55μ m, given the largely defovarable SNR at this wavelength regime, but to reproduce a beating signal between a broadband source of radiation and a laser. It should also be noted that for test purposes, dedicated simulated numerical signals could also be used. Once these modulations are applied to the EOMs, a fringe peak is observed at the modulation frequency $\frac{f_G}{f_S}\Delta f_{OL} = 175\,\text{kHz}$, according to Eq. (3), where f_S is the recording sampling frequency and f_G is the generation sampling frequency. This fringe signal is visible in the power spectral density of the photocurrent (PSD), as shown in Fig. 4. In order to estimate the degradation introduced by the photonic correlator on the signal, we measured the noise factor NF = $\frac{(S/N)_{in}}{(S/N)_{out}}$, defined as the ratio of input and output S/N.

We estimated input S/N from the two recorded waveforms, by computing numerically the interference term in Eq.(3). Fringe power and noise are estimated on two defined frequency windows, as shown if Fig.4, by computing the integrated power in the peak and the standard deviation of the noise floor, respectively. Output S/N is then estimated with the same method on the PSD of the photodiode output, on the same exact frequency windows. This analysis provides a ratio of the output S/N on the input S/N : 1/NF = 87%$\pm$5% that is, a S/N degradation of 13%, also corresponding to NF = 1.15. This result is limited by a non-negligible oscilloscope dark current, as seen in the histogram of Fig.3, and a strong contribution of a low-frequency $1/f$, as visible in Fig.4, which artificially degrade the S/N of the fringe peak, but are not fundamentally due to the optical correlator.
In addition, we assessed the temporal properties of our correlation signal to observe its coherence envelope and give an additional verification that the fringe peak observed could not be produced by a parasitic signal. To do so, a numerical delay is introduced at the level of one AWG, for each value for which we measured the fringe peak power. The coherence envelope is shown on Fig.4, and superposed to the coherence envelope computed numerically. The experimental profile fits a Gaussian with a full width at half maximum (FWHM) $\tau \approx 20\,\text{ns}$, which corresponds to an equivalent bandwidth $\Delta f = 1/\tau \sim 50\,\text{MHz}$. This is consistent with the maximum bandwidth of our regenerated signal with a sampling frequency $f_S = 50\,\text{MS/s}$. Moreover, this measurement removes the possibility that the fringe peak is a parasitic signal.

3.5 Fibered delay, fringe rotation

At this point, we have not yet addressed the problem of delay compensation and earth rotation. Earth rotation translates into two features, which have to be compensated for. First, a phase velocity that can be computed and easily compensated for at the level of a local oscillator by a dedicated frequency shift, which is also called lobe rotation, as it was routinely done on the ISI for example. More complex, the group delay has to be adjusted to track the maximum of the correlation envelope within a coherence length l_c. This delay can be covered both in the RF domain or directly in the photonic correlator, using a combination of switchable fibered delay, compensating for the large delays, and a continuously adjustable fibered delay line, covering small delays and relaxing the minimum resolution of the switchable module. We note that the design complexity of such a movable delay line, at telecom wavelength and on a very narrow spectral band, would be considerably lower than the design complexity of a direct mid-infrared vacuum delay line. As in telecom networks, dispersion could be managed with the use of dispersion compensating fibers, over a bandwidth of 100 GHz in this case, but with propagation distances significantly smaller than that encountered in telecom, up to a few kilometers in this case. The speed of the movable delay line could be relaxed by a careful control of the frequency shift of lobe rotation. In practice, these considerations could benefit from the strong compatibility with telecom technologies, and the emergence of commercial fibered delay lines.

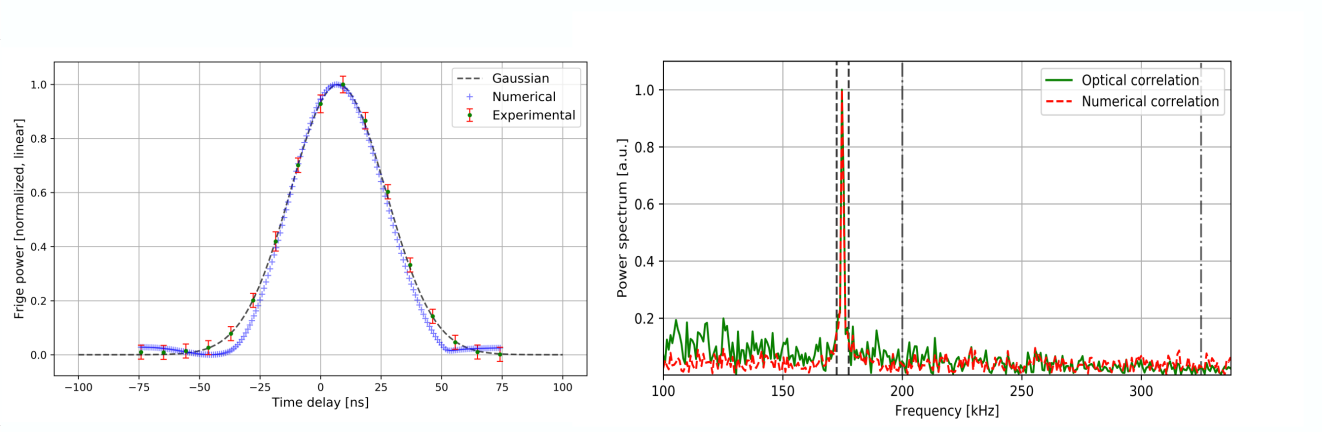

Figure 4. Left: Fringe peak at the outptut of the correlator (y-axis, in linear scale). The red dashed line indicates the numerical correlation of the input signal. The green solid line shows the correlation of the signal through the optical correlator. Right: The coherence envelope of the fringe signal (green dot), and the envelope computed numerically (blue cross) are shown. The experimental envelope fits a Gaussian profile, which differs from the numerical computation only at the feet of the envelope. This could be imputed both to the experimental measurement uncertainties and to the estimation of the impulse response of the AWG.

4. EXTENSION TO AN IMAGING ARRAY AND A LARGE NUMBER OF SPECTRAL CHANNELS

In this section, we discuss the possible extension of the photonic correlation concept demonstrated with two telescopes to an array with a larger number of telescopes. In contrast with classical interferometry, the signals detected in heterodyne interferometry can be conveniently splitted and amplified without significant additional noise or losses [5]. As a consequence, point source SNR in heterodyne interferometry scales as N_{tel}, compared to $\sqrt{N_{\mathrm{tel}}}$ in classical* interferometry. An additional advantages, though not directly related to the number of telescopes, of the use of heterodyne detection, is the ability to calibrate simultaneously the photometry without further degradation of the SNR, contrarily to classical interferometry. At this stage of the study, we propose two prospective schemes, the first one based on pair-wise combination of each baseline, which can be seen as the most intuitive scaling of the concept demonstrated with two telescopes, and the second one based direct imaging, already proposed in a different context by [20].

4.1 Extension to a large number of telescope

4.1.1 Pair-wise correlation

The most direct extrapolation of the phase modulation scheme to a large number telescopes consists in the pair-wise combination of each baseline. This pairwise combination is necessary to stabilize each baseline at a quadratic functioning point of the Mach-Zehnder (intensity minimum or maximum). It also enables to have access to the relative phase perturbations between each baselines, although the monitoring of the phase perturbations would necessitate only a subsytem of N_{tel} independent measurements.

To this end, pairwise combination could be done directly in integrated optics combiners, which were also developed within the frame of astronomical applications, in particular for infrared interferometry [21–23]. In that case, the use of such an integrated optic component would take full advantage of the fact that optical carrier is a monochromatic laser at telecom wavelength, with potentially large optical power and a controlled

*Except for an hypertelescope architecture (densified pupil), which is not anticipated to be part of the PFI design, for reasons exposed in [2]

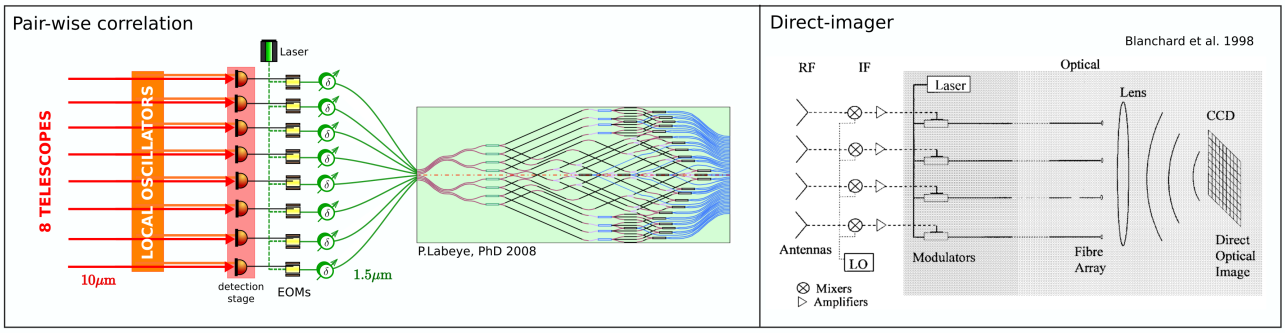

Figure 5. Possible extrapolation of photonic correlation concept with phase modulation to N telescopes. *Left, Pair-wise combination* : each telescope pair is formed and detected separately in an integrated optic combiner, from which the interferometric visibilities are extracted. . *Right, Direct Imaging combination* : a scaled version of the telescope array is formed in the pupil plane of lens, and the image through the array is directly registered on a camera [20].

linear polarization. As mentioned above, it has to be underlined that the division of the optical carrier does not cause fundamental losses of sensitivity here given that the signal can be amplified, as long as the noise of the photonic processing chain does not degrade the global SNR. A careful noise analysis of the photonic processing should be carried in this direction. From a more practical point of view, a 4T to 8T combiner could be directly implemented for a combination up to 8T, using the AC-combiner developed within the frame of PIONIER instrument and VSI study [22]. Here, the AC design would enable to monitor both the null and bright output of the Mach-Zehnder i.e. the quadratic minimum and maximum, whereas a simple pairwise combination would produce alternately a bright and a dark output depending of the baseline, given that a π-phase shift could not be obtained simultaneously between all baseline on a simple pairwise combiner.

4.1.2 Direct imaging mode

We have described so far a recombination method which enables to extract the correlation product for each baseline i.e. is sensible to the visibility amplitude and phase (or closure phase, in the absence of fringe-tracking), on which model fitting or image reconstruction can be perform. A second method of recombination could consist in directly forming an image from the pupil plane, in a so-called "direct imager" mode, similar to a Fizeau recombination mode. In the case of a photonic processed signal, this mode consist in forming a scaled replica of the telescope array in the pupil plane of a lens, with the ends of the fibers on which the RF-signal is encoded. The interferometric image then formed directly in the focal plane of the lens, and can be recorded on a camera in real-time. Such a technique would mostly by advantageous for the combination of a large number of telescope, the separate measurement of each visibility amplitude being more preferable.

A similar concept has already been proposed in [20] in the context of millimiter wave array imaging. Together with this concept, Blanchard et al. present a proof-of-principle demonstration, implemented with a so-called Redundant Space Calibration (RSC) procedure to correct the phase perturbations in single-shot acquisition, although the noise budget of this concept is not evaluated. This concept was then revived and developed by different authors in [24, 25], in the context of aerospace and defense applications, and advanced demonstrations of a complete imaging system with 224 millimetric apertures are presented in [24], with a special emphasis on the optimization of the noise figure of the detection chain. The system developed in [24] already reach a technological level compatible with commercial systems, which gives good confidence on the scaling of such a concept, although a thorough signal-to-noise analysis should be conducted in the perspective of application to infrared heterodyne interferometry.

4.2 Spectral channel multiplexing

At this stage, we have addressed the question of the correlation of a large number of telescopes, but not the additional correlation of a large number of *spectral* channels. In what follows, we will consider only the pairwise correlation scheme, given that it enables to extract the interferometric visibilities for each baseline.

Here we propose that the extrapolation of this phase modulation scheme to a large number of spectral channels can be enabled by the use of telecom technologies developed in a similar frame, in particular through WDM/DWDM techniques. This multiplexing can be perform by encoding the RF signal coming from each detector, each one associated to one tooth of the frequency comb, onto a laser with a specific wavelength through a dedicated EOM, all these fibers being recombined and transported in the same output fiber to the integrated combiner. These encoding wavelengths have to be sufficiently close to each other, so that the same fibers and integrated components could be used without prohibitive chromatic effect. On the other part, they have to be sufficiently separated to be demultiplexed by standard DWDM at the output of the integrated optics combiner. At the output of the integrated combiner, each detector, spectrally demultiplexed, is then associated to one given spectral channel of the mid-infrared comb.

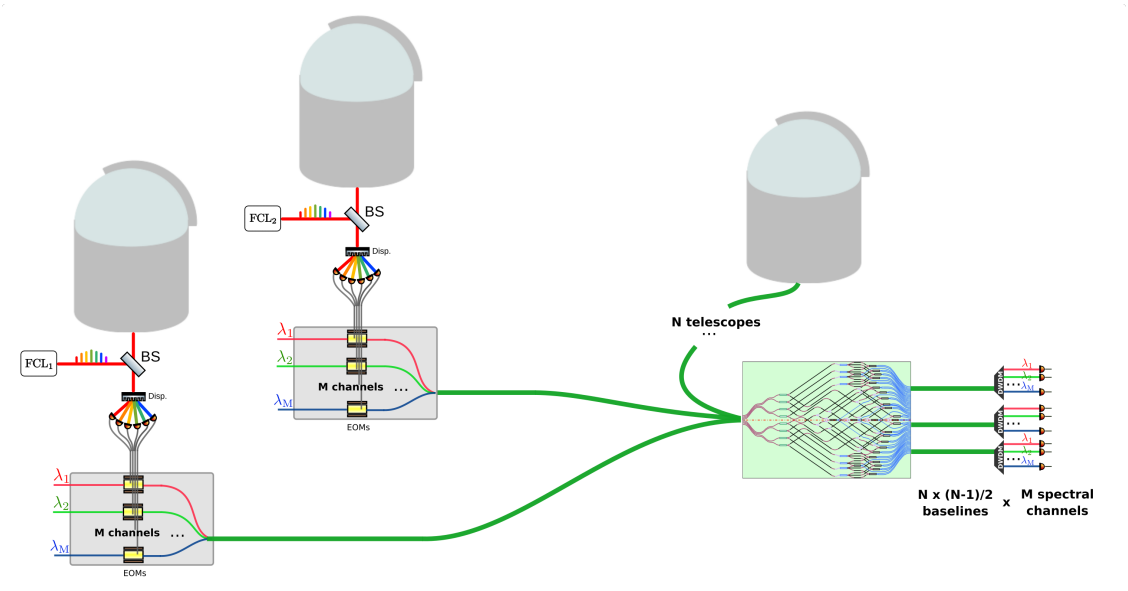

Figure 6. Possible extrapolation of photonic correlation to N telescopes, M spectral channels. Each spectral channel is encoded on a different wavelegth λ_1, λ_2... λ_M near 1.5μm, and separated with a DWDM after the pairwise correlation.

5. AN ALTERNATIVE CORRELATION SCHEME WITH AMPLITUDE MODULATION

In this section, we propose a second preliminary correlation scheme, based on amplitude modulation, and discuss its difference with the phase stabilization scheme, in particular in terms of phase stabilization.

We consider a Mach-Zehnder in which each EOM presented in Sec.3.2 are replaced by amplitude modulators. These amplitude modulators consist themselves in integrated Mach-Zehnder, whose relative phase difference between each arm can be controlled by internal EOM modulators. At the output of a single amplitude modulator, the electric field is written $E_1(t) = E_0 e^{i\omega_0 t}\left(1 + e^{i\pi\, s_1(t)/V_\pi} \cdot e^{i\phi_0}\right)$, with ϕ_0 the relative phase between each arms inside the modulator. ϕ_0 generally remains stable in time over timescale of the order of few minutes, and can be controlled easily, even with commercial systems, to lock the functioning point of the modulator.

We first consider that each amplitude modulator operates at the intensity minimum, with $s(t)$ small compared to V_π. In this case, the electric field is written $E_{1,2}(t) \approx -iE_0 \left(\frac{\pi\, s_{12}(t)}{V_\pi}\right) e^{i\omega_0 t}$, and the total intensity at the output of the interferometer is :

$$I(t) = I_0 \left[\left(\frac{\pi\, s_1(t)}{V_{\pi,1}}\right)^2 + \left(\frac{\pi\, s_2(t)}{V_{\pi,2}}\right)^2 + 2\left(\frac{\pi^2}{V_{\pi,1}V_{\pi,2}}\right) s_1(t)s_2(t)\cos(\phi_{12}(t)) \right] \tag{4}$$

with $\phi_{12}(t)$ the relative phase shift between each arm of the interferometer, which can vary in time. Here, the correlation term $\langle s_1(t) \cdot s_2(t) \rangle$ appears directly in the beating term at the output of the interferometer. However, in the absence of phase stabilization, this term is multiplied by $\cos(\phi_{12}(t))$, which perturbs the measure of the correlation product.

A way to circumvent this problem consists in introducing a relative frequency shift between each arm of the interferometer, for example with the AOMs presented previously. In such a case, the output intensity becomes :

$$I(t) = I_0 \left[\left(\frac{\pi\, s_1(t)}{V_{\pi,1}}\right)^2 + \left(\frac{\pi\, s_2(t)}{V_{\pi,2}}\right)^2 + 2\left(\frac{\pi^2}{V_{\pi,1}V_{\pi,2}}\right) s_1(t)s_2(t)\cos\left(2\pi f_s t + \phi_{12}(t)\right) \right] \tag{5}$$

with f_s the relative frequency shift introduced between each arms of the interferometer. Considering the expression of double-sideband correlation term $\langle s_1(t)s_2(t) \rangle$, if the frequency difference between each mid-infrared laser f_{LO} is null, the fringes are encoded at a single frequency peak at f_s ; if $f_{\mathrm{LO}} \neq 0$, the correlation peak is encoded at two frequency peaks centered around f_s, at $f_s - f_{\mathrm{LO}}$ and $f_s + f_{\mathrm{LO}}$. In this scheme, the correlation product $\langle s_1(t)s_2(t) \rangle$ is modulated at frequency f_s, and does not have to be stabilized exclusively at a given functioning point, in contrast to phase modulation. However, as the phase perturbation term acts in the same way as an atmospheric piston, the correlation product has to be measured in an integration time smaller than the typical time of the phase vibrations. In the case where these vibrations are negligible or have a typical time greater than the coherent integration time dictated by the atmosphere, this term has a negligible effect. Otherwise, a phase stabilization loop of the same type of the phase stabilization scheme has to be implemented, to avoid a loss of coherent flux.

These developments on amplitude modulation, along with a laboratory proof-of-principle demonstrators, phase stabilization scheme, and noise properties of the chain, are on-going work at IPAG and LIPhy, and offer an interesting alternative to phase modulation scheme. In particular, the extrapolation to a large number of telescopes and spectral channels could be facilitated and will be explored further in a future work.

6. CONCLUSION

Heterodyne interferometry has been proposed as a practical alternative to recombine a large number of telescope over kilometric baseline, despite a poorer sensitivity partly due to a limited available bandwidth. Herein, we have proposed to introduce the concept of a photonic correlation capable of transporting and processing signals up to 100 GHz with telecom components. We have presented an implementation of this concept and the preliminary results on a two element double-sideband continuum photonic correlator, for which a dedicated phase stabilization scheme was developed. This concept could be extended to a larger number telescopes with two possible combination schemes, one based on pair-wise combination with integrated optics, and an other based on a direct-imager combination. Finally, a second architecture based on amplitude modulation is proposed, and could enable to circumvent part of the phase-locking constrain inherent to the phase modulation scheme. Taken together, these concepts could offer a practical path toward the correlation of an imaging heterodyne interferometer with kilometric baseline.

ACKNOWLEDGMENTS

This project is currently funded by the Institut National des Sciences de l'Univers (INSU-CNRS) through Action Spécifique Hauté Résolution Angulaire (ASHRA) and CSAA and by the LabEx FOCUS.

REFERENCES

[1] Monnier, J. D., Kraus, S., Ireland, M. J., Baron, F., Bayo, A., Berger, J.-P., Creech-Eakman, M., Dong, R., Duchêne, G., Espaillat, C., Haniff, C., Hönig, S., Isella, A., Juhasz, A., Labadie, L., Lacour, S., Leifer, S., Merand, A., Michael, E., Minardi, S., Mordasini, C., Mozurkewich, D., Olofsson, J., Paladini, C., Petrov, R., Pott, J.-U., Ridgway, S., Rinehart, S., Stassun, K., Surdej, J., Brummelaar, T. t., Turner, N., Tuthill, P., Vahala, K., van Belle, G., Vasisht, G., Wishnow, E., Young, J., and Zhu, Z., "The planet formation imager," *Experimental Astronomy* **46**, 517–529 (Dec. 2018).

[2] Ireland, M. J., Monnier, J. D., Kraus, S., Isella, A., Minardi, S., Petrov, R., ten Brummelaar, T., Young, J., Vasisht, G., Mozurkewich, D., Rinehart, S., Michael, E. A., van Belle, G., and Woillez, J., "Status of the Planet Formation Imager (PFI) concept," **9907**, 99071L (Aug. 2016).

[3] Ireland, M. J. and Monnier, J. D., "A dispersed heterodyne design for the planet formation imager," **9146**, 914612 (July 2014).

[4] Townes, C. H., "Spatial interferometry in the mid-infrared region," *Journal of Astrophysics and Astronomy* **5**, 111–130 (June 1984).

[5] Hale, D. D. S., Bester, M., Danchi, W. C., Fitelson, W., Hoss, S., Lipman, E. A., Monnier, J. D., Tuthill, P. G., and Townes, C. H., "The Berkeley Infrared Spatial Interferometer: A Heterodyne Stellar Interferometer for the Mid-Infrared," *The Astrophysical Journal* **537**, 998–1012 (July 2000).

[6] Hale, D. D. S., Fitelson, W., Monnier, J. D., Weiner, J., and Townes, C. H., "Techniques for measuring phase closure at 11 microns," **4838**, 387–397 (Feb. 2003).

[7] Lopez, B., Danchi, W. C., Bester, M., Hale, D. D. S., Lipman, E. A., Monnier, J. D., Tuthill, P. G., Townes, C. H., Degiacomi, C. G., Geballe, T. R., Greenhill, L. J., Cruzalèbes, P., Lefèvre, J., Mékarnia, D., Mattei, J. A., Nishimoto, D., and Kervin, P. W., "Nonspherical Structures and Temporal Variations in the Dust Shell of o Ceti Observed with a Long Baseline Interferometer at 11 microns," *The Astrophysical Journal* **488**, 807–826 (Oct. 1997).

[8] Monnier, J. D., Danchi, W. C., Hale, D. S., Lipman, E. A., Tuthill, P. G., and Townes, C. H., "Mid-Infrared Interferometry on Spectral Lines. II. Continuum (Dust) Emission Around IRC +10216 and VY Canis Majoris," *The Astrophysical Journal* **543**, 861–867 (Nov. 2000).

[9] Townes, C. H., Wishnow, E. H., Hale, D. D. S., and Walp, B., "A Systematic Change with Time in the Size of Betelgeuse," *The Astrophysical Journal Letters* **697**, L127–L128 (June 2009).

[10] Swenson, G. W., "Radio-astronomy precedent for optical interferometer imaging," *J. Opt. Soc. Am. A, JOSAA* **3**, 1311–1319 (Aug. 1986).

[11] Palaferri, D., Todorov, Y., Bigioli, A., Mottaghizadeh, A., Gacemi, D., Calabrese, A., Vasanelli, A., Li, L., Davies, A. G., Linfield, E. H., Kapsalidis, F., Beck, M., Faist, J., and Sirtori, C., "Room-temperature nine-µm-wavelength photodetectors and GHz-frequency heterodyne receivers," *Nature* **556**, 85–88 (Apr. 2018).

[12] Hakl, M., Lin, Q. Y., Lepillet, S., Billet, M., Lampin, J.-F., Pirotta, S., Colombelli, R., Wan, W. J., Cao, J. C., Li, H., Peytavit, E., and Barbieri, S., "Ultra-fast quantum-well infared photodetectors operating at 10μm with flat response up to 70GHz at room temperature," *arXiv e-prints* , arXiv:2007.00299 (July 2020).

[13] Wang, N., Cakmakyapan, S., Lin, Y.-J., Javadi, H., and Jarrahi, M., "Room-temperature heterodyne terahertz detection with quantum-level sensitivity," *Nature Astronomy* **3**, 977–982 (July 2019).

[14] Bourdarot, G., Guillet de Chatellus, H., and Berger, J. P., "Toward a large bandwidth photonic correlator for infrared heterodyne interferometry. A first laboratory proof of concept," *Astronomy & Astrophysics* **639**, A53 (July 2020).

[15] Boyd, R. W., "Radiometry and the detection of optical radiation," *Wiley Series in Pure and Applied Optics, New York: Wiley, |c1983* (1983).

[16] Thompson, A. R., Moran, J. M., and Swenson, Jr., G. W., "Interferometry and Synthesis in Radio Astronomy, 3rd Edition," *Interferometry and Synthesis in Radio Astronomy, by A. Richard Thompson, James M. Moran, and George W. Swenson, Jr. 3rd ed. Springer, 2017.* (2017).

[17] Monnier, J. D., *Infrared interferometry and spectroscopy of circumstellar envelopes*, PhD thesis (1999).

[18] Burla, M., Hoessbacher, C., Heni, W., Haffner, C., Fedoryshyn, Y., Werner, D., Watanabe, T., Massler, H., Elder, D. L., Dalton, L. R., and Leuthold, J., "500 GHz plasmonic Mach-Zehnder modulator enabling sub-THz microwave photonics," *APL Photonics* **4**, 056106 (May 2019).

[19] Gabor, P., Chazelas, B., Brachet, F., Ollivier, M., Decaudin, M., Jacquinod, S., Labèque, A., and Léger, A., "Stabilising a nulling interferometer using optical path difference dithering," *Astronomy and Astrophysics* **483**, 365–369 (May 2008).

[20] Blanchard, P. M., Greenaway, A. H., Harvey, A. R., and Webster, K., "Coherent Optical Beam Forming with Passive Millimeter-Wave Arrays," *Journal of Lightwave Technology* **17**, 418–425 (Mar. 1999).

[21] Berger, J. P., Rousselet-Perraut, K., Kern, P., Malbet, F., Schanen-Duport, I., Reynaud, F., Haguenauer, P., and Benech, P., "Integrated optics for astronomical interferometry. II. First laboratory white-light interferograms," *Astronomy & Astrophysics* **139**, 173–177 (Oct. 1999).

[22] Labeye, P., "Integrated optics components for stellar interferometry," *arXiv e-prints* , arXiv:0904.3030 (Apr. 2009).

[23] Perraut, K., Jocou, L., Berger, J. P., Chabli, A., Cardin, V., Chamiot-Maitral, G., Delboulbé, A., Eisenhauer, F., Gambérini, Y., Gillessen, S., Guieu, S., Guerrero, J., Haug, M., Hausmann, F., Joulain, F., Kervella, P., Labeye, P., Lacour, S., Lanthermann, C., Lapras, V., Le Bouquin, J. B., Lippa, M., Magnard, Y., Moulin, T., Noël, P., Nolot, A., Patru, F., Perrin, G., Pfuhl, O., Pocas, S., Poulain, S., Scibetta, C., Stadler, E., Templier, R., Ventura, N., Vizioz, C., Amorim, A., Brandner, W., and Straubmeier, C., "Single-mode waveguides for GRAVITY. I. The cryogenic 4-telescope integrated optics beam combiner," *Astronomy & Astrophysics* **614**, A70 (June 2018).

[24] Schuetz, C., Martin, R., Dillon, T., Yao, P., Mackrides, D., Harrity, C., Zablocki, A., Shreve, K., Bonnett, J., Curt, P., and Prather, D., "Realization of a video-rate distributed aperture millimeter-wave imaging system using optical upconversion," in [*Passive and Active Millimeter-Wave Imaging XVI*], Wikner, D. A. and Luukanen, A. R., eds., *Society of Photo-Optical Instrumentation Engineers (SPIE) Conference Series* **8715**, 87150I (May 2013).

[25] Nova Lavado, E., *Millimeter-wave and terahertz imaging techniques*, ph.D. Thesis, Universitat Politècnica de Catalunya (July 2013).

V8: an 8 beam mid-infrared heterodyne instrument concept for the VLTI

Jean-Philippe Berger[a], Guillaume Bourdarot[a,b], and Hugues Guillet de Chatellus[b]

[a]Univ. Grenoble Alpes, CNRS, IPAG, F-38000 Grenoble, France
[b]Univ. Grenoble Alpes, CNRS, LIPhy, F-38000 Grenoble, France

ABSTRACT

The extension of infrared interferometry to an array with a large number of telescopes and kilometric baselines such as the Planet Formation Imager represents an exciting but formidable challenge. Such an infrastructure will require major technological developments, with several key aspects still to be solved on a mid and long term horizon. Mid-infrared heterodyne interferometry is considered as one potential technology despite its well documented lower sensitivity but its stronger scalability and lower hard infrastructure requirements. Exploring pathfinder instruments is a way to increase the maturity of interferometric technologies. In this study we propose to use the 8 VLTI telescopes (Unit and Auxiliary) as a coherent array using infrared heterodyne interferometry by exploiting the potential of state of the art technology in the field of high bandwidth detectors, laser frequency combs, fiber links and innovative photonics correlator. We analyze the sensitivity of an eight beam combining heterodyne instrument called V8 and present a possible sub-system breakdown. By comparing its performances with the ones advertised by ESO for MATISSE we conclude that V8, despite its lower sensitivity, has an interesting science potential since it allows to trade a higher limiting magnitude with an incomparable better mapping capability. As such it should be a formidable tool to explore evolved stars complex mass-loss processes. Moreover, it should allow the interferometry community to explore pathways for future long-baseline arrays, combining or not, direct and heterodyne interferometry.

Keywords: Interferometry, Heterodyne, Mid-Infrared, VLTI, Photonics, Laser, Frequency-combs

1. INTRODUCTION

From the birth of stars and planetary systems to supermassive black-holes, the recent observations of astronomical objects at the highest angular resolution have profoundly changed our vision of our surrounding universe. In this field, aperture synthesis with Very Long Baseline interferometry (VLBI) and optical infrared interferometry such as the Very Large Telescope Interferometer (VLTI) are currently the two techniques that provide the highest angular resolution achievable. With its shorter wavelength, infrared interferometry, still confined at 100m scale baseline, could be envisioned as one of the most promising technique to go even further. The extension of this techniques to a large number (N$\geq$20) of telescopes and kilometric baselines would represent a major step for observational astronomy. Nevertheless, such an infrastructure, as proposed in the context of the Planet Formation Imager (PFI) initiative[1] will also require challenging technological developments that cannot be extrapolated simply from existing instrumentation.[2]

In the current status of PFI, direct interferometry is the privileged option since it provides a major sensitivity gain in the short part of the mid-infrared spectrum (the 3-5 μm window) with respect to heterodyne. A fundamental quantum noise with a dramatically increasing effect at high frequencies explains its poor performance. However, this advantage is less strong in the N and Q mid-infrared bands.

Because it is less demanding on the infrastructure, and because the gain of direct interferometry at $\approx 10\mu$m is not so superior, heterodyne detection offers a still valuable and complementary path to address the problem of kilometric baseline and aperture synthesis with a large number of telescopes. In the past, through the pioneering work of maser inventor and Nobel Prize C.H. Townes and his team, heterodyne detection was the first

Further author information: (Send correspondence to Jean-Philippe Berger)
E-mail: jean-philippe.berger@univ-grenoble-alpes.fr

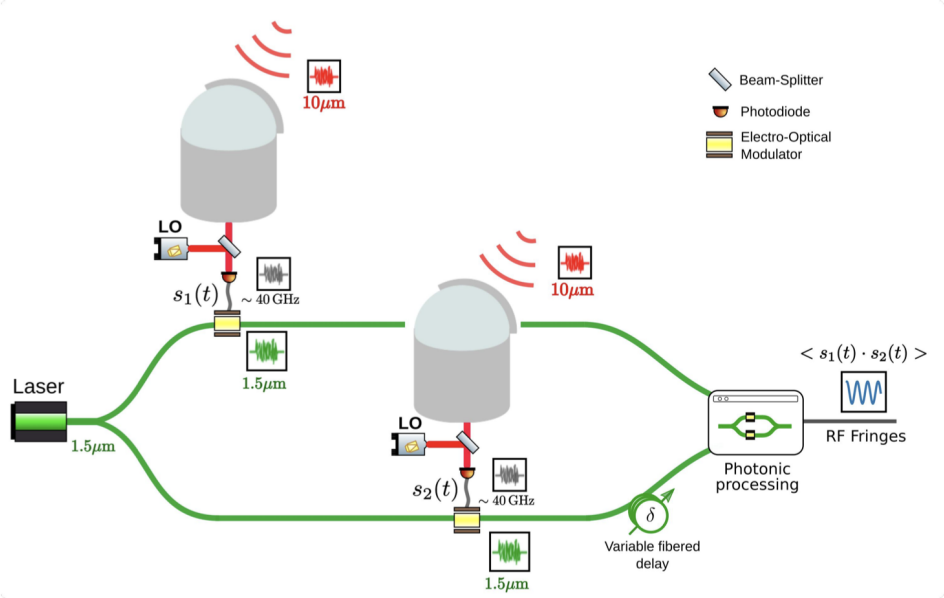

Figure 1. Conceptual scheme of a two telescope heterodyne optical chain

technique able to combine 2 telescopes in the mid-infrared and to measure closure phases with 3 telescopes, on the Infrared Spatial Interferometer (ISI) in UC Berkeley.[3–5] ISI provided valuable scientific results well ahead of its time, anticipating the following generation of direct mid-infrared interferometric instruments such as MIDI and MATISSE. Despite the sensitivity disadvantage in the 10 μm regime by a few factors (and almost none in the Q band), its strength deserves to be further explored, particularly in the context of an array of several tenths of telescopes (see also Ernest Michael's work in this conference Paper 11446-66)

We present here the idea that mid-infrared heterodyne interferometry is currently the sole technique capable of combining all the eight VLTI telescopes with very limited infrastructure modifications. We describe a concept of a simple instrument, code-named V8 that would bring an unprecedented imaging capability at VLTI, albeit limited to bright sources. It relies on technological advances on many fields pushed by the world-wide interest in developing mid-infrared photonics technologies. Our overarching goal is to push technology towards a complete fiber-linked mid-infrared interferometric facility.

2. THE MID-INFRARED HETERODYNE INSTRUMENT BUILDING BLOCKS

2.1 Conceptual design

Figure 1 shows a conceptual scheme of a two-telescope heterodyne instrument which forms the basis of our proposition. The incoming celestial light of each telescope interferes (is "mixed") with a local-oscillator on a high temporal bandwidth detector. Local-oscillators are synchronized in phase between the telescopes. In such a process, the mixed mid-infrared signal is down-converted to radio-frequencies signal that can be correlated with other telescopes'. Unlike the classical architecture inspired by radio interferometry, we do not digitize the beating signal but rather use it to modulate a stable laser in such a way that it acts as a carrier of the amplitude information and can be carried through fiber links. We refer to Bourdarot et al. in this conference (paper 11446-61) for a full description of this photonics scheme. Interference between the two arms of the fiber link allow a measurement of the correlation between the incoming electromagnetic fields to be made. This provides a direct measurement of the object spatial coherence.

t

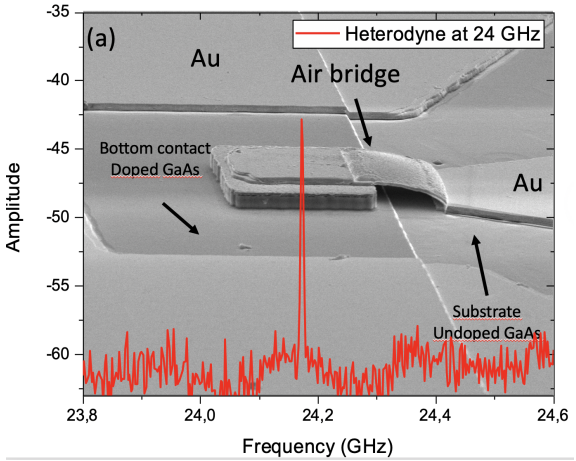

Figure 2. Mid-infrared high bandwidth unipolar detector developed by LPENS with an heterodyne-locked QCL signal at 25GHz (courtesy of Carlo Sirtori), see e.g.[6,7]

2.2 Detection

The ISI used ≈ 3 GHz detectors corresponding to a ≈ 10000 spectral resolution power, which explains partly its limited sensitivity. Improving the detector bandwidth is the first way to increase the sensitivity of the heterodyne scheme as it allows a broader portion of the spectrum to be sampled. Considerable progresses have been made since the ISI in this field driven, by the needs of hyperspectral imaging, chemical sensing, Lidar and quantum applications. For example Cakmakyapan et al.[8] report high responsivity high bandwidth (50GHz) using detectors made of gold-patched graphene nano-structures. The application of this technology to heterodyne interferometry is contemplated by E. Michael's group (see[9] and this conference proceedings).

We are exploring with Laboratoire de Physique de l'Ecole Normale de Physique (LP-ENS) unipolar mid-infrared ($4\mu\text{m} < \lambda < 12\mu\text{m}$) detectors for a high speed operation up to room temperature.[6] These detectors are based on a quantum well absorbing medium embedded into a metallic metamaterial that provide strong sub-wavelength confinement. Such architectures increase the device responsivity and also the detector operating temperature thanks to a reduction of the thermally generated dark current. In addition, unipolar detectors have a unique property which is their very short excited carrier lifetime, on the order of few picoseconds, leading to a frequency bandwidth of several tens of GHz. Using a heterodyne setup made with two quantum cascade lasers, frequency response above 20 GHz have been already demonstrated.[6,7] This is about 10 times better than what was reported at ISI. LPENS is currently revisiting the overall photonic architecture of the unipolar detectors in order to enhance the quantum efficiency up to 50%. Moreover, an adapted RF packaging can be implemented to further increase the bandwidth and flatten the frequency response. The fabrication processing can be optimized in order to reach a yield that allows to get several identical detectors from one round of fabrication. The high yield could be also exploited to realize few elements linear arrays with the detector next to each other. This would allow the incoming signal to be dispersed onto the array and mixed with a mid-infrared frequency comb.

2.3 Local oscillator

The ISI used a CO_2 laser as a local oscillator (LO) which presents the interest of generating many lines in the 9-12 μm band that can be further enriched depending on the isotope used. In order to further increase the spectral coverage of an heterodyne setup mid-infrared frequency combs should be considered. However, only a few broad bandwidth mid-infrared lasers exist. As a consequence nonlinear frequency down-conversion is the priviledged way to generate frequency combs in this spectral region. The specific constraint of the heterodyne interferometric technique requires to generate combs with line spacing corresponding to detector bandwidths which, in our particular case, should be of the order of a few 10GHz. There are currently no commercially

available products. However, we note that several applications such as gas sensing, precision spectroscopy and kinetics chemical reactions monitoring require such light sources. With that in mind Kowligy et al.[10] have reported the first mid-infrared frequency combs with 10GHz repetition rate around a wavelength of 4 mic and have explored the extension to the 7-11 window using OP-GaP crystals as non-linear conversion material. Other technologies, based on QCL lasers are close to maturity and provide another path for mid-infrared frequency combs.[11]

The distribution of a phase-locked mid-infrared local oscillator is another challenge. In ISI this was done by propagating physically the CO_2 laser towards the telescopes. This is more difficult to envision for a kilometric baseline infrastructure with many telescopes as it would require a dedicated optical train. Instead, we note that the recent work by Argence et al. ([12]) has demonstrated the possibility to lock a mid-infrared QCL laser to an atomic clock located 47 km away thanks to the phase-controlled propagation of a near infrared ultra-stable laser. The adaptation of this scheme to long-baseline interferometry would not necessarily require the locking on an atomic clock since we are interested in relative phase stability.

For practical purposes, the technologies we have exposed above are still in need of maturation. For an immediate application we note that two commercially available quantum cascade lasers locked together provide a sufficiently stable local oscillator as demonstrated by Gacemi et al.[7] This will be our baseline for the conceptual designed provided later.

2.4 Correlation and delay.

Radio interferometric arrays such as ALMA require correlation techniques that can handle several tens of telescopes with the maximum possible spectral bandpass and resolution. Dedicated electronic technologies are required, starting at the antenna end with high bandwidth digitizers, optical data links to the central correlator. As pointed out by Ireland et al.,[14] the extrapolation of radio-techniques for a mid-infrared array such as PFI lead to not-yet available computing power requirements. Moreover, the perspective of having to deal with high bandwidth RF signals (several 10s of GHz) complicates further the matter. Finally, the bandwidth over frequency ratio being so different between the radio and the mid-infrared, it is highly likely that specific architectures would have to be conceived in order to retrieve the spectral information.

For a small number of telescopes such as ISI or the 2 telescope near-infrared demonstrator proposed in Besser et al.[15] the electronic approach is the most direct method. In particular, in the context of a visitor instrument, the use of a Reconfigurable Open Architecture Computing Hardware (2nd Generation ROACH-2) board with the capacity of four parallel 1.25 GHz bandwidth digitization is particularly simple and elegant.[15] But, for of an 8 beam guest instrument at VLTI with potential detector bandwidths superior do 25 GHz such an approach might be difficult to extend. Instead we revisited the idea of carrying an *analogical correlation* by converting the RF signal over to a stable telecom laser carrier using electro-optics modulators. Using off-the-shelf components, we demonstrated in Bourdarot et al.,[13] that the correlation between two telescopes could be done (see figure 3). The main interest of this approach is that it provides a simple way to handle both high bandwidth signals (up to 50GHz), many telescopes and several spectral channels with telecom technologies (DWDM). In this conference Bourdarot et al. (Paper 11446-61) present in more detail our photonics analogical approach. The delay compensation can be achieved using commercially available discrete delay line that can generate delays of several 100s of meters and a continuous small range one. Indeed, since we are in this analogical correlation scheme we are limited neither by losses nor by chromatic dispersion.

2.5 Fringe tracking

Whatever the final architecture (direct or heterodyne), if long integration times have to be achieved, fringe tracking (or co-phasing) is requested in order to overcome the atmosphere's short coherent time adverse effects. Gravity's fringe tracker[16] has proven essential to reach limiting magnitudes sufficient to study the galactic center close environment. In the context of a technological approach of interferometry relying on fiber links one has to find a way to provide a companion instrument to the heterodyne correlator that stabilizes the fringes using fibers and a direct combination scheme. The easiest and cheapest way is to use the astronomical H band that corresponds to telecommunication wavelengths. However, broadband propagation through fibers is strongly affected by chromatic dispersion and we are left with the additional conundrum of how to secure the optical path

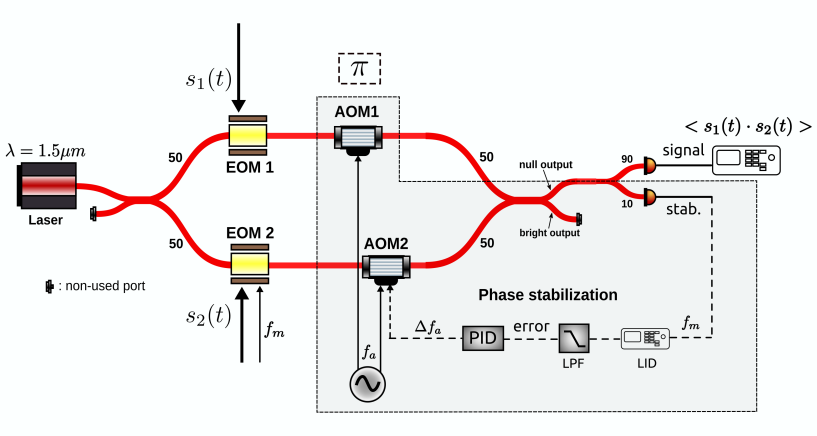

Figure 3. An analogical 2-way photonics correlator based on a Mach-Zehnder interferometer stabilized at the zero null (Bourdarot et al. 2020[13]). Incoming signals modulate EOMs placed in each arm. In this configuration, the output of the photodiode contains a term proportional to the product of the RF signals at the input of each modulator. Abbreviations as follows: LO: local oscillator; BS: beam splitter; PD: photo-diode; LNA: low-noise amplifier; LID: lock-in detection; LPF: low-pass filter; PID: proportional integral derivator; AOM: acousto-optic modulator; EOM: electro-optic modulator.

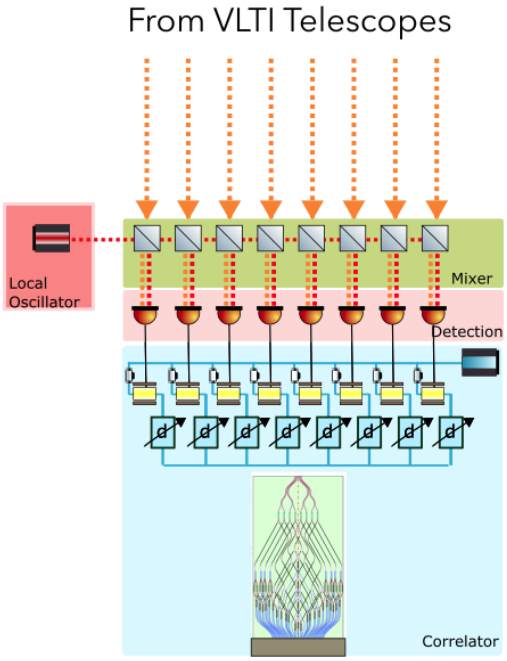

Figure 4. Schematic of the proposed V8 optical layout inside the VLTI laboratory.

SNRc=10 (SNR_V2=5) per 20min incoherent integration t0>120ms @10.5µm ***per spectral channel***	**V8**			**MATISSE**		
**which was typically reported on ISI*	AT	AT-UT (approx. with simple geometrical mean)	UT	*in parentheses, all spectral channels combined*	AT	UT
BW = 2.5 GHz, QE=0.4, + noise penalty 2x2.5 from ideal (one polarization)	120* Jy	26 Jy	5.8 Jy	Low N, full vis.	25 Jy (4.2 Jy)	1 Jy (0.17 Jy)
BW = 2.5 GHz, QE=0.4, + noise penalty 2 (one polarization)	48 Jy	10 Jy	2.3 Jy	Low N, coh. flux	4 Jy (0.68 Jy)	0.2 Jy (0.034 Jy)
BW = 25 GHz, QE=0.5, + noise penalty 2x2.5 from ideal (one polarization)	30 Jy	6.2 Jy	1.3 Jy	High N, coh. flux (rel.)	35 Jy (2.4 Jy)	0.7 Jy (0.047 Jy)
BW = 25 GHz, QE=0.5, + noise penalty 2 (one polarization)	15 Jy	2.7 Jy	0.5 Jy			

Figure 5. Performance comparison between MATISSE, ISI and V8 at the VLTI. Required fluxes to reach an SNR of 5 on squared visibility measurement after a 20 minutes incoherent integration time. For the heterodyne side a double-side band correlator on a single polarisation was considered.

compensation. At the time of this writing we have to acknowledge that we have no operational scheme. However, we note that, despite the recent progresses in fiber technology, there has been a relatively small effort of research and technology in our community to elaborate dispersion compensating fiber links that include optical path compensation. At the time of this writing we are exploring White or Herriot cell schemes to secure broadband, fiber-linked optical path compensation.

3. V8: AN 8 BEAM HETERODYNE CORRELATOR AT VLTI

3.1 Conceptual layout

In the absence of an operational way to distribute the local oscillator to the telescopes, which would increase sensitivity by a factor of 4, we propose that the 8 beam heterodyne correlator could be entirely located inside the VLTI laboratory. Figure 4 shows a conceptual layout of such an instrument. The eight beams originating from the four Unit Telescopes and Auxiliary Telescopes would have to be brought back to the VLTI laboratory. A QCL-based mid-infrared local oscillator stabilized in frequency is distributed and interferes with the incoming celestial light onto the high-bandwidth unipolar detectors. As the laser is polarized, a specific care to the polarization state of the incoming signal would have to be taken. The resulting beating signals modulates the electro-optics modulators of the photonic correlator. We use an 8-beam photonics chip to ensure a pairwise correlation function using the same technique that we used for PIONIER and GRAVITY.[17,18]

On the VLTI side two main modifications would have to be undertaken:

- insertion of additional mirrors to redirect the light of all eight telescopes to the VLTI laboratory;
- adapt the VLTI software and organization to handle the simultaneous operation of eight telescopes.

3.2 Sensitivity analysis

Although the quantum noise still limits heterodyne sensitivity in the N band the gap between direct interferometry and heterodyne can be significantly reduced (and almost cancelled in the Q band). In order to quantify

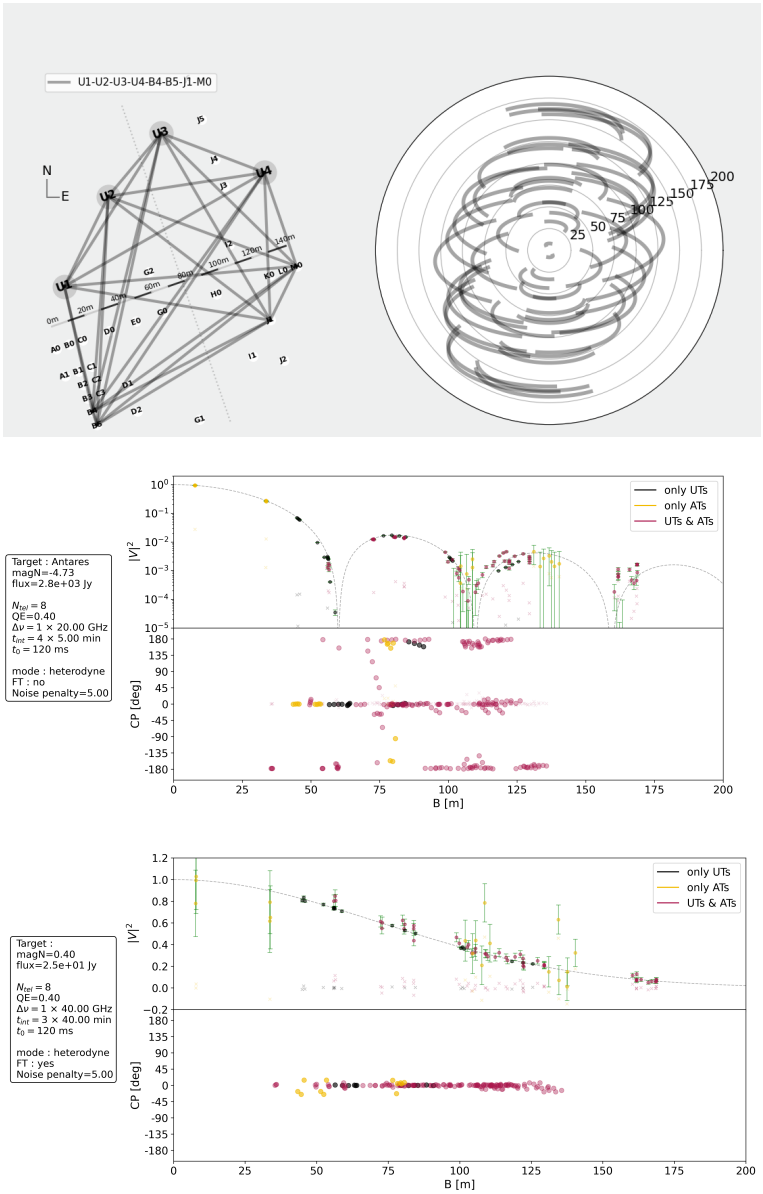

Figure 6. Top: Example of possible 4AT-4UT configuration and corresponding (u,v) coverage for Antares. Bottom: Simulation of expected squared visibility and closure phase with corresponding errors as a function of spatial frequency expected with V8. UT-UT, AT-AT and mixed AT-UT baselines are separated by color code. *Top:* Antares *Bottom:* Star with 25 Jy flux at 10 microns with 50 GHz detectors and an external 8 beam fringe tracker and 3 × 20mn coherent integration points.

this difference we have compared MATISSE performances as advertised on the ESO official web pages with ISI performances and our putative heterodyne instrument V8. V8 improves on ISI by having state of the art high bandwidth detectors (25 GHz bandpass), better quantum efficiency (0.5) and an improved noise penalty (2) with respect to the one described in Hale 2000. We employed the formula demonstrated in Thompson (2017)[19] (see Eq.(6.49), p.228 and Eq (9.89), p.419 for coherent integration) which is equivalent to the one used by Hale et al. 2000.[3] We used Hale et al. 2004[5] to verify that the computed SNR were close to what had been actually measured.

The table in figure 5 summarizes the limiting flux at 10.5 microns necessary to reach a coherent signal-to-noise ratio of 10 (5 on the squared visibility) after a 20min incoherent integration for an atmospheric coherence time of 120ms. MATISSE performance is extracted from each of its advertised instrumental configurations. For MATISSE, limiting fluxes obtained by averaging all spectral pixels is shown in parenthesis.

This analysis leads us to conclude that, despite the systematic better sensitivity of MATISSE with respect to ISI and V8, both heterodyne instruments fare globally well in terms of sensitivity by reaching limiting fluxes compatible with many sources in the southern hemisphere. This is particularly the case for Red Super Giants, Asymptotic Giant Branch stars and post AGB stars for which several tens are significantly brighter than the limits computed here. We note that coupling AT with UTs allows decent limiting fluxes per spectral channel to be obtained. Those are comparable with MATISSE's performance per spectral channel on the AT's.

Our conclusion is that a simple heterodyne instrument at VLTI would be perfectly capable of mapping tens of evolved sources and massive young embedded stars, even without a fringe tracker. Our scientific motivation to pursue this instrumental research avenue is therefore the trade between sensitivity and an incomparable mapping capability since V8 would sample 28 baselines instead of 6 with MATISSE.

3.3 V8-VLTI spatial frequency sampling

We were able to explore the (u,v) coverage that V8 would allow by adapting Antoine Mérand's public code (`https://github.com/amerand/UTILS`) and including a noise estimation presented in section 3.2. As can be seen in figure 6, the instantaneous coverage is considerably denser than with available four beam instruments. Furthermore, the heterodyne scheme would allow a *full sky coverage*, unlike what is currently offered with direct interferometry. Our sensitivity estimation shows that, even under the assumption of an incoherent integration, we should be able to reach a 5σ signal to noise ratio on squared visibilities in 20 minutes on a hundred of science targets. If one includes a conservative bracketing calibration of 20 minutes on both sides of the science measurement V8 should be able to provide a calibrated measurement every hour. An example of the instantaneous spatial frequency coverage that could be obtained on the Red Super Giant α Sco (Antares) with V8 is shown in the middle of figure 6. Bottom of figure shows a typical visibility curve of a 25 Jansky source if fringe tracking allows 40 min coherent integration.

4. CONCLUSION

In this work we propose to explore the idea of using all 8 VLTI telescope in a coherent mode using heterodyne interferometry in the mid-infrared. We argue that, with limited developments, currently available photonics technologies provide a relatively simple path to build a mid-infrared instrument, V8, which could be a possible precursor to PFI mid-infrared technologies. Such an instrument would bring an unprecedented imaging capability at VLTI on several tens of bright mid-infrared sources allowing for the spatio-kinematical monitoring of the still mysterious mass-loss processes in evolved stars.

Our overarching technological motivation is to explore the feasibility of an all-fibered-linked mid-infrared facility. To achieve even higher performances we also need to advance in the conceptual design of a fiber-fed near-infrared direct combination companion fringe tracker. Therefore by pushing forward V8 we are helping advancing both direct and heterodyne interferometry. Our next step is to demonstrate in the laboratory a complete two-way mid-infrared instrument concept and show that sensitivity performances are indeed as predicted and to test its operational robustness.

ACKNOWLEDGMENTS

We thank Carlo Sirtori and Azzurra Bigioli (LPENS) for fruitful discussions and their support. This project is currently funded by the Institut National des Sciences de l'Univers (INSU-CNRS) through Action Spécifique Haute Résolution Angulaire (ASHRA) and CSAA and by the LabEx FOCUS.

REFERENCES

[1] Monnier, J. D., Kraus, S., Ireland, M. J., Baron, F., Bayo, A., Berger, J.-P., Creech-Eakman, M., Dong, R., Duchêne, G., Espaillat, C., Haniff, C., Hönig, S., Isella, A., Juhasz, A., Labadie, L., Lacour, S., Leifer, S., Merand, A., Michael, E., Minardi, S., Mordasini, C., Mozurkewich, D., Olofsson, J., Paladini, C., Petrov, R., Pott, J.-U., Ridgway, S., Rinehart, S., Stassun, K., Surdej, J., Brummelaar, T. t., Turner, N., Tuthill, P., Vahala, K., van Belle, G., Vasisht, G., Wishnow, E., Young, J., and Zhu, Z., "The planet formation imager," *Experimental Astronomy* **46**, 517–529 (Dec. 2018).

[2] Ireland, M. J., Monnier, J. D., Kraus, S., Isella, A., Minardi, S., Petrov, R., ten Brummelaar, T., Young, J., Vasisht, G., Mozurkewich, D., Rinehart, S., Michael, E. A., van Belle, G., and Woillez, J., "Status of the Planet Formation Imager (PFI) concept," 99071L (Aug. 2016).

[3] Hale, D. D. S., Bester, M., Danchi, W. C., Fitelson, W., Hoss, S., Lipman, E. A., Monnier, J. D., Tuthill, P. G., and Townes, C. H., "The Berkeley Infrared Spatial Interferometer: A Heterodyne Stellar Interferometer for the Mid-Infrared," *The Astrophysical Journal* **537**, 998 (July 2000).

[4] Danchi, W. C., Townes, C. H., Fitelson, W., Hale, D. D. S., Monnier, J. D., Tevosjan, S., and Weiner, J., "Status and progress on the upgraded infrared spatial interferometer," in [*Interferometry for Optical Astronomy II*], **4838**, 33–44, International Society for Optics and Photonics (Feb. 2003).

[5] Hale, D. D. S., Weiner, J., and Townes, C. H., "ISI: recent technology and science," 490 (Oct. 2004).

[6] Palaferri, D., Todorov, Y., Bigioli, A., Mottaghizadeh, A., Gacemi, D., Calabrese, A., Vasanelli, A., Li, L., Davies, A. G., Linfield, E. H., Kapsalidis, F., Beck, M., Faist, J., and Sirtori, C., "Room-temperature nine-µm-wavelength photodetectors and GHz-frequency heterodyne receivers," *Nature* **556**, 85–88 (Apr. 2018).

[7] Gacemi, D., Todorov, Y., Bigioli, A., Palaferri, D., and Sirtori, C., "Ultra-Stable Heterodyne Detection in the Mid-IR," in [*2018 43rd International Conference on Infrared, Millimeter, and Terahertz Waves (IRMMW-THz)*], 1–1, IEEE, Nagoya (Sept. 2018).

[8] Cakmakyapan, S., Lu, P. K., Navabi, A., and Jarrahi, M., "Gold-patched graphene nano-stripes for high-responsivity and ultrafast photodetection from the visible to infrared regime," *Light: Science & Applications* **7**, 20 (Dec. 2018).

[9] Michael, E., "Towards a Broadband Q-Band," 51 (July 2019).

[10] Kowligy, A. S., Kowligy, A. S., Carlson, D. R., Hickstein, D. D., Timmers, H., Lind, A. J., Lind, A. J., Schunemann, P. G., Papp, S. B., Papp, S. B., Diddams, S. A., and Diddams, S. A., "Mid-infrared frequency combs at 10 GHz," *Optics Letters* **45**, 3677–3680 (July 2020).

[11] Hugi, A., Villares, G., Blaser, S., Liu, H. C., and Faist, J., "Mid-infrared frequency comb based on a quantum cascade laser," *Nature* **492**, 229–233 (Dec. 2012).

[12] Argence, B., Chanteau, B., Lopez, O., Nicolodi, D., Abgrall, M., Chardonnet, C., Daussy, C., Darquié, B., Le Coq, Y., and Amy-Klein, A., "Quantum cascade laser frequency stabilization at the sub-Hz level," *Nature Photonics* **9**, 456–460 (July 2015).

[13] Bourdarot, G., Guillet de Chatellus, H., and Berger, J.-P., "Toward a large bandwidth photonic correlator for infrared heterodyne interferometry: A first laboratory proof of concept," *Astronomy & Astrophysics* **639**, A53 (July 2020).

[14] Ireland, M. J. and Monnier, J. D., "A dispersed heterodyne design for the planet formation imager," in [*Optical and Infrared Interferometry IV*], **9146**, 914612, International Society for Optics and Photonics (July 2014).

[15] Besser, F. E., Ramos, N., Rates, A., Ortega, N., Sepulveda, S., Parvex, T., Piña, M., Pollarolo, C., Jara, R. E., Espinoza, K. R., Rodriguez, A., Becerra, A., Martin, P., Cadiz, M. D., Henriquez, N. N., Carrasco, J., Martin, C. S., Rearte, C., Diaz, J., Moreno, E., and Michael, E. A., "Fiber-based infrared heterodyne technology for the PFI: development of a prototype test system," in [*Optical and Infrared Interferometry and Imaging VI*], **10701**, 107012L, International Society for Optics and Photonics (July 2018).

[16] Lacour, S., Dembet, R., Abuter, R., Fédou, P., Perrin, G., Choquet, E., Pfuhl, O., Eisenhauer, F., Woillez, J., Cassaing, F., Wieprecht, E., Ott, T., Wiezorrek, E., Tristram, K. R. W., Wolff, B., Ramírez, A., Haubois, X., Perraut, K., Straubmeier, C., Brandner, W., and Amorim, A., "The GRAVITY fringe tracker," *Astronomy & Astrophysics* **624**, A99 (Apr. 2019).

[17] Benisty, M., Berger, J.-P., Jocou, L., Labeye, P., Malbet, F., Perraut, K., and Kern, P., "An integrated optics beam combiner for the second generation VLTI instruments," *Astronomy & Astrophysics* **498**, 601–613 (May 2009).

[18] Perraut, K., Jocou, L., Berger, J. P., Chabli, A., Cardin, V., Chamiot-Maitral, G., Delboulbé, A., Eisenhauer, F., Gambérini, Y., Gillessen, S., Guieu, S., Guerrero, J., Haug, M., Hausmann, F., Joulain, F., Kervella, P., Labeye, P., Lacour, S., Lanthermann, C., Lapras, V., Le Bouquin, J. B., Lippa, M., Magnard, Y., Moulin, T., Noël, P., Nolot, A., Patru, F., Perrin, G., Pfuhl, O., Pocas, S., Poulain, S., Scibetta, C., Stadler, E., Templier, R., Ventura, N., Vizioz, C., Amorim, A., Brandner, W., and Straubmeier, C., "Single-mode waveguides for GRAVITY: I. The cryogenic 4-telescope integrated optics beam combiner," *Astronomy & Astrophysics* **614**, A70 (June 2018).

[19] Thompson, A. R., Moran, J. M., and Swenson, Jr., G. W., [*Interferometry and Synthesis in Radio Astronomy, 3rd Edition*], Astronomy and Astrophysics Library, Springer International Publishing, Cham (2017).

Architecture of photonics correlation for infrared heterodyne interferometry

Demonstration of amplitude-modulation based correlation

GUILLAUME BOURDAROT[1,2*], JEAN-PHILIPPE BERGER[1], AND HUGUES GUILLET DE CHATELLUS[2]

[1] *Univ. Grenoble Alpes, CNRS, IPAG, F-38000 Grenoble, France*
[2] *Univ. Grenoble Alpes, CNRS, LIPhy, F-38000 Grenoble, France*
[*] *guillaume.bourdarot@univ-grenoble-alpes.fr*

Compiled August 25, 2021

In the context of mid-infrared astronomical aperture synthesis, heterodyne interferometry has been identified as a potential solution to combine a large number of telescopes in the $10\,\mu\mathrm{m} - 20\,\mu\mathrm{m}$ wavelength regime. In search for an alternative to costly and technologically difficult digital correlation, we have proposed to correlate wide bandwidth radio-frequency (RF) signals in the analog domain, using photonics components developed in the frame of telecommunication applications. In this paper, we propose an extension to amplitude modulation of our initial proposition, in which the encoding of the heterodyne signal was performed through phase modulation. Both schemes are compared, and an experimental demonstration of correlation between two signals using amplitude modulation is presented. Our experiment shows that this concept has important advantages over phase modulation, in particular with regards to the requirements on the phase stabilization. The possibility to scale-up the photonics concept to the recombination of a large number of telescopes, and a large number of spectral channels in order to increase the instantaneous bandwidth coverage of infrared heterodyne interferometry, is discussed. This study shows that the necessary technological building blocks of a pathfinder instrument adaptable to existing astronomical facilities are available. © 2021 Optical Society of America

http://dx.doi.org/10.1364/ao.XX.XXXXXX

1. INTRODUCTION

Astronomical long-baseline interferometry is a technique that enables astrophysical objects to be studied at the highest angular resolution by looking at the spatial coherence properties of the incident light, which can be related to the object intensity distribution through the Zernike-van Cittert theorem [1, 2]. The interferometric combination of a large number of telescopes over kilometric baselines in the mid-infrared currently represents one of the most exciting challenges of astronomical instrumentation, and a future decisive step toward the imaging of the key processes of planet formation [3]. As an alternative to classical Michelson interferometry, which necessitates a complex infrastructure to transport and combine the light coming from multiple telescopes, heterodyne interferometry, in which the light is coherently detected at the level of each telescopes, has been proposed as a practical way to combine signals in the $10\,\mu$m - $20\,\mu$m wavelength regime [4–6]. Despite a less demanding infrastructure, one of the limitations of heterodyne interferometry resides in its particularly narrow detection bandwidth, which severely restricts the sensitivity and the spectral coverage of this type of detection. The advent of wide-bandwidth mid-infrared detectors, in particular QWIP and QCD, with laboratory demonstration up to 20 GHz [7, 8] and up to 70 GHz [9], and the current development of mid-infrared frequency combs, have recently enabled to envision both an increase of the instantaneous bandwidth of a detector by more than one order of magnitude, and, by dispersing the light of a frequency comb on multiple photodiodes, to record simultaneously multiple spectral channels in order to cover a larger bandwidth [5, 6]. These new features push back the former limitations of heterodyne detection and bear the promise of renewed sensitivity limits, which open major scientific opportunities in astronomy [6, 10].

This potential increase of bandwidth raises at the same time the question of the correlation of hundreds of channels, each one with dozens to a hundred GHz bandwidth. For that purpose, a first estimation applied to digital correlation, which is routinely used, for example, in millimeter-wave interferometry, converged to the need of a computing power more than two orders of magnitude larger than the current capabilities of the world's largest facilities [6]. In this context, the concept of an analog correlation based on the use of photonics components to process wide bandwidth RF signals was proposed specifically

for infrared heterodyne interferometry [11].

The general idea behind the concept of photonic correlation is to encode the wide bandwidth RF signals originating from each telescope on a continuous wave (CW) laser at a telecommunication wavelength, through the use of e.g. a phase modulator, and then extracting the mean multiplication product i.e. the correlation product at one delay, from the photodetection of the optical signal. A first version of this concept based on phase modulation, along with a laboratory proof-of-principle using standard telecom components, has enabled the correlation of two simulated single channel telescope signals, using fibered Electro-Optical Modulators (EOMs) and a dedicated phase stabilization scheme, with a noise figure compatible with sensitive application [11].

In this paper, we propose to formalize and extend the concept of photonic correlation to both phase and amplitude modulation, and to provide an experimental proof-of-principle of the latter. Section 2 recalls the basics of infrared heterodyne detection and the classical expressions of the correlation of heterodyne signals. Section 3 describes two possible photonic correlation architectures, based on phase and amplitude modulation respectively. The experimental implementation of the amplitude modulation scheme is given in Section 4. Finally, Section 5 discusses the extension of this concept to an astronomical interferometer with a large number of telescopes and a broad wavelength coverage through multiple spectral channels, along with the different constraints encountered in practice to correlate astronomical signals. Overall, this study points towards an advantage of the amplitude modulation scheme over phase modulation.

2. INFRARED HETERODYNE INTERFEROMETRY

A. Infrared Heterodyne Detection

The principle of heterodyne interferometry consists in detecting the electro-magnetic field of the astronomical signal, by mixing the incident astronomical light with a local oscillator (LO) on a detector squaring the field. In the infrared regime, the LOs are stable lasers, the detectors are fast infrared photodiodes, and the overlap between the astronomical signal and the LO produces an interference term, whose voltage is written, once the DC component is filtered :

$$\begin{cases} s_1(t) &= \eta_{\mathrm{IR},1} E_{\mathrm{LO},1} \left(E_s(\theta,\omega_s) e^{i\Phi_1(t)} + \mathrm{c.c.} \right) \\ s_2(t) &= \eta_{\mathrm{IR},2} E_{\mathrm{LO},2} \left(E_s(\theta,\omega_s) e^{i\Phi_2(t) + i\phi_{\mathrm{tot}}(\theta,\omega_s)} + \mathrm{c.c.} \right) \end{cases} \quad (1)$$

with c.c. the abbreviation of complex conjugate, $\eta_{\mathrm{IR,k}}$ the total throughput at telescope k, including detector quantum efficiency, $E_{\mathrm{LO,k}}$ the LO field, $E_s(\theta,\omega_s)$ the astronomical field originating from an angular direction θ and at angular frequency ω_s. $\phi_{\mathrm{tot}}(\theta,\omega_s)$, whose expression is detailed in Appendix A Eq (18), is the phase difference associated with the optical path difference between telescopes 1 and 2 as well as additional radio-frequency delays.

Of particular importance are the phase terms $\phi_{\mathrm{tot}}(\theta,\omega_s)$ and $\Phi_k(t)$, that enclose the coherence properties of the interferometric signal. $\Phi_k(t)$ is written as :

$$\Phi_{\mathrm{k}}(t) = (\omega_s - \omega_{\mathrm{LO,k}})t - \phi_{\mathrm{LO,k}}(t) \quad (2)$$

with $\phi_{\mathrm{LO,k}}(t)$ the phase of the local oscillator at telescope k. Eq (1) and Eq (2) express the fundamental properties of heterodyne detection : the observed signal is a downconverted version of the incident field, observed at the frequency difference between

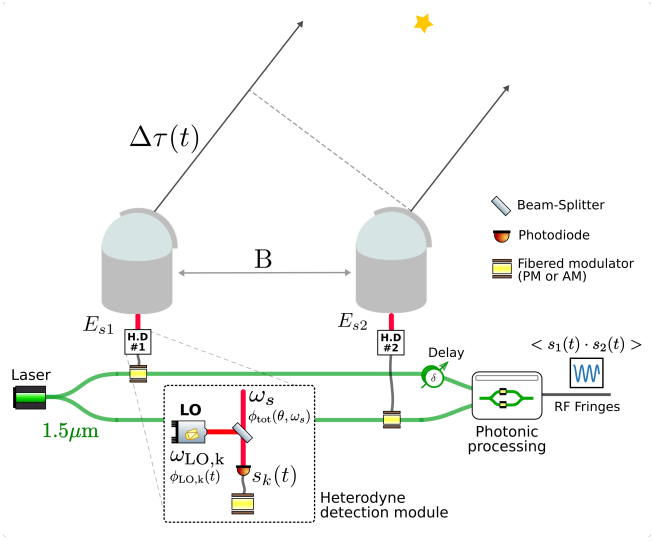

Fig. 1. General schematic of an infrared heterodyne interferometer with a photonics correlator. The inset shows a heterodyne detection module, placed at the level of each telescope. See Section 2 for notation.

the signal and the LO frequency, and this signal preserved the phase of the incident astronomical field. The frequency at which the incident signal is downconverted is usually called the intermediate frequency (IF) [12], written ω_{if}, which verifies the relation :

$$\omega_s = \omega_{\mathrm{LO}} \pm \omega_{\mathrm{if}} \quad (3)$$

The $\pm$ refers to the two possible incident optical frequencies which can be folded on the same intermediate frequency ω_{if} in the RF domain. The higher frequency refers to the so called upper-sideband, and lower to the lower-sideband. For more details on heterodyne detection, we refer to the aforementioned references [12–14].

B. Correlation

The signal detected at the output of each telescope is proportional to the electric field of the incident astronomical light. The visibility of the astronomical field can thus be extracted by computing the correlation product of the IF signals detected at the level of each telescopes. This operation basically consists in the multiplication product of the two incident signals, integrated in time. According to Eq (1) , this operation is :

$$\langle s_1(t) s_2(t) \rangle \propto \left(|E_s(\theta,\omega_s)|^2 e^{i[\Phi_2(t) - \Phi_1(t)]} e^{+i\phi_{\mathrm{tot}}(\theta,\omega_s)} + \mathrm{c.c.} \right) \quad (4)$$

where the terms corresponding to the sum of the frequency averaged out [13]. Without further operation, this correlation product will result in the integration of all the intermediate frequencies ω_{if} over the detection bandwidth $\Delta\nu$. In the infrared $\Delta\nu$ is equivalent to a very high spectral resolution. By contrast, in radio-interferometry it is usually of interest to further decompose the detection bandwidth into smaller sections to perform spectroscopy. [15, 16]. Integrated over the detection bandwidth, the correlation product is (see Appendix A for a detailed derivation from Eq (4)) :

$$\begin{aligned} \langle s_1(t) s_2(t + \Delta\tau(t)) \rangle = {} & |F_c(B/\lambda,\omega_s)| e^{i\phi_{\mathrm{V}}(B/\lambda,\omega_s)} e^{2i\pi f_{12} t} \\ & \times |G(\Delta\tau(t))| e^{\pm i\phi_{\mathrm{G}}} e^{\pm i\omega_c \Delta\tau(t)} + \mathrm{c.c} \end{aligned} \quad (5)$$

with $F_c(B/\lambda, \omega_s)$ the coherent flux of the source at spatial frequency B/λ, ϕ_V the phase of the astrophysical object, ω_c the central angular frequency of the RF integration bandwidth, and $|G(\Delta\tau(t))|e^{i\phi_G} = 2H_0^2\Delta\nu\left[\frac{\sin(\pi\Delta\nu\Delta\tau(t))}{\pi\Delta\nu\Delta\tau(t)}\right]$ the complex response of the detection chain, that has an amplitude H_0, and a phase ϕ_G resulting from the phase difference of the amplifiers and filters in the detection and correlation chain [12]. We have also introduced the delay difference $\Delta\tau(t)$ between the two interferometric arms, which takes into account both the elevation of the astrophysical objects and the potential delay introduced downstream in the processing chain, and f_{12} the frequency at which the fringes are encoded, which takes into account the relative phase difference of the local oscillators and the continuous variation of the phase of the fringes due to earth rotation, sometimes called the "natural fringe frequency" (see Appendix A). The expression of Eq (5) is also detailed in Appendix A, and is similar to radio-astronomy [12, 13].

The expression Eq (5) represents the response of a correlator for a single sideband (upper or lower) separately, which provides the basis to describe the correlator response. In practice, these sidebands are not necessarily measured separately, which will require to introduce a distinction between single-sideband and double-sideband operation.

B.1. Double-sideband correlation

In the case where the two signals are multiplied and integrated without additional operations, the upper- and the lower-sideband are added. In this case, the response of the correlator is :

$$\begin{aligned}\langle s_1(t)s_2(t)\rangle_{\text{DSB}} &= |F_c(B/\lambda,\omega_s)|e^{i\phi_V(B/\lambda,\omega_s)}e^{2i\pi f_{12}t}|G(\Delta\tau(t))| \\ &\times\left(e^{+i\phi_G}e^{+i\omega_c\Delta\tau(t)} + e^{-i\phi_G}e^{-i\omega_c\Delta\tau(t)}\right) + \text{c.c.} \\ &= |F_c(B/\lambda,\omega_s)|\cdot|G(\Delta\tau(t))|\cos\left(\omega_c\Delta\tau(t)+\phi_G\right) \\ &\cos\left(2\pi f_{12}t + \phi_V(B/\lambda,\omega_s)\right)\end{aligned} \quad \textbf{(6)}$$

In the following, the photonics scheme considered here will mainly rely on double-sideband operation.

B.2. Single-sideband correlation

In the case where it is possible to isolate a single-sideband, the correlator output is given by Eq(5) , which is written :

$$\begin{aligned}\langle s_1(t)s_2(t)\rangle_{\text{SSB}} &= |F_c(B/\lambda,\omega_s)|\cdot|G(\Delta\tau(t))|\times \\ &\cos\left(2\pi f_{12}t + \omega_c\Delta\tau(t) + \phi_V(B/\lambda,\omega_s) + \phi_G\right)\end{aligned} \quad \textbf{(7)}$$

3. PHOTONIC CORRELATION : PHASE AND AMPLITUDE MODULATION

In a general manner, photonic correlation can be performed both in phase and in amplitude modulation. The respective principles of these approaches are presented in this section. Amplitude modulation is favored, given its convenient use to encode the fringe frequency and the less demanding requirements on phase stabilization.

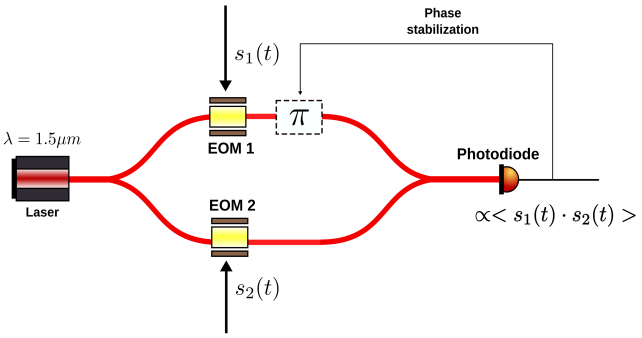

Fig. 2. Photonic correlation using phase modulation.

A. Phase modulation

A.1. Principles

We first consider a Mach-Zehnder interferometer in which each arm is modulated by an EOM. In practice, the modulators can be placed directly at each telescope, at the RF output of the heterodyne detection unit, the modulated optical signal being then propagated through fibers over the array to the recombination unit. Assuming an incident carrier laser E_0 at frequency ω_0, and a transmission t_k for the channel associated to each telescope (two telescope combination here), the field at the output of the interferometer is :

$$E(t) = E_0 e^{i\omega_0 t}\left(t_1 e^{i\beta_1 s_1(t)} + t_2 e^{i\beta_2 s_2(t)} e^{i\phi_0}\right) \quad \textbf{(8)}$$

with $\beta_k = \frac{\pi}{V_{\pi,k}}$, and $V_{\pi,k}$ the half-voltage of the modulator, which is defined as the input tension necessary to introduce a relative phase-shift of π between the arm of the modulator. Using a balanced detection, which enables to reject common mode noise and DC component, the intensity detected is :

$$I(t) = 4I_0 \mathrm{V}_i \cos(\beta_1 s_1(t) - \beta_2 s_2(t) - \phi_0) \quad \textbf{(9)}$$

with $\mathrm{V}_i = 2t_1t_2/(t_1^2+t_2^2)$. Assuming that the relative phase between each arm is set at $\phi_0 = 0$ or $\phi_0 = \pi$, and that the incident RF signal is sufficiently small compared to V_π, Eq (9) becomes

$$I(t) = 4I_0\mathrm{V}_i\left(\frac{1}{2}\left(\beta_1^2 s_1^2(t) + \beta_2^2 s_2^2(t)\right) \pm \beta_1\beta_2 s_1(t)s_2(t)\right) \quad \textbf{(10)}$$

where the $+$ sign corresponds to $\phi_0 = 0$, and $-$ sign to $\phi_0 = \pi$. These quadratic functioning points permit the product term $s_1(t)s_2(t)$ to appear, which corresponds to the correlation product of the two incident signals, and is precisely the term we seek to compute. Two broad noise signals $s_k^2(t)$ are also present in the spectrum, but can be considered as negligible as their power is distributed over the entire detection bandpass. As detailed in Sec B.1 , the product term can be encoded as a fringe peak, whose frequency f_k can be adjusted by the difference of the mid-infrared LOs. The width Δf of this fringe peak is given by the total integration time $\Delta f \approx 1/t$, set ideally by the maximum time during which the relative phase between the two telescopes channel is stable, i.e. the coherence time.

A.2. Phase stabilization

The main constraint of phase modulation resides in the fact that the Mach-Zehnder has to be placed in a quadratic regime. As mentioned earlier, this imposes a given 0 or π phase difference, which has to be stabilized at a fraction of 1.55μm over time. Such a phase stabilization loop was demonstrated in [11]. In

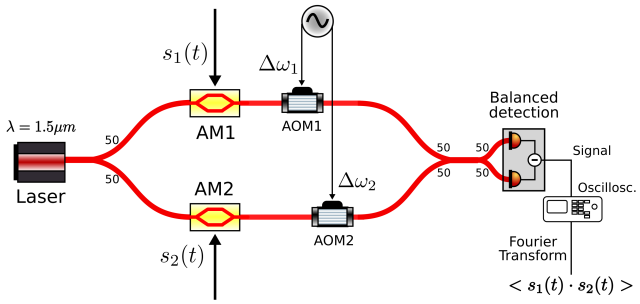

Fig. 3. Photonic correlation in amplitude modulation with frequency shift. The signal is split in two by a 1:2 coupler, modulated in amplitude in each arm by Amplitude Modulators (AM), shifted in frequency by Acousto-Optic Modulators (AOM), combined in a 2:2 coupler and detected on a balanced photodiode. The ratio of the 1:2 and 2:2 couplers are indicated next to the arms of these couplers.

the following, we will see a second possible correlation scheme, based on amplitude modulation, and how it relaxes, in part, the requirements on this phase stabilization.

B. Amplitude modulation

B.1. Amplitude modulation without frequency shift

We now consider a Mach-Zehnder in which the EOMs of Sec A are replaced by amplitude modulators. These amplitude modulators consist themselves in integrated Mach-Zehnder Modulators (MZM), which are driven by the telescope RF signals.

Here, we assume that each amplitude modulator is at the minimum of transmission. Using the same notation as Sect A, and the same small signal approximation, the field at the output of each MZM prior to combination is

$$E_k(t) = t_k E_0 e^{i\omega_0 t} e^{i\phi_k} \left(1 - e^{i\beta_k s_k(t)}\right) \approx -i t_k E_0 \beta_k s_k(t) e^{i\omega_0 t + i\phi_k(t)} \quad \textbf{(11)}$$

Using a single photodiode, the intensity detected is

$$I(t) = I_0 \Big(t_1^2 \beta_1^2 s_1^2(t) + t_2^2 \beta_2^2 s_2^2(t) + 2 t_1 t_2 \beta_1 \beta_2 s_1(t) s_2(t) \cos\left(\Delta\phi_{12}(t)\right) \Big) \quad \textbf{(12)}$$

with $\Delta\phi_{12}(t) = \phi_2(t) - \phi_1(t)$ the relative phase difference between the arms of the Mach-Zehnder interferometer. This signal is almost identical to Eq (10). It also necessitates a given functioning point and requires the same kind of stabilization loop as in phase modulation. In this case, the phase and this amplitude set-up are comparable. Contrary to phase modulation, the square components $s_k^2(t)$ can be removed here by the use of a balanced detection.

The regime in which this small signal approximation is valid is detailed in Appendix B. In addition, we assume that the phase perturbation $\phi_k(t)$ is much smaller than π and much smaller than the rms phase value originating from the signal $\beta_k s_{k,\mathrm{rms}}(t)$, in order not to affect the value of the correlation product, which sets the tolerance on the stabilization of the null of the MZMs.

B.2. Amplitude modulation with frequency shift

Let us now assume that a frequency shift is applied between each arm of the Mach-Zehnder, upstream or downstream of the amplitude modulator. In practice, this frequency shift is applied with an Acousto Optical Modulator (AOM) in one arm, or two AOMs with slightly different driver frequencies, the latter solution being generally preferred. We note $\Delta\omega_k$ the angular frequency shift introduced by the AOM in each arm. The electric field at the output of the AOM in each arm is

$$E_k(t) = -i t_k E_0 \beta_k s_k(t) e^{i(\omega_0 + \Delta\omega_k)t + i\phi_k(t)}$$

Using a single photodiode, the detected signal becomes

$$I(t) = I_0 \Big(t_1^2 \beta_1^2 s_1^2(t) + t_2^2 \beta_2^2 s_2^2(t) + 2 t_1 t_2 \beta_1 \beta_2 s_1(t) s_2(t) \cos\left((\Delta\omega_2 - \Delta\omega_1)t + \Delta\phi_{12}(t)\right) \Big) \quad \textbf{(13)}$$

Using a balanced detector, this signal is

$$I(t) = 4 I_0 \mathrm{V}_i \beta_1 \beta_2 s_1(t) s_2(t) \cos\left((\Delta\omega_2 - \Delta\omega_1)t + \Delta\phi_{12}(t)\right) \quad \textbf{(14)}$$

Here, the fringes are encoded directly at a frequency difference that can be tuned inside the photonic correlator through the frequency difference between the AOMs. At this point, we note three fundamental advantages of this type of recombination over phase modulation. First, the correlation product does not depend of a particular functioning point, but only needs to be relatively phase-stabilized over a coherent integration time. Second, it enables another degree of freedom on the frequency encoding of the fringes, which does not need to be controlled exclusively at the level of the infrared LOs. Third, it definitely eliminates the broadband terms $s_k^2(t)$.

These different reasons, along with its ease of use in a practical set-up, tends to favor the use of amplitude modulation over phase modulation.

B.3. Double-sideband correlation

In the following, we only consider a set-up with amplitude modulation and frequency shift.
For the set-up described in Sec B.1, the upper- and lower sidebands add together, and the correlation product is given by the response of a double sideband correlator Eq (6) . For $f_{12} = 0$, where the LOs have the same frequency, and the natural fringe frequency is also 0, the correlation product is encoded on a single peak at angular frequency $(\Delta\omega_2 - \Delta\omega_1)$; for $f_{12} \neq 0$, the instantaneous phase of the signal at the ouput of the correlator is :

$$\phi_\pm(t) = (\Delta\omega_2 - \Delta\omega_1)t \pm 2\pi f_{12} t \pm \phi_\mathrm{V}(B/\lambda, \omega_s) + \Delta\phi_{12}(t) \quad \textbf{(15)}$$

According to this expression of the instantaneous, the correlation product is encoded on two peaks centered on both sides of $(\Delta\omega_2 - \Delta\omega_1)$, whose frequencies are $((\Delta\omega_2 - \Delta\omega_1) \pm 2\pi f_{12})$, and where the phase under each peak is $(\pm\phi_\mathrm{V}(B/\lambda, \omega_s) + \Delta\phi_{12}(t))$. From Eq (15) , the coherent flux and the interferometric phase can be extracted from the amplitude and the phase (respectively) of these two peaks :

$$\begin{cases} \tilde{I} & = 2 I_0 \mathrm{V}_i \beta_1 \beta_2 |F_c(B/\lambda, \omega_s)| \cdot |G(\Delta\tau(t))| \cos\left(\omega_c \Delta\tau(t) + \phi_G\right) \\ \tilde{\phi}_V & = \frac{1}{2}(\phi_+ - \phi_-) \end{cases} \quad \textbf{(16)}$$

For more than 2 telescopes, additional common observables, and in particular closure-phase, can be constructed from Eq(16) , as in optical and radio-interferometry.

B.4. Phase stabilization

As above-mentioned, in both phase and amplitude modulations, the overall photonics (fibered) link still has to be phase-stabilized, however the exact requirements on this phase stabilization are different in each case. In the case of phase modulation (Sec A.1, Eq (9)) and of amplitude modulation without frequency shift (Sec B.1, Eq (12)), the phase functioning point must be stabilized and locked at a specific value (0 or π). In the case of amplitude modulation with frequency modulation, the phase between each arm has to be stabilized in time but does not have to be fixed to a specific value, which is a significant advantage of this method.

4. EXPERIMENTAL DEMONSTRATION OF AMPLITUDE CORRELATION

In this section, we present a proof of principle of the double-sideband amplitude correlator described in B.3. The methodology and the results obtained with amplitude correlation share strong similarities with the previous demonstration of phase modulation [11].

A. Experimental set-up

The schematic of our experimental proof-of-princples is shown in Fig.3, and is implemented with standard fibered components at telecom wavelength 1.55μm. The references and the characteristics of these components are given in Appendix C.

A sub-kHz laser is divided in two arms using a fibered 1:2 coupler (50:50). Each arm is modulated in amplitude with fibered MZMs with 10 GHz bandwidth, and then shifted in frequency through AOMs. The frequency difference of the AOMs drives the frequency at which the fringes are encoded, as described in Eq(15) . The AOMs are fed with 81 MHz and 82.7 MHz respectively, which were chosen to avoid potential parasitic RF signals at 80 MHz and small residual amplitude modulation signals of the AOMs at 80 MHz. Finally, the signal is recombined through a fibered 2:2 coupler (50:50) on a balanced photodiode. The signal at the output of the balanced photodiode is recorded on a rapid oscilloscope, downloaded on a computer and then Fourier transformed.

Two correlated heterodyne signals, previously registered in a heterodyne detection bench described in [11], are generated *a posteriori* through Arbitrary Waveform Generators (AWGs) and applied to the MZMs. A set of 2^{16} samples were generated at a rate of 100 MSa/s, and encode the fringes at a frequency difference of $f_{12} = 350$ kHz after generation, thus creating two fringe peaks at 1.7 ± 0.35MHz at the output of the amplitude correlators, according to Eq (15). The frequency difference f_{12} contained in our heterodyne signals arises from the initial set-up described [11], based itself on the method used in the Infrared Spatial Interferometer (ISI, [17]) to encode the fringes. In the initial set-up in [11], before the detection of the heterodyne signals, the fringe are encoded through a fixed frequency difference introduced between the infrared local oscillators (7 MHz, sampled at 2 GSa/s), which translates into a frequency $\frac{0.1}{2} \times 7\,\text{MHz} = 350\,\text{kHz}$ after generation, taking into account the playback rate of AWGs.

B. Fringe signal and coherence envelope

The typical fringe peaks registered at the output of the amplitude correlator are shown in Fig.4. As described in Eq (16) , the amplitude of each peak is proportional to the coherent flux, and will constitute the main observable in the following. We will not focus on the phase of the fringes, which can be exploited here, but do not contain particular information in this demonstration.

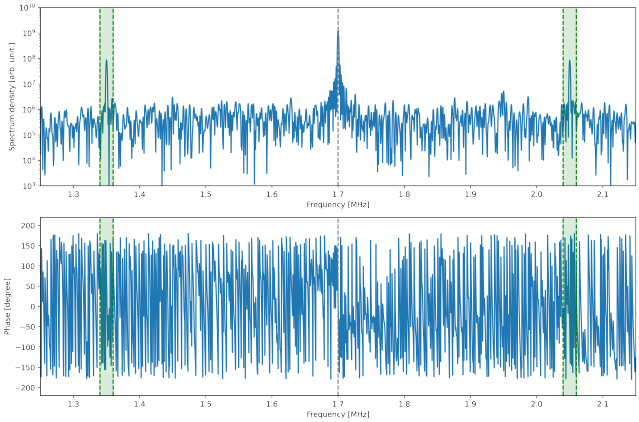

Fig. 4. Intensity (top) and phase (bottom) of the correlated signals. Coherent flux peaks at the output of the amplitude photonic correlator can be seen and are highlighted in green. These peaks are centered around the AOMs frequency difference at 1.7MHz.

The coherent flux is estimated by integrating the coherent peaks in frequency and computing the average of the amplitude obtained on the two peaks. This operation is repeated for several relative delays between each correlator arm. Experimentally, the numerical ns-delay is introduced at the level of the AWGs between the two RF signals. The change in the coherent flux peaks with respect to the relative delay shows the coherence envelope $G(\Delta\tau)$ of the incident signals, as shown in Fig.5. The coherence envelope retrieved in Fig.5 from this measurement exhibits a Gaussian shape, consistent with the noise statistics of the incident signal, and a typical full-width at half maximum (FWHM) of 12ns, consistent with the AWG playback rate and the minimum rise-time of the AWGs.

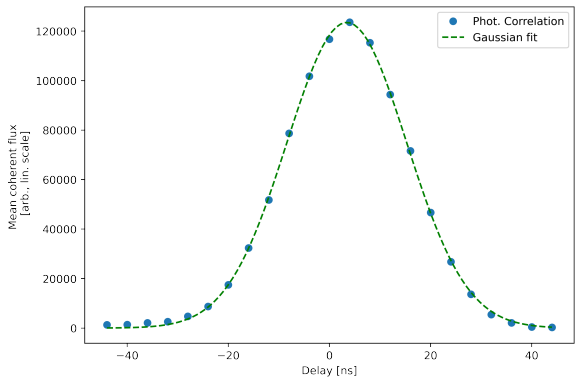

Fig. 5. Coherent flux versus delay for noise signal. The Gaussian envelope is the coherence envelope of the signal.

The comparison between the numerical correlation of the signals and the actual correlation obtained through photonic processing in Fig.4 shows a ratio of Signal-to-Noise Ratio (SNR) larger than 90%. This value is comparable or better than in phase modulation.

C. Phase stabilization

Given the relatively short acquisition time considered here, not greater than a few tens of milliseconds, the relative phase variations between the arms of the photonics correlator do not limit the coherent integration time. The typical phase variations of the optical bench are of the order of few milli-seconds to a second typically. In this case, the correlator is operating in a truly passive way, in contrast to correlators based on phase modulation for the same typical integration time, which had to be locked at a precise functioning point.
Depending on whether the maximum coherent time is set by the atmosphere, or by the environmental phase perturbations inside the photonic processing, a phase stabilization loop would be needed to counter the environmental phase perturbations to reach the ultimate sensitivity of the correlator, for which part of the phase stabilization strategy developed in [11] could be used.

5. DISCUSSION

The general framework of this study is an heterodyne interferometer such as PFI[3], combining a large number of telescopes and covering a large bandwidth with a dispersed frequency comb at each telescope. In this section, we discuss the extension of the photonic correlation scheme in this perspective, taking into account the compensation in the photonic correlator of the optical delay between telescopes (Sec A), and the extension of the correlation scheme to a large number of telescopes (Sec B) and a large number of spectral channels (Sec C).

A. Optical delay difference compensation

For astronomical applications, one has to take into account that the source crosses the sky due to sidereal motion, which causes a propagation delay difference between the telescope. Moreover, the finite width of the coherence envelope $|G(\Delta\tau(t))|$ of the signal constrains the optical delay between each arm to within a coherence length $c\Delta\tau(t) \ll c/\Delta\nu$. This delay can be compensated in the RF domain, by introducing RF cables with different lengths as was done in the ISI [17], or any time downstream in the photonic processing chain with a fibered optical delay. This latter solution is the preferred option envisioned to handle large delays. This stage of the fibered delay line could consist in a set of different fiber lengths, switched at a relatively low rate (of the order of few seconds). This first stage could benefit from standard fibered components developed in the frame of telecom industry or phased array applications.
In this approach, the minimum length difference between each fiber would then be covered by a second stage, covering this smaller range with a higher precision (coherence length) and continuous variations, given that the relative position of the zero delay varies in time, depending on the elevation of the object and on the telescope baseline. This second stage is also currently under study.
Finally, a last consequence of earth rotation is the non-zero phase velocity of the fringes, as mentioned in Section 2, and detailed in Appendix A. As a phase variation, it can be compensated by a frequency shift, either at the level of the LOs or downstream in the photonic correlator itself. In particular, in the case of the amplitude correlation with frequency shift (Section B.3), this effect can be simply compensated by computing the correction frequency in advance and applying it to the AOMs.

B. Extension to a large number of telescopes

The beam combination scheme described so far enables the correlation of the signal coming from two photodiodes i.e. only two telescopes, with one spectral channel integrated over the whole detection bandpass. In our experiments it is carried with a fiber coupler. In the context of a future facility such as PFI, we have to extend this concept to a large number of telescopes ($N_t \approx 30$). The use of photonics technologies borrowed from the telecommunication industry allows integrated-optics-based beam combination solutions to be used for the final beam interference function of the correlator. For example, four beam combiners have been developed for astronomical direct interferometry [18] and 8 beam combiners have been designed [19]. The fact that, here, the correlation works with a narrow spectral line laser simplifies the chromaticity and throughput constraints previously encountered in astronomical broadband applications. There are several architectures that can ensure the beam-interfering function inside the correlator depending on the type of correlation flux encoding (e.g. spatial, temporal or static-phase shifting) and the beam routing, (e.g. pair-wise, all-in one, hybrid) as described in [20]. Theoretically all architectures should be applicable provided the instrumental encoding can handle the 66 baselines requested in PFI minimum configuration [3] or the 435 baselines requested in a more ambitious 30 telescope array. In a general manner, all architectures (spatial, temporal, static-phase shifting) and all modulation schemes (phase and amplitude modulation) discussed here require a stabilization of the relative phase of the channels. This requires either a separate dedicated metrology sub-system or to use a beam combination architecture compatible with high cadence single-pixel telecommunication detectors, such as demonstrated in [11]. The latter option is preferred because it allows for the integration of the metrology system in the same channel that the signal channel. The need for an architecture compatible with high cadence detection leads us to prefer temporally-encoded pair-wise or all-in one schemes, compatible with this high cadence operations, compared to spatial or static phase-shifting encoding.

B.1. Pair-wise combination

The first immediate application of photonic correlation to a larger number of telescopes consists in the pairwise correlation of each telescope signal individually. This could be done via phase or amplitude modulation, by combining each pair of telescope signals as described in Eq (10) or Eq (14) respectively. At the output of the combiner, $N_t(N_t-1)/2 \times n_c$ outputs are simultaneously detected, with n_c the number of outputs registered simultaneously at one baseline. In particular, $n_c = 2$ for operation using balanced detection (Eq (10) and Eq (14) respectively), corresponding to two outputs with opposite phases.
In practice, as aforementioned, such a pairwise correlation of photonic signals is already done in classical interferometry for more than two decades, and the integrated optics combiners developed for this purpose [18, 19] could be directly used in photonic correlation. In particular, the AC combination scheme, which offers two opposite phases output per baseline, would be favored as they are perfectly adapted to operate with a balanced detector.
Notably, contrary to classical interferometry, where the splitting of the telescope signals induces a decrease of the optical carrier

flux coming from each telescope, splitting the signal in heterodyne interferometry does not induced a fundamental loss of sensitivity, as long as the noise figure of the photonic processing does not dominate the budget of the detection chain. This problem, together with the figures of merit to evaluate the quality of the photonic processing chain, enters precisely in the frame of microwave-photonics developments [21]. However, a pairwise combination scheme for more than 12 telescopes might prove a technological challenge since the integrated optics would need to interfere at least 66 telescope combinations. Massive progress in the field of highly confined photonics (e.g. silicon based, see [22]) might provide a way out but this remains to be explored and led us to examine the all-in-one scheme.

B.2. All-in-one with frequency encoding

The alternative to this pair-wise concept consists in summing together all the telescope signals at once, and then separating each baseline with a non-redundant frequency encoding. This is the so-called all-in-one combiner.

In this scheme, each telescope still has a carrier light with a designated MZM and AOM, with angular frequency shift $\Delta\omega_k$. These different channels are summed together and detected on a photodiode. The expression of the intensity detected by the photodiode can be written :

$$\left|\sum_k \beta_k s_k(t) e^{i\Delta\omega_k t}\right|^2 = \sum_k (\beta_k s_k(t))^2 + 2\mathrm{Re}\left(\sum_{k\neq l} \beta_k \beta_l s_k(t) s_l(t) e^{i[(\Delta\omega_k - \Delta\omega_l)t + \phi_k(t) - \phi_l(t)]}\right) \quad (17)$$

where the frequency differences $(\Delta\omega_k - \Delta\omega_l)$ are chosen so that they are non-redundant for every $k \neq l$. Each baseline associated to the telescope pair (k,l) is thus encoded at a given frequency difference $\Delta\omega_k - \Delta\omega_l$, which does not overlap with any other pair of telescopes.

The fundamental advantages here would rely on the fact that the information is encoded in the frequency domain, which can bear a massive multiplexing capability with simple hardware requirements and less complex combination routing, since it could rely on a cascade of directional couplers. For an array of 30 telescopes, there are 435 unique combinations. The ratio between the smallest and largest spacing in the frequency domain for a non-redundant encoding scheme is approximately 1000 [23]. For a frequency minimum spacing of 10 kHz, which is constrained by the atmospheric coherence time, the non-redundant frequency series extends to 10 MHz, where this is certainly compatible with telecom photodiodes and electronics. Such a combination would represent a major simplification of the design of the combiner compared to pairwise correlation, as it would only require summing N_t channels, rather than physically performing $N_t(N_t-1)/2$ combinations, where N_t is the number of telescopes.

B.3. Direct-imager

The two previous correlation techniques are derived from current radio and optical infrastructure architectures, which are built to measure the spatio-spectral coherence of the incoming electro-magnetic field at as many spatial frequencies as possible. This, in turn, makes it possible to reconstruct an image. A significantly different option could consist in forming directly the image of the astronomical object. This could be done by arranging the outputs of the fibers coming from each telescope in a scaled-down version of the entrance pupil of the telescope array and imaging the direct combination. In this way, the image is convolved by the response of the array and forms in the focal plane of the lens, where it can be recorded on a camera. This principle was already proposed in the context of millimeter wave imaging by Blanchard et al. [24] and shares intrinsic similarities with optical beamforming technologies. In principle, it also shares analogous ideas with the Fizeau and densified pupil (hypertelescope) modes in classical interferometry [25].

Direct-imager mode requires stringent operating conditions on the fiber link in order to observe a proper image of the object. First and foremost, every baseline has to be coherenced and cophased simultaneously, otherwise the final image will be blurred. This condition imposes a simultaneous phase stabilization of the entire fibered link, based either on a potential external phase stabilization mechanism, or on Redundant Phase Calibration (RSC) as proposed in [24]. The extrapolation of this second solution remains problematic in the case of an astronomical array with low redundancy. Phase stabilization still remains an open question to be solved in the case of the direct imager.

Notably, the principle proposed by Blanchard et al. was regained and extensively developed in the context of millimeter wave imaging, to combine simultaneously 224 apertures with a 75 GHz bandwidth and a Noise Equivalent Temperature Difference (NETD) compatible with sensitive imaging in this wavelength regime [26]. An additional nuance of this method lies in the fact that one of the sidebands of the modulated optical carrier has to be suppressed in order to avoid the superposition of two centro-symmetric replicas of the image [24]. Sideband suppression can be performed by the use of dual parallel Mach-Zehnder modulators or by very narrowband optical filters [27].

Overall, it is more likely that the direct combination is fully advantageous for a significantly large number of telescopes ($N_t > 30$), for which pairwise correlation would appear cumbersome. For $N_t \leq 30$, pair-wise and all-in-one schemes appear as the preferred options, as they enable the independent control and registration of each baseline, and to post-process the whole visibility information in the UV-plane. Given its much less demanding requirements on the beam combination unit, all-in-one appears as a particularly interesting perspective for both a small and a large number of telescopes.

C. Extension to a large number of spectral channels

The general framework of this study is an heterodyne interferometer with a large number of telescopes and covering a large bandwidth. In this interferometer architecture, the extension in bandwidth is achieved by a frequency comb, which by definition emits discrete laser lines, equally spaced in frequency, and with a stable relative phase between them. Before the detection, these lines, which we refer to as "teeth" in the following, are dispersed by a spectrograph on multiple photodiodes, where each of them act as a mid-infrared local oscillator, to record simultaneously a large number of spectral channels. As a consequence, in addition to a large number of telescopes, the photonic architecture considered in this paper aimed at correlating simultaneously a large number of detectors associated to these spectral channels. In this section, we propose two main strategies to handle this multiplexing in the photonic correlator.

C.1. Wavelength multiplexing

The first approach consists in multiplexing the information associated to the mid-infrared spectral channel in the wavelength domain of the photonics correlator. The schematic principle of

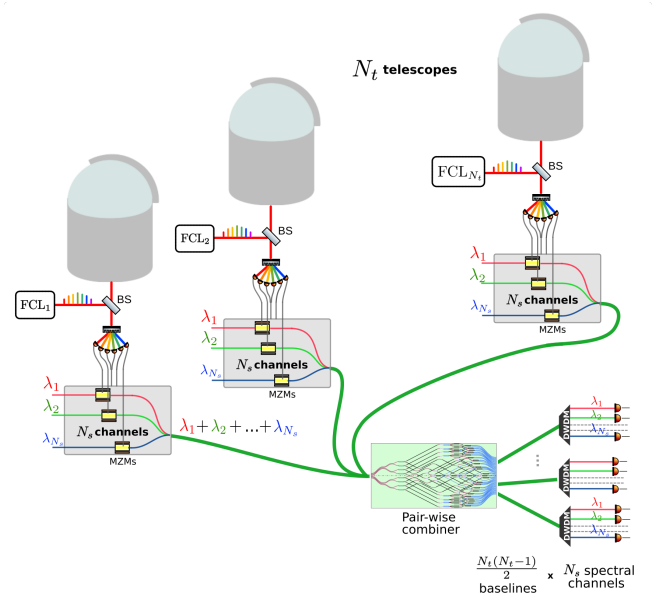

Fig. 6. Extension of the photonic correlator to the correlation of a large number of spectral channels with wavelength multiplexing. After the detection stage, the signals are encoded on an individual wavelength, transported in the same fiber, and combined to extract the different baselines (here in a pair-wise combiner). The individual spectral channels are finally retrieved through a demultiplexing with DWDMs.

this architecture is represented in Fig 6. At the level of each telescopes, the modulators associated to one mid-infrared detector (i.e. one tooth of the frequency comb, Fig 6) could be associated to one telecommunication wavelength (i.e. Dense Wavelength Dispersed Multiplexing DWDM). Then, all the telecommunication wavelengths could be transported in the same transport fiber, and injected in the same pair-wise combiner described in Sec B.1 (or the all-in-one combiner of Sec B.2). At the output of the combiner, the spectral information is then recovered by dispersing the light, producing $N_t(N_t-1)/2 \times N_s$ outputs (or N_s for an all-in-one combiner) , with N_s the number of spectral channels processed simultaneously. To this end, this wavelength multiplexing scheme benefits from the DWDM technology of the telecom industry. The principal constraint here would be to limit the chromatic dispersion during the propagation through the fiber, which could be facilitated by the relatively modest distance considered here (up to 1km or a few kms typically) compared to typical distances in telecom (several 100kms). Phase stabilization can be achieved using the frequency modulation system demonstrated in [11], where each spectral channel can be stabilized separately using the AOMs.

C.2. Frequency multiplexing

A second potential path could encode the spectral information non-redundantly in the frequency domain. In particular, this strategy could exploit techniques used by dual-comb spectroscopy [28, 29].

The schematic principle is shown in Fig 7. Let us first consider a pair-wise combination (Sec B.1), and a telescope array on which a mid-infrared frequency comb is placed at level of each telescope station. As in dual comb spectroscopy, the frequency spacing f_s of the teeth for each comb can be chosen to N_t distinct values : given that the output RF signals are encoded at the frequency difference between each LO frequency, plus a possible adjustment at the level of the AOM, the correlation signal produced at the output of the combiner will consist in the difference of two combs with slightly distinct frequency spacing $f_{s,1}$ and $f_{s,2}$. This frequency difference results in a RF comb with frequency spacing $f_{s,2} - f_{s,1}$. In that respect, the output of the combiner will be made of $N_t(N_t-1)/2$ physical outputs, from which N_s spectral channels could be extracted from such a RF comb in the frequency domain. Here, we have implicitly considered that the carrier envelope offset frequency (f_{ceo}) of each mid-infrared comb are set to the same fixed common value.

The main advantage of the frequency multiplexing approach would be to put aside the need of physical demultiplexing with DWDM at the output of the beam combiner, the signal being multiplexed in the RF frequency domain. This approach would take full benefit of the massive multiplexing capability that can be performed in the RF domain, and would relax the requirements on the hardware. On a prospective basis, it could be envisioned that a specific non-redundant computation of both the repetition rate and of the carrier envelope offset frequency (f_{ceo}) of the frequency combs of each telescope could enable to multiplex both the different spectral channels and the different baselines, possibly avoiding part or all of the need of a pair-wise combiner, at the benefit of an all-in-one combiner.

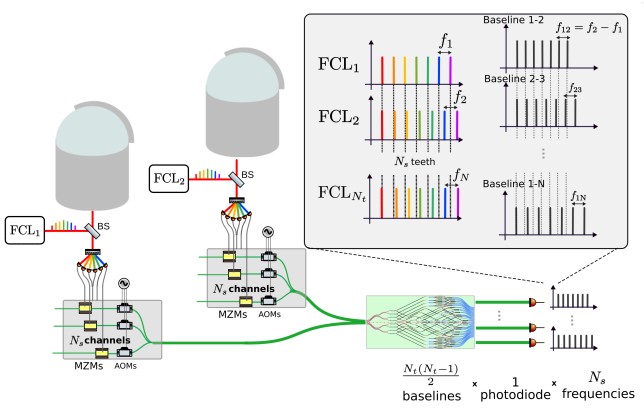

Fig. 7. Extension to the correlation of a large number of spectral channels with frequency multiplexing. After the mid-infrared detection stage of one telescope, the signals are encoded on MZMs, plus a possible ajustement with AOM, and transported in the same fiber. The signals originating from the different telescopes are then combined in a pair-wise combiner. At the output of the combiner, the demultiplexing is achieved in the frequency domain, by looking at the frequency difference of the initial mid-infrared combs, in an analogous way to dual-comb techniques.

6. CONCLUSION

In this paper, we have shown that photonic correlation of two heterodyne signals can be performed both by using the intermediate frequency signal to modulate in phase or in amplitude a narrow line laser source. The amplitude modulation scheme has been implemented experimentally, with a performance comparable to that of phase modulation. Amplitude modulation

is preferred over phase modulation given its simple implementation and less demanding requirement on phase stabilization, and its capability to add an additional degree of freedom on frequency encoding of the fringes. This concept could be potentially extended to a large number of telescopes ($N_t \leq 30$) with the use of integrated optics combiners. Direct imaging combination proposed in the context of millimetric imaging could also be applied, presumably with an advantage for a larger number of telescopes ($N_t \geq 30$). Photonic correlation could be scaled to a larger number of spectral channels through the use of DWDM technologies, and more prospectively through the use of concepts derived from dual comb spectroscopy. The noise analysis of these different types of photonics correlator is the subject of a forthcoming work.

In its simple form ($N_t \leq 8$, and one or a few spectral channels), the photonics correlator could be coupled to a set of modular heterodyne detection units adaptable to existing astronomical infrastructures. A remaining item is the development of fibered delay lines at telecommunication wavelengths. Altogether, these elements could enable exploitation of the full imaging capabilities of current infrared interferometric facilities, such as VLTI [10], and serve as a basis of a demonstration of technology for a kilometric baseline imaging interferometer in the mid-infrared.

7. ACKNOWLEDGMENTS

This work was partially funded by INSU-CNRS through the Commission Spécialisée Astronomie & Astrophysique (CSAA) and the Action Spécifique Haute Résolution Angulaire (ASHRA) co-funded by CNES. It was partially funded by LabEx FOCUS ANR-11-LABX-0013. We acknowledge the additional funding of Agence Nationale de la Recherche (“ANR FROST”, ANR-14-CE32-0022).

Disclosures. The authors declare no conflicts of interest.

REFERENCES

1. P. H. van Cittert, “Die Wahrscheinliche Schwingungsverteilung in Einer von Einer Lichtquelle Direkt Oder Mittels Einer Linse Beleuchteten Ebene,” Physica **1**, 201–210 (1934).
2. F. Zernike, “The concept of degree of coherence and its application to optical problems,” Physica **5**, 785–795 (1938).
3. J. D. Monnier, S. Kraus, M. J. Ireland, F. Baron, A. Bayo, J.-P. Berger, M. Creech-Eakman, R. Dong, G. Duchêne, C. Espaillat, C. Haniff, S. Hönig, A. Isella, A. Juhasz, L. Labadie, S. Lacour, S. Leifer, A. Merand, E. Michael, S. Minardi, C. Mordasini, D. Mozurkewich, J. Olofsson, C. Paladini, R. Petrov, J.-U. Pott, S. Ridgway, S. Rinehart, K. Stassun, J. Surdej, T. t. Brummelaar, N. Turner, P. Tuthill, K. Vahala, G. van Belle, G. Vasisht, E. Wishnow, J. Young, and Z. Zhu, “The planet formation imager,” Exp. Astron. **46**, 517–529 (2018).
4. C. H. Townes, “Spatial interferometry in the mid-infrared region,” J. Astrophys. Astron. **5**, 111–130 (1984).
5. G. W. Swenson, “Radio-astronomy precedent for optical interferometer imaging,” J. Opt. Soc. Am. A, JOSAA **3**, 1311–1319 (1986).
6. M. J. Ireland and J. D. Monnier, “A dispersed heterodyne design for the planet formation imager,” in *Optical and Infrared Interferometry IV,* vol. 9146 of *Society of Photo-Optical Instrumentation Engineers (SPIE) Conference Series* J. K. Rajagopal, M. J. Creech-Eakman, and F. Malbet, eds. (2014), p. 914612.
7. D. Palaferri, Y. Todorov, A. Bigioli, A. Mottaghizadeh, D. Gacemi, A. Calabrese, A. Vasanelli, L. Li, A. G. Davies, E. H. Linfield, F. Kapsalidis, M. Beck, J. Faist, and C. Sirtori, “Room-temperature nine-µm-wavelength photodetectors and GHz-frequency heterodyne receivers,” Nature **556**, 85–88 (2018).
8. A. Bigioli, G. Armaroli, A. Vasanelli, D. Gacemi, Y. Todorov, D. Palaferri, L. Li, A. G. Davies, E. H. Linfield, and C. Sirtori, “Long-wavelength infrared photovoltaic heterodyne receivers using patch-antenna quantum cascade detectors,” Appl. Phys. Lett. **116**, 161101 (2020).
9. M. Hakl, Q. Y. Lin, S. Lepillet, M. Billet, J.-F. Lampin, S. Pirotta, R. Colombelli, W. J. Wan, J. C. Cao, H. Li, E. Peytavit, and S. Barbieri, “Ultra-fast quantum-well infared photodetectors operating at 10μm with flat response up to 70GHz at room temperature,” arXiv e-prints arXiv:2007.00299 (2020).
10. J.-P. Berger, G. Bourdarot, and H. Guillet de Chatellus, “V8: an 8 beam mid-infrared heterodyne instrument concept for the VLTI,” in *Society of Photo-Optical Instrumentation Engineers (SPIE) Conference Series,* vol. 11446 of *Society of Photo-Optical Instrumentation Engineers (SPIE) Conference Series* (2020), p. 1144613.
11. G. Bourdarot, H. Guillet de Chatellus, and J. P. Berger, “Toward a large bandwidth photonic correlator for infrared heterodyne interferometry. A first laboratory proof of concept,” Astron. & Astrophys. **639**, A53 (2020).
12. A. R. Thompson, J. M. Moran, and J. Swenson, George W., *Interferometry and Synthesis in Radio Astronomy, 3rd Edition, Chapter 6 "Response of the Receiving System"* (2017).
13. J. D. Monnier, “Infrared interferometry and spectroscopy of circumstellar envelopes,” Ph.D. thesis (1999).
14. R. H. Kingston, “Detection of optical and infrared radiation,” Springer Ser. Opt. Sci. Berlin: Springer, 1978 (1978).
15. R. P. Escoffier, G. Comoretto, J. C. Webber, A. Baudry, C. M. Broadwell, J. H. Greenberg, R. R. Treacy, P. Cais, B. Quertier, P. Camino, A. Bos, and A. W. Gunst, “The ALMA correlator,” Astron. Astrophys. **462**, 801–810 (2007).
16. O. Gentaz, “PolyFiX: Lessons learned from the NOEMA Wideband Correlator System,” in *ALMA Development Workshop,* (2019), p. 16.
17. D. D. S. Hale, M. Bester, W. C. Danchi, W. Fitelson, S. Hoss, E. A. Lipman, J. D. Monnier, P. G. Tuthill, and C. H. Townes, “The Berkeley Infrared Spatial Interferometer: A Heterodyne Stellar Interferometer for the Mid-Infrared,” The Astrophys. J. **537**, 998–1012 (2000).
18. M. Benisty, J.-P. Berger, L. Jocou, P. Labeye, F. Malbet, K. Perraut, and P. Kern, “An integrated optics beam combiner for the second generation VLTI instruments,” Astron. Astrophys. **498**, 601–613 (2009).
19. P. Labeye, “Composants optiques intégrés pour l’Interférométrie astronomique,” Theses, Institut National Polytechnique de Grenoble - INPG (2008).
20. J.-B. J. Lebouquin, J.-P. Berger, P. R. Labeye, E. Tatulli, F. Malbet, K. Rousselet-Perraut, and P. Y. Kern, “Comparison of integrated optics concepts for a near-infrared multi-telescope beam combiner,” in *New Frontiers in Stellar Interferometry,* vol. 5491 of *Society of Photo-Optical Instrumentation Engineers (SPIE) Conference Series* W. A. Traub, ed. (2004), p. 1362.
21. D. Marpaung, C. Roeloffzen, R. Heideman, A. Leinse, S. Sales, and J. Capmany, “Integrated microwave photonics,” arXiv:1211.4114 [physics] (2012). ArXiv: 1211.4114.
22. S. A. Miller, Y.-C. Chang, C. T. Phare, M. C. Shin, M. Zadka, S. P. Roberts, B. Stern, X. Ji, A. Mohanty, O. A. J. Gordillo, U. D. Dave, and M. Lipson, “Large-scale optical phased array using a low-power multi-pass silicon photonic platform,” Optica **7**, 3–6 (2020).
23. E. N. Ribak, E. B. Hochberg, N. A. Page, S. P. Synnott, and J. B. Breckinridge, “Beam combination in a multi-telescope, monolithic interferometer.” in *European Southern Observatory Conference and Workshop Proceedings,* vol. 29 of *European Southern Observatory Conference and Workshop Proceedings* (1988), pp. 1105–1116.
24. P. M. Blanchard, A. H. Greenaway, A. R. Harvey, and K. Webster, “Coherent Optical Beam Forming with Passive Millimeter-Wave Arrays,” J. Light. Technol. **17**, 418–425 (1999).
25. A. Labeyrie, “Resolved imaging of extra-solar planets with future 10-100km optical interferometric arrays.” Astron. & Astrophys. **118**, 517–524 (1996).
26. C. Schuetz, R. Martin, T. Dillon, P. Yao, D. Mackrides, C. Harrity, A. Zablocki, K. Shreve, J. Bonnett, P. Curt, and D. Prather, “Realization of a video-rate distributed aperture millimeter-wave imaging system using optical upconversion,” in *Passive and Active Millimeter-Wave*

Imaging XVI, vol. 8715 of *Society of Photo-Optical Instrumentation Engineers (SPIE) Conference Series* D. A. Wikner and A. R. Luukanen, eds. (2013), p. 87150I.
27. C. A. Schuetz, J. Murakowski, G. J. Schneider, and D. W. Prather, "Radiometric Millimeter-wave detection via optical upconversion and carrier suppression," IEEE Transactions on Microw. Theory Tech. **53**, 1732–1738 (2005).
28. N. Picqué and T. W. Hänsch, "Frequency comb spectroscopy," Nat. Photonics **13**, 146–157 (2019).
29. I. Coddington, N. Newbury, and W. Swann, "Dual-comb spectroscopy," Optica **3**, 414 (2016).
30. I. Cox, Charles H., *Analog Optical Links* (2004).

APPENDIX A : CORRELATION OF ASTRONOMICAL HETERODYNE SIGNALS

In this section, we detail further the expression of the correlation signal and of the fringe frequency at the output of an heterodyne interferometer, as provided in Eq. (5). For a complete description in the context of radio-astronomy, we refer the reader to [12].
First, the phase term of the fringes can be broken down into its different contributions, by introducing $\vec{S}_0$ the center of the interferometric field of view, $\vec{\sigma}$ the angular position relative to the center of this field of view, and τ_{off} the delay introduced in the RF domain to compensate for the delay between each telescopes :

$$\begin{aligned}\phi_{\text{tot}}(\theta,\omega_s) &= \omega_s \frac{B}{c}\left(\vec{S}_0(t)+\vec{\sigma}\right) - (\pm\omega_{\text{if}}\tau_{\text{off}}) \\ &= \omega_s \underbrace{\frac{B}{c}\vec{S}_0(t)}_{\tau_B(t)} + \underbrace{\omega_s \frac{B}{c}\vec{\sigma}}_{\phi(\theta,\omega_s)} - (\pm\omega_{\text{if}}\tau)\end{aligned} \tag{18}$$

, with $\tau_B(t)$ the delay between each telescope, $\phi(\theta,\omega_s)$ the astrophysical phase of the object and τ the additional delay introduced in the RF chain downstream the correlator.

The correlator performs the multiplication product of the heterodyne signals described in Eq (1), which results in Eq (4) for one incident frequency ω_s of the intermediate frequency bandpass and one angular direction θ in the interferometric field of view. Without further operations, all the angular directions as well as all the wavelengths are integrated in the output, which results in :

$$\begin{aligned}\langle s_1(t)s_2(t)\rangle &\propto \int_{\omega_{\text{if}}}\int_{\theta}\Big(|E_s(\theta,\omega_s)|^2 e^{i[\Phi_2(t)-\Phi_1(t)]}e^{i[\omega_s\tau_B(t)-(\pm\omega_{\text{if}}\tau)]} \\ &\qquad e^{i\phi(\theta,\omega_s)} + \text{c.c.}\Big)\,\mathrm{d}\theta\mathrm{d}\omega_{\text{if}} \\ &\propto \int_{\omega_{\text{if}}}\Big(|F_c(B/\lambda,\omega_s)|e^{i\phi_V(B/\lambda,\omega_s)}e^{i[\Phi_2(t)-\Phi_1(t)]} \\ &\qquad e^{i[\omega_s\tau_B(t)-(\pm\omega_{\text{if}}\tau)]} + \text{c.c.}\Big)\,\mathrm{d}\omega_{\text{if}} \\ &\propto |F_c(B/\lambda,\omega_s)|e^{i\phi_V(B,\omega_s)}e^{i[\Delta\Phi(t)+\omega_{\text{L0},1}\tau_B(t)]} \\ &\qquad \times |G(\Delta\tau(t))|e^{\pm i\phi_G}e^{\pm i\omega_c\Delta\tau(t)} + \text{c.c}\end{aligned}$$

with $\Delta\tau = \tau_B(t) - \tau$, and $\Delta\Phi_{21}(t) = \Phi_2(t) - \Phi_1(t)$
The last equation corresponds exactly to Eq (5), with the fringes frequency described by :

$$\Delta\Phi(t) + \omega_{\text{L0},1}\tau_B(t) = 2\pi f_k t \tag{19}$$

The frequency of the fringes is thus described by two terms : first, the phase difference between the two mid-infrared LOs $\Delta\Phi_{21}(t)$, and second, $\omega_{\text{L0},1}\tau_B(t)$, which corresponds to the so-called natural fringe frequency. Eq (19) makes clear how a small frequency difference between the mid-infrared LOs can compensate for the natural fringe frequency. More generally, Eq (19) summarizes how the fringe frequency at the output of the correlator are encoded, taking into account the relative phase stabilization of the LOs and the contribution of the natural fringe frequency.

APPENDIX B : VALIDITY OF THE SMALL SIGNAL APPROXIMATION

The small signal approximation assumed in the case of amplitude modulation is valid within the range of values for which the non-linearities of the modulator can be neglected. In our case, the terms of order 2 are either suppressed by the balanced detection $\langle s_k^2(t)\rangle$, or are the terms we seek to compute to obtain the correlation product $\langle s1(t)s2(t)\rangle$. The first non-linearity that affects our measurements is thus the non-linearity of order 3. In a Mach-Zehnder, this quantity is usually characterized by the Intercept Point of order 3 (IP3), which corresponds to the input RF power on the modulator at which the power of the 3rd order intermodulation (IMD) is equal to the fundamental signal [30]. In the same way, the Intercept Point of order 2, can be defined as the input RF power where 2nd order IMD is equal to the fundamental signal.

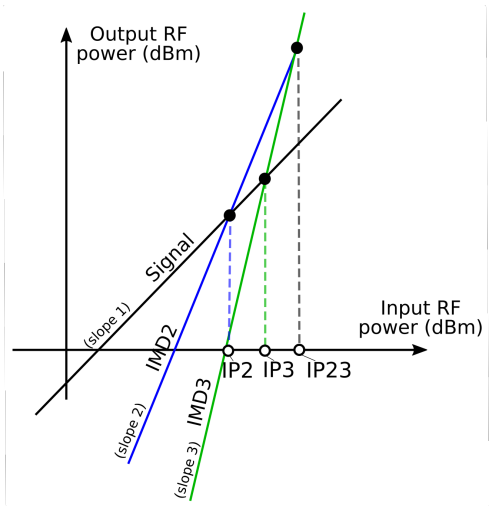

Fig. 8. The relation between input and output RF power in the Mach-Zehnder modulator (log scale), which illustrates the relation between IP_2, IP_3 and IP_{23} geometrically. See the text for notations definition.

In Mach-Zehnder modulators, the expression of IP_3 and IP_3 are [21] :

$$\text{IP}_3 = \frac{4}{R_L}\frac{V_\pi^2}{\pi^2} \quad ; \quad \text{IP}_2 = \frac{2}{R_L}\frac{V_\pi^2}{\pi^2} \tag{20}$$

The small signal approximation is fulfilled when the power of the 3rd order IMD signal is negligible (typically 10dB smaller) compared to the 2nd order IMD. We define IP_{23} the input electrical power at which the 3rd order IMD is equal to the 2nd order IMD. In Fig 8, it can be seen from basic geometrical arguments

that IP_{23} follows the relation (in logarithmic scale) :

$$\begin{aligned} &IP_2 + 2(IP_{23} - IP_2) = IP_3 + 3(IP_{23} - IP_3) \\ \Rightarrow &IP_{23} = 2\,IP_3 - IP_2 \text{ (log scale)} \end{aligned}$$

This last equation, combined with the expression of IP_3 and IP_2 in Eq (20), enables us to simply express IP_{23} as a function of IP_3 :

$$IP_{23} = 2\,IP_3 \text{ (linear scale)} = IP_3 + 3\,\text{dB (log scale)} \qquad \textbf{(21)}$$

The 2nd order and the 3rd order IMD are respectively a power of 2 and 3 of the input electrical power (slope 2 and slope 3 in Fig 8. If we take as a criteria that the 3rd order IMD is 10dB smaller than 2nd order IMD, and taking into account the dependence of each IMD with the input power (slope 2 and slope 3), the maximum input electric power on the modulator is equal to :

$$IP_{23} = IP3 - 2/3 \times 10\,\text{dB} = IP3 - 3\,\text{dB (log scale)} \qquad \textbf{(22)}$$

In our modulators (IXBlue MXAN-LN-10), the specifications for IP3 is 30dBm, which leads to a maximum incident power of 27dBm, or 25 dBm (4Vrms) if we take some margins, which sets the maximum input value that can be used in our set-up.

APPENDIX C : COMPONENTS USED IN THE EXPERIMENTAL SET-UP

In this appendix, we provide basic details about the components and their operation. All the components in the following are commercial off-the-shelf components.

The laser source is a Koheras E15, operating at 1.55 μm with sub-kHz linewidth and an optical power up to 40mW. The laser is fibered, and every component after the laser in the chain are polarization maintaining fibered components. The couplers are standard 1:2 and 2:2 couplers. Concerning the modulators, we used Mach-Zehnder Modulators (MZMs) from the company IXBlue (MXAN-LN-10), with 10 GHz input analog bandwidth, typical half-wave voltage $V_\pi = 10\,$GHz, IP3=30 dBm, and input load $R_L = 50\,\Omega$. We used Acousto-Optic Modulators (AOMs) from the company AA-OPTO (MT80), and are also fibered and polarization maintaining. These modulators operate at a frequency shift of $+80\,$MHz, with a tuning range of $\pm 5\,$MHz around this value. We used a balanced detector Thorlabs PDB470C, with a detection bandwidth DC - 400 MHz, a typical responsivity 0.9 A/W at 1.55 μm and a common mode rejection ratio 25 dB. The rapid oscilloscope is a Lecroy HRO 64Zi, with 400 MHz analog input bandwidth, 2GSa/s maximum sampling rate, and 12 bit ADC resolution. The Arbitrary Waveform Generators (AWGs) are Keysight 33612A, with 80 MHz analog bandwidth, a maximum sampling rate of 1 GSa/s, and typical rise time of the of 2.9 ns. In order to playback the heterodyne signals $s_1(t)$ and $s_2(t)$ previously registered (the generation of these signals is described in [11]), we loaded a set of 2^{16} points of these traces $s_1(t)$ and $s_2(t)$ into the memory of the AWGs. In the AWGs, a Direct Digital Synthesis (DDS) generates the two output analog voltage from these numerical waveforms. We used either a unique AWG with two output channels to generate $s_1(t)$ and $s_2(t)$, or two channels on two different AWGs. In the latter case, the AWGs were synchronized to each other through a standard 10 MHz synchronization channel included in the AWGs.

SF2A 2021
A. Siebert, K. Bailli, E. Lagadec, N. Lagarde, J. Malzac , J.-B. Marquette, M. NDiaye, J. Richard, O. Venot (eds)

V8 CONCEPT AND PHOTONIC CORRELATION FOR MID-INFRARED INTERFEROMETRY

G.Bourdarot[1,2], J.-P. Berger[1] and Hugues Guillet de Chatellus[2]

Abstract. The recombination of a large number of telescopes over kilometric baselines in an infrared interferometric array, such as proposed in the Planet Formation Imager (PFI) initiative, requires the investigation of renewed interferometric architectures. In the mid-infrared, heterodyne interferometry represents a potential solution, appropriate for the recombination of a large number of telescopes and the practical transport of interferometric signals. A major challenge of heterodyne interferometry is the limitation in terms of detection bandwidth, which requires the development of detectors and correlators handling detection bandwidth up to tens of GHz. Here, we report on the status of our technological demonstration in this direction. We present an update of the concepts of photonic correlation, including both phase and amplitude modulation schemes, and their proof-of-principle demonstration in the laboratory. Together with the advent of new mid-infrared high bandwidth detectors and Quantum Cascade Lasers (QCLs), the current state of mid-infrared technologies could be applied to the simultaneous combination of the eight telescopes of the VLTI, so-called V8 concept. We describe the first step in this direction, with the development of mid-infrared test bench at 10.6 μm with 2 detection channels, including a QCL, commercial high-bandwidth detectors and a photonic correlator.

Keywords: Planet Formation Imager, Heterodyne Interferometry, VLTI, Photonic Correlation, QCL

1 Introduction

The development of an infrared interferometric array recombining a large number of telescopes over kilometric baselines represents a major step in observational astrophysics, in particular for the study and the image reconstruction of protoplanetary environments with milli-arcsecond (mas) and sub-mas resolution in the infrared, such as proposed in the Planet Formation Imager (PFI) initiative (Monnier et al. 2018; Ireland & Monnier 2014). In the mid-infrared, heterodyne interferometry, which consists in detecting the amplitude of the field (coherent detection) as a radio-frequency (RF) signal and in correlating these RFs signal between each pair of telescopes, offers a practical solution while relaxing the requirement on a hard infrastructure. In this perspective, the V8 concept (this work and Berger et al. in the same proceedings) proposes to take advantage of the scalability of heterodyne interferometry and of the current state of mid-infrared technologies to combine the 8 telescopes of VLTI simultaneously in the VLTI lab through an heterodyne combiner, which handles the correlation and the delay function on the heterodyne signal, in order to exploit the full imaging capability of VLTI. In the following, we complement the photonic correlation proposed in this perspective and present a preliminary 2 beams combiner at 10.6 μm dedicated to the validation of a complete detection and correlation chain.

2 Photonic correlation

The principles of photonic correlation consists in encoding a wide band RF signal through a photonic modulator on a optical carrier, typically at telecom wavelength, which is then transported and combined on a photodiode. The scheme that enables to extract the correlation product of the signal can be based either on phase modulation or amplitude modulation. In both cases, the signal that is extracted is proportional to the multiplication product of the two input RF channels integrated in time i.e. the correlation product of the input RF signals at one delay. This principle is very similar to the analog RF correlator implemented on the Infrared Spatial Interferometer (Hale et al. 2000).

[1] Univ. Grenoble Alpes, CNRS, IPAG, F-38000 Grenoble, France
[2] Univ. Grenoble Alpes, CNRS, LIPhy, F-38000 Grenoble, France

© Société Francaise d'Astronomie et d'Astrophysique (SF2A) 2021

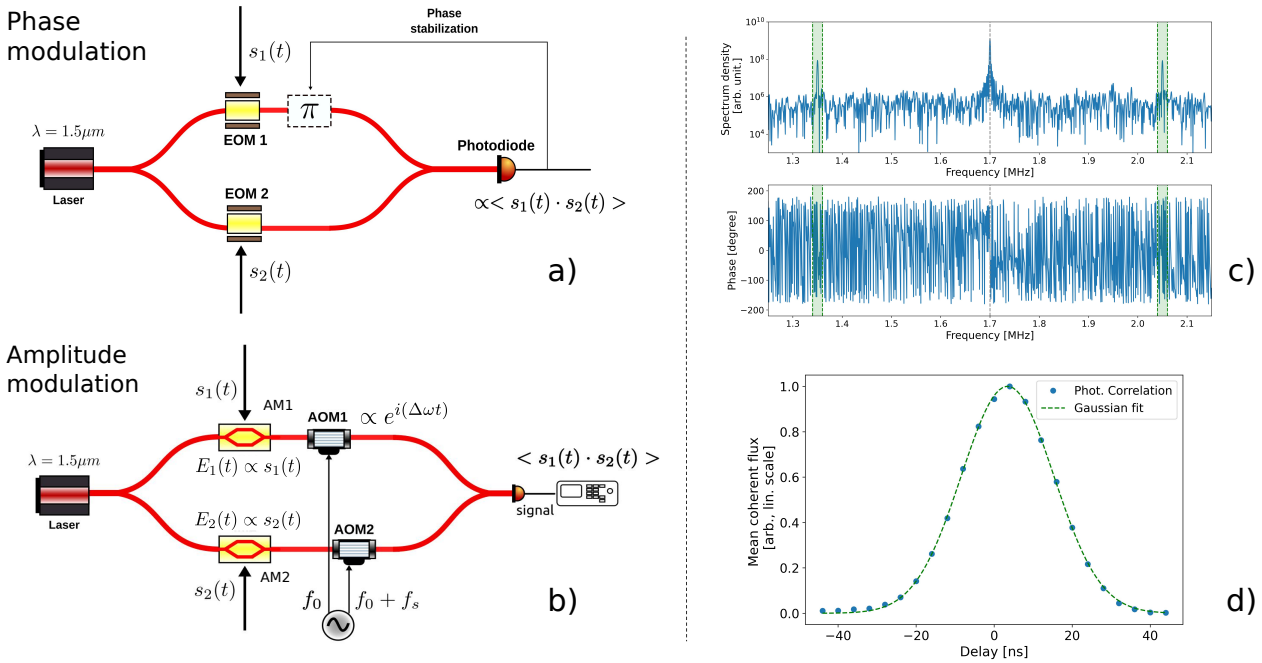

Fig. 1. a) : Phase modulation scheme (EOM : Electro-Optical Modulator) **b) :** Amplitude modulation scheme **c) :** Correlation of heterodyne signals in amplitude modulation (fringe peak in green area). **d) :** Coherence envelope of the correlated signals.

2.1 Photonic correlation in phase modulation

In the phase modulation scheme, the RF signal at the output of the rapid mid-infrared photodiode is encoded on the optical carrier through a phase modulator, placed at the level of each telescope. This signal then propagates in telecom fiber and is combined with an arm coming from an other telescope, which forms a Mach-Zehnder, as shown in Fig 1. The key idea of phase modulation consists in noticing that at a minimum or at a maximum of intensity of a Mach-Zehnder, the output intensity of the Mach-Zehnder varies as the square of the relative phase modulation between the arm. Since the phase modulation is proportional to the input RF signal, the output intensity contains the product term of the two input RF signals, which is the correlation product we seek to compute. A detailed description of the functioning principle as well as its experimental demonstration is given in Bourdarot et al. (2020). The stabilization of the Mach-Zehnder to a given functioning point (maximum or minimum of intensity) is an important constraint of this scheme. In the next section, we describe a second correlation scheme, based on *amplitude* modulation, which enables to relax the requirement on phase stabilization.

2.2 Photonic correlation in amplitude modulation

In the amplitude modulation, an amplitude modulator, on which is imposed the output RF signal of the heterodyne detection stage, is placed in each arm of the Mach-Zehnder, and used at the null of transmission. The optical field $E_k(t)$ in each arm (numbered k) after these two components is :

$$E_k(t) = E_0 e^{i\omega_0 t} e^{i\phi_k} \left(1 - e^{i\beta_k s_k(t)}\right) \approx -iE_0\beta_k s_k(t) e^{i\omega_0 t + i\phi_k(t)} \tag{2.1}$$

where we have assumed that each modulator is at a minimum of intensity, with E_0 the amplitude of the optical carrier at telecom wavelength (carrier), ω_0 the angular frequency of the optical carrier, $\beta_k = \frac{\pi}{V_\pi}$ with V_π the half-voltage of the modulator, $s_k(t)$ the RF signals coming from the heterodyne stage, and $\phi_k(t)$ the phase perturbation in the fiber link. In addition, a fiber frequency shifter (Acousto-Optic Modulator abrev. AOM) can be placed downstream the amplitude modulator, and has the effect of shifting the central frequency of the optical field i.e. multiplying the electric field by $e^{i\Delta\omega_k t}$, with $\Delta\omega_k$ the angular frequency shift in arm k. The

beating term at the output of the Mach-Zehnder (measured with a balanced detection for example) is finally :

$$I(t) = 4I_0 \mathrm{V}_i \beta_1 \beta_2 s_1(t) s_2(t) \cos\left((\Delta\omega_2 - \Delta\omega_1)t + \Delta\phi_{12}(t)\right) \tag{2.2}$$

with $I_0 = |E_0|^2$ and $\Delta\phi_{12}(t) = \phi_2 - \phi_1$. At the output of the correlator, the correlation product $\langle s_1(t) s_2(t) \rangle$ is thus encoded at a given (angular) frequency $(\Delta\omega_2 - \Delta\omega_1)$. In this way, the correlator does not require the stabilization to a given functioning point, but only a relative stabilization over the coherent integration time.

2.3 Experimental demonstration

Following the same methodology than in (Bourdarot et al. 2020), the amplitude modulation scheme was implemented with commercial fibred components, and enables to demonstrate the correlation of heterodyne signals that were previously registered and generated a posteriori with Arbitrary Waveform Generator (AWG). We measure the correlation fringes with a noise factor $> 90\,\%$, and we measure the coherence envelop of the incident signal by varying numerically the relative delay between each arm of the Mach-Zehnder. The results of this proof-of-principles are shown in Fig 1.

2.4 Extension to a large number of telescopes

The photonic correlation scheme described so far is adapted to the correlation of two channels. This scheme can be extended to the correlation of a larger number of telescopes. Different architectures can be envisioned, as in direct interferometry (Lebouquin et al. 2004). These beam combinations can be categorized in different type of flux encoding (spatial, temporal, static phase-shifting) and beam routing (pair-wise, all-in-one, hybrid), cf Fig. 2. In our photonic scheme, temporal techniques are favoured, as they are more suited to the temporal encoding of the fringes in the architecture presented so far, and to the integration of a metrology system in the same channel that the signal channel. In temporal techniques, all-in one combinations based on frequency multiplexing of the fringes, and pair-wise combination, are both compatible to the correlation of a large number of channels. Alternatively, direct-imager combiner, such as proposed in (Blanchard et al. 1999), could also be envisioned, but are less suited to the correlation of a large number of spectral channels, contrary to temporal techniques. These different techniques and the parallel with direct interferometry are summarized in Fig. 2.

3 Preliminary 2 channels heterodyne demonstrator at $10.6\,\mu$m

We propose the implementation of a 2 beam heterodyne combiner at $10.6\,\mu$m in order to demonstrate the detection and correlation architecture devised earlier, to produce a complete sensitivity analysis of this chain, and to validate in the laboratory the technological sub-systems required for V8. The current layout of the

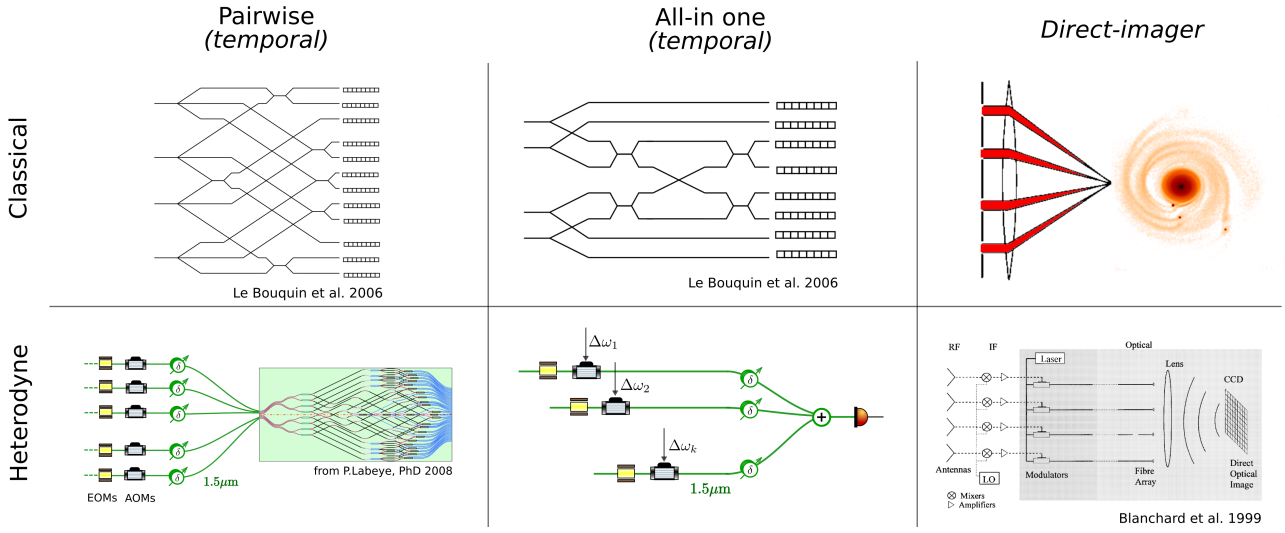

Fig. 2. Extension of the photonic correlation scheme to a larger number of telescopes.

demonstrator is shown in Fig. 3. In this demonstrator, the local oscillator (LO) is a Quantum Cascade Laser (QCL), splitted in two channels to two detectors, which naturally ensures the relative phase stability of the LO between the two channels. The signal channel can be either fed by a laser signal (e.g. the initial QCL) or an independent source (laser, black-body). The current detectors are commercial detectors (VIGO company, 1 GHz bandwidth) , and the correlator is a photonic correlator in amplitude modulation, identical to Sec 2.2. The demonstrator is currently under development, and is designed to observe an heterodyne interferometric signal on a black-body at 900K.

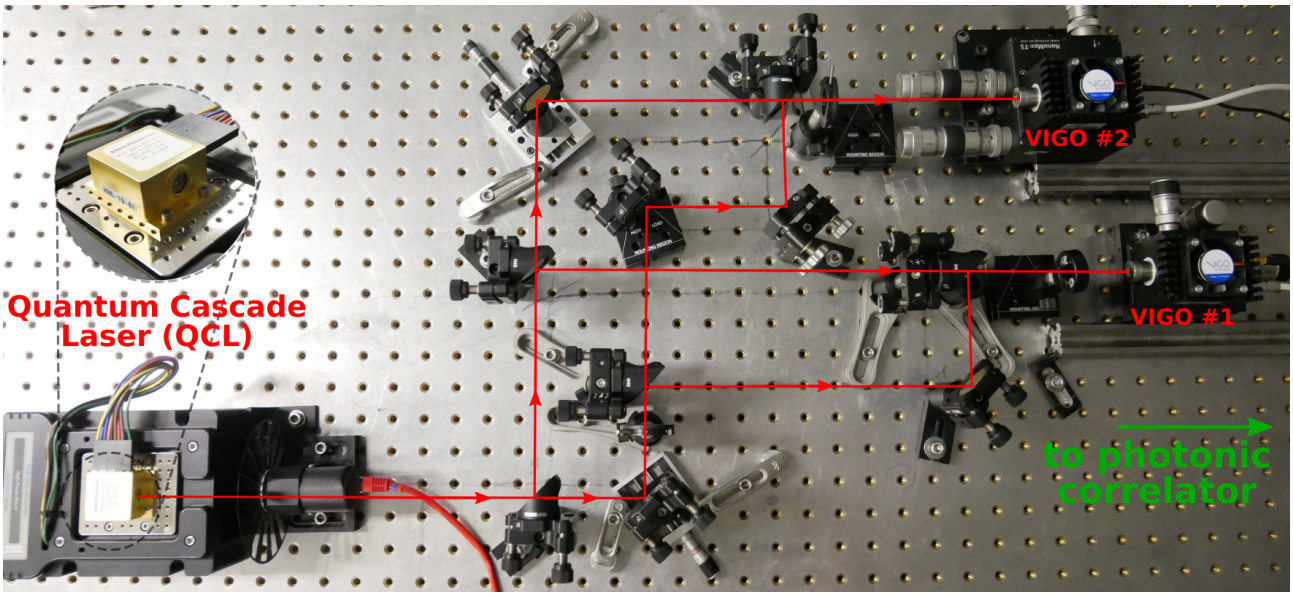

Fig. 3. Mid-infrared optics of the two beam heterodyne interferometric demonstrator at 10.6 μm.

4 Conclusions

The recombination of large number of telescope over kilometric baselines in the mid-infrared can benefit from the use of heterodyne interferometry. We complement the photonic correlation architecture proposed in this purpose with the introduction of amplitude modulation and the extension of this technique to the correlation of a larger number of telescopes. We present the preliminary implementation of a 2 channels heterodyne combiner at 10.6 μm whose goal is to validate the complete detection and correlation chain of our renewed heterodyne architecture, its sensitivity budget, and its essential technological blocks. Once demonstrated, this essential step could be scalable to the correlation of a larger number of telescopes and adaptable to existing infrastructures, in particular to the simultaneous correlation of the eight telescopes of VLTI in the mid-infrared, so-called V8 concept.

This work was partially funded by INSU-CNRS through the Commission Spcialise Astronomie & Astrophysique (CSAA) and the Action Spcique Haute Rsolution Angulaire (ASHRA) co-funded by CNES. It was partially funded by LabEx FOCUS ANR-11-LABX-0013. We acknowledge the additional funding of Agence Nationale de la Recherche (ANR FROST, ANR-14-CE32-0022).

References

Blanchard, P. M., Greenaway, A. H., Harvey, A. R., & Webster, K. 1999, Journal of Lightwave Technology, 17, 418

Bourdarot, G., Guillet de Chatellus, H., & Berger, J.-P. 2020, Astronomy & Astrophysics, 639, A53

Hale, D. D. S., Bester, M., Danchi, W. C., et al. 2000, The Astrophysical Journal, 537, 998

Ireland, M. J. & Monnier, J. D. 2014, in Society of Photo-Optical Instrumentation Engineers (SPIE) Conference Series, Vol. 9146, Optical and Infrared Interferometry IV, ed. J. K. Rajagopal, M. J. Creech-Eakman, & F. Malbet, 914612

Lebouquin, J.-B. J., Berger, J.-P., Labeye, P. R., et al. 2004, in SPIE, Vol. 5491, New Frontiers in Stellar Interferometry, ed. W. A. Traub, 1362

Monnier, J. D., Kraus, S., Ireland, M. J., et al. 2018, Experimental Astronomy, 46, 517

Multi-delay photonic correlator for wideband RF signal processing

GUILLAUME BOURDAROT,[1,2] JEAN-PHILIPPE BERGER,[2] AND HUGUES GUILLET DE CHATELLUS[1,*]

[1] *Laboratoire Interdisciplinaire de Physique, UGA/CNRS, 38000 Grenoble, France*
[2] *Institut de Planétologie et d'Astrophysique de Grenoble, UGA/CNRS, 38000 Grenoble, France*
[*] *hugues.guilletdechatellus@univ-grenoble-alpes.fr*

Abstract: Correlation of RF signals is a fundamental operation in many fields such as information processing, detection and imaging techniques at large. Because of the intrinsic limitations of electronic techniques, standard digital correlators, which rely on the acquisition of signals and their processing, become very complex to implement for the real-time analysis of signals whose bandwidth exceeds a few hundred MHz. In this article, we report a novel analog correlator architecture based on multi-heterodyne interferometry implemented in a simple photonic platform, suitable for wideband RF signal processing. It gives access in real time, to the entire analog correlation function of two signals, by computing the cross-correlation coefficients at 200 delay time steps simultaneously. The delay time step can be adjusted, from a few ns, down to a few tens of ps, enabling to process signals with multi-GHz bandwidth. We have applied this architecture to the localization of RF transmitters by TDoA, and achieved a precision close to 10 ps for a 100 ms integration time. This architecture is expected to find practical applications in various domains, from radar and electronic warfare to telecommunications, imaging, and radio-astronomy.

© 2021 Optical Society of America

1. Introduction

Correlation is a general concept, that characterizes the degree of similarity between data sets. It finds many practical applications in information processing, for statistical analysis, pattern recognition, classification and data extraction tasks [1]. Correlation is also particularly useful for processing time-dependent signals. If one considers two real signals $s_1(t)$ and $s_2(t)$, the cross-correlation (CC) function defined as $C_{1,2}(\tau) = \langle s_1(t)s_2(t \quad \tau)\rangle$ (where $\langle\rangle$ stands for an average over a given time-window) quantifies the mutual degree of correlation of the two signals as a function of their relative time delay τ. Determining the value of τ that maximizes the degree of correlation is at the basis of time-delay analysis employed in numerous detection and imaging techniques [2]. In active techniques such as radar, lidar, or sonar, the distance to the target is deduced from the measurement of the time of flight (ToF) from the transmitter to the target [3]. In passive systems such as global positioning systems and radio-location systems at large, the position of the receiver can be inferred from time difference of arrival (TDoA) analysis of signals emitted by several transmitters, whose positions are known [5]. Conversely, TDoA makes it possible to locate transmitters by comparing the signals received at different locations, a concept employed in various applications, e.g. for locating natural disaster victims, hunting down interference in mobile communication networks, tracking radio-frequency (RF) jammers, and identifying threats in a war zone [5, 6]. In both ToF and TDoA, when short pulsed signals are transmitted, location information is generally obtained from direct measurement of the signal times of arrival. On the contrary, in the case of long or continuous transmitted waveforms, correlation is employed, since it makes it possible to retrieve a temporal resolution limited by the bandwidth of the transmitted waveform, rather than by its duration [2]. In addition, the process of correlation is closely related to convolution and to matched filtering, a feature that guarantees

the optimization of the SNR in the case of additive stochastic noise [7]. Finally, beside simple time-delay analysis, a deeper analysis of the correlation function can be useful for advanced high-resolution imaging techniques such as aperture synthesis in radio-astronomy [8].

For all these reasons, the development of correlators for RF signals is a major challenge. Beyond simplicity and low size, weight, power and cost, a significant requirement of correlators is their capability to process broadband signals in real-time. Indeed, depending of the targeted application, broadband signals are intrinsically related to a high density of information and to a high temporal resolution. Additionally, real-time capability is an important feature of correlation, in order to avoid blind times and to offer a 100 % probability of interception. This capability is particularly important for defense applications, or for the observation of low intensity sources in radio-astronomy, among others.

In practice, many correlation techniques have been used so far, both in the frequency and in the time domain. Nowadays, most of correlation techniques are digital, where the signals are quantized and digitized in discrete data series [9]. Frequency domain approaches are based on the Wiener-Khinchin theorem, which states that the CC function can be retrieved from the inverse Fourier transform (FT) of the product $\tilde{s}_1(f)\tilde{s}_2^*(f)$, where $\tilde{s}_1(f)$ and $\tilde{s}_2(f)$ are the respective FTs of $s_1(t)$ and $s_2(t)$. In time domain approaches, the CC function is calculated by term-by-term products and successive relative shifts of the two series. However, in practice, digital CC in real time is constrained by two limitations. First, according to the sampling theorem, digital processing of wideband signals requires a sampling rate higher than twice the signal bandwidth. Digitizers with sampling rates exceeding a few tens of GS/s are commercially available, but their effective number of bits is severely constrained by the jitter of the clock signal [10]. Second, such data rates are still way beyond the limits of conventional real-time processing techniques. Indeed, the bandwidth of commercial real-time analyzers does not exceed a few hundreds of MHz [11]. These two constraints set a compromise between the signal bandwidth and the probability of interception. In practice, cutting edge applications can overcome these limitations, but at the price of a high degree of complexity: to give an example, the state-of-art ALMA correlator (Atacama Large Millimeter/Submillimiter Array) uses more than 100 millions of processors to process in the real time all 8 GHz-bandwidth signals coming from 66 antennas [12].

On the contrary, analog approaches are a priori very attractive, because they do not require to acquire the signals, nor to process them digitally. Analog correlation of RF signals can be performed in the frequency domain, a feature widely employed in radar and sonar, where the received signal passes through the matched filter, achieving pulse compression [3] (Fig. 1). However in practice, the technique is restricted to the cases where the signal to be detected (i.e. the matched filter) is known. Moreover, this technique is not easily reconfigurable. In turn, time domain analog correlators have been used in the early days of radio interferometry [8], as well as in heterodyne optical interferometry [13]. The product of the signals is calculated by a square-law detector, and the duration of the time-average window is set by the detector response time and by additional low-pass filters. Time domain approaches are intrinsically sequential: the measurement of the CC function is done point by point, by varying the relative time delay between the signals. In addition to the technical challenge related to the control of the relative time delay by moving parts, this mode of operation renders the technique intrinsically slow and unsuitable for non-stationary signals. Implementations of parallelized correlation schemes, or lag correlators, have been reported: they enable to calculate the correlation function for several values of the delay simultaneously [14, 15]. However, despite their potential advantages, analog cross correlation techniques remain less developed than digital ones, mostly because of the poor bandwidth acceptance of analog RF components, and of the limited scalability of RF analog circuits.

Recently, the field of photonics has shown to offer efficient solutions for analog processing of RF signals, by taking advantage of the huge bandwidth of the optical spectrum, and of the

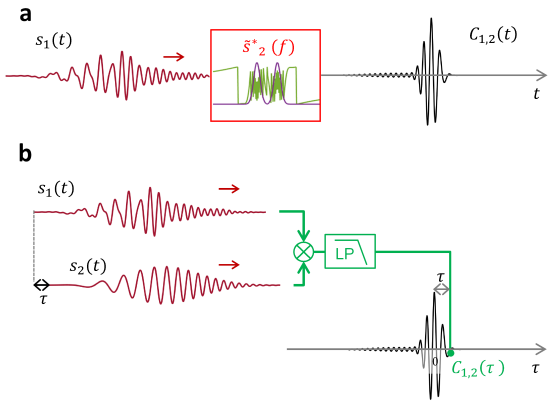

Fig. 1. a: Analog cross-correlation (CC) of two signals $s_1(t)$ and $s_2(t)$ in the frequency domain. $s_1(t)$ passes through a filter, whose transfer function is the complex conjugate of $\tilde{s}_2(f)$ (magenta: amplitude, green: phase). The output signal is $C_{1,2}(t)$. When $s_1 = s_2$, the process corresponds to auto-correlation (AC), or matched filtering. b: Analog CC in the time domain. Analog multiplication of the signals time-shifted by τ is followed by low-pass filtering (LP) to calculate the CC coefficient $C_{1,2}(\tau)$. The measurement is repeated while varying the delay, to reconstruct the whole CC function $C_{1,2}(\tau)$.

availability of cheap and efficient components at the telecom wavelength [16, 17]. Moreover, photonic architectures are immune to electromagnetic interference. Microwave photonics, which offers solutions for the processing of wideband signals through photonic architectures, has thus emerged and greatly developed in the past decades [18]. Besides, correlation is a common process in optics: it is at the heart of FT spectroscopy [19] and aperture synthesis in optical stellar interferometry [20], while non-linear AC techniques are widely used to characterize ultra-short optical pulses [21]. Therefore, several photonic-aided approaches have been proposed for RF signal correlation so far, and have demonstrated the capability of processing multi GHz-wide signals. Implementation in the spectral domain rely generally on the use of tailored linear filters [22–24], while temporal approaches make use of non-linear techniques [25–28], or of direct up-conversion of the RF signal to the optical domain followed by photodetection [29]. Other architectures of correlators based on free-space optics have been demonstrated in the frame of optical computing [30, 31], and adapted to the correlation of millimeter-waves by frequency up-conversion [32–34]. Finally, wideband correlators based on diffraction in cryogenically cooled crystals doped with rare-earth ions have been developed and commercialized [35, 36]. However, generally speaking, photonic solutions turn to have the same limitations as analog electronic ones: a high degree of complexity, a lack of reconfigurability in spectral approaches, and the need for point-by-point measurements in temporal ones.

In this article, we propose a novel analog correlation technique of RF signals based on a simple photonic architecture, which surpasses the capabilities of analog and digital conventional techniques. It relies on the multiplexing of the relative delay between the input signals τ, which avoids the need for point-by-point measurements of the CC function, and makes it possible to calculate the entire correlation function in parallel (i.e. for about 200 values of the delay τ simultaneously), and in real time. The architecture contains no moving part, and is easily reconfigurable: the delay-time step can be controlled over orders of magnitude down to the tens of ps scale, enabling the processing of multi GHz-wideband signals [37].

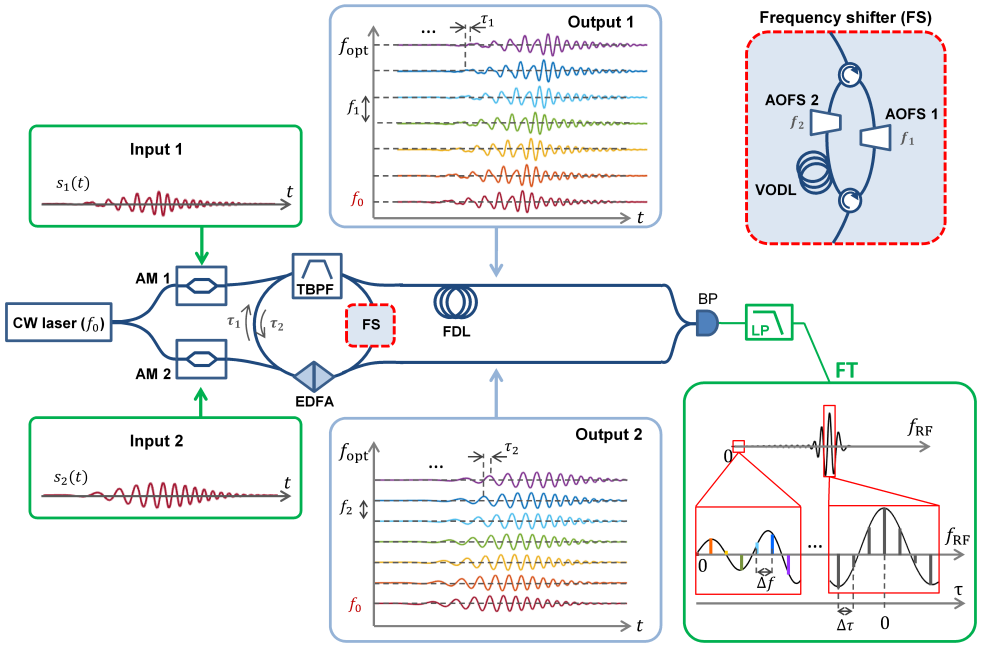

Fig. 2. Sketch of the analog photonic correlator. A bidirectional fiber frequency shifting loop is seeded in both ways by a CW laser at 1550 nm, modulated in amplitude (AM) by two RF signals $s_1(t)$ and $s_2(t)$. Two variable optical attenuators (not shown) enable to control the light power injected in the loop. The non-reciprocal frequency shifter (FS) is sketched in the inset (top right). A variable optical delay line (VODL) enables to control the time delay between both ways $\Delta\tau = \tau_2 - \tau_1$. The loop contains an amplifier (EDFA) and a tunable bandpass filter (TBPF), both bidirectional. The loop produces replicas of the input signals transferred in the optical domain, shifted both in time and in frequency. Photodetection by the balanced detector (BP) produces multi-heterodyne beatings. After low-pass filtering (LP), the Fourier transform (FT) of the photocurrent (i.e. the RF spectrum) sampled at multiples of $\Delta f = f_1 - f_2$ provides the CC coefficients for values of the relative delay multiples of $\Delta\tau$ (see text). A fiber delay line (noted FDL) is inserted in path #1 in order to bring the position of the null delay (i.e. $\tau = 0$) to the center of the RF spectrum.

The article is structured as follows. First, we provide a concise description of the photonic correlator. Then, we report both AC and CC of arbitrary RF signals. In particular, we demonstrate the reconfigurability of the architecture by performing CC with two different values of the delay-time step (125 ps and 4 ns). Next, we characterize the performance of the architecture for time-delay analysis of RF signals, and report a precision approaching 10 ps for a 100 ms integration time. Then, we provide a practical demonstration of transmitter localization by TDoA. In the conclusion, we discuss the perspectives and the limitations of the technique for practical applications. A Supplement regroups complementary theoretical and experimental details on the operation of the correlator, as well as additional examples of correlation measurements.

2. Architecture of the photonic correlator

In this part, we provide a brief description of the correlator (Fig. 2). Its principle is the following. We consider two input RF signals, $s_1(t)$ and $s_2(t)$. Both of them are transferred into the optical

domain, so as to to generate a large number ($N > 200$) of time-shifted replicas. The values of the delay-time steps for the two signals are different, and are written τ_1 and τ_2 for $s_1(t)$ and $s_2(t)$ respectively. Moreover, the time-delayed replicas of the signals are simultaneously shifted in frequency, so that the replica that has been delayed n times, has also experienced n frequency-shifts. Similarly, the frequency shifts are slightly different, and are respectively noted f_1 and f_2. The replicas of the two signals are combined on a photodiode (which plays the role of the square-law detector) followed by a low-pass filter. The photocurrent contains a large number of spectral components, each of them corresponding to the heterodyne beating between a specific pair of replicas of the two signals. Fourier processing of the photocurrent gives access to the CC coefficients of the two signals.

The practical implementation of this concept utilizes a pair of frequency shifting loops, or FSLs [38]. A FSL consists of a fiber loop containing a frequency shifter (usually, an acousto-optic frequency shifter, or AOFS), an amplifier to compensate for the losses of the system (here, an Erbium-doped fiber amplifier, EDFA), and a tunable bandpass filter (TBPF). The role of the filter is to limit the amplified spontaneous emission (ASE) of the amplifier, and to control the spectral bandwidth, i.e. N the number of roundtrips of the light in the loop. The FSL can be seeded by a CW laser (frequency: f_0), modulated in amplitude by the RF signal under test, owing to an amplitude modulator (AM) biased at the null point. In this case, the FSL generates replicas of the RF input signal (transferred in the optical domain). The delay-time step of the replicas is simply equal to the travel time in the loop, while their separation in frequency is equal to the frequency shift per turn in the loop. As such, FSLs have proven many applications in the field of microwave photonics, for the processing and the generation of RF signals [39–43], as well as in spectroscopy and ranging [44, 45].

Here, the correlator architecture involves a pair of two FSLs, whose travel times are τ_1 and τ_2. We define $\Delta\tau = \tau_2 - \tau_1$. The frequency shifts per turn are equal respectively to f_1 and f_2, and we define similarly $\Delta f = f_1 - f_2$. The values of the frequency shifts are sufficiently close, to match the condition $N\Delta f < f_2/2, f_1/2$. The two FSLs are seeded by the same CW laser, modulated by $s_1(t)$ and $s_2(t)$, respectively. In order to preserve the optical coherence between the signals, the FSLs are implemented in a bidirectional configuration [46, 47]. The two signals travel in opposite directions in the same fiber loop, except a short non-reciprocal section where they experience different time delays and frequency shifts (Inset Fig. 2). Output couplers enable to extract a fraction of the counterpropagating optical fields.

It can be shown that after the output couplers, the electric fields $E_1(t)$ and $E_2(t)$ write:

$$E_{1,2}(t) = E_0 e^{i2\pi f_0 t} \sum_{n=0}^{N} s_{1,2}(t - n\tau_{1,2}) e^{i2\pi n f_{1,2} t} e^{-i\pi f_{1,2}\tau_{1,2} n^2}. \quad (1)$$

Both fields are recombined on a balanced photodetector. The photocurrent passes trough a low-pass filter (cutoff-frequency: $N\Delta f$). Simple calculations derived in the Supplement show that the photocurrent, defined in complex formalism, by $I(t) \propto E_1(t)E_2^*(t)$ writes, after low-pass filtering:

$$I(t) \propto \sum_n \langle s_1(t) s_2(t - n\Delta\tau)\rangle e^{i2\pi n\Delta f t} e^{-i\pi(f_1\tau_1 - f_2\tau_2)n^2}. \quad (2)$$

This expression proves that the CC function sampled at multiples of $\Delta\tau$ can be retrieved by computing the FT of $I(t)$:

$$\tilde{I}(n\Delta f) \propto \langle s_1(t) s_2(t - n\Delta\tau)\rangle e^{-i\pi(f_1\tau_1 - f_2\tau_2)n^2}. \quad (3)$$

In other words, the CC function is mapped in the RF spectrum (the FT of the photocurrent): the amplitude of the heterodyne beatnote at frequency $n\Delta f$ is proportional to the value of the CC function at a relative delay of $n\Delta\tau$.

Advantageously, the system parameters can be adjusted, so that $f_1\tau_1 - f_2\tau_2$ is an even integer. In this case, the FT of the photocurrent after filtering provides directly the CC function of the input signals. When this condition is not met, the square modulus of the the FT of the photocurrent simply provides the square of the CC function. Interestingly, the operation mode of the correlator is closely related to multi-heterodyne interferometry as implemented in dual-comb techniques [48, 49]: the information sought (here: the CC coefficients; in dual-comb techniques: the amplitude and phase of the comb lines) is contained in the low frequency beatnotes in the RF spectrum produced by the interference of the teeth of the first comb, with their closest neighbor (in terms of frequency) in the second one.

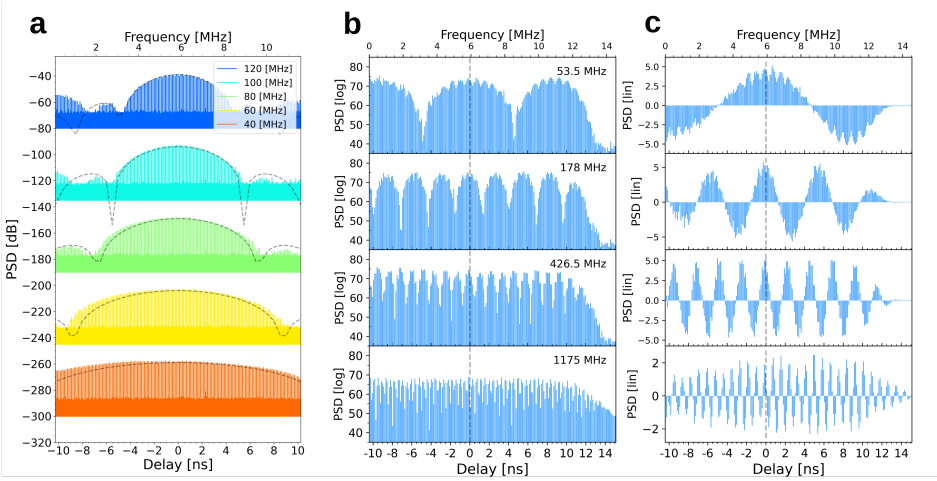

Fig. 3. a: Square modulus of the AC of a white noise with different bandwidths (120 MHz to 40 MHz) (acq. time: 200 ms, log. scale). The dashed line is the expected (numerical) AC trace. b: Square modulus of the AC of sine waves with different frequencies (log. scale, acq. time: 100 ms). The noise background in the AC traces has been numerically filtered out (see text). c: Real part of the AC (linear scale). The residual modulations in the traces are due to sampling effects in the RF spectrum. The vignetting in the real part traces comes from a small residual quadratic phase in the RF spectrum.

As said, the sampling delay-time step of the CC function $\Delta\tau$ is directly set by the path difference of the bidirectional FSL. In practice, this value can be precisely tuned by means of a variable optical delay line (VODL). It can be set arbitrarily small, leading to the possibility of processing signals with tens of GHz bandwidth. Ultimately, the processing bandwidth is limited by the bandwidth of the TBPF inserted in the loop, i.e. Nf_1 ($\simeq Nf_2$). Typically, this value approaches 20 GHz (assuming $N = 250$ and $f_1 \simeq 80$ MHz). The advantage of the system is the capability to compute simultaneously and in real time, the CC coefficients for more than 200 values of the delay simultaneously, with no moving part. Therefore, the technique is not restricted to stationary signals, but can also be applied to the processing of time-dependent signals, provided that their change rate is smaller than the processing time of the system. The latter is about $N\tau_1$ ($\simeq N\tau_2$), typically close to 20 μs ($N = 200$ and $\tau_1 \simeq 100$ ns).

3. Experimental results

In a first set of experiments, we demonstrate the capability of the setup to measure the entire AC and CC functions of different input RF signals.

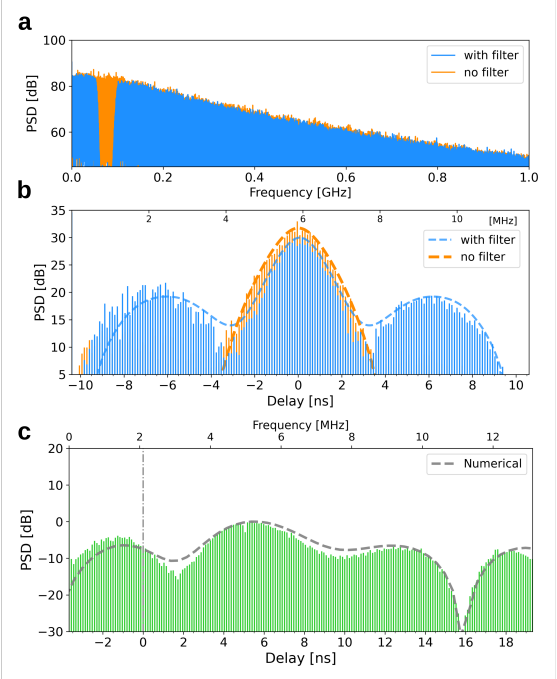

Fig. 4. a: Spectrum of a 120 MHz-bandwidth noise, in orange, and of the same signal after a bandstop filter (65-85 MHz), in blue. b: Square modulus of the ACs of both signals (acq. time: 200 ms). c: CC trace between the unfiltered and the filtered signals (acq. time: 200 ms). In all plots, the experimental AC and CC traces are compared to the expected ones (in dashed line).

3.1. Examples of cross- and auto-correlation of RF signals

We have implemented the photonic correlator with two different values of the delay-time step $\Delta\tau$. In the first case, $\Delta\tau$ is set to 115 ps. This configuration is suitable for signal correlation, the bandwidth of which can be up to 8 GHz. Considering, $N = 200$, the delay range between the two input signals reaches $N\Delta\tau = 23$ ns. In order to measure a CC function whose zero delay corresponds to the center of the RF spectrum of the photo-current, we compensate the paths mismatch by inserting about 3 meters of fiber on the path of the output # 1 (FDL in Fig. 2). To satisfy the condition $f_1\tau_1 = f_2\tau_2$, f_1 and f_2 were respectively equal to 80.0657 and 80.0000 MHz ($\Delta f = 65.7$ kHz).

First, we measure the AC functions of simple waveforms (white noise and sine waves). In Fig. 3.a, we show the RF power spectra obtained by seeding the system with white noise of variable bandwidth (from 120 MHz down to 40 MHz). The traces consist of well defined beatnotes (more than 200), whose power is proportional to the square of the AC coefficient. The beatnotes dominate a noise background, that mostly comes from the ASE circulating in the FSL. Since the frequency of the beatnotes is precisely known (their frequency is an integer multiple of Δf), the noise background can readily be filtered out numerically. In the data shown in the following of the article, this filtering has been implemented. As said, the relationship between the frequency axis of the RF spectrum and the time delay is linear, with a proportionality coefficient equal to $\Delta f/\Delta\tau$. As expected, the width of the AC function (i.e. the coherence time of the applied signal) decreases with the spectral bandwidth of the signal. We also compare the AC traces obtained by

the photonic correlator, with the expected ones. The latter are calculated by recording the RF signal with a fast digital oscilloscope, and computing the AC function. A good agreement is found between the experimental, and the expected traces. In Fig. 3.b, we plot the AC functions of sine waves with different frequencies. Interestingly, since $\tilde{I}(f)$ maps the real part of the AC function, it is possible to retrieve the sign of the AC function. Examples of real values of the AC function are plotted in Fig. 3.c.

In Fig. 4, we demonstrate the capability of the setup for CC. Two different RF signals are used: the first one is a 120 MHz-bandwidth white noise, the second one is the same signal after notch filtering (stopband: 65-85 MHz). The spectra of the input RF signals are displayed in Fig. 4.a. In Fig. 4.b, we recall the AC traces obtained separately with each of these signals. Then, both signals are sent to the system, and the experimental CC trace is shown in Fig. 4.c. Similarly to the previous case, the expected CC trace is computed numerically, and plotted for comparison.

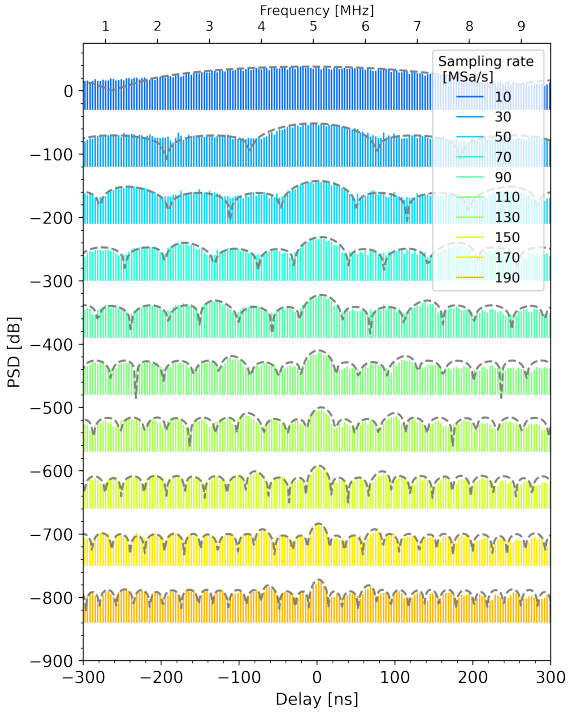

Fig. 5. Solid lines: experimental AC traces of a specifically designed noise-like input signal. The time step of the correlator is set to $\Delta\tau = 4$ ns. The sampling rate of the input signal is increased, from 10 to 190 MSa/s. Dashed lines are the expected AC traces (acq. time : 100 ms).

As said, depending on the signal under test, the delay time step is simply reconfigurable by changing the optical path delay $\tau_2 - \tau_1$. To show the flexibility of the concept, we have increased the value of the delay time step by inserting 1 m of optical fiber next to AOFS 2. (Simultaneously, to bring the position of the null relative delay at the center of the RF spectrum, we have added a 100 m long fiber delay line on the path of output # 1.) In this case, the value of τ is about 4 ns, which makes this configuration suitable for signals with bandwidth up to 250 MHz. The maximum delay range is now close to 0.8 μs. A numerical signal has been specifically designed, so as to exhibit a relatively complex AC function with many side lobes.

This noise-like signal is sent to the system with different sampling rates (from 10 to 190 MSa/s), so as to vary its bandwidth. The results are displayed in Fig.5. In this case too, the experimental traces obtained through the analog photonic correlator show an excellent agreement with the numerical correlation traces.

3.2. Time-delay analysis

A major application of correlation measurement is the possibility to measure the time delay T between two mutually-delayed replicas of the same signal (written as $s(t)$ and $s(t-T)$). The value of τ that maximizes $\langle s(t)s(t-T \quad \tau)\rangle$ is simply equal to T, the time delay. As said, the main advantage of time-delay analysis based on correlation is the matched-filtering effect: the delay information is contained in a correlation peak, whose duration is set by the spectral bandwidth of the signal [2]. This peak can be very narrow, even in the case of quasi CW signals. As said, this pulse compression effect is particularly useful to enhance the signal-to-noise ratio, e.g. in radar techniques based on matched filtering. Here, the system offers the capability to perform such time delay measurements directly in the time domain. To demonstrate this feature, we apply to the AMs two mutually-delayed replicas of the same signal (a numerically synthesized white noise with a 120 MHz bandwidth). The relative time delay between the replicas is controlled digitally. We record the CC traces for different values of the time delay. As expected, the delay measured through the photonic correlator matches closely the digital delay applied to the input signals (Fig. 6.a). Then, we characterize the precision of the time delay measurement offered by the technique. To do so, we acquire a 1 s-long time trace, and clip it numerically into sequences of duration equal to a multiple (labelled by q) of 15.2 μs (i.e. $1/\Delta f$). For each value of q, we calculate the position of the AC peak (i.e. the value of the delay) by a numerical fitting procedure, and determine the deviation of this measurement repeated over the full-length trace. The results are given in Fig. 6.b. As expected the deviation decreases as the square root of the integration time. Beyond 100-ms integration times, the experimental results tend to deviate from this law, presumably due to the smaller number of statistical samples available. Nevertheless, the precision is close to 10 ps for 100 ms integration time, a value significantly smaller than the 8.3 ns-coherence time of the signal under test (1/120 MHz). It is also much smaller than the average period of the signal (16.7 ns), which means that the time delay is measured with a precision better than one thousandth of a wavelength (in 100 ms).

3.3. Application to time difference of arrival

In a last set of experiments, we demonstrate the capability of the system for the localization of an RF transmitter by TDoA. Here, we provide a 2D proof of concept at the lab scale with a single transmitter and two receivers, but the technique could be generalized to more complex antenna networks, e.g. to enable passive radar by triangulation. A complex noise-like signal is synthesized by combining a white noise generator and frequency multipliers with low- and high-pass filters. The spectrum of the resulting RF signal ranges between 0.4 and 1.2 GHz (Fig. 7.a). The RF signal is sent to a whip (monopole) antenna (Tx). Two receiving antennas (Rx1 and Rx2), identical to the transmitter, are placed at a distance of about 1 meter from Tx (see Fig. 7.b). Rx2 can be moved, to change the relative delay between the signals received by the antennas. These two signals are amplified, and applied to the AMs at the correlator input. The measured CC functions are displayed in Fig. 7.c. As expected, the CC traces shift with the position of Rx2. In this case also, the delay retrieved from the analog photonic correlation matches precisely the geometrical delay between the antennas, demonstrating the capability of the system for TDoA analysis.

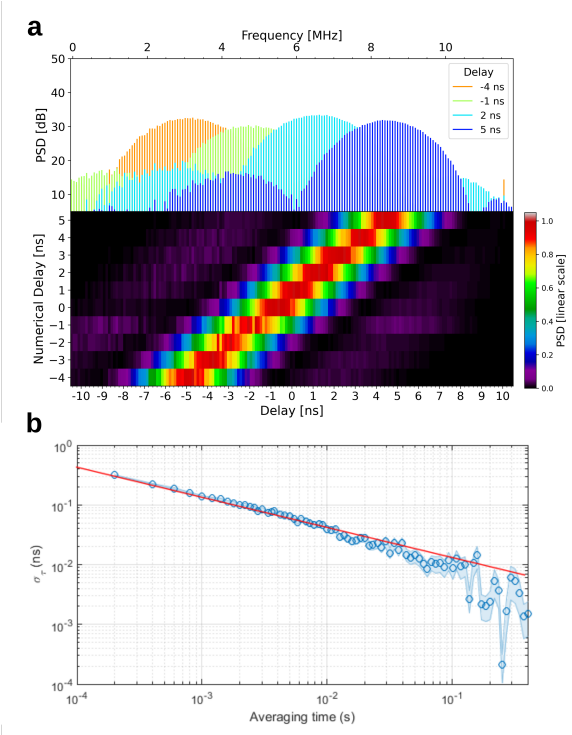

Fig. 6. a: Top, experimental AC traces measured for time-delayed replicas of a 120 MHz-bandwidth white noise. Bottom: 2-D plot of the AC traces as a function of the delay. c: Allan deviation of the time delay measurement, as a function of the averaging time (see text). The red line is a guide for the eyes (slope: $-1/2$).

4. Conclusion

In this paper, we have reported the first analog photonic-based architecture that enables to compute the cross-correlation of wideband RF signals for more than 200 values of the delay simultaneously. The architecture is considerably simpler than conventional analog or digital wideband correlators. Here, the optical circuitry is based on off-the-shelf telecom components. No broabdand laser source is needed, but a low linewidth single frequency laser. Contrary to most conventional analog approaches in the time domain which rely on point-by-point measurements of the CC coefficients, our architecture contains no moving part, and computes the CC function as a whole, through 200 simultaneous values of the relative delay, enabling real-time signal processing. On a dynamic point of view, the typical computation time of the CC function is about 20 μs, a value significantly lower than any other point-by-point CC technique. This value is also the time response of the correlator. Moreover, no truncation is applied to the input signal, which means that our architecture performs correlation with a 100% probability of interception.

The spectral bandwidth of the signals to be processed is an important parameter of the system. In our architecture, it is set by two factors. The first one is the delay-time step. In the reported experiments, it could reach 125 ps, but this value could be arbitrarily smaller. The second limiting factor is the optical spectral bandwidth set by the TBPF (i.e. $Nf_1 \simeq Nf_2$). One could imagine increasing the spectral bandwidth of the filter, which would simultaneously result in an increase of the number N of roundtrips, and of the signal bandwidth supported by the system. However, the saturation of the gain of the amplifier would lead to a decrease of the power as the

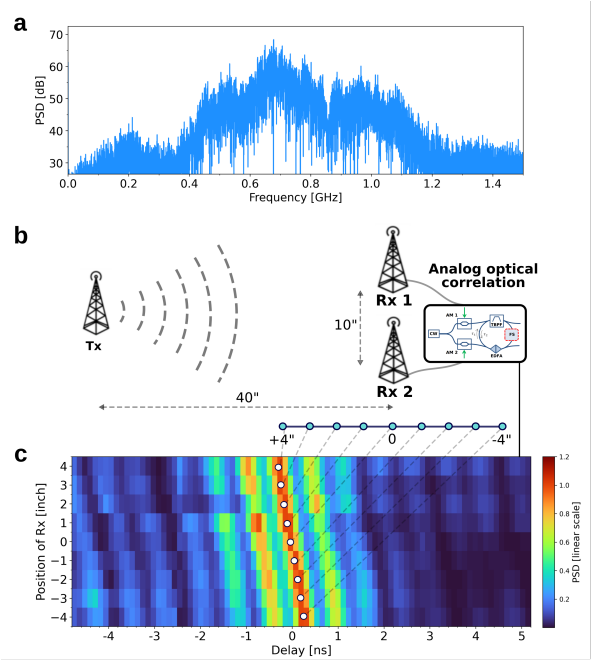

Fig. 7. Proof of concept of TDoA. a: RF spectrum of the transmitted signal. b: Sketch of the experimental setup. c: 2D plot of the CC traces as a function of the positions of the antennas (100 ms acq. time).

signal circulates in the loop [50]. The use of frequency shifters with a larger nominal frequency shift (e.g. electro-optic single-sideband frequency shifters) could enable to increase the filter's spectral bandwidth while keeping the number of roundtrips constant, avoiding the problem of saturation. This solution could be attractive, but presumably at the cost of increased ASE [50]. In addition to the capability of processing signals with multi-GHz bandwidth, our architecture shows another advantage. In digital techniques, the data collected at each antenna must be accurately time-stamped to accurate clock signals. This requires to have an absolute time reference shared between all antennas and the correlator. In our architecture, a phase stabilization of the optical link between the antennas and the correlator is sufficient and can be achieved with standard fiber stabilization techniques. This leads to the possibility of performing signal correlation over very long baselines, a feature that could find applications in sub-millimetric astronomy. Interestingly, this architecture could also open perspectives to optical interferometry. Infrared heterodyne interferometry, which replaces the correlation of the optical signals received by the telescopes, by the correlation of RF signals obtained by mixing the optical signals with a local oscillator on a photo-detector, could benefit from the proposed correlation technique [13, 29]. Beside synthetic aperture imaging in astronomy, other applications based on time delay analysis are conceivable, including passive radar and localization of transmitters/receivers, among others. For most of these applications, the extension of the correlator to more than two signals would represent a significant advantage, e.g. to achieve long baseline interferometry with a large array of antennas, or to enable transmitter's localization by triangulation. The extension of the architecture proposed here to more than two signals is underway. On the long term, perspective of integration of this architecture are foreseeable. All components used in the dual FSL, including the frequency shifter, can be integrated [51]. The combination of all components on a single chip could be

accessible, presumably via hybrid integration techniques, and could open many possibilities of practical applications of the architecture.

Acknowledgments

We acknowledge support from Université Grenoble Alpes (grant IDEX- IRS 2020), from the Ecole Doctorale de Physique de Grenoble, and from the INSU-CNRS (ASHRA and CSAA) for their financial support. We also acknowledge Vicente Duran for his work at the early stages of the system's implementation.

Disclosures

The authors declare no conflicts of interest.

Data Availability Statement

Data underlying the results presented in this paper may be obtained from the authors upon request.

References

1. R. S. Witte, and J. S. Witte, "Statistics," 11th Ed., John Wiley and Sons (2017).
2. J. Y. Stein, "Digital Signal Processing: A Computer Science Perspective", John Wiley and Sons Inc., Ch. 9 (2000).
3. N. Levanon, and E. Mozeson, "Radar signals," John Wiley and Sons Inc., (2004).
4. H. D. Griffiths, and C. J. Baker, "An introduction to passive radar," Artech House, Boston/London (2017).
5. A.-M. Roxin, J. Gaber, M. Wack, A. N. Sidi Moh, "Survey of Wireless Geolocation Techniques," IEEE Globecom Workshops, Washington DC (2007).
6. H. Liu, H. Darabi, P. Banerjee and J. Liu, "Survey of Wireless Indoor Positioning Techniques and Systems," IEEE Transactions on Systems, Man, and Cybernetics, Part C (Applications and Reviews), 37, 1067-1080 (2007).
7. R. E. Ziemer and W. H. Tranter, "Principles of Communications," John Wiley and Sons Inc., 1988.
8. A. R. Thompson, J. M. Moran, and G. W. Swenson, Jr. "Interferometry and Synthesis in Radio Astronomy," 3rd ed. Springer, 2017.
9. S. N. Kuo, B. H. Lee, and W. Tian, "Real-Time Digital Signal Processing: Fundamentals, Implementations and Applications," 3rd Ed., John Wiley and Sons (2013).
10. B. Murmann, "The race for the extra decibel: A brief review of current ADC performance trajectories", IEEE Solid-State Circuits Mag., 7, 58–66 (2015).
11. Fondamentalsofreal-timespectrumanalysis,https://download.tek.com/document/37W_17249_5_HR_Letter.pdf, Tektronix 2015.
12. R. P. Escoffier et al., "The ALMA correlator," Astronomy and Astrophysics, 462, 801-810 (2006).
13. D. D. S. Hale, and al., "The Berkeley Infrared Spatial Interferometer: A Heterodyne Stellar Interferometer for the Mid-Infrared," The Astrophysical Journal, 537, 598 (2000).
14. L. Chao-Te Li et al., "Amiba wideband analog correlator", The Astrophysical Journal, 716, 746-757 (2010).
15. C. M. Holler, M. E. Jones, A. C. Taylor, A. I. Harris and S. A. Maas, "A 2–20-GHz Analog Lag Correlator for Radio Interferometry," in IEEE Transactions on Instrumentation and Measurement, 61, 2253-2261 (2012).
16. R. A. Minasian, "Photonic signal processing of microwave signals," IEEE Transactions on Microwave Theory and Techniques, 54, 832-846 (2006).
17. H. Caulfield, and S. Dolev, "Why future supercomputing requires optics," Nat. Photonics, 4 (2010).
18. D. Marpaung, J. Yao, and J. Capmany, "Integrated microwave photonics," Nature Photon. 13, 80–90 (2019).
19. S. P. Davis, M. C. Abrams and J. W. Brault, Fourier transform spectrometry, Academic Press (2001).
20. John D Monnier, "Optical interferometry in astronomy," Rep. Prog. Phys. 66, 789 (2003).
21. C. Monat et al., "Integrated optical auto-correlator based on third-harmonic generation in a silicon photonic crystal waveguide," Nat Commun.,5, 3246 (2014).
22. M. S. Rasras et al., "A Programmable 8-bit Optical Correlator Filter for Optical Bit Pattern Recognition," IEEE Photonics Technology Letters, 20, 694-696 (2008).
23. Y. Dai, and J. Yao, "Microwave Correlator Based on a Nonuniformly Spaced Photonic Microwave Delay-Line Filter", IEEE Photonics Technology Letters 21, 969-971 (2009).
24. J. Yao, "Photonics to the Rescue: A Fresh Look at Microwave Photonic Filters," in IEEE Microwave Magazine, 16, 46-60 (2015).
25. R. Kibria, L. A. Bui and M. W. Austin, "Nonlinear mixing based photonic correlator," IEEE International Topical Meeting on Microwave Photonics, pp. 30-33 (2012).
26. M. Ziyadi, et al., "Tunable optical correlator using an optical frequency comb and a nonlinear multiplexer," Opt. Express 22, 84-89 (2014).

27. M. Shoeiby, A. Mitchell, L. Bui, "Real time all optical correlator for serialized time encoded signals," Optics Commun. 338, 34-39 (2015).
28. A. E. Willner, A. Fallahpour, K. Zou, F. Alishahi and H. Zhou, "Optical Signal Processing Aided by Optical Frequency Combs," IEEE Journal of Selected Topics in Quantum Electronics, 27, 1-16 (2021).
29. G. Bourdarot, H. Guillet de Chatellus, and J-P. Berger, "Toward a large bandwidth photonic correlator for infrared heterodyne interferometry," Astronomy and Astrophysics, 639, A53 (2020).
30. P. Ambs, "Optical Computing: A 60-Year Adventure", Advances in Optical Technologies, 2010, 372652 (2021).
31. T. Manzur 1, J. Zeller, S. Serati, "Optical correlator based target detection, recognition, classification, and tracking," Appl. Opt. 51, 4976-4983 (2012).
32. P. M. Blanchard, A. H. Greenaway, A. R. Harvey, and K. Webster, "Coherent optical beam forming with passive milimeter-wave arrays," J. of. Lightwave Technol. 17, 418-425 (1999).
33. C. A. Schuetz, R. D. Martin, I. Biswas, M. S. Mirotznik, S. Shi, G. J. Schneider, J. Murakowski, D. W. Prather, "Sparse aperture millimeter-wave imaging using optical detection and correlation techniques," Proc. SPIE 6548, Passive Millimeter-Wave Imaging Technology X, 65480 B (2007).
34. C. Wang, X. Xin, M. Kashif and J. Miao, "A Compact Analog Complex Cross-Correlator for Passive Millimeter-Wave Imager," IEEE Transactions on Instrumentation and Measurement, 66, 2997-3006 (2017).
35. K. D. Merkel et al., "A Photonics-based Broadband RF Spectrum Analysis and Geolocation System," IEEE Research and Applications of Photonics In Defense Conference (RAPID), 1-4 (2018).
36. W. R. Babbitt, "Microwave photonic processing with spatial-spectral holographic materials," Proc. SPIE 11296, Optical, Opto-Atomic, and Entanglement-Enhanced Precision Metrology II, 112963L (2020).
37. Patent FR2012782, "Dispositif large-bande de mesure de la corrélation croisée de signaux", CNRS/Université Grenoble Alpes.
38. H. Guillet de Chatellus, E. Lacot, W. Glastre, O. Jacquin, and O. Hugon, "Theory of Talbot lasers," Phys. Rev. A 88, 033828 (2013).
39. H. Guillet de Chatellus, O. Jacquin, O. Hugon, W. Glastre, E. Lacot, and J. Marklof, "Generation of ultrahigh and tunable repetition rates in CW injection-seeded frequency-shifted feedback lasers," Opt. Express 21, 15065-15074 (2013).
40. H. Guillet de Chatellus, L. Romero Cortés, and J. Azana, "Optical real-time Fourier transformation with kilohertz resolutions," Optica 3, 1-8 (2016).
41. C. Schnébelin, and H. Guillet de Chatellus, "Agile photonic fractional Fourier transformation of optical and RF signals," Optica 4, 907 (2017).
42. H. Guillet de Chatellus, L. Romero Cortés, et al., "Reconfigurable photonic generation of broadband chirped waveforms using a single CW laser and low-frequency electronics," Nat. Commun. 9, 2438 (2018).
43. C. Schnébelin, J. Azana, and H. Guillet de Chatellus, "Programmable broadband optical field spectral shaping with megahertz resolution using a simple frequency shifting loop," Nat. Commun. 10, 4654 (2019).
44. V. Duran, C. Schnébelin, and H. Guillet de Chatellus, "Coherent multi-heterodyne spectroscopy using acousto-optic frequency combs," Opt. Express 26, 13800-13809 (2018).
45. J. Clement, C. Schnébelin, H. Guillet de Chatellus, and C. R. Fernández-Pousa, "Laser ranging using coherent pulse compression with frequency shifting loops," Opt. Express 27, 12000-12010 (2019).
46. V. Duran, L. Djevarhidjian, and H. Guillet de Chatellus, "Bidirectional frequency-shifting loop for dual-comb spectroscopy," Opt. Lett. 44, 3789-3792 (2019).
47. V. Billault, V. Duran, C. R. Fernández-Pousa, V. Crozatier, D. Dolfi, and H. Guillet de Chatellus, "All-optical coherent pulse compression for dynamic laser ranging using an acousto-optic dual comb," Opt. Express 29, 21369-21385 (2021).
48. I. Coddington, N. Newbury, and W. Swann, "Dual-comb spectroscopy," Optica 3, 414-426 (2016).
49. N. Picqué, T. W. Hänsch, "Frequency comb spectroscopy," Nature Photon. 13, 146–157 (2019).
50. N. Kanagaraj, L. Djevarhidjian, et al., "Optimization of acousto-optic optical frequency combs," Opt. Express 27, 14842-14852 (2019).
51. L. Shao, N. Sinclair, et al., "Integrated microwave acousto-optic frequency shifter on thin-film lithium niobate," Opt. Express 28, 23728-23738 (2020).

Bibliography

ALMA Partnership, C. L. Brogan, L. M. Perez, et al. (July 1, 2015). „The 2014 ALMA Long Baseline Campaign: First Results from High Angular Resolution Observations toward the HL Tau Region“. In: *The Astrophysical Journal* 808, p. L3 (cit. on p. 16).

Andre, Philippe and Thierry Montmerle (Jan. 1, 1994). „From T Tauri Stars to Protostars: Circumstellar Material and Young Stellar Objects in the rho Ophiuchi Cloud“. In: *The Astrophysical Journal* 420, p. 837 (cit. on pp. 6, 8).

Andrews, Sean M. (Aug. 2020). „Observations of Protoplanetary Disk Structures“. In: *Annual Review of Astronomy and Astrophysics, vol. 58, p.483-528* 58, p. 483 (cit. on p. 16).

Andrews, Sean M., Jane Huang, Laura M. Pérez, et al. (Dec. 26, 2018). „The Disk Substructures at High Angular Resolution Project (DSHARP). I. Motivation, Sample, Calibration, and Overview“. In: *The Astrophysical Journal* 869.2, p. L41 (cit. on p. 16).

Argence, Berengère, Bruno Chanteau, Olivier Lopez, et al. (July 2015). „Quantum cascade laser frequency stabilization at the sub-Hz level“. In: *Nature Photonics* 9.7, pp. 456–460 (cit. on p. 100).

Armitage, Philip J. (Sept. 22, 2011). „Dynamics of Protoplanetary Disks“. In: *Annual Review of Astronomy and Astrophysics* 49.1, pp. 195–236 (cit. on pp. 9, 12).

– (2020). *Astrophysics of Planet Formation*. 2nd ed. Cambridge: Cambridge University Press (cit. on pp. 7, 13–15).

Armitage, Philip J., Mario Livio, and J. E. Pringle (June 1, 2001). „Episodic accretion in magnetically layered protoplanetary discs“. In: *Monthly Notices of the Royal Astronomical Society* 324, pp. 705–711 (cit. on pp. 45, 58–60, 220).

Audard, M., P. abraham, M. M. Dunham, et al. (2014). „Episodic Accretion in Young Stars“. In: *Protostars and Planets VI*, pp. 387–410 (cit. on pp. 45, 59).

Bae, Jaehan, Lee Hartmann, Zhaohuan Zhu, and Richard P. Nelson (Nov. 1, 2014). „Accretion Outbursts in Self-gravitating Protoplanetary Disks“. In: *The Astrophysical Journal* 795, p. 61 (cit. on p. 45).

Balbus, Steven A. and John F. Hawley (July 1, 1991). „A Powerful Local Shear Instability in Weakly Magnetized Disks. I. Linear Analysis“. In: *The Astrophysical Journal* 376, p. 214 (cit. on p. 10).

Bayo, A., P. Mardones, S. Castillo, et al. (Dec. 2, 2020). „NPF update: Light-weight mirror development in Chile“. In: *arXiv:2012.01560 [astro-ph]*. arXiv: 2012.01560 (cit. on p. 101).

Bell, K. R. and D. N. C. Lin (June 1, 1994). „Using FU Orionis outbursts to constrain self-regulated protostellar disk models“. In: *The Astrophysical Journal* 427, pp. 987–1004 (cit. on pp. 45, 58–60).

Benisty, M., J.-P. Berger, L. Jocou, et al. (May 1, 2009). „An integrated optics beam combiner for the second generation VLTI instruments“. In: *Astronomy and Astrophysics* 498, pp. 601–613 (cit. on p. 150).

Benisty, M., F. Malbet, C. Dougados, et al. (July 1, 2010). „The 2008 outburst in the young stellar system Z CMa. I. Evidence of an enhanced bipolar wind on the AU-scale“. In: *Astronomy and Astrophysics* 517, p. L3 (cit. on pp. 17, 18, 67).

Berger, J.-P., F. Malbet, F. Baron, et al. (June 1, 2012). „Imaging the heart of astrophysical objects with optical long-baseline interferometry“. In: *Astronomy and Astrophysics Review* 20, p. 53 (cit. on p. 25).

Berger, Jean Philippe and Damien Segransan (Oct. 1, 2007). „An introduction to visibility modeling“. In: *New Astronomy Reviews* 51, pp. 576–582 (cit. on p. 51).

Berger, Jean-Philippe, Guillaume Bourdarot, and Hugues Guillet de Chatellus (Dec. 1, 2020). „V8: an 8 beam mid-infrared heterodyne instrument concept for the VLTI“. In: 11446, p. 1144613 (cit. on p. 200).

Bigioli, Azzurra (Feb. 2, 2021). „Uncooled unipolar receivers for 9μm wavelength heterodyne detection“. These de doctorat. Univsersité de Paris (cit. on pp. 97, 98).

Bigioli, Azzurra, Giovanni Armaroli, Angela Vasanelli, et al. (Apr. 20, 2020). „Long-wavelength infrared photovoltaic heterodyne receivers using patch-antenna quantum cascade detectors“. In: *Applied Physics Letters* 116.16, p. 161101 (cit. on p. 97).

Billault, Vincent, Guillaume Arpison, Vincent Crozatier, et al. (June 2021). „Coherent Optical Fiber Sensing Based on a Frequency Shifting Loop“. In: *Journal of Lightwave Technology, vol. 39, issue 12, pp. 4118-4123* 39.12, p. 4118 (cit. on pp. 164, 184).

Bitner, M. A., M. J. Richter, J. H. Lacy, et al. (Dec. 2008). „The TEXES Survey For H2 Emission From Protoplanetary Disks“. In: *The Astrophysical Journal* 688.2, pp. 1326–1344. arXiv: 0808.1099 (cit. on p. 214).

Blanchard, P. M., A. H. Greenaway, A. R. Harvey, and K. Webster (Mar. 1, 1999). „Coherent Optical Beam Forming with Passive Millimeter-Wave Arrays“. In: *Journal of Lightwave Technology* 17, pp. 418–425 (cit. on p. 152).

Blandford, R. D. and D. G. Payne (June 1, 1982). „Hydromagnetic flows from accretion disks and the production of radio jets.“ In: *Monthly Notices of the Royal Astronomical Society* 199, pp. 883–903 (cit. on p. 10).

Boccaletti, A., E. Di Folco, E. Pantin, et al. (May 18, 2020). „Possible evidence of ongoing planet formation in AB Aurigae. A showcase of the SPHERE/ALMA synergy“. In: *arXiv:2005.09064 [astro-ph]*. arXiv: 2005.09064 (cit. on pp. 17, 214).

Boekel, R. van, M. Min, Ch Leinert, et al. (Nov. 2004). „The building blocks of planets within the ‘terrestrial’ region of protoplanetary disks“. In: *Nature* 432.7016, pp. 479–482 (cit. on pp. 18, 214).

Bonnell, Ian and Pierre Bastien (Dec. 1, 1992). „A binary origin for FU Orionis stars“. In: *The Astrophysical Journal Letters* 401, pp. L31–L34 (cit. on p. 59).

Born, Max and Emil Wolf (Jan. 1, 1980). „Principles of Optics Electromagnetic Theory of Propagation, Interference and Diffraction of Light“. In: *Principles of Optics Electromagnetic Theory of Propagation* (cit. on p. 23).

Bouquin, Jean-Baptiste Le (Dec. 15, 2005). „Imagerie par synthèse d'ouverture optique, application aux etoiles chimiquement particulières“. PhD thesis. Universite Joseph-Fourier - Grenoble I (cit. on p. 122).

Bouvier, J., K. Perraut, J.-B. Le Bouquin, et al. (Apr. 2, 2020). „Probing the magnetospheric accretion region of the young pre-transitional disk system DoAr 44 using VLTI/GRAVITY“. In: *arXiv:2004.00848 [astro-ph]*. arXiv: 2004.00848 (cit. on p. 18).

Boyd, Robert W. (1983). „Radiometry and the detection of optical radiation“. In: *Wiley Series in Pure and Applied Optics, New York: Wiley, |c1983* (cit. on pp. 83, 103, 106).

Bracewell, Ron (Jan. 1, 1965). *The Fourier Transform and its applications*. ADS Bibcode: 1965ftia.book.....B (cit. on p. 83).

Burla, Maurizio, Claudia Hoessbacher, Wolfgang Heni, et al. (May 1, 2019). „500 GHz plasmonic Mach-Zehnder modulator enabling sub-THz microwave photonics“. In: *APL Photonics* 4.5, p. 056106 (cit. on p. 131).

Callen, Herbert B. and Theodore A. Welton (July 1, 1951). „Irreversibility and Generalized Noise“. In: *Physical Review* 83.1, pp. 34–40 (cit. on p. 111).

Calvet, N., L. Hartmann, and S. E. Strom (May 1, 2000). „Evolution of Disk Accretion“. In: *Protostars and Planets IV*, p. 377 (cit. on p. 44).

Calvet, Nuria, Lee Hartmann, and Stephen E. Strom (Feb. 23, 1999). „Evolution of Disk Accretion“. In: *arXiv:astro-ph/9902335*. arXiv: astro-ph/9902335 (cit. on p. 12).

Capmany, Jose, Jose Mora, Ivana Gasulla, et al. (Feb. 2013). „Microwave Photonic Signal Processing“. In: *Journal of Lightwave Technology* 31.4, pp. 571–586 (cit. on p. 130).

Caves, Carlton M. (Oct. 15, 1982). „Quantum limits on noise in linear amplifiers“. In: *Physical Review D* 26.8, pp. 1817–1839 (cit. on pp. 107, 108, 126).

Chauvin, G. (Oct. 1, 2018). „Direct Imaging of Exoplanets at the Era of the Extremely Large Telescopes“. In: *arXiv e-prints*, arXiv:1810.02031 (cit. on p. 17).

Chiang, E. and A. N. Youdin (May 1, 2010). „Forming Planetesimals in Solar and Extrasolar Nebulae“. In: *Annual Review of Earth and Planetary Sciences* 38, pp. 493–522 (cit. on p. 11).

Chiavassa, A., B. Freytag, T. Masseron, and B. Plez (Nov. 2011). „Radiative hydrodynamics simulations of red supergiant stars: IV. Gray versus non-gray opacities“. In: *Astronomy & Astrophysics* 535, A22 (cit. on pp. 208, 209).

Chiavassa, A., B. Plez, E. Josselin, and B. Freytag (Nov. 2009). „Radiative hydrodynamics simulations of red supergiant stars: I. interpretation of interferometric observations“. In: *Astronomy & Astrophysics* 506.3, pp. 1351–1365 (cit. on pp. 208, 209).

Clement, Juan, Come Schnebelin, Hugues Guillet de Chatellus, and Carlos R. Fernandez-Pousa (Apr. 1, 2019). „Laser ranging using coherent pulse compression with frequency shifting loops“. In: *Optics Express* 27, p. 12000 (cit. on p. 163).

Coddington, Ian, Nathan Newbury, and William Swann (Apr. 2016). „Dual-comb spectroscopy“. In: *Optica, vol. 3, issue 4, p. 414* 3.4, p. 414 (cit. on p. 165).

Cohen-Tannoudji, C., B. Diu, and F. Laloë (1973). *Mecanique quantique*. Collection Enseignement des sciences vol. 1. Masson (cit. on pp. 112, 118).

Collaboration, Gravity, A. Caratti o Garatti, R. Fedriani, et al. (Mar. 2020). „The GRAVITY young stellar object survey. II. First spatially resolved observations of the CO bandhead emission in a high-mass YSO“. In: *Astronomy & Astrophysics, Volume 635, id.L12, <NUMPAGES>9</NUMPAGES> pp.* 635, p. L12 (cit. on p. 18).

Consolino, Luigi, Malik Nafa, Francesco Cappelli, et al. (July 3, 2019). „Fully phase-stabilized quantum cascade laser frequency comb“. In: *Nature Communications* 10.1, p. 2938 (cit. on p. 98).

Cuello, Nicolas, Fabien Louvet, Daniel Mentiplay, et al. (Jan. 1, 2020). „Flybys in protoplanetary discs - II. Observational signatures“. In: *Monthly Notices of the Royal Astronomical Society* 491, pp. 504–514 (cit. on p. 59).

Danchi, Dr William C (Sept. 2, 2003). „The Beauty and Limitations of Infrared Heterodyne Interferometry: (U.C. Berkeley Infrared Spatial Interferometer)“. In: p. 28 (cit. on p. 132).

Darré, P., R. Baudoin, J. -T. Gomes, et al. (Dec. 2016). „First On-Sky Fringes with an Up-Conversion Interferometer Tested on a Telescope Array“. In: *Physical Review Letters* 117. ADS Bibcode: 2016PhRvL.117w3902D, p. 233902 (cit. on p. 27).

De Graauw, Th and H. Van De Stadt (Dec. 1973). „Infrared Heterodyne Detection of the Moon, Planets and Stars at 10 μm“. In: *Nature Physical Science* 246.153, pp. 73–75 (cit. on p. 33).

Dullemond, C. P., C. Dominik, and A. Natta (Oct. 20, 2001). „Passive Irradiated Circumstellar Disks with an Inner Hole“. In: *The Astrophysical Journal* 560.2, pp. 957–969 (cit. on p. 214).

Dullemond, C.P. and J.D. Monnier (Aug. 2010). „The Inner Regions of Protoplanetary Disks“. In: *Annual Review of Astronomy and Astrophysics* 48.1, pp. 205–239 (cit. on pp. 9, 17, 18).

Duran, Vicente, Leo Djevarhidjian, and Hugues Guillet de Chatellus (Aug. 1, 2019). „Bidirectional frequency-shifting loop for dual-comb spectroscopy“. In: *Optics Letters* 44, p. 3789 (cit. on p. 164).

Duran, Vicente, Come Schnebelin, and Hugues Guillet de Chatellus (May 1, 2018). „Coherent multi-heterodyne spectroscopy using acousto-optic frequency combs“. In: *Optics Express* 26, p. 13800 (cit. on p. 163).

Duvert, Gilles, John Young, and Christian A. Hummel (Jan. 1, 2017). „OIFITS 2: the 2nd version of the data exchange standard for optical interferometry“. In: *Astronomy and Astrophysics* 597, A8 (cit. on p. 206).

Efron, Bradley (1982). „The Jackknife, the Bootstrap and other resampling plans“. In: *CBMS-NSF Regional Conference Series in Applied Mathematics, Philadelphia: Society for Industrial and Applied Mathematics (SIAM), 1982* (cit. on p. 52).

Ferreira, J., C. Dougados, and S. Cabrit (July 2006). „Which jet launching mechanism(s) in T Tauri stars?“ In: *Astronomy and Astrophysics, Volume 453, Issue 3, July III 2006, pp.785-796* 453.3, p. 785 (cit. on p. 10).

Gaia Collaboration (Nov. 1, 2020). „VizieR Online Data Catalog: Gaia EDR3 (Gaia Collaboration, 2020)“. In: *VizieR Online Data Catalog* 1350 (cit. on p. 69).

Gaia Collaboration, A. G. A. Brown, A. Vallenari, et al. (Aug. 1, 2018). „Gaia Data Release 2. Summary of the contents and survey properties“. In: *Astronomy and Astrophysics* 616, A1 (cit. on p. 69).

Gaia Collaboration, T. Prusti, J. H. J. de Bruijne, et al. (Nov. 1, 2016). „The Gaia mission“. In: *Astronomy and Astrophysics* 595, A1 (cit. on p. 69).

Gammie, Charles F. (Jan. 1, 1996). „Layered Accretion in T Tauri Disks“. In: *The Astrophysical Journal* 457, p. 355 (cit. on pp. 10–12, 59).

Gardiner, C., P. Zoller, and P. Zoller (2004). *Quantum Noise: A Handbook of Markovian and Non-Markovian Quantum Stochastic Methods with Applications to Quantum Optics*. Springer Series in Synergetics. Springer (cit. on pp. 108, 115, 120).

Gay, J. and A. Journet (July 1975). „An infrared astrometric interferometer“. In: *Space Science Reviews* 17.5, pp. 687–688 (cit. on p. 33).

Gay, J., A. Journet, B. Christophe, and M. Robert (May 1973). „Heterodyne detection of blackbody radiation“. In: *Applied Physics Letters* 22.9, pp. 448–449 (cit. on pp. 27, 33).

Gay, J and Y Rabbia (Apr. 2014). „Heterodyne Interferometry in InfraRed at OCA-Calern Observatory in the seventies“. In: ed. by L. Arnold, H. Le Coroller, and J. Surdej, p. 9 (cit. on p. 34).

Glauber, Roy J. (Sept. 15, 1963a). „Coherent and Incoherent States of the Radiation Field“. In: *Physical Review* 131.6, pp. 2766–2788 (cit. on pp. 112, 114, 119, 120).

– (June 15, 1963b). „The Quantum Theory of Optical Coherence“. In: *Physical Review* 130.6, pp. 2529–2539 (cit. on pp. 108, 112).

Goldreich, P. and S. Tremaine (Nov. 1, 1979). „The excitation of density waves at the Lindblad and corotation resonances by an external potential.“ In: *The Astrophysical Journal* 233, pp. 857–871 (cit. on p. 15).

Goldreich, Peter and William R. Ward (Aug. 1, 1973). „The Formation of Planetesimals“. In: *The Astrophysical Journal* 183, pp. 1051–1062 (cit. on p. 13).

Goodman, Joseph W. (Jan. 1, 1985). „Statistical Optics“. In: *Statistical Optics by Joseph W. Goddman New York* (cit. on pp. 23, 27).

Gottesman, Daniel, Thomas Jennewein, and Sarah Croke (Aug. 16, 2012). „Longer-Baseline Telescopes Using Quantum Repeaters“. In: *Physical Review Letters* 109.7, p. 070503. arXiv: 1107.2939 (cit. on p. 125).

Gravity Collaboration, R. Abuter, M. Accardo, et al. (June 1, 2017). „First light for GRAVITY: Phase referencing optical interferometry for the Very Large Telescope Interferometer“. In: *Astronomy and Astrophysics* 602, A94 (cit. on pp. 31, 101).

Gravity Collaboration, R. Garcia Lopez, A. Natta, et al. (Aug. 1, 2020). „A measure of the size of the magnetospheric accretion region in TW Hydrae“. In: *Nature* 584, pp. 547–550 (cit. on p. 18).

Gravity Collaboration, K. Perraut, L. Labadie, et al. (Dec. 1, 2019). „The GRAVITY Young Stellar Object survey. I. Probing the disks of Herbig Ae/Be stars in terrestrial orbits“. In: *Astronomy and Astrophysics* 632, A53 (cit. on p. 50).

Gravity, M. Koutoulaki, R. Garcia Lopez, et al. (Nov. 11, 2020). „The GRAVITY Young Stellar Object survey IV. The CO overtone emission in 51 Oph at sub-au scales“. In: *arXiv:2011.05955 [astro-ph]*. arXiv: 2011.05955 (cit. on p. 67).

Guerin, W., J. -P. Rivet, M. Fouché, et al. (Oct. 2018). „Spatial intensity interferometry on three bright stars“. In: *Monthly Notices of the Royal Astronomical Society* 480. ADS Bibcode: 2018MNRAS.480..245G, pp. 245–250 (cit. on p. 27).

Guillet de Chatellus, Hugues, Luis Romero Cortes, and Jose Azana (Jan. 1, 2016). „Optical real-time Fourier transformation with kilohertz resolutions“. In: *Optica* 3, p. 1 (cit. on p. 163).

Guillet de Chatellus, Hugues, Luis Romero Cortes, Come Schnebelin, Maurizio Burla, and Jose Azana (June 1, 2018). „Reconfigurable photonic generation of broadband chirped waveforms using a single CW laser and low-frequency electronics“. In: *Nature Communications* 9, p. 2438 (cit. on p. 163).

Haffert, S. Y., A. J. Bohn, J. de Boer, et al. (June 1, 2019). „Two accreting protoplanets around the young star PDS 70“. In: *Nature Astronomy* 3, pp. 749–754 (cit. on p. 17).

Hakl, M, Q Y Lin, S Lepillet, et al. (n.d.). „Ultrafast quantum-well photodetectors operating at 10μm with flat frequency response up to 70GHz at room temperature“. In: (), p. 28 (cit. on p. 97).

Hale, D. D. S., M. Bester, W. C. Danchi, et al. (July 1, 2000). „The Berkeley Infrared Spatial Interferometer: A Heterodyne Stellar Interferometer for the Mid-Infrared“. In: *The Astrophysical Journal* 537, pp. 998–1012 (cit. on pp. 34, 40, 86, 87, 89, 107, 203).

Hale, David D. S., Walter Fitelson, John D. Monnier, Jonathon Weiner, and Charles H. Townes (Feb. 24, 2003). „Techniques for measuring phase closure at 11 microns“. In: Astronomical Telescopes and Instrumentation. Ed. by Wesley A. Traub. Waikoloa, Hawai'i, United States, p. 387 (cit. on pp. 34, 203).

Hanbury Brown, R. (Nov. 1956). „A Test of a New Type of Stellar Interferometer on Sirius“. In: *Nature* 178. ADS Bibcode: 1956Natur.178.1046H, pp. 1046–1048 (cit. on p. 27).

Hartmann, Lee and Nuria Calvet (Apr. 1, 1995a). „Observational constraints on FU ORI winds“. In: *The Astronomical Journal* 109, pp. 1846–1855 (cit. on p. 12).

– (Apr. 1, 1995b). „Observational constraints on FU ORI winds“. In: *The Astronomical Journal* 109, pp. 1846–1855 (cit. on p. 68).

Hartmann, Lee, Nuria Calvet, Erik Gullbring, and Paola D'Alessio (Mar. 1, 1998). „Accretion and the Evolution of T Tauri Disks“. In: *The Astrophysical Journal* 495, pp. 385–400 (cit. on p. 7).

Hartmann, Lee and Scott J. Kenyon (1996). „The FU Orionis Phenomenon“. In: *Annual Review of Astronomy and Astrophysics* 34, pp. 207–240 (cit. on pp. 44, 45, 50).

Heffner, H. (July 1962). „The Fundamental Noise Limit of Linear Amplifiers“. In: *Proceedings of the IRE* 50.7, pp. 1604–1608 (cit. on pp. 107, 126).

Helstrom, Carl W and Carl W Helstrom (1976). *Quantum detection and estimation theory*. Vol. 84. Academic press New York (cit. on p. 121).

Herbig, G. H. (Nov. 1977). „Eruptive phenomena in early stellar evolution“. In: *The Astrophysical Journal* 217, pp. 693–715 (cit. on p. 46).

Herbig, George H. (Mar. 1, 1960). „The Spectra of Be- and Ae-Type Stars Associated with Nebulosity“. In: *The Astrophysical Journal Supplement Series* 4, p. 337 (cit. on p. 6).

Hirose, Shigenobu (Apr. 1, 2015). „Magnetic turbulence and thermodynamics in the inner region of protoplanetary discs“. In: *Monthly Notices of the Royal Astronomical Society* 448, pp. 3105–3120 (cit. on p. 59).

Holler, C. M., M. E. Jones, A. C. Taylor, A. I. Harris, and S. A. Maas (Dec. 1, 2011). „A 2-20 GHz Analog Lag-Correlator for Radio Interferometry“. In: *arXiv e-prints* 1112, arXiv:1112.1982 (cit. on pp. 99, 161).

Hugi, Andreas, Gustavo Villares, Stephane Blaser, H. C. Liu, and Jerome Faist (Dec. 2012). „Mid-infrared frequency comb based on a quantum cascade laser“. In: *Nature* 492.7428, pp. 229–233 (cit. on p. 98).

Ireland, Michael J. and John D. Monnier (July 1, 2014). „A dispersed heterodyne design for the planet formation imager“. In: 9146, p. 914612 (cit. on pp. 42, 79, 90, 99, 221).

Ireland, Michael J., John D. Monnier, Stefan Kraus, et al. (Aug. 1, 2016). „Status of the Planet Formation Imager (PFI) concept“. In: 9907, p. 99071L (cit. on p. 88).

Johnson, M A, A L Betz, and C H Townes (1974). „10-/zm Heterodyne Stellar Interferometer“. In: *PHYSICAL REVIEW LETTERS* 33.27, p. 4 (cit. on pp. 2, 27, 33).

Johnson, M. A. and C. H. Townes (May 1, 2000). „Quantum effects and optimization of heterodyne detection“. In: *Optics Communications* 179, pp. 183–187 (cit. on p. 107).

Joy, Alfred H. (Sept. 1, 1945). „T Tauri Variable Stars.“ In: *The Astrophysical Journal* 102, p. 168 (cit. on p. 6).

Kaeufl, H. U. (Jan. 1, 1984). „Construction of a 10-micron-wavelength heterodyne receiver for use at the Cassegrain focus of astronomical telescopes and spectroscopic investigation of the atmospheres of Mars and Venus“. PhD thesis (cit. on p. 33).

Kanagaraj, Nithyanandan, Leo Djevarhidjian, Vicente Duran, Come Schnebelin, and Hugues Guillet de Chatellus (May 13, 2019). „Optimization of acousto-optic optical frequency combs“. In: *Optics Express* 27.10, p. 14842 (cit. on pp. 167–169).

Kenyon, Scott J. and Lee W. Hartmann (Jan. 1, 1990). „On the apparent positions of T Tauri stars in the H-R diagram“. In: *The Astrophysical Journal* 349, pp. 197–207 (cit. on pp. 12, 44).

Keppler, M., M. Benisty, A. Müller, et al. (Sept. 2018). „Discovery of a planetary-mass companion within the gap of the transition disk around PDS 70“. In: *Astronomy & Astrophysics* 617, A44 (cit. on p. 17).

Kerr, A.R. (Mar. 1999). „Suggestions for revised definitions of noise quantities, including quantum effects“. In: *IEEE Transactions on Microwave Theory and Techniques* 47.3, pp. 325–329 (cit. on p. 108).

Kerr', A R and M J Feldman (1997). „Receiver Noise Temperature, the Quantum Noise Limit, and the Role of the Zero-Point Fluctuations“. In: p. 11 (cit. on p. 108).

Kervella, P., D. Segransan, and V. Coude du Foresto (Oct. 1, 2004). „Data reduction methods for single-mode optical interferometry. Application to the VLTI two-telescopes beam combiner VINCI“. In: *Astronomy and Astrophysics* 425, pp. 1161–1174 (cit. on pp. 49, 52).

Khabiboulline, Emil T., Johannes Borregaard, Kristiaan De Greve, and Mikhail D. Lukin (Aug. 15, 2019). „Optical Interferometry with Quantum Networks“. In: *Physical Review Letters* 123.7, p. 070504. arXiv: 1809.01659 (cit. on p. 125).

Kikuchi, Kazuro (Jan. 1, 2016). „Fundamentals of Coherent Optical Fiber Communications“. In: *Journal of Lightwave Technology* 34.1, pp. 157–179 (cit. on p. 106).

Kingston, R. H. (1978). „Detection of optical and infrared radiation“. In: *Springer Series in Optical Sciences, Berlin: Springer, 1978* (cit. on pp. 31, 82, 83, 103, 192).

Kluska, J., J.-P. Berger, F. Malbet, et al. (Apr. 3, 2020). „A family portrait of disk inner rims around Herbig Ae/Be stars: Hunting for warps, rings, self shadowing, and misalignments in the inner astronomical units“. In: *arXiv:2004.01594 [astro-ph]*. arXiv: 2004.01594 (cit. on pp. 17, 18).

Kratter, Kaitlin M. and Giuseppe Lodato (Sept. 19, 2016). „Gravitational Instabilities in Circumstellar Disks“. In: *Annual Review of Astronomy and Astrophysics* 54.1, pp. 271–311. arXiv: 1603.01280 (cit. on pp. 9, 14).

Kraus, S., K.-H. Hofmann, M. Benisty, et al. (Oct. 2008). „The origin of hydrogen line emission for five Herbig Ae/Be stars spatially resolved by VLTI/AMBER spectro-interferometry“. In: *Astronomy & Astrophysics* 489.3, pp. 1157–1173 (cit. on p. 18).

Kraus, Stefan, John D. Monnier, Michael J. Ireland, et al. (Aug. 4, 2016). „Planet Formation Imager (PFI): science vision and key requirements“. In: SPIE Astronomical Telescopes + Instrumentation. Ed. by Fabien Malbet, Michelle J. Creech-Eakman, and Peter G. Tuthill. Edinburgh, United Kingdom, 99071K (cit. on p. 19).

Kraus, Stefan, John Monnier, Tim Harries, et al. (July 24, 2014). „The Science Case for the Planet Formation Imager (PFI)“. In: *arXiv:1407.7033 [astro-ph]*, p. 914611. arXiv: 1407.7033 (cit. on p. 19).

Labdon, Aaron, Stefan Kraus, Claire L Davies, et al. (Nov. 1, 2020). „Viscous Heating and Boundary Layer Accretion in the Disk of Outbursting Star FU Orionis“. In: *arXiv e-prints* 2011, arXiv:2011.07865 (cit. on pp. 45, 47, 48, 55, 63, 64).

Labeye, Pierre (Feb. 6, 2008). „Composants optiques integres pour l'Interferometrie astronomique“. PhD thesis. Institut National Polytechnique de Grenoble - INPG (cit. on p. 150).

Labeyrie, A. (Mar. 1, 1975). „Interference fringes obtained on Vega with two optical telescopes.“ In: *The Astrophysical Journal* 196, pp. L71–L75 (cit. on pp. 27, 28).

– (Sept. 1996). „Resolved imaging of extra-solar planets with future 10-100 km optical interferometric arrays“. In: *Astronomy and Astrophysics Supplement Series* 118.3, pp. 517–524 (cit. on p. 152).

Lachaume, R. (Mar. 2003). „On marginally resolved objects in optical interferometry“. In: *Astronomy and Astrophysics, v.400, p.795-803 (2003)* 400, p. 795 (cit. on p. 26).

Lachaume, Regis, Markus Rabus, Andres Jordan, et al. (Apr. 1, 2019). „Towards reliable uncertainties in IR interferometry: the bootstrap for correlated statistical and systematic errors“. In: *Monthly Notices of the Royal Astronomical Society* 484, pp. 2656–2673 (cit. on p. 53).

Lada, Charles J. (Jan. 1, 1987). „Star formation: from OB associations to protostars.“ In: 115, p. 1 (cit. on pp. 6, 8).

Lambrechts, M. and A. Johansen (Aug. 2012). „Rapid growth of gas-giant cores by pebble accretion“. In: *Astronomy & Astrophysics, Volume 544, id.A32, <NUMPAGES>13</NUMPAGES> pp.* 544, A32 (cit. on p. 13).

Landi, Gabriel T (n.d.). „Quantum Information and Quantum Noise“. In: (), p. 149 (cit. on p. 114).

Lawson, Peter R. (2000). „Principles of Long Baseline Stellar Interferometry“. In: (cit. on pp. 91–93, 107).

Lazareff, B., J.-P. Berger, J. Kluska, et al. (Mar. 1, 2017). „Structure of Herbig AeBe disks at the milliarcsecond scale . A statistical survey in the H band using PIONIER-VLTI“. In: *Astronomy and Astrophysics* 599, A85 (cit. on pp. 18, 50).

Le Bouquin, J.-B., J.-P. Berger, B. Lazareff, et al. (Nov. 1, 2011). „PIONIER: a 4-telescope visitor instrument at VLTI“. In: *Astronomy and Astrophysics* 535, A67 (cit. on pp. 31, 48, 49).

Le Coarer, E., A. Chalabaev, and G. Duvert (Apr. 1, 2014). „Prospects of Optical Heterodyne Detection for Astronomy and One Photon Interferometry“. In: pp. 191–195 (cit. on pp. 97, 106, 107).

LeBouquin, Jean-Baptiste J. B., Jean-Philippe Berger, Pierre R. Labeye, et al. (Oct. 20, 2004). „Comparison of integrated optics concepts for a near-infrared multi-telescope beam combiner“. In: SPIE Astronomical Telescopes + Instrumentation. Ed. by Wesley A. Traub. USA, p. 1362 (cit. on p. 149).

Lehmann, Lucien, Ludovic Grossard, Laurent Delage, et al. (May 1, 2019). „Towards a mid-infrared L band up-conversion interferometer: first on-sky sensitivity test on a single arm“. In: *Monthly Notices of the Royal Astronomical Society* 485. ADS Bibcode: 2019MNRAS.485.3595L, pp. 3595–3599 (cit. on p. 27).

Léna, P. (Jan. 1, 1988). „The interferometric mode of the European Very Large Telescope.“ In: 29, pp. 899–908 (cit. on p. 223).

Lena, Pierre, Daniel Rouan, François Lebrun, François Mignard, and Didier Pelat (Jan. 1, 2012). „Observational Astrophysics“. In: *Observational Astrophysics:* (cit. on pp. 23, 25).

Lin, D. N. C., P. Bodenheimer, and D. C. Richardson (Apr. 1, 1996). „Orbital migration of the planetary companion of 51 Pegasi to its present location“. In: *Nature* 380, pp. 606–607 (cit. on p. 15).

Lin, D. N. C. and J. Papaloizou (Mar. 1, 1979). „Tidal torques on accretion discs in binary systems with extreme mass ratios.“ In: *Monthly Notices of the Royal Astronomical Society* 186, pp. 799–812 (cit. on p. 15).

Liu, Hauyu Baobab, Antoine Merand, Joel D. Green, et al. (Oct. 1, 2019). „Diagnosing 0.1-10 au Scale Morphology of the FU Ori Disk Using ALMA and VLTI/GRAVITY“. In: *The Astrophysical Journal* 884, p. 97 (cit. on pp. 45, 50, 56, 64, 65).

Lobanov, Andrei (Feb. 2015). „Brightness temperature constraints from interferometric visibilities“. In: *Astronomy & Astrophysics* 574, A84 (cit. on p. 90).

Lodato, G. and C. J. Clarke (Sept. 1, 2004). „Massive planets in FU Orionis discs: implications for thermal instability models“. In: *Monthly Notices of the Royal Astronomical Society* 353, pp. 841–852 (cit. on p. 59).

Lopez, B., S. Lagarde, W. Jaffe, et al. (Sept. 1, 2014). „An Overview of the MATISSE Instrument — Science, Concept and Current Status“. In: *The Messenger* 157, pp. 5–12 (cit. on p. 31).

Louvet, F., C. Dougados, S. Cabrit, et al. (Oct. 2018). „The HH30 edge-on T Tauri star. A rotating and precessing monopolar outflow scrutinized by ALMA“. In: *Astronomy & Astrophysics, Volume 618, id.A120, <NUMPAGES>28</NUMPAGES> pp.* 618, A120 (cit. on p. 11).

Lynden-Bell, D. and J. E. Pringle (Sept. 1, 1974). „The evolution of viscous discs and the origin of the nebular variables.“ In: *Monthly Notices of the Royal Astronomical Society* 168, pp. 603–637 (cit. on p. 58).

Lyra, W. and H. Klahr (Mar. 2011). „The baroclinic instability in the context of layered accretion. Self-sustained vortices and their magnetic stability in local compressible unstratified models of protoplanetary disks“. In: *Astronomy & Astrophysics, Volume 527, id.A138, <NUMPAGES>20</NUMPAGES> pp.* 527, A138 (cit. on p. 13).

Malbet, F., J.-P. Berger, M. M. Colavita, et al. (Nov. 1, 1998). „FU Orionis Resolved by Infrared Long-Baseline Interferometry at a 2 AU Scale“. In: *The Astrophysical Journal Letters* 507, pp. L149–L152 (cit. on p. 45).

Malbet, F., R. Lachaume, J.-P. Berger, et al. (July 1, 2005). „New insights on the AU-scale circumstellar structure of FU Orionis“. In: *Astronomy and Astrophysics* 437, pp. 627–636 (cit. on pp. 45–47, 49, 51, 60, 63).

Malbet, Fabien (Dec. 1, 1992). „Circumstellar Surroundings of Young Stellar Objectse“. PhD thesis (cit. on p. 64).

Mandel, Leonard and Emil Wolf (Sept. 1, 1995). „Optical Coherence and Quantum Optics“. In: *Optical Coherence and Quantum Optics, by Leonard Mandel and Emil Wolf, pp. 1192. ISBN 0521417112. Cambridge, UK: Cambridge University Press, September 1995.* (Cit. on pp. 120, 121).

Marois, Christian, Bruce Macintosh, Travis Barman, et al. (Nov. 1, 2008). „Direct Imaging of Multiple Planets Orbiting the Star HR 8799“. In: *Science* 322, p. 1348 (cit. on p. 14).

Marpaung, David, Chris Roeloffzen, Rene Heideman, et al. (Nov. 17, 2012). „Integrated microwave photonics“. In: *arXiv:1211.4114 [physics]*. arXiv: 1211.4114 (cit. on pp. 141, 193).

Marpaung, David, Jianping Yao, and Jose Capmany (Feb. 2019). „Integrated microwave photonics“. In: *Nature Photonics* 13.2, pp. 80–90 (cit. on p. 130).

Martin, R. G. and S. H. Lubow (Oct. 1, 2011). „The Gravo-magneto Limit Cycle in Accretion Disks“. In: *The Astrophysical Journal Letters* 740, p. L6 (cit. on p. 60).

Mège, Pierre (Jan. 1, 2002). „Interférométrie avec des guides d'ondes optiques : théorie et applications“. These de doctorat. Université Joseph Fourier (Grenoble) (cit. on p. 30).

Michael, Ernest A. and Felipe E. Besser (2018). „On the Possibility of Breaking the Heterodyne Detection Quantum Noise Limit With Cross-Correlation“. In: *IEEE Access* 6, pp. 45299–45316 (cit. on pp. 97, 106–108, 125).

Michelson, A. A. and F. G. Pease (May 1, 1921). „Measurement of the Diameter of alpha Orionis with the Interferometer.“ In: *The Astrophysical Journal* 53, pp. 249–259 (cit. on pp. 27, 28).

Millan-Gabet, R., J. D. Monnier, R. L. Akeson, et al. (Apr. 1, 2006). „Keck Interferometer Observations of FU Orionis Objects“. In: *The Astrophysical Journal* 641, pp. 547–555 (cit. on pp. 45, 64).

Millan-Gabet, Rafael, F. Peter Schloerb, and Wesley A. Traub (Jan. 1, 2001). „Spatially Resolved Circumstellar Structure of Herbig AE/BE Stars in the Near-Infrared“. In: *The Astrophysical Journal* 546, pp. 358–381 (cit. on p. 17).

Milli, J., M. Kasper, P. Bourget, et al. (July 1, 2018). „Low wind effect on VLT/SPHERE: impact, mitigation strategy, and results“. In: 0703, 107032A (cit. on p. 49).

Monnier, John D., Jean-Philippe Berger, Jean-Baptiste Le Bouquin, et al. (July 1, 2014). „The 2014 interferometric imaging beauty contest“. In: 9146, 91461Q (cit. on p. 210).

Monnier, John D., Michael Ireland, Stefan Kraus, et al. (July 1, 2018a). „Planet formation imager: project update“. In: 0701, p. 1070118 (cit. on p. 206).

Monnier, John D., Stefan Kraus, Michael J. Ireland, et al. (Dec. 2018b). „The Planet Formation Imager“. In: *Experimental Astronomy* 46.3, pp. 517–529. arXiv: 1807.11559 (cit. on pp. 18, 22, 23, 79).

Monnier, John David (1999). „Infrared interferometry and spectroscopy of circumstellar envelopes“. PhD thesis (cit. on pp. 35, 39, 41, 86, 93, 94, 160).

Mordasini, C., Y. Alibert, H. Klahr, and T. Henning (Nov. 2012). „Characterization of exoplanets from their formation: I. Models of combined planet formation and evolution“. In: *Astronomy & Astrophysics* 547, A111 (cit. on p. 14).

Mumma, M. J., D. Buhl, G. Chin, et al. (Apr. 3, 1981). „Discovery of Natural Gain Amplification in the 10-Micrometer Carbon Dioxide Laser Bands on Mars: A Natural Laser“. In: *Science* 212.4490, pp. 45–49 (cit. on pp. 34, 176).

Ohnaka, K., G. Weigelt, and K.-H. Hofmann (Aug. 2017). „Vigorous atmospheric motion in the red supergiant star Antares“. In: *Nature* 548.7667, pp. 310–312 (cit. on p. 211).

Palaferri, Daniele, Yanko Todorov, Azzurra Bigioli, et al. (Apr. 2018). „Room-temperature nine-μm-wavelength photodetectors and GHz-frequency heterodyne receivers“. In: *Nature* 556.7699, pp. 85–88 (cit. on p. 97).

Parriaux, Alexandre, Kamal Hammani, and Guy Millot (Sept. 1, 2019). „Electro-optic dual-comb spectrometer in the thulium amplification band for gas sensing applications“. In: *Optics Letters* 44.17, pp. 4335–4338 (cit. on p. 98).

– (Mar. 31, 2020). „Electro-optic frequency combs“. In: *Advances in Optics and Photonics* 12.1, p. 223 (cit. on p. 98).

Perez, Laura M., John M. Carpenter, Sean M. Andrews, et al. (Sept. 1, 2016). „Spiral density waves in a young protoplanetary disk“. In: *Science* 353, pp. 1519–1521 (cit. on p. 16).

Perrin, G. and J. Woillez (May 1, 2019). „Single-mode interferometric field of view in partial turbulence correction. Application to the observation of the environment of Sgr A* with GRAVITY“. In: *Astronomy and Astrophysics* 625, A48 (cit. on pp. 30, 48, 50).

Petrov, Romain G., Fatme Allouche, Alexis Matter, et al. (Dec. 30, 2020). „Commissioning MATISSE: operation and performances“. In: *Optical and Infrared Interferometry and Imaging VII*. Optical and Infrared Interferometry and Imaging VII. Ed. by Antoine Merand, Stephanie Sallum, and Peter G. Tuthill. Online Only, United States: SPIE, p. 19 (cit. on pp. 92, 101, 204).

Petrov, Romain G., Abdelkarim Boskri, Yves Bresson, et al. (Aug. 4, 2016). „Hierarchical fringe tracker to co-phase and coherence very large optical interferometers“. In: SPIE Astronomical Telescopes + Instrumentation. Edinburgh, United Kingdom, 99071F (cit. on p. 101).

Picque, Nathalie and Theodor W. Hänsch (Feb. 2019). „Frequency comb spectroscopy“. In: *Nature Photonics, Volume 13, Issue 3, p.146-157* 13.3, p. 146 (cit. on p. 165).

Pinte, C., D. J. Price, F. Menard, et al. (Feb. 1, 2020). „Nine Localized Deviations from Keplerian Rotation in the DSHARP Circumstellar Disks: Kinematic Evidence for Protoplanets Carving the Gaps“. In: *The Astrophysical Journal* 890, p. L9 (cit. on p. 17).

Popham, Robert, Scott Kenyon, Lee Hartmann, and Ramesh Narayan (Dec. 1, 1996). „Spectra and Line Profiles of FU Orionis Objects: Comparisons between Boundary Layer Models and Observations“. In: *The Astrophysical Journal* 473, p. 422 (cit. on pp. 61, 64).

Pueyo, Laurent, Lynne Hillenbrand, Gautam Vasisht, et al. (Sept. 1, 2012). „Constraining Mass Ratio and Extinction in the FU Orionis Binary System with Infrared Integral Field Spectroscopy“. In: *The Astrophysical Journal* 757, p. 57 (cit. on p. 61).

Quanz, S. P., Th. Henning, J. Bouwman, Th. Ratzka, and Ch. Leinert (Sept. 1, 2006). „FU Orionis: The MIDI VLTI Perspective“. In: *The Astrophysical Journal* 648, pp. 472–483 (cit. on p. 45).

Ravi, V., E. H. Wishnow, C. H. Townes, et al. (Oct. 10, 2011). „THE NON-UNIFORM, DYNAMIC ATMOSPHERE OF BETELGEUSE OBSERVED AT MID-INFRARED WAVELENGTHS“. In: *The Astrophysical Journal* 740.1, p. 24 (cit. on p. 90).

Ribak, E. N., E. B. Hochberg, N. A. Page, S. P. Synnott, and J. B. Breckinridge (1988). „Beam combination in a multi-telescope, monolithic interferometer.“ In: 29, pp. 1105–1116 (cit. on pp. 151, 183).

Ridgway, Richard W., Carl L. Dohrman, and Joshua A. Conway (Oct. 1, 2014). „Microwave Photonics Programs at DARPA“. In: *Journal of Lightwave Technology* 32, pp. 3428–3439 (cit. on p. 194).

Schnebelin, Come (Oct. 1, 2018). „Analyse et generation de signaux dans les boucles optiques à decalage de frequence : analogie spatiale et nouveaux concepts d'auto-imagerie“. These de doctorat. Universite Grenoble Alpes (ComUE) (cit. on pp. 162, 163).

Schnebelin, Come, Jose Azana, and Hugues Guillet de Chatellus (Oct. 1, 2019). „Programmable broadband optical field spectral shaping with megahertz resolution using a simple frequency shifting loop“. In: *Nature Communications* 10, p. 4654 (cit. on p. 163).

Schuetz, C.A., J. Murakowski, G.J. Schneider, and D.W. Prather (May 2005). „Radiometric Millimeter-wave detection via optical upconversion and carrier suppression“. In: *IEEE Transactions on Microwave Theory and Techniques* 53.5, pp. 1732–1738 (cit. on p. 152).

Schuetz, Christopher, Richard Martin, Thomas Dillon, et al. (May 31, 2013). „Realization of a video-rate distributed aperture millimeter-wave imaging system using optical upconversion“. In: SPIE Defense, Security, and Sensing. Ed. by David A. Wikner and Arttu R. Luukanen. Baltimore, Maryland, USA, p. 87150I (cit. on p. 152).

Serber, R. and C. H. Townes (1960). „Limits on Electromagnetic Amplification due to Complementarity“. In: p. 233 (cit. on p. 119).

Shaklan, Stuart and Francois Roddier (June 1, 1988). „Coupling starlight into single-mode fiber optics“. In: *Applied Optics* 27, pp. 2334–2338 (cit. on p. 30).

Shakura, N. I. and R. A. Sunyaev (June 1973). „Reprint of 1973A&A....24..337S. Black holes in binary systems. Observational appearance.“ In: *Astronomy and Astrophysics* 500, pp. 33–51 (cit. on p. 7).

Stassun, Keivan G., Ryan J. Oelkers, Martin Paegert, et al. (Oct. 1, 2019). „The Revised TESS Input Catalog and Candidate Target List“. In: *The Astronomical Journal* 158, p. 138 (cit. on p. 69).

Stupar, Dušan, Jürgen Krieg, Peter Krötz, et al. (May 1, 2008). „Fully reflective external-cavity setup for quantum-cascade lasers as a local oscillator in mid-infrared wavelength heterodyne spectroscopy“. In: *Applied Optics* 47, pp. 2993–2997 (cit. on p. 190).

Sudarshan, E. C. (Apr. 1963). „Equivalence of Semiclassical and Quantum Mechanical Descriptions of Statistical Light Beams“. In: *Physical Review Letters, vol. 10, Issue 7, pp. 277-279* 10.7, p. 277 (cit. on p. 120).

Swenson, George W. (Aug. 1, 1986). „Radio-astronomy precedent for optical interferometer imaging“. In: *JOSA A* 3.8, pp. 1311–1319 (cit. on pp. 42, 79, 221).

Szemendera, L., L. Grossard, L. Delage, and F. Reynaud (July 2017). „In-laboratory ALOHA mid-infrared up-conversion interferometer in the photon counting regime at l = 3.39 m“. In: *Monthly Notices of the Royal Astronomical Society* 468. ADS Bibcode: 2017MNRAS.468.3484S, pp. 3484–3488 (cit. on p. 27).

Takami, Michihiro, Guangwei Fu, Hauyu Baobab Liu, et al. (Sept. 1, 2018). „Near-infrared High-resolution Imaging Polarimetry of FU Ori-type Objects: Toward a Unified Scheme for Low-mass Protostellar Evolution“. In: *The Astrophysical Journal* 864, p. 20 (cit. on p. 50).

Teich, M.C. (Jan. 1968). „Infrared heterodyne detection“. In: *Proceedings of the IEEE* 56.1, pp. 37–46 (cit. on p. 106).

Thompson, A. Richard, James M. Moran, and George W. Swenson Jr. (2017). „Interferometry and Synthesis in Radio Astronomy, 3rd Edition“. In: *Interferometry and Synthesis in Radio Astronomy, by A. Richard Thompson, James M. Moran, and George W. Swenson, Jr. 3rd ed. Springer, 2017.* (Cit. on pp. 27, 35, 36, 38, 39, 82–87, 90, 106, 108, 111, 122, 123).

Townes, C. H. (June 1, 1984). „Spatial interferometry in the mid-infrared region“. In: *Journal of Astrophysics and Astronomy* 5, pp. 111–130 (cit. on pp. 33, 86, 87, 107, 123).

Townes, C. H. and E. C. Sutton (1981). „Multiple telescope infrared interferometry“. In: (cit. on p. 34).

Tsang, Mankei (Dec. 1, 2011). „Quantum Nonlocality in Weak-Thermal-Light Interferometry“. In: *Physical Review Letters* 107, p. 270402 (cit. on pp. 108, 121, 123, 221).

Tucker, John R. and Marc J. Feldman (Oct. 1, 1985). „Quantum detection at millimeter wavelengths“. In: *Reviews of Modern Physics* 57.4, pp. 1055–1113 (cit. on p. 108).

Turner, N. J., S. Fromang, C. Gammie, et al. (Jan. 1, 2014). *Transport and Accretion in Planet-Forming Disks*. eprint: arXiv:1401.7306 (cit. on pp. 9–11).

Valon, A. de, C. Dougados, S. Cabrit, et al. (Feb. 2020). „ALMA reveals a large structured disk and nested rotating outflows in DG Tauri B“. In: *Astronomy & Astrophysics, Volume 634, id.L12, <NUMPAGES>11</NUMPAGES> pp.* 634, p. L12 (cit. on pp. 11, 16).

Varga, J., P. abraham, L. Chen, et al. (Sept. 2018). „VLTI/MIDI atlas of disks around low- and intermediate-mass young stellar objects“. In: *Astronomy & Astrophysics* 617, A83. arXiv: 1805.02939 (cit. on pp. 211–215).

Weidenschilling, S. J. (July 1, 1977). „Aerodynamics of solid bodies in the solar nebula.“ In: *Monthly Notices of the Royal Astronomical Society* 180, pp. 57–70 (cit. on p. 13).

Woillez, Julien, Olivier Lai, Guy Perrin, et al. (June 2017). „AGILIS: Agile Guided Interferometer for Longbaseline Imaging Synthesis: Demonstration and concepts of reconfigurable optical imaging interferometers“. In: *Astronomy & Astrophysics* 602, A116 (cit. on pp. 79, 81, 100, 210).

Zari, E., A. G. A. Brown, J. de Bruijne, C. F. Manara, and P. T. de Zeeuw (Dec. 1, 2017). „Mapping young stellar populations toward Orion with Gaia DR1“. In: *Astronomy and Astrophysics* 608, A148 (cit. on p. 69).

Zernike, F. (Aug. 1, 1938). „The concept of degree of coherence and its application to optical problems“. In: *Physica* 5, pp. 785–795 (cit. on p. 25).

Zhao, Peiqian, Jean-Marie Mariotti, Vincent Coudé du Foresto, Pierre J. Lena, and Guy Perrin (June 1, 1995). „Multistage fiber optic delay line for astronomical interferometry“. In: 2476, pp. 108–119 (cit. on p. 148).

Zhu, Zhaohuan, Lee Hartmann, Charles Gammie, and Jonathan C. McKinney (Aug. 1, 2009). „Two-dimensional Simulations of FU Orionis Disk Outbursts“. In: *The Astrophysical Journal* 701, pp. 620–634 (cit. on p. 45).

List of Figures

1.1 Classes of Young Stellar Objects (Lada, 1987; Andre and Montmerle, 1994). Figure from A. de Valon (2021). 8

1.2 *Up :* Structure of a protoplanetary disks and resolution range of each high-angular resolution techniques, from (C. Dullemond and J. Monnier, 2010). *Bottom :* Physical regimes relevant to angular momentum transport in disks (from (Armitage, 2011)). In the inner region of the disk and for high accretion rates, viscous accretion dominates the transport of angular momentum. The temperature of ionization of alkali metals provide the range where MRI can be activated. In the outer part, the disk is gravitationally unstable (Q<1). The overall conditions of the disk set the environment where planet formation occurs e.g. location of the snowline. 9

1.3 Mechanism of magnetorotational instability (MRI). Extracted from Harvard Astronomy 201b lecture. 10

1.4 Layered disk model and dead zone in protoplanetary disks (from (Armitage, 2011), and initially proposed in (Gammie, 1996)). 12

1.5 *Left :* Accretion luminosity of a $1\,M_J$ proto-planet at 5.2 AU. (Mordasini et al., 2012) (blue : core luminosity, green : envelope luminosity, red : total luminosity). The luminosity peak on the right corresponds to the runaway accretion following the collapse of the core. *Right :* Type II migration, with the opening of a gap and the apparition of disk Lindblad resonances (Armitage, 2020). 14

1.6 **a)**: Size-luminosity relation in YSOs (C. Dullemond and J. Monnier, 2010) **b)**: Spectro-astrometry of bipolar wind in ZCma (Benisty et al., 2010) **c)**: Image reconstruction of a Herbig Ae/Be star (Kluska et al., 2020). 17

2.1 Top level requirements of a Planet Formation Imager, extracted from (John D. Monnier et al., 2018b). 23

2.2 *Left :* Pupil-plane of an optical system : the pupil can be seen as the decomposition of a multiple two element Young interferometer. *Right :* Frequency space of the image (so-called UV plane), in which one separation corresponds to the measurement of one spatial frequency. As an example, the visibility function of an arbitrary object was generated using `Aspro2` (developed by JMMC). 24

2.3 Domain of application of the astronomical interferometric techniques demonstrated at the time of writing. For each technique, the solid line represents the domain where the technique has been demonstrated (cf Tab 2.2), the dashed line represents the domain could be potentially extended, but where the demonstration is not yet done or is on-going. The order of coherence measured by each technique is indicated on the y-axis. 28

2.4 Principles of infrared interferometer (amplitude interferometry), credits ESO. . 29

2.5 Overview of the Very Large Telescope Interferometer (VLTI) at Cerro Paranal. . 30

2.6 Schematic of a infrared heterodyne detection (from (Kingston, 1978)). 31

2.7 General layout of a two element infrared heterodyne interferometer. 33

2.8 *Left :* Simplified block diagram of the Infrared Spatial Interferometer (ISI, figure from **Danchi2002**). *Right :* ISI on the Mt Wilson : the periscopes from which the local-oscillators are launched are visible on the left. 34

2.9 Simplified schematic of the propagation of signals in a heterodyne interferometer, inspired from Thompson, Moran, and Swenson, 2017. The different points a), b) and c) are used in the calculation of the phase in the text. HD: Heterodyne Detection, see the text for the definition of $\tau(\theta, t)$ and $\tau_d(t)$. 36

3.1 *Left* : Classical picture of FU Orionis outburst, exctracted from (Lee Hartmann and Kenyon, 1996). *Right* : Optical image of FU Orionis at large spatial scales (PanSTARRS/DR1). The remnant of the infalling envelope in which FU Orionis is embedded is visible. 44

3.2 Lightcurve of FU Orionis, extracted from G. H. Herbig, 1977 and AAVSO database (https://www.aavso.org). 46

3.3 Visibility squared as a function of the projected baseline, observed with MIRCX instrument in year 2019 (see logs Tab 3.1). Red dashed line shows the minor and major axis of the gaussian inner disk ; black solid lines and black arrows show the contribution of the compact flux f_c and of the over-resolved flux f_e. . 51

3.4 Size of the resolved emission as a function of time, plotted in H band *(up)* and K band *(bottom)*. The temporal slope is estimated through bootstrap (dashed line : median of the bootstrap trials), the individual trials being over-plotted in the graph (green lines). Yellow and red regions highlight respectively the 1σ and 3σ contours of the fit. The red point in H band (PIONIER, 2017) is discarded from the estimation of the slope with bootstrap, due to an observational bias identified for this point. 56

3.5 Proportion of the flux of the extended envelope over the total flux measured in the interferometric field of view, in K band. A chromatic dependency is visible in GRAVI21 and GRAVI16 data. The offset between these two curves is due to the smaller interferometric field of view in GRAVI21. 57

3.6 Schematic of the disk structure in a layered disk model. Figure extracted from Armitage, Livio, and Pringle, 2001. 59

3.7 Radial profile of the effective temperature of the disk as function of time (y-axis : radius, x-axis : time). *Left :* MRI+GI model, including TI instability at the innermost scale *Right :* pure TI model, based on the opacities provided in (Bell and Lin, 1994). 60

3.8 Typical observables deduced from the simulation, here given for Simulation 5. *Upper left :* Effective temperature profiles (solid line) obtained at the output of the numerical simulation of the outburst, corrected in the inner part of the disk (dashed line). *Lower left :* Visibility profiles deduced from the corrected effective temperature profile. The dashed line corresponds to the minor axis of the disk (less resolved), solid line to the major axis (more resolved). *Middle right :* SED deduced from the corrected effective temperature profile. Effective temperature profiles, Visibilities, and SEDs are plotted at the different time stamp, that are indicated in the legend to show the evolution of these observables in time. . . . 62
3.9 Simulated size of the emission zone compared to interferometric observations. The simulations are labeled with the number provided in Tab.3.5. 63
3.10 SED of the extended envelope deduced from GRAVITY observations in K band, and MIRC-X and PIONIER non-detection in H band. The total SED of FU Orionis was obtained with archival X-shooter data. 65
3.11 Extrapolation of the flux of the extended envelope deduced from interferometric observations, and available spectral bands in the mid-infrared. 66
3.12 H band : output of the fitting procedure of the interferometric observations. **Left :** The visibility model is represented in dashed line, the minor axis of the gaussian disk is associated to the upper visibility curve and the major axis to the lower visibility curve. Residuals are shown in red scattered points. **Middle :** Bootstrap values of the fwhm estimate. **Right :** (u,v)-coverage associated to each observation. 70
3.13 K band : output of the fitting procedure. See Fig.3.14 for the second part. . . . 71
3.14 K band (continuation). 72
3.15 PION19 bootstrap output, computed over $N = 1000$ iterations. 73
3.16 GRAVI17 bootstrap output, computed over $N = 1000$ iterations. 74

4.1 System architecture of the mid-infrared heterodyne interferometer considered in this work for a PFI. 80
4.2 Block diagram of a single channel heterodyne detection chain in radiometer mode, adapted from Kingston, 1978. 82
4.3 Point source sensitivity and brightness temperature for an angular resolution $\theta = 2\,\mathrm{mas}$, based on the parameters in Tab 4.3. 91
4.4 Ratio of the noise density in heterodyne and direct interferometry. The exact parameters used in this comparison are provided in Tab 4.4. 92
4.5 Ratio of the noise density in heterodyne and direct interferometry for a single spectral channel as a function of detection bandwidth, with the same parameters as in Fig 4.4. 95
4.6 QCD technology, from Bigioli, 2021. Upper-left: band diagram of the detector; Upper-right: SEM (Scanning Electron Microscope) image of an array of detector; Lower right: sketch of the array 98
4.7 Equivalent background noise temperature of direct detection, computed with the same parameters as Fig 4.4. 104

5.1 Probability distribution to measure a thermal field with a coherent deteciton in phase space. 119

6.1 General picture of a photonic correlator scheme. 131
6.2 Principle of the ISI analog correlator (from (Danchi, 2003)). 132
6.3 Principle of a photonic correlation based on phase modulation 133
6.4 Two-telescope interferometric set-up at telecom wavelength. 135
6.5 a) Set-up of the photonic correlator based on phase modulation. Abbreviations as follows: LO: local oscillator; BS: beam splitter; PD: photo-diode; LNA: low-noise amplifier; LID: lock-in detection; LPF: low-pass filter; PID: proportional integral derivator; AOM: acousto-optic modulator; EOM: electro-optic modulator. b) Quadratic regime of the Mach-Zehnder output : at the exact null, the second harmonic (first harmonic respectively) of any sinusoidal phase modulation (orange signal) will be maximized (resp. minimized). The first harmonic can then be used as an error signal of the PID (c) that drives the frequency difference between each arm of the interferometer. 137
6.6 Implementation of the phase modulation scheme in the lab. 138
6.7 Closing of the phase stabilization loop Top: Open-loop is highlighted in red, closed-loop in green. The photodiode output signal (green line) is just above the oscilloscope dark current (gray), which limits the effective contrast of the null. Bottom: Histogram of the photodiode output is shown. Asymmetric shape of the photodiode output is typical of a null output. 139
6.8 Left: Fringe peak at the ouptut of the correlator (linear scale in y-axis). The red dashed line indicates the numerical correlation of the input signal. The green solid line shows the correlation of the signal through the optical correlator. Right: The coherence envelope of the fringe signal (green dot), and the envelope computed numerically (blue cross) are shown. 140
6.9 Principle of a photonic correlation based on amplitude modulation, with no additional frequency modulation 142
6.10 Principle of a photonic correlation based on amplitude modulation, with two AOMs which encode the fringe frequency. 143
6.11 Implementation of the amplitude modulation scheme in the lab. 145
6.12 Top : Spectrum modulus of the output signal of the photonic correlator with amplitude modulation. Bottom : phase signal. The position of the peak encoding the fringe information are highlighted in green. These peaks are centered around the central AOM frequency difference at 1.7MHz. 145
6.13 Coherence envelope of the correlated heterodyne signals, obtained by measuring the coherent flux for different numerical delays in the correlator. 146
6.14 Principles of a photonic correlation with amplitude modulation and frequency shift, extended to 3 telescopes. The encoding of the fringes is ensured by choosing a non-redundant frequency shift differences. 147
6.15 Analogy between classical and heterodyne multi-telescopes combinations. . . . 150
6.16 Processing of multiple spectral channels in the photonics correlator through wavelength multiplexing. 153
6.17 Calibraiton of $V_{\pi,\mathrm{eff}}$ for different functioning point in open-loop. Left : acquisitions with $10\,Vpp$ driving amplitude ; Right : $5\,Vpp$ amplitude. 156

6.18 Left : Fit of $\frac{A_I}{A_{II}}$ data with the model of Eq.6.15. Right : fit of the standard deviation experimental data with Eq.6.16. A noticeable deviation between the model starts to be visible for large Vpp, where the driving voltage is not negligible against V_π of the modulators. 157

7.1 Schematic diagram of the two possible correlation approaches. The temporal approach (green) consists in retrieving the value of the correlation function at each time step τ by multiplying and integrating the two signals delayed by a relative amount τ ; in the case where the correlation function is mapped for a large number of delays τ, the spectro-visibility can be obtained by computing the Fourier transform of the correlation function $C_{12}(\tau)$. The frequency approach consists in computing directly the Fourier transform of each signals, and in multiplying one spectrum with the complex conjugate of the other. At the end, temporal and frequency approach enables to obtain the same observable. 161

7.2 Principle of a Frequency Shifting Loop (FSL) : an input field $E_{\text{in}}(t)$ enters the loop, where it is shifted in frequency f_s by the AOFS and delayed by a time τ_c. An optical amplifier (EDFA : Erbium Doped Fiber Amplifier) is inserted in the loop in order to compensate for the propagation losses and the output coupling losses to extract part of the flux. The output field E_{out} is carried by a comb with frequency separation f_s and which exhibits a quadratic phase (see text), where each tooth is associated to a replica of the incident field delayed by a time $n\Delta\tau$. 164

7.3 Principle of the analog photonic correlator : the correlator consists in two FSLs, implemented in a bidirectional configuration. The input of the loop is composed of a CW laser seed, splitted in two arms, which are modulated by broadband amplitude modulator. The frequency shifts f_1 and f_2 and delays τ_1 and τ_2 are introduced in the non-reciprocal part of the loop, where the two respective loops are directed along two different paths by means of circulators. A Variable Optical Delay Line (VODL) is inserted in one arm, and enables to easily reconfigure the relative delay between each loops. Finally, the two arms are recombined on a balanced photodiode, which is low-pass filtered. The beating of the two combs with slightly different frequency separation creates a down-converted RF comb, in a similar way to dual-comb spectroscopy, where each tooth is here associated to the product of the input RF signals at different relative delays $\langle s_1(t)s_2(t-\tau)\rangle$. In this way, this output RF combs gives directly access to the value of the cross-correlation function, evaluated for a large number N of relative delays. An additional portion of fiber is introduced in one arm in order to position the zero delay $\Delta\tau = 0$ at the center of the frequency window. 166

7.4 Actual implementation of the analog photonic correlator in the laboratory. . . . 167

7.5 Regimes of the FSL depending of the gain of the amplifier relative to the passive losses. The power of the teeth and of the ASE are both represented. Adapted from (Kanagaraj et al., 2019). 168

7.6 a) Auto-correlation of a sine function for increasing amplitude value. The plot is divided in 5 frequency bins, corresponding to each local peak of the auto-correlation function (bin 1 : 0.2 to 1.5 MHz ; bin 2 : 1.5 to 3.5 MHz ; bin 3 : 3.5 to 5.5 MHz ; bin 4 : 5.5 to 7.5 MHz ; bin 5 : 7.5 to 9.5 MHz). b) The maximum PSD amplitude of each frequency bin is extracted for each voltage, and plotted versus corresponding input RF power. The dashed line corresponds to the theoretical quadratic growth of the auto-correlation PSD. 169
7.7 a) Auto-correlation of a noise waveform signal with 120 MHz bandwidth. b) Maximum amplitude of the correlation envelope versus input input RF power. A dashed line corresponding to a linear growth is over-plotted in comparison. . . 170
7.8 a) Auto-correlation of a noise waveform signal with 120 MHz bandwidth. b) Maximum amplitude of the correlation envelope versus input input RF power. A dashed line corresponding to a linear growth is over-plotted in comparison. . . 172
7.9 Auto-correlation of PN3 (left) and PN4 signal (right). 173
7.10 Auto-correlation of sinusoidal signals modulated in frequency. The parameters of the input signals are (see text for the notation used) $f = 100\,\mathrm{MHz}$, $f_\Delta = 10\,\mathrm{MHz}$ and *(Left)* $f_r = 100\,\mathrm{Hz}$; *(Center)* $f_r = 400\,\mathrm{Hz}$; *(Right)* $f_r = 4\,\mathrm{kHz}$ (note the different scale on time axis). 174
7.11 a) Auto-correlation of broad noise signals with temporal resolution $\Delta\tau = 115\,\mathrm{ps}$. The PSD is proportional to the square modulus of the auto-correlation. b) Auto-correlation of noise signals (heterodyne signals generated in Sec 6.4.1) with temporal resolution $\Delta\tau = 4\,\mathrm{ns}$. Both : the theoretical autocorrelation traces are superimposed in dashed lines. 175
7.12 a) Spectrum of noise signals with 120 MHz bandwidth (orange), and the same signal on which a notch filter is applied (65 MHz - 85 MHz). b) Square modulus of the auto-correlation function. One can notice the significant side-lobes on the filtered signal (acquisition time : 200ms). c) Square modulus of the cross-correlation of the two signals (acquisition time : 200ms). All : the theoretical autocorrelation traces are superimposed in dashed lines. 177
7.13 Autocorrelation of 120 MHz noise signals : a relative digital delay is applied between each channel, which can be compared to the delay measured by the photonic correlator. 178
7.14 a) Spectrum of the signal emitted by the Tx antenna. b) Experimental set-up used to correlate two monopole antennas. c) Plot of the cross-correlation traces with respect to their position (100ms acquisition time). 180
7.15 Schematic diagram of the scale-up of the analog correlator to a large number of channels. In an analogous way to the simple amplitude photonic correlator, the basic idea consists in encoding each pair of correlation signal in a non-redundant frequency pattern at the output of the correlator. 184

8.1 Optical layout of H2T10 alignment *Left:* QCL+QCL beating *Right:* QCL+black body beating. *Gray area :* In the first implementation, only one QCL we be used as the same local oscillator for each detection channel. The final goal will be to phase-locked two QCLs together in order to obtain two separated local-oscillators. Schematic adapted from G. Bruel. 190

8.2 Current implementation of the optical set-up of H2T10 at $10\,\mu$m, with one QCL and two detection channels. See description in Sec 8.2. 191

9.1 Overview of the VLT on Cerro Paranal, with the 4 UTs (8.2m diameter) and 4 ATs (1.8m diameter), and the VLTI infrastructure. 200
9.2 General schematic of V8 concept. 202
9.3 Structure of the code (upper) and an example of a 8 telescopes uv-track (left) and the associated dirty map and the sampling of the input image (middle). . . 207
9.4 **Left:** VLTI baseline map **Left (middle):** Sky-coverage of the 8 telescopes combination, the sky coverage is limited by the shadow of the UT only **Right (middle):** uv-plane associated to the 8 telescopes combination **Right:** Dirty beam associated to the 8 telescopes combination, the dimension of the beam at 10.5 μm are indicated in upper left corner. 209
9.5 The output image of `CO5BOLD-OPTIM3D` model (Chiavassa et al., 2009; Chiavassa et al., 2011) the visibility function (amplitude and phase) associated to this image. The image and the dirty beam are at the same spatial scale. 209
9.6 Simulated observation of α Sco, 12 sequences of 5min incoherent integration. . 210
9.7 *Up :* Compact VLTI telescope configuration chosen to simulate the YSO observations.*From left to right :* VLTI telescope base ; Sky coverage ; UV-coverage ; Dirty Beam. *(Bottom :)* Simulated observation of a bright YSO (AB Aurigae), whose morphology is taken from MIDI observation (Varga et al., 2018). The MIDI observation (coherent flux) is inserted on the right. 212
9.8 Point source sensitivity and brightness temperature of a V8, assuming the telescope configuration shown in Fig 9.7. We note that the point source sensitivity is smaller than the point source sensitivity criteria given in Tab 9.1, which was assuming the combination of only 2 telescopes, whereas the present estimation take into account the 8 telescopes of the array for the image reconstruction. . . 213
9.9 Simulated observation of a non-resolved point source with a total flux of 70 Jy/polar. The parameters of the observation are indicated in the legend. 217
9.10 Similar simulation to 9.9, with a total flux of 5 Jy/polar. 217

List of Tables

0.1 List of the acronyms used in the manuscript. xxii

2.1 Interferometric observables obtained from the measurement of the spatial coherence of light. 26

2.2 Summary of astronomical interferometric techniques demonstrated in the visible and the infrared. References: (1):Fizeau (1864) ; (2): Michelson and Pease, 1921 ; (3): Labeyrie, 1975 ; (4): M A Johnson, Betz, and C H Townes, 1974 ; (5): J. Gay et al., 1973; (6): Thompson, Moran, and Swenson, 2017 ; (7):Darré et al., 2016 ; (8): Szemendera et al., 2017 ; (9): Hanbury Brown, 1956 ; (10): Guerin et al., 2018 27

3.1 Logs of FU Orionis interferometric observations in H and K Band. The data for which the data-reduction was done in this study are indicated with '*data reduced*'. 47

3.2 Components of the geometrical model used to fit FU Orionis visibility. 52

3.3 Fitted parameters of the geometrical modeling of FU Orionis. The reference datasets in each band, on which are fixed the sparse dataset (see text), are indicated in bold. 54

3.4 Estimation of the size and the temporal slope of the resolved emission 55

3.5 Parameters of the different numerical simulations of FU Orionis outburst. These simulations were performed by Geoffroy Lesur. 62

3.6 Table of photometric data used in our SED of FU Orionis. 69

4.1 Technical requirements of a baseline PFI architecture in the mid-infrared (N and Q band) 78

4.2 Scaling of the performances on the point-source sensitivity of a heterodyne interferometer. The point source sensitivity of the ISI was typically 50-100 Jy in t=1h *incoherent* integration. 89

4.3 Technological parameters chosen for the sensitivity calculation of the array. . . . 90

4.4 Parameters of the array considered for the comparison of direct and heterodyne detection sensitivity. The values of direct detection are based on the design of the MATISSE instrument in N band. 94

4.5 Signal-to-noise ratio in SSB and DSB correlation. 103

8.1 Characteristics of the main optical components of the bench. 191

8.2 Noise budget of the detection and amplification/correlation chain. *This number originates from the specifications of our detectors, but at not yet characterized in the lab. This noise contribution has the strongest impact on the total noise budget.194

8.3 Signal-to-noise estimation of H2T10 on black-body at 900K. 195

8.4 Parameters of the photonic correlator implemented in H2T10. 197

9.1 SNR sensitivity limits (in Jy/polar), assuming $t_0 = 150\,\mathrm{ms}$ (at $\lambda = 10.5\,\mu\mathrm{m}$), QE=0.4, and a noise penalty of 1.5 (reported on ISI) ; each cell is divided in two, corresponding to $\mathrm{T} = 0.6 \times 0.4 = 0.24$ (total transmission, including VLTI beam train, left part) and $\mathrm{T} = 0.6$ (transmission to the telescope focus and projection on the mode of the laser, based on ISI typical results, right part) **Top :** sensitivity limits defined as the lowest flux to obtain a SNR=10 in t=1 min integration **Bottom :** idem with SNR=5 and t=20 min integration. For MATISSE, sensitivity limits are taken from (Petrov et al., 2020), and divided by two in order to compare both number in Jy/polarization. For heterodyne detection, the point source sensitivity is computed only for 2 telescope combinations. See the next section for a calculation including all the 8 telescopes of the array. 204

Colophon

This thesis was typeset with LaTeX 2$_\varepsilon$. It uses the *Clean Thesis* style developed by Ricardo Langner. The design of the *Clean Thesis* style is inspired by user guide documents from Apple Inc.

Download the *Clean Thesis* style at http://cleanthesis.der-ric.de/.